frontiers | Research Topics

Radiation belt dynamics: theory, observation and modeling

Edited by
Qianli Ma, Xinliang Gao and Dedong Wang

Published in
Frontiers in Astronomy and Space Sciences
Frontiers in Physics

ISSN 1664-8714
ISBN 978-2-8325-5736-5
DOI 10.3389/978-2-8325-5736-5

About Frontiers

Frontiers is more than just an open access publisher of scholarly articles: it is a pioneering approach to the world of academia, radically improving the way scholarly research is managed. The grand vision of Frontiers is a world where all people have an equal opportunity to seek, share and generate knowledge. Frontiers provides immediate and permanent online open access to all its publications, but this alone is not enough to realize our grand goals.

Frontiers journal series

The Frontiers journal series is a multi-tier and interdisciplinary set of open-access, online journals, promising a paradigm shift from the current review, selection and dissemination processes in academic publishing. All Frontiers journals are driven by researchers for researchers; therefore, they constitute a service to the scholarly community. At the same time, the *Frontiers journal series* operates on a revolutionary invention, the tiered publishing system, initially addressing specific communities of scholars, and gradually climbing up to broader public understanding, thus serving the interests of the lay society, too.

Dedication to quality

Each Frontiers article is a landmark of the highest quality, thanks to genuinely collaborative interactions between authors and review editors, who include some of the world's best academicians. Research must be certified by peers before entering a stream of knowledge that may eventually reach the public - and shape society; therefore, Frontiers only applies the most rigorous and unbiased reviews. Frontiers revolutionizes research publishing by freely delivering the most outstanding research, evaluated with no bias from both the academic and social point of view. By applying the most advanced information technologies, Frontiers is catapulting scholarly publishing into a new generation.

What are Frontiers Research Topics?

Frontiers Research Topics are very popular trademarks of the *Frontiers journals series*: they are collections of at least ten articles, all centered on a particular subject. With their unique mix of varied contributions from Original Research to Review Articles, Frontiers Research Topics unify the most influential researchers, the latest key findings and historical advances in a hot research area.

Find out more on how to host your own Frontiers Research Topic or contribute to one as an author by contacting the Frontiers editorial office: frontiersin.org/about/contact

Radiation belt dynamics: theory, observation and modeling

Topic editors

Qianli Ma — Boston University, United States

Xinliang Gao — University of Science and Technology of China, China

Dedong Wang — GFZ German Research Centre for Geosciences, Germany

Citation

Ma, Q., Gao, X., Wang, D., eds. (2024). *Radiation belt dynamics: theory, observation and modeling*. Lausanne: Frontiers Media SA. doi: 10.3389/978-2-8325-5736-5

Table of contents

frontiers | Frontiers in Astronomy and Space Sciences

TYPE Editorial
PUBLISHED 15 November 2024
DOI 10.3389/fspas.2024.1503963

OPEN ACCESS

EDITED AND REVIEWED BY
Joseph E. Borovsky,
Space Science Institute (SSI), United States

*CORRESPONDENCE
Qianli Ma,
qma@bu.edu

RECEIVED 30 September 2024
ACCEPTED 04 November 2024
PUBLISHED 15 November 2024

CITATION
Ma Q, Gao X and Wang D (2024) Editorial: Radiation belt dynamics: theory, observation and modeling.
Front. Astron. Space Sci. 11:1503963.
doi: 10.3389/fspas.2024.1503963

Editorial: Radiation belt dynamics: theory, observation and modeling

Qianli Ma[1,2]*, Xinliang Gao[3,4,5] and Dedong Wang[6]

[1]Center for Space Physics, Boston University, Boston, MA, United States, [2]Department of Atmospheric and Oceanic Sciences, University of California, Los Angeles, CA, United States, [3]Deep Space Exploration Laboratory, School of Earth and Space Sciences, University of Science and Technology of China, Hefei, China, [4]CAS Center for Excellence in Comparative Planetology, Hefei, China, [5]Collaborative Innovation Center of Astronautical Science and Technology, Harbin, China, [6]GFZ German Research Centre for Geosciences, Potsdam, Germany

KEYWORDS

Earth's radiation belts, relativistic electron fluxes, magnetospheric plasma waves, wave–particle interactions, space weather modeling and prediction

Editorial on the Research Topic
Radiation belt dynamics: theory, observation and modeling

The relativistic electron fluxes in Earth's radiation belts are highly dynamic due to various source and loss processes (Reeves et al., 2003; Thorne, 2010; Turner et al., 2014). Satellite observations revealed that the outer radiation belt fluxes are strongly affected by solar wind and geomagnetic activities (e.g., Baker et al., 2019). The most important drivers of the radiation belt variability are radial diffusion due to ultra-low frequency waves (e.g., Mann et al., 2016) and local wave–particle interactions due to whistler-mode waves (e.g., Horne and Thorne, 1998), electron cyclotron harmonic waves (e.g., Zhang et al., 2015), and electromagnetic ion cyclotron (EMIC) waves (e.g., Summers and Thorne, 2003). Quasilinear and nonlinear theories were developed to demonstrate and quantify the importance of each process in the radiation belts (e.g., Albert, 1999; Omura et al., 2008). Numerical simulations generally reproduce the overall source and loss of radiation belt particles (e.g., Ma et al., 2016), but detailed quantification of the observed features is challenging. The machine learning technique has proven to be a useful tool in reproducing and forecasting the particle fluxes in radiation belts (e.g., Bortnik et al., 2018). Although the Van Allen Probes provided a great opportunity to improve the understanding of Earth's radiation belt dynamics, many science questions regarding the wave and particle properties, distributions, variability, and evolution remained unexplored after the end of the spacecraft mission (Li and Hudson, 2019).

This Research Topic, "*Radiation Belt Dynamics: Theory, Observation and Modeling*," aims in advancing the understanding of radiation belt dynamics and improving the capability to model and forecast the energetic particles and plasma waves in the magnetosphere. This Research Topic collected 11 research articles and 1 mini review article. The published papers address a wide range of topics in the theory, observation, and modeling of radiation belt dynamics.

Most of the radiation belt models are drift-averaged and consider the radial transport as a one-dimensional radial diffusion process. Lejosne and Albert developed a theoretical framework to retain drift phase information and resolve the effects of the bulk motion

and diffusion of trapped particles. The authors derived formulas to evaluate the drift phase resolved diffusion coefficients and impacts of particle drift, as well as radial diffusion.

Following their theoretical work, Lejosne et al. applied their theory to model the trapped particle transport under the influence of random electric potential fluctuations. Numerical experiments were performed to track the radial diffusion and drift of trapped particles. Modeling resolves how the particle distribution function changes from being determined by drift motion to being well-described by diffusion. By considering the localized transport processes, the developed drift-diffusion equation provides a better spatiotemporal resolution than the standard radial diffusion model.

Chan et al. developed a radiation belt simulation model (K2) by combining global MHD simulations with guiding-center test-particle methods. The model resolves important global scale processes of particle motion in self-consistent MHD fields, as well as local wave–particle interactions. The authors used the K2 model to simulate the electron phase space density evolution during a strong geomagnetic storm event. The simulation indicates the importance of combined influences of local energization by chorus waves and radial transport in the electron flux enhancement during disturbed times.

Drozdov et al. combined the data assimilation method with the machine learning technique to reconstruct radiation belt electron fluxes. They used the multivariate linear regression and neural network methods to map Polar Orbiting Environmental Satellite (POES) measurements to the equator. The electron fluxes were then used in data assimilation with the Versatile Electron Radiation Belt model. Improved accuracy of radiation belt electron modeling was demonstrated using the above method after comparison with satellite observations.

Huang et al. used a neural network to model the total electron density and hiss wave variations in the radiation belts during a geomagnetic storm event. The simulation revealed detailed features of plasmasphere, plume, and hiss waves on a global scale. The authors modeled energetic electron evolution to explain the observed electron flux decay. The simulation quantified the relative roles of plasmaspheric hiss and plume hiss. The dynamic evolution of hiss waves was suggested to be important to study the radiation belt electron evolution.

Hua et al. analyzed the geomagnetic conditions favorable for radiation belt electron acceleration. Their study suggested that intense substorms contribute to the elevated source and seed electron fluxes. These electron populations are critical for the multi-MeV electron flux enhancements due to chorus waves. The correlation analysis suggests that the accumulative substorm impact is directly related to the high electron fluxes in the outer radiation belt.

Liu and Su reviewed the impacts of solar wind dynamic pressure pulses on the whistler-mode waves in the magnetosphere. The spatiotemporal variability of whistler-mode waves is ultimately driven by solar wind conditions. The authors reviewed several studies highlighting the enhancement and disappearance of chorus and hiss wave powers, following large variations in solar wind dynamic pressures. Liu and Su summarized the underlying mechanisms and raised outstanding questions.

Ma et al. evaluated the empirical model performances for the total electron density and whistler-mode wave amplitudes using Van Allen Probes measurements. The modeled electron densities align with satellite observations; the chorus and hiss wave models generally agree with satellite observations when the modeled plasmapause agrees with the observation or when the wave amplitudes are moderate. Significant discrepancies between the model and observation are found near the plasmapause boundary or in the plumes.

Qin et al. investigated the magnetospheric oscillations, the simultaneous whistler-mode chorus wave modulation, and the energetic electron precipitation, as evidenced by BARREL X-ray observations. The authors performed quasi-linear analysis to evaluate electron precipitation. The electron precipitation variations are directly driven by chorus wave amplitude modulation, aided by the modulation of background plasma conditions. The spatial scale of the magnetospheric oscillations is large, suggesting their significant role in global electron precipitation.

Hanzelka et al. performed test-particle simulations to analyze electron scattering and precipitation due to EMIC waves in Earth's radiation belts. By considering oblique wave normal angles, the authors confirmed the importance of multiple harmonic resonances in the electron scattering loss. The nonlinear force bunching causing positive advection at low pitch angles is balanced by the transport of electrons into the loss cone. The authors also revealed the contribution of fractional resonances to electron precipitation at energies below the minimum resonance energy.

Hanzelka et al. performed full-wave modeling of EMIC wave propagation in Earth's outer radiation belt using finite-difference time-domain simulations. The simulations suggest cold plasma density gradients could guide the quasiparallel EMIC waves and influence the wave mode conversion and wave reflection. For unducted waves, the wave normal angles increase rapidly with latitude and the waves are reflected when the wave frequency becomes the local ion hybrid frequency. The modeled wave fields are useful to study particle precipitation by EMIC waves in the future.

Shao et al. performed one-dimensional particle-in-cell simulations to study the magnetosonic wave propagation when the waves encounter density structures in Earth's magnetosphere. The simulations indicate the roles of wave energy absorption and wave reflection, both of which strongly depend on the height and width of local density structures. Magnetosonic wave power absorption was suggested to be important to understand the wave distribution in Earth's magnetosphere.

Author contributions

QM: conceptualization, investigation, writing–original draft, and writing–review and editing. XG: investigation and writing–review and editing. DW: writing–review and editing.

Funding

The author(s) declare that financial support was received for the research, authorship, and/or publication of this article. QM would like to acknowledge the NSF grant AGS-2225445.

Acknowledgments

The authors are grateful to the authors and reviewers of the papers collected in this Frontiers Research Topic. They also thank the Frontiers editorial team for their assistance.

Conflict of interest

The author declares that the research was conducted in the absence of any commercial or financial relationships that could be construed as a potential conflict of interest.

Publisher's note

All claims expressed in this article are solely those of the authors and do not necessarily represent those of their affiliated organizations, or those of the publisher, the editors, and the reviewers. Any product that may be evaluated in this article, or claim that may be made by its manufacturer, is not guaranteed or endorsed by the publisher.

References

Albert, J. M. (1999). Analysis of quasi-linear diffusion coefficients. *J. Geophys. Res.* 104 (A2), 2429–2441. doi:10.1029/1998JA900113

Baker, D. N., Hoxie, V., Zhao, H., Jaynes, A. N., Kanekal, S., Li, X., et al. (2019). Multiyear measurements of radiation belt electrons: acceleration, transport, and loss. *J. Geophys. Res. Space Phys.* 124, 2588–2602. doi:10.1029/2018JA026259

Bortnik, J., Chu, X.-N., Ma, Q., Li, W., Zhang, X.-J., Thorne, R. M., et al. (2018). "Artificial neural networks for determining magnetospheric conditions," in *Machine learning techniques for space weather* (Elsevier), 279–300. doi:10.1016/B978-0-12-811788-0.00011-1

Horne, R. B., and Thorne, R. M. (1998). Potential waves for relativistic electron scattering and stochastic acceleration during magnetic storms. *Geophys. Res. Lett.* 25 (15), 3011–3014. doi:10.1029/98GL01002

Li, W., and Hudson, M. K. (2019). Earth's van allen radiation belts: from discovery to the van allen Probes era. *J. Geophys. Res. Space Phys.* 124, 8319–8351. doi:10.1029/2018JA025940

Ma, Q., Li, W., Thorne, R. M., Nishimura, Y., Zhang, X., Reeves, G. D., et al. (2016). Simulation of energy-dependent electron diffusion processes in the Earth's outer radiation belt. *J. Geophys. Res. Space Phys.* 121, 4217–4231. doi:10.1002/2016JA022507

Mann, I. R., Ozeke, L. G., Murphy, K. R., Claudepierre, S. G., Turner, D. L., Baker, D. N., et al. (2016). Explaining the dynamics of the ultra-relativistic third Van Allen radiation belt. *Nat. Phys.* 12, 978–983. doi:10.1038/nphys3799

Omura, Y., Katoh, Y., and Summers, D. (2008). Theory and simulation of the generation of whistler-mode chorus. *J. Geophys. Res.* 113, A04223. doi:10.1029/2007JA012622

Reeves, G. D., McAdams, K. L., Friedel, R. H. W., and O'Brien, T. P. (2003). Acceleration and loss of relativistic electrons during geomagnetic storms. *Geophys. Res. Lett.* 30, 1529. doi:10.1029/2002gl016513

Summers, D., and Thorne, R. M. (2003). Relativistic electron pitch-angle scattering by electromagnetic ion cyclotron waves during geomagnetic storms. *J. Geophys. Res.* 108, 1143. doi:10.1029/2002ja009489

Thorne, R. M. (2010). Radiation belt dynamics: the importance of wave-particle interactions. *Geophys. Res. Lett.* 37, L22107. doi:10.1029/2010GL044990

Turner, D. L., Angelopoulos, V., Li, W., Bortnik, J., Ni, B., Ma, Q., et al. (2014). Competing source and loss mechanisms due to wave-particle interactions in Earth's outer radiation belt during the 30 September to 3 October 2012 geomagnetic storm. *J. Geophys. Res. Space Phys.* 119, 1960–1979. doi:10.1002/2014JA019770

Zhang, X.-J., Angelopoulos, V., Ni, B., and Thorne, R. M. (2015). Predominance of ECH wave contribution to diffuse aurora in Earth's outer magnetosphere. *J. Geophys. Res. Space Phys.* 120, 295–309. doi:10.1002/2014JA020455

frontiers | Frontiers in Astronomy and Space Sciences

TYPE Original Research
PUBLISHED 05 April 2023
DOI 10.3389/fspas.2023.1168636

OPEN ACCESS

EDITED BY
Xinliang Gao,
University of Science and Technology of China, China

REVIEWED BY
Si Liu,
Changsha University of Science and Technology, China
Huayue Chen,
Auburn University, United States

*CORRESPONDENCE
Man Hua,
manhua@ucla.edu

SPECIALTY SECTION
This article was submitted to Space Physics, a section of the journal Frontiers in Astronomy and Space Sciences

RECEIVED 17 February 2023
ACCEPTED 24 March 2023
PUBLISHED 05 April 2023

CITATION
Hua M, Bortnik J, Spence HE and Reeves GD (2023), Testing the key processes that accelerate outer radiation belt relativistic electrons during geomagnetic storms.
Front. Astron. Space Sci. 10:1168636.
doi: 10.3389/fspas.2023.1168636

Testing the key processes that accelerate outer radiation belt relativistic electrons during geomagnetic storms

Man Hua[1]*, Jacob Bortnik[1], Harlan E. Spence[2] and Geoffrey D. Reeves[3,4]

[1]Department of Atmospheric and Oceanic Sciences, UCLA, Los Angeles, CA, United States, [2]Institute for the Study of Earth, Oceans and Space, University of New Hampshire, Durham, NH, United States, [3]Space Science and Applications Group, Los Alamos National Laboratory, Los Alamos, NM, United States, [4]The New Mexico Consortium, Los Alamos, NM, United States

Since the discovery of the Earth's radiation belts in 1958, it has always been a challenge to determine the dominant physical mechanisms, whether local acceleration by chorus or inward radial diffusion, that leads to outer radiation belt relativistic electron flux enhancements. In this study, we test a chain of processes with several potential successive steps that is believed to accelerate outer belt relativistic electrons. By performing correlation analysis of different part of this chain, including the geomagnetic condition, evolution of source and seed electron fluxes, chorus wave activity, and maximum fluxes (j_{max}) of relativistic electrons, we aim to identify the critical steps that lead to acceleration of MeV electrons. Based on 5-years of Van Allen Probes observations, our results confirm the repeatable response of both source and seed electrons to the storms, showing a significant flux enhancement during the main phase of storms, followed by either a gradual decay or flux persistence at a stable level. However, it is the intense and prolonged occurrence of substorms that contributes to the long-lasting existence of both source and seed electrons, which is also strongly associated with the j_{max} of relativistic electrons. The significant correlation (Correlation Coefficient, CC~0.8) between the seed electron fluxes and j_{max} reveal that the prolonged and pronounced seed electrons are the prerequisite for the significant flux enhancement of relativistic electrons regardless of the acceleration mechanism. The slightly smaller CC (~0.5–0.7) between source electron fluxes and j_{max} of relativistic electrons indicates that while local acceleration by chorus wave plays an important role to accelerate relativistic electrons to j_{max}, other mechanisms such as inward radial diffusion are still needed in this process. The CC between the source electrons and the chorus wave amplitude increases with increasing levels of substorms, showing (CC)max of ~0.8, which further supports the crucial role of chorus waves in accelerating the relativistic electrons during intense substroms.

KEYWORDS

radiation belt, electron acceleration, source and seed electrons, upper limit of fluxes, whistler-mode chorus waves, statistical distribution

1 Introduction

Understanding the main processes that control the dynamics of the outer radiation belt relativistic electrons has been a fundamental question in space physics since the discovery of the Earth's radiation belts in 1958. The fluxes of these relativistic electrons, also known as "killer electrons" (Reeves, 1997), can vary by several orders of magnitude on timescales of hours to days, especially during geomagnetically active times (Baker et al., 2004; Baker et al., 2019; Reeves et al., 2016; Turner et al., 2019). It is fundamentally important to understand the underlying physical mechanisms that control these relativistic electrons, which can pose a hazard to operating satellites in geospace as well as to modern society that strongly relies on the space-based communications, navigation, commerce, and other functions (Baker et al., 1998; Baker, 2001; Horne et al., 2013; Horne et al., 2021).

Several recent studies have been dedicated to understanding the upper limit of radiation belt electron fluxes during geomagnetic storms based on Van Allen Probes (Mauk et al., 2013) observations (Olifer et al., 2021; Olifer et al., 2022; Zhang et al., 2021; Hua et al., 2022a; Hua et al., 2022b; Mourenas et al., 2022). Zhang et al. (2021) reported the energy spectrum of maximum fluxes observed by the DEMETER and Van Allen Probes, with the maximum fluxes at 100 keV—1 MeV roughly varying inversely proportional to the kinetic energy in the outer belt, which is consistent with the Kennel-Petschek (KP) theory of self-limited electron fluxes through the generation of whistler-mode chorus waves that can further cause electron precipitations (Kennel and Petschek, 1966; Summers and Shi, 2014). In the KP theory, the maximum electron fluxes are controlled by a self-limited process. The pitch-angle diffusion due to wave-particle interactions causes electron precipitations into the ionosphere, leading to anisotropic trapped electron populations. These anisotropic electrons can give free energies to the excitation of whistler-mode waves, which results in further precipitation. Meanwhile, the wave growth rate is limited by the wave damping. In the KP theory, the wave-driven energy diffusion is assumed to be negligible compared to the pitch-angle diffusion. Furthermore, a recent statistical study showed that electron fluxes below ~850 keV can quickly reach the KP limit (Olifer et al., 2021), while the relativistic electron fluxes below ~2.6 MeV can only approach the KP limit during the strongest enhancement events (Olifer et al., 2022). Nevertheless, the observed upper limit of multi-MeV electron fluxes in all of these studies was not well captured by the KP limit. The study of Hua et al. (2022a) provided a different paradigm and revealed for the first time the natural upper limit of electron acceleration by chorus waves, which explained the observed maximum fluxes from ~0.1 to ~10 MeV during the storm that produced almost the highest upper limit during the Van Allen Probe era. In addition, they clearly demonstrated that such a natural upper limit strongly depends on the substorm injected electrons from a simulation perspective, which still needs statistical observational evidence. Mourenas et al. (2022) further developed an analytical steady-state solution of electron fluxes due to scattering effects by chorus waves, which produced similar energy spectra as the numerical simulation results from Hua et al. (2022a). Moreover, the study of Hua et al. (2022b) reported that the radial profiles of both maximum fluxes of relativistic electrons and chorus wave amplitude peak at the heart of the outer belt at L ~ 4.7, further supporting the potentially important role of chorus waves in producing the maximum fluxes. In addition, they unraveled the crucial impact of time-integrated AL index, which acts as a proxy for the accumulation of substorm activities, on producing the upper limit of relativistic electron fluxes, whose acceleration process can take several hours to several days (e.g., Thorne et al., 2013; Tu et al., 2014; Li et al., 2016; Ma et al., 2018; Agapitov et al., 2019).

There are two primary mechanisms that are believed to accelerate outer belt relativistic electrons: local heating by chorus waves and inward radial diffusion by Ultra-Low-Frequency (ULF) waves (Hudson et al., 2008; Reeves et al., 2013; Thorne et al., 2013; Tu et al., 2013; Li et al., 2016a; Ma et al., 2018; Zhao et al., 2018; Li and Hudson, 2019; Ozeke et al., 2020; Lejosne et al., 2022). However, it is still a challenge to determine which mechanism is primarily responsible for the observed maximum fluxes of relativistic electrons, especially as this may vary from storm to storm (Ma et al., 2018).

Figure 1 schematically illustrates the potential key processes that are believed to be responsible for relativistic electrons to reach their maximum fluxes, and will serve as a convenient framework for organizing the results in this study. The different steps include: (1) the continuous substorm injections that provide (2) a sustained source of electrons (tens of keV) that provide a source of free energy for the (4) excitation of chorus waves (Li et al., 2010), and (3) seed (hundreds of keV) electrons that can be accelerated to higher energies (~1 MeV) (Miyoshi et al., 2013; Turner et al., 2015; Boyd et al., 2016; Tang et al., 2017; Bingham et al., 2018; Jaynes et al., 2018; Ripoll et al., 2020); (5) Then, the outer belt relativistic electrons are continuously locally accelerated by chorus waves through energy diffusion (e.g., Summers et al., 1998; Thorne et al., 2013); (6) Finally, the relativistic electrons reach their maximum fluxes either when their acceleration by chorus waves reaches its natural upper limit or when the source or seed electrons are no longer present due to the cessation of substorm injections, or removal of the source electrons by precipitation (due to chorus waves) into the upper atmosphere (Hua et al., 2022a). At the same time, (7) the enhanced inward radial diffusion during geomagnetically active times can contribute to electron flux enhancement of both source and seed electrons and relativistic electrons.

In this letter, we examine the chain of events illustrated in Figure 1 in order to test which mechanism is primarily responsible for the outer belt relativistic electrons to reach their maximum fluxes during geomagnetic storms. Especially, we will focus on the region at L = 4.5–5.0, which is close to the peak of the radial profile of the maximum fluxes of relativistic electron at L ~ 4.7 (Hua et al., 2022b). To determine whether the local acceleration by chorus waves or inward radial diffusion plays a more important role, we investigate the correlation among different parts of the chain of relativistic electron acceleration displayed in Figure 1, including the necessary geomagnetic conditions, the evolution of source and seed electrons, chorus wave activity, and maximum fluxes of relativistic electrons. If the prolonged substorm injections play a key role in providing continuous source and seed electrons, a high correlation between substorm activity and the evolution of both source and seed electron fluxes would be expected. If the local acceleration by chorus waves dominantly contributes to the maximum fluxes of relativistic

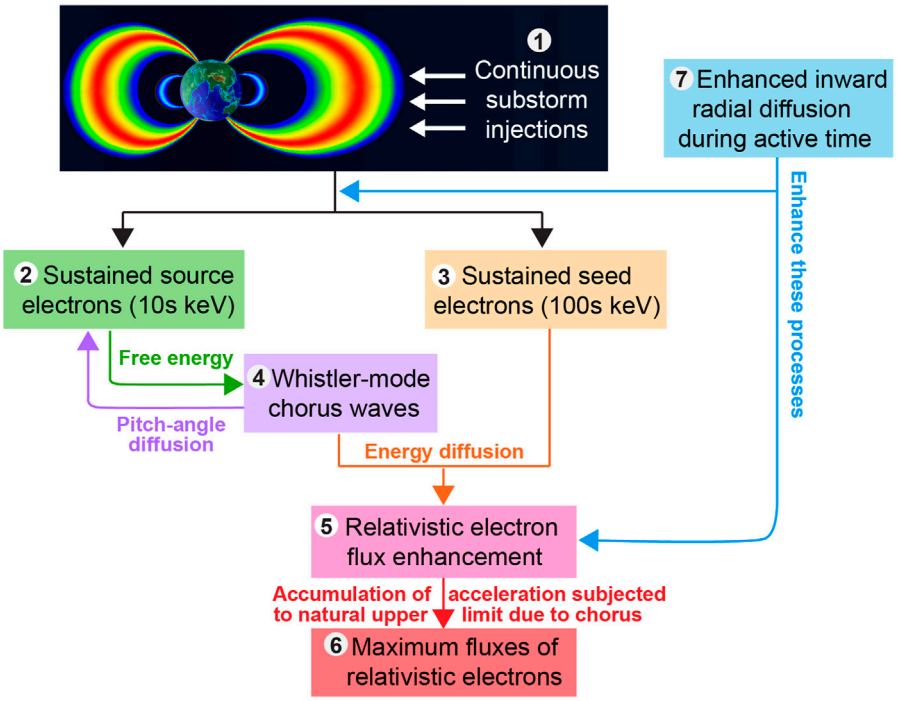

FIGURE 1
Schematic illustration of the key processes believed to be responsible for the acceleration of relativistic electrons and their ability to reach their maximum fluxes.

electrons, we would expect the correlation between the maximum fluxes of relativistic electrons and the sustained source and seed electrons to be high, with chorus acting as the intermediary energy transfer mechanism. Recent studies have found a strong correlation between seed electron dynamics and the acceleration of relativistic electrons (Boyd et al., 2016; Tang et al., 2017; Tang et al., 2023; Bingham et al., 2018; Jaynes et al., 2018). Similarly, we would expect the correlation between the source electrons and whistler-mode chorus wave activity to increase with the increasing level of substorm activity. Previous statistical studies have reported the strong correlation between source electron fluxes and chorus wave activities (Li et al., 2010; Li et al., 2012; Simms et al., 2019). On the contrary, if inward radial diffusion plays a more important role in producing the maximum fluxes of relativistic electrons, there would be a small correlation between the maximum fluxes of relativistic electrons and the source electron fluxes. Comprehensively investigating the correlation of different parts of this chain enables us to develop a deeper understanding of what mechanisms dominates the outer belt relativistic electron acceleration.

2 Superposed epoch analysis of source and seed electron fluxes during geomagnetic storms

In the present study, we utilize the electron flux data from the Energetic Particle Composition and Thermal Plasma suite (ECT; Spence et al., 2013) onboard both Van Allen Probes (Mauk et al., 2013). We use the ECT combined spin-averaged cross-calibrated fitting data with 127 energy channels logarithmically spaced over 10 eV—20 MeV (Boyd et al., 2019). The L-shell used in this study is the McIlwain L calculated in the T89D model (Tsyganenko, 1989). OMNI data are used to provide various geomagnetic indices, including SYM-H, AE, and AL indices at 1-min resolution.

To examine the evolution of both the source and seed electron fluxes during geomagnetic storms in a statistical sense, we select 110 storm events with $(\text{SYM-H})_{\text{min}} < -50$ nT during 2013—2017 when the observations of both SYM-H and AL indices are available, which are the same events as those used in Hua et al. (2022b). In the present study, we focus on the region close to the peak of the radial profile of the maximum fluxes of relativistic electron at L ~ 4.7 (Hua et al., 2022b). The electron fluxes are binned into a 0.1 L × 6 h UT grid. Since Van Allen Probes had a highly elliptical orbit period of ~9 h, the time bin size of 6 h here ensures that there is at least one available measurement in each bin for most of the time. This bin size has also been used in previous studies (e.g., Turner et al., 2015; Turner et al., 2019; Hua et al., 2022a; Hua et al., 2022b). Although both time scale of whistler-mode chorus wave activities and inward radial diffusion can vary significantly in different storm events (e.g., Ma et al., 2018; Ozeke et al., 2020; Hua et al., 2023), the time bin size of 6 h is usually smaller than the time scale of the relativistic electron acceleration processes during the storm recovery phase that takes several hours to several days (e.g., Thorne et al., 2013; Tu et al., 2014; Li et al., 2016a; Ma et al., 2018). Figure 2 presents the superposed epoch analysis of the source and seed electron fluxes in the heart of the radiation belt acceleration region at L = 4.5, for various energies from ~30 to 300 keV spanning

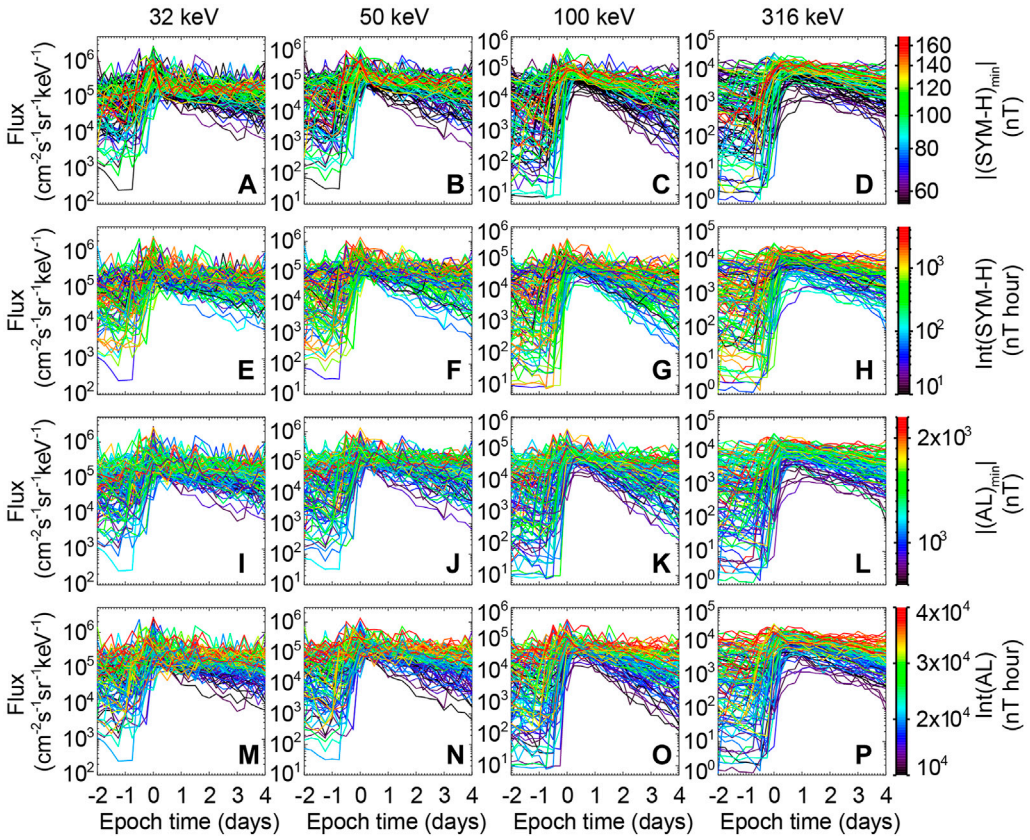

FIGURE 2
Superposed epoch analysis of source and seed electron fluxes at L = 4.5 at indicated energies, from left to right: 32 keV, 50 keV, 100 keV, and 316 keV, for all the geomagnetic storms with (SYM-H)$_{min}$ below −50 nT during the years 2013–2017. Each storm is color-coded by the corresponding geomagnetic index, shown in each of the rows, including **(A–D)** (SYM-H)$_{min}$, **(E–H)** Int(SYM-H), **(I–L)** |(AL)$_{min}$|, and **(M–P)** Int(AL) in each storm.

the source-seed energy range (shown in different columns), color-coded by the corresponding geomagnetic index shown in rows, which includes (panels A–D) (SYM-H)$_{min}$, (panels E–H) Int(SYM-H), (panels I–L) |(AL)$_{min}$|, and (panels M–P) Int(AL) of all the selected storms during 2013—2017. In the present study, the time of (SYM-H)$_{min}$, i.e., t_0 defined below, is taken as the epoch 0. Similar to those in Hua et al. (2022b), the Int(SYM-H) is the time-integral of the absolute value of SYM-H when it remained below −50 nT during the time interval of $[t_0 - 2, t_0 + 4]$ (in units of days), where t_0 corresponds to (SYM-H)$_{min}$ in each storm. Therefore, Int(SYM-H) represents continuous periods of high geomagnetic storm activity. While |(AL)$_{min}$| is the absolute value of the minimum AL during $[t_0 - 2, t_0 + 4]$ in each storm to represent the strongest substorm activities, the Int(AL) is the time-integral of absolute value of AL index during the same time interval to represent the continuous substorm activities. Note that t_0 is not necessarily associated with (AL)$_{min}$.

Overall, the behavior of both source and seed electrons strongly depends on the storm activity, showing a significant flux enhancement during the main phase of the storm at t_{epoch} ~0 day, after which, electron fluxes either remain at that level or gradually decrease. This is the typical repeatable response of the outer belt electrons during storms (Murphy et al., 2018). Although both source and seed electron fluxes tend to decrease faster during weaker storms as shown by the dark blue lines in Figures 2A–D, the persistently enduring fluxes at a high level show a smaller dependence on the magnitude of the storm as indicated by the (SYM-H)$_{min}$. Although the both source and seed electron fluxes remain at a high level during large (SYM-H)$_{min}$ events, some events with small and medium (SYM-H)$_{min}$ (shown in dark blue and green colors) can also remain at a high level. Therefore, the sustained and intense source and seed electron fluxes are not necessarily associated with a large (SYM-H)$_{min}$.The trend is even worse when the results are sorted by the Int(SYM-H) (Figures 2E–H) or by the |(AL)$_{min}$| (Figures 2I–L). However, the evolution of electron fluxes seems to be best organized by the Int(AL) (Figures 2M–P) compared to the (SYM-H)$_{min}$, Int(SYM-H), and |(AL)$_{min}$|. Both source and seed electron fluxes remain at a high level for several days after the sudden flux enhancements due to consecutive substorm injections that occur during larger Int(AL) events, while the flux decay of these electrons reaches up to several orders of magnitude within ~4 days after t_{epoch} = 0 during smaller Int(AL) events. Consequently, during the larger Int(AL) events, the persistent high intensity of the source electrons at tens of keV that can potentially contribute to the generation of chorus waves, accompanied by the continuously guaranteed seed electrons at hundreds of keV, are more favorable to accelerate relativistic

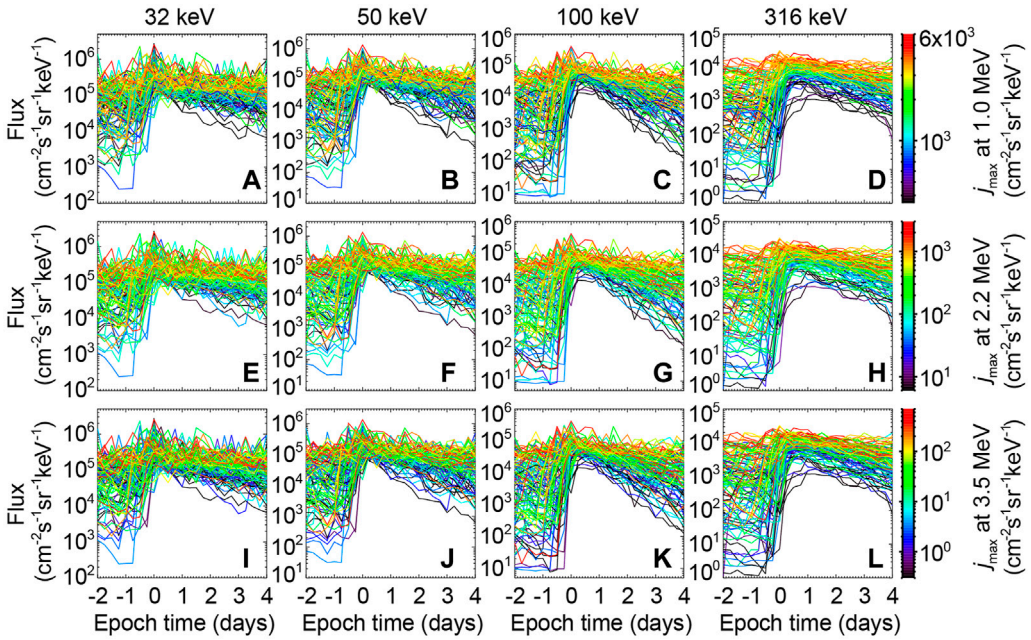

FIGURE 3
Similar to Figure 2 but for the results color-coded by the corresponding maximum fluxes of relativistic electrons at energies of **(A–D)** 1.0 MeV, **(E–H)** 2.2 MeV, and **(I–L)** 3.5 MeV in each storm.

electrons to a higher upper limit (Hua et al., 2022b). In addition, the intensified inward radial diffusion during more active time can further enhance the fluxes (Ozeke et al., 2014).

In order to provide further evidence that links the source and seed electron fluxes with the upper limit of relativistic electron fluxes, Figure 3 is similar as Figure 2 but for the results color-coded by the corresponding maximum fluxes of relativistic electrons at various energies (shown in different rows). Here, we employ the same method to obtain the maximum fluxes (j_{max}) of relativistic electrons as Hua et al. (2022b), which is the maximum value for each energy at different times during the interval of $[t_0 - 2, t_0 + 4]$ (in units of days). Since it typically takes several hours to several days for the relativistic electron fluxes to reach their maximum values during the storm recovery phase, j_{max} usually does not correspond to t_0. The results indicated that j_{max} significantly depends on the overall evolution of the source and seed electron fluxes, showing a similar trend from 1.0 to 3.5 MeV. Both source and seed electron fluxes persist at a stable high level after the sudden flux jump at t_{epoch} ~0 day during the storm events associated with larger j_{max} as shown by the red lines, comparing to the quick flux drop of source and seed electrons during the storm events that produce smaller j_{max} as shown by the dark blue lines. The persistent and intense source electron fluxes are more favorable to provide free energy for the generation of whistler-mode chorus waves comparing to the events that source electron fluxes decay significantly after t_{epoch} ~0 day. In addition, previous study has demonstrated that local acceleration by chorus waves can produce a larger j_{max} of relativistic electrons when the seed electrons at hundreds of keV are continuously provided (Hua et al., 2022a). Considering all these factors, this linkage between the overall evolution of both source and seed electrons and j_{max} indicates the potentially important role of local heating by chorus waves in producing the upper limit of relativistic electron fluxes during storms.

3 Correlation analysis results

3.1 Correlations between time-integrated source and seed electron fluxes and time-integrated geomagnetic activities

To quantitatively analyze the significance of cumulative substorm activities on providing the prolonged source and seed electrons, Figures 4A–D show the time-integrated source and seed electron fluxes (Int(Flux)) during 6 days of each storm over the time interval $[t_0 - 2, t_0 + 4]$ at various energies, observed near the heart of the outer belt, versus the corresponding Int(AL). Overall, a significant correlation exists between the Int(Flux) of both source and seed electrons and Int(AL) as suggested by the correlation coefficients (CC) reaching ~0.8, confirming the essential role of time-integrated substorm activities in providing the persistent supply of source and seed electrons. Nevertheless, we note that the smaller CC of ~0.6–0.7 between Int(Flux) at 32 keV and Int(AL) compared to other energies indicating that other sources apart from direct injections may be present, such as transport of electrons due to enhanced magnetospheric convection (Lyons et al., 2005; Rodger et al., 2022) and inward radial diffusion caused by ULF waves (Tang et al., 2018). For comparison of the major dependence of the integrated fluxes, Figures 4E–H present the correlation between the Int(Flux) and Int(SYM-H). The significantly reduced CC between them indicates that the long-lasting source and seed electrons are only weakly dependent on the magnitude of storms.

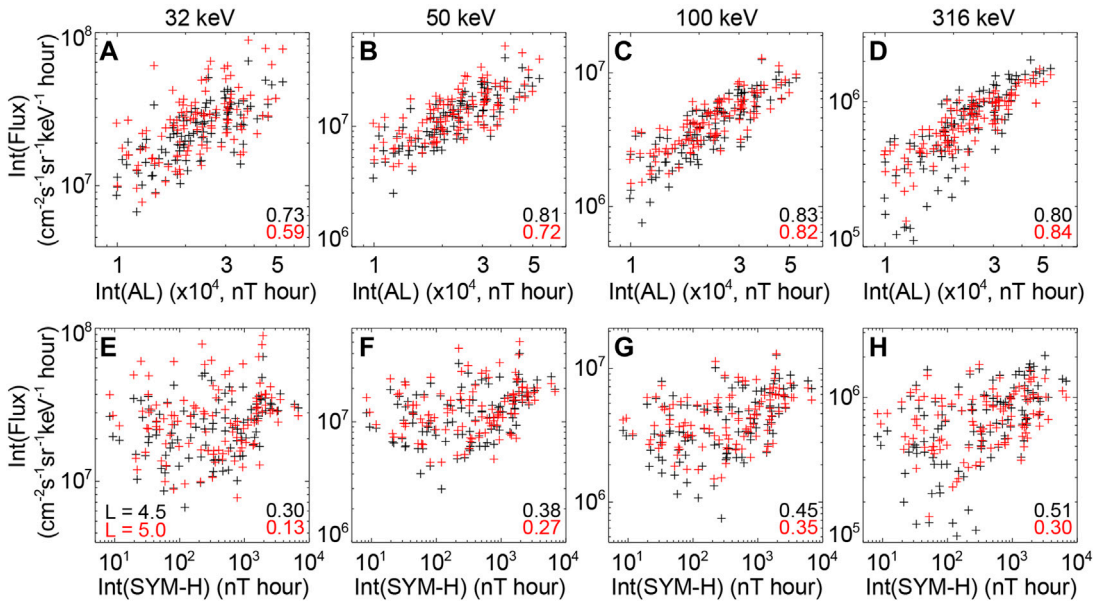

FIGURE 4
Time-integrated electron fluxes at L = 4.5 (black) and L = 5.0 (red) at different energies, from left to right: 32, 50, 100, and 316 keV, versus the corresponding integrated geomagnetic indices including **(A–D)** Int(AL) and **(E–H)** Int(SYM-H) in each storm, with the correlation coefficients marked on the bottom. Each plus symbol represents an individual storm event.

3.2 Correlations between time-integrated source and seed electron fluxes and maximum fluxes of relativistic electrons

Figure 5 shows the Int(Flux) of both source and seed electrons at different energies corresponding to the different rows, plotted against the j_{max} of relativistic electrons at various energies shown in different columns. Although the larger Int(Flux) of source electrons tends to be related to a higher j_{max} of relativistic electrons (Figures 5A–F), the correlation between them is less significant as indicated by the CC varying from ~0.5 to ~0.7 compared to the much stronger correlation between Int(Flux) of seed electrons and j_{max} (Figures 5G–L). Since these source electrons are primarily responsible for the excitation of chorus waves, stronger chorus waves are more likely to occur during the storms with larger Int(Flux) at tens of keV, which contribute to locally accelerated relativistic electron to a higher j_{max}. Nevertheless, this less significant CC between Int(Flux) of source electrons and j_{max} indicates that other mechanisms such as inward radial diffusion driven by ULF waves still play an important role in outer belt relativistic electron acceleration. In contrast, the Int(Flux) of seed electrons are strongly related to the j_{max}, with the highest CC reaching 0.91, indicating the prolonged and pronounced seed electrons are the prerequisite for the significant flux enhancement of relativistic electrons despite the acceleration mechanism. Such a strong correlation also supports idea that the Int(Flux) of seed electrons can be regarded as a proxy for the j_{max} of relativistic electrons (Li et al., 2005; Nasi et al., 2020).

3.3 Correlations between source electron fluxes and whistler-mode chorus wave activity

To directly demonstrate the correlation between the source electron fluxes and chorus wave activity, the simultaneously observed lower band whistler-mode chorus wave amplitude integrated over 0.05 f_{ce}—0.5 f_{ce} (where f_{ce} is the equatorial electron gyrofrequency) versus the source electron fluxes at 32 keV during different levels of AL* index near the equator ($|$MLAT$| \leq 10°$) at L = 4.5 and L = 5.0 are shown in Figures 6A, D, respectively. Due to the less significant role of upper-band chorus waves comparing to the lower-band chorus waves in local acceleration of relativistic electrons (Hua et al., 2022a), we limit our analysis to the lower-band chorus waves in the current study. The wave measurements by Electric and Magnetic Field Instrument Suite and Integrated Science (EMFISIS; Kletzing et al., 2013) instrument are used, with the same chorus identification criteria as Li et al. (2016b). Here, each plus symbol represents one 6-h averaged result when measurements of both chorus waves and electron fluxes at 32 keV are available, and the AL* represents the minimum AL in the corresponding 6-h time bin. We exclude observations over the interval 15–21 MLT since this region is known for its weak intensity of chorus waves (e.g., Li et al., 2016b; Meredith et al., 2020). Clearly, the more intense chorus waves tend to be associated with larger source electron fluxes though there is a large amount of scatter in the data, with the CC between them when considering observations during all levels of AL* reaching ~0.6. During weak substorm activity as indicated by the black and blue colors, the majority of the observed chorus wave amplitude is only

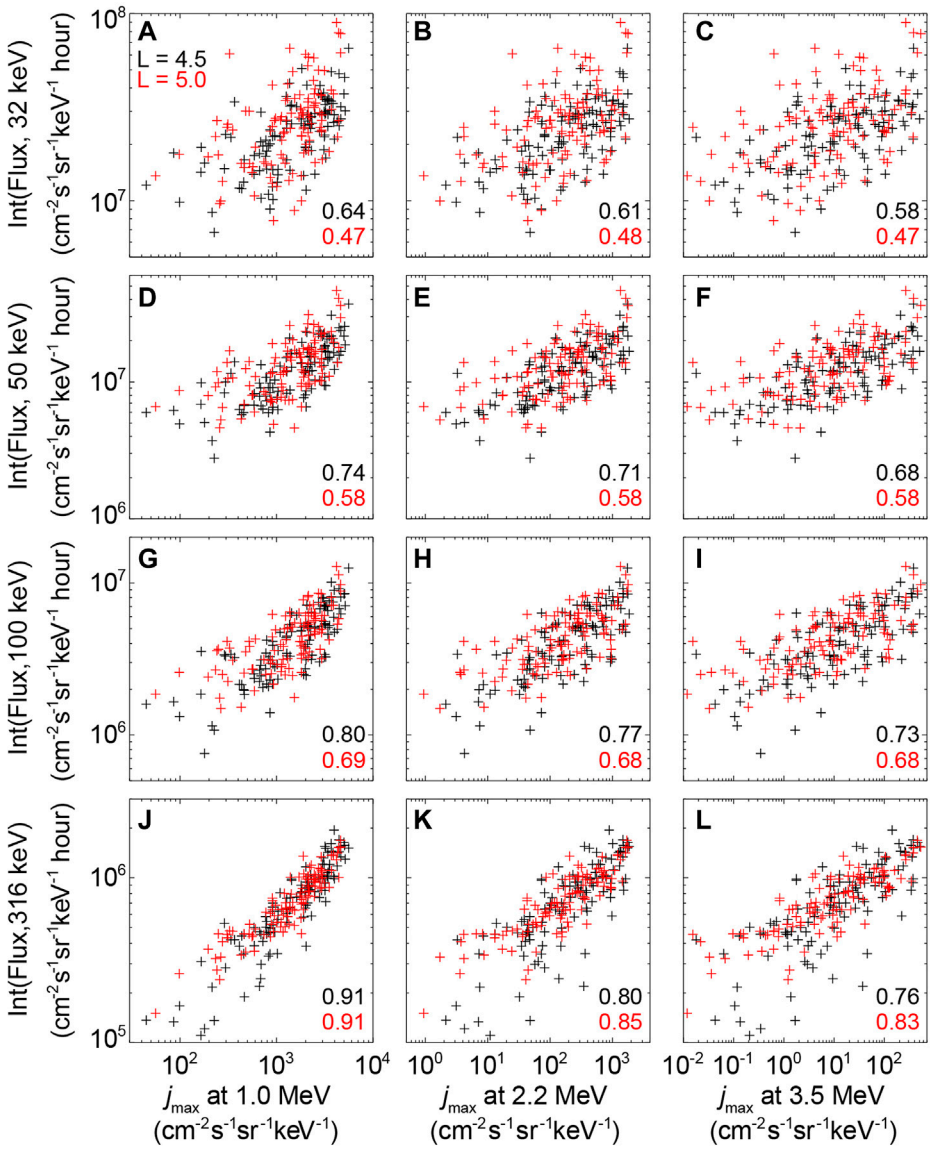

FIGURE 5
Time-integrated electron fluxes at L = 4.5 (black) and L = 5.0 (red) at different energies, from top to bottom: **(A-C)** 32 keV, **(D-F)** 50 keV, **(G-I)** 100 keV, and **(J-L)** 316 keV, versus the corresponding maximum fluxes of relativistic electrons at various energies, from left to right: 1.0, 2.2, and 3.5 MeV, with the correlation coefficients marked at the bottom right of each panel. Each plus symbol represents an individual storm event.

several pT, which is seen to be almost independent of the source electron fluxes, and has low CC values varying from 0.13 to 0.46. However, chorus wave amplitude significantly increases with increasing source electron fluxes during strong substorm activity as indicated by the green and purple color, showing a much stronger CC of >0.7 during the most intense substorms. Figure 6G presents the time-integrated chorus wave amplitude (Int(B_w)) plotted against the time-integrated source electron fluxes based on 6-h averaged results shown in Figures 6A, D. The strong CC reaching 0.7–0.8 confirms the strong correlation between the continuously replenished source electrons by substorm injections and the prolonged and pronounced chorus waves. This is consistent with the most recent study of Tang et al. (2023) that revealed the dominant role of local acceleration in causing the relativistic electron flux enhancements during the continuous intense substorms comparing to the non-continuous intense substorms.

Since the variation of the total electron density (n_e) significantly influences the acceleration of relativistic electron by chorus waves (Thorne et al., 2013; Agapitov et al., 2019; Allison et al., 2021; Hua et al., 2023), we further investigate the distribution of electron density in relation with source electron fluxes (Figures 6B, E, H) and with chorus wave amplitude (Figures 6C, F, I). The electron density inferred from the upper hybrid resonance frequency (Kurth et al., 2015) is adopted whenever it is available, otherwise, the electron density estimated by the Electric Fields and Waves (EFW; Breneman and Wygant, 2022; Wygant et al., 2013) instrument is adopted. Due to the fact that the total electron density is related to the cold plasma (few eV; Lemaire and

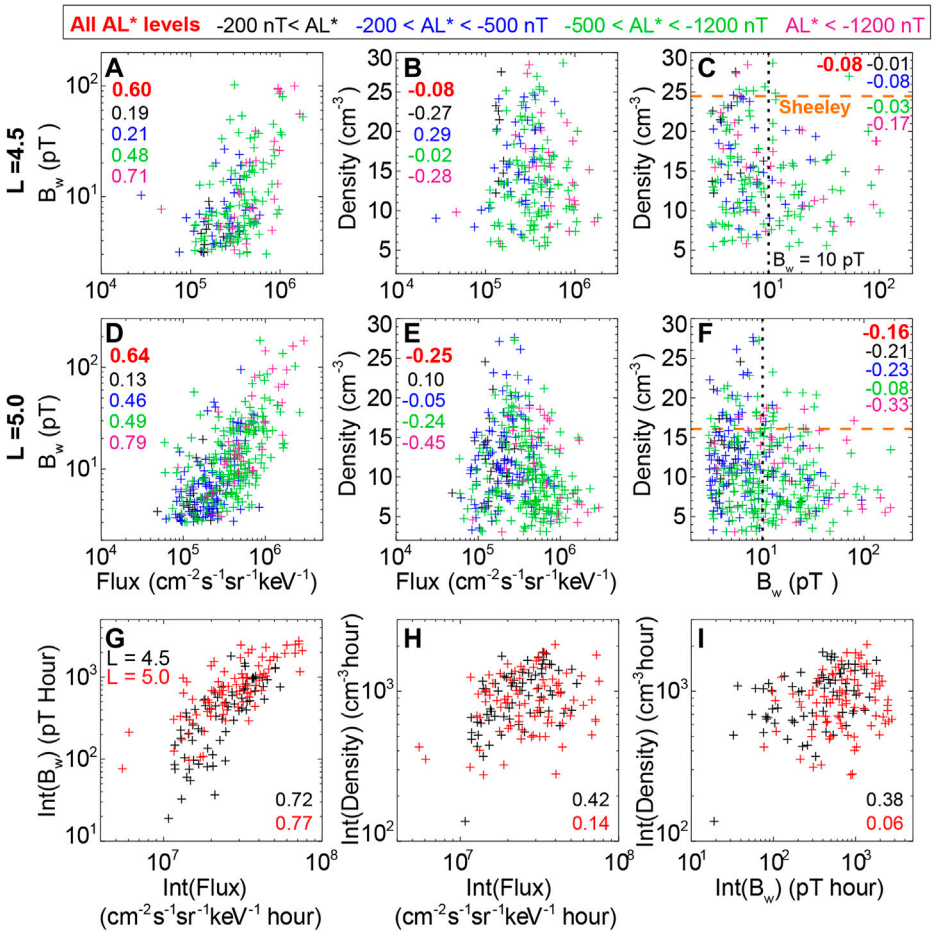

FIGURE 6
(A) Simultaneously observed whistler-mode chorus wave amplitudes versus the source electron fluxes at 32 keV near the equator (|MLAT| ≤10°) at L = 4.5 during different levels of AL* index as shown by different colors, with the corresponding correlation coefficients marked on the top left. The correlation coefficient calculated using observations during all levels of AL* is marked in red in bold font. Here, each plus symbol corresponds to one 6-h averaged result when measurements of both chorus waves and electron fluxes at 32 keV are available. The measurements over 15—21 MLT are excluded. **(B)** Similar format to **(A)** except for the cold plasma density shown on the vertical axis. **(C)** Similar format to **(B)** except for the whistler-mode chorus wave amplitude shown on the *x*-axis. The orange dashed line represents the electron density at L = 4.5 from the empirical model of Sheeley et al. (2001) without considering the MLT factor. The black dotted line marks B_w = 10 pT. **(D–F)** Similar to **(A–C)** but for the results at L = 5.0. **(G)** Time-integrated chorus wave amplitude at L = 4.5 (black) and L = 5.0 (red) versus time-integrated electron fluxes at 32 keV, with the correlation coefficients marked on the bottom. Each plus symbol represents one storm event. **(H)** Similar to **(G)** except for the time-integrated cold plasma density shown on the vertical axis. **(I)** Similar to **(H)** except for the time-integrated chorus wave amplitude shown on the horizontal axis.

Gringauz, 1998), there is no clear dependence of electron density on the source electron fluxes at 32 keV for either instantaneous values or the time-integrated values. Thus, there is no strong correlation that can be detected between electron density and chorus wave amplitude, consistent with the small correlation shown in Hua et al. (2023). Nevertheless, the majority of the intense chorus waves (e.g., with B_w > 10 pT) are mostly associated with the extremely low electron density, which is much lower than the results from the empirical density model shown as the orange dashed lines (Sheeley et al., 2001) that gives n_e = 24.5 cm^{-3} at L = 4.5, and n_e = 16.1 cm^{-3} at L = 5.0 without considering the MLT factor, respectively. The changing electron density strongly affects the f_{pe}/f_{ce} ratio (electron plasma frequency to electron gyrofrequency ratio), which control the efficiency of resonance conditions for wave-particle interactions between relativistic electrons and chorus waves. Multiple previous studies have demonstrated that very low (~10 cm^{-3}) electron density creates preferential conditions for local heating of relativistic electrons by resonant interacting with whistler-mode chorus waves (Thorne et al., 2013; Agapitov et al., 2019; Allison et al., 2021; Camporeale et al., 2016; Hua et al., 2023) Such events with extremely low density and intense chorus waves are favorable to locally accelerate relativistic electrons by chorus waves.

As we have determined the strong correlation between the source electrons and chorus wave activity, we aim to identify the energy channel of source electrons that gives the highest CC with chorus wave amplitude. Similar as the calculation of CC shown in Figures 6A, D, we further calculate the CC with electron fluxes at various energies that can potentially contribute to the excitation of lower-band chorus waves (e.g., Li et al., 2010), which is displayed in Figure 7. Under weak substorm conditions (shown in black and blue

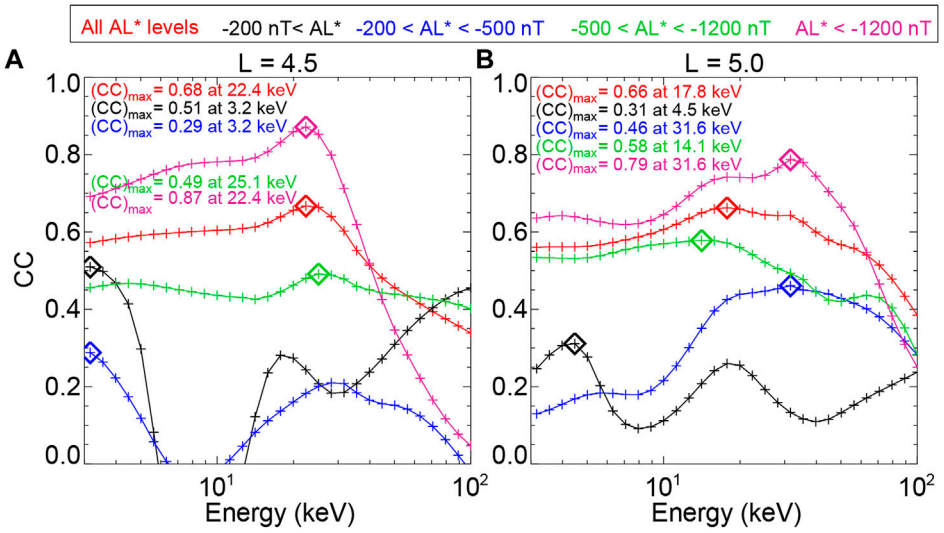

FIGURE 7
The correlation coefficients (CC) between the simultaneously observed whistler-mode chorus wave amplitude and the source electron fluxes at various energies at **(A)** L = 4.5, and **(B)** L = 5.0 at different levels of AL* index as shown by different colors, with the diamond symbols marking the maximum CC, whose values and the corresponding energies are given in each panel.

colors), the noise-like distributions of the CC with energies suggest a weak correlation between the chorus wave activity and the source electrons. However, the CC at energies below ~40 keV overall increases with the increasing substorm intensity (from green to purple colors). The maximum of CC reaching ~0.8 during the most intense substorms indicates that more intense substorms are more favorable to provide long-lasting source electrons, which in turn significantly contribute to the excitation of chorus waves. Moreover, the CC slightly increases from several keV to ~30 keV, peaking at 20–30 keV, and then sharply drops at energies above ~30–40 keV, demonstrating that source electrons from several keV up to ~30 keV compared to the higher energies play a more important role in the generation of chorus waves.

4 Conclusions and discussions

In this study, we systematically investigate the linkage between different parts of the chain, that is believed to accelerate outer radiation belt relativistic electrons to their maximum fluxes as shown graphically in Figure 1, which enables us to determine the crucial elements during this process. Based on 5-year Van Allen Probes observations during geomagnetic storms we investigated the correlation among the background geomagnetic conditions, the evolution of the source and seed electrons, the corresponding chorus wave activity, and the resulting maximum fluxes of relativistic electrons. Our principal conclusions are as follows:

1. Although both source and seed electrons demonstrate a repeatable response to the storms, showing a significant flux enhancement at t_{epoch} ~0 day followed by either a gradual decay or long-lasting existence at a stable level, the evolutions of these electrons demonstrate stronger dependence on the Int(AL) than the Int(SYM-H). This dependence on the integrated AL history suggests that stronger cumulative substorm activities comparing to the weaker substorms are more favorable for providing both sustained source and seed electron fluxes.
2. The CC between the Int(Flux) of source electrons at tens of keV and j_{max} of relativistic electrons varies from ~0.5 to ~0.7 which is relatively modest. Therefore, while local acceleration by chorus wave plays an important role in accelerating relativistic electrons to their saturation level j_{max}, other mechanisms such as inward radial diffusion are still needed in this process.
3. The significant correlation between the Int(Flux) of seed electrons (hundreds of keV) and j_{max} of relativistic electrons indicates that the prolonged and pronounced seed electrons are the prerequisite for significant flux enhancement of relativistic electrons regardless of the acceleration mechanism, and these ~100 keV electron fluxes can also serve as a proxy for j_{max} of MeV electrons.
4. The CC between chorus waves and source electrons increases with increasing levels of substorm activity, with $(CC)_{max}$ reaching ~0.8 at 20—30 keV during the most intense substorms, when it is favorable to observe intense chorus waves. The strong correlation between Int(B_w) and Int(Flux) of source electrons confirms the strong correlation between the continuously replenished source electrons by substorm injections and the prolonged and pronounced chorus waves.

Although it has been well acknowledged that local acceleration by chorus waves and inward radial diffusion due to ULF waves are the two major processes responsible for outer belt electron flux enhancements, other mechanisms such as time domain structures (Mozer et al., 2015), direct injections deep in to the inner magnetosphere (Reeves et al., 2016), and non-linear acceleration processes (e.g., Kubota & Omura, 2018; Artemyev et al., 2022; Foster and Erickson, 2022) can also play an important role in the outer belt electron acceleration. Furthermore, the present study focuses on the

region near the heart of the outer belt (L = 4.5–5.0), which is close to the peak of the radial profile of the maximum fluxes of relativistic electrons at L ~ 4.7. It is worth noting that the electric radial diffusion coefficients at L = 4.5 can be about one-tenth of that at L = 6.0 (Liu et al., 2016). Therefore, the inward radial diffusion can contribute significantly to the relativistic electron acceleration at higher L-shells. Nevertheless, since both L = 4.5 and L = 5.0 are very close to the heart of the outer belt, and the chorus wave amplitudes at these two L-shells are also similar based on previous statistical study using Van Allen Probes data (Aryan et al., 2021), the dominant acceleration mechanism could be similar at these two L-shells. Moreover, we analyze the correlation of the source electrons with the chorus wave activity whenever the observations were available, which means these chorus waves can be observed near or away from their source region. Therefore, the analysis of the correlation of the anisotropy of the source electron and the locally generated chorus waves near the source region will be needed in future studies. In addition, the electron kinetic energy range analyzed in the present study are also usually regarded as the lower energy boundary in the quasi-linear diffusion simulation to reproduce the observed electron acceleration by chorus (e.g., Xiao et al., 2009; Thorne et al., 2013; Glauert et al., 2014; Li et al., 2014; Su et al., 2015; Hua et al., 2018; Hua et al., 2023; Ma et al., 2018). The superposed epoch analysis of the evolution of both source and seed electron fluxes in the present study help us to systematically understand how long their fluxes can be elevated and sustain at that high level, which is fundamentally important for the estimation of the upper limit of outer belt electron acceleration (Hua et al., 2022a).

Data availability statement

The Van Allen probes data from the EMFISIS instrument were obtained from http://emfisis.physics.uiowa.edu/Flight. The ECT data were obtained from https://rbsp-ect.newmexicoconsortium.org/data_pub/. The geomagnetic indices were obtained from the OMNI data set (https://omniweb.gsfc.nasa.gov/ow_min.html). The source data used to produce figures in the present study are publicly available in the [figshare] [https://doi.org/10.6084/m9.figshare.21956627.v1].

Author contributions

MH designed and led the study, performed data analysis, and wrote the initial manuscript. JB supervised the project, contributed significantly to explain the results, finalized the manuscript through review and edits. All coauthors reviewed the manuscript and discussed the results.

Funding

The authors gratefully acknowledge subgrant 1559841 to the University of California, Los Angeles, from the University of Colorado Boulder under NASA Prime Grant agreement 80NSSC20K1580.

Acknowledgments

We acknowledge the Van Allen Probes mission, particularly the ECT team for providing the particle data and the EMFISIS team for providing the wave data.

Conflict of interest

The authors declare that the research was conducted in the absence of any commercial or financial relationships that could be construed as a potential conflict of interest.

Publisher's note

References

Agapitov, O., Mourenas, D., Artemyev, A., Hospodarsky, G., and Bonnell, J. W. (2019). Time scales for electron quasi-linear diffusion by lower-band chorus waves: The effects of ωpe/Ωce dependence on geomagnetic activity. *Geophys. Res. Lett.* 46, 6178–6187. doi:10.1029/2019GL083446

Allison, H. J., Shprits, Y. Y., Zhelavskaya, I. S., Wang, D., and Smirnov, A. G. (2021). Gyroresonant wave-particle interactions with chorus waves during extreme depletions of plasma density in the Van Allen radiation belts. *Sci. Adv.* 7 (5), eabc0380. doi:10.1126/sciadv.abc0380

Artemyev, A. V., Mourenas, D., Zhang, X.-J., and Vainchtein, D. (2022). Extreme energy spectra of relativistic electron flux in the outer radiation belt. *J. Geophys. Res. Space Phys.* 127, e2022JA031038. e2022JA030853. doi:10.1029/2022JA031038

Aryan, H., Bortnik, J., Meredith, N. P., Horne, R. B., Sibeck, D. G., and Balikhin, M. A. (2021). Multi-parameter chorus and plasmaspheric hiss wave models. *J. Geophys. Res. Space Phys.* 126, e2020JA028403. doi:10.1029/2020JA028403

Baker, D. N., Allen, J. H., Kanekal, S. G., and Reeves, G. D. (1998). Disturbed space environment may have been related to pager satellite failure. *Eos Trans. AGU* 79 (40), 477–483. doi:10.1029/98EO00359

Baker, D. N., Hoxie, V., Zhao, H., Jaynes, A. N., Kanekal, S., Li, X., et al. (2019). Multiyear measurements of radiation belt electrons: Acceleration, transport, and loss. *J. Geophys. Res. Space Phys.* 124, 2588–2602. doi:10.1029/2018JA026259

Baker, D. N., Kanekal, S., Li, X., Monk, S. P., Goldstein, J., and Burch, J. L. (2004). An extreme distortion of the Van Allen belt arising from the 'Hallowe'en' solar storm in 2003. *Nature* 432, 878–881. doi:10.1038/nature03116

Baker, D. N. (2001). "Satellite anomalies due to space storms," in *Space storms and space weather hazards, NATO science series (series II: Mathematics, physics and chemistry)* Editor I. A. Daglis (Dordrecht: Springer), 285–311.

Bingham, S. T., Mouikis, C. G., Kistler, L. M., Boyd, A. J., Paulson, K., Farrugia, C. J., et al. (2018). The outer radiation belt response to the storm time development of seed electrons and chorus wave activity during CME and CIR driven storms. *J. Geophys. Res. Space Phys.* 123 (10), 157. 139– 10. doi:10.1029/2018JA025963

Boyd, A. J., Reeves, G. D., Spence, H. E., Funsten, H. O., Larsen, B. A., Skoug, R. M., et al. (2019). RBSP-ECT combined spin-averaged electron flux data product. *J. Geophys. Res. Space Phys.* 124, 9124–9136. doi:10.1029/2019JA026733

Boyd, A. J., Spence, H. E., Huang, C.-L., Reeves, G. D., Baker, D. N., Turner, D. L., et al. (2016). Statistical properties of the radiation belt seed population. *J. Geophys. Res. Space Phys.* 121, 7636–7646. doi:10.1002/2016JA022652

Breneman, A. W., Wygant, J. R., Tian, S., Cattell, C. A., Thaller, S. A., Goetz, K., et al. (2022). The van allen probes electric field and waves instrument: Science results, measurements, and access to data. *Space Sci. Rev.* 218, 69. doi:10.1007/s11214-022-00934-y

Camporeale, E., Shprits, Y., Chandorkar, M., Drozdov, A., and Wing, S. (2016). On the propagation of uncertainties in radiation belt simulations. *Space Weather.* 14, 982–992. doi:10.1002/2016SW001494

Foster, J. C., and Erickson, P. J. (2022). Offequatorial effects of the nonlinear interaction of VLF chorus waves with radiation belt electrons. *Front. Astron. Space Sci.* 9, 986814. doi:10.3389/fspas.2022.986814

Glauert, S. A., Horne, R. B., and Meredith, N. P. (2014). Three-dimensional electron radiation belt simulations using the BAS Radiation Belt Model with new diffusion models for chorus, plasmaspheric hiss, and lightning-generated whistlers. *J. Geophys. Res. Space Phys.* 119, 268–289. doi:10.1002/2013JA019281

Horne, R. B., Glauert, S. A., Kirsch, P., Heynderickx, D., Bingham, S., Thorn, P., et al. (2021). The satellite risk prediction and radiation forecast system (SaRIF). *Space weather.* 19, e2021SW002823. doi:10.1029/2021SW002823

Horne, R. B., Glauert, S. A., Meredith, N. P., Boscher, D., Maget, V., Heynderickx, D., et al. (2013). Space weather impacts on satellites and forecasting the Earth's electron radiation belts with SPACECAST. *Space weather.* 11, 169–186. doi:10.1002/swe.20023

Hua, M., Bortnik, J., Chu, X., Aryan, H., and Ma, Q. (2022b). Unraveling the critical geomagnetic conditions controlling the upper limit of electron fluxes in the Earth's outer radiation belt. *Geophys. Res. Lett.* 49, e2022GL101096. doi:10.1029/2022GL101096

Hua, M., Bortnik, J., Kellerman, A. C., Camporeale, E., and Ma, Q. (2023). Ensemble modeling of radiation belt electron acceleration by chorus waves: Dependence on key input parameters. *Space weather.* 21, e2022SW003234. doi:10.1029/2022SW003234

Hua, M., Bortnik, J., and Ma, Q. (2022a). Upper limit of outer radiation belt electron acceleration driven by whistler-mode chorus waves. *Geophys. Res. Lett.* 49, e2022GL099618. doi:10.1029/2022GL099618

Hua, M., Ni, B., Fu, S., Gu, X., Xiang, Z., Cao, X., et al. (2018). Combined scattering of outer radiation belt electrons by simultaneously occurring chorus, exohiss, and magnetosonic waves. *Geophys. Res. Lett.* 45, 067. doi:10.1029/2018GL079533

Hudson, M. K., Kress, B. T., Mueller, H.-R., Zastrow, J. A., and Blake, J. B. (2008). Relationship of the Van Allen radiation belts to solar wind drivers. *J. Atmos. Solar-Terrestrial Phys.* 70 (5), 708–729. doi:10.1016/j.jastp.2007.11.003

Jaynes, A. N., Ali, A. F., Elkington, S. R., Malaspina, D. M., Baker, D. N., Li, X., et al. (2018). Fast diffusion of ultrarelativistic electrons in the outer radiation belt: 17 march 2015 storm event. *Geophys. Res. Lett.* 45 (20), 10874–10882. doi:10.1029/2018GL079786

Kennel, C. F., and Petschek, H. E. (1966). Limit on stably trapped particle fluxes. *J. Geophys. Res.* 71 (1), 1–28. doi:10.1029/JZ071i001p00001

Kletzing, C. A., Kurth, W. S., Acuna, M., MacDowall, R. J., Torbert, R. B., Averkamp, T., et al. (2013). The electric and magnetic field instrument suite and integrated science (EMFISIS) on RBSP. *Space Sci. Rev.* 179 (1-4), 127–181. doi:10.1007/s11214-013-9993-6

Kubota, Y., and Omura, Y. (2018). Nonlinear dynamics of radiation belt electrons interacting with chorus emissions localized in longitude. *J. Geophys. Res. Space Phys.* 123, 4835–4857. doi:10.1029/2017JA025050

Kurth, W. S., De Pascuale, S., Faden, J. B., Kletzing, C. A., Hospodarsky, G. B., Thaller, S., et al. (2015). Electron densities inferred from plasma wave spectra obtained by the Waves instrument on Van Allen Probes. *J. Geophys. Res. Space Phys.* 120, 904–914. doi:10.1002/2014JA020857

Lejosne, S., Allison, H. J., Blum, L. W., Drozdov, A. Y., Hartinger, M. D., Hudson, M. K., et al. (2022). Differentiating between the leading processes for electron radiation belt acceleration. *Front. Astronomy Space Sci.* 144. doi:10.3389/fspas.2022.896245

Lemaire, J. F., and Gringauz, K. I. (1998). *The earth's plasmasphere*. Cambridge, U. K: Cambridge Univ. Press.

Li, W., and Hudson, M. K. (2019). Earth's van allen radiation belts: From discovery to the van allen probes era. *J. Geophys. Res. Space Phys.* 124, 8319–8351. doi:10.1029/2018JA025940

Li, W., Ma, Q., Thorne, R. M., Bortnik, J., Zhang, X. J., Li, J., et al. (2016a). Radiation belt electron acceleration during the 17 March 2015 geomagnetic storm: Observations and simulations. *J. Geophys. Res. Space Phys.* 121 (6), 5520–5536. doi:10.1002/2016JA022400

Li, W., Santolik, O., Bortnik, J., Thorne, R. M., Kletzing, C. A., Kurth, W. S., et al. (2016b). New chorus wave properties near the equator from Van Allen Probes wave observations. *Geophys. Res. Lett.* 43, 4725–4735. doi:10.1002/2016GL068780

Li, W., Thorne, R., Bortnik, J., McPherron, R., Nishimura, Y., Angelopoulos, V., et al. (2012). Evolution of chorus waves and their source electrons during storms driven by corotating interaction regions. *J. Geophys. Res.* 117, A08209. doi:10.1029/2012JA017797

Li, W., Thorne, R. M., Ma, Q., Ni, B., Bortnik, J., Baker, D. N., et al. (2014). Radiation belt electron acceleration by chorus waves during the 17 March 2013 storm. *J. Geophys. Res. Space Phys.* 119, 4681–4693. doi:10.1002/2014JA019945

Li, W., Thorne, R. M., Nishimura, Y., Bortnik, J., Angelopoulos, V., McFadden, J. P., et al. (2010). THEMIS analysis of observed equatorial electron distributions responsible for the chorus excitation. *J. Geophys. Res.* 115, A00F11. doi:10.1029/2009JA014845

Li, X., Baker, D. N., Temerin, M., Reeves, G., Friedel, R., and Shen, C. (2005). Energetic electrons, 50 keV to 6 MeV, at geosynchronous orbit: Their responses to solar wind variations. *Space weather.* 3, S04001. doi:10.1029/2004SW000105

Liu, W., Tu, W., Li, X., Sarris, T., Khotyaintsev, Y., Fu, H., et al. (2016). On the calculation of electric diffusion coefficient of radiation belt electrons with *in situ* electric field measurements by THEMIS. *Geophys. Res. Lett.* 43, 1023–1030. doi:10.1002/2015GL067398

Lyons, L. R., Lee, D.-Y., Thorne, R. M., Horne, R. B., and Smith, A. J. (2005). Solar wind-magnetosphere coupling leading to relativistic electron energization during high-speed streams. *J. Geophys. Res.* 110, A11202. doi:10.1029/2005JA011254

Ma, Q., Li, W., Bortnik, J., Thorne, R. M., Chu, X., Ozeke, L. G., et al. (2018). Quantitative evaluation of radial diffusion and local acceleration processes during GEM challenge events. *J. Geophys. Res. Space Phys.* 123, 1938–1952. doi:10.1002/2017JA025114

Mauk, B. H., Fox, N. J., Kanekal, S. G., Kessel, R. L., Sibeck, D. G., and Ukhorskiy, A. (2013). Science objectives and rationale for the radiation belt storm probes mission. *Space Sci. Rev.* 179, 3. doi:10.1007/s11214-012-9908-y

Meredith, N. P., Horne, R. B., Shen, X.-C., Li, W., and Bortnik, J. (2020). Global model of whistler mode chorus in the near-equatorial region ($|\lambda_{<i>m</i>}| < 18^{\circ}$). *Geophys. Res. Lett.* 47, e2020GL087311. doi:10.1029/2020GL087311

Miyoshi, Y., Kataoka, R., Kasahara, Y., Kumamoto, A., Nagai, T., and Thomsen, M. F. (2013). High-speed solar wind with southward interplanetary magnetic field causes relativistic electron flux enhancement of the outer radiation belt via enhanced condition of whistler waves. *Geophys. Res. Lett.* 40, 4520–4525. doi:10.1002/grl.50916

Mourenas, D., Artemyev, A. V., Zhang, X.-J., and Angelopoulos, V. (2022). Extreme energy spectra of relativistic electron flux in the outer radiation belt. *J. Geophys. Res. Space Phys.* 127, e2022JA031038. doi:10.1029/2022JA031038

Mozer, F. S., Agapitov, O. V., Artemyev, A., Drake, J. F., Krasnoselskikh, V., Lejosne, S., et al. (2015). Time domain structures: What and where they are, what they do, and how they are made. *Geophys. Res. Lett.* 42, 3627–3638. doi:10.1002/2015GL063946

Murphy, K. R., Watt, C. E. J., Mann, I. R., Jonathan Rae, I., Sibeck, D. G., Boyd, A. J., et al. (2018). The global statistical response of the outer radiation belt during geomagnetic storms. *Geophys. Res. Lett.* 45 (9), 3783–3792. doi:10.1002/2017GL076674

Nasi, A., Daglis, I. A., Katsavrias, C., and Li, W. (2020). Interplay of source/seed electrons and wave-particle interactions in producing relativistic electron PSD enhancements in the outer Van Allen belt. *J. Atmos. Solar-Terrestrial Phys.* 210, 105405. doi:10.1016/j.jastp.2020.105405

Olifer, L., Mann, I. R., Claudepierre, S. G., Baker, D. N., Spence, H. E., and Ozeke, L. G. (2022). A natural limit to the spectral hardness of worst case electron radiation in the terrestrial van allen belt. *J. Geophys. Res. Space Phys.* 127, e2022JA030506. doi:10.1029/2022JA030506

Olifer, L., Mann, I. R., Kale, A., Mauk, B. H., Claudepierre, S. G., Baker, D. N., et al. (2021). A tale of two radiation belts: The energy-dependence of self-limiting electron space radiation. *Geophys. Res. Lett.* 48, e2021GL095779. doi:10.1029/2021GL095779

Ozeke, L. G., Mann, I. R., Dufresne, S. K. Y., Olifer, L., Morley, S. K., Claudepierre, S. G., et al. (2020). Rapid outer radiation belt flux dropouts and fast acceleration during the march 2015 and 2013 storms: The role of ultra-low frequency wave transport from a dynamic outer boundary. *J. Geophys. Res. Space Phys.* 125, e2019JA027179. doi:10.1029/2019JA027179

Ozeke, L. G., Mann, I. R., Murphy, K. R., Jonathan Rae, I., and Milling, D. K. (2014). Analytic expressions for ULF wave radiation belt radial diffusion coefficients. *J. Geophys. Res. Space Phys.* 119, 1587–1605. doi:10.1002/2013JA019204

Reeves, G. D., Friedel, R. H. W., Larsen, B. A., Skoug, R. M., Funsten, H. O., Claudepierre, S. G., et al. (2016). Energy-dependent dynamics of keV to MeV electrons in the inner zone, outer zone, and slot regions. *J. Geophys. Res. Space Phys.* 121, 397–412. doi:10.1002/2015JA021569

Reeves, G. D., Spence, H. E., Henderson, M. G., Morley, S. K., Friedel, R. H. W., Funsten, H. O., et al. (2013). Electron acceleration in the heart of the Van Allen radiation belts. *Science* 341 (6149), 991–994. doi:10.1126/science.1237743

Reeves, G. D. (1997). *Workshop on the earth's trapped particle environment proceedings*. United States: American Institutes of Physics.

Ripoll, J.-F., Claudepierre, S. G., Ukhorskiy, A. Y., Colpitts, C., Li, X., Fennell, J., et al. (2020). Particle dynamics in the Earth's radiation belts: Review of current research and open questions. *J. Geophys. Res. Space Phys.* 125 (5), e2019JA026735. doi:10.1029/2019JA026735

Rodger, C. J., Hendry, A. T., Clilverd, M. A., Forsyth, C., and Morley, S. K. (2022). Examination of radiation belt dynamics during substorm clusters: Activity drivers and dependencies of trapped flux enhancements. *J. Geophys. Res. Space Phys.* 127, e2021JA030003. doi:10.1029/2021JA030003

Sheeley, B. W., Moldwin, M. B., Rassoul, H. K., and Anderson, R. R. (2001). An empirical plasmasphere and trough density model: CRRES observations. *J. Geophys. Res.* 106 (11), 25631. doi:10.1029/2000JA000286

Simms, L. E., Engebretson, M. J., Rodger, C. J., Gjerloev, J. W., and Reeves, G. D. (2019). Predicting lower band chorus with autoregressive-moving average transfer function (ARMAX) models. *J. Geophys. Res. Space Phys.* 124, 5692–5708. doi:10.1029/2019JA026726

Spence, H. E., Reeves, G. D., Baker, D. N., Blake, J. B., Bolton, M., Bourdarie, S., et al. (2013). Science goals and overview of the radiation belt storm probes (RBSP) energetic

particle, composition, and thermal plasma (ECT) suite on NASA's van allen probes mission. *Space Sci. Rev.* 179, 311–336. doi:10.1007/s11214-013-0007-5

Su, Z., Zhu, H., Xiao, F., Zheng, H., Wang, Y., Zong, Q., et al. (2015). Quantifying the relative contributions of substorm injections and chorus waves to the rapid outward extension of electron radiation belt. *J. Geophys. Res. Space Phys.* 119, 10040. doi:10.1002/2014JA020709

Summers, D., and Shi, R. (2014). Limiting energy spectrum of an electron radiation belt. *J. Geophys. Res. Space Phys.* 119, 6313–6326. doi:10.1002/2014JA020250

Summers, D., Thorne, R. M., and Xiao, F. (1998). Relativistic theory of wave-particle resonant diffusion with application to electron acceleration in the magnetosphere. *J. Geophys. Res.* 103 (9), 20487–20500. doi:10.1029/98JA01740

Tang, C. L., Wang, Y. X., Ni, B., Zhang, J.-C., Reeves, G. D., Su, Z. P., et al. (2017). Radiation belt seed population and its association with the relativistic electron dynamics: A statistical study. *J. Geophys. Res. Space Phys.* 122, 5261–5276. doi:10.1002/2017JA023905

Tang, C. L., Xie, X. J., Ni, B., Su, Z. P., Reeves, G. D., Zhang, J.-C., et al. (2018). Rapid enhancements of the seed populations in the heart of the earth's outer radiation belt: A multicase study. *J. Geophys. Res. Space Phys.* 123, 4895–4907. doi:10.1029/2017JA025142

Tang, C. L., Yang, C., Chen, J. R., Wang, X., Ni, B. B., Su, Z. P., et al. (2023). Rapid enhancements of relativistic electrons in the Earth's outer radiation belt caused by the intense substorms: A statistical study. *J. Geophys. Res. Space Phys.* 128, e2022JA031089. doi:10.1029/2022JA031089

Thorne, R. M., Li, W., Ni, B., Ma, Q., Bortnik, J., Chen, L., et al. (2013). Rapid local acceleration of relativistic radiation-belt electrons by magnetospheric chorus. *Nature* 504 (7480), 411–414. doi:10.1038/nature12889

Tsyganenko, N. A. (1989). A magnetospheric magnetic field model with a warped tail current sheet. *Planet. Space Sci.* 37 (1), 5–20. doi:10.1016/0032-0633(89)90066-4

Tu, W., Cunningham, G. S., Chen, Y., Henderson, M. G., Camporeale, E., and Reeves, G. D. (2013). Modeling radiation belt electron dynamics during GEM challenge intervals with the DREAM3D diffusion model. *J. Geophys. Res. Space Phys.* 118, 6197–6211. doi:10.1002/jgra.50560

Tu, W., Cunningham, G. S., Chen, Y., Morley, S. K., Reeves, G. D., Blake, J. B., et al. (2014). Event-specific chorus wave and electron seed population models in DREAM3D using the Van Allen Probes. *Geophys. Res. Lett.* 41, 1359–1366. doi:10.1002/2013GL058819

Turner, D. L., Kilpua, E. K. J., Hietala, H., Claudepierre, S. G., O'Brien, T. P., Fennell, J. F., et al. (2019). The response of Earth's electron radiation belts to geomagnetic storms: Statistics from the Van Allen Probes era including effects from different storm drivers. *J. Geophys. Res. Space Phys.* 124, 1013–1034. doi:10.1029/2018JA026066

Turner, D. L., O'Brien, T. P., Fennell, J. F., Claudepierre, S. G., Blake, J. B., Kilpua, E. K. J., et al. (2015). The effects of geomagnetic storms on electrons in Earth's radiation belts. *Geophys. Res. Lett.* 42, 9176–9184. doi:10.1002/2015GL064747

Wygant, J. R., Bonnell, J. W., Goetz, K., Ergun, R. E., Mozer, F. S., Bale, S. D., et al. (2013). "The electric field and waves instruments on the radiation belt storm probes mission," in *The van allen probes mission* Editors N. Fox, and J. L. Burch (Boston: Springer), 183–220. doi:10.1007/978-1-4899-7433-4_6

Xiao, F., Su, Z., Zheng, H., and Wang, S. (2009). Modeling of outer radiation belt electrons by multidimensional diffusion process. *J. Geophys. Res.* 114, A03201. doi:10.1029/2008JA013580

Zhang, K., Li, X., Zhao, H., Xiang, Z., Khoo, L. Y., Zhang, W., et al. (2021). Upper limit of electron fluxes observed in the radiation belts. *J. Geophys. Res. Space Phys.* 126, e2020JA028511. doi:10.1029/2020JA028511

Zhao, H., Baker, D. N., Li, X., Jaynes, A. N., and Kanekal, S. G. (2018). The acceleration of ultrarelativistic electrons during a small to moderate storm of 21 april 2017. *Geophys. Res. Lett.* 91, 5818–5825. doi:10.1029/2018GL078582

frontiers | Frontiers in Astronomy and Space Sciences

TYPE Original Research
PUBLISHED 19 April 2023
DOI 10.3389/fspas.2023.1163515

OPEN ACCESS

EDITED BY
Xiao-Jia Zhang,
The University of Texas at Dallas, United States

REVIEWED BY
Jay M. Albert,
Air Force Research Lab, United States
Xin An,
University of California, Los Angeles, United States

*CORRESPONDENCE
Miroslav Hanzelka,
mirekhanzelka@gmail.com

SPECIALTY SECTION
This article was submitted to Space Physics, a section of the journal Frontiers in Astronomy and Space Sciences

RECEIVED 10 February 2023
ACCEPTED 27 March 2023
PUBLISHED 19 April 2023

CITATION
Hanzelka M, Li W and Ma Q (2023), Parametric analysis of pitch angle scattering and losses of relativistic electrons by oblique EMIC waves. *Front. Astron. Space Sci.* 10:1163515. doi: 10.3389/fspas.2023.1163515

Parametric analysis of pitch angle scattering and losses of relativistic electrons by oblique EMIC waves

Miroslav Hanzelka[1,2]*, Wen Li[1] and Qianli Ma[1,3]

[1]Center for Space Physics, Boston University, Boston, MA, United States, [2]Department of Space Physics, Institute of Atmospheric Physics of the Czech Academy of Sciences, Prague, Czechia, [3]Department of Atmospheric and Oceanic Sciences, University of California, Los Angeles, Los Angeles, CA, United States

This study analyzes the effects of electromagnetic ion cyclotron (EMIC) waves on relativistic electron scattering and losses in the Earth's outer radiation belt. EMIC emissions are commonly observed in the inner magnetosphere and are known to reach high amplitudes, causing significant pitch angle changes in primarily >1 MeV electrons *via* cyclotron resonance interactions. We run test-particle simulations of electrons streaming through helium band waves with different amplitudes and wave normal angles and assess the sensitivity of advective and diffusive scattering behaviors to these two parameters, including the possibility of very oblique propagation. The numerical analysis confirms the importance of harmonic resonances for oblique waves, and the very oblique waves are observed to efficiently scatter both co-streaming and counter-streaming electrons. However, strong finite Larmor radius effects limit the scattering efficiency at high pitch angles. Recently discussed force-bunching effects and associated strong positive advection at low pitch angles are, surprisingly, shown to cause no decrease in the phase space density of precipitating electrons, and it is demonstrated that the transport of electrons into the loss cone balances out the scattering out of the loss cone. In the case of high-amplitude obliquely propagating waves, weak but non-negligible losses are detected well below the minimum resonance energy, and we identify them as the result of non-linear fractional resonances. Simulations and theoretical analysis suggest that these resonances might contribute to subrelativistic electron precipitation but are likely to be overshadowed by non-resonant effects.

KEYWORDS

electron scattering, EMIC waves, non-linear wave–particle interactions, test-particle simulation, radiation belts, fractional resonance, loss cone, electron precipitation

1 Introduction

Electromagnetic ion cyclotron (EMIC) waves are naturally occurring electromagnetic emissions in the Earth's magnetosphere generated by unstable anisotropic hot ion populations (Kennel and Petschek, 1966; Anderson et al., 1996). Each ion component of the space plasma has a corresponding EMIC frequency band located below the gyrofrequency of the ion, with the hydrogen band (H+) and helium band (He+) being the most commonly observed (Min et al., 2012; Meredith et al., 2014; Saikin et al., 2015; Wang X. Y. et al., 2017; Jun et al., 2021). In the outer radiation belt, the wave frequencies in the near-equatorial

source (Loto'aniu et al., 2005; Allen et al., 2015) fall mainly into the Pc1 range 0.2–5 Hz (Saito, 1969; Usanova et al., 2012). Initially generated in the left-handed mode, the waves may convert to the right-handed mode at higher latitudes (Rauch and Roux, 1982; Perraut et al., 1984; Kim and Johnson, 2016). These polarized waves can scatter relativistic electrons (kinetic energies E_k around 1 MeV and larger) in pitch angle α through cyclotron resonance interactions (Horne and Thorne, 1998; Summers et al., 1998), which leads to significant losses of radiation belt electrons to the atmosphere (Thorne and Kennel, 1971; Usanova et al., 2014; Clilverd et al., 2015; Kurita et al., 2018; Li and Hudson, 2019).

During geomagnetically active times, EMIC waves at lower L-shells ($L < 6$) can reach peak magnetic field amplitudes B_w higher than 1% of the background magnetic field strength B_0 (Meredith et al., 2003; Engebretson et al., 2015). Trajectories of particles resonating with strong waves experience large perturbations, and a variety of associated non-linear effects appear (Karpman, 1974; Artemyev et al., 2018; Grach et al., 2022). Phase trapping of ions in the wave potential leads to non-local transport to higher pitch angles and the formation of phase space density (PSD) holes in the gyrophase space (Omura et al., 2010; Shoji et al., 2021), while phase-trapped electrons experience a decrease in pitch angle (Omura and Zhao, 2012; Zheng et al., 2019). At $\alpha \approx 0°$, the force-bunched electrons are transported predominantly to higher pitch angles; Bortnik et al. (2022) proposed that this non-linear effect may result in precipitation blocking due to the removal of electrons from the loss cone. Below the fundamental cyclotron resonance energy, non-resonant scattering by amplitude-modulated waves takes place and may extend the energy range of precipitating electrons down to hundreds of keV (Chen et al., 2016; An et al., 2022).

When the wave normal angle θ_k (WNA) of EMIC waves increases and the propagation becomes oblique, finite Larmor radius effects enable interaction with higher cyclotron harmonics. Approximate quasilinear formulas for pitch angle diffusion coefficients of waves with a given wave normal distribution can be found in the study by Albert (2008). Wang G. et al. (2017) studied the interaction of electrons with moderately oblique monochromatic EMIC waves through non-linear test-particle simulations and quasilinear diffusive modeling. They have shown that with increasing θ_k, harmonic resonances at ultrarelativistic energies can lead to significant scattering loss, while the fundamental resonance becomes weaker for oblique waves. Lee et al. (2018) analyzed the WNA and ellipticity of a set of EMIC waves detected by Van Allen Probe A, ran test-particle simulations of electron interaction with very powerful and oblique EMIC waves, and highlighted the complexity of pitch angle evolution due to higher-order resonance with the elliptically polarized wave. They also emphasized the advective aspects of non-linear scattering and noted the importance of ellipticity and WNA distributions in modeling the radiation belt electron transport.

In this paper, we perform test-particle simulations of non-linear electron interactions with quasiparallel and very oblique monochromatic EMIC waves, with the overall goal of describing the dependence of advection, diffusion, and subsequent particle losses on the wave amplitude and wave normal angle—special attention is given to the PSD evolution at low pitch angles. After describing the simulation setup in **Section 2**, we analyze the average and standard deviation of equatorial pitch angle changes for very oblique waves and discuss the influence of higher harmonics on advection and diffusion in **Section 3.1**. In **Section 3.2**, we demonstrate through Liouville mapping of phase space density in backward-in-time simulations that the force-bunching effects at low pitch angles are balanced out by transport from higher pitch angles and that there is no apparent precipitation blocking in the sense of decreasing precipitating electron PSD below the trapped PSD. **Section 3.3** describes fractional resonances, a type of resonance acting below the fundamental resonance energy, and considers their effects on subrelativistic electrons. A summary of the most salient results and a discussion of the impacts of our findings on radiation belt electron modeling can be found in **Section 4**.

2 Methods and simulation setup

Before choosing representative wave and plasma parameters for our particle simulation, we must first consider which quantities can influence the behavior of resonant electrons. Wave amplitude B_w controls the transition from quasilinear to non-linear interaction, and wave normal angle θ_k is related to the perpendicular component of the wave vector and associated harmonic resonances. Varying the values of B_w or θ_k leads to major qualitative changes in the resonant behavior; therefore, they are the essential parameters in our simulation. We choose four values of wave normal angle $\{5°, 45°, 70°, 80°\}$ to cover quasiparallel, moderately oblique, and very oblique wave propagation. The WNA values are combined with three values of amplitude $B_{w0} = \{100\ \text{pT}, 400\ \text{pT}, 1.6\ \text{nT}\}$, which approximately correspond to B_{w0}/B_{0eq} ratios of $\{0.04\%, 0.16\%, 0.64\%\}$ for equatorial field strength $B_{0eq} = 248$ nT at $L = 5$. This choice of L-shell is consistent with regions of enhanced EMIC wave activity identified by Meredith et al. (2014) and Jun et al. (2021) in spacecraft measurements during active geomagnetic conditions.

There are also several parameters that influence the value of the minimum resonance energy, which is given by the formula

$$E_{\text{Rmin}} = mc^2 \left(\frac{n\omega\Omega_e - k_\parallel c\sqrt{n^2\Omega_e^2 + k_\parallel^2 c^2 - \omega^2}}{\omega^2 - k_\parallel^2 c^2} - 1 \right) \approx mc^2 \left(\sqrt{1 + \frac{n^2\Omega_e^2}{k_\parallel^2 c^2}} - 1 \right) \approx \left| \frac{n}{k_\parallel} \right| mc\Omega_e, \tag{1}$$

where m is the electron mass, c is the speed of light, $k_\parallel$ is the component of the wave vector parallel to $\boldsymbol{B_0}$, ω is the wave frequency, Ω_e is the local electron gyrofrequency, and n is an integer determining the resonance harmonic (positive/negative for electrons streaming against/along the wave). The first approximation assumes $\omega \ll \Omega_e$ and $\omega_{pe}^2 \gg \Omega_e^2$, and the second one is the ultrarelativistic approximation. The energy E_{Rmin} is dependent on the normalized frequency ω/Ω_e, and through the cold plasma dispersion relation $k(\omega)$, it also depends on the electron plasma frequency ω_{pe} and the concentration of ion species. These dependencies are evaluated and plotted in **Figure 1**, where we plot E_{Rmin} with $n = -1$ for a monochromatic left-handed EMIC wave propagating from the magnetic equator along a dipole field line up to magnetic latitude $\lambda_m = 30°$. We consider high ($\omega_{pe0}/\Omega_{e0} = 15$) and low ($\omega_{pe0}/\Omega_{e0} = 5$) densities at the equator, and

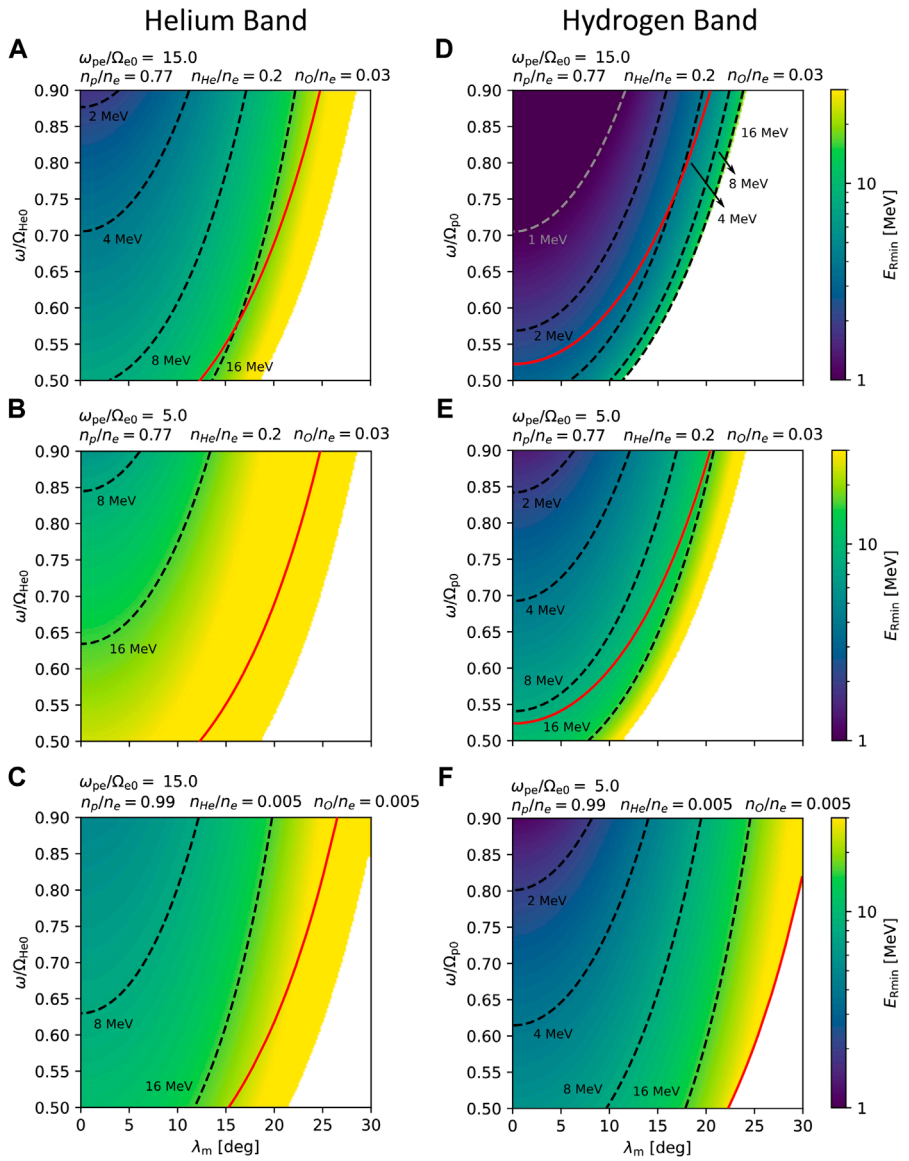

FIGURE 1
Minimum resonance energies E_{Rmin} of electrons interacting with a left-hand polarized parallel-propagating EMIC wave. Each panel shows a map of energies as a function of wave frequency and magnetic latitude. **(A)** Minimum resonance energies for interaction with a helium band wave in a high-density plasma with a high relative concentration of heavier ions—these conditions are used in our simulations. **(B)** Same as panel A, but in a low-density plasma. **(C)** Same as panel A, but with a low concentration of heavier ions. **(D–F)** E_{Rmin} for a hydrogen band wave under the same plasma conditions as in **(A–C)**, except for panel F, where both the electron density and heavier ion concentrations are kept low. In all panels, dashed lines represent energy contours, and the solid red line signifies the crossover frequency. Note that for oblique waves, the left-handed dispersion branch is coupled to the right-handed branch, so the energies right of the red curve would have to be calculated for right-hand polarized waves.

we compare the high concentrations of heavy ions ($n_p/n_e = 0.77$, $n_{He}/n_e = 0.2$, and $n_O/n_e = 0.03$), which were used in the simulations by Jordanova et al. (2008) and Bortnik et al. (2022), with lower concentrations ($n_p/n_e = 0.99$, $n_{He}/n_e = 0.005$, and $n_O/n_e = 0.005$). Latitudinal dependence of density follows the formula given by Denton et al. (2002), $n_e = n_{e0}(\cos\lambda_m)^{-2a}$, with $a = 0.5$ in the high-density case and $a = 1.0$ in the low-density case (and the relative ion concentrations remain constant). We observe that changes to the density, ion concentration, and frequency band manifest mostly through a rescaling of E_{Rmin}. Therefore, we limit our investigations to the helium band and choose the higher values of density ($\omega_{pe0}/\Omega_{e0} = 15 \sim n_{e0} = 134$ cm^{-3}) and ion concentrations, which is in agreement with the observations of Meredith et al. (2014) and Horwitz et al. (1981). The wave frequency is set to $\omega/\Omega_{He0} = 0.80 \sim 0.76$ Hz, a slightly higher value that allows the waves to reach higher latitudes before experiencing the polarization reversal. **Figure 1A** can be referred to for the particle motion analysis from **Section 3.1** to infer resonance latitudes of particles with a given energy propagating through quasiparallel waves; the plotted energy values can be further multiplied by $|n|$ to get higher-order resonance latitudes as long as the ultrarelativistic approximation from Eq. **1** is valid.

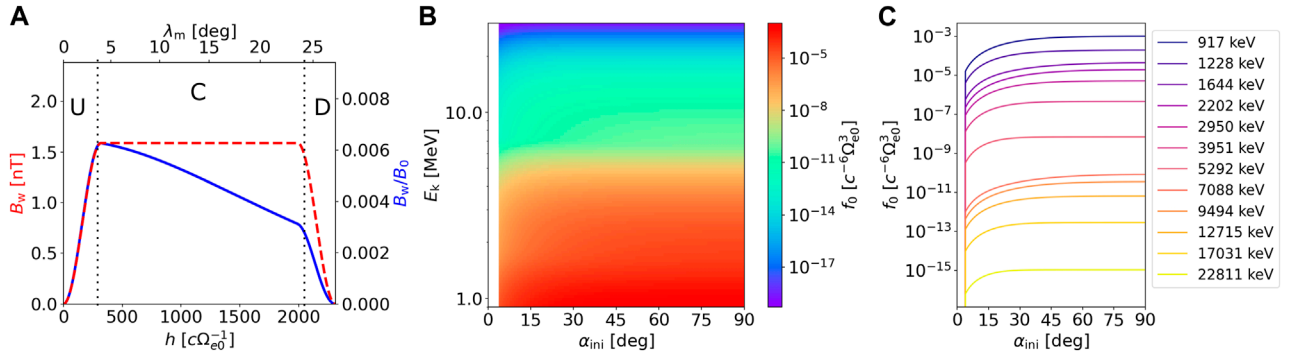

FIGURE 2
(A) Distribution of wave amplitudes along the field line. The wave experiences smooth growth in region *U*, stays constant in region *C* (1.6 nT in this example), and decreases back to zero in region *D*, as shown by the dashed red line. The solid blue line shows the relative wave amplitude with respect to the background field B_0. **(B)** Phase space density distribution at the equator plotted in the energy–pitch angle space. The empty loss cone corresponds to the white region at $\alpha_{ini} < \alpha_{loss} = 3.7°$. Normalized PSD is used in the simulation code. **(C)** Line plots of pitch angle profiles from the previous panel for representative energies. Note that the $\sin\alpha$ term from Jacobian is not included; therefore, the decrease in PSD near the loss cone indicates a positive pitch angle anisotropy.

Apart from the strong interaction near resonance energies, electrons can also experience non-resonant scattering due to wave amplitude gradients (Chen et al., 2016) or, equivalently, due to the spectral broadening of amplitude-modulated waves (An et al., 2022). To simplify our analysis, we suppress the non-resonant scattering by introducing a slow and smooth amplitude change at the edges of the wave packet. This is performed by multiplying the wave envelope by a half-period of the $\cos^2$ function, with a field-aligned distance from the minimum to the maximum of the function set to $\Delta h = 2{,}200$ km. Symbolically,

$$= B_{w0}\cos^2\left(\frac{\pi}{2}\left(\frac{h}{\Delta h} - 1\right)\right) \quad \text{for } 0 < h < \Delta h, \tag{2}$$

$$B_w(h) = B_{w0} \quad \text{for } \Delta h < h < (h_{max} - \Delta h), \tag{3}$$

$$= B_{w0}\cos^2\left(\frac{\pi}{2}\left(\frac{h - h_{max}}{\Delta h} + 1\right)\right) \quad \text{for } (h_{max} - \Delta h) < h < h_{max}. \tag{4}$$

This amplitude profile is similar to the tanh model in the study by Bortnik et al. (2022). The envelope shape is plotted in **Figure 2A**. The packet ends at a field-aligned distance h_{max}, where the normalized frequency reaches $\omega/\Omega_O = 1.25$. At this frequency, the helium wave is already right-handed, and the resonance energy of very oblique waves rapidly increases (Stix, 1992).

The test-particle simulation method is based on the solution of the Lorentz force law by a relativistic Boris algorithm with a phase angle correction, as described by Zenitani and Umeda (2018). The components of the electromagnetic wave field are defined according to the analysis of elliptically polarized waves presented by Omura et al. (2019); see also Eqs **8**–**11**, Eqs **15**–**19** in **Section 5**. Wave packet motion can be neglected on short timescales since the group velocity of EMIC waves is much smaller than the velocity of relativistic electrons. In forward-in-time simulations, the particles start either at the equator and propagate until they reach the end of the wave packet (or their mirror point) or at the end of the wave packet and propagate back to the equator. Mirroring particles are not allowed to return to the equator so that we can separate the resonant effects experienced by co-streaming and counter-streaming electrons. In both cases, the initial particle energy is spaced logarithmically from 900 keV to 30 MeV with 96 bins, initial pitch angles go from 0° to 90° (or 180°–90° for counter-streaming electrons) with 90 linear steps, and the initial gyrophases φ uniformly cover the full 360° angle with 72 steps. It is of note that the grid boundaries in the (E_k, α, φ) space represent bin edges. In backward-in-time simulations, the pitch angle range is limited to 0°–20° (or 180°–160° for counter-streaming electrons) with 90 linear steps, providing increased resolution of the loss cone ($\alpha_{loss} = 3.6°$ at the equator and 6.1° at the end of the packet). The time step of the Boris solver is adaptive and always stays at 128 steps per local electron gyroperiod.

The backward-in-time simulations are used to map the phase space density of an initial, unperturbed distribution to the final state and assess the PSD evolution due to resonant interactions (Nunn and Omura, 2015; Hanzelka et al., 2021). We assume that the initial hot (relativistic) distribution is in the form of a sum of subtracted bi-Maxwellian distributions that preserves phase space density along adiabatic trajectories (Summers et al., 2012; Omura, 2021). At a distance h, this distribution can be written for relativistic momenta $u_\parallel = \gamma v_\parallel$ and $u_\perp = \gamma v_\perp$ as

$$f(h, u_\parallel, u_\perp) = \sum_{i=1}^{N} f_i(h, u_\parallel, u_\perp), \tag{5}$$

with

$$\begin{aligned} & f_i(h, u_\parallel, u_\perp) \\ &= \frac{n_{he0i}}{(2\pi)^{3/2} U_{t\parallel i} U_{t\perp i}^2 (1 - \rho_i \beta_i)} \exp\left(-\frac{u_\parallel^2}{2U_{t\parallel i}^2}\right) \\ &\times \left[\exp\left(-\left(\frac{1 - B_{0eq}/B_0(h)}{2B_0(h) U_{t\perp i}^2} + \frac{B_{0eq}}{2B_0(h) U_{t\perp i}^2}\right) u_\perp^2\right)\right. \\ &\left. - \rho_i \exp\left(-\left(\frac{1 - B_{0eq}/B_0(h)}{2B_0(h) U_{t\parallel i}^2} + \frac{B_{0eq}}{2\beta_i B_0(h) U_{t\parallel i}^2}\right) u_\perp^2\right)\right]. \end{aligned} \tag{6}$$

We set $N = 5$ and choose the following values of distribution parameters: loss cone width $\beta_i = 0.5 \forall i$, loss cone height $\rho_i = 1.0 \forall i$, parallel and perpendicular thermal momenta $U_{t\parallel i}/c = U_{t\perp i}/c = \{0.2, 0.5, 1.0, 2.5, 9.0\}$, and hot electron density

$n_{he0i} = \{2.2, 0.22, 0.022, 0.0022, 2.2 \times 10^{-7}\}$ cm^{-3}. PSD inside the loss cone is set to zero for all values of h. The equatorial distribution is plotted in **Figure 2B** in the (E_k, α_{ini}) space. The energy profile up to 10 MeV is constructed to loosely follow the Van Allen Probes measurements analyzed by Zhao et al. (2019); however, the energy distribution is of little importance for EMIC-electron resonance since the acceleration caused by this interaction is negligible (Summers et al., 1998). Line plots of pitch angle distributions for several initial energies are presented in **Figure 2C**. Although each component of the initial distribution has a zero temperature anisotropy $A_t = U_{t\perp}^2/U_{t\parallel}^2 - 1$, the pitch angle anisotropy (Chen et al., 1999) can reach positive values up to approximately 0.6 due to the subtraction in the PSD distribution model. This model is consistent with the assumption that previous weaker wave–particle interactions already eroded the pitch angle profile.

3 Results

3.1 Advection and diffusion

When studying the non-linear interactions between plasma waves and charged particles, it is illustrative to start by inspecting individual trajectories. In **Figure 3**, we plot the spatial evolution of the equatorial pitch angle for electrons propagating through a high-amplitude ($B_{w0}/B_{0eq} = 0.0064$) moderately oblique ($\theta_k = 45°$) EMIC wave. The equatorial minimum resonance energy for this wave is $E_{Rmin} \approx 3.3$ MeV for $n = \pm 1$ and $E_{Rmin} \approx 7.1$ MeV for $n = \pm 2$. Particles starting at the equator with initial pitch angle $\alpha = 0.5°$ and energy $E_k = 3.95$ MeV experience a significant increase in equatorial pitch angle $\Delta\alpha_{eq} \approx 11°$ due to the $n = -1$ resonance, with almost no dependence on the initial gyrophase (**Figure 3A**). This is the advective behavior caused by force bunching, as previously described by Grach and Demekhov (2020), Grach et al. (2022), and Albert et al. (2022). This type of scattering has also been called "anomalous phase trapping" in the whistler-mode wave case studied by Kitahara and Katoh (2019).

Particles starting at larger pitch angles ($\alpha_{eq} = 29.5°$, **Figure 3B**) experience a large spread in α_{eq} across the gyrophases, exhibiting a predominantly diffusive behavior. The asymmetry in $\Delta\alpha_{eq}$ toward lower values is caused by phase locking of φ to the wave phase ψ, but the particles never become fully phase-trapped in this particular case. In **Figure 3C**, we increase the initial energy to $E_k = 8.51$ MeV and observe that particles first undergo scattering due to the $n = -2$ harmonic resonance and then encounter the $n = -1$ resonance at latitudes from 11° to 16°, resulting in pitch angle diffusion.

Figures 3D–F show particle trajectories of electrons starting at the end of the wave packet and streaming against the wave. Here, resonant interaction is enabled by the right-handed component of the elliptically polarized wave. Keeping the initial energies and initial equatorial pitch angles similar to the co-streaming case, we observe that the advective and diffusive effects of the $n = 1$ resonance are comparable to the $n = -1$ resonance. However, the maximum change in pitch angle is smaller, and the phase-locking effect does not appear. In the case with $E_k = 8.51$ MeV, the counter-streaming particles first encounter the stronger $n = 1$ resonance, and the weaker $n = 2$ resonance then has only a small effect on the spread in $\Delta\alpha_{eq}$.

To evaluate the pitch angle evolution of relativistic electrons across all initial pitch angles and energies, we introduce two statistical measures: the average $\langle\Delta\alpha_{eq}\rangle_\varphi$ (first central moment), which is related to the advection coefficient, and the standard deviation $\sigma_\varphi(\alpha_{eq})$ (second central moment), which is related to the diffusion coefficient. We intentionally eschew the standard advection and diffusion coefficients (Zheng et al., 2019) as they are often bounce-averaged in practical applications, while we do not let the particles finish the half-bounce, which is to separate between $n > 0$ and $n < 0$ resonances. The average change in equatorial pitch angle for co-streaming particles is plotted in **Figure 4** in (α_{ini}, E_k) coordinates, with each plot corresponding to one of the 3 combinations of wave amplitude and wave normal angle. Starting with quasiparallel propagation ($\theta_k = 5°$, **Figures 4A–C**), we first note the different scales of color bars, which have a range of $\pm\max_{(\alpha_{ini},E_k)}|\langle\Delta\alpha_{eq}\rangle_\varphi|$ separately for each plot. An outstanding feature, high positive advection, appears at low pitch angles near the $n = -1$ resonance, confirming the force-bunching effects observed on trajectories in **Figure 3A**. Another prominent feature is the two red (positive) and blue (negative) curved stripes that follow the dependence of $n = -1$ resonance energy on pitch angle. For the case with the largest wave amplitude (**Figure 4C**), the negative advection at higher pitch angles dominates over the positive one, indicating significant non-linear phase-trapping effects. It is of note that the strongest interaction happens slightly off-equator, where the wave amplitude peaks, corresponding to resonance energies slightly higher than the equatorial resonance energy plotted by green lines in **Figure 4**.

The appearance of strong negative advection associated with phase trapping can be explained through the behavior of the inhomogeneity parameter S. This parameter is proportional to the magnetic field gradient and inversely proportional to the wave amplitude and has a complicated dependence on wave dispersion properties (see Omura and Zhao (2012) and Omura (2021) for a detailed analysis and overview). When $|S|$ drops below 1, a resonance island forms in the phase space, and non-linear phase trapping becomes possible. For parallel wave propagation, the absolute value of the parameter decreases with the equatorial pitch angle. In the case of fundamental resonance $n = -1$, $|S|$ increases with the wave normal angle, while a decrease is seen in the case of harmonic resonances (Wang G. et al., 2017). However, scattering by very oblique waves becomes inefficient at high WNA. Therefore, the most favorable case for phase trapping is the fundamental resonance with high-amplitude quasiparallel waves at moderate-to-high pitch angles, as seen in **Figure 4C**. However, the inhomogeneity parameter is derived from the pendulum approximation of electron motion and cannot describe the behavior at low pitch angles. An extension of the electron motion analysis to small α based on the two-valley Hamiltonian was presented by Albert et al. (2021), where they concluded that as the initial pitch angle goes to zero, all particles are expected to experience force bunching, which can be understood as a special case of phase trapping.

The interaction with oblique waves (**Figures 4D–L**) introduces some new effects. First, we may notice the alternating blue and red vertical lines at high pitch angles, with almost no dependence on energy. These are the result of non-resonant oscillations at mirror

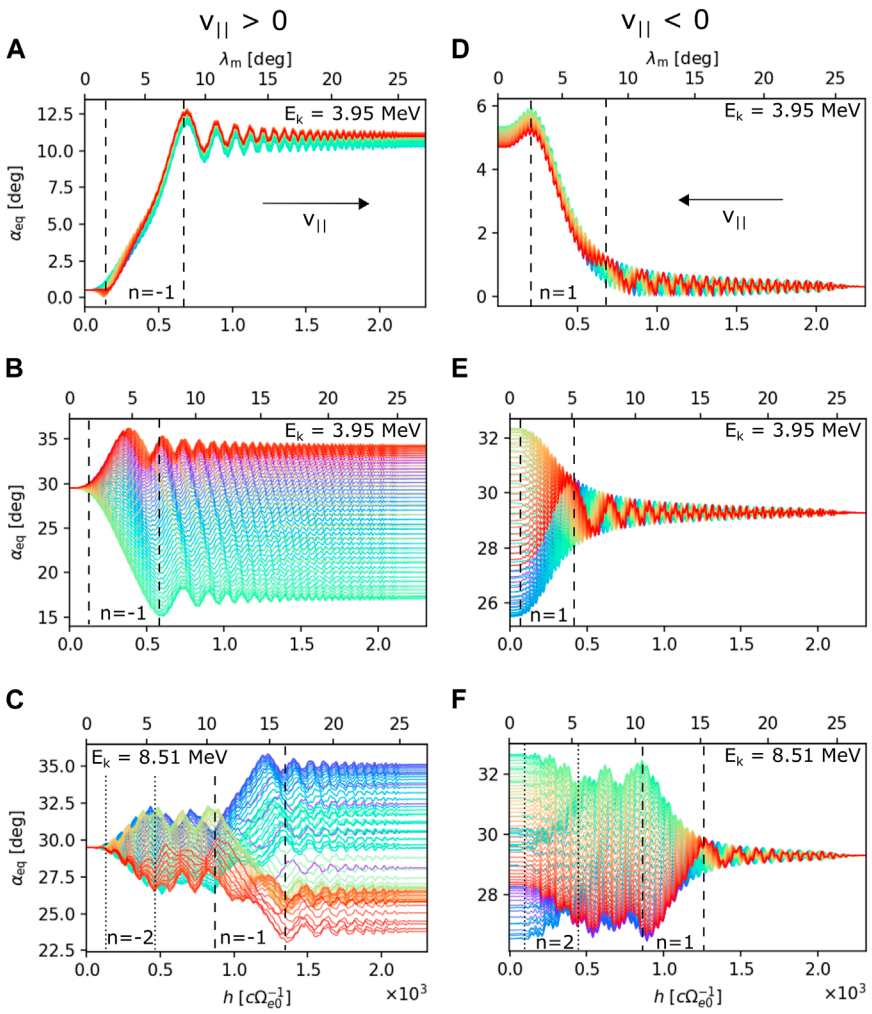

FIGURE 3
Trajectory examples showing the change in equatorial pitch angle over latitude due to interaction with a high-amplitude, moderately oblique wave (B_{w0}/B_{0eq} = 0.0064 and θ_k = 45°). **(A–C)** Electrons propagating along the wave (from the equator), and **(D–F)** propagation against the wave (toward the equator). In each panel, electrons have the same initial energy, pitch angle, and latitude, and the line colors represent the initial uniform sampling in gyrophase. Pairs of dashed lines represent the approximate spatial interval on which the fundamental cyclotron resonance produces strong scattering; for the harmonic resonances $n = \pm 2$, the interval is marked by dotted lines.

points and would completely disappear if the particles were allowed to bounce back to the equator—the lines are not relevant to our analysis of the cyclotron resonance and will be omitted in the following sections. Harmonic resonances become visible at higher amplitudes, adding new pairs of positive and negative advective stripes along the corresponding resonance energy curves. However, as the wave normal angle increases, advective effects disappear at higher pitch angles; for $\theta_k = 80°$, the average change in pitch angle becomes negligible for particles with $\alpha_{ini} > 30°$. Moreover, a fine stripe structure traversing the resonance energy curves appears in the high-amplitude plots. These new effects will be explained when discussing diffusive behavior, where their origin becomes more apparent.

The standard deviation in the equatorial pitch angle of co-streaming particles is plotted in Figure 5, following the panel format of Figure 4. The color bars of each individual panel go from zero to $\max_{(\alpha_{ini},E_k)}\sigma_\varphi(\alpha_{eq})$. Starting again with the quasiparallel propagation ($\theta_k = 5°$, Figures 5A–C), we can see the suppressed diffusion at low pitch angles, consistent with the lack of spread in pitch angles observed in the particle trajectories (Figure 3A). The largest values of $\sigma_\varphi(\alpha_{eq})$ are localized along the resonance energy curve, with slight changes appearing for B_{w0} = 1.6 nT at higher pitch angles, where the phase trapping and bunching effects may enhance or decrease the standard deviation. In the oblique case, diffusion at higher pitch angles gets weaker with growing wave normal angle. Unlike in the analysis of advection, we detect a clear structure of maxima and minima along each resonant curve, which is related to the zeros of Bessel functions that arise in the derivation of harmonic resonances (see Section 5; Eqs 12–14, Eqs 22–24). The fine structure appearing in the energy range of harmonic resonances is now also more evident, especially in the high-amplitude case (Figures 5F, I, L). By inspecting trajectory plots, its origin can be traced to multi-resonance interactions, when particles phase-organized by the resonance of order $|n|$ at lower latitudes experience a $|n-1|$ resonance at higher latitudes. It is of note that the fine structure is also present in the quasiparallel case, showing that

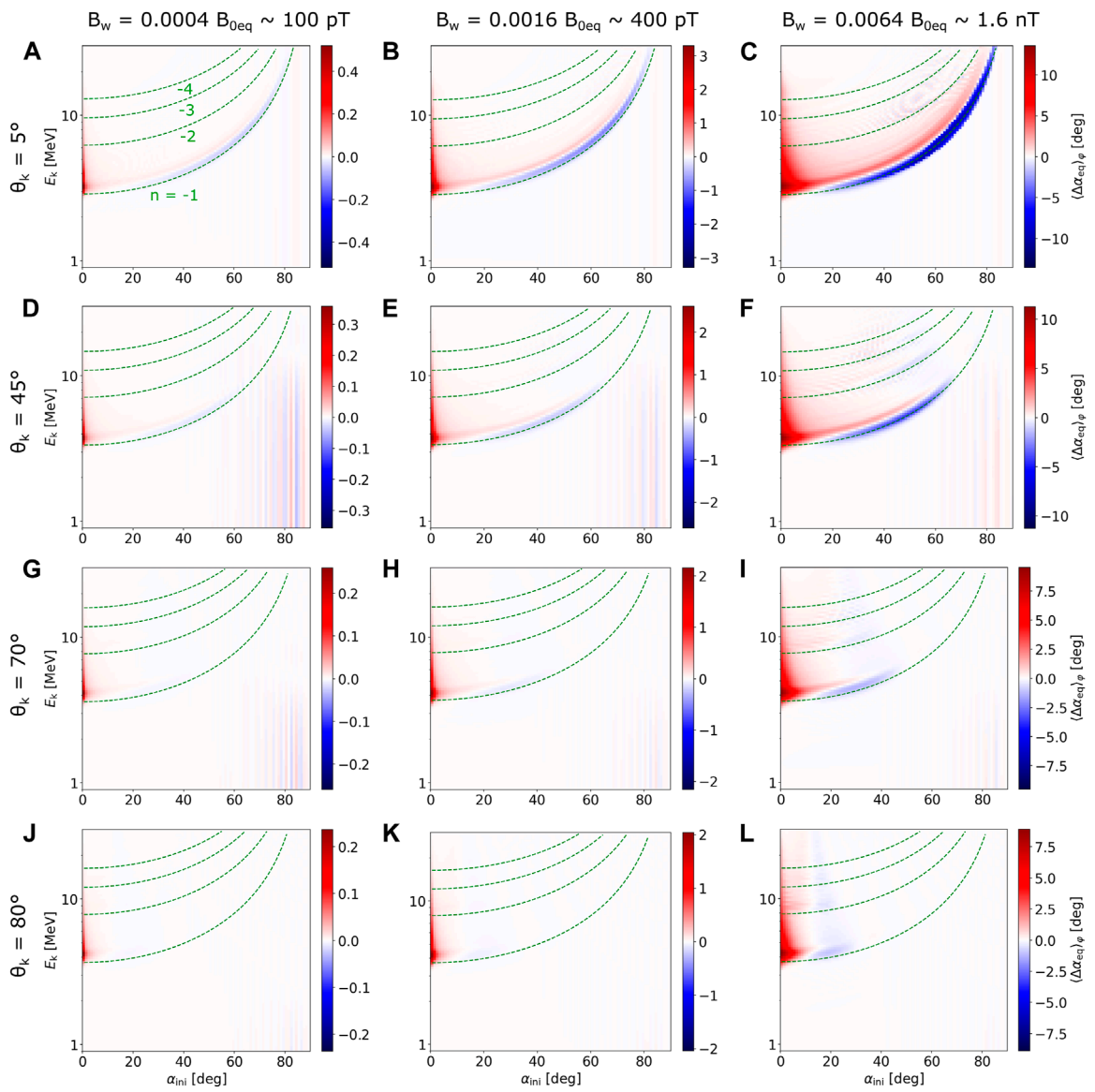

FIGURE 4
Average change $\langle\Delta\alpha_{eq}\rangle_\varphi$ in electron equatorial pitch angle for propagation along the EMIC wave packet (stopping point is the end of the wave packet or the mirror point). All particles start at the equator, so the initial pitch angle α_{ini} on the abscissa is equal to the initial α_{eq}. The columns are parametrized by wave amplitude (left to right: 100 pT, 400 pT, and 1.6 nT), and the rows are parametrized by wave normal angle (top to bottom: 5°, 45°, 70°, and 80°), forming a grid of twelve panels labeled **(A–L)**. The color bars associated with each panel range from $-\max_{(\alpha_{ini},E_k)}|\langle\Delta\alpha_{eq}\rangle_\varphi|$ to $+\max_{(\alpha_{ini},E_k)}|\langle\Delta\alpha_{eq}\rangle_\varphi|$. Vertical stripes at higher pitch angles are related to non-resonant oscillations at mirror points and would disappear after a complete half-bounce. The green dashed lines represent resonance energy curves calculated at $\lambda_m = 0°$.

the harmonic resonances are important even at WNA as low as $\theta_k = 5°$.

Concerning the strength of diffusion at lower pitch angles, the test-particle simulations show a decreasing trend in $\sigma_\varphi(\alpha_{eq})$ with increasing WNA at energies close to the $n = -1$ resonance. Harmonic resonances get stronger compared to fundamental resonances, but the overall diffusion at higher energies does not change much because the increased strength of near-equatorial harmonic interaction is compensated by the weaker fundamental resonance encountered at higher latitudes. An exception is the extreme ultrarelativistic energies ($E_k \gtrsim 15$ MeV), where the interaction with very oblique waves causes slightly stronger diffusion (**Figures 5I, L**). This behavior will impact the transport of electrons into the loss cone, as discussed in the next section.

3.2 Phase space density near the loss cone

The scattering effects analyzed in **Section 3.1** transport particles into the loss cone and, thus, contribute to the atmospheric precipitation of relativistic electrons. As described in **Section 2**, we trace particles back in time from the end of the wave packet to the equator and map the PSD values of a known equatorial distribution

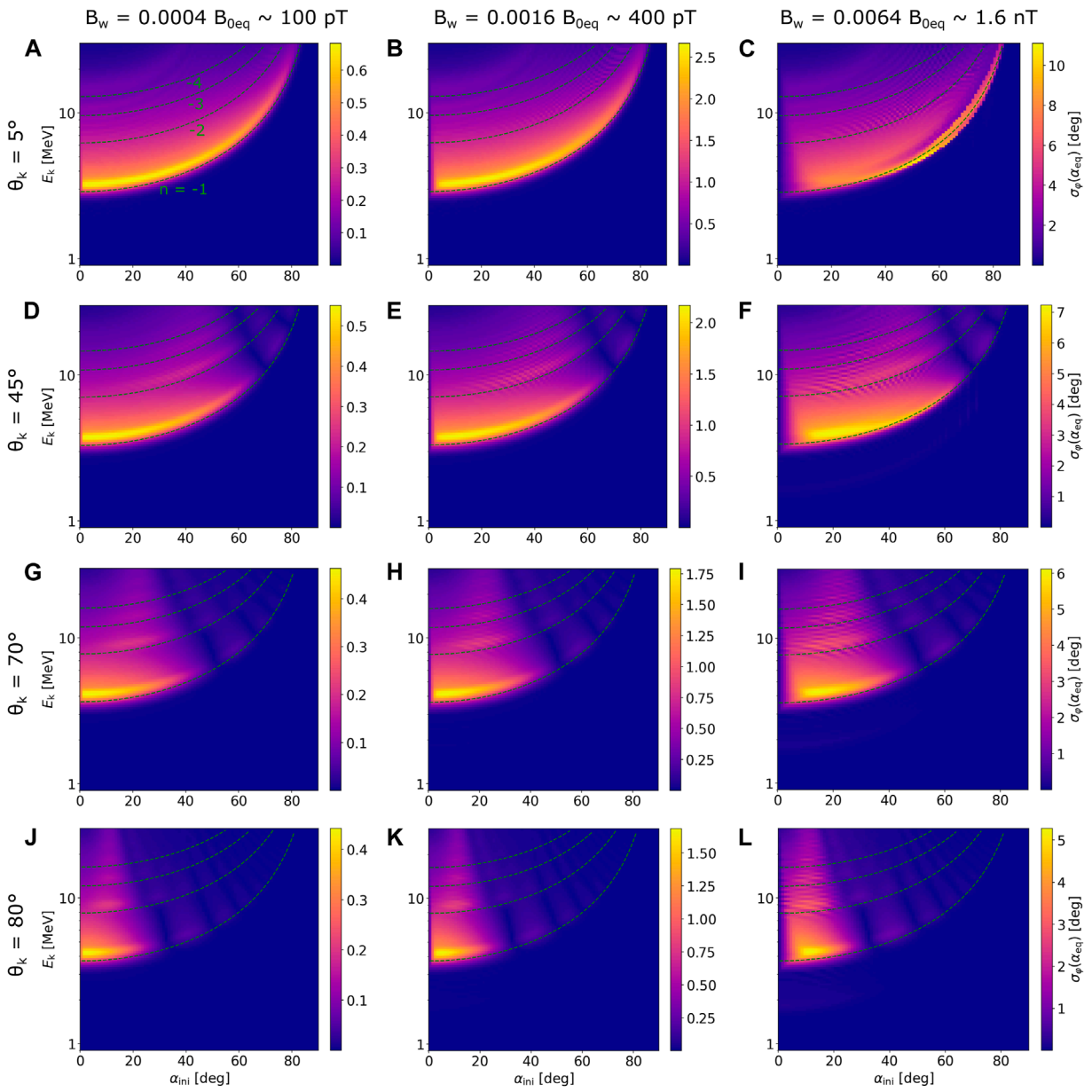

FIGURE 5
Standard deviation $\sigma_\varphi(\alpha_{eq})$ in electron equatorial pitch angle for propagation along the EMIC wave packet. **(A–L)** correspond to the same combinations of wave parameters as the respective panels in **Figure 4**, but the color bars in each panel now go from 0 to $\max_{(\alpha_{ini},E_k)}\sigma_\varphi(\alpha_{eq})$.

along particle trajectories to the starting point. The resulting PSD distributions at the end of the packet are plotted in **Figure 6** in the (α_{end}, E_k) space, where α_{end} is the initial pitch angle value in the sense of backward-in-time propagation. Since the number density of relativistic electrons in our model is not scaled to any specific spacecraft observation, we keep the normalized phase space density units $c^{-6}\Omega_{e0}^3$ used in the simulation code.

The quasiparallel EMIC wave manages to completely fill the loss cone near fundamental resonance energy when its amplitude is set to $B_{w0} = 400$ pT (**Figure 6B**). Increasing the amplitude to $B_{w0} = 1.6$ nT extends the range of energies, with the complete loss cone filling up to 10 MeV (**Figure 6C**). There are several noteworthy features to this strongly perturbed PSD distribution. First, we observe that particles near $E_k = 13$ MeV reach deeper into the loss cone, a feature not seen in the low-amplitude wave precipitation profile. This irregularity arises from the fast polarization reversal experienced by quasiparallel waves, which abruptly stops the resonant interaction—mild oscillations in $\sigma_\varphi(\alpha_{eq})$ across energy are seen in the top left corners of **Figures 5A–C**, but the effect on precipitation becomes clear only for strong waves. Second, the energy profile of trapped particles immediately above α_{loss} has a local maximum near the fundamental resonance—this peak appears due to pitch angle anisotropy when particles from high PSD regions at higher pitch angles undergo scattering toward lower pitch angles.

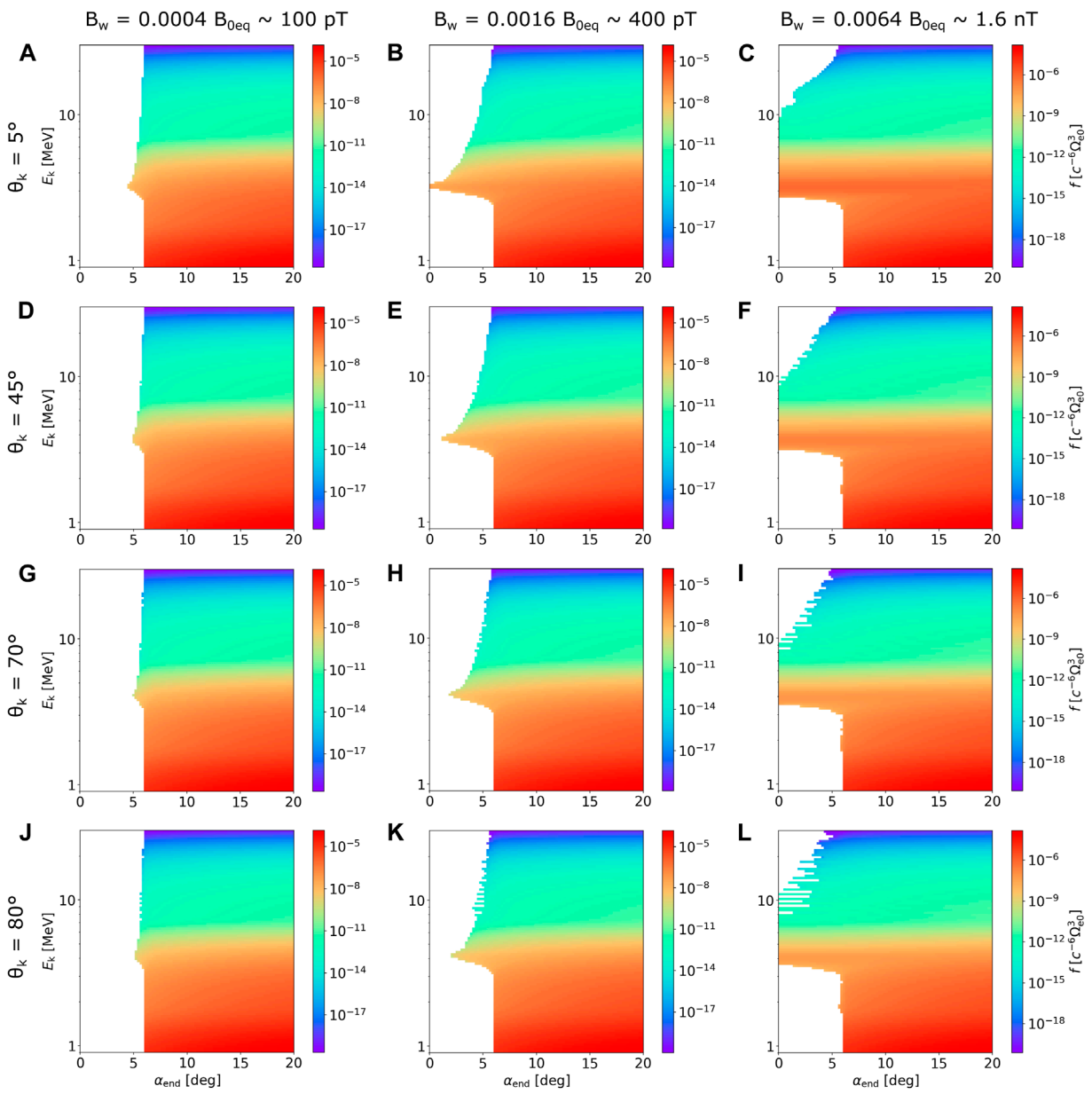

FIGURE 6
Electron phase space density distribution after resonant interaction with the EMIC wave captured at the end of the wave packet. Range in pitch angles is limited to 0°–20° to focus on the loss cone. **(A–L)** correspond to the same combinations of wave parameters as the respective panels in **Figures 4**, **5**, but because the co-streaming particles were traced back in time, the pitch angle α_{end} on the abscissa now represents the initial value at the end of the subpacket. The curious small bumps on the boundary between zero and finite PSD values near 2 MeV in **(F, I, L)** arise due to fractional resonances—see **Section 3.3**; **Figure 8**.

Third, the pitch angle distribution at energies from 3 MeV to 10 MeV is flattened, signifying a marked decrease in pitch angle anisotropy. Fourth, as a consequence of the third point, there is no apparent precipitation blocking, so phase space density inside the loss cone reaches the value of trapped particle PSD.

The lack of precipitation blocking contradicts the predictions of Bortnik et al. (2022) and may seem counterintuitive, especially after seeing the strong upward advection at low pitch angles in **Figure 4C**. To explain this observation, we consider the consequences of Liouville's theorem (i.e., constancy of PSD along phase space trajectories), which is known to hold in the Hamiltonian system of charged particles and electromagnetic waves constituting a collisionless plasma (Ichimaru, 2004). Let us first assume that a state has been reached where the PSD of precipitating and trapped electrons are equal at a certain energy. Because EMIC waves cannot efficiently accelerate electrons and change their energy, the PSD along trajectories will always be the same. Therefore, no amount of force bunching or other non-linear effects can disturb the uniform pitch angle distribution. If the PSD in the loss cone were initially higher than outside, the EMIC-induced scattering would mix the

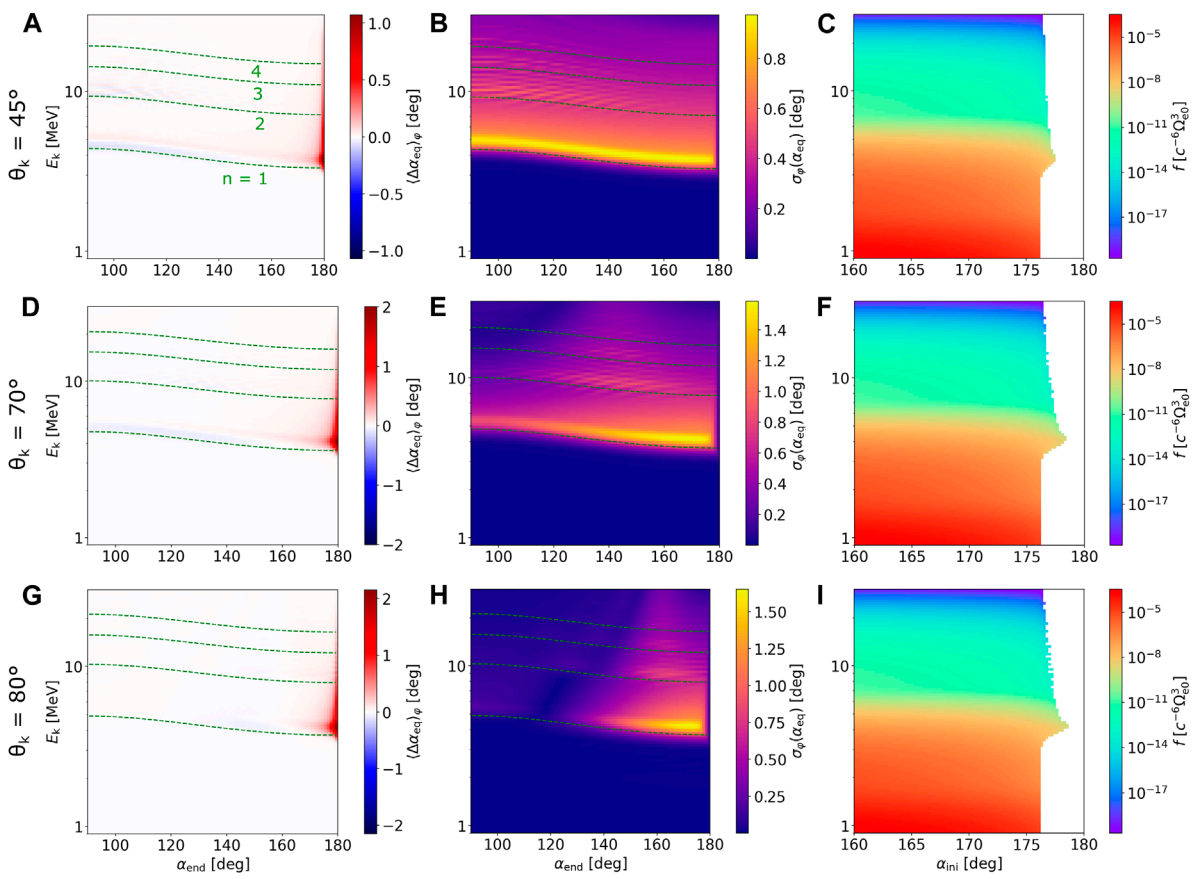

FIGURE 7
Effect of resonant interactions on electrons propagating against the EMIC wave packet. Physical quantities plotted in the first **(A, D, G)**, second **(B, E, H)**, and third **(C, F, I)** columns correspond to **Figures 4–6**, respectively. Only a single amplitude value is used, B_{w0} = 400 pT, and the wave normal parametrization over rows of panels skips the quasiparallel case θ_k = 5°, where the resonance effects would be negligible except for extremely ultrarelativistic energies ($E_k \gtrsim 15$ MeV). Note that because the electrons are now counter-streaming, the pitch angles on the abscissas α_{ini} and α_{end} were swapped, and particles with initial equatorial pitch angles >39° are missing from the forward-in-time simulations.

distribution, thus decreasing the precipitating PSD, but it would not push it below the value of the trapped PSD. Non-uniformity along the field line could complicate the argument if a broader range of $v_\parallel$ were considered, but the spread in $v_\parallel$ at low pitch angles at a fixed energy level is negligible. The apparent discrepancy between backward-in-time PSD mapping and the transport coefficients from **Section 3.1** can be resolved by considering the initial distributions of particles in the forward simulation. A uniform distribution in (α, E_k, φ) is not uniform in (v_x, v_y, v_z); consequently, the number of particles per unit velocity space volume in the forward simulation is much higher at lower pitch angles than at higher pitch angles. Symbolically, we can write the unit volume as (working in a non-relativistic setting for simplicity)

$$\mathrm{d}V = \mathrm{d}v_x \mathrm{d}v_y \mathrm{d}v_z = m^{-3/2}\sqrt{2E_k}\sin\alpha\,\mathrm{d}E_k\,\mathrm{d}\varphi. \tag{7}$$

The sin α term in the Jacobian expresses the smallness of velocity space volume near $\alpha = 0$. Therefore, the few test particles scattered into the loss cone can have the same weight as all the force-bunched particles escaping from the loss cone.

The effect of increasing obliquity on the PSD evolution displayed in **Figure 6D–L** agrees with the analysis of diffusion from **Section 3.1**. The loss cone is only partially filled near the fundamental resonance energy for waves with B_{w0} = 400 pT, and the range of complete loss cone filling with B_{w0} = 1.6 nT becomes narrower with increasing θ_k. The penetration of non-zero PSD into the loss cone at higher energies turns out to be mostly independent of wave normal angle, except for ultrarelativistic energies, where the very oblique waves show larger increases in precipitating PSD. The jagged boundary between finite and zero values of PSD in the case of strong, oblique waves (mainly **Figures 6I, L**) comes from the fine multi-resonance structure observed in corresponding diffusion plots in **Figures 5I, L**. The weak losses near half of the fundamental resonance energy are related to non-linear fractional resonances, which will be analyzed in depth in **Section 3.3**. Finally, we note that the rapid decrease of $\sigma_\varphi(\alpha_{eq})$ with rising WNA at higher pitch angles is not reflected in the PSD perturbations after a single quarter-bounce but might become important after multiple bounces due to the weak transport of particles from high-density regions of the initial anisotropic distribution.

So far, we have investigated electron scattering and related losses for propagation along the wave. However, as indicated by **Figures 3D–F**, counter-streaming particles are also efficiently

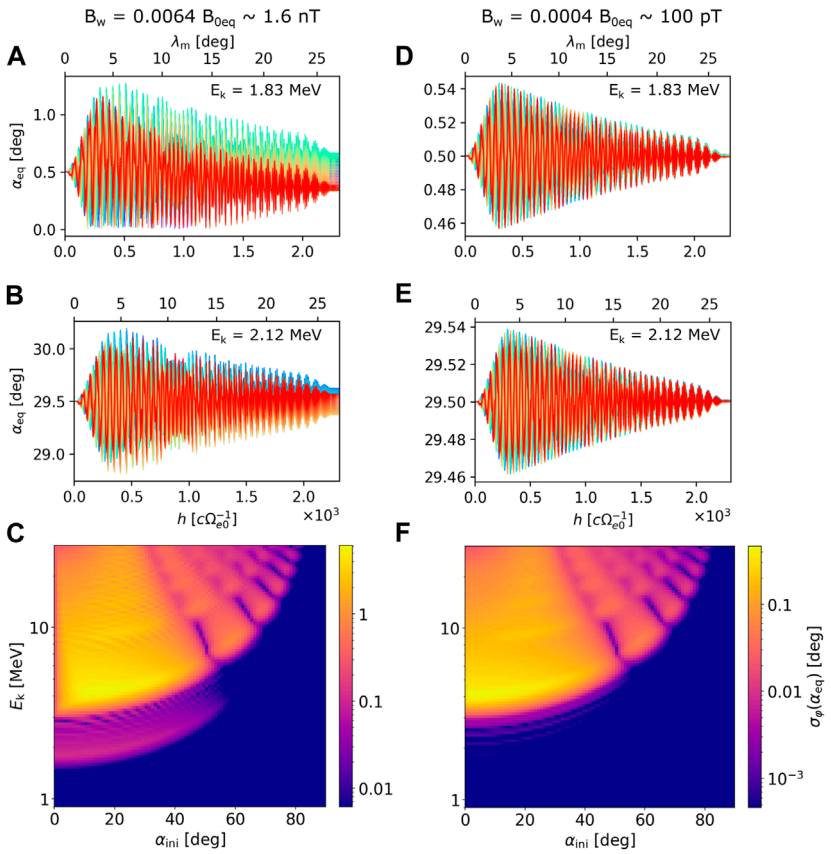

FIGURE 8
Behavior of fractional resonances explained by particle trajectories and standard deviations in equatorial pitch angle for an EMIC wave with wave normal angle $\theta_k = 70°$. **(A–B)** Changes in pitch angle along the field line at energies well below the equatorial fundamental resonance energy $E_{Rmin} \approx 4$ MeV. The wave amplitude is $B_{w0} = 1.6$ nT. **(C)** Standard deviation in equatorial pitch angle plotted in logarithmic scale that spans three orders of magnitude. Weak resonant effects near 2 MeV become apparent. **(D–F)** Same as **(A–C)**, but for a 16 times smaller wave amplitude. The resonant effects near $E_{Rmin}/2$ are now insubstantial compared to the fundamental resonance.

scattered by oblique EMIC waves, and significant particle losses are to be expected. In Figure 7, we plot the quantities $\langle \Delta\alpha_{eq} \rangle_{\varphi}$, $\sigma_{\varphi}(\alpha_{eq})$, and f for electrons streaming against the medium-amplitude wave ($B_{w0} = 400$ pT) with oblique wave vectors. The quasiparallel case is omitted because the right-handed wave component is negligible until the polarization crossover at higher latitudes is reached, where the resonance energies are already near the upper limit of our E_k range. The first thing to notice is that the forward-in-time propagating particles start away from the equator and have a limited range of equatorial pitch angles; therefore, the resonance energy curves appear stretched in the (α_{end}, E_k) space. Unlike in the co-streaming case, the advection and diffusion caused by fundamental resonance grow with increasing WNA because the polarization becomes more linear and the right-handed wave component gets larger. This behavior is reflected in the PSD plots, where the precipitating particles can travel deeper into the loss cone when interacting with very oblique waves. For $\theta_k = 80°$, the advection and diffusion (and, as a consequence, the electron losses) become comparable to the co-streaming case, showing the importance of $n > 0$ resonances for the analysis of relativistic electron precipitation by oblique EMIC waves.

3.3 Non-linear fractional resonances

In the discussion of Figures 6I, L, we mentioned the surprising detection of electron scattering into loss cone at energies $E_k \approx 2$ MeV, far below the fundamental resonance energy. These losses cannot have origin in non-resonant scattering because we use a slowly varying amplitude profile along h, and also because the non-resonant scattering would show as a broadening of the fundamental resonance and not as a separate peak in energy profile (An et al., 2022). Trajectories of particles with energies $E_k = 1.83$ MeV and $E_k = 2.12$ MeV propagating along the high-amplitude wave with $\theta_k = 70°$ (Figures 8A, B) reveal a spread in α_{eq} that does not disappear even after the particles leave the wave field. This spread is somewhat weaker than the oscillations caused by the fundamental cyclotron resonance. The oscillations can be understood as the maximum possible non-resonant scattering in a wave with a rectangular amplitude distribution along the field line.

Since the spread in α_{eq} is too small to be clearly visible in the $\sigma_{\varphi}(\alpha_{eq})$ plot from Figure 5I, we re-plot the diffusion with a logarithmic color bar and show the results in Figure 8C. It becomes apparent that we are observing a new type of resonance with

a minimum resonance energy near $E_{Rmin}/2$. This new resonance causes much weaker scattering than the fundamental resonance but is roughly comparable to non-resonant oscillations. However, when we look at the particle trajectories and diffusion from the simulation with a small-amplitude wave ($B_{w0} = 100$ pT), the new resonance becomes much weaker than the non-resonant oscillations, and the corresponding $\sigma_\varphi(\alpha_{eq})$ values are more than three orders of magnitude below the fundamental resonance effect (**Figures 8D–F**).

Based on the numerical observations presented in **Figure 8**, we identify the new behavior as the non-linear fractional resonance of order $n = -1/2$. A simplified analytical derivation is provided in **Section 5**, where we also identify fractional resonances of order $n = \{\pm 1/3, \pm 1/2, \pm 2/3, \pm 3/2\}$ and suggest that the non-linear resonance energy spectrum is dense in the sense of rational numbers. These resonances seem to be analogous to the sub-cyclotron resonance of electrons with whistler waves described within the Hamiltonian framework by Fu et al. (2015). The concept of fractional resonances does not appear in quasilinear theory because it arises from integration along perturbed trajectories (compare with the integration along unperturbed trajectories employed in quasilinear theory, as mentioned in the theoretical works of Kennel and Engelmann (1966) and Allanson et al. (2022)). In the non-linear treatment of whistler-electron scattering presented by Omura et al. (2019), an integer resonance is chosen first, and the non-linear scattering effects are obtained from perturbations of near-resonant electrons. Suppose we instead implement a model of large perturbations without specifying a resonance velocity/energy, as in the example given in Eqs **27**, **28**, and proceed to analyze power transfer between waves and particles (which is directly related to pitch angle scattering through resonance diffusion curves, as explained by Summers et al. (1998)). In that case, fractional resonances will arise from the Bessel function expansion of gyrophase evolution. An important property of the $n = -1/2$ is the scaling of scattering strength with the square of wave amplitude—theoretically proven in Eqs **45**, **46**—which differs from the known linear dependence for integer resonances. The non-linear fractional resonances are, thus, expected to play a role only in precipitation induced by very strong oblique waves.

4 Summary and discussion

We have numerically analyzed the dependence of relativistic electron scattering on the wave normal angle and magnetic field amplitude of helium band EMIC waves. Unlike in the previous studies by Wang G. et al. (2017); Lee et al. (2018), we allow for very oblique wave normal angles, $\theta_k = 70°$ and $\theta_k = 80°$, and keep the amplitudes more moderate ($B_{w0}/B_{0eq} < 1\%$). The presented analysis of advective and diffusive behavior is comparable to the analysis by Bortnik et al. (2022), where, however, much lower energy and pitch angle resolution was adopted for parallel waves only. On the other hand, the results of Bortnik et al. (2022) include a simulation of scattering induced by hydrogen band waves. We opted not to show figures from our hydrogen band simulations, as the only major difference from the helium band case is the shift in resonance energies. The input parameters for hydrogen band simulations differed in the following: wave frequency $\omega = 0.6\Omega_{p0} = 2.3$ Hz, plasma frequency $\omega_{pe0}/\Omega_{e0} = 5$, and density model coefficient $a = 1.0$, and h_{max} is at the point where $\omega = 1.25\Omega_{He}$. The evaluation of diffusive and advective properties and PSD perturbations similar to **Figures 4–7** is available in the **Supplementary Material**.

Our overall results can be summarized in three blocks:

1) Confirmation of previous results:
   a) Harmonic resonances $n < -1$ substantially affect the scattering of relativistic electrons at low pitch angles for waves with wave normal angles as small as $\theta_k = 5°$ (Wang G. et al., 2017). The contribution from $n > 0$ resonances requires at least moderate obliquity to become significant.
   b) Positive advection of resonant particles at very low pitch angles was detected and shown to dominate over diffusion as wave amplitude increases. This is the effect described as boundary reflection by Zhu et al. (2020) and non-linear force bunching by Grach and Demekhov (2020) and Bortnik et al. (2022).
   c) The advective behavior of resonant particles can be positive or negative, depending on their initial pitch angle and energy (Lee et al., 2018). Particles that start at energies lower than the resonance energy for a given pitch angle will, on average (over gyrophases), experience a decrease in pitch angle, while particles starting at higher energies will encounter the resonance curve at higher latitudes and experience an average increase in pitch angle. This is visualized by the blue–red stripe pairs in **Figure 4**.
   d) Increasing obliquity weakens the effects of $n = -1$ resonance but enhances the resonant interaction for $|n| > 1$ and $n = 1$ (Wang G. et al., 2017).
   e) Crossings of multiple resonance energies during one passage through the waves result in a more stochastic pitch angle evolution, described by Lee et al. (2018) as "complicated and time-dependent phase trapping and bunching effects." Under our simplified wave model, these multi-resonance effects appear after one quarter-bounce as a fine structure in the plots of advection and diffusion when the EMIC wave is strong and oblique (**Figures 4I, L**, **5I, L**).
2) Disagreement with previous results:
   a) Oblique waves seem to weaken the advection effects at low pitch angles, contrary to the observations by Lee et al. (2018).
   b) We do not observe any effects of precipitation blocking in the PSD analysis (**Figure 6**), which is in disagreement with the suggestion presented by Bortnik et al. (2022) that force bunching caused by strong EMIC waves will decrease the electron fluxes/PSD at low pitch angles.
3) New discoveries:
   a) Losses of relativistic electrons by quasiparallel waves are comparable to losses induced by oblique waves (**Figure 6**). This behavior changes for ultrarelativistic electrons ($E_k \gtrsim 15$ MeV, depending on wave parameters), where the very oblique waves cause stronger precipitation.
   b) Very oblique waves cannot efficiently scatter electrons at higher pitch angles ($\alpha > 30°$ for $\theta_k = 80°$, see **Figure 5J–L**). Transport from high PSD regions at large pitch angles toward the loss cone is facilitated only by quasiparallel waves.
   c) Very oblique waves scatter co-streaming and counter-streaming electrons with similar efficiency due to the high

ellipticity, or in other words, due to comparable magnitude of right-handed and left-handed amplitude components (compare **Figure 6K** with **Figure 7I**).

d) High-amplitude oblique waves can scatter electrons below minimum resonance energy through non-linear fractional resonances. The pitch angle changes caused by $n = -1/2$ scale with the square of wave amplitude are faster than the linear scaling for $n = -1$ resonance.

When comparing our results to previous literature, a few points must be made to avoid confusion: under our sign convention, the interaction of right-handed waves with electrons happens at resonances of order $n \geq 1$, and the interaction with left-handed waves corresponds with $n \leq 1$, opposite to the convention used by Wang G. et al. (2017). Furthermore, the strongest wave we use has a relative amplitude $B_{w0}/B_0 = 0.64\%$, while that by Lee et al. (2018) goes up to 10% (above the amplitude of the extremely intense EMIC wave observations presented by Engebretson et al. (2015)); as a consequence, phase trapping has minimal impact on our PSD mapping results, especially for oblique waves.

The disagreement in the dependence of advection on obliquity between our results and those of Lee et al. (2018) comes from the different approaches to wave modeling. Lee et al. (2018) implement one wave field that is elliptically polarized but remains parallel, and another wave field where the wave normal angle is non-zero, but the polarization remains circular. According to the cold plasma dispersion relation, which is strictly followed in our study, oblique waves always have elliptical polarization (linear being considered as a special case of elliptical), and parallel waves are always circularly polarized, except for the singularity at the crossover frequency. Deviations from circular polarization decrease the advection effects, reconciling our results with those of Lee et al. (2018).

The lack of precipitation blocking is demonstrated in **Section 3.2** through numerical PSD mapping and supported by arguments based on Liouville's theorem. The concept of EMIC precipitation blocking was likely first introduced by Grach and Demekhov (2020), who concluded that due to competition between phase trapping and force bunching, the precipitating fluxes would reach the strong diffusion limit, with no apparent decrease near $\alpha = 0°$. Our observations corroborate this conclusion, except that the transport of particles to low pitch angles is due to the symmetric ("diffusive") scattering, as observed in **Figure 3B**, where the particles stay in the phase-trapping region only for a short time and do not become phase-locked. Bortnik et al. (2022) suggested that Van Allen Probes (RBSP) observations of dips in precipitating flux by Zhu et al. (2020) could be explained by force bunching. However, the EMIC-induced precipitating electron flux shown by Zhu et al. (2020) has a local maximum at $\alpha = 0°$, while the force-bunching effects should be most effective at removing particles from this region. The spacecraft observations are consistent with the simulation results of Grach and Demekhov (2020), where the PSD distribution sometimes peaked inside the loss cone. This effect is not clearly visible in the perturbed distribution from **Figure 6C** because it requires strong phase trapping. Such trapping may be possible with $B_w/B_0 > 1\%$ rising-tone EMIC emissions reported by Zhu et al. (2020) but not with the monochromatic waves at moderate amplitudes implemented in our simulations. We recall that transport caused by phase trapping is non-local, allowing the mixing of phase space density from distant points along the field line and violating the assumption of localized scattering processes that were used in our simplified argument against precipitation blocking (**Section 3.2**). Finally, we must emphasize that the force bunching indeed removes particles from the loss cone, but the important quantity for precipitation is the net effect of upward and downward pitch angle motion.

Most of our new and original results are related to very oblique propagation, which was omitted in previous literature on EMIC-induced precipitation. We have shown that the precipitation of relativistic electrons by very oblique waves is comparable to quasiparallel waves, except for electron energies corresponding to high-order resonances ($n < -4$). Note that we are not making a comparison to the routinely investigated purely parallel waves with $\theta_k = 0°$ because *in situ* spacecraft measurements (Allen et al., 2015) always show at least a small amount of obliquity. Nevertheless, when we consider the increased scattering effects of very oblique waves on counter-streaming electrons, bounce-averaged diffusion might be significantly increased compared to quasiparallel waves. Unfortunately, we do not know how strong the oblique EMIC waves can be, as we are not aware of any study that shows the distribution of wave power over WNA and frequencies. Van Allen Probes observations presented by Saikin et al. (2015) suggest that strong helium band waves (average wave power >0.1 nT^2/Hz) have a lower average WNA than weak waves (average wave power from 0.01 nT^2/Hz to 0.1 nT^2/Hz). Nevertheless, strong waves with $\theta_k > 60°$ at $L = 5$ were occasionally detected, justifying our parameter choice.

To our knowledge, the non-linear fractional resonances were never described before in the context of EMIC–electron interaction. They are, however, conceptually identical to the sub-cyclotron resonance of electrons with whistler waves, which was studied by Fu et al. (2015). Kramer et al. (2012) detected fractional resonances in fusion devices in the context of ion drift-orbit resonance with magnetohydrodynamic waves. Given the different physical settings, the theoretical approach taken by Kramer et al. (2012) is not the same as ours, but they arrive at a formula consisting of a multi-index sum over a product of Bessel functions, not unlike our Eqs **38**–**40**. Non-linear interactions at fractions of the plasma frequency were theoretically described by Lewak and Chen (1969) and used to explain the observations made by the Alouette II spacecraft. The EMIC-electron fractional resonances, especially the resonance of order $n = -1/2$, might provide a possible explanation for the precipitation of subrelativistic electrons (Hendry et al., 2017; 2019; Capannolo et al., 2019) if we consider a high-density plasma where the fundamental resonance energy can drop to 1 MeV (compare with the ω_{pe} dependence plotted in **Figure 1**). However, to evaluate how competitive this mechanism is in comparison to the non-resonant scattering (Chen et al., 2016; An et al., 2022), we need to obtain a realistic distribution of wave power/amplitude over wave normal angles, as mentioned earlier. Endeavors in this direction are left for future study.

5 Derivation of fractional resonances

The existence of fractional resonances from **Section 3.3** can be derived from the equations of motion for an electron interacting

with an elliptically polarized wave. We start by defining the wave fields.

$$\boldsymbol{E}_{\mathbf{w}} = \hat{\boldsymbol{x}} E_x^{\mathrm{w}} \sin\psi - \hat{\boldsymbol{y}} E_y^{\mathrm{w}} \cos\psi + \hat{\boldsymbol{z}} E_z^{\mathrm{w}} \sin\psi, \tag{8}$$

$$\boldsymbol{B}_{\mathbf{w}} = \hat{\boldsymbol{x}} B_x^{\mathrm{w}} \cos\psi + \hat{\boldsymbol{y}} B_y^{\mathrm{w}} \sin\psi - \hat{\boldsymbol{z}} B_z^{\mathrm{w}} \cos\psi, \tag{9}$$

where $E_x^{\mathrm{w}} < 0$ and $B_y^{\mathrm{w}} < 0$ for left-hand polarized waves. The three hatted vectors form the standard basis of a Cartesian system. The wave phase seen by a particle with gyrophase φ is

$$\psi = \omega t - k_z z - k_x \rho_{\mathrm{L}} \sin\varphi + \mathrm{const.} \equiv \psi_{\mathrm{B}} - \beta \sin\varphi, \tag{10}$$

and it includes the effects of finite Larmor radius (FLR) ρ_{L} through the quantity

$$\beta = \frac{\gamma v_\perp k_x}{\Omega_{\mathrm{e}}}, \tag{11}$$

while ψ_{B} represents the wave phase at the gyrocenter. The constant initial phase will be dropped in the following analysis.

The equations of motion for an electron with the gyrocenter at $x = y = 0$ propagating through the wave field on a homogeneous background field $\boldsymbol{B}_0 \| \hat{\boldsymbol{z}}$ (field inhomogeneity is not important for the following resonance spectrum analysis) can be written as

$$\frac{\mathrm{d}(\gamma v_z)}{\mathrm{d}t} = \frac{e}{m}\left(v_\perp B_{\mathrm{R}}^{\mathrm{w}} \sin(\varphi - \psi) + v_\perp B_{\mathrm{L}}^{\mathrm{w}} \sin(\varphi + \psi) - E_z^{\mathrm{w}} \sin\psi\right), \tag{12}$$

$$\frac{\mathrm{d}(\gamma v_\perp)}{\mathrm{d}t} = \frac{e}{m}\left((U_{\mathrm{R}} - v_z) B_{\mathrm{R}}^{\mathrm{w}} \sin(\varphi - \psi) + (U_{\mathrm{L}} - v_z) B_{\mathrm{L}}^{\mathrm{w}} \sin(\varphi + \psi)\right), \tag{13}$$

$$\frac{\mathrm{d}\varphi}{\mathrm{d}t} = \frac{e}{m}\left(\frac{U_{\mathrm{R}} - v_z}{\gamma v_\perp} B_{\mathrm{R}}^{\mathrm{w}} \cos(\varphi - \psi) + \frac{U_{\mathrm{L}} - v_z}{\gamma v_\perp} B_{\mathrm{L}}^{\mathrm{w}} \cos(\varphi + \psi) - \frac{B_z^{\mathrm{w}}}{\gamma} \cos\psi + \frac{B_0}{\gamma}\right). \tag{14}$$

Here, we decomposed the wave field into left-hand and right-hand circularly polarized components (Omura et al., 2019)

$$\boldsymbol{E}_{\mathbf{R}} = E_{\mathrm{R}}^{\mathrm{w}} (\hat{\boldsymbol{x}} \sin\psi - \hat{\boldsymbol{y}} \cos\psi), \quad E_{\mathrm{R}}^{\mathrm{w}} = \frac{E_x^{\mathrm{w}} + E_y^{\mathrm{w}}}{2}, \tag{15}$$

$$\boldsymbol{E}_{\mathbf{L}} = E_{\mathrm{L}}^{\mathrm{w}} (-\hat{\boldsymbol{x}} \sin\psi - \hat{\boldsymbol{y}} \cos\psi), \quad E_{\mathrm{L}}^{\mathrm{w}} = \frac{E_y^{\mathrm{w}} - E_y^{\mathrm{w}}}{2}, \tag{16}$$

$$\boldsymbol{B}_{\mathbf{R}} = B_{\mathrm{R}}^{\mathrm{w}} (\hat{\boldsymbol{x}} \cos\psi + \hat{\boldsymbol{y}} \sin\psi), \quad B_{\mathrm{R}}^{\mathrm{w}} = \frac{B_x^{\mathrm{w}} + B_y^{\mathrm{w}}}{2}, \tag{17}$$

$$\boldsymbol{B}_{\mathbf{L}} = B_{\mathrm{L}}^{\mathrm{w}} (\hat{\boldsymbol{x}} \cos\psi - \hat{\boldsymbol{y}} \sin\psi), \quad B_{\mathrm{L}}^{\mathrm{w}} = \frac{B_x^{\mathrm{w}} - B_y^{\mathrm{w}}}{2}, \tag{18}$$

and defined the ratios

$$U_{\mathrm{R}} = \frac{E_{\mathrm{R}}^{\mathrm{w}}}{B_{\mathrm{R}}^{\mathrm{w}}}, \quad U_{\mathrm{L}} = \frac{E_{\mathrm{L}}^{\mathrm{w}}}{B_{\mathrm{L}}^{\mathrm{w}}}, \tag{19}$$

which are related to phase velocities (they reduce exactly to phase velocities in the case of circularly polarized parallel-propagating waves). In further calculations, we will also use the normalized amplitude components $\Omega_{\mathrm{R}}^{\mathrm{w}} = B_{\mathrm{R}}^{\mathrm{w}} e/m$, $\Omega_{\mathrm{L}}^{\mathrm{w}} = B_{\mathrm{L}}^{\mathrm{w}} e/m$, and $\Omega_z^{\mathrm{w}} = B_z^{\mathrm{w}} e/m$.

The average change in electron kinetic energy per one wave period T can be expressed as

$$\left\langle \frac{\mathrm{d}E_{\mathrm{k}}}{\mathrm{d}t} \right\rangle_T = -\frac{e}{T}\int_0^T \mathrm{d}t (\boldsymbol{v} \cdot \mathbf{E}_{\mathbf{w}}) = -\frac{e}{T}\int_0^T \mathrm{d}t \left(v_\perp (E_{\mathrm{R}}^{\mathrm{w}} - E_{\mathrm{L}}^{\mathrm{w}}) \cos\varphi \sin\psi - v_\perp (E_{\mathrm{R}}^{\mathrm{w}} + E_{\mathrm{L}}^{\mathrm{w}}) \sin\varphi \cos\psi + v_z E_z^{\mathrm{w}} \sin\psi\right), \tag{20}$$

where we used the decompositions from Eqs 15–18. Let us denote the integrand I and restate it in the form

$$I = -\frac{e}{T}\left(-v_\perp (E_{\mathrm{R}}^{\mathrm{w}} \sin(\varphi - \psi) + E_{\mathrm{L}}^{\mathrm{w}} \sin(\varphi + \psi)) + v_z E_z^{\mathrm{w}} \sin\psi\right). \tag{21}$$

We may now apply the Jacobi–Anger expansion (Abramowitz and Stegun, 1965) and express the trigonometric functions in terms of Bessel functions of the first kind.

$$\sin(\varphi - \psi) = \sin(\varphi - \psi_{\mathrm{B}} + \beta \sin\varphi) = \sum_{n=-\infty}^{\infty} J_{n-1}(\beta) \sin\zeta_n = \sum_{n=-\infty}^{\infty} J_n(\beta) \sin\zeta_{n+1}, \tag{22}$$

$$\sin(\varphi + \psi) = \sin(\varphi + \psi_{\mathrm{B}} - \beta \sin\varphi) = -\sum_{n=-\infty}^{\infty} J_{n+1}(\beta) \sin\zeta_n = -\sum_{n=-\infty}^{\infty} J_n(\beta) \sin\zeta_{n-1}, \tag{23}$$

$$\sin(\psi) = \sin(\psi_{\mathrm{B}} - \beta \sin\varphi) = -\sum_{n=-\infty}^{\infty} J_n(\beta) \sin\zeta_n, \tag{24}$$

where

$$\zeta_n = n\varphi - \psi_B \tag{25}$$

is the relative phase angle for the nth resonance. Note that while the changes in kinetic energy of electrons interacting with EMIC waves are typically negligible, these small energy changes are directly related to large changes in pitch angle through the particle motion along resonant diffusion curves (Summers et al., 1998).

The non-linear effect of individual resonances is usually studied by performing an expansion in v_z about the nth resonance velocity.

$$V_{\mathrm{R}n} = \frac{1}{k_z}\left(\omega + \frac{n\Omega_{\mathrm{e}}}{\gamma}\right). \tag{26}$$

Here, we instead expand the gyrophase to the first order of perturbations due to wave—particle interactions and plug them into the Jacobi—Anger expansions from Eqs 22–24. We write $\varphi \approx \varphi_0 + \varphi_1$ with

$$\frac{\mathrm{d}\varphi_0}{\mathrm{d}t} = \frac{\Omega_{\mathrm{e}}}{\gamma}, \tag{27}$$

$$\frac{\mathrm{d}\varphi_1}{\mathrm{d}t} = -\frac{v_z}{\gamma v_\perp} \Omega_{\mathrm{R}}^{\mathrm{w}} \cos(\varphi - \psi) - \frac{v_z}{\gamma v_\perp} \Omega_{\mathrm{R}}^{\mathrm{w}} \cos(\varphi + \psi), \tag{28}$$

where we have used the inequalities $|U_{\mathrm{L}}| \ll |v_z|$ and $|U_{\mathrm{R}}| \ll |v_z|$ for EMIC waves and relativistic electrons, and we also removed the Ω_z^{w} term by focusing on low pitch angle regions where $\Omega_z^{\mathrm{w}} \ll \Omega_{\mathrm{R,L}}^{\mathrm{w}} v_z / \gamma v_\perp$. For simplicity, we will further neglect the perturbations to v_z and $v_\perp$. In the case of $v_\perp$, the factors in front of sines in Eq. 13, divided by $\gamma v_\perp$, are the same as the factors in front of cosines in Eq. 14, suggesting that the relative perturbations in $v_\perp$ and φ are comparable. However, $v_\perp$ enters the computation either through $\mathrm{d}\varphi_1/\mathrm{d}t$, so we can consider that perturbation to be of second order, or through β, which simply scales the FLR effects and can, thus, be kept constant without losing information about resonant behavior. In the case of v_z, the approximation can be justified only for low pitch angles since comparing the factors in Eqs 12, 14 sets the requirement

$v_\perp/v_z \ll v_z/v_\perp$ (v_z enters directly into ψ through $k_z z = k_z v_z t$, so the perturbation would be of the first order if we did not use the low α approximation).

To cut off the perturbation expansion, we replace ψ with ψ_B in Eqs 27, 28. Then, by integrating φ_1 over time, we can obtain the gyrophase perturbation,

$$\varphi_1 = -R_1 \sin(\varphi_0 - \psi_B) - L_1 \sin(\varphi_0 + \psi_B). \tag{29}$$

Here, we introduced the substitutions

$$R_1 = \frac{v_z}{v_\perp}\frac{\Omega_R}{v_1}, \tag{30}$$

$$L_1 = \frac{v_z}{v_\perp}\frac{\Omega_L}{v_{-1}}, \tag{31}$$

where

$$v_{\pm 1} = \Omega_e \mp \omega \pm k_z v_z \tag{32}$$

is a quantity expressing the deviation from the fundamental resonances $n = \pm 1$.

Going back to the Bessel function expansion from Eqs 22–24, we can now write

$$\begin{aligned}\sin\zeta_n &\approx \sin(n(\varphi_0+\varphi_1) - \psi_B)\\ &= \sin(n\varphi_0 - nR_1\sin(\varphi_0-\psi_B))\cos(-\psi_B - nL_1\sin(\varphi_0+\psi_B))\\ &\quad + \cos(n\varphi_0 - nR_1\sin(\varphi_0-\psi_B))\sin(-\psi_B - nL_1\sin(\varphi_0+\psi_B)).\end{aligned} \tag{33}$$

Using the second form of the expansions, we can expand each of the trigonometric functions from Eq. 35 into

$$\begin{aligned}&\sin(n\varphi_0 - nR_1\sin(\varphi_0-\psi_B))\\ &\quad = -\sum_{r=-\infty}^{\infty} J_r(nR_1)\sin(r(\varphi_0-\psi_B) - n\varphi_0),\end{aligned} \tag{34}$$

$$\begin{aligned}&\cos(-\psi_B - nL_1\sin(\varphi_0+\psi_B))\\ &\quad = \sum_{l=-\infty}^{\infty} J_l(nL_1)\cos(l(\varphi_0+\psi_B) + \psi_B),\end{aligned} \tag{35}$$

$$\begin{aligned}&\cos(n\varphi_0 - nR_1\sin(\varphi_0-\psi_B))\\ &\quad = \sum_{r=-\infty}^{\infty} J_r(nR_1)\cos(r(\varphi_0-\psi_B) - n\varphi_0),\end{aligned} \tag{36}$$

$$\begin{aligned}&\sin(-\psi_B - nL_1\sin(\varphi_0+\psi_B))\\ &\quad = -\sum_{l=-\infty}^{\infty} J_l(nL_1)\sin(l(\varphi_0+\psi_B) + \psi_B).\end{aligned} \tag{37}$$

Since R_1 and L_1 are proportional to the relative wave magnetic field B_w/B_0, we can limit the summations to $|r| \le 1$ and $|l| \le 1$. As a further simplification, we will limit the resonance number n to $-1, 0, 1$, which is a reasonable approximation when $\beta^2 \ll 1$; i.e., when pitch angles are low and θ_k is not too close to the resonance cone. We then insert Eqs 34–37 into Eqs 33, 22 and finally obtain

$$\begin{aligned}\sin(\varphi-\psi) \approx -\sum_{n,r,l=-1}^{1} &J_n(\beta)J_r((n+1)R_1)J_l((n+1)L_1)\\ &\times\sin((r-n+l-1)\varphi_0 + (l-r+1)\psi_B),\end{aligned} \tag{38}$$

$$\begin{aligned}\sin(\varphi+\psi) \approx \sum_{n,r,l=-1}^{1} &J_n(\beta)J_r((n-1)R_1)J_l((n-1)L_1)\\ &\times\sin((r-n+l+1)\varphi_0 + (l-r+1)\psi_B),\end{aligned} \tag{39}$$

$$\begin{aligned}\sin(\psi) \approx -\sum_{n,r,l=-1}^{1} &J_n(\beta)J_r(nR_1)J_l(nL_1)\\ &\times\sin((r-n+l)\varphi_0 + (l-r+1)\psi_B).\end{aligned} \tag{40}$$

Comparing the prefactors of φ_0 and ψ_B results in resonant fractions.

$$q_R = -\frac{r-n+l-1}{l-r+1}, \tag{41}$$

$$q_L = -\frac{r-n+l+1}{l-r+1}, \tag{42}$$

$$q_z = -\frac{r-n+l}{l-r+1}. \tag{43}$$

Apart from the integer values (which represent fundamental and harmonic resonances), the fractions can also evaluate to $\pm 1/3$, $\pm 1/2$, $\pm 2/3$, and $\pm 3/2$; other fractional values would appear if we extended the summation range in n and removed the approximation $\beta^2 \ll 1$.

We now focus on the resonance $-1/2$, which contributes to electron diffusion near $E_k = 2$ MeV in Figure 8C. The related relative phase angle $\varphi_0 + 2\psi_B$ corresponds to resonance velocity

$$V_{R-1/2} = \frac{1}{k_z}\left(\omega - \frac{\Omega_e}{2\gamma}\right). \tag{44}$$

Going back to the average change in energy defined in Eq. 21, we can perform the Taylor expansion of Bessel function to the first order and show that the term with E_R^w does not contribute to the $-1/2$ resonance, while the E_L^w term contributes to the integrand by

$$-\frac{e\gamma k_x v_\perp v_z E_L^w \Omega_R^w}{2T\Omega_e v_1}, \tag{45}$$

where we have used Eqs 30, 11. The E_z^w also has a non-zero contribution to the integrand

$$-\frac{e v_z^2 E_z^w \Omega_L^w}{2T v_\perp v_{-1}}. \tag{46}$$

Due to the terms $E_L^w\Omega_R^w$ and $E_z^w\Omega_L^w$, the energy change caused by $-1/2$ resonance scales with a square of the wave amplitude. On the other hand, for the integer resonance terms with $r = l = 0$, the quantities Ω_R^w and Ω_L^w disappear, and the scaling reduces to the first power in amplitude. This analytical result explains the diminishing of the $-1/2$ resonance in Figure 8 when the amplitude is decreased. Notice that due to the term $1/v_{-1}$, fractional resonances very close to $n = -1$ retain non-negligible strength and contribute to resonance broadening.

The derivation provided in this section works for whistler-mode waves as well, except for the approximations $U_R \ll v_z$, $U_L \ll v_z$.

Data availability statement

The datasets presented in this study can be found in online repositories. The names of the repository/repositories and accession number(s) can be found at: https://doi.org/10.6084/m9.figshare.22061159.v1.

Author contributions

MH wrote and ran the simulation code, analyzed the resulting data, derived the equations for fractional resonances, and prepared the original draft. WL initiated the study and provided frequent consultations. QM helped in validating the code. WL and QM provided advice during the pre-submission review and editing of the manuscript.

Funding

The research at Boston University was supported by NASA grants 80NSSC20K0698, 80NSSC20K1270, and 80NSSC21K1312, as well as the NSF grant AGS-2019950. QM would like to acknowledge the NASA grant 80NSSC20K0196 and the NSF grant AGS-2225445.

Acknowledgments

The authors gratefully acknowledge the discussion with Jacob Bortnik and Xin An on the topic of precipitation blocking.

Conflict of interest

The authors declare that the research was conducted in the absence of any commercial or financial relationships that could be construed as a potential conflict of interest.

Publisher's note

All claims expressed in this article are solely those of the authors and do not necessarily represent those of their affiliated organizations, or those of the publisher, the editors, and the reviewers. Any product that may be evaluated in this article, or claim that may be made by its manufacturer, is not guaranteed or endorsed by the publisher.

Supplementary Material

The Supplementary Material for this article can be found online at: https://www.frontiersin.org/articles/10.3389/fspas.2023.1163515/full#supplementary-material

References

Abramowitz, M., and Stegun, I. A. (1965). *Handbook of mathematical functions: With formulas, graphs, and mathematical tables*. New York: Dover Books on Advanced Mathematics (Dover Publications.

Albert, J. M., Artemyev, A., Li, W., Gan, L., and Ma, Q. (2022). Analytical results for phase bunching in the pendulum model of wave-particle interactions. *Front. Astron. Space Sci.* 9, 971358. doi:10.3389/fspas.2022.971358

Albert, J. M., Artemyev, A. V., Li, W., Gan, L., and Ma, Q. (2021). Models of resonant wave-particle interactions. *J. Geophys. Res. Space Phys.* 126, e29216. doi:10.1029/2021JA029216

Albert, J. M. (2008). Efficient approximations of quasi-linear diffusion coefficients in the radiation belts. *J. Geophys. Res. Space Phys.* 113, A06208. doi:10.1029/2007JA012936

Allanson, O., Elsden, T., Watt, C., and Neukirch, T. (2022). Weak turbulence and quasilinear diffusion for relativistic wave-particle interactions via a Markov approach. *Front. Astron. Space Sci.* 8, 232. doi:10.3389/fspas.2021.805699

Allen, R. C., Zhang, J. C., Kistler, L. M., Spence, H. E., Lin, R. L., Klecker, B., et al. (2015). A statistical study of EMIC waves observed by cluster: 1. Wave properties. *J. Geophys. Res. Space Phys.* 120, 5574–5592. doi:10.1002/2015JA021333

An, X., Artemyev, A., Angelopoulos, V., Zhang, X., Mourenas, D., and Bortnik, J. (2022). Nonresonant scattering of relativistic electrons by electromagnetic ion cyclotron waves in Earth's radiation belts. *Phys. Rev. Lett.* 129, 135101. doi:10.1103/PhysRevLett.129.135101

Anderson, B. J., Denton, R. E., Ho, G., Hamilton, D. C., Fuselier, S. A., and Strangeway, R. J. (1996). Observational test of local proton cyclotron instability in the Earth's magnetosphere. *J. Geophys. Res.* 101, 21527–21543. doi:10.1029/96JA01251

Artemyev, A. V., Neishtadt, A. I., Vainchtein, D. L., Vasiliev, A. A., Vasko, I. Y., and Zelenyi, L. M. (2018). Trapping (capture) into resonance and scattering on resonance: Summary of results for space plasma systems. *Commun. Nonlinear Sci. Numer. Simulat.* 65, 111–160. doi:10.1016/j.cnsns.2018.05.004

Bortnik, J., Albert, J. M., Artemyev, A., Li, W., Jun, C.-W., Grach, V. S., et al. (2022). Amplitude dependence of nonlinear precipitation blocking of relativistic electrons by large amplitude EMIC waves. *Geophys. Res. Lett.* 49, e2022GL098365. doi:10.1029/2022GL098365

Capannolo, L., Li, W., Ma, Q., Chen, L., Shen, X. C., Spence, H. E., et al. (2019). Direct observation of subrelativistic electron precipitation potentially driven by EMIC waves. *Geophys. Res. Lett.* 46 (12), 12711–12721. 711–12. doi:10.1029/2019GL084202

Chen, L., Thorne, R. M., Bortnik, J., and Zhang, X.-J. (2016). Nonresonant interactions of electromagnetic ion cyclotron waves with relativistic electrons. *J. Geophys. Res. Space Phys.* 121, 9913–9925. doi:10.1002/2016JA022813

Chen, M. W., Roeder, J. L., Fennell, J. F., Lyons, L. R., Lambour, R. L., and Schulz, M. (1999). Proton ring current pitch angle distributions: Comparison of simulations with CRRES observations. *J. Geophys. Res.* 104, 17379–17389. doi:10.1029/1999JA900142

Clilverd, M. A., Duthie, R., Hardman, R., Hendry, A. T., Rodger, C. J., Raita, T., et al. (2015). Electron precipitation from EMIC waves: A case study from 31 may 2013. *J. Geophys. Res. Space Phys.* 120, 3618–3631. doi:10.1002/2015JA021090

Denton, R. E., Goldstein, J., Menietti, J. D., and Young, S. L. (2002). Magnetospheric electron density model inferred from Polar plasma wave data. *J. Geophys. Res. Space Phys.* 107, 1386. doi:10.1029/2001JA009136

Engebretson, M. J., Posch, J. L., Wygant, J. R., Kletzing, C. A., Lessard, M. R., Huang, C. L., et al. (2015). Van Allen probes, NOAA, GOES, and ground observations of an intense EMIC wave event extending over 12 h in magnetic local time. *J. Geophys. Res. Space Phys.* 120, 5465–5488. doi:10.1002/2015JA021227

Fu, X., Guo, Z., Dong, C., and Gary, S. P. (2015). Nonlinear subcyclotron resonance as a formation mechanism for gaps in banded chorus. *Geophys. Res. Lett.* 42, 3150–3159. doi:10.1002/2015GL064182

Grach, V. S., Artemyev, A. V., Demekhov, A. G., Zhang, X.-J., Bortnik, J., Angelopoulos, V., et al. (2022). Relativistic electron precipitation by EMIC waves: Importance of nonlinear resonant effects. *Geophys. Res. Lett.* 49, e99994. doi:10.1029/2022GL099994

Grach, V. S., and Demekhov, A. G. (2020). Precipitation of relativistic electrons under resonant interaction with electromagnetic ion cyclotron wave packets. *J. Geophys. Res. Space Phys.* 125, e27358. doi:10.1029/2019JA027358

Hanzelka, M., Santolík, O., Omura, Y., and Kolmašová, I. (2021). Measurability of the nonlinear response of electron distribution function to chorus emissions in the Earth's radiation belt. *J. Geophys. Res. Space Phys.* 126, e29624. doi:10.1029/2021JA029624

Hendry, A. T., Rodger, C. J., and Clilverd, M. A. (2017). Evidence of sub-MeV EMIC-driven electron precipitation. *Geophys. Res. Lett.* 44, 1210–1218. doi:10.1002/2016GL071807

Hendry, A. T., Santolik, O., Kletzing, C. A., Rodger, C. J., Shiokawa, K., and Baishev, D. (2019). Multi-instrument observation of nonlinear EMIC-driven electron precipitation at sub-MeV energies. *Geophys. Res. Lett.* 46, 7248–7257. doi:10.1029/2019GL082401

Horne, R. B., and Thorne, R. M. (1998). Potential waves for relativistic electron scattering and stochastic acceleration during magnetic storms. *Geophys. Res. Lett.* 25, 3011–3014. doi:10.1029/98GL01002

Horwitz, J. L., Baugher, C. R., Chappell, C. R., Shelley, E. G., Young, D. T., and Anderson, R. R. (1981). ISEE 1 observations of thermal plasma in the vicinity of the plasmasphere during periods of quieting magnetic activity. *J. Geophys. Res.* 86, 9989–10001. doi:10.1029/JA086iA12p09989

Ichimaru, S. (2004). *Statistical plasma Physics: Basic principles*. 1st ed. CRC Press.

Jordanova, V. K., Albert, J., and Miyoshi, Y. (2008). Relativistic electron precipitation by EMIC waves from self-consistent global simulations. *J. Geophys. Res. Space Phys.* 113, A00A10. doi:10.1029/2008JA013239

Jun, C.-W., Miyoshi, Y., Kurita, S., Yue, C., Bortnik, J., Lyons, L., et al. (2021). The characteristics of EMIC waves in the magnetosphere based on the van allen probes and arase observations. *J. Geophys. Res. Space Phys.* 126, e29001. doi:10.1029/2020JA029001

Karpman, V. I. (1974). Nonlinear effects in the ELF waves propagating along the magnetic field in the magnetosphere. *Space Sci. Rev.* 16, 361–388. doi:10.1007/BF00171564

Kennel, C. F., and Engelmann, F. (1966). Velocity space diffusion from weak plasma turbulence in a magnetic field. *Phys. Fluids* 9, 2377–2388. doi:10.1063/1.1761629

Kennel, C. F., and Petschek, H. E. (1966). Limit on stably trapped particle fluxes. *J. Geophys. Res.* 71, 1–28. doi:10.1029/JZ071i001p00001

Kim, E.-H., and Johnson, J. R. (2016). Full-wave modeling of EMIC waves near the He^+ gyrofrequency. *Geophys. Res. Lett.* 43, 13–21. doi:10.1002/2015GL066978

Kitahara, M., and Katoh, Y. (2019). Anomalous trapping of low pitch angle electrons by coherent whistler mode waves. *J. Geophys. Res. Space Phys.* 124, 5568–5583. doi:10.1029/2019JA026493

Kramer, G. J., Chen, L., Fisher, R. K., Heidbrink, W. W., Nazikian, R., Pace, D. C., et al. (2012). Fractional resonances between waves and energetic particles in tokamak plasmas. *Phys. Rev. Lett.* 109, 035003. doi:10.1103/PhysRevLett.109.035003

Kurita, S., Miyoshi, Y., Shiokawa, K., Higashio, N., Mitani, T., Takashima, T., et al. (2018). Rapid loss of relativistic electrons by EMIC waves in the outer radiation belt observed by arase, van allen probes, and the PWING ground stations. *Geophys. Res. Lett.* 45, 12,720–12,729. doi:10.1029/2018GL080262

Lee, D.-Y., Shin, D.-K., and Choi, C.-R. (2018). Effects of oblique wave normal angle and noncircular polarization of electromagnetic ion cyclotron waves on the pitch angle scattering of relativistic electrons. *J. Geophys. Res. Space Phys.* 123, 4556–4573. doi:10.1029/2018JA025342

Lewak, G. J., and Chen, C. S. (1969). Higher order resonances in a plasma. *J. Plasma Phys.* 3, 481–497. doi:10.1017/S0022377800004554

Li, W., and Hudson, M. K. (2019). Earth's van allen radiation belts: From discovery to the van allen probes era. *J. Geophys. Res. Space Phys.* 124, 8319–8351. doi:10.1029/2018JA025940

Loto'aniu, T. M., Fraser, B. J., and Waters, C. L. (2005). Propagation of electromagnetic ion cyclotron wave energy in the magnetosphere. *J. Geophys. Res. Space Phys.* 110, A07214. doi:10.1029/2004JA010816

Meredith, N. P., Horne, R. B., Kersten, T., Fraser, B. J., and Grew, R. S. (2014). Global morphology and spectral properties of EMIC waves derived from CRRES observations. *J. Geophys. Res. Space Phys.* 119, 5328–5342. doi:10.1002/2014JA020064

Meredith, N. P., Thorne, R. M., Horne, R. B., Summers, D., Fraser, B. J., and Anderson, R. R. (2003). Statistical analysis of relativistic electron energies for cyclotron resonance with EMIC waves observed on CRRES. *J. Geophys. Res. Space Phys.* 108, 1250. doi:10.1029/2002JA009700

Min, K., Lee, J., Keika, K., and Li, W. (2012). Global distribution of EMIC waves derived from THEMIS observations. *J. Geophys. Res. Space Phys.* 117, A05219. doi:10.1029/2012JA017515

Nunn, D., and Omura, Y. (2015). A computational and theoretical investigation of nonlinear wave-particle interactions in oblique whistlers. *J. Geophys. Res. Space Phys.* 120, 2890–2911. doi:10.1002/2014JA020898

Omura, Y., Hsieh, Y.-K., Foster, J. C., Erickson, P. J., Kletzing, C. A., and Baker, D. N. (2019). Cyclotron acceleration of relativistic electrons through landau resonance with obliquely propagating whistler-mode chorus emissions. *J. Geophys. Res. Space Phys.* 124, 2018JA026374–2810. doi:10.1029/2018JA026374

Omura, Y. (2021). Nonlinear wave growth theory of whistler-mode chorus and hiss emissions in the magnetosphere. *Earth Planets Space* 73, 95. doi:10.1186/s40623-021-01380-w

Omura, Y., Pickett, J., Grison, B., Santolik, O., Dandouras, I., Engebretson, M., et al. (2010). Theory and observation of electromagnetic ion cyclotron triggered emissions in the magnetosphere. *J. Geophys. Res. Space Phys.* 115, A07234. doi:10.1029/2010JA015300

Omura, Y., and Zhao, Q. (2012). Nonlinear pitch angle scattering of relativistic electrons by EMIC waves in the inner magnetosphere. *J. Geophys. Res. Space Phys.* 117, A08227. doi:10.1029/2012JA017943

Perraut, S., Gendrin, R., Roux, A., and de Villedary, C. (1984). Ion cyclotron waves: Direct comparison between ground-based measurements and observations in the source region. *J. Geophys. Res.* 89, 195–202. doi:10.1029/JA089iA01p00195

Rauch, J. L., and Roux, A. (1982). Ray tracing of ULF waves in a multicomponent magnetospheric plasma: Consequences for the generation mechanism of ion cyclotron waves. *J. Geophys. Res.* 87, 8191–8198. doi:10.1029/JA087iA10p08191

Saikin, A. A., Zhang, J. C., Allen, R. C., Smith, C. W., Kistler, L. M., Spence, H. E., et al. (2015). The occurrence and wave properties of H^+-He^+-and O^+-band EMIC waves observed by the Van Allen Probes. *J. Geophys. Res. Space Phys.* 120, 7477–7492. doi:10.1002/2015JA021358

Saito, T. (1969). Geomagnetic pulsations. *Space Sci. Rev.* 10, 319–412. doi:10.1007/BF00203620

Shoji, M., Miyoshi, Y., Kistler, L. M., Asamura, K., Matsuoka, A., Kasaba, Y., et al. (2021). Discovery of proton hill in the phase space during interactions between ions and electromagnetic ion cyclotron waves. *Sci. Rep.* 11, 13480. doi:10.1038/s41598-021-92541-0

Stix, T. (1992). *Waves in plasmas*. Melville NY: American Institute of Physics.

Summers, D., Omura, Y., Miyashita, Y., and Lee, D.-H. (2012). Nonlinear spatiotemporal evolution of whistler mode chorus waves in Earth's inner magnetosphere. *J. Geophys. Res. Space Phys.* 117, A09206. doi:10.1029/2012JA017842

Summers, D., Thorne, R. M., and Xiao, F. (1998). Relativistic theory of wave-particle resonant diffusion with application to electron acceleration in the magnetosphere. *J. Geophys. Res.* 103, 20487–20500. doi:10.1029/98JA01740

Thorne, R. M., and Kennel, C. F. (1971). Relativistic electron precipitation during magnetic storm main phase. *J. Geophys. Res.* 76, 4446–4453. doi:10.1029/JA076i019p04446

Usanova, M. E., Drozdov, A., Orlova, K., Mann, I. R., Shprits, Y., Robertson, M. T., et al. (2014). Effect of EMIC waves on relativistic and ultrarelativistic electron populations: Ground-based and Van Allen Probes observations. *Geophys. Res. Lett.* 41, 1375–1381. doi:10.1002/2013GL059024

Usanova, M. E., Mann, I. R., Bortnik, J., Shao, L., and Angelopoulos, V. (2012). THEMIS observations of electromagnetic ion cyclotron wave occurrence: Dependence on AE, SYMH, and solar wind dynamic pressure. *J. Geophys. Res. Space Phys.* 117, A10218. doi:10.1029/2012JA018049

Wang, G., Su, Z., Zheng, H., Wang, Y., Zhang, M., and Wang, S. (2017a). Nonlinear fundamental and harmonic cyclotron resonant scattering of radiation belt ultrarelativistic electrons by oblique monochromatic EMIC waves. *J. Geophys. Res. Space Phys.* 122, 1928–1945. doi:10.1002/2016JA023451

Wang, X. Y., Huang, S. Y., Allen, R. C., Fu, H. S., Deng, X. H., Zhou, M., et al. (2017b). The occurrence and wave properties of EMIC waves observed by the Magnetospheric Multiscale (MMS) mission. *J. Geophys. Res. Space Phys.* 122, 8228–8240. doi:10.1002/2017JA024237

Zenitani, S., and Umeda, T. (2018). On the Boris solver in particle-in-cell simulation. *Phys. Plasmas* 25, 112110. doi:10.1063/1.5051077

Zhao, H., Johnston, W. R., Baker, D. N., Li, X., Ni, B., Jaynes, A. N., et al. (2019). Characterization and evolution of radiation belt electron energy spectra based on the van allen probes measurements. *J. Geophys. Res. Space Phys.* 124, 4217–4232. doi:10.1029/2019JA026697

Zheng, L., Chen, L., and Zhu, H. (2019). Modeling energetic electron nonlinear wave-particle interactions with electromagnetic ion cyclotron waves. *J. Geophys. Res. Space Phys.* 124, 3436–3453. doi:10.1029/2018JA026156

Zhu, H., Chen, L., Claudepierre, S. G., and Zheng, L. (2020). Direct evidence of the pitch angle scattering of relativistic electrons induced by EMIC waves. *Geophys. Res. Lett.* 47, e85637. doi:10.1029/2019GL085637

frontiers | Frontiers in Astronomy and Space Sciences

TYPE Mini Review
PUBLISHED 17 May 2023
DOI 10.3389/fspas.2023.1193600

OPEN ACCESS

EDITED BY
Qianli Ma,
Boston University, United States

REVIEWED BY
David Paul Hartley,
The University of Iowa, United States

*CORRESPONDENCE
Nigang Liu,
liung5@mail.sysu.edu.cn
Zhenpeng Su,
szpe@mail.ustc.edu.cn

RECEIVED 25 March 2023
ACCEPTED 03 May 2023
PUBLISHED 17 May 2023

CITATION
Liu N and Su Z (2023), Prompt responses of magnetospheric whistler-mode waves to solar wind dynamic pressure pulses. *Front. Astron. Space Sci.* 10:1193600. doi: 10.3389/fspas.2023.1193600

Prompt responses of magnetospheric whistler-mode waves to solar wind dynamic pressure pulses

Nigang Liu[1,2]* and Zhenpeng Su[3,4,5]*

[1]Planetary Environmental and Astrobiological Research Laboratory (PEARL), School of Atmospheric Sciences, Sun Yat-sen University, Zhuhai, China, [2]Key Laboratory of Tropical Atmosphere-Ocean System, Sun Yat-sen University, Ministry of Education, Zhuhai, China, [3]CAS Center for Excellence in Comparative Planetology/CAS Key Laboratory of Geospace Environment/Mengcheng National Geophysical Observatory, University of Science and Technology of China, Hefei, China, [4]Deep Space Exploration Laboratory/School of Earth and Space Sciences, University of Science and Technology of China, Hefei, China, [5]Collaborative Innovation Center of Astronautical Science and Technology, Hefei, China

Whistler-mode waves play a critical role in shaping the Earth's radiation belts, and their spatiotemporal distribution is vital for forecasting and modeling geospace weather. Previous works have extensively investigated the influences of geomagnetic activities, such as storms and substorms, on the modification of whistler-mode waves, but the direct impacts of solar wind disturbances have received relatively less attention. Recently, increasing research has highlighted the prompt impacts of solar wind dynamic pressure pulses on magnetospheric whistler-mode waves. This paper reviews the current progress in this field, specifically the prompt responses of chorus waves and plasmaspheric hiss to the solar wind dynamic pressure pulses. It will summarize the underlying mechanisms and pose some outstanding questions.

KEYWORDS

whistler-mode waves, solar wind-magnetosphere coupling, chorus, plasmaspheric hiss, plasma wave instability

1 Introduction

Whistler-mode waves are very low-frequency (VLF) right-handed circularly polarized electromagnetic emissions that are commonly observed in the magnetosphere (Laakso and Blomberg, 2005; Anderson and Vasko, 2018). Depending on their spatial location, whistler-mode waves are divided into chorus (outside high-density plasmasphere) and plasmaspheric hiss (inside high-density plasmasphere or plume). Chorus waves typically exhibit a structured and discrete emission pattern, with a frequency range of 0.1–0.8 f_{ce} (equatorial electron cyclotron frequency) (Tsurutani and Smith, 1974; Tsurutani and Smith, 1977; Meredith et al., 2001; Santolík et al., 2003; Gao et al., 2017). In contrast, plasmaspheric hiss is typically observed as an incoherent and structureless band, with a frequency range from ~0.1 kHz to several kilohertz (Russell et al., 1969; Thorne et al., 1973; Hayakawa and Sazhin, 1992; Summers et al., 2008). Once plasmaspheric hiss leaks out of the plasmasphere, it is referred to as exohiss (Russell et al., 1969; Thorne et al., 1973). Note that low frequency chorus below 0.1 f_{ce} (Meredith et al., 2014; Cattell et al., 2015; Gao et al., 2016) and coherent plasmaspheric hiss with fine structures (Summers et al., 2014; Tsurutani et al., 2015; Su et al., 2018; Liu et al., 2020a) have also been reported. The fundamental role of whistler-mode

waves in radiation belt dynamics has made them a subject of considerable interest in the space-physics community. Through cyclotron resonance, whistler-mode waves contribute to the acceleration and loss of radiation belt electrons (Summers et al., 2002; Horne et al., 2005; Reeves et al., 2013; Thorne et al., 2013b; Su et al., 2014a; c; Xiao et al., 2014; Lyons and Thorne, 1973; Abel and Thorne, 1998; Albert, 1994; Su et al., 2011; Nishimura et al., 2013; Kasahara et al., 2018; Thorne et al., 2013a; Ni et al., 2014; Breneman et al., 2015; Zhu et al., 2015; Li et al., 2017; Ma et al., 2017; Zhang et al., 2019; Liu et al., 2020b). Through landau resonance, plasmaspheric hiss is able to accelerate suprathermal electrons (Woodroffe et al., 2017; Li et al., 2019; Wang et al., 2020), and probably transfer energy toward the ionospheric plasma (Wang et al., 2020). Thus, a detailed understanding of the spatiotemporal distribution of whistler-mode waves is of great importance for forecasting and modeling geospace weather.

Storms and substorms are remarkable geomagnetic activities caused by solar wind disturbances (McPherron et al., 1986; Gonzalez et al., 1989; Gonzalez et al., 1999; Sergeev et al., 2012). Their important role in modifying whistler-mode waves has been extensively investigated (Wilson et al., 2011; Agapitov et al., 2013; Li et al., 2013b; Tsurutani et al., 2018; Shi et al., 2019; Liu et al., 2020a; Meredith et al., 2020; Meredith et al., 2021). However, previous works commonly highlight the influences of electron injection in the course of storms and substorms. In fact, there might be variations in the magnetospheric plasma environment during the initial phase of a storm (Gosling et al., 1967; Tsurutani et al., 1995; Gonzalez et al., 1999; Samsonov et al., 2007) which could also impact whistler-mode waves. Moreover, regarding solar wind disturbances that are incapable of triggering storms or substorms, there is a relative lack of studies on their influence on whistler-mode waves. One of the most frequently observed solar wind disturbances at 1 AU is the solar wind dynamic pressure pulses (Wu et al., 1993; Dalin et al., 2002; Neugebauer, 2006; Zuo et al., 2015). They are characterized by abrupt jumps or depressions in solar wind dynamic pressure, corresponding to the positive or negative pressure pulse, respectively. Solar wind dynamic pressure pulses are usually associated with interplanetary shocks or other discontinuities (Hudson, 1970; Dalin et al., 2002; Neugebauer, 2006; Zuo et al., 2015). The fast-forward interplanetary shock (simply termed interplanetary shock in the following), which is the most common type of interplanetary shock, can be treated as a positive pressure pulse (Kennel et al., 1985). As important manifestations of solar wind-magnetosphere coupling, the prompt impacts of solar wind dynamic pressure pulses on the magnetospheric current systems (Zesta et al., 2000), particle fluxes (Lee et al., 2004; Zong et al., 2009; Li et al., 2013a), and auroral activities (Zhou et al., 2009; Zhou et al., 2017) have been investigated. Given the geoeffective nature of solar wind dynamic pressure pulses, it is reasonable to expect the prompt responses of magnetospheric whistler-mode waves to these disturbances.

This paper reviews the recent progress in the prompt responses of magnetospheric whistler-mode waves to solar wind dynamic pressure pulses. Here the "prompt response" refers to variations in whistler-mode waves occurring within several minutes (depending on solar wind velocity) after the arrival of pressure pulses at the magnetopause. Advanced magnetospheric missions such as the Van Allen Probes (Mauk et al., 2013) and THEMIS (Angelopoulos, 2008), which carry various instruments including the Electric and Magnetic Field Instrument Suite and Integrated Science suite (EMFISIS) (Kletzing et al., 2013), the Energetic particle, Composition and the Thermal plasma suite (ECT) (Spence et al., 2013), the Electric Field and Waves (EFW) (Wygant et al., 2013), the Search Coil Magnetometer (SCM) (Le Contel et al., 2008), and the Electric Field Instrument (EFI) (Bonnell et al., 2008), have provided high-quality and comprehensive data, allowing for a detailed investigation into the underlying mechanisms.

2 Prompt responses of chorus waves

Anisotropic energetic electrons from a few to tens of keV provide the free energy for the excitation of chorus waves (Kennel and Engelmann, 1966; LeDocq et al., 1998; Li et al., 2009; Su et al., 2014b). Though the generation mechanism of chorus waves has not been fully revealed, current works have proposed a widely accepted scenario: the background thermal noise grows linearly to a specific threshold wave amplitude for the further amplification through nonlinear process (Omura et al., 2008; Katoh and Omura, 2013; Tao, 2014; Nakamura et al., 2016; Omura, 2021). By modifying the linear and nonlinear wave growth processes, solar wind dynamic pressure pulses can cause the prompt response of chorus waves.

The modification of equatorial energetic electron fluxes by pressure pulses can alter the chorus wave intensity. Fu et al. (2012) reported a chorus intensification in response to an interplanetary shock using THEMIS observations. The shock compression increased the magnetic field strength and triggered PC4-5 ultra-low-frequency (ULF) waves, which further enhanced the temperature anisotropy of energetic electrons through local betatron acceleration and radial diffusion processes. These increased the maximum linear growth rate by 50%, resulting in chorus intensification. Peng et al. (2020) also reported such compression-related chorus intensifications associated with adiabatic acceleration of energetic electron fluxes using MMS observations. In contrast, Liu et al. (2017a) reported a sudden disappearance of chorus waves triggered by an interplanetary shock. The shock produced a drastic increase in dynamic pressure which compressed the dayside magnetopause earthward to about $L = 7$, abruptly eliminating the preexisting dayside chorus waves and the associated source electrons.

As well as impacting the local energetic electron populations, solar wind dynamic pressure pulses can also affect the background magnetic field configuration and consequently the nonlinear growth process of chorus. Zhou et al. (2015) analyzed 20 interplanetary shock events which occurred between 1 January 2008 and 31 December 2014 with simultaneous observations of chorus waves made by three THEMIS satellites, and found that the chorus intensification events preferentially occurred at high L shells (greater than 8) and on the dayside (MLT from 6 to 18). Utilizing the TS04 geomagnetic mode (Tsyganenko and Sitnov, 2005), they showed that the background magnetic field configurations became more homogeneous (a smaller background magnetic field gradient) following shock compression, which is favorable for

the nonlinear growth of chorus (Omura et al., 2008; Katoh and Omura, 2013). Zhou et al. (2015) claimed there were no significant changes in the energetic electron distribution to be responsible for the chorus intensifications, contrary to the interpretation of Fu et al. (2012). Liu et al. (2017b) reported a sudden disappearance of chorus waves triggered by a negative pressure pulse using THEMIS observations. The negative pulse caused no significant changes in the background plasma populations associated with the generation of chorus waves, but an increase in background magnetic field inhomogeneity. Liu et al. (2017b) proposed that the dayside geomagnetic field configuration with the enhanced inhomogeneity became unfavorable for the nonlinear growth of chorus, which can be interpreted as an "inverse" process of that described in Zhou et al. (2015).

Recently, a statistical study was conducted by Jin et al. (2022) to investigate the immediate impacts of dynamic pressure pulses, both positive and negative, on inner magnetospheric chorus waves. The study analyzed Van Allen Probes data from 2012 to 2019 and demonstrated that a stronger pulse has a greater likelihood of changing the chorus amplitude particularly on the dayside. Specifically, positive pulses were associated with an enhancement in chorus amplitudes, while negative pulses resulted in a weakening of these waves. The disappearance of chorus waves triggered by positive pulses due to the losses of source electrons to the magnetopause (Reeves et al., 2003; Ukhorskiy et al., 2006; Turner et al., 2012) has not been observed in the inner magnetosphere in this work. As supported by direct observations, these pulses alter the linear growth of waves by modifying energetic electron distributions. On the other hand, geomagnetic field modeling indicates no significant changes in the background magnetic field inhomogeneity controlling the nonlinear growth threshold of waves. The inconsistency between this result and previous works (Zhou et al., 2015; Liu et al., 2017b) which investigated chorus waves in the outer magnetosphere (8 <L<12) can be attributed to the low sensitivity of equatorial magnetic field inhomogeneity to solar wind disturbances in the inner magnetosphere.

3 Prompt responses of plasmaspheric hiss

The generation mechanism of plasmaspheric hiss remains a topic of intense debate. Two main categories of candidate mechanisms have been proposed: 1) internal generation, which involves the linear or nonlinear amplification of ambient electromagnetic noise by unstable energetic electrons inside the plasmasphere (Thorne et al., 1979); 2) external origination, which involves the entry of lightning-associated whistlers or source chorus to the plasmasphere (Church and Thorne, 1983; Draganov et al., 1992; Green et al., 2005; Bortnik et al., 2008; Bortnik et al., 2009; Chen et al., 2009; Li et al., 2015). An identification of plasmaspheric hiss with different generation mechanisms is based on the wave Poynting fluxes, where the internally-generated hiss has poleward uni-directional Poynting fluxes near its source region before undergoing magnetospheric reflections, and the externally-originated hiss has bi-directional Poynting fluxes. Studying the prompt impacts of solar wind dynamic pressure pulses on plasmaspheric hiss provides an opportunity to examine the wave generation mechanisms.

For the externally-originated plasmaspheric hiss, variations of source chorus triggered by solar wind pressure pulses can subsequently cause corresponding responses within the plasmasphere. As introduced in the previous section, an intense interplanetary shock can eliminate energetic electrons and chorus waves on the dayside outer magnetosphere (Liu et al., 2017a), and a negative solar wind dynamic pressure pulse can cause the disappearance of chorus waves by enhancing the dayside magnetic field inhomogeneity (Liu et al., 2017b). In both cases, the plasmaspheric hiss ceased as a result of the quenching of source chorus. A similar event to that of Liu et al. (2017a) has been lately reported by Chakraborty et al. (2021). It also should be mentioned that, by using the conjunctive observations from three satellites of Van Allen Probes and THEMIS, Liu et al. (2017b) observed for the first time the simultaneous disappearances of chorus, plasmaspheric hiss, and exohiss over a vast region on the dayside, providing direct observational evidence for the link between different types of magnetospheric whistler-mode waves.

Another important factor affecting the externally-originated plasmaspheric hiss is the propagation of source chorus into the plasmasphere. Su et al. (2015) gave the first report on the shock-induced disappearances of plasmaspheric hiss observed by the Van Allen Probes. The hot electron fluxes were expected to be increased through adiabatic process after shock, which could favor the excitation of chorus. However, the increased hot electron fluxes also enhanced the Landau damping for obliquely propagating chorus waves, thus leading to the quenching of plasmaspheric hiss by damping the chorus before it can enter the plasmasphere. Later, Yue et al. (2017) conducted a statistical study on the prompt responses of whistler-mode waves to fast forward shocks using the Van Allen Probes and THEMIS missions. The statistical results showed that chorus waves were intensified following shock arrival at all MLTs, which is consistent with the results for positive pressure pulses in Jin et al. (2022). In contrast, plasmaspheric hiss mainly disappeared/weakened on the dayside and intensified on the nightside, which cannot be explained solely by the variations of source chorus. Such different dependences of chorus and plasmaspheric hiss on the solar wind dynamic pressure have also been reported recently by Tang et al. (2023). Through simple ray tracing modeling, Yue et al. (2017) found that a more stretched magnetic field configuration on the nightside caused by shock compression favors the entry of chorus waves with more field-aligned wave normal into the plasmasphere, which are generally the majority of observed chorus waves in the equatorial region (Burton and Holzer, 1974; Goldstein and Tsurutani, 1984; Santolík et al., 2014a; Santolík et al., 2014b; Hartley et al., 2019). It also should be noticed that the occurrence of oblique chorus waves increases close to the plasmapause on the nightside (Li et al., 2016), which may make this less favorable. Generally, these results qualitatively explain the enhancements of plasmapsheric hiss on the nightside. Yue et al. (2017) proposed that the weakening of plasmaspheric hiss on the dayside can be attributed to the enhanced Landau damping from the observed enhancements in suprathermal electron flux (Su et al., 2015). Another possibility could be related to the abrupt erosion of the plasmapause caused by the shock compression. It has been shown that the presence of azimuthal density gradients associated

with plasmaspheric plumes allows for a broader range of chorus wave normal angles to propagate into the plasmasphere (Chen et al., 2009; Hartley et al., 2019; Hartley et al., 2022). As such, the absence of azimuthal density gradient or plume after shock compression might reduce the amount of source chorus that can propagate into the plasmasphere and evolve into plasmaspheric hiss.

Compared to the externally-originated plasmaspheric hiss, there has been relatively little research on the prompt response of internally-generated hiss to solar wind dynamic pressure pulses. Two plausible explanations for this are: 1) some solar wind dynamic pressure pulses may not be strong enough to affect the plasma environment associated with whistler-mode wave generation in the plasmasphere within synchronous orbit; 2) due to the overlapping of different whistler rays, it is difficult to identify internally-generated plasmaspheric hiss through uni-directional Poynting fluxes. Nonetheless, there is still observational evidence showing the direct impact of dynamic pressure pulses on internally-generated plasmaspheric hiss. Fu et al. (2021) reported a frequency-dependent response of plasmaspheric hiss to an interplanetary shock. Based on wave Poynting fluxes, they found that hiss waves with frequencies below 3.5 kHz (~0.18f_{ce}) probably originated from chorus waves outside the plasmasphere, while hiss waves with frequencies above 3.5 kHz were generated near the local magnetic equator. A recent statistical work has proposed the combination of these two different generation mechanisms as the origin of banded plasmaspheric hiss (Ni et al., 2023). The interplanetary shock changed magnetic field configuration and weakened hiss waves below 3.5 kHz by preventing the entry of source chorus into the plasmasphere, which is coincident with the scenario in Yue et al. (2017). Note the shock compression could also change the position of minimum B pockets where source chorus is generated (Tsurutani et al., 2019) and the Landau damping rate along the raypaths (Su et al., 2015), which both affect the propagation of the source chorus into plasmasphere and need further studies. In contrast, the shock-induced acceleration of hot electron fluxes intensified the hiss waves above 3.5 kHz. Recently, Liu et al. (2022) reported the evolution of internally-generated plasmaspheric hiss during a heliospheric plasma sheet (HPS) in the dusk-side plasmasphere (L ~6.7, MLT ~16.8). The long duration impingement of high-density solar wind HPS onto the magnetosphere produced hot anisotropy electrons and caused excitation of plasmaspheric hiss. The subsequent cessation of the HPS led to decreases in hot electron fluxes and the prompt disappearance of the compression-related plasmaspheric hiss. Here, the cessation of the HPS can be treated as a negative solar wind dynamic pressure pulse. The hot proton fluxes and EMIC waves also exhibited similar evolutions in this event, highlighting the importance of solar wind conditions for Earth's space weather.

4 Discussion and conclusion

As a new consequence of solar wind-magnetosphere coupling, the prompt responses of magnetospheric whistler-mode waves to solar wind dynamic pressure pulses has attracted increasing interest in recent years. The prominent effects of solar wind dynamic pressure pulse on the magnetospheric plasma environment associated with whistler-mode waves include: 1) influences of magnetopause movements on electron drift paths; 2) adiabatic variations of energetic electron fluxes caused by sudden changes in magnetic field intensity; 3) acceleration of energetic electrons by compression-related ULF waves; 4) the variation of magnetic field configuration due to the movement of field lines; 5) variations of cold plasma density and plasmasphere structure. In general, the influences to the whistler-mode waves can be summarized as: 1) variations of electron populations can modify the linear wave growth process or the Landau damping (Fu et al., 2012; Su et al., 2015; Jin et al., 2022); 2) variations of both electron populations and magnetic field configuration control the nonlinear growth process (Omura et al., 2008; Katoh and Omura, 2013; Omura, 2021); 3) the magnetic field configuration and cold plasma density determine the raypaths of whistler-mode waves (Chen et al., 2009; Yue et al., 2017; Hartley et al., 2019; Hartley et al., 2022). For chorus waves and internally-generated plasmaspheric hiss, their prompt responses to the solar wind dynamic pressure pulse are directly linked to the local linear or nonlinear growth processes. For plasmaspheric hiss originated from chorus waves, their prompt responses are associated with both the intensity of source chorus and the accessibility of source chorus into the plasmasphere.

Recent studies investigating the prompt impacts of solar wind dynamic pressure pulses on magnetospheric whistler-mode waves have enhanced our understanding of the wave spatiotemporal distribution and generation mechanism. However, several questions remain open, for instance, whether there is a frequency dependence in the response of chorus waves to solar wind dynamic pressure pulses? Can we make a further step in clarifying the plasmaspheric hiss generation mechanisms by statistically analyzing their prompt response to solar wind dynamic pressure pulses? Current studies mainly focus on the variations of wave intensity triggered by pressure pulses, are there any variations in wave frequencies? How do solar wind dynamic pressure pulses affect the propagation process of whistler-mode waves by altering the background magnetic field configuration? The impacts of solar wind dynamic pressure pulses on whistler-mode waves can last for how long, and to what extent do these affect radiation belt electron dynamics? In the future, detailed simulations including the event-specific parameters and statistical analyses using more comprehensive data set are required for a better knowledge.

Author contributions

ZS and NL designed the study. NL wrote the manuscript with contributions from ZS. All authors listed have made a substantial, direct, and intellectual contribution to the work and approved it for publication. All authors contributed to the article and approved the submitted version.

Funding

This work was supported by the National Natural Science Foundation of China grants 42004140, 42130204, 42188101, and 42274198, the Strategic Priority Research Program of Chinese Academy of Sciences grant XDB 41000000, and the Key

Research Program of the Chinese Academy of Sciences grant ZDRE-KT-2021-3.

Conflict of interest

The authors declare that the research was conducted in the absence of any commercial or financial relationships that could be construed as a potential conflict of interest.

Publisher's note

References

Agapitov, O., Artemyev, A., Krasnoselskikh, V., Khotyaintsev, Y. V., Mourenas, D., Breuillard, H., et al. (2013). Statistics of whistler mode waves in the outer radiation belt: Cluster STAFF-SA measurements. *J. Geophys. Res.* 118, 3407–3420. doi:10.1002/jgra.50312

Abel, B., and Thorne, R. M. (1998). Electron scattering loss in Earth's inner magnetosphere 1. Dominant physical processes. *J. Geophys. Res.* 103, 2385–2396. doi:10.1029/97JA02919

Albert, J. M. (1994). Quasi-linear pitch angle diffusion coefficients: Retaining high harmonics. *J. Geophys. Res.* 99, 23741. doi:10.1029/94JA02345

Anderson, R. R., and Vasko, I. Y. (2018). "Whistler waves and their effects on radiation belt dynamics," in *Radiation belt science and exploration* (Amsterdam, Netherlands: Elsevier), 117–135. doi:10.1016/B978-0-12-811788-5.00005-1

Angelopoulos, V. (2008). The THEMIS mission. *Space Sci. Rev.* 141, 5–34. doi:10.1007/s11214-008-9336-1

Bonnell, J. W., Mozer, F. S., Delory, G. T., Hull, A. J., Ergun, R. E., Cully, C. M., et al. (2008). The electric field instrument (EFI) for THEMIS. *Space Sci. Rev.* 141, 303–341. doi:10.1007/s11214-008-9469-2

Bortnik, J., Thorne, R. M., and Meredith, N. P. (2008). The unexpected origin of plasmaspheric hiss from discrete chorus emissions. *Nature* 452, 62–66. doi:10.1038/nature06741

Bortnik, J., Li, W., Thorne, R. M., Angelopoulos, V., Cully, C., Bonnell, J., et al. (2009). An observation linking the origin of plasmaspheric hiss to discrete chorus emissions. *Science* 324, 775–778. doi:10.1126/science.1171273

Breneman, A., Halford, A., Millan, R., McCarthy, M., Fennell, J., Sample, J., et al. (2015). Global-scale coherence modulation of radiation-belt electron loss from plasmaspheric hiss. *Nature* 523, 193–195. doi:10.1038/nature14515

Burton, R. K., and Holzer, R. E. (1974). The origin and propagation of chorus in the outer magnetosphere. *J. Geophys. Res.* 79, 1014–1023. doi:10.1029/JA079i007p01014

Cattell, C. A., Breneman, A. W., Thaller, S. A., Wygant, J. R., Kletzing, C. A., and Kurth, W. S. (2015). Van Allen Probes observations of unusually low frequency whistler mode waves observed in association with moderate magnetic storms: Statistical study. *Geophys. Res. Lett.* 42, 7273–7281. doi:10.1002/2015GL065565

Chakraborty, S., Chakrabarty, D., Reeves, G. D., Baker, D. N., Claudepierre, S. G., Breneman, A. W., et al. (2021). Van allen probe observations of disappearance, recovery and patchiness of plasmaspheric hiss following two consecutive interplanetary shocks: First results. *J. Geophys. Res. (Space Phys.* 126, e28873. doi:10.1029/2020JA028873

Chen, L., Bortnik, J., Thorne, R. M., Horne, R. B., and Jordanova, V. K. (2009). Three-dimensional ray tracing of VLF waves in a magnetospheric environment containing a plasmaspheric plume. *Geophys. Res. Lett.* 36, L22101. doi:10.1029/2009GL040451

Church, S. R., and Thorne, R. M. (1983). On the origin of plasmaspheric hiss - ray path integrated amplification. *J. Geophys. Res.* 88, 7941–7957. doi:10.1029/JA088iA10p07941

Dalin, P. A., Zastenker, G. N., Paularena, K. I., and Richardson, J. D. (2002). A Survey of large, rapid solar wind dynamic pressure changes observed by Interball-1 and IMP 8. *Ann. Geophys.* 20, 293–299. doi:10.5194/angeo-20-293-2002

Draganov, A. B., Inan, U. S., Sonwalkar, V. S., and Bell, T. F. (1992). Magnetospherically reflected whistlers as a source of plasmaspheric hiss. *Geophys. Res. Lett.* 19, 233–236. doi:10.1029/91GL03167

Fu, H. S., Cao, J. B., Mozer, F. S., Lu, H. Y., and Yang, B. (2012). Chorus intensification in response to interplanetary shock. *J. Geophys. Res. (Space Phys.* 117, A01203. doi:10.1029/2011JA016913

Fu, H., Yue, C., Ma, Q., Kang, N., Bortnik, J., Zong, Q.-g., et al. (2021). Frequency-dependent responses of plasmaspheric hiss to the impact of an interplanetary shock. *Geophys. Res. Lett.* 48, e2021GL094810. doi:10.1029/2021GL094810

Gao, Z., Su, Z., Chen, L., Zheng, H., Wang, Y., and Wang, S. (2017). Van Allen Probes observations of whistler-mode chorus with long-lived oscillating tones. *Geophys. Res. Lett.* 44, 5909–5919. doi:10.1002/2017GL073420

Gao, Z., Su, Z., Zhu, H., Xiao, F., Zheng, H., Wang, Y., et al. (2016). Intense low-frequency chorus waves observed by Van Allen Probes: Fine structures and potential effect on radiation belt electrons. *Geophys. Res. Lett.* 43, 967–977. doi:10.1002/2016GL067687

Goldstein, B. E., and Tsurutani, B. T. (1984). Wave normal directions of chorus near the equatorial source region. *J. Geophys. Res. Space Phys.* 89, 2789–2810. doi:10.1029/JA089iA05p02789

Gonzalez, W. D., Gonzalez, A. L. C., Tsurutani, B. T., Smith, E. J., Tang, F., and Akasofu, S. I. (1989). Solar wind-magnetosphere coupling during intense magnetic storms (1978-1979). *J. Geophys. Res.* 94, 8835–8851. doi:10.1029/JA094iA07p08835

Gonzalez, W. D., Tsurutani, B. T., and Clúa de Gonzalez, A. L. (1999). Interplanetary origin of geomagnetic storms. *Space Sci. Rev.* 88, 529–562. doi:10.1023/A:1005160129098

Gosling, J. T., Asbridge, J. R., Bame, S. J., Hundhausen, A. J., and Strong, I. B. (1967). Discontinuities in the solar wind associated with sudden geomagnetic impulses and storm commencements. *J. Geophys. Res.* 72, 3357–3363. doi:10.1029/JZ072i013p03357

Green, J. L., Boardsen, S., Garcia, L., Taylor, W. W. L., Fung, S. F., and Reinisch, B. W. (2005). On the origin of whistler mode radiation in the plasmasphere. *J. Geophys. Res.* 110, A03201. doi:10.1029/2004JA010495

Hartley, D. P., Chen, L., Christopher, I. W., Kletzing, C. A., Santolik, O., Li, W., et al. (2022). The angular distribution of lower band chorus waves near plasmaspheric plumes. *Geophys. Res. Lett.* 49, e2022GL098710. doi:10.1029/2022GL098710

Hartley, D. P., Kletzing, C. A., Chen, L., Horne, R. B., and Santolík, O. (2019). Van allen probes observations of chorus wave vector orientations: Implications for the chorus-to-hiss mechanism. *Geophys. Res. Lett.* 46, 2337–2346. doi:10.1029/2019GL082111

Hayakawa, M., and Sazhin, S. S. (1992). Mid-latitude and plasmaspheric hiss - a review. *Planet. Space Sci.* 40, 1325–1338. doi:10.1016/0032-0633(92)90089-7

Horne, R. B., Thorne, R. M., Shprits, Y. Y., Meredith, N. P., Glauert, S. A., Smith, A. J., et al. (2005). Wave acceleration of electrons in the Van Allen radiation belts. *Nature* 437, 227–230. doi:10.1038/nature03939

Hudson, P. D. (1970). Discontinuities in an anisotropic plasma and their identification in the solar wind. *Planet. Space Sci.* 18, 1611–1622. doi:10.1016/0032-0633(70)90036-X

Jin, Y., Liu, N., Su, Z., Zheng, H., Wang, Y., and Wang, S. (2022). Immediate impact of solar wind dynamic pressure pulses on whistler-mode chorus waves in the inner magnetosphere. *Geophys. Res. Lett.* 49, e2022GL097941. doi:10.1029/2022GL097941

Kasahara, S., Miyoshi, Y., Yokota, S., Mitani, T., Kasahara, Y., Matsuda, S., et al. (2018). Pulsating aurora from electron scattering by chorus waves. *Nature* 554, 337–340. doi:10.1038/nature25505

Katoh, Y., and Omura, Y. (2013). Effect of the background magnetic field inhomogeneity on generation processes of whistler-mode chorus and broadband hiss-like emissions. *J. Geophys. Res.* 118, 4189–4198. doi:10.1002/jgra.50395

Kennel, C. F., Edmiston, J. P., Hada, T., and Wu, C. S. (1985). The quasi-parallel shock wave: Theory and particle simulations. *J. Geophys. Res. Space Phys.* 90, 2199–2208. doi:10.1029/JA090iA11p12199

Kennel, C. F., and Engelmann, F. (1966). Velocity space diffusion from weak plasma turbulence in a magnetic field. *Phys. Fluids* 9, 2377–2388. doi:10.1063/1.1761629

Kletzing, C. A., Kurth, W. S., Acuna, M., MacDowall, R. J., Torbert, R. B., Averkamp, T., et al. (2013). The electric and magnetic field instrument suite and integrated science (EMFISIS) on RBSP. *Space Sci. Rev.* 179, 127–181. doi:10.1007/s11214-013-9993-6

Laakso, H., and Blomberg, L. G. (2005). A survey of magnetospheric whistler-mode waves: Occurrence statistics. *J. Geophys. Res. Space Phys.* 110. doi:10.1029/2004JA010684

Le Contel, O., Roux, A., Robert, P., Coillot, C., Bouabdellah, A., de La Porte, B., et al. (2008). First results of the THEMIS Search Coil magnetometers. *Space Sci. Rev.* 141, 509–534. doi:10.1007/s11214-008-9371-y

LeDocq, M. J., Gurnett, D. A., and Hospodarsky, G. B. (1998). Chorus source locations from VLF poynting flux measurements with the polar spacecraft. *Geophys. Res. Lett.* 25, 4063–4066. doi:10.1029/1998GL900071

Lee, D. Y., Lyons, L. R., and Yumoto, K. (2004). Sawtooth oscillations directly driven by solar wind dynamic pressure enhancements. *J. Geophys. Res. (Space Phys.* 109, A04202. doi:10.1029/2003JA010246

Li, J., Ma, Q., Bortnik, J., Li, W., An, X., Reeves, G. D., et al. (2019). Parallel acceleration of suprathermal electrons caused by whistler-mode hiss waves. *Geophys. Res. Lett.* 46, 12675,675–12,684. doi:10.1029/2019GL085562

Li, L. Y., Cao, J. B., Yang, J. Y., and Dong, Y. X. (2013). Joint responses of geosynchronous magnetic field and relativistic electrons to external changes in solar wind dynamic pressure and interplanetary magnetic field. *J. Geophys. Res. (Space Phys.* 118, 1472–1482. doi:10.1002/jgra.50201

Li, L. Y., Yu, J., Cao, J. B., Yang, J. Y., Li, X., Baker, D. N., et al. (2017). Roles of whistler mode waves and magnetosonic waves in changing the outer radiation belt and the slot region. *J. Geophys. Res. (Space Phys.* 122, 5431–5448. doi:10.1002/2016JA023634

Li, W., Chen, L., Bortnik, J., Thorne, R. M., Angelopoulos, V., Kletzing, C. A., et al. (2015). First evidence for chorus at a large geocentric distance as a source of plasmaspheric hiss: Coordinated THEMIS and Van Allen Probes observation. *Geophys. Res. Lett.* 42, 241–248. doi:10.1002/2014GL062832

Li, W., Santolik, O., Bortnik, J., Thorne, R. M., Kletzing, C. A., Kurth, W. S., et al. (2016). New chorus wave properties near the equator from van allen probes wave observations. *Geophys. Res. Lett.* 43, 4725–4735. doi:10.1002/2016GL068780

Li, W., Thorne, R. M., Angelopoulos, V., Bonnell, J. W., McFadden, J. P., Carlson, C. W., et al. (2009). Evaluation of whistler-mode chorus intensification on the nightside during an injection event observed on the THEMIS spacecraft. *J. Geophys. Res.* 114, A00C14. doi:10.1029/2008JA013554

Li, W., Thorne, R. M., Bortnik, J., Reeves, G. D., Kletzing, C. A., Kurth, W. S., et al. (2013). An unusual enhancement of low-frequency plasmaspheric hiss in the outer plasmasphere associated with substorm-injected electrons. *Geophys. Res. Lett.* 40, 3798–3803. doi:10.1002/grl.50787

Liu, N., Jin, Y., He, Z., Yu, J., Li, K., and Cui, J. (2022). Simultaneous evolutions of inner magnetospheric plasmaspheric hiss and EMIC waves under the influence of a heliospheric plasma sheet. *Geophys. Res. Lett.* 49, e2022GL098798. doi:10.1029/2022GL098798

Liu, N., Su, Z., Gao, Z., Reeves, G. D., Zheng, H., Wang, Y., et al. (2017a). Shock-induced disappearance and subsequent recovery of plasmaspheric hiss: Coordinated observations of RBSP, THEMIS, and POES satellites. *J. Geophys. Res. (Space Phys.* 122, 10,421–10,435. doi:10.1002/2017JA024470

Liu, N., Su, Z., Gao, Z., Zheng, H., Wang, Y., Wang, S., et al. (2020a). Comprehensive observations of substorm-enhanced plasmaspheric hiss generation, propagation, and dissipation. *Geophys. Res. Lett.* 47, e86040. doi:10.1029/2019GL086040

Liu, N., Su, Z., Gao, Z., Zheng, H., Wang, Y., Wang, S., et al. (2017b). Simultaneous disappearances of plasmaspheric hiss, exohiss, and chorus waves triggered by a sudden decrease in solar wind dynamic pressure. *Geophys. Res. Lett.* 44, 52–61. doi:10.1002/2016GL071987

Liu, S., Xie, Y., Zhang, S., Shang, X., Yang, C., Zhou, Q., et al. (2020b). Unusual loss of van allen belt relativistic electrons by extremely low-frequency chorus. *Geophys. Res. Lett.* 47, e89994. doi:10.1029/2020GL089994

Lyons, L. R., and Thorne, R. M. (1973). Equilibrium structure of radiation belt electrons. *J. Geophys. Res.* 78, 2142–2149. doi:10.1029/JA078i013p02142

Ma, Q., Mourenas, D., Li, W., Artemyev, A., and Thorne, R. M. (2017). VLF waves from ground-based transmitters observed by the Van Allen Probes: Statistical model and effects on plasmaspheric electrons. *Geophys. Res. Lett.* 44, 6483–6491. doi:10.1002/2017GL073885

Mauk, B. H., Fox, N. J., Kanekal, S. G., Kessel, R. L., Sibeck, D. G., and Ukhorskiy, A. (2013). Science objectives and rationale for the radiation belt storm probes mission. *Space Sci. Rev.* 179, 3–27. doi:10.1007/s11214-012-9908-y

McPherron, R. L., Terasawa, T., and Nishida, A. (1986). Solar wind triggering of substorm expansion onset. *J. Geomagnetism Geoelectr.* 38, 1089–1108. doi:10.5636/jgg.38.1089

Meredith, N. P., Bortnik, J., Horne, R. B., Li, W., and Shen, X.-C. (2021). Statistical investigation of the frequency dependence of the chorus source mechanism of plasmaspheric hiss. *Geophys. Res. Lett.* 48, e92725. doi:10.1029/2021GL092725

Meredith, N. P., Horne, R. B., and Anderson, R. R. (2001). Substorm dependence of chorus amplitudes: Implications for the acceleration of electrons to relativistic energies. *J. Geophys. Res.* 106, 13165–13178. doi:10.1029/2000JA900156

Meredith, N. P., Horne, R. B., Li, W., Thorne, R. M., and Sicard-Piet, A. (2014). Global model of low-frequency chorus (f_{LHR}<f<0.1f_{ce}) from multiple satellite observations. *Geophys. Res. Lett.* 41, 280–286. doi:10.1002/2013GL059050

Meredith, N. P., Horne, R. B., Shen, X.-C., Li, W., and Bortnik, J. (2020). Global model of whistler mode chorus in the near-equatorial region ($|\lambda_m| < 18°$). *Geophys. Res. Lett.* 47, e87311. doi:10.1029/2020GL087311

Nakamura, S., Omura, Y., and Angelopoulos, V. (2016). A statistical study of EMIC rising and falling tone emissions observed by THEMIS. *J. Geophys. Res. (Space Phys.* 121, 8374–8391. doi:10.1002/2016JA022353

Neugebauer, M. (2006). Comment on the abundances of rotational and tangential discontinuities in the solar wind. *J. Geophys. Res. (Space Phys.* 111, A04103. doi:10.1029/2005JA011497

Ni, B., Li, W., Thorne, R. M., Bortnik, J., Ma, Q., Chen, L., et al. (2014). Resonant scattering of energetic electrons by unusual low-frequency hiss. *Geophys. Res. Lett.* 41, 1854–1861. doi:10.1002/2014GL059389

Ni, B., Summers, D., Xiang, Z., Dou, X., Tsurutani, B. T., Meredith, N. P., et al. (2023). Unique banded structures of plasmaspheric hiss waves in the Earth's magnetosphere. *J. Geophys. Res. (Space Phys.* 128, e2023JA031325. doi:10.1029/2023JA031325

Nishimura, Y., Bortnik, J., Li, W., Thorne, R. M., Ni, B., Lyons, L. R., et al. (2013). Structures of dayside whistler-mode waves deduced from conjugate diffuse aurora. *J. Geophys. Res. (Space Phys.* 118, 664–673. doi:10.1029/2012JA018242

Omura, Y., Katoh, Y., and Summers, D. (2008). Theory and simulation of the generation of whistler-mode chorus. *J. Geophys. Res.* 113, A04223. doi:10.1029/2007JA012622

Omura, Y. (2021). Nonlinear wave growth theory of whistler-mode chorus and hiss emissions in the magnetosphere. *Earth, Planets Space* 73, 95. doi:10.1186/s40623-021-01380-w

Peng, Q., Li, H., Tang, R., Zhong, Z., Zhang, H., and Li, Q. (2020). Variation of dayside chorus waves associated with solar wind dynamic pressure based on MMS observations. *Adv. Space Res.* 65, 2551–2558. doi:10.1016/j.asr.2020.03.006

Reeves, G. D., McAdams, K. L., Friedel, R. H. W., and O'Brien, T. P. (2003). Acceleration and loss of relativistic electrons during geomagnetic storms. *Geophys. Res. Lett.* 30, 1529. doi:10.1029/2002GL016513

Reeves, G. D., Spence, H. E., Henderson, M. G., Morley, S. K., Friedel, R. H. W., Funsten, H. O., et al. (2013). Electron acceleration in the heart of the van allen radiation belts. *Science* 341, 991–994. doi:10.1126/science.1237743

Russell, C. T., Holzer, R. E., and Smith, E. J. (1969). OGO 3 observations of ELF noise in the magnetosphere. 1. Spatial extent and frequency of occurrence. *J. Geophys. Res.* 74, 755–777. doi:10.1029/JA074i003p00755

Samsonov, A. A., Sibeck, D. G., and Imber, J. (2007). MHD simulation for the interaction of an interplanetary shock with the Earth's magnetosphere. *J. Geophys. Res. (Space Phys.* 112, A12220. doi:10.1029/2007JA012627

Santolík, O., Gurnett, D. A., Pickett, J. S., Parrot, M., and Cornilleau-Wehrlin, N. (2003). Spatio-temporal structure of storm-time chorus. *J. Geophys. Res.* 108, 1278. doi:10.1029/2002JA009791

Santolík, O., Kletzing, C. A., Kurth, W. S., Hospodarsky, G. B., and Bounds, S. R. (2014a). Fine structure of large-amplitude chorus wave packets. *Geophys. Res. Lett.* 41, 293–299. doi:10.1002/2013GL058889

Santolík, O., Macúšová, E., Kolmašová, I., Cornilleau-Wehrlin, N., and Conchy, Y. (2014b). Propagation of lower-band whistler-mode waves in the outer Van Allen belt: Systematic analysis of 11 years of multi-component data from the Cluster spacecraft. *Geophys. Res. Lett.* 41, 2729–2737. doi:10.1002/2014GL059815

Sergeev, V. A., Angelopoulos, V., and Nakamura, R. (2012). Recent advances in understanding substorm dynamics. *Geophys. Res. Lett.* 39, L05101. doi:10.1029/2012GL050859

Shi, R., Li, W., Ma, Q., Green, A., Kletzing, C. A., Kurth, W. S., et al. (2019). Properties of whistler mode waves in Earth's plasmasphere and plumes. *J. Geophys. Res. (Space Phys.* 124, 1035–1051. doi:10.1029/2018JA026041

Spence, H. E., Reeves, G. D., Baker, D. N., Blake, J. B., Bolton, M., Bourdarie, S., et al. (2013). Science goals and overview of the radiation belt storm probes (RBSP) energetic particle, composition, and thermal plasma (ECT) suite on NASA's van allen probes mission. *Space Sci. Rev.* 179, 311–336. doi:10.1007/s11214-013-0007-5

Su, Z., Liu, N., Zheng, H., Wang, Y., and Wang, S. (2018). Large-amplitude extremely low frequency hiss waves in plasmaspheric plumes. *Geophys. Res. Lett.* 45, 565–577. doi:10.1002/2017GL076754

Su, Z., Xiao, F., Zheng, H., He, Z., Zhu, H., Zhang, M., et al. (2014a). Nonstorm time dynamics of electron radiation belts observed by the Van Allen Probes. *Geophys. Res. Lett.* 41, 229–235. doi:10.1002/2013GL058912

Su, Z., Xiao, F., Zheng, H., and Wang, S. (2011). CRRES observation and STEERB simulation of the 9 October 1990 electron radiation belt dropout event. *Geophys. Res. Lett.* 38, L06106. doi:10.1029/2011GL046873

Su, Z., Zhu, H., Xiao, F., Zheng, H., Wang, Y., He, Z., et al. (2014b). Intense duskside lower band chorus waves observed by Van Allen Probes: Generation and potential acceleration effect on radiation belt electrons. *J. Geophys. Res.* 119, 4266–4273. doi:10.1002/2014JA019919

Su, Z., Zhu, H., Xiao, F., Zheng, H., Wang, Y., Shen, C., et al. (2015). Disappearance of plasmaspheric hiss following interplanetary shock. *Geophys. Res. Lett.* 42, 3129–3140. doi:10.1002/2015GL063906

Su, Z., Zhu, H., Xiao, F., Zheng, H., Wang, Y., Zong, Q.-G., et al. (2014c). Quantifying the relative contributions of substorm injections and chorus waves to the rapid

outward extension of electron radiation belt. *J. Geophys. Res. Space Phys.* 119, 10–023. doi:10.1002/2014JA020709

Summers, D., Ma, C., Meredith, N. P., Horne, R. B., Thorne, R. M., Heynderickx, D., et al. (2002). Model of the energization of outer-zone electrons by whistler-mode chorus during the October 9, 1990 geomagnetic storm. *Geophys. Res. Lett.* 29, 27-1–27-4. doi:10.1029/2002GL016039

Summers, D., Ni, B., Meredith, N. P., Horne, R. B., Thorne, R. M., Moldwin, M. B., et al. (2008). Electron scattering by whistler-mode ELF hiss in plasmaspheric plumes. *J. Geophys. Res.* 113, A04219. doi:10.1029/2007JA012678

Summers, D., Omura, Y., Nakamura, S., and Kletzing, C. A. (2014). Fine structure of plasmaspheric hiss. *J. Geophys. Res. (Space Phys.* 119, 9134–9149. doi:10.1002/2014JA020437

Tang, R., Yuan, A., Li, H., Ouyang, Z., and Deng, X. (2023). Influence of solar wind dynamic pressure on distribution of whistler mode waves based on van allen probe observations. *J. Geophys. Res. Space Phys.* 128, e2022JA031181. doi:10.1029/2022ja031181

Tao, X. (2014). A numerical study of chorus generation and the related variation of wave intensity using the DAWN code. *J. Geophys. Res. (Space Phys.* 119, 3362–3372. doi:10.1002/2014JA019820

Thorne, R. M., Church, S. R., and Gorney, D. J. (1979). On the origin of plasmaspheric hiss - the importance of wave propagation and the plasmapause. *J. Geophys. Res.* 84, 5241–5247. doi:10.1029/JA084iA09p05241

Thorne, R. M., Li, W., Ni, B., Ma, Q., Bortnik, J., Baker, D. N., et al. (2013a). Evolution and slow decay of an unusual narrow ring of relativistic electrons near *L* ~ 3.2 following the september 2012 magnetic storm. *Geophys. Res. Lett.* 40, 3507–3511. doi:10.1002/grl.50627

Thorne, R. M., Li, W., Ni, B., Ma, Q., Bortnik, J., Chen, L., et al. (2013b). Rapid local acceleration of relativistic radiation-belt electrons by magnetospheric chorus. *Nature* 504, 411–414. doi:10.1038/nature12889

Thorne, R. M., Smith, E. J., Burton, R. K., and Holzer, R. E. (1973). Plasmaspheric hiss. *J. Geophys. Res.* 78, 1581–1596. doi:10.1029/JA078i010p01581

Tsurutani, B. T., Falkowski, B. J., Pickett, J. S., Santolik, O., and Lakhina, G. S. (2015). Plasmaspheric hiss properties: Observations from polar. *J. Geophys. Res. (Space Phys.* 120, 414–431. doi:10.1002/2014JA020518

Tsurutani, B. T., Gonzalez, W. D., Gonzalez, A. L. C., Tang, F., Arballo, J. K., and Okada, M. (1995). Interplanetary origin of geomagnetic activity in the declining phase of the solar cycle. *J. Geophys. Res.* 100, 21717–21733. doi:10.1029/95JA01476

Tsurutani, B. T., Park, S. A., Falkowski, B. J., Bortnik, J., Lakhina, G. S., Sen, A., et al. (2019). Low frequency (f ¡ 200 hz) polar plasmaspheric hiss: Coherent and intense. *J. Geophys. Res. Space Phys.* 124, 10063–10084. doi:10.1029/2019JA027102

Tsurutani, B. T., Park, S. A., Falkowski, B. J., Lakhina, G. S., Pickett, J. S., Bortnik, J., et al. (2018). Plasmaspheric hiss: Coherent and intense. *J. Geophys. Res. (Space Phys.* 123, 10,009–10,029. doi:10.1029/2018JA025975

Tsurutani, B. T., and Smith, E. J. (1974). Postmidnight chorus: A substorm phenomenon. *J. Geophys. Res.* 79, 118–127. doi:10.1029/JA079i001p00118

Tsurutani, B. T., and Smith, E. J. (1977). Two types of magnetospheric ELF chorus and their substorm dependences. *J. Geophys. Res.* 82, 5112–5128. doi:10.1029/JA082i032p05112

Tsyganenko, N. A., and Sitnov, M. I. (2005). Modeling the dynamics of the inner magnetosphere during strong geomagnetic storms. *J. Geophys. Res.* 110, A03208. doi:10.1029/2004JA010798

Turner, D. L., Shprits, Y., Hartinger, M., and Angelopoulos, V. (2012). Explaining sudden losses of outer radiation belt electrons during geomagnetic storms. *Nat. Phys.* 8, 208–212. doi:10.1038/nphys2185

Ukhorskiy, A. Y., Anderson, B. J., Brandt, P. C., and Tsyganenko, N. A. (2006). Storm time evolution of the outer radiation belt: Transport and losses. *J. Geophys. Res.* 111, A11S03. doi:10.1029/2006JA011690

Wang, Z., Su, Z., Liu, N., Dai, G., Zheng, H., Wang, Y., et al. (2020). Suprathermal electron evolution under the competition between plasmaspheric plume hiss wave heating and collisional cooling. *Geophys. Res. Lett.* 47, e89649. doi:10.1029/2020GL089649

Wilson, L., Cattell, C., Kellogg, P., Wygant, J., Goetz, K., Breneman, A., et al. (2011). The properties of large amplitude whistler mode waves in the magnetosphere: Propagation and relationship with geomagnetic activity. *Geophys. Res. Lett.* 38, L17107. doi:10.1029/2011GL048671

Woodroffe, J. R., Jordanova, V. K., Funsten, H. O., Streltsov, A. V., Bengtson, M. T., Kletzing, C. A., et al. (2017). Van Allen Probes observations of structured whistler mode activity and coincident electron Landau acceleration inside a remnant plasmaspheric plume. *J. Geophys. Res. (Space Phys.* 122, 3073–3086. doi:10.1002/2015JA022219

Wu, B.-H., Mandt, M. E., Lee, L. C., and Chao, J. K. (1993). Magnetospheric response to solar wind dynamic pressure variations: Interaction of interplanetary tangential discontinuities with the bow shock. *J. Geophys. Res.* 98, 21297–21311. doi:10.1029/93JA01013

Wygant, J. R., Bonnell, J. W., Goetz, K., Ergun, R. E., Mozer, F. S., Bale, S. D., et al. (2013). The electric field and waves instruments on the radiation belt storm probes mission. *Space Sci. Rev.* 179, 183–220. doi:10.1007/s11214-013-0013-7

Xiao, F., Yang, C., He, Z., Su, Z., Zhou, Q., He, Y., et al. (2014). Chorus acceleration of radiation belt relativistic electrons during March 2013 geomagnetic storm. *J. Geophys. Res.* 119, 3325–3332. doi:10.1002/2014JA019822

Yue, C., Chen, L., Bortnik, J., Ma, Q., Thorne, R. M., Angelopoulos, V., et al. (2017). The characteristic response of whistler mode waves to interplanetary shocks. *J. Geophys. Res. (Space Phys.* 122, 10,047–10,057. doi:10.1002/2017JA024574

Zesta, E., Singer, H. J., Lummerzheim, D., Russell, C. T., Lyons, L. R., and Brittnacher, M. J. (2000). The effect of the january 10, 1997, pressure pulse on the magnetosphere-ionosphere current system. *Geophys. Monogr. Ser.* 118, 217–226. doi:10.1029/GM118p0217

Zhang, W., Ni, B., Huang, H., Summers, D., Fu, S., Xiang, Z., et al. (2019). Statistical properties of hiss in plasmaspheric plumes and associated scattering losses of radiation belt electrons. *Geophys. Res. Lett.* 46, 5670–5680. doi:10.1029/2018GL081863

Zhou, C., Li, W., Thorne, R. M., Bortnik, J., Ma, Q., An, X., et al. (2015). Excitation of dayside chorus waves due to magnetic field line compression in response to interplanetary shocks. *J. Geophys. Res. (Space Phys.* 120, 8327–8338. doi:10.1002/2015JA021530

Zhou, X., Haerendel, G., Moen, J. I., Trondsen, E., Clausen, L., Strangeway, R. J., et al. (2017). Shock aurora: Field-aligned discrete structures moving along the dawnside oval. *J. Geophys. Res. (Space Phys.* 122, 3145–3162. doi:10.1002/2016JA022666

Zhou, X. Y., Fukui, K., Carlson, H. C., Moen, J. I., and Strangeway, R. J. (2009). Shock aurora: Ground-based imager observations. *J. Geophys. Res. (Space Phys.* 114, A12216. doi:10.1029/2009JA014186

Zhu, H., Su, Z., Xiao, F., Zheng, H., Wang, Y., Shen, C., et al. (2015). Plasmatrough exohiss waves observed by Van Allen Probes: Evidence for leakage from plasmasphere and resonant scattering of radiation belt electrons. *Geophys. Res. Lett.* 42, 1012–1019. doi:10.1002/2014GL062964

Zong, Q., Zhou, X., Wang, Y. F., Li, X., Song, P., Baker, D. N., et al. (2009). Energetic electron response to ULF waves induced by interplanetary shocks in the outer radiation belt. *J. Geophys. Res.* 114, A10204. doi:10.1029/2009JA014393

Zuo, P., Feng, X., Xie, Y., Wang, Y., Li, H., and Xu, X. (2015). Automatic detection algorithm of dynamic pressure pulses in the solar wind. *Astrophysical J.* 803, 94. doi:10.1088/0004-637X/803/2/94

frontiers | Frontiers in Astronomy and Space Sciences

TYPE Original Research
PUBLISHED 19 May 2023
DOI 10.3389/fspas.2023.1072795

OPEN ACCESS

EDITED BY
Qianli Ma,
Boston University, United States

REVIEWED BY
Binbin Ni,
Wuhan University, China
Yue Chen,
Los Alamos National Laboratory (DOE), United States

*CORRESPONDENCE
Dmitri Kondrashov,
dkondras@atmos.ucla.edu

RECEIVED 17 October 2022
ACCEPTED 03 May 2023
PUBLISHED 19 May 2023

CITATION
Drozdov AY, Kondrashov D, Strounine K and Shprits YY (2023), Reconstruction of electron radiation belts using data assimilation and machine learning. *Front. Astron. Space Sci.* 10:1072795. doi: 10.3389/fspas.2023.1072795

Reconstruction of electron radiation belts using data assimilation and machine learning

Alexander Y. Drozdov[1], Dmitri Kondrashov[2]*, Kirill Strounine[3] and Yuri Y. Shprits[1,3,4]

[1]Department of Earth, Planetary, and Space Sciences, University of California, Los Angeles, Los Angeles, CA, United States, [2]Department of Atmospheric and Oceanic Sciences, University of California, Los Angeles, Los Angeles, CA, United States, [3]Space Sciences Innovations Inc., Seattle, WA, United States, [4]GFZ German Centre for Geosciences, Potsdam, Germany

We present a reconstruction of radiation belt electron fluxes using data assimilation with low-Earth-orbiting Polar Orbiting Environmental Satellites (POES) measurements mapped to near equatorial regions. Such mapping is a challenging task and the appropriate methodology should be selected. To map POES measurements, we explore two machine learning methods: multivariate linear regression (MLR) and neural network (NN). The reconstructed flux is included in data assimilation with the Versatile Electron Radiation Belts (VERB) model and compared with Van Allen Probes and GOES observations. We demonstrate that data assimilation using MLR-based mapping provides a reasonably good agreement with observations. Furthermore, the data assimilation with the flux reconstructed by NN provides better performance in comparison to the data assimilation using flux reconstructed by MLR. However, the improvement by adding data assimilation is limited when compared to the purely NN model which by itself already has a high performance of predicting electron fluxes at high altitudes. In the case an optimized machine learning model is not possible, our results suggest that data assimilation can be beneficial for reconstructing outer belt electrons by correcting errors of a machine learning based LEO-to-MEO mapping and by providing physics-based extrapolation to the parameter space portion not included in the LEO-to-MEO mapping, such as at the GEO orbit in this study.

KEYWORDS

radiation belts, neural network, multiple linear regression, VERB code, data assimilation, machine learning

1 Introduction

The radiation belts consist of electrons and protons trapped by the Earth's magnetic field (Lyons and Thorne, 1973) and are a major source of damaging space weather effects on near-Earth spacecraft. The inner electron belt is located typically between 1.2 and 2.0 Earth radii R_E, while the outer belt extends from about 3 to ~8 R_E. Relativistic electron fluxes in the outer belt are highly variable; this variability is due to the competing effects of source and loss processes, both of which are forced by solar-wind-driven magnetospheric dynamics and by resonant interactions of plasma waves and particles (Thorne, 2010; Shprits et al., 2008a; 2008b).

Understanding the mechanisms of build-up and decay of radiation belt electron fluxes is one of the fundamental problems of modern space physics having an important application in relation to human technological systems. While significant progress has been achieved in understanding the electron radiation belt dynamics using physics-based models, it is still incomplete, due to the limited number of satellites in mapping the global radiation environment in space at any given time. Here, data assimilation techniques become very important and helpful, as they combine measurements that are irregularly distributed in space and time with a physics-based model to estimate the evolution of the system's state in time; both the model and observations typically include errors. The Kalman filter (K-filter, hereafter) (Kalman, 1960) technique of data assimilation represents so-called sequential filtering or sequential estimation, and its various generalizations have been successfully applied in various engineering fields, including autonomous or assisted navigation systems, as well as in atmospheric, oceanic, and climate studies (Ghil and Malanotte-Rizzoli, 1991; Kalnay, 2003). Data assimilation for radiation belts by K-filter techniques had been pioneered at UCLA in collaboration with Richard Thorne and Michael Ghil (Kondrashov et al., 2007; Shprits et al., 2007; Daae et al., 2011; Kondrashov et al., 2011) starting with the Versatile Electron Radiation Belt (VERB) 1-D code, where only radial diffusion is included, similar to study of (Koller et al., 2007) about the same time. For the VERB-3D code, where the state vector is of a very large size $\mathcal{O}(10^6 - 10^7)$ and the computational requirements of the standard K-filter become very large, Shprits et al. (2013) developed a novel efficient approximation of a K-filter inspired by the operator splitting technique. This method still applies the standard formulation of a K-filter, but only for the 1D diffusion operators of VERB-3D model in L-shell, energy, and pitch-angle, thus operating sequentially on matrices of much smaller size for each grid line. Utilizing the split-operator technique, the first operational data-assimilative radiation belt forecast model was developed at UCLA (e.g., Kellerman et al., 2014; Shprits et al., 2023). Additionally, the approach of using data assimilation with the VERB model was successfully used to study radiation belt source and loss mechanisms (Cervantes et al., 2020a; Cervantes et al., 2020b), although so far no reconstructed measurements based on LEO observations were used for data assimilation. Recently, K-filter type approaches have been extended into a complex high-dimensional magnetosphere model, where it has been demonstrated that missing physics in global MHD models can be successfully compensated for by data assimilation, namely that pressure gradients in the inner magnetosphere can be generated *via* the imposition of an observed low-latitude current system (Merkin et al., 2016).

Before the launch of the Van Allen Probes (Mauk et al., 2013) that provided unprecedented measurements of the radiation belts, several works attempted reconstruction of the electron flux variation at geostationary orbit using a neural network (e.g., Koons and Gorney, 1991; Fukata et al., 2002; Ling et al., 2010; Kitamura et al., 2011), which was important for space weather applications and for the understanding of the physical processes driving radiation belt dynamics. The neural network approach of the electron flux prediction showed decent agreement with observations and other models (Perry et al., 2010). Lately, machine learning methods including neural networks became increasingly commonly used in reconstructing and forecasting relativistic electrons in radiation belts, using solar wind conditions, geomagnetic indices and other inputs (e.g., Batusov et al., 2018; Pires de Lima et al., 2020; Sarma et al., 2020; Chu et al., 2021; Landis et al., 2022; Ma et al., 2022; Wing et al., 2022; Zhelavskaya et al., 2016; 2017; 2018; 2021).

Kanekal et al. (2001) have found a remarkable global coherency in ultrarelativistic electron populations (>2MeV) throughout the outer zone observed on satellites in distinct orbits, ranging from polar low-Earth to geosynchronous altitudes. Recently, Chen et al. (2016) have established cross-energy, cross-pitch-angle coherence between the trapped MeV electrons observed by Van Allen-Probes and precipitating 100 s of keV electrons at LEO. These findings naturally motivated more studies and model development on forecasting and nowcasting of outer belt electrons using LEO measurements.

Chen et al. (2019) developed a linear filter model to predict distributions of electrons within Earth's outer radiation belt using measurements from the Polar Operational Environmental Satellite (POES) and LANL GEO. This PreMevE model provided a prediction spanning several hours as well as a 1-day forecasts of the spin-averaged ~MeV radiation belt electrons near the equator. The extended PreMevE 2.0 (Pires de Lima et al., 2020) and 2E (Sinha et al., 2021) models further evaluated multiple machine learning models that fall into four different classes of linear and neural network architectures and utilized electron intensities from Polar Operational Environmental Satellite (POES) and LANL GEO to map into 1 MeV and >2MeV trapped spin-averaged electron fluxes with the focus on extended prediction (up to 2 days), taking as input also solar wind parameters.

Claudepierre and O'Brien (2020) also developed the neural net SHELLS model nowcasting daily 350 keV and 1 MeV electron fluxes in the outer radiation belt by using as input the electron fluxes from the POES satellite, and the model was built for spin-averaged flux. A new version of the SHELLS model was recently developed by Boyd et al. (2023) which incorporates the radial, angular and energy dependence as well as finer temporal resolution, and can accurately nowcast the outer electron radiation belt dynamics using both out-of-sample data from the Van Allen Probes and GPS.

In this work, we use machine learning to enhance existing satellite observations for data assimilation purposes. Our main goal is to build a model that will map the low-Earth-orbit satellite data to near-equatorial regions. Mapping the POES data to the equatorial region enables data assimilation (DA) of the electron radiation belts with the Versatile Electron Radiation Belt (VERB) code, in particular providing the state of the radiation belts in the wide range of equatorial pitch-angles and energies. The fully reconstructed state of the radiation belts is particularly useful for space weather applications, as it allows to fly virtual satellites with arbitrary orbital parameters. Using POES data is ideal for this task because of its long history and availability in the near future.

Our work extends earlier studies and is different in several important ways. First, we use POES data for mapping (nowcasting) the newly available Van Allen Probes ECT dataset (Boyd et al., 2021) in an extended range of available energies and equatorial pitch angles, which is essential for the DA and radiation belts reconstruction because it is necessary for the computation of the PSD in the adiabatic invariant space, that is used in the physics-based model, e.g. VERB. Secondly, we explore two machine learning

methods for mapping: multivariate linear regression (MLR) and neural net (NN).

This is an initial study that is aimed to test if the considered machine learning models (MLR and NN) can be used by data assimilation to reconstruct radiation belts. We test the entire workflow including first mapping to the equator and then assimilating ML model results into the VERB model. In the particular case described in this study, we only use POES satellites (specifically, NOAA-15, NOAA-16, NOAA-18, and NOAA-19) for mapping from LEO to MEO (Van Allen Probes), to reconstruct the entire radiation belts and along any satellite trajectory, such as GOES. Furthermore, data assimilation allows us to combine measurements from different sources and different satellites, and this will be explored in future studies.

To summarize, the machine learning (ML) based mapping of LEO to MEO can be interpreted as creating high-quality Van Allen Probes-like satellite measurements even after the end of the Van Allen Probes mission, and which can be used to reconstruct radiation belts *via* data assimilation. Such use of ML-based "virtual satellite" is a very powerful and novel concept that could be potentially applied to other Earth sciences. Our approach represents the combination of physics-based (*via* data assimilation with VERB) and ML approaches, known as gray box (Camporeale, 2019), and takes into account errors (uncertainties) in both.

2 Data and methods

2.1 Data

In this study, we utilize measurements from the National Aeronautics and Space Administration (NASA) Van Allen Probes (Mauk et al., 2013) and from the National Oceanic and Atmospheric Administration (NOAA) Polar Orbiting Environmental Satellites (POES) (Evans and Greer, 2004).

The Van Allen Probes included two identical spacecraft (RBSP-A and RBSP-B) that were orbiting through the Earth's radiation belts between a perigee and apogee of 1.1 and 5.8 RE (medium Earth orbit, MEO), respectively, with a low inclination (~10°). Each probe maintains an orbital period of 9 h, providing near-equatorial electron measurements. On board the satellites are multiple instruments that are a part of the Energetic Particle, Composition and Thermal Plasma Suite (ECT) (Spence et al., 2013), providing the measurements of electrons in a wide energy range (from 1 eV up to 20 MeV). In this study, we use a new ECT data product that incorporates the pitch-angle-resolved electron flux measurements on a consistent cross-calibrated data set (Boyd et al., 2021). **Figure 1A** illustrates 1 month of electron flux measurements at local pitch angle $\alpha_{loc} = 90°$ with corresponding equatorial pitch-angle coverage on **Figure 1B**.

The POES are multiple Sun-synchronous low-orbiting satellites (altitude of ~800 km or lower Earth orbit, LEO), which provide comprehensive coverage in L-shell and magnetic local time (MLT). The orbital period of each satellite is ~100 min. The satellites provide measurements with two telescopes oriented to zenith (0°) and perpendicular (90°). Two telescopes enable us to distinguish between particles in the loss cone and trapped (or quasi-trapped) population. In this study, we use 4 satellites: NOAA-15, NOAA-16, NOAA-18, and NOAA-19. We use a contamination-corrected dataset of differential electron flux that is available from 1998 until 11 May 2014 (Peck et al., 2015). In this study, we limit the energy range in the selected dataset from ~30 keV up to ~1.9 MeV, providing 20 energy channels. **Figure 1C** shows electron flux measurements from a single POES satellite (NOAA-15) using the perpendicular telescope-maximizing corresponding equatorial pitch-angle coverage on **Figure 1D**. In comparison to the Van Allen Probes, observations from POES are limited in equatorial pitch-angle coverage but have a much finer temporal resolution, which makes them highly advantageous for the reconstruction of the radiation belts.

GOES spacecraft at geosynchronous orbit measures electrons in several integral flux channels using the Energetic Proton, Electron, and Alpha particle Detector (EPEAD) (e.g., Rodriguez et al., 2014). In this study we use >800 keV and >2 MeV channels and calculate differential electron flux between those energies using Gaussian fit of the spectrum. We use 2 spacecraft available for the time of interest, GOES-13 and GOES-15.

For all missions, the adiabatic invariants μ, K, and L* (Roederer, 1970) are computed with The International Radiation Belt Environment Modeling (IRBEM) library, utilizing the International Geomagnetic Reference Field (IGRF) internal field model, and the T89 external field model (Tsyganenko, 1989).

2.2 Versatile electron radiation belt (VERB) code

The adiabatic motion of energetic charged particles in these belts consists of three basic periodic components: gyro-motion about Earth's magnetic field lines; bounce motion of the gyration center up and down a given magnetic field line; and the azimuthal drift of particles around the Earth, perpendicular to the meridional planes formed by the magnetic polar axis and the field lines. There are three adiabatic invariants, each associated with one of these motions, and by averaging over the gyro, bounce, and drift motions, we can describe the evolution of the particles' phase-space density (PSD) solely in terms of these invariants — (μ, J, Φ), respectively. In the collisionless magnetospheric plasma, resonant wave-particle interactions provide the dominant mechanism for violation of the adiabatic invariants, resulting in changes in the outer radiation belt structure. For small wave amplitudes and a broad wave spectrum, such resonant interaction can be described within a framework of the quasi-linear (QL) theory, which is based on the 3-D Fokker-Planck diffusion equation (Shultz and Lanzerotti, 1974). The three-dimensional Versatile Electron Radiation Belt (VERB-3D) code (Subbotin and Shprits, 2009) solves the Fokker-Planck equations for PSD of electrons f written in term operators describing the radial diffusion, equatorial pitch angle (α_{eq}) and energy (or momentum p) diffusion:

$$\frac{\partial f}{\partial t} = \frac{1}{G}\frac{\partial}{\partial L^*}\left(GD_{L^*L^*}\frac{\partial f}{\partial L^*}\right) + \frac{1}{G}\frac{\partial}{\partial p}\left(GD_{pp}\frac{\partial f}{\partial p}\right) + \frac{1}{G}\frac{\partial}{\partial \alpha_{eq}}\left(GD_{\alpha_{eq}\alpha_{eq}}\frac{\partial f}{\partial \alpha_{eq}}\right) - \frac{f}{\tau}, \quad (1)$$

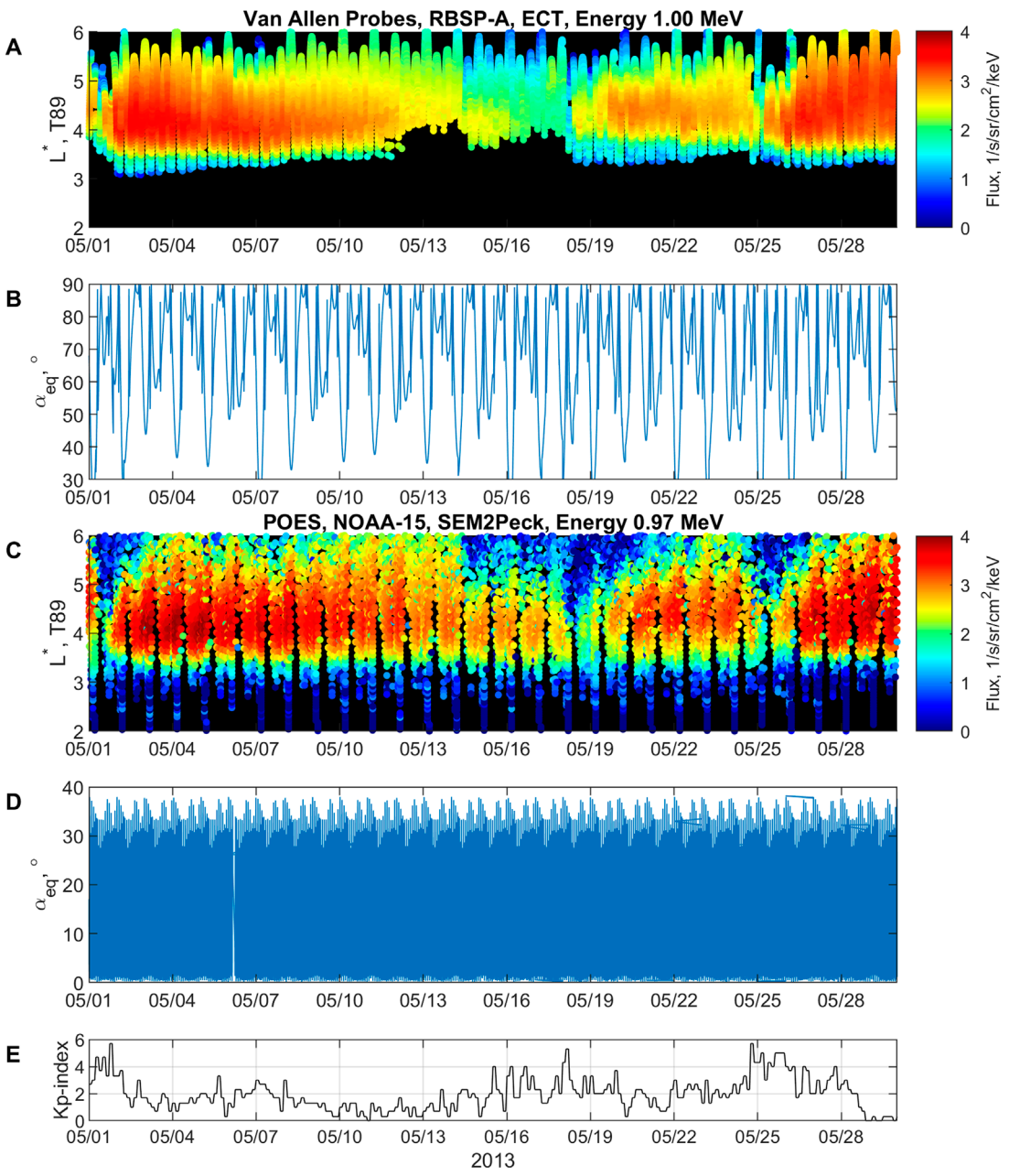

FIGURE 1
Example of the data used in this study: **(A)** Van Allen Probes observation from RBSP-A satellite (ETC data set), 1 MeV electron flux and **(B)** corresponding equatorial pitch angle α_{eq}. **(C)** POES observations from NOAA-15 satellite (SEM2Peck data set), 0.97 MeV electron flux and **(D)** corresponding equatorial pitch angle α_{eq}. **(E)** Kp index.

where $G = \frac{8\pi R_E^3}{m_0} p^s \sin(2\alpha_{eq}) L^{*2} T(\sin(\alpha_{eq}))$ is the Jacobian of the transformation from an adiabatic invariant system (μ, J, Φ) to (p, α_{eq}, L^*); L^* is a form of the third invariant Φ; m_0 is the particle's rest mass; R_E is Earth's radius; and $T(\sin(\alpha_{eq}))$ is a function corresponding to the bounce frequency Shultz and Lanzerotti (1974). The diffusion coefficients $D_{L^*L^*}$, D_{pp}, $D_{\alpha_{eq}\alpha_{eq}}$ of Eq. 1 incorporate radial and energy diffusion and pitch angle scattering, respectively, and are estimated using QL diffusion theory and statistical hiss and chorus wave properties (Brautigam and Albert, 2000; Zhu et al., 2019). The mixed terms are not included for simplicity of the use of the VERB code in data assimilation (see **Section 2.3**). The lifetime parameter τ accounts for electron losses due to collisions with neutral particles, which is modeled by setting up lifetimes equal to the quarter bounce time for electrons inside of the loss cone and infinite outside of the loss cone. The VERB model was successfully validated on time scales from several months to several years (e.g. Drozdov et al., 2015; Drozdov et al., 2017; Zhu et al., 2019; Drozdov et al., 2020; Wang et al., 2020; Drozdov et al., 2021; Saikin et al., 2021).

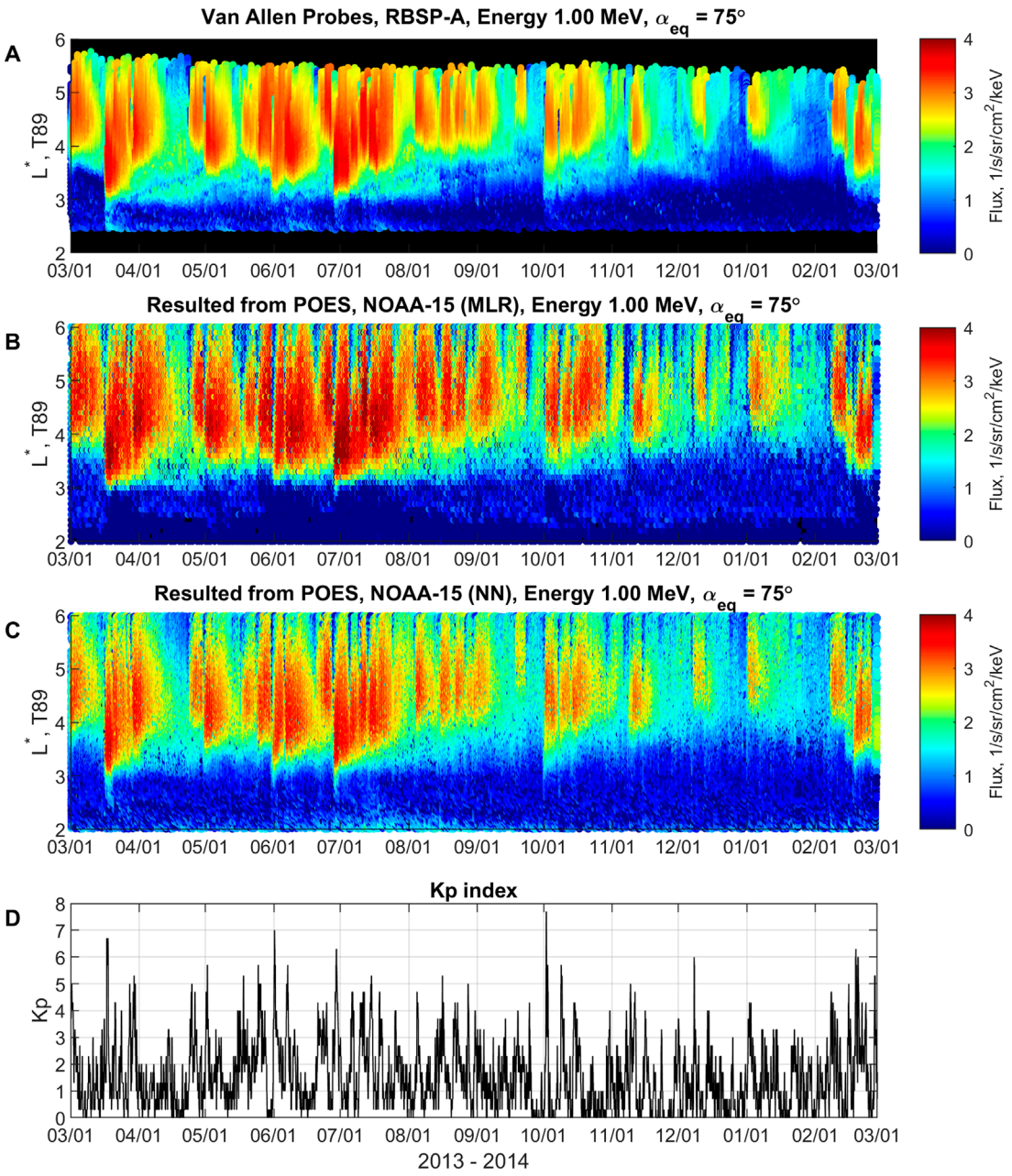

FIGURE 2
Observed and reconstructed using NOAA-15 satellite electron flux at 1 MeV and α_{eq} =75° for the training/testing period of 1 year from 01 March 2013 until 01 March 2014. **(A)** Van Allen Probes observations. **(B)** Reconstructed with multivariate linear regression analysis flux. **(C)** Reconstructed with neural network flux. **(D)** Kp index.

2.3 Data assimilation (DA)

By using common nomenclature for data assimilation (DA), in the K-filter formulation for a numerically discretized model (such as VERB-3D), the observational data $\mathbf{y}^o$ and dynamically evolving fields of the model forecast $\mathbf{x}^f$ are combined into analysis $\mathbf{x}^a$:

$$\mathbf{x}^a_{k+1} = \mathbf{M}_k \mathbf{x}^f_k + \mathbf{K}_k \left(\mathbf{y}^o_k - \mathbf{H}_k \mathbf{x}^f_k \right) \tag{2}$$

Here $\mathbf{x}_k$ represents a state column vector composed of all model variables on a numerical grid–for our case, it is PSD f in Eq. 1, k is the time-stepping index, and the time-dependent matrix $\mathbf{M}_k$ of the VERB numerical model is obtained by numerically discretizing the partial differential equations that govern the physical system under study, i.e. Fokker-Plank equations for PSD (Eq. (1)). The use of the full Kalman filter for a three-dimensional model is a challenging task, as it requires the operation of $O(N^3)$ in computational complexity, where N is the number of all points in

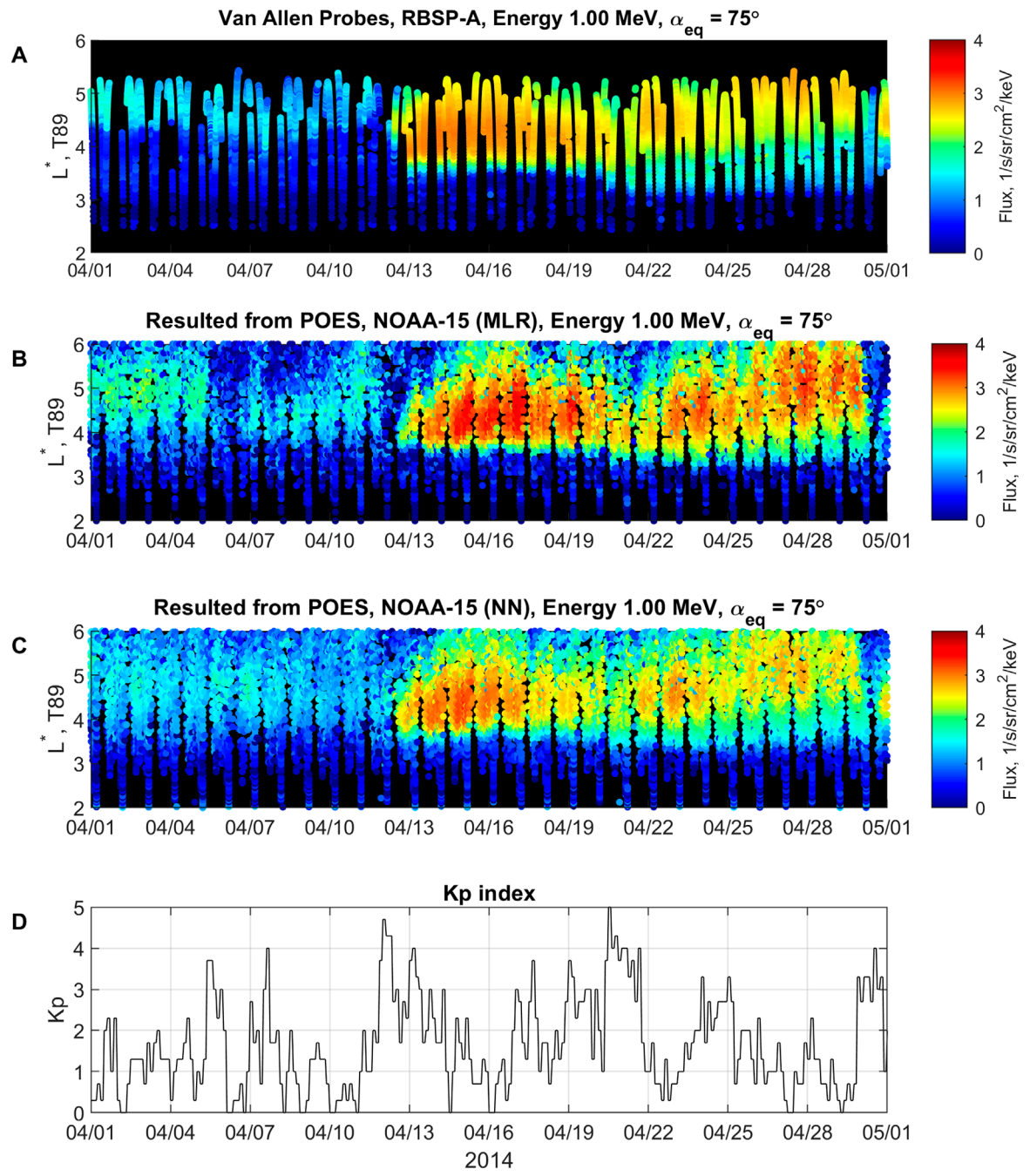

FIGURE 3
Observations and reconstruction using NOAA-15 satellite electron flux at 1 MeV and α_{eq} =75° for the interval outside of the training/testing period, from 01 April 2014 until 01 May 2014. **(A)** Van Allen Probes observations. **(B)** Reconstructed with multivariate linear regression analysis flux. **(C)** Reconstructed with neural network flux. **(D)** Kp index.

the grid. In this study, we use a 31 × 30 × 29 grid in the coordinates of L^*, p, α_{eq}, respectively. Instead of using the full Kalman filter, we use an alternative method of split-operator approach Shprits et al. (2013), where the Kalman filter is applied for each grid direction. The model matrices $\mathbf{M}_k$ correspond to each of the diffusion operators in Eq. 1. The grid is selected to cover the $L^* \in [1,7]$, with pitch angle and energy covering $\alpha_{eq} \in [0.3°, 89.7°], E \in [0.01, 10]$ MeV at $L^* = 7$.

The matrix $\mathbf{H}_k$ represents a map between the model state $\mathbf{x}_k$ and the observations of that state. The last term on the right-hand side of Eq. 2,

$$\mathbf{z}_k \equiv \mathbf{y}_k^{\mathrm{o}} - \mathbf{H}\mathbf{x}_k^{\mathrm{f}}, \tag{3}$$

is the innovation vector that represents the mismatch between the model and observations and is used to drive the model state closer to the observations.

Specifying the model and observational errors **Q** and **R** allows us to follow the time evolution of the forecast-error $\mathbf{P}^f$ and analysis-error $\mathbf{P}^a$ covariance matrices.

This knowledge of the error-covariance matrices provides, in turn, the optimal Kalman gain matrix $\mathbf{K}_k$, which gives the proper weight to the observations vs. the model prediction:

$$\begin{aligned}\mathbf{P}_k^f &= \mathbf{M}_k\mathbf{P}_{k-1}^a\mathbf{M}_k^T + \mathbf{Q_k},\\ \mathbf{P}_k^a &= (\mathbf{I} - \mathbf{K}_k\mathbf{H}_k)\,\mathbf{P}_k^f,\\ \mathbf{K}_k &= \mathbf{P}_k^f\mathbf{H}_k^T\left(\mathbf{H}_k\mathbf{P}_k^f\mathbf{H}_k^T + \mathbf{R}_k\right)^{-1}.\end{aligned} \tag{4}$$

Information obtained in the error-covariance matrices is crucial in modifying the state vector $\mathbf{x}_k$ in observation-void regions.

In the standard formulation of the Kalman filter, the noise covariances **Q** and **R** are assumed to be known. This rarely happens in practice, and usually, some simple approximations are made. Assuming the log-normal distribution of errors for PSD and uncorrelated errors in different locations, both **Q** and **R** are specified as diagonal matrices, and the diagonal terms of **Q** and **R** are taken simply as $\zeta_{o,m}f_{o,m}^2$, where $f_{o,m}^2$ is the observed or modeled PSD value, and $\zeta_{o,m}$ is a specified factor corresponding to observational or model error (Kondrashov et al., 2011). This heuristic approach worked well in previous DA studies using VERB. Note that the exact values of $\zeta_{o,m}$ are not important: it is their respective ratio that determines the weight given to the observations vs. the model solution in the analysis, or update, the step of the data assimilation. In this study, we use $\zeta_o = 0.5$ and $\zeta_m = 0.5$.

2.4 Multivariate linear regression model (MLR)

To map POES measurements to the high equatorial pitch-angle region, we use the following data processing. Van Allen Probes data is interpolated into the regular grid of equatorial pitch angles from 5° to 85° with a step of 10°. Then the data is interpolated onto the same energy grid as the energy channels on the POES satellites. The interpolated flux from RBSP-A and RBSP-B is merged and binned in time and L^* (j_{RBSP}^{binned}). For the binning, we use a time step of 3 h and a L^* step of 0.1.

Next, we calculated the standard deviation of the log_{10} of POES flux (j) at all POES energies and found very high variations as revealed by very high standard deviation values. The high variation of the flux is considered to be an outlier of the unrealistically low or high values of the measured fluxes. To remove the unrealistic measurements, we exclude the data that is below the threshold based on the visual inspection of measurements. The threshold is calculated for the 1-year period of 01 March 2013–01 March 2014 for each energy channel for the entire L^* range

$$threshold = 10^{<\log_{10}(j) - std(\log_{10}(j))/4>} \tag{5}$$

The results of this method were inspected at all energies for several months of POES measurements. The inspection included the analysis of the flux vs. L^* dependence with a determined threshold level. The threshold level was selected to be significantly below the reliable flux level.

To obtain the extrapolated pitch-angle distribution, we assume a simplified functional dependence of the flux as shown by the following equation:

$$j\left(\alpha_{eq}\right) = j_0 \cdot \sin\left(\alpha_{eq}\right) \tag{6}$$

where α_{eq} is an equatorial pitch angle and j_0 is the flux of the trapped population at 90°. Then the POES measurements are extrapolated to the equatorial pitch angles on the grid (α_{eq}^{grid}) from 5° to 85° grid with a fixed step of 10°:

$$j\left(t, E, \alpha_{eq}^{grid}\right) = \sin\left(\alpha_{eq}^{grid}\right)\frac{j\left(t, E, \alpha_{eq}\right)}{\sin\left(\alpha_{eq}\right)} \tag{7}$$

where $j(t, E, \alpha_{eq}^{grid})$ is flux extrapolated to the new equatorial pitch angle grid, and $j(t, E, \alpha_{eq})$ is flux observed by POES at the time t, energy E and equatorial pitch angle α_{eq}. At each point in time, POES provided flux measurements for two local pitch angles. We selected one measurement of the flux that corresponded to the higher pitch angle to calculate extrapolated flux values. The extrapolated POES flux is binned in a similar manner as Van Allen Probes (j_{POES}^{binned}). The simplified sin approximation is used to establish a baseline method of that described in this section. As discussed in **Section 4**, the use of advanced pitch-angle approximation will be a subject of future research.

Then, we calculate the ratio $r(t, E, \alpha_{eq}^{grid}) = j_{RBSP}^{binned}/j_{POES}^{binned}$ of the binned Van Allen Probes and binned POES fluxes for a 1-year period (01 March 2013–01 March 2014). We first take the median of this ratio for each Kp value and then bin by Kp, L^*, energy, and equatorial pitch angle. Typically, inter-calibration coefficients are used to describe differences between instruments. Here we use obtained ratio r to capture not only the bias of the instrument but also the bias of the extrapolation to the high pitch angles procedure which may depend on Kp and L^*.

TABLE 1 Coefficients of determination (r^2) and correlation coefficients calculated in logarithmic (r_{log}) and linear (r_{lin}) space between Van Allen Probes, RBSP-A and reconstituted from POES NOAA-15 data using MLR and NN models.

	MLR			NN		
Energy/Pitch angle	r^2	r_{log}	r_{lin}	r^2	r_{log}	r_{lin}
Training period of 1 year, 01 March 2013–01 March 2014						
E = 1.0 MeV, α_{eq} = 75°	0.78	0.86	0.79	0.91	0.92	0.88
E = 1.0 MeV, α_{eq} = 55°	0.82	0.88	0.82	0.91	0.92	0.89
E = 1.0 MeV, α_{eq} = 35°	0.83	0.88	0.82	0.91	0.92	0.90
E = 0.5 MeV, α_{eq} = 75°	0.47	0.85	0.81	0.82	0.89	0.88
E = 1.5 MeV, α_{eq} = 75°	0.71	0.78	0.72	0.85	0.87	0.85
Outside of the training period, 01 April 2014–01 May 2014						
E = 1.0 MeV, α_{eq} = 75°	0.79	0.83	0.69	0.90	0.90	0.85
E = 1.0 MeV, α_{eq} = 55°	0.79	0.84	0.75	0.88	0.89	0.84
E = 1.0 MeV, α_{eq} = 35°	0.81	0.86	0.77	0.86	0.89	0.84
E = 0.5 MeV, α_{eq} = 75°	0.63	0.87	0.80	0.83	0.89	0.89
E = 1.5 MeV, α_{eq} = 75°	0.66	0.71	0.65	0.77	0.80	0.84

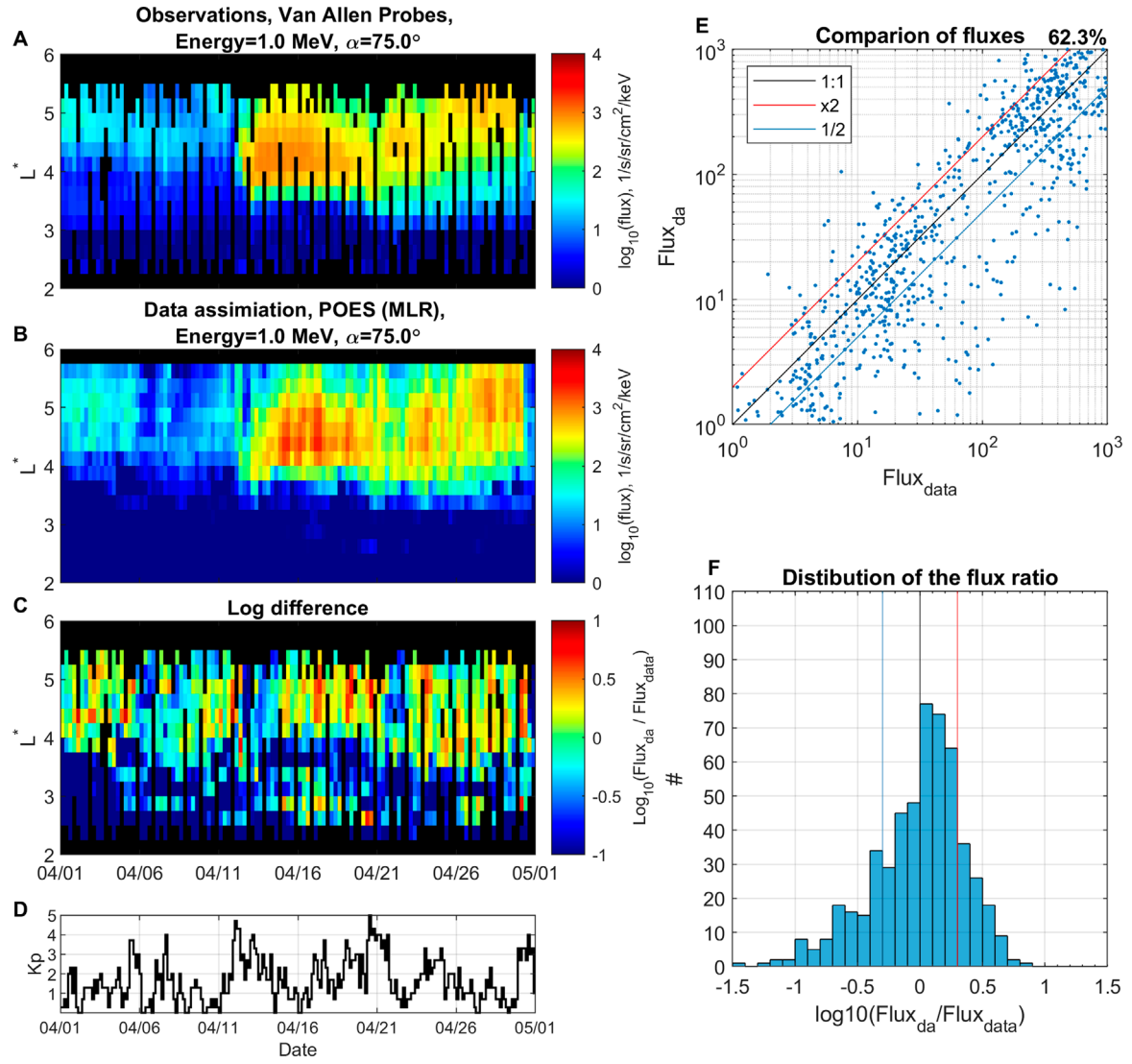

FIGURE 4
Data assimilation using reconstructed with multivariate linear regression analysis data. Electron flux at 1 MeV and α_{eq} =75° for the period from 01 April 2014 until 01 May 2014. **(A)** Binned Van Allen Probe observations. **(B)** Data assimilation using reconstructed flux from POES data. **(C)** Logarithmic difference between flux from data assimilation and observations. **(D)** Kp index. **(E)** Comparison of fluxes between observations $Flux_{data}$ and DA results $Flux_{da}$, **(F)** distribution of the logarithmic flux ratio.

Using the logarithm of the obtained ratio ($\log_{10}(r)$), we perform a multivariate linear regression analysis. We obtain calibration coefficients (ξ) that depend on Kp, L^*, energy (E) and pitch angle (α_{eq}) based on this analysis:

$$\xi\left(Kp, L^*, E, \alpha_{eq}\right) = b_0 + b_1 \cdot Kp + b_2 \cdot L^* + b_3 \cdot E + b_4 \cdot \alpha_{eq} \qquad (8)$$

where $b_0 \ldots b_4$ are regression coefficients. The calibration coefficients ξ can be used to obtain the fluxes at given α_{eq}, namely $j_{\alpha_{eq}^{grid}} = 10^{\xi} \cdot j_{POES}$, for each of the α_{eq}^{grid} and POES energy. Figure 2 illustrates that the flux resulted from MLR method is in reasonable agreement with Van Allen Probe measurements. The resulted flux for the period from 01 April 2014 until 01 May 2014 (see Figure 3), which is outside of the 1-year interval used to construct MLR calibration coefficients, is included in the data assimilation in Section 3.

2.5 Neural network (NN) model

The constructed neural network (NN) model predicts Van Allen Probes ECT electron flux j_{RBSP} for a specific energy channel and a local pitch angle channel using one fully connected layer with 32 neurons and the rectified linear unit ("relu") activation function in the hidden layer. Our NN model design choices are generated by using best practices and an extensive parameter search and testing. We have compared various designs of NN model with different number of hidden layers and neurons (not shown here),

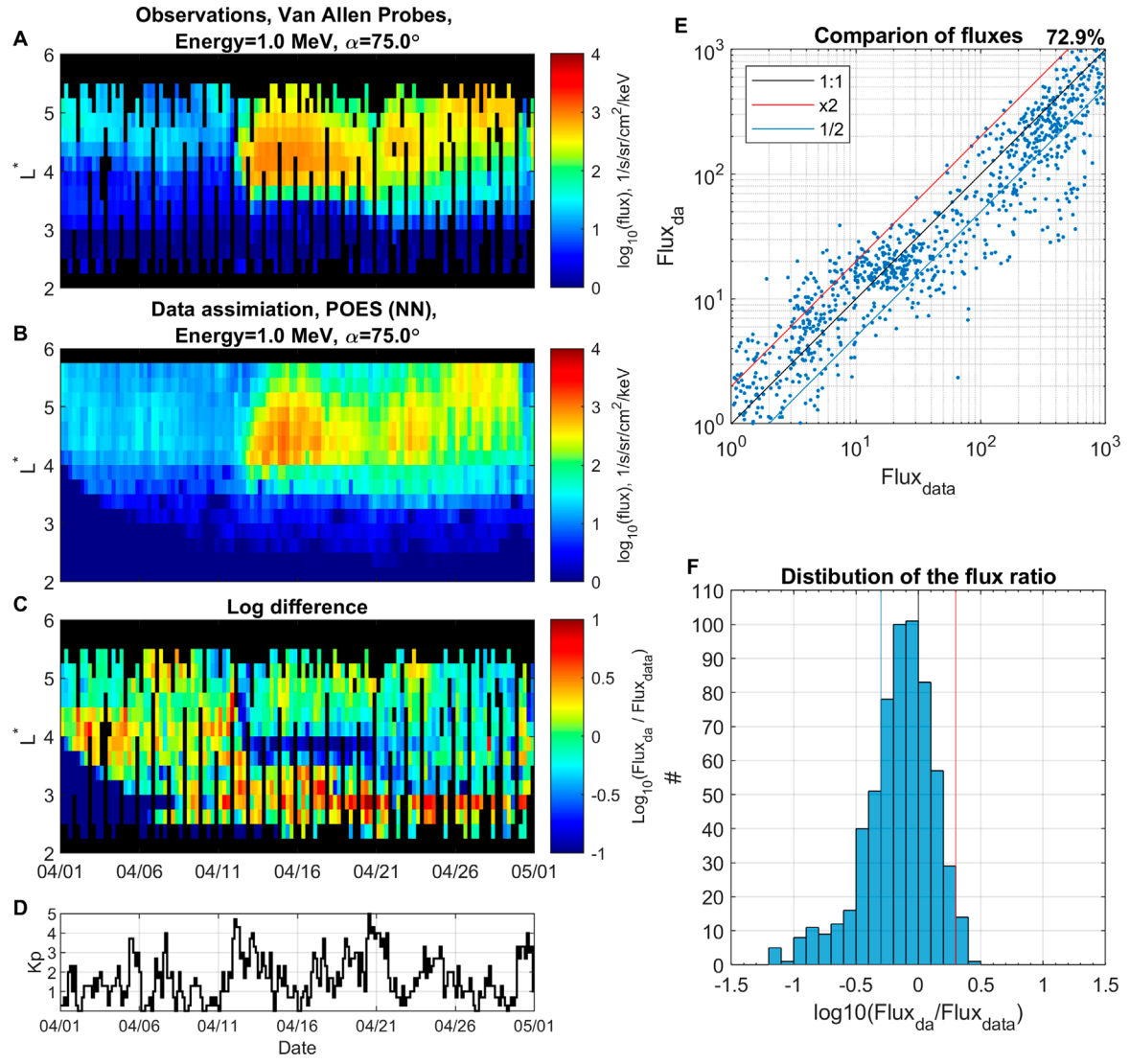

FIGURE 5
Data assimilation using reconstructed with neural network data. Electron flux at 1 MeV and α_{eq} =75° for period from 01 April 2014 until 01 May 2014. **(A)** Binned Van Allen Probe observations. **(B)** Data assimilation using reconstructed flux from POES data. **(C)** Logarithmic difference between flux from data assimilation and observations. **(D)** Kp index, **(E)** comparison of fluxes between observations $Flux_{data}$ and DA results $Flux_{da}$, **(F)** distribution of the logarithmic flux ratio.

and selected 32 hidden neurons based on the minimal validation error.

Thus, in total, we independently train $N_E * N_\alpha = 180$ NN models, where $N_E = 20$ and $N_\alpha = 9$ are the number of selected energy and local pitch angle channels from the ECT dataset, respectively. The 20 selected energy channels from the ECT dataset are chosen to be close to the selected energy channels from POES dataset by Peck et al. (2015). The pitch angles are selected from 10° up to 90° with the step of 10°. Thus, the single network input data consists of the POES fluxes in all 20 energy channels (1.20), one POES equatorial pitch angle (selected only from a perpendicular telescope), and one Van Allen Probes equatorial pitch angle (selected from a local pitch angle channel) and L^* (as explained below and computed with T89 model), as well as Kp index:

$$j_{RBSP}(t,\alpha_{loc},E_{RBSP}) = NN\left(j_{POES}(t,E_{1.20}),\alpha_{eq}^{POES}(t),\ \alpha_{eq}^{RBSP}(t),L^*(t),Kp(t)\right) \quad (9)$$

Both POES and Van Allen Probes fluxes are transformed into logarithmic space and normalized before fitting the network. The outliers of the unrealistically low or high values of the POES flux measured are removed similarly as described in **Section 2.4**. All of the inputs and output are aggregated to and averaged at specific time t (within 1 hour) and L^* location (within 0.1 L^*) of ECT output, and are also standardized to have zero mean and unit variance. The network minimizes the mean-squared error loss (MSE) function using the stochastic gradient descent 'adam' method

with initial learning rate as 0.005, piecewise learn rate schedule for dropping the learning rate every 125 epochs by multiplying by a factor of 0.2. In order to avoid overfitting, we have used training, validation, and test datasets. We randomly select 90% of data from 01 March 2013 until 01 March 2014 as training, and 10% as the validation set (see **Figure 2**). We have used validation-based early stopping, that is the training process stops when the MSE of the validation set stops improving for several consecutive epochs.

The test period from 01 April 2014 until 01 May 2014 (see **Figure 3**) is used to assess out-of-sample model performance and is included into data assimilation (**Section 3**). Once the neural network is trained, the Van Allen Probes data are no longer needed; only the POES fluxes, locations in space and pitch angle, and the Kp index are required to specify the outer electron belt environment. While $\alpha_{eq}^{RBSP}(t)$ is changing in time during the training of the NN model, we use a constant value from α_{eq}^{grid} (see Section 2.4) in a predictive mode specific to assessment, comparison, and data assimilation. The NN that corresponds to the selected value of α_{eq}^{grid} is chosen based on the time median for corresponding during training $\alpha_{eq}^{RBSP}(t)$.

3 Results

3.1 POES-to-RBSP reconstruction by NN and MLR models

Figure 2 shows the electron flux at 1 MeV and $\alpha_{eq} = 75°$ for a 1-year period (01 March 2013–01 March 2014). This period is used to obtain calibration coefficients using the MLR method (**Figure 2B**) and to train and validate the NN (**Figure 2C**). **Figure 2** serves an illustrative purpose and demonstrated both methods (MLR and NN) provide a reasonable reconstruction of the electron flux at a higher equatorial pitch angle than POES can observe. For the testing of the methods and for the following data assimilation, we use a different period (01 April 2014–01 May 2014), which is shown in **Figure 3**. For the quantitative estimation of the MLR and NN models, we use metrics presented in Claudepierre and O'Brien (2020). Namely, we use coefficients of determination [r^2; Eq. **(1)** from (Claudepierre and O'Brien, 2020)] and correlation coefficients calculated in logarithmic (r_{log}) and linear (r_{lin}) space between Van Allen Probes, RBSP-A and reconstituted flux from NOAA-15. The metrics are calculated for the full range of L^* and since RBSP-A and NOAA-15 data have different time resolutions, the data is binned with the time step of 4 h and L^* step of 0.1 prior to calculating the coefficients. The coefficients are presented in **Table 1** and are computed values for 3 energies (0.5, 1.0, 1.5 MeV) and separately for 3 different pitch-angle values (35°, 55°, 75°). Although the selection of energy and pitch angle is limited, both models indicate similar performance albeit the NN model is at least noticeably better than MLR in term of r^2.

3.2 VERB data assimilation using NN- and MLR-reconstructed data

The predicted flux j by MLR and NN models is converted to PSD f as $f = j/(p \cdot c)^2$ for convenience, where p is momentum, and c is the speed of light. The first (μ) and second (K) invariants are calculated from the energy and equatorial pitch angles using a dipole field and preserving the third adiabatic invariant (L^*) that is calculated using the T89 magnetic field. The resulting PSD from POES-based MLR- and NN- reconstructed fluxes at multiple energies based on POES data and equatorial pitch angles (α_{eq}^{grid}) are used as observations (y^o in Eq **(2)**) for assimilation with the VERB model. Hence, each point reconstructed in time from a single POES satellite covering 20 energy values and 9 α_{eq}^{grid} values is interpolated to the simulation grid and included in DA.

Next we compare DA results using POES-based NN- and MLR-reconstructed fluxes in the validation period from 01 April 2014 until 01 May 2014. **Figure 4A** shows the binned Van Allen Probes observations as a ground truth at 1 MeV and $\alpha_{eq} = 75°$, in comparison to DA results using MLR-reconstructed fluxes, shown in **Figure 4B**. **Figure 4C** show the logarithmic difference between Van Allen Probes observations and DA results.

Figure 4E shows a quantitative comparison of fluxes between observations $Flux_{data}$ and data assimilation using MLR-reconstructed fluxes $Flux_{da}$, with 62.3% of points being within a factor of 2. **Figure 4F** shows a histogram of their corresponding logarithmic ratio. The histogram is nearly normally distributed with slight overestimation of $Flux_{da}$ in comparison to $Flux_{data}$.

Figure 5 is in the same format as **Figure 4** but shows DA results with NN-reconstructed fluxes and indicating an improved accuracy with 72.9% of points within the factor of 2 (**Figure 5E**). The histogram on **Figure 5F** shows that data assimilation using NN-reconstructed fluxes results in almost no overestimation larger than a factor of 2, and its peak is shifted towards underestimation of $Flux_{da}$ in comparison to $Flux_{data}$.

TABLE 2 Coefficients of determination (r^2) and correlation coefficients calculated in logarithmic (r_{log}) and linear (r_{lin}) space between Van Allen Probes, RBSP-A and reconstituted from POES NOAA-15 data using MLR and NN models (first 5 rows, similar to **Table 1**); and the same comparison with data assimilation with POES NOAA-15 using MLR and NN models (last 5 rows). The calculation of coefficients is limited to $L^* \in [3.5,6.0]$, which represents the heart of the radiation belts.

	MLR			NN		
Energy/Pitch angle	r^2	r_{log}	r_{lin}	r^2	r_{log}	r_{lin}
From ML reconstruction, 01 April 2014–01 May 2014						
$E = 1.0$ MeV, $\alpha_{eq} = 75°$	0.60	0.79	0.66	0.86	0.89	0.83
$E = 1.0$ MeV, $\alpha_{eq} = 55°$	0.61	0.80	0.72	0.84	0.89	0.83
$E = 1.0$ MeV, $\alpha_{eq} = 35°$	0.67	0.83	0.75	0.82	0.88	0.83
$E = 0.5$ MeV, $\alpha_{eq} = 75°$	0.51	0.87	0.78	0.85	0.90	0.88
$E = 1.5$ MeV, $\alpha_{eq} = 75°$	0.22	0.68	0.62	0.84	0.89	0.82
From data assimilation reconstruction, 01 April 2014–01 May 2014						
$E = 1.0$ MeV, $\alpha_{eq} = 75°$	0.73	0.83	0.65	0.88	0.88	0.80
$E = 1.0$ MeV, $\alpha_{eq} = 55°$	0.78	0.83	0.70	0.89	0.88	0.82
$E = 1.0$ MeV, $\alpha_{eq} = 35°$	0.79	0.83	0.72	0.90	0.89	0.81
$E = 0.5$ MeV, $\alpha_{eq} = 75°$	0.64	0.86	0.76	0.90	0.92	0.86
$E = 1.5$ MeV, $\alpha_{eq} = 75°$	0.39	0.73	0.59	0.89	0.88	0.79

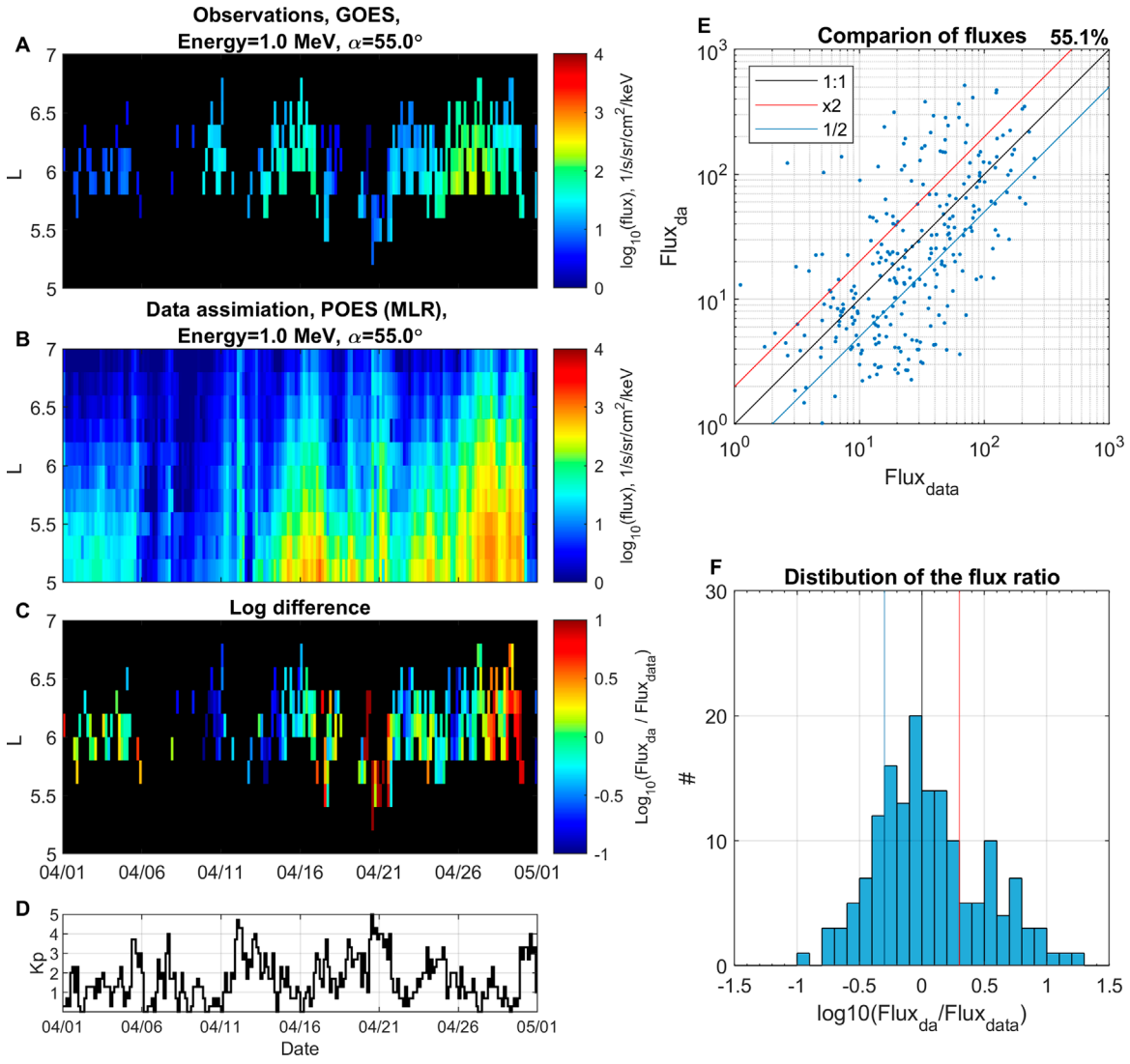

FIGURE 6
Data assimilation using reconstructed with multivariate linear regression analysis data. Electron flux at 1 MeV and α_{eq} =55° for the period from 01 April 2014 until 01 May 2014. **(A)** Binned GOES observations. **(B)** Data assimilation using reconstructed flux from POES data. **(C)** Logarithmic difference between flux from data assimilation and observations. **(D)** Kp index. **(E)** Comparison of fluxes between observations $Flux_{data}$ and DA results $Flux_{da}$, **(F)** distribution of the logarithmic flux ratio.

Furthermore, Table 2 shows that DA improves accuracy (as measured by r^2) of reconstructed fluxes in the heart of radiation belts ($L^* \in [3.5, 6.0]$, where election dynamics is the most significant) in comparison with standalone machine learning model results. Such improvement by DA is more pronounced when using MLR-based fluxes, and accuracy is only marginally better when using NN-based fluxes. We chose the narrower L^* region because physics-based VERB code simulation provides a very low PSD level in the slot region in comparison to the observations for the selected period as seen on Figure 3, which are defined by the instrumental noise level. The similar comparison at lower $L^* < 3.5$ (below heart of radiation belts Reeves et al. (2013)) results in fitting to observations when DA is applied to NN-based fluxes (not shown).

One of the main advantages of using DA is that it provides a full and complete reconstruction of radiation belts. This enables a virtual flyby of arbitrary satellites retrieving the accurate representation of electron flux/PSD along the trajectory, similar to the Observing System Simulation Experiments (OSSEs) study recently supported by NOAA (Schiller et al., 2022) in so called "fraternal twin" assimilation experiments (Kondrashov et al., 2007; Shprits et al., 2007; Kondrashov et al., 2011), where synthetic data from virtual satellites along different orbits (LEO, GTO, MEO) of VERB simulation with one set of physical parameters is assimilated into VERB with different physical parameter settings with a goal to best reconstruct at GEO. We achieve such reconstruction using physics-based extrapolation of LEO observations with VERB code and machine learning. To demonstrate such capability, Figures 6,

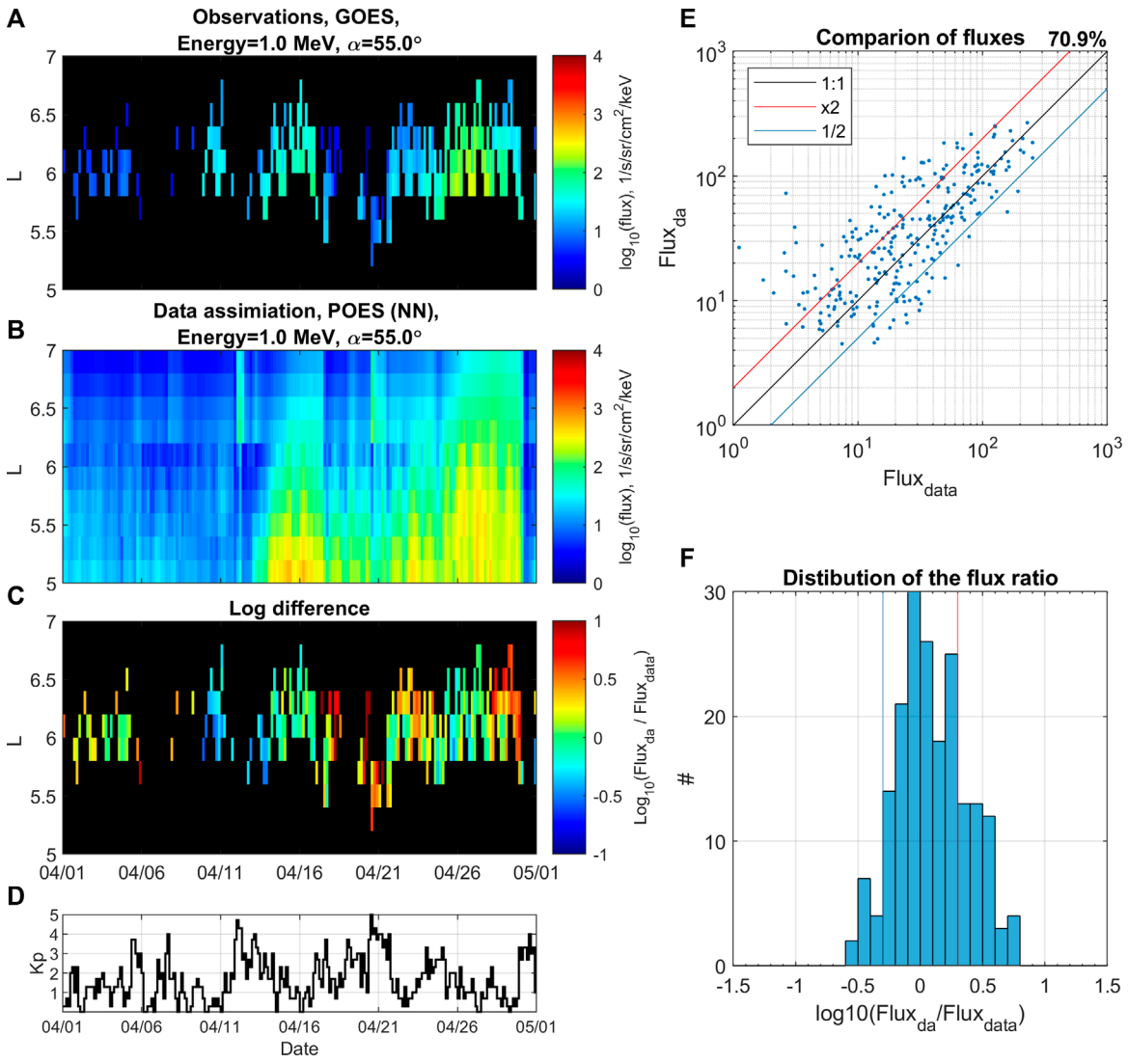

FIGURE 7
Data assimilation using reconstructed with neural network data. Electron flux at 1 MeV and α_{eq} =55° for period from 01 April 2014 until 01 May 2014. **(A)** Binned GOES observations. **(B)** Data assimilation using reconstructed flux from POES data. **(C)** Logarithmic difference between flux from data assimilation and observations. **(D)** Kp index, **(E)** comparison of fluxes between observations $Flux_{data}$ and DA results $Flux_{da}$, **(F)** distribution of the logarithmic flux ratio.

7 show DA results in comparison to GOES observations at 1 MeV and α_{eq} = 55° in the validation period from 01 April 2014 until 01 May 2014 and using the same format as in Figures 4, 5. As one can see, the accuracy of DA reconstruction using NN-based fluxes is significantly better than using the MLR method, such as 70.9% of points being within a factor of 2 for the former vs. 55.1% for the latter. In addition, we perform a comparison of the GOES fluxes reconstructed from LEO using ML methods and DA. The wide L-shell coverage provided by POES allow us to reconstruct the flux level in the region of GEO. However, none of our ML models (MLR and NN) were trained on the data outside of Van Allen Probes spatial coverage in L^*, which is below GEO. Hence, the physics-based extrapolation imposed by DA may become more important for such a task. Table 3 provides details of the comparison of DA and our ML models at extrapolation to GEO at different energies and pitch angles, in a format similar to Table 2. The agreement of the observed and reconstructed fluxes at GEO using DA is better than for our ML models, although the accuracy of the DA-NN model is lower than in Table 2. This is expected result because our ML models did not include training on GEO data. Also, there already exist much better predictive ML models that includes GEO electron data for training (e.g., Boynton et al., 2013; Shin et al., 2016; Zhang et al., 2020; Wang et al., 2023). However, such models usually rely on the knowledge of the solar wind data, while demonstrated in this paper DA technique only use Kp-index as a indicator of geomagnetic activity, with is available at near real-time (e.g., Matzka et al., 2021). Also, the demonstrated method of reconstruction of the fluxes at GEO using LEO measurements is of an interest of the community (e.g., Drozdov et al., 2022).

TABLE 3 Coefficients of determination (r^2) and correlation coefficients calculated in logarithmic (r_{log}) and linear (r_{lin}) space between GOES-13, GOES-15 and reconstituted from POES NOAA-15 data using MLR and NN models (first 5 rows); and the same comparison with data assimilation with POES NOAA-15 using MLR and NN models (last 5 rows). The calculation of coefficients is limited to $L^*\epsilon$ [5.0,7.0], the GOES coverage.

	MLR			NN		
Energy/Pitch angle	r^2	r_{log}	r_{lin}	r^2	r_{log}	r_{lin}
From ML reconstruction, 01 April 2014–01 May 2014						
E = 1.0 MeV, α_{eq} = 75°	−0.09	0.60	0.53	0.48	0.64	0.71
E = 1.0 MeV, α_{eq} = 55°	0.12	0.63	0.49	0.73	0.59	0.66
E = 1.0 MeV, α_{eq} = 35°	−0.01	0.53	0.42	0.64	0.52	0.70
E = 0.5 MeV, α_{eq} = 75°	−3.03	0.50	0.59	0.45	0.57	0.68
E = 1.5 MeV, α_{eq} = 75°	−1.85	0.67	0.40	0.61	0.75	0.70
From data assimilation reconstruction, 01 April 2014–01 May 2014						
E = 1.0 MeV, α_{eq} = 75°	0.29	0.57	0.44	0.76	0.75	0.80
E = 1.0 MeV, α_{eq} = 55°	0.38	0.54	0.41	0.66	0.66	0.70
E = 1.0 MeV, α_{eq} = 35°	0.29	0.53	0.45	0.69	0.71	0.75
E = 0.5 MeV, α_{eq} = 75°	−1.01	0.58	0.64	0.70	0.65	0.72
E = 1.5 MeV, α_{eq} = 75°	−1.62	0.60	0.24	0.83	0.83	0.77

4 Conclusion

In this work, we demonstrated that electron radiation belt flux observed by the MEO satellite can be successfully reconstructed using LEO POES measurements with various machine learning methods. We used 2 ML methods: multivariate linear regression analysis (MLR) and neural network (NN). The reconstructed flux was included in data assimilation (DA) with VERB code and compared with Van Allen Probes and GOES observations. The MLR method represents a reference model which is easy to implement in space weather applications that require reconstruction of the radiation belt dynamics. We found that data assimilation using MLR-reconstructed flux can provide a reasonable agreement with observations. However, the data assimilation with the flux reconstructed using a NN provided only a limited improvement. Therefore, our main conclusion is that, in the case an optimized machine learning model is not possible, our preliminary results suggest that data assimilation can be beneficial for reconstructing outer belt electrons by correcting errors of a subpar machine learning based LEO-to-MEO mapping (e.g., the MLR case), as well as by providing physics-based extrapolation to the parameter space portion that is inadequately covered by existing measurements (e.g., GEO is used as the pretended case here). Meanwhile, when a well-trained ML model is feasible (e.g., the NN case), the application of DA shows only limited improvement.

Although both methods (MLR and NN) in combination with DA showed applicability in the reconstruction of radiation belts, this study includes several assumptions and limitations. The selected implementation of the MLR reconstructed flux has limitations, as we used a simplified sin-function extrapolation of electron flux. The use of the more realistic reconstruction of the pitch-angle distribution (e.g., Allison et al., 2018; Zhao et al., 2018; Smirnov et al., 2022), as well as MLT dependence, may be used in future studies to improve the results. Additionally, we used the convenient for this study POES data set presented by Peck et al. (2015), which has limited temporal coverage (1998–2014) and thus short overlap with Van-Allen Probes to allow for robust comparison of DA-MLR and DA-NN results between quiet and disturbed geomagnetic activity, including extreme geomagnetic storms. The future work will consider the near real-time POES measurements, a comprehensive analysis of PSD (e.g., Wing et al., 2022), as well as, the detailed analysis of a wider range of energies and pitch angles remains a subject of future research. In addition, future work will include the combination of different measurements with various errors into a data assimilative model.

The main advantage of data assimilation is that it can help with the reduction of the errors that can arise from the inaccuracies of measurements, inaccuracies associated with the mixing of trapped and quasi-trapped populations, and inaccuracies associated with extrapolation to the equator. In the case an optimized machine learning model is not possible, our results suggest that data assimilation can be beneficial for reconstructing outer belt electrons by correcting errors of a machine learning based LEO-to-MEO mapping and by providing physics-based extrapolation to the parameter space portion not included in the LEO-to-MEO mapping, such as at GEO orbit. Machine learning models can be also inaccurate especially when applied outside of the training interval and during extreme geomagnetic conditions. In these situations, we may consider rebalancing using a similar approach as by Shprits et al. (2019) or using different machine learning models (e.g., MLR and NN) depending on the geomagnetic activity, when DA can compensate for the possible machine learning errors during extreme geomagnetic storms (see Zhelavskaya et al., 2021).

The ML and DA-based reconstruction of the radiation belts with the presented methodology enables continuous monitoring of the radiation belt state even without *in situ* near-equatorial radiation belt measurements. This is particularly crucial for space weather applications and space weather prediction. Such an approach can also be used to study the global long-term dynamics of radiation belts. Furthermore, analysis of the pitch-angle distributions of the reconstructed from LEO measurements radiation belts can inform about the dominant physical mechanism that drives radiation belts dynamics and will be addressed in future research.

Data availability statement

We thank the Van Allen Probe ECT team for providing the data: https://rbsp-ect.newmexicoconsortium.org/. The POES measurements are available at the NOAA NGDC website: https://satdat.ngdc.noaa.gov/sem/poes/data/processed/ngdc/corrected/peck/. The GOES measurements are available at the NOAA-NGDC website: https://www.ngdc.noaa.gov/stp/. The authors used geomagnetic indices provided by OMNIWeb: https://omniweb.gsfc.nasa.gov/.

Author contributions

AD led the work, performed the analyses, and assisted in writing the paper. DK developed the NN model, advised AD on the DA details and interpretation of the results, and wrote the paper. KS assisted in DA analysis. YS conceptualized the study. All authors contributed to the article and approved the submitted version.

Funding

This research is funded by contract FA9453-19-C-0619 submitted to ARFL STTR topic AF17C-T03. DK is supported by NSF grant AGS-2211345.

Acknowledgments

The authors acknowledge the developers of the International Radiation Belt Environment Modeling (IRBEM) library. We thank Drew Turner, Quintin Schiller and Geoff Reeves for their useful discussions and Sharon Uy for proofreading this manuscript.

Conflict of interest

AD, KS and YS have a significant financial interest in Space Sciences Innovations Inc.

The remaining author declares that the research was conducted in the absence of any commercial or financial relationships that could be construed as a potential conflict of interest.

Publisher's note

All claims expressed in this article are solely those of the authors and do not necessarily represent those of their affiliated organizations, or those of the publisher, the editors and the reviewers. Any product that may be evaluated in this article, or claim that may be made by its manufacturer, is not guaranteed or endorsed by the publisher.

Author disclaimer

The views expressed are those of the author and do not necessarily reflect the official policy or position of the Department of the Air Force, the Department of Defense, or the U.S. government. The appearance of external hyperlinks does not constitute endorsement by the United States Department of Defense (DoD) of the linked websites, or the information, products, or services contained therein. The DoD does not exercise any editorial, security, or other control over the information you may find at these locations.

References

Allison, H. J., Horne, R. B., Glauert, S. A., and Del Zanna, G. (2018). Determination of the equatorial electron differential flux from observations at low Earth orbit. *J. Geophys. Res. Space Phys.* 123, 9574–9596. doi:10.1029/2018ja025786

Batusov, R., Dolenko, S., and Myagkova, I. (2018). Neural network prediction of daily relativistic electrons fluence in the outer radiation belt of the earth: Selection of delay embedding method ∗ ∗this study has been conducted at the expense of Russian science foundation, grant no. 16-17-00098. *Procedia Comput. Sci.* 123, 86–91. doi:10.1016/j.procs.2018.01.014

Boyd, A. J., Spence, H. E., Reeves, G. D., Funsten, H. O., Skoug, R. M., Larsen, B. A., et al. (2021). RBSP-ECT combined pitch angle resolved electron flux data product. *J. Geophys. Res. Space Phys.* 126. doi:10.1029/2020ja028637

Boynton, R. J., Balikhin, M. A., Billings, S. A., Reeves, G. D., Ganushkina, N., Gedalin, M., et al. (2013). The analysis of electron fluxes at geosynchronous orbit employing a narmax approach. *J. Geophys. Res. Space Phys.* 118, 1500–1513. doi:10.1002/jgra.50192

Brautigam, D. H., and Albert, J. M. (2000). Radial diffusion analysis of outer radiation belt electrons during the october 9, 1990, magnetic storm. *J. Geophys. Res.* 105, 291–309. doi:10.1029/1999ja900344

Camporeale, E. (2019). The challenge of machine learning in space weather: Nowcasting and forecasting. *Space Weather* 17, 1166–1207. doi:10.1029/2018SW002061

Cervantes, S., Shprits, Y. Y., Aseev, N. A., and Allison, H. J. (2020a). Quantifying the effects of emic wave scattering and magnetopause shadowing in the outer electron radiation belt by means of data assimilation. *J. Geophys. Res. Space Phys.* 125, e2020JA028208. doi:10.1029/2020ja028208

Cervantes, S., Shprits, Y. Y., Aseev, N. A., Drozdov, A. Y., Castillo, A., and Stolle, C. (2020b). Identifying radiation belt electron source and loss processes by assimilating spacecraft data in a three-dimensional diffusion model. *J. Geophys. Res. Space Phys.* 125. doi:10.1029/2019ja027514

Chen, Y., Reeves, G. D., Cunningham, G. S., Redmon, R. J., and Henderson, M. G. (2016). Forecasting and remote sensing outer belt relativistic electrons from low Earth orbit. *Geophys. Res. Lett.* 43, 1031–1038. doi:10.1002/2015GL067481

Chen, Y., Reeves, G. D., Fu, X., and Henderson, M. (2019). Premeve: New predictive model for megaelectron-volt electrons inside Earth's outer radiation belt. *Space Weather* 17, 438–454. doi:10.1029/2018SW002095

Chu, X., Ma, D., Bortnik, J., Tobiska, W. K., Cruz, A., Bouwer, S. D., et al. (2021). Relativistic electron model in the outer radiation belt using a neural network approach. *Space Weather* 19, e2021SW002808. doi:10.1029/2021SW002808

Claudepierre, S. G., and O'Brien, T. P. (2020). Specifying high-altitude electrons using low-altitude leo systems: The shells model. *Space Weather* 18, e2019SW002402. doi:10.1029/2019sw002402

Daae, M., Shprits, Y. Y., Ni, B., Koller, J., Kondrashov, D., and Chen, Y. (2011). Reanalysis of radiation belt electron phase space density using various boundary conditions and loss models. *Adv. Space Res.* 48, 1327–1334. doi:10.1016/j.asr.2011.07.001

Drozdov, A., Schiller, Q., Shprits, Y., Kondrashov, D., and Strunin, K. (2022). "An OSSE using the VERB code for outer electron radiation belt," in Presented at 2022 mini-GEM, 11 Dec.

Drozdov, A. Y., Allison, H. J., Shprits, Y. Y., Elkington, S. R., and Aseev, N. A. (2021). A comparison of radial diffusion coefficients in 1-d and 3-d long-term radiation belt simulations. *J. Geophys. Res. Space Phys.* 126. doi:10.1029/2020ja028707

Drozdov, A. Y., Shprits, Y. Y., Orlova, K. G., Kellerman, A. C., Subbotin, D. A., Baker, D. N., et al. (2015). Energetic, relativistic, and ultrarelativistic electrons: Comparison of long-term verb code simulations with van allen probes measurements. *J. Geophys. Res. Space Phys.* 120, 3574–3587. doi:10.1002/2014JA020637

Drozdov, A. Y., Shprits, Y. Y., Usanova, M. E., Aseev, N. A., Kellerman, A. C., and Zhu, H. (2017). Emic wave parameterization in the long-term verb code simulation. *J. Geophys. Res. Space Phys.* 122, 8488–8501. doi:10.1002/2017JA024389

Drozdov, A. Y., Usanova, M. E., Hudson, M. K., Allison, H. J., and Shprits, Y. Y. (2020). The role of hiss, chorus, and emic waves in the modeling of the dynamics of the Multi-MeV radiation belt electrons. *J. Geophys. Res. Space Phys.* 125, 2628. doi:10.1029/2020JA028282

Evans, D. S., and Greer, M. S. (2004). "Polar orbiting environmental satellite space environment monitor - 2 instrument descriptions and archive data documentation," in *NOAA technical memorandum OAR SEC* (Boulder, Colorado), 93.

Fukata, M., Taguchi, S., Okuzawa, T., and Obara, T. (2002). Neural network prediction of relativistic electrons at geosynchronous orbit during the storm recovery phase: Effects of recurring substorms. *Ann. Geophys.* 20, 947–951. doi:10.5194/angeo-20-947-2002

Ghil, M., and Malanotte-Rizzoli, P. (1991). "Data assimilation in meteorology and oceanography," in *Advances in geophysics* (New York: Academic Press), 33, 141–266.

Kalman, R. E. (1960). A new approach to linear filtering and prediction problems. *Trans. ASME–Journal Basic Eng.* 82, 35–45. doi:10.1115/1.3662552

Kalnay, E. (2003). *Atmospheric modeling, data assimilation and predictability*. Cambridge University Press.

Kanekal, S. G., Baker, D. N., and Blake, J. B. (2001). Multisatellite measurements of relativistic electrons: Global coherence. *J. Geophys. Res. Space Phys.* 106, 29721–29732. doi:10.1029/2001JA000070

Kellerman, A. C., Shprits, Y. Y., Kondrashov, D., Subbotin, D., Makarevich, E., Donovan, R. A., et al. (2014). Three-dimensional data assimilation and reanalysis of radiation belt electrons: Observations of a four-zone structure using five spacecraft and the VERB code. *J. Geophys. Res. Space Phys.* 119, 8764–8783. under review. doi:10.1002/2014ja020171

Kitamura, K., Nakamura, Y., Tokumitsu, M., Ishida, Y., and Watari, S. (2011). Prediction of the electron flux environment in geosynchronous orbit using a neural network technique. *Artif. Life Robot.* 16, 389–392. doi:10.1007/s10015-011-0957-1

Koller, J., Chen, Y., Reeves, G. D., Friedel, R. H. W., Cayton, T. E., and Vrugt, J. A. (2007). Identifying the radiation belt source region by data assimilation. *J. Geophys. Res. Space Phys.* 112. doi:10.1029/2006JA012196

Kondrashov, D., Ghil, M., and Shprits, Y. (2011). Lognormal kalman filter for assimilating phase space density data in the radiation belts. *Space Weather* 9. doi:10.1029/2011sw000726

Kondrashov, D., Shprits, Y., Ghil, M., and Thorne, R. (2007). A Kalman filter technique to estimate relativistic electron lifetimes in the outer radiation belt. *J. Geophys. Res.* 112, A10227. doi:10.1029/2007JA012583

Koons, H. C., and Gorney, D. J. (1991). A neural network model of the relativistic electron flux at geosynchronous orbit. *J. Geophys. Res.* 96, 5549. doi:10.1029/90ja02380

Landis, D. A., Saikin, A. A., Zhelavskaya, I., Drozdov, A. Y., Aseev, N., Shprits, Y. Y., et al. (2022). Title: Narx neural network derivations of the outer boundary radiation belt electron flux. *Space Weather* 20. doi:10.1029/2021sw002774

Ling, A. G., Ginet, G. P., Hilmer, R. V., and Perry, K. L. (2010). A neural network–based geosynchronous relativistic electron flux forecasting model. *Space Weather* 8. doi:10.1029/2010SW000576

Lyons, L. R., and Thorne, R. M. (1973). Equilibrium structure of radiation belt electrons. *J. Geophys. Res.* 78, 2142–2149. doi:10.1029/ja078i013p02142

Ma, D., Chu, X., Bortnik, J., Claudepierre, S. G., Tobiska, W. K., Cruz, A., et al. (2022). Modeling the dynamic variability of sub-relativistic outer radiation belt electron fluxes using machine learning. *Space Weather* 20, e2022SW003079. doi:10.1029/2022sw003079

Matzka, J., Stolle, C., Yamazaki, Y., Bronkalla, O., and Morschhauser, A. (2021). The geomagnetic kp index and derived indices of geomagnetic activity. *Space Weather* 19. doi:10.1029/2020sw002641

Mauk, B. H., Fox, N. J., Kanekal, S. G., Kessel, R. L., Sibeck, D. G., and Ukhorskiy, A. (2013). Science objectives and rationale for the radiation belt storm probes mission. *Space Sci. Rev.* 179, 3–27. doi:10.1007/s11214-012-9908-y

Merkin, V. G., Kondrashov, D., Ghil, M., and Anderson, B. J. (2016). Data assimilation of low-altitude magnetic perturbations into a global magnetosphere model. *Space Weather* 14, 165–184. doi:10.1002/2015sw001330

Peck, E. D., Randall, C. E., Green, J. C., Rodriguez, J. V., and Rodger, C. J. (2015). POES MEPED differential flux retrievals and electron channel contamination correction: POES MEPED correction. *J. Geophys. Res. Space Phys.* 120, 4596–4612. doi:10.1002/2014ja020817

Perry, K. L., Ginet, G. P., Ling, A. G., and Hilmer, R. V. (2010). Comparing geosynchronous relativistic electron prediction models. *Space Weather* 8. doi:10.1029/2010sw000581

Pires de Lima, R., Chen, Y., and Lin, Y. (2020). Forecasting megaelectron-volt electrons inside earth's outer radiation belt: PreMevE 2.0 based on supervised machine learning algorithms. *Space Weather* 18, e2019SW002399. doi:10.1029/2019SW002399

Reeves, G. D., Spence, H. E., Henderson, M. G., Morley, S. K., Friedel, R. H. W., Funsten, H. O., et al. (2013). Electron acceleration in the heart of the van allen radiation belts. *Science* 341, 991–994. doi:10.1126/science.1237743

Rodriguez, J. V., Krosschell, J. C., and Green, J. C. (2014). Intercalibration of goes 8-15 solar proton detectors. *Space Weather* 12, 92–109. doi:10.1002/2013sw000996

Roederer, J. G. (1970). *Dynamics of geomagnetically trapped radiation*. Springer Berlin Heidelberg. doi:10.1007/978-3-642-49300-3

Saikin, A. A., Shprits, Y. Y., Drozdov, A. Y., Landis, D. A., Zhelavskaya, I. S., and Cervantes, S. (2021). Reconstruction of the radiation belts for solar cycles 17–24 (1933–2017). *Space Weather* 19, e2020SW002524. doi:10.1029/2020SW002524

Sarma, R., Chandorkar, M., Zhelavskaya, I., Shprits, Y., Drozdov, A., and Camporeale, E. (2020). Bayesian inference of Quasi-Linear radial diffusion parameters using van allen probes. *J. Geophys. Res. Space Phys.* 125, A04222. doi:10.1029/2019JA027618

Schiller, Q., Shprits, Y., Drozdov, A., Kondrashov, D., and Strunin, K. (2022). "An OSSE using the VERB code for outer electron radiation belt situational awareness," in Presented at 2022 Fall Meeting, 12-16 Dec (AGU).

Shin, D.-K., Lee, D.-Y., Kim, K.-C., Hwang, J., and Kim, J. (2016). Artificial neural network prediction model for geosynchronous electron fluxes: Dependence on satellite position and particle energy. *Space Weather* 14, 313–321. doi:10.1002/2015sw001359

Shprits, Y. Y., Castillo, A. M., Aseev, N., Cervantes, S., Michaelis, I., Zhelavskaya, I., et al. (2023). "Data assimilation in the near-earth electron radiation environment," in *Applications of data assimilation and inverse problems in the earth sciences*. Editor A. Ismail-Zadeh (Cambridge University Press - IUGG Special Publication Series). (In Press).

Shprits, Y. Y., Elkington, S. R., Meredith, N. P., and Subbotin, D. A. (2008a). Review of modeling of losses and sources of relativistic electrons in the outer radiation belt I: Radial transport. *J. Atmos. Sol. Terr. Phys.* 70 (14), 1679–1693. doi:10.1016/j.jastp.2008.06.008

Shprits, Y., Kellerman, A., Kondrashov, D., and Subbotin, D. (2013). Application of a new data operator-splitting data assimilation technique to the 3-D VERB diffusion code and CRRES measurements. *Geophys. Res. Lett.* 40, 4998–5002. doi:10.1002/grl.50969

Shprits, Y., Kondrashov, D., Chen, Y., Thorne, R., Ghil, M., Friedel, R., et al. (2007). Reanalysis of relativistic radiation belt electron fluxes using CRRES satellite data, a radial diffusion model, and a Kalman filter. *J. Geophys. Res.* 112, A12216. doi:10.1029/2007JA012579

Shprits, Y. Y., Subbotin, D. A., Meredith, N. P., and Elkington, S. R. (2008b). Review of modeling of losses and sources of relativistic electrons in the outer radiation belt II: Local acceleration and loss. *J. Atmos. Sol. Terr. Phys.* 70 (14), 1694–1713. doi:10.1016/j.jastp.2008.06.014

Shprits, Y. Y., Vasile, R., and Zhelavskaya, I. S. (2019). Nowcasting and predicting the k p index using historical values and real-time observations. *Space Weather* 17, 1219–1229. doi:10.1029/2018sw002141

Shultz, M., and Lanzerotti, L. (1974). *Particle diffusion in the radiation belt*. New York: Springer.

Sinha, S., Chen, Y., Lin, Y., and Pires de Lima, R. (2021). Premeve update: Forecasting ultra-relativistic electrons inside Earth's outer radiation belt. *Space Weather* 19. doi:10.1029/2021SW002773

Smirnov, A., Shprits, Y., Allison, H., Aseev, N., Drozdov, A., Kollmann, P., et al. (2022). Storm-time evolution of the equatorial electron pitch angle distributions in Earth's outer radiation belt. *Front. Astron. Space Sci.* 9. doi:10.3389/fspas.2022.836811

Spence, H. E., Reeves, G. D., Baker, D. N., Blake, J. B., Bolton, M., Bourdarie, S., et al. (2013). Science goals and overview of the radiation belt storm probes (RBSP) energetic particle, composition, and thermal plasma (ECT) suite on NASA's van allen probes mission. *Space Sci. Rev.* 179, 311–336. doi:10.1007/s11214-013-0007-5

Subbotin, D. A., and Shprits, Y. Y. (2009). Three-dimensional modeling of the radiation belts using the versatile electron radiation belt (VERB) code. *Space Weather* 7, S10001. doi:10.1029/2008SW000452

Thorne, R. M. (2010). Radiation belt dynamics: The importance of wave-particle interactions. *Geophys. Res. Lett.* 37. doi:10.1029/2010GL044990

Tsyganenko, N. A. (1989). A magnetospheric magnetic field model with a warped tail current sheet. *Planet. Space Sci.* 37, 5–20. doi:10.1016/0032-0633(89)90066-4

Wang, D., Shprits, Y. Y., Zhelavskaya, I. S., Effenberger, F., Castillo, A., Drozdov, A. Y., et al. (2020). The effect of plasma boundaries on the dynamic evolution of relativistic radiation belt electrons. *J. Geophys. Res. Space Phys.* 125. doi:10.1029/2019JA027422

Wang, J., Guo, D., Xiang, Z., Ni, B., Liu, Y., and Dong, J. (2023). Prediction of geosynchronous electron fluxes using an artificial neural network driven by solar wind parameters. *Adv. Space Res.* 71, 275–285. doi:10.1016/j.asr.2022.10.013

Wing, S., Turner, D. L., Ukhorskiy, A. Y., Johnson, J. R., Sotirelis, T., Nikoukar, R., et al. (2022). Modeling radiation belt electrons with information theory informed neural networks. *Space Weather* 20, e2022SW003090. doi:10.1029/2022SW003090

Zhang, H., Fu, S., Xie, L., Zhao, D., Yue, C., Pu, Z., et al. (2020). Relativistic electron flux prediction at geosynchronous orbit based on the neural network and the quantile regression method. *Space Weather* 18. doi:10.1029/2020sw002445

Zhao, H., Friedel, R. H. W., Chen, Y., Reeves, G. D., Baker, D. N., Li, X., et al. (2018). An empirical model of radiation belt electron pitch angle distributions based on van allen probes measurements. *J. Geophys. Res. Space Phys.* 123, 3493–3511. doi:10.1029/2018JA025277

Zhelavskaya, I. S., Aseev, N. A., and Shprits, Y. Y. (2021). A combined neural network- and physics-based approach for modeling plasmasphere dynamics. *J. Geophys. Res. Space Phys.* 126. doi:10.1029/2020ja028077

Zhelavskaya, I. S., Shprits, Y. Y., and Spasojevic, M. (2018). "Chapter 12 - Reconstruction of plasma electron density from satellite measurements via artificial neural networks," in *Machine learning techniques for space weather*. Editors E. Camporeale, S. Wing, and J. R. Johnson (Elsevier), 301–327. doi:10.1016/B978-0-12-811788-0.00012-3

Zhelavskaya, I. S., Shprits, Y. Y., and Spasojević, M. (2017). Empirical modeling of the plasmasphere dynamics using neural networks: Global dynamic plasmasphere model. *J. Geophys. Res. Space Phys.* 122 (11), 11,227–11,244. doi:10.1002/2017JA024406

Zhelavskaya, I. S., Spasojevic, M., Shprits, Y. Y., and Kurth, W. S. (2016). Automated determination of electron density from electric field measurements on the Van Allen Probes spacecraft. *J. Geophys. Res. Space Phys.* 121 (5), 2015JA022132. doi:10.1002/2015JA022132

Zhu, H., Shprits, Y. Y., Spasojevic, M., and Drozdov, A. Y. (2019). New hiss and chorus waves diffusion coefficient parameterizations from the van allen probes and their effect on long-term relativistic electron radiation-belt VERB simulations. *J. Atmos. Sol. Terr. Phys.* 193, 105090. doi:10.1016/j.jastp.2019.105090

frontiers | Frontiers in Astronomy and Space Sciences

TYPE Original Research
PUBLISHED 04 July 2023
DOI 10.3389/fspas.2023.1200485

OPEN ACCESS

EDITED BY
Qianli Ma,
Boston University, United States

REVIEWED BY
Paul O'Brien,
The Aerospace Corporation, United States
Zhenpeng Su,
University of Science and Technology of China, China

*CORRESPONDENCE
Solène Lejosne,
solene@berkeley.edu

RECEIVED 05 April 2023
ACCEPTED 08 June 2023
PUBLISHED 04 July 2023

CITATION
Lejosne S and Albert JM (2023), Drift phase resolved diffusive radiation belt model: 1. Theoretical framework. *Front. Astron. Space Sci.* 10:1200485. doi: 10.3389/fspas.2023.1200485

Drift phase resolved diffusive radiation belt model: 1. Theoretical framework

Solène Lejosne[1]* and Jay M. Albert[2]

[1]Space Sciences Laboratory, University of California, Berkeley, Berkeley, CA, United States, [2]Air Force Research Laboratory, Kirtland AFB, Albuquerque, NM, United States

Most physics-based models provide a coarse three-dimensional representation of radiation belt dynamics at low time resolution, of the order of a few drift periods. The description of the effect of trapped particle transport on radiation belt intensity is based on the random phase approximation, and it is in one dimension only: the third adiabatic invariant coordinate, akin to a phase-averaged radial distance. This means that these radiation belt models do not resolve the drift phase or, equivalently, the magnetic local time. Yet, *in situ* measurements suggest that radiation belt intensity frequently depends on magnetic local time, at least transiently, such as during active times. To include processes generating azimuthal variations in trapped particle fluxes and to quantify their relative importance in radiation belt energization, an improvement in the spatiotemporal resolution of the radiation belt models is required. The objective of this study is to pave the way for a new generation of diffusive radiation belt models capable of retaining drift phase information. Specifically, we highlight a two-dimensional equation for the effects of trapped particle transport on radiation belt intensity. With a theoretical framework that goes beyond the radial diffusion paradigm, the effects of trapped particle bulk motion, as well as diffusion, are quantified in terms of Euler potentials, (α, β), quantities akin to the radial and azimuthal directions. This work provides the theoretical foundations underlying the drift phase resolved transport equation for radiation belt dynamics. It also brings forward the concept of azimuthal diffusion as a phase-mixing agent.

KEYWORDS

radiation belts, Fokker–Planck equation, adiabatic invariants, Euler potentials, radial transport, radial diffusion, azimuthal diffusion

1 Introduction

The motion of energetic particles trapped in planetary radiation belts is a superposition of three quasi-periodic motions, each evolving on a very distinct spatiotemporal scale, with an amplitude quantified by an adiabatic invariant (e.g., Northrop and Teller, 1960; Schulz and Lanzerotti, 1974):

(1) A very fast and small motion of gyration around the magnetic field direction.
(2) A slower and bigger bounce motion between the planet's hemispheres, along the magnetic field direction.
(3) A slow and large drift motion around the planet in a direction perpendicular to the magnetic field direction.

The scale separation between these three quasi-periodic motions spans several orders of magnitude in time and space.

Combining adiabatic invariant theory with Fokker–Planck formalism yields the theoretical framework for a *probabilistic* model of radiation belt dynamics (e.g., Roederer and Zhang, 2014). The Fokker–Planck formalism accounts for uncertainties in electromagnetic field characterization. The adiabatic theory allows for a three-dimensional *phase-averaged* representation of radiation belt dynamics rather than a full six-dimensional description in phase space.

The description of radiation belt dynamics as a three-dimensional Fokker–Planck equation reduced to a diffusion equation requires minimal computational resources. This quality has enabled the development of many radiation belt computer codes over the years: Salammbô (e.g., Beutier and Boscher, 1995; Nénon et al., 2017), Diffusion in (I,L,B) Energetic Radiation Tracker (DILBERT) (Albert et al., 2009), Versatile Electron Radiation Belt (VERB) (Subbotin and Shprits, 2009), Storm-Time Evolution of Electron Radiation Belt (STEERB) (Su et al., 2010), DREAM3D, as part of the Dynamic Radiation Environment Assimilation Model (DREAM) project (Tu et al., 2013), and British Antarctic Survey Radiation Belt Model (BAS RBM) (Glauert et al., 2014; Woodfield et al., 2014) are all examples of radiation belt codes relying on the same theoretical basis. While first implemented in the case of terrestrial radiation belts, the three-dimensional Fokker–Planck equation has also been transposed to the radiation belts of Jupiter and Saturn. The resulting codes are widely used for scientific research (e.g., Varotsou et al., 2005; Woodfield et al., 2018; Drozdov et al., 2020) and for space weather purposes (e.g., Glauert et al., 2018; Horne et al., 2021).

On the technical side, these computer codes consist of solving a diffusion equation that provides an *approximate* description for the time evolution of the radiation belts:

$$\frac{\partial f}{\partial t} = \sum_{i,j} \frac{\partial}{\partial J_i}\left(D_{i,j} \frac{\partial f}{\partial J_j} \right) + Sources - Losses, \quad (1)$$

where $f(t,J_1,J_2,J_3)$ is the phase-averaged phase space density, $J_{i=1,2,3}$ are the action variables, which are proportional to the adiabatic invariants by physical constants, and $D_{i,j}$ are the phase-averaged diffusion coefficients. According to Eq. **1**, radiation belts are primarily driven by very small, uncorrelated perturbations to the particle trajectories, at all spatiotemporal scales, from the gyro-scale up to the drift scale. The "*Sources*" and "*Losses*" terms account for other non-diffusive processes affecting the distribution function (e.g., Schulz and Lanzerotti, 1974). It is worth emphasizing that all quantities in Eq. **1** are *drift-averaged*, i.e., they are phase-averaged over all three phases. It means that this theoretical formulation cannot resolve the drift phase of trapped particles, or equivalently, the magnetic local time (*MLT*) dimension: the resulting modeled radiation belt intensity, $f(t,J_1,J_2,J_3)$, is independent of magnetic local time.

From a theoretical standpoint, it is a reasonable first approximation to consider that radiation belt intensity is independent of magnetic local time: any *MLT*-dependent structure is expected to dissipate rapidly, on a timescale of a few drift periods, because of the mechanism of phase mixing (e.g., Schulz and Lanzerotti, 1974; Ukhorskiy and Sitnov, 2013). Yet, in practice, *in situ* measurements of trapped particle fluxes suggest that radiation belt intensity frequently depends on the magnetic local time, at least transiently. Both inner and outer terrestrial radiation belt fluxes typically display drift-periodic oscillations. Depending on the situation, these drift-periodic signatures can be interpreted as drift echoes following *MLT*-localized injections, dropout echoes following *MLT*-localized losses, or evidence of trapped particles' drift resonance with ULF waves (e.g., Sauvaud et al., 2013; Hao et al., 2016; Patel et al., 2019; Lejosne and Mozer, 2020; Zhao et al., 2022). Drift echoes have also been reported in Saturnian radiation belt fluxes (e.g., Hao et al., 2020).

In all cases, processes generating drift-periodic signatures are important due to their connection to radiation belt energization (e.g., Hudson et al., 2020). Yet, three-dimensional radiation belt models cannot account for the generation of drift-periodic signatures. Instead, drift-periodic signatures are usually modeled independently of other processes, by tracking the drift motion of test particles (guiding centers) in prescribed electric and magnetic fields, omitting local processes occurring along the gyration and bounce motions (such as local acceleration by chorus waves for instance) (e.g., Li et al., 1993; Hudson et al., 2017).

In that context, it is necessary to introduce a general equation for radiation belt dynamics that includes *MLT*-localized effects, and that can account for both local processes, at the gyro-scale, and large-scale effects associated with the radial transport. An equation that meets these requirements is detailed in the following section. It relies on the work by Birmingham et al. (1967), in which a two-dimensional drift-diffusion equation was derived assuming conservation of the first two adiabatic invariants. It is straightforward to generalize the proposed equation to include diffusion in the first two adiabatic invariants. We present a compact way to retrieve the equation proposed by Birmingham et al. (1967), combining Fokker–Planck formalism with relationships derived from the Hamiltonian theory. While adjustments to the three-dimensional diffusion Eq. **1** have already been proposed to resolve the drift phase in radiation belt models (e.g., Bourdarie et al., 1997; Shprits et al., 2015) and ring current models can resolve local time (e.g., Jordanova et al., 1997; 2022; Fok et al., 2014), we propose an alternative from the first principles and describe its underlying theoretical assumptions. Similar to the theoretical framework for ring current models (e.g., Fok and Moore, 1997; Yu et al., 2016), the work discussed thereafter relies on the representation of the inner magnetosphere in terms of Euler potentials (e.g., Stern, 1967). That is why the outline of the remainder is as follows: in Section 2, we provide the theoretical background necessary to derive the equation proposed by Birmingham et al. (1967). In particular, we recall how to derive the standard radial diffusion equation before deconstructing it. We introduce the Euler potential coordinates and relate the Euler coordinates to the third adiabatic invariant. In Section 3, we show how the Fokker–Planck equation in terms of Euler potential coordinates yields a two-dimensional drift-diffusion equation when Hamiltonian relationships between the Euler coordinates are taken into account.

Since this work focuses on improving the modeling of drift effects on radiation belt intensity, we first assume conservation of the first two adiabatic invariants. Thus, all considered quantities are bounce-averaged. We also omit any significant source or loss mechanism. A generalization of the resulting transport equation

to include diffusion of the first two adiabatic invariants is straightforward. It is provided at the end of Section 3.

2 Theoretical background

We briefly recall how to derive the standard radial diffusion equation. This informs how to derive the same equation as the one proposed by Birmingham et al. (1967) (Section 3). We also detail the concept of Euler potentials and highlight their connection to the third adiabatic invariant.

2.1 Derivation of the standard radiation belt radial diffusion equation

In the following section, the third adiabatic invariant, J_3, is abbreviated to J out of convenience. The objective is to describe the time evolution of a distribution function, f, that quantifies the number of particles per unit of J (assuming conservation of the first two adiabatic invariants). This quantity is proportional to the drift-averaged phase space density by a physical constant (e.g., Roederer and Zhang, 2014, their chapter 4). The usual assumption is that many very small uncorrelated random changes of the variable, J, occur between times t and $t+\Delta t$, with a very small total effect ($\Delta J/J \ll 1; \Delta t \ll f/(\partial f/\partial t)$). In this case, the time evolution of the distribution function, f, is provided by a Fokker–Planck equation (e.g., Roederer, 1970; Walt, 1994):

$$\frac{\partial f}{\partial t} = -\frac{\partial}{\partial J}(\langle \Delta J\rangle f) + \frac{1}{2}\frac{\partial^2}{\partial J^2}(\langle (\Delta J)^2\rangle f), \tag{2}$$

where $\langle \Delta J\rangle = [\Delta J]/\Delta t$ is the rate of change for the expected value of the third invariant variation, $[\Delta J] = [J(t+\Delta t) - J(t)]$, and $\langle (\Delta J)^2\rangle = [(\Delta J)^2]/\Delta t$ is the rate of change for the expected value of the third invariant squared variation. A rewriting of the right-hand side of Eq. 2 provides a mathematically equivalent formulation:

$$\frac{\partial f}{\partial t} = \frac{\partial}{\partial J}\left(-\langle \Delta J\rangle f + \frac{1}{2}\frac{\partial}{\partial J}(\langle (\Delta J)^2\rangle f)\right), \tag{3}$$

which can also be written as

$$\frac{\partial f}{\partial t} = \frac{\partial}{\partial J}\left(\left(-\langle \Delta J\rangle + \frac{1}{2}\frac{\partial \langle (\Delta J)^2\rangle}{\partial J}\right)f + \frac{\langle (\Delta J)^2\rangle}{2}\frac{\partial f}{\partial J}\right). \tag{4}$$

To transform this equation into a radial diffusion equation, we use the fact that the two coefficients $\langle \Delta J\rangle$ and $\langle (\Delta J)^2\rangle$ are not independent of each other:

$$\langle \Delta J\rangle = \frac{1}{2}\frac{\partial \langle (\Delta J)^2\rangle}{\partial J} \tag{5}$$

(e.g., Lichtenberg and Lieberman, 1992, their section 5.4a; Lejosne and Kollmann, 2020, their section 2.3.2). This relationship (Eq. 5) relies on the assumption of drift phase homogeneity, also known as random drift phase approximation, meaning that each drift phase location is equiprobable. In this context, the Fokker–Planck Eq. 2 reduces to a diffusion equation:

$$\frac{\partial f}{\partial t} = \frac{\partial}{\partial J}\left(D\frac{\partial f}{\partial J}\right), \tag{6}$$

where $D = \langle (\Delta J)^2\rangle/2$ is the diffusion coefficient in J. The diffusion equation is often rewritten in terms of $L^* \propto 1/J$:

$$\frac{\partial f}{\partial t} = L^{*2}\frac{\partial}{\partial L^*}\left(\frac{D_{LL}}{L^{*2}}\frac{\partial f}{\partial L^*}\right), \tag{7}$$

where $D_{LL} = \left\langle \left(\Delta L^*\right)^2\right\rangle/2$ is the radial diffusion coefficient.

2.2 Euler potentials

An appropriate coordinate to discuss radial diffusion is the L^* coordinate (Roederer, 1967), inversely proportional to the third adiabatic invariant, J (Eq. 7). In the following section, we argue that L^* is not suited when the objective is to resolve the drift phase. Instead, we introduce the best-suited coordinate, $\mathbb{L}$ ("double-struck L" or "L-Euler"). We discuss the relationship between $\mathbb{L}$ and L^* by detailing the underlying role of the Euler potentials.

2.2.1 Third adiabatic invariant, deconstructed in terms of Euler potentials

The radial diffusion equation, retrieved in Section 2.1 (Eq. 7), describes the time evolution of the number of particles per unit of third adiabatic invariant, J, or equivalently, L^*. The quantities J and L^* are *MLT-averaged* by design. Indeed, the third invariant of a trapped population, J, is proportional to the magnetic flux encompassed by the guiding drift shell:

$$J \propto \iint_\Sigma \boldsymbol{B}\bullet\boldsymbol{dS} = \oint_\Gamma \boldsymbol{A}\bullet\boldsymbol{dl}, \tag{8}$$

where $\boldsymbol{A}$ is the magnetic vector potential ($\nabla\times\boldsymbol{A} = \boldsymbol{B}$), and Σ is the surface encompassed by the instantaneous drift contour, Γ, of the trapped population. The instantaneous drift contour, Γ, can be viewed as the intersection of the guiding drift shell with a surface, such as the minimum B-surface (see also, Roederer, 1970, p. 76–79). In other words, to quantify the third adiabatic invariant, J, it is necessary to know the guiding drift shell, that is, the set of guiding center locations *at all magnetic local times*, treating the electromagnetic fields as stationary.

An important underlying requirement to sort trapped particle fluxes using the third adiabatic invariant is the so-called *frozen field condition*, where in the presence of magnetic field time variations, the cold (frozen) plasma $\boldsymbol{E}\times\boldsymbol{B}$ drifts to remain on the same magnetic field line (Birmingham and Jones, 1968). This assumption requires the Earth's surface to be a perfect conductor and no component of the electric field to be parallel to the magnetic field direction. In this context, the footpoints of a magnetic field line are rooted at fixed locations at ionospheric altitudes, while the rest of the field line can "move" (stretch, compress, distort) in the magnetosphere in the presence of magnetic field time variations. Thus, the frozen field condition enables a tempting, yet disputed, concept of field line "flagging" and its corollary, field line "motion" (Fälthammar and Mozer, 2007). It is indeed worth emphasizing that a field line is an imaginary concept that aids to visualize the magnitude and direction of a vector field, so there should be no way of differentiating a field line from the other. We assume nonetheless that we can label field lines based on the locations of their rooted ionospheric footpoints. In this context, to determine a guiding drift shell or an instantaneous drift contour, Γ, and to compute

the third adiabatic invariant, we now have to know the set of field lines that were scanned by the drifting guiding centers *at all magnetic local times*. In other words, we need information on the field line label at each magnetic local time. This can be done by leveraging the Euler potentials, as discussed in the following.

The Euler potentials (α,β) are a convenient tool for labeling field lines. They are analogous to the stream function in an incompressible flow in fluid mechanics. They offer a representation of the magnetic field intrinsically dependent on its topology (e.g., Stern, 1967, 1970). Their characterization relies on the fact that the magnetic field is a solenoidal vector field, i.e., $\nabla \bullet \boldsymbol{B} = 0$. The Euler potentials are such that

$$\boldsymbol{B} = \nabla\alpha \times \nabla\beta. \tag{9}$$

Thus, the Euler potentials are constant along the magnetic field lines. Since the vector potential can be viewed as $\boldsymbol{A} = \alpha\nabla\beta$, a reformulation of Eq. 8 in terms of Euler potential yields

$$J \propto \oint_\Gamma \alpha d\beta. \tag{10}$$

Although there is no uniformity in the definition of the Euler potentials, a suitable set of Euler potentials in a magnetic dipole field is

$$\begin{cases} \alpha = -\dfrac{B_E R_E^3}{r}\sin^2\theta \\ \beta = \varphi, \end{cases} \tag{11}$$

where $B_E = 30{,}000$ nT is the magnetic equatorial field at the surface of the Earth, $R_E = 6370\,km$ is one Earth radius, and (r,θ,φ) are the radial distance, magnetic colatitude, and azimuthal (i.e., MLT) location with respect to the center of the dipole magnetic moment, respectively.

In the presence of a distorted magnetic field, the expressions provided in Eq. 11 are not valid anymore. That said, it is possible to leverage the facts that (a) the field line footpoints are rooted at ionospheric altitudes, a region where the ambient magnetic field is mainly dipolar, so the Euler potentials can be described by Eq. 11 at ionospheric altitudes and (b) the Euler potentials are constant along the magnetic field lines. With that in mind, we can define a set of Euler potentials (α,β) such that at the footpoints (R_E,θ_E,φ_E), and thus all along the field lines:

$$\begin{cases} \alpha = -B_E R_E^2 \sin^2\theta_E \\ \beta = \varphi_E, \end{cases} \tag{12}$$

where $(\theta_E,\ \varphi_E)$, respectively, indicate the magnetic colatitude and longitude of the field line footpoint at $r = R_E$, the Earth's surface.

If a distorted magnetic field were to change into a dipole field, each field line would "move" in geospace, adopting a dipolar shape, while its footpoints would stay rooted at fixed ionospheric latitudes. Leveraging Eq. 11 in the newly transformed dipole field, a dipolar field line with footpoints at (R_E,θ_E,φ_E) would have its equatorial apex $(r_o,\theta=\pi/2,\varphi_o)$ such that $\alpha(r_o,\theta=\pi/2,\varphi_o) = \alpha(R_E,\theta_E,\varphi_E)$ and $\beta(r_o,\theta=\pi/2,\varphi_o) = \beta(R_E,\theta_E,\varphi_E)$. Thus, the intersection of the dipolar field line footpoint and the magnetic equator $(\theta=\pi/2)$ would be at

$$\begin{cases} r_o = \dfrac{R_E}{\sin^2\theta_E} \\ \varphi_o = \varphi_E. \end{cases} \tag{13}$$

The physical interpretation of this thought experiment is similar to the physical interpretation of the L^* parameter. The L^* coordinate corresponds to the normalized equatorial radius of the circular guiding contour on which trapped particles would drift after all non-dipolar contributions to the magnetic field and all electric field components have been turned off adiabatically. Here, we introduce the parameter $\mathbb{L}$ ("double-struck L" or "L-Euler") such that

$$\mathbb{L} = \frac{1}{\sin^2\theta_E}, \tag{14}$$

where θ_E is the magnetic colatitude of the footpoint at $r = R_E$ for the field line passing through the location considered. It corresponds to the normalized equatorial radius of the *field line* on which trapped particles would bounce if all non-dipolar contributions to the magnetic field were turned off relatively fast (a few bounce periods). As for the angle variable, β, one can reasonably assume no significant longitudinal bending of the field lines when the magnetic field is stretched or compressed. Thus, in terms of Euler potentials, we have in general that

$$\begin{cases} \alpha = -\dfrac{B_E R_E^2}{\mathbb{L}} \\ \beta = \varphi_E \cong \varphi. \end{cases} \tag{15}$$

Combining Eqs 10, 15, given that $\oint_\Gamma \alpha d\beta = -2\pi B_E R_E^2/L^*$, we obtain

$$\frac{1}{L^*} = \frac{1}{2\pi}\oint_\Gamma \frac{d\varphi}{\mathbb{L}}. \tag{16}$$

The parameter L^* is the harmonic mean of the $\mathbb{L}$ coordinate along the guiding contour, Γ, a relationship that can be utilized to quantify L^* (e.g., Lejosne, 2014). In the presence of quasi-trapped particles, i.e., guiding centers drifting along on open drift contour, the parameter L^* cannot be defined. On the other hand, the $\mathbb{L}$ coordinate can still be defined on open drift contour, as long as we are dealing with a closed field line.

An illustration to the concepts discussed here is provided in Figure 1.

2.2.2 Euler potentials as appropriate variables to describe bounce-average drift motion of trapped and quasi-trapped particles

The Euler potentials α and β are proportional to canonical variables, that is,

$$\begin{cases} \dot{\alpha} = -\dfrac{\partial H}{\partial \beta} \\ \dot{\beta} = \dfrac{\partial H}{\partial \alpha}, \end{cases} \tag{17}$$

where H is a Hamiltonian proportional to the total energy of the guiding center (Northrop and Teller, 1960; Birmingham et al., 1967):

$$H = \frac{T}{q} + V, \tag{18}$$

where T is the kinetic energy, q is the charge of the population considered, and V is the electric potential.

One consequence of Eq. 17 is that the variations of the Euler potentials are related:

$$\frac{\partial}{\partial\alpha}(\dot{\alpha}) + \frac{\partial}{\partial\beta}(\dot{\beta}) = 0. \tag{19}$$

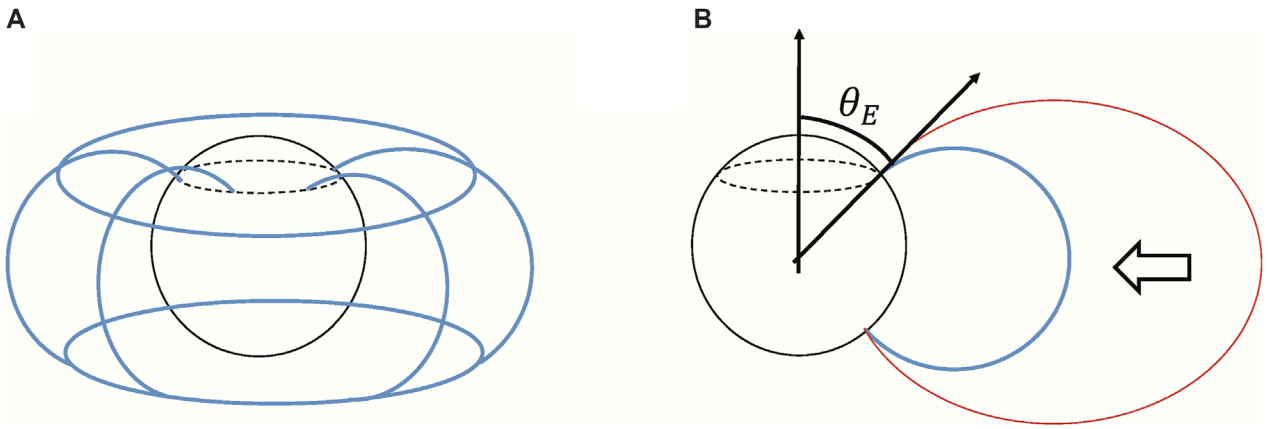

FIGURE 1
(A) A few magnetic field lines constitutive of a trapped particle drift shell, together with the locations of the field line footpoints, necessary to determine the L* parameter—adapted from Roederer (1970). **(B)** A stretch magnetic field line (in red) is relaxed into its dipolar shape (in blue). The field line footpoint remains rooted at the same ionospheric colatitude, θ_E, a parameter that determines the $\mathbb{L}$ parameter, of use for field line labeling. The parameter $\mathbb{L}$ corresponds to the normalized equatorial radius of the dipolar field line (in blue)—adapted from Lejosne (2014).

This property will be leveraged to transform a two-dimensional Fokker–Planck equation in terms of Euler potentials, (α,β), in a two-dimensional drift-diffusion equation.

3 New derivation of Birmingham et al.'s transport equation to describe trapped particle transport effects on radiation belt intensity

Here, we present a compact way to retrieve the equation proposed by Birmingham et al. (1967). This equation represents the time evolution of radiation belt intensity due to transport processes. We describe the time evolution of a distribution function, F, that quantifies the number of particles per unit of Euler potential surface $d\alpha d\beta$. This function, F, is proportional to the phase space density averaged over both gyration and bounce phases by a physical constant. It relates to the drift-averaged distribution function, f, introduced in Section 2.1, since the number of particles per unit of third invariant, J, is $fdJ = \oint_{\beta\in\Gamma} Fd\alpha(\beta)d\beta$ (with $dJ = \oint_{\beta\in\Gamma} d\alpha(\beta)d\beta$). We assume that many very small random changes of the Euler coordinates occur between times t and $t+\Delta t$, with a very small total effect. The resulting two-dimensional Fokker–Planck equation is

$$\begin{aligned}\frac{\partial F}{\partial t} = &-\frac{\partial}{\partial\alpha}(\langle\Delta\alpha\rangle F) - \frac{\partial}{\partial\beta}(\langle\Delta\beta\rangle F)\\ &+\frac{1}{2}\frac{\partial^2}{\partial\alpha^2}(\langle(\Delta\alpha)^2\rangle F) + \frac{1}{2}\frac{\partial^2}{\partial\beta^2}(\langle(\Delta\beta)^2\rangle F)\\ &+\frac{1}{2}\frac{\partial^2}{\partial\alpha\partial\beta}(\langle\Delta\alpha\Delta\beta\rangle F) + \frac{1}{2}\frac{\partial^2}{\partial\beta\partial\alpha}(\langle\Delta\beta\Delta\alpha\rangle F),\end{aligned} \tag{20}$$

where the angle bracket sign, $\langle\,\rangle$, indicates the rate of change of the expected value for the bracketed variable and $\Delta X = X(t+\Delta t) - X(t)$.

Just like in Section 2.1 (Eq. 3), we rewrite Eq. 20 as

$$\begin{aligned}\frac{\partial F}{\partial t} = &\frac{\partial}{\partial\alpha}\left(-\langle\Delta\alpha\rangle F + \frac{1}{2}\frac{\partial}{\partial\alpha}(\langle(\Delta\alpha)^2\rangle F) + \frac{1}{2}\frac{\partial}{\partial\beta}(\langle\Delta\alpha\Delta\beta\rangle F)\right)\\ &+\frac{\partial}{\partial\beta}\left(-(\langle\Delta\beta\rangle F) + \frac{1}{2}\frac{\partial}{\partial\beta}(\langle(\Delta\beta)^2\rangle F) + \frac{1}{2}\frac{\partial}{\partial\alpha}(\langle\Delta\beta\Delta\alpha\rangle F)\right).\end{aligned} \tag{21}$$

The terms between the large parentheses in Eq. 21 are

$$\begin{aligned}&-\langle\Delta\alpha\rangle F + \frac{1}{2}\frac{\partial}{\partial\alpha}\left(\langle(\Delta\alpha)^2\rangle F\right) + \frac{1}{2}\frac{\partial}{\partial\beta}(\langle\Delta\alpha\Delta\beta\rangle F)\\ &= \left(-\langle\Delta\alpha\rangle + \frac{1}{2}\frac{\partial\langle(\Delta\alpha)^2\rangle}{\partial\alpha} + \frac{1}{2}\frac{\partial\langle\Delta\alpha\Delta\beta\rangle}{\partial\beta}\right)F + \frac{\langle(\Delta\alpha)^2\rangle}{2}\frac{\partial F}{\partial\alpha} + \frac{\langle\Delta\alpha\Delta\beta\rangle}{2}\frac{\partial F}{\partial\beta}\end{aligned} \tag{22}$$

and

$$\begin{aligned}&-(\langle\Delta\beta\rangle F) + \frac{1}{2}\frac{\partial}{\partial\beta}\left(\langle(\Delta\beta)^2\rangle F\right) + \frac{1}{2}\frac{\partial}{\partial\alpha}(\langle\Delta\beta\Delta\alpha\rangle F)\\ &= \left(-\langle\Delta\beta\rangle + \frac{1}{2}\frac{\partial\langle(\Delta\beta)^2\rangle}{\partial\beta} + \frac{1}{2}\frac{\partial\langle\Delta\beta\Delta\alpha\rangle}{\partial\alpha}\right)F + \frac{\langle(\Delta\beta)^2\rangle}{2}\frac{\partial F}{\partial\beta} + \frac{\langle\Delta\beta\Delta\alpha\rangle}{2}\frac{\partial F}{\partial\alpha}.\end{aligned} \tag{23}$$

Using the Hamiltonian relationships between the Euler potentials (Eq. 17), we have shown in the **Appendix** that

$$\begin{cases}-\langle\Delta\alpha\rangle + \frac{1}{2}\frac{\partial\langle(\Delta\alpha)^2\rangle}{\partial\alpha} + \frac{1}{2}\frac{\partial\langle\Delta\alpha\Delta\beta\rangle}{\partial\beta} = -[\dot{\alpha}]\\ -\langle\Delta\beta\rangle + \frac{1}{2}\frac{\partial\langle(\Delta\beta)^2\rangle}{\partial\beta} + \frac{1}{2}\frac{\partial\langle\Delta\beta\Delta\alpha\rangle}{\partial\alpha} = -[\dot{\beta}],\end{cases} \tag{24}$$

provided that the time interval, Δt, is very small in comparison with the characteristic time for the time variation of the Hamiltonian ($\Delta t \ll H/(\partial H/\partial t)$). In practice, the time interval, Δt, is of the order of a few bounce periods, that is, very small in comparison with the drift period. The squared brackets, [ ], indicate the expected value of the bracketed variable.

Combining Eqs 21–24, Eq. 20 becomes a drift-diffusion equation:

$$\frac{\partial F}{\partial t} = -\frac{\partial}{\partial \alpha}([\dot{\alpha}]F) - \frac{\partial}{\partial \beta}\left([\dot{\beta}]F\right) + \frac{\partial}{\partial \alpha}\left(\frac{\langle(\Delta\alpha)^2\rangle}{2}\frac{\partial F}{\partial \alpha}\right) + \frac{\partial}{\partial \alpha}\left(\frac{\langle\Delta\alpha\Delta\beta\rangle}{2}\frac{\partial F}{\partial \beta}\right) + \frac{\partial}{\partial \beta}\left(\frac{\langle\Delta\beta\Delta\alpha\rangle}{2}\frac{\partial F}{\partial \alpha}\right) + \frac{\partial}{\partial \beta}\left(\frac{\langle(\Delta\beta)^2\rangle}{2}\frac{\partial F}{\partial \beta}\right). \quad (25)$$

Given Eq. 19, this simplifies to

$$\frac{\partial F}{\partial t} = -[\dot{\alpha}]\frac{\partial F}{\partial \alpha} - [\dot{\beta}]\frac{\partial F}{\partial \beta} + \frac{\partial}{\partial \alpha}\left(D_{\alpha\alpha}\frac{\partial F}{\partial \alpha}\right) + \frac{\partial}{\partial \alpha}\left(D_{\alpha\beta}\frac{\partial F}{\partial \beta}\right) + \frac{\partial}{\partial \beta}\left(D_{\beta\alpha}\frac{\partial F}{\partial \alpha}\right) + \frac{\partial}{\partial \beta}\left(D_{\beta\beta}\frac{\partial F}{\partial \beta}\right), \quad (26)$$

where $D_{\alpha\alpha} = \langle(\Delta\alpha)^2\rangle/2$, $D_{\beta\beta} = \langle(\Delta\beta)^2\rangle/2$, $D_{\alpha\beta} = \langle\Delta\alpha\Delta\beta\rangle/2$, and $D_{\beta\alpha} = \langle\Delta\beta\Delta\alpha\rangle/2$ are the diffusion coefficients, and $[\dot{\alpha}]$ and $[\dot{\beta}]$ are the mean bounce-averaged time rates of change of α and β, respectively. This transport equation coincides with the one provided by Birmingham et al. (1967), their equation (4.11). A change of variables (using Eq. 15) yields:

$$\frac{\partial F}{\partial t} = -[\dot{\mathbb{L}}]\frac{\partial F}{\partial \mathbb{L}} - [\dot{\varphi}]\frac{\partial F}{\partial \varphi} + \mathbb{L}^2\frac{\partial}{\partial \mathbb{L}}\left(\frac{D_{\mathbb{L}\mathbb{L}}}{\mathbb{L}^2}\frac{\partial F}{\partial \mathbb{L}}\right) + \mathbb{L}^2\frac{\partial}{\partial \mathbb{L}}\left(\frac{D_{\mathbb{L}\varphi}}{\mathbb{L}^2}\frac{\partial F}{\partial \varphi}\right) + \frac{\partial}{\partial \varphi}\left(D_{\varphi\mathbb{L}}\frac{\partial F}{\partial \mathbb{L}}\right) + \frac{\partial}{\partial \varphi}\left(D_{\varphi\varphi}\frac{\partial F}{\partial \varphi}\right). \quad (27)$$

The term depending on $D_{\mathbb{L}\mathbb{L}}$ mistakenly resembles the one present in the standard radial diffusion equation (Eq. 7): $D_{\mathbb{L}\mathbb{L}}$ and D_{LL} are different. The distribution function, f, the coefficient for the standard radiation diffusion equation (Eq. 7), D_{LL}, and more generally, the quantities used for the three-dimensional equation for radiation belt dynamics (Eq. 1) are *drift-averaged*, i.e., they are independent of the drift phase. Here, the drift phase is resolved: the distribution function and coefficients are *bounce-averaged* quantities that depend on the drift phase. Thus, they must be evaluated at each location (α,β), or similarly $(\mathbb{L},\varphi)$, and at each time, t.

The transport parameters of Eq. 27 are all statistically averaged quantities. The coefficients $[\dot{\mathbb{L}}]$ and $[\dot{\varphi}]$ (or equivalently $[\dot{\alpha}]$ and $[\dot{\beta}]$) indicate ensemble averages of time derivatives for the quantities considered. The ensemble averages are computed at each location and at each time, t, over an ensemble of field fluctuations. The diffusion coefficients are proportional to the time rates of change of the covariances for the quantities considered. Specifically, when considering two variables X and Y (where (X,Y) could be any combination of (α,β) or $(\mathbb{L},\varphi)$), the diffusion coefficient is

$$D_{XY} = \frac{[(\mathrm{X(t+\Delta t)} - \mathrm{X(t)})(\mathrm{Y(t+\Delta t)} - \mathrm{Y(t)})]}{2\Delta \mathrm{t}}. \quad (28)$$

That is, it is half the time rate of change of the ensemble average for the product of the time variations of X and Y during a time interval, Δt. A worked example will be provided in the second part of this work. It will detail how to compute all transport parameters of Eq. 27 in a particular model of field fluctuations.

According to Eq. 26, variations in the distribution function are due to the bulk motion of the plasma in the presence of density gradients and to diffusive effects in both the localized radial ($\mathbb{L}$) and azimuthal (φ) directions. Local effects acting at smaller scales can be readily reinstated by adding relevant coefficients modeling local diffusion, source, and loss mechanisms:

$$\frac{\partial F}{\partial t} = -[\dot{\mathbb{L}}]\frac{\partial F}{\partial \mathbb{L}} - [\dot{\varphi}]\frac{\partial F}{\partial \varphi} + \mathbb{L}^2\frac{\partial}{\partial \mathbb{L}}\left(\frac{D_{\mathbb{L}\mathbb{L}}}{\mathbb{L}^2}\frac{\partial F}{\partial \mathbb{L}}\right) + \mathbb{L}^2\frac{\partial}{\partial \mathbb{L}}\left(\frac{D_{\mathbb{L}\varphi}}{\mathbb{L}^2}\frac{\partial F}{\partial \varphi}\right) + \frac{\partial}{\partial \varphi}\left(D_{\varphi\mathbb{L}}\frac{\partial F}{\partial \mathbb{L}}\right) + \frac{\partial}{\partial \varphi}\left(D_{\varphi\varphi}\frac{\partial F}{\partial \varphi}\right) + \sum_{1\le i,j\le 2}\frac{\partial}{\partial J_i}\left(D_{i,j}\frac{\partial F}{\partial J_j}\right) + Sources - Losses, \quad (29)$$

where all quantities are *bounce-averaged* quantities that depend on the drift phase.

4 Conclusion

The objective of this work is to contribute toward improving the spatiotemporal resolution of physics-based diffusive radiation belt models. The resulting transport Eq. 27 can resolve the drift phase, and the outputs are bounce-averaged rather than drift-averaged. This is of use when the objective is to model fast radiation belt dynamics, such as times of fast radiation belt acceleration or losses occurring during the main phase of geomagnetic storms (e.g., Ripoll et al., 2020; Lejosne et al., 2022). It can also be used to increase the energy range modeled, by including ring current energies.

Although Eq. 27 contains some localized (in $\mathbb{L}$, MLT) diffusion coefficients, its scope is beyond the long-established radial diffusion paradigm used to summarize transport effects on radiation belt intensity. The inclusion of the effects of bulk motion and the diffusion in the azimuthal coordinate enable the modeling of MLT-localized structures, drift-periodic flux oscillations, and their subsequent attenuation due to phase-mixing processes.

Current works leveraging *in situ* measurements to quantify radial diffusion coefficients require information on average over all magnetic local times of a drift shell. Yet, a spacecraft can only scan the electromagnetic environment along its orbit, limiting the accuracy with which the outputs can be determined (e.g., Sandhu et al., 2021). Because the coefficients introduced in this work depend on magnetic local time, these may be easier to quantify experimentally. Furthermore, describing the effect of drift motion on radiation belt intensity in terms of Euler potentials, or similarly with $(\mathbb{L},\varphi)$, is computationally more advantageous than working with the action-angle variables (J_3, φ_3): the latter requires tracing the instantaneous drift contour at every time step, while the former only requires local field line tracing. In addition, the definition of the Euler potentials only requires closed field lines, while the definition of the action-angle variables is more restrictive, requiring a closed instantaneous drift contour. Thus, working in terms of Euler potentials allows for the inclusion of quasi-trapped particles from the drift loss cone.

The second part of this work will deal with characterizing the coefficients introduced in Eq. 27 (i.e., $[\dot{\mathbb{L}}], [\dot{\varphi}], D_{\mathbb{L}\mathbb{L}}, D_{\mathbb{L}\varphi}, D_{\varphi\mathbb{L}}, D_{\varphi\varphi}$) in the special case of electric potential fluctuations in a magnetic dipole field. It will show how to implement the theoretical framework presented in this work.

Data availability statement

The original contributions presented in the study are included in the article/Supplementary Material, further inquiries can be directed to the corresponding author.

Author contributions

We describe contributions to the paper using the CRediT (Contributor Roles Taxonomy) categories (Brand et al., 2015). Conceptualization, writing—original draft, and writing—review and editing: all authors. Visualization: SL. All authors contributed to the article and approved the submitted version.

Acknowledgments

SL's work was performed under NASA Grants 80NSSC18K1223 and 80NSSC20K1351. The author thanks S.D. Walton for helpful comments on a draft version of this manuscript.

Conflict of interest

The authors declare that the research was conducted in the absence of any commercial or financial relationships that could be construed as a potential conflict of interest.

Publisher's note

All claims expressed in this article are solely those of the authors and do not necessarily represent those of their affiliated organizations, or those of the publisher, the editors, and the reviewers. Any product that may be evaluated in this article, or claim that may be made by its manufacturer, is not guaranteed or endorsed by the publisher.

References

Albert, J. M., Meredith, N. P., and Horne, R. B. (2009). Three-dimensional diffusion simulation of outer radiation belt electrons during the 9 October 1990 magnetic storm. *J. Geophys. Res.* 114, A09214. doi:10.1029/2009JA014336

Beutier, T., and Boscher, D. (1995). A three-dimensional analysis of the electron radiation belt by the Salammbô code. *J. Geophys. Res.* 100 (8), 14853–14861. doi:10.1029/94JA03066

Birmingham, T. J., and Jones, F. C. (1968). Identification of moving magnetic field lines. *J. Geophys. Res.* 73 (17), 5505–5510. doi:10.1029/JA073i017p05505

Birmingham, T. J., Northrop, T. G., and Fälthammar, C. G. (1967). Charged particle diffusion by violation of the third adiabatic invariant. *Phys. Fluids* 10 (11), 2389. doi:10.1063/1.1762048

Bourdarie, S., Boscher, D., Beutier, T., Sauvaud, J.-A., and Blanc, M. (1997). Electron and proton radiation belt dynamic simulations during storm periods: A new asymmetric convection-diffusion model. *J. Geophys. Res.* 102 (8), 17541–17552. doi:10.1029/97JA01305

Brand, A., Allen, L., Altman, M., Hlava, M., and Scott, J. (2015). Beyond authorship: Attribution, contribution, collaboration, and credit. *Learn. Pub.* 28, 151–155. doi:10.1087/20150211

Drozdov, A. Y., Usanova, M. E., Hudson, M. K., Allison, H. J., and Shprits, Y. Y. (2020). The role of hiss, chorus, and EMIC waves in the modeling of the dynamics of the multi-MeV radiation belt electrons. *J. Geophys. Res. Space Phys.* 125, e2020JA028282. doi:10.1029/2020JA028282

Fälthammar, C.-G., and Mozer, F. S. (2007). [Comment on "Bringing space physics concepts into introductory electromagnetism"] on the concept of moving magnetic fields lines. *Eos Trans. AGU* 88, 169–170. doi:10.1029/2007EO150002

Fok, M.-C., Buzulukova, N. Y., Chen, S.-H., Glocer, A., Nagai, T., Valek, P., et al. (2014). The comprehensive inner magnetosphere-ionosphere model. *J. Geophys. Res. Space Phys.* 119, 7522–7540. doi:10.1002/2014JA020239

Fok, M. C., and Moore, T. E. (1997). Ring current modeling in a realistic magnetic field configuration. *J. Geophys. Res.* 24 (14), 1775–1778. doi:10.1029/97GL01255

Glauert, S. A., Horne, R. B., and Meredith, N. P. (2018). A 30-year simulation of the outer electron radiation belt. *Space weather.* 16, 1498–1522. doi:10.1029/2018SW001981

Glauert, S. A., Horne, R. B., and Meredith, N. P. (2014). Three-dimensional electron radiation belt simulations using the BAS Radiation Belt Model with new diffusion models for chorus, plasmaspheric hiss, and lightning-generated whistlers. *J. Geophys. Res. Space Phys.* 119, 268–289. doi:10.1002/2013JA019281

Hao, Y. X., Sun, Y. X., Roussos, E., Liu, Y., Kollmann, P., Yuan, C. J., et al. (2020). The formation of saturn's and jupiter's electron radiation belts by magnetospheric electric fields. *Astrophysical J.* 905 (1), L10. doi:10.3847/2041-8213/abca3f

Hao, Y. X., Zong, Q. G., Zhou, X. Z., Fu, S. Y., Rankin, R., Yuan, C. J., et al. (2016). Electron dropout echoes induced by interplanetary shock: Van Allen Probes observations. *Geophys. Res. Lett.* 43, 5597–5605. doi:10.1002/2016GL069140

Horne, R. B., Glauert, S. A., Kirsch, P., Heynderickx, D., Bingham, S., Thorn, P., et al. (2021). The satellite risk prediction and radiation forecast system (SaRIF). *Space weather.* 19, e2021SW002823. doi:10.1029/2021SW002823

Hudson, M., Jaynes, A., Kress, B. T., Li, Z., Patel, M., Shen, X.-C., et al. (2017). Simulated prompt acceleration of multi-MeV electrons by the 17March 2015 interplanetary shock. *J. Geophys. Research:Space Phys.* 122, 10,036–10,046. doi:10.1002/2017JA024445

Hudson, M. K., Elkington, S. R., Li, Z., and Patel, M. (2020). Drift echoes and flux oscillations: A signature of prompt and diffusive changes in the radiation belts. *J. Atmos. Solar-Terrestrial Phys.* 207, 105332. doi:10.1016/j.jastp.2020.105332

Jordanova, V. K., Kozyra, J. U., Nagy, A. F., and Khazanov, G. V. (1997). Kinetic model of the ring current-atmosphere interactions. *J. Geophys. Res.* 102 (7), 14279–14291. doi:10.1029/96JA03699

Jordanova, V. K., Morley, S. K., Engel, M. A., Godinez, H. C., Yakymenko, K., Henderson, M. G., et al. (2022). The RAM-SCB model and its applications to advance space weather forecasting. *Adv. Space Res.* doi:10.1016/j.asr.2022.08.077

Lejosne, S., Allison, H. J., Blum, L. W., Drozdov, A. Y., Hartinger, M. D., Hudson, M. K., et al. (2022). Differentiating between the leading processes for electron radiation belt acceleration. *Front. Astron. Space Sci.* 9, 896245. doi:10.3389/fspas.2022.896245

Lejosne, S. (2014). An algorithm for approximating the L * invariant coordinate from the real-time tracing of one magnetic field line between mirror points. *J. Geophys. Res. Space Phys.* 119, 6405–6416. doi:10.1002/2014JA020016

Lejosne, S., and Kollmann, P. (2020). Radiation belt radial diffusion at Earth and beyond. *Space Sci. Rev.* 216, 19. doi:10.1007/s11214-020-0642-6

Lejosne, S., and Mozer, F. S. (2020). Experimental determination of the conditions associated with "zebra stripe" pattern generation in the earth's inner radiation belt and slot region. *J. Geophys. Res. Space Phys.* 125, e2020JA027889. doi:10.1029/2020JA027889

Li, X., Roth, I., Temerin, M., Wygant, J. R., Hudson, M. K., and Blake, J. B. (1993). Simulation of the prompt energization and transport of radiation belt particles during the March 24, 1991 SSC. *Geophys. Res. Lett.* 20 (22), 2423–2426. doi:10.1029/93gl02701

Lichtenberg, A. J., and Lieberman, M. A. (1992). "Regular and chaotic dynamics," in *Applied mathematical Sciences*. 2nd (New York: Springer).

Nénon, Q., Sicard, A., and Bourdarie, S. (2017). A new physical model of the electron radiation belts of Jupiter inside Europa's orbit. *J. Geophys. Res. Space Phys.* 122, 5148–5167. doi:10.1002/2017JA023893

Northrop, T. G., and Teller, E. (1960). Stability of the adiabatic motion of charged particles in the earth's field. *Phys. Rev.* 117 (1), 215–225. doi:10.1103/PhysRev.117.215

Patel, M., Li, Z., Hudson, M., Claudepierre, S., and Wygant, J. (2019). Simulation of prompt acceleration of radiation belt electrons during the 16 July 2017 storm. *Geophys. Res. Lett.* 46, 7222–7229. doi:10.1029/2019GL083257

Ripoll, J.-F., Claudepierre, S. G., Ukhorskiy, A. Y., Colpitts, C., Li, X., Fennell, J., et al. (2020). Particle dynamics in the earth's radiation belts: Review of current research and open questions. *J. Geophys. Res. Space Phys.* 125, e2019JA026735. doi:10.1029/2019JA026735

Roederer, J. G. (1970). *Dynamics of geomagnetically trapped radiation*. Heidelberg: Springer Berlin.

Roederer, J. G. (1967). On the adiabatic motion of energetic particles in a model magnetosphere. *J. Geophys. Res.* 72 (3), 981–992. doi:10.1029/JZ072i003p00981

Roederer, J. G., and Zhang, H. (2014). "Dynamics of magnetically trapped particles," in *Foundations of the physics of radiation belts and space plasmas. Astrophysics and space science library* (Berlin: Springer).

Sandhu, J. K., Rae, I. J., Wygant, J. R., Breneman, A. W., Tian, S., Watt, C. E. J., et al. (2021). ULF wave driven radial diffusion during geomagnetic storms: A statistical analysis of van allen probes observations. *J. Geophys. Res. Space Phys.* 126, e2020JA029024. doi:10.1029/2020JA029024

Sauvaud, J.-A., Walt, M., Delcourt, D., Benoist, C., Penou, E., Chen, Y., et al. (2013). Inner radiation belt particle acceleration and energy structuring by drift resonance with ULF waves during geomagnetic storms. *J. Geophys. Res. Space Phys.* 118, 1723–1736. doi:10.1002/jgra.50125

Schulz, M., and Lanzerotti, L. J. (1974). *Particle diffusion in the radiation belts*. Heidelberg: Springer Berlin.

Shprits, Y. Y., Kellerman, A. C., Drozdov, A. Y., Spence, H. E., Reeves, G. D., and Baker, D. N. (2015), Combined convective and diffusive simulations: VERB-4D comparison with 17 march 2013 van allen probes observations, *Geophys. Res. Lett.* 42, 9600–9608. doi:10.1002/2015GL065230

Stern, D. (1967). Geomagnetic euler potentials. *J. Geophys. Res.* 72 (15), 3995–4005. doi:10.1029/jz072i015p03995

Stern, D. P. (1970). Euler potentials. *Am. J. Phys.* 38, 494–501. doi:10.1119/1.1976373

Su, Z., Xiao, F., Zheng, H., and Wang, S. (2010). Steerb: A three-dimensional code for storm-time evolution of electron radiation belt. *J. Geophys. Res.* 115, A09208. doi:10.1029/2009JA015210

Subbotin, D. A., and Shprits, Y. Y. (2009). Three-dimensional modeling of the radiation belts using the Versatile Electron Radiation Belt (VERB) code. *Space weather.* 7, S10001. doi:10.1029/2008SW000452

Tu, W., Cunningham, G. S., Chen, Y., Henderson, M. G., Camporeale, E., and Reeves, G. D. (2013). Modeling radiation belt electron dynamics during GEM challenge intervals with the DREAM3D diffusion model. *J. Geophys. Res. Space Phys.* 118, 6197–6211. doi:10.1002/jgra.50560

Ukhorskiy, A. Y., and Sitnov, M. I. (2013). Dynamics of radiation belt particles. *Space Sci. Rev.* 179, 545–578. doi:10.1007/s11214-012-9938-5

Varotsou, A., Boscher, D., Bourdarie, S., Horne, R. B., Glauert, S. A., and Meredith, N. P. (2005). Simulation of the outer radiation belt electrons near geosynchronous orbit including both radial diffusion and resonant interaction with Whistler-mode chorus waves. *Geophys. Res. Lett.* 32, L19106. doi:10.1029/2005GL023282

Walt, M. (1994). *Introduction to geomagnetically trapped radiation*. Cambridge: Cambridge University Press. doi:10.1017/CBO9780511524981

Woodfield, E. E., Horne, R. B., Glauert, S. A., Menietti, J. D., Shprits, Y. Y., and Kurth, W. S. (2018). Formation of electron radiation belts at Saturn by Z-mode wave acceleration. *Nat. Commun.* 9, 5062. doi:10.1038/s41467-018-07549-4

Woodfield, E. E., Horne, R. B., Glauert, S. A., Menietti, J. D., and Shprits, Y. Y. (2014). The origin of Jupiter's outer radiation belt. *J. Geophys. Res. Space Phys.* 119, 3490–3502. doi:10.1002/2014JA019891

Yu, Y., Jordanova, V. K., Ridley, A. J., Albert, J. M., Horne, R. B., and Jeffery, C. A. (2016). A new ionospheric electron precipitation module coupled with RAM-SCB within the geospace general circulation model. *J. Geophys. Res. Space Phys.* 121, 8554–8575. doi:10.1002/2016JA022585

Zhao, H., Sarris, T. E., Li, X., Huckabee, I. G., Baker, D. N., Jaynes, A. J., et al. (2022). Statistics of multi-MeV electron drift-periodic flux oscillations using Van Allen Probes observations. *Geophys. Res. Lett.* 49, e2022GL097995. doi:10.1029/2022GL097995

Appendix

Here, we detail how to obtain Eq. 24, leveraging the fact that the Euler potentials (α,β) are proportional to canonical variables (Eq. 17).

We assume some small variations in α and β during t and $t+\Delta t$. In which case, a Taylor approximation of the time variations of α and β, to the second order, yields

$$\begin{cases} \alpha(t+\Delta t) = \alpha(t) + \dot{\alpha}(t)\Delta t + \dfrac{\ddot{\alpha}(t)}{2}\Delta t^2 \\ \beta(t+\Delta t) = \beta(t) + \dot{\beta}(t)\Delta t + \dfrac{\ddot{\beta}(t)}{2}\Delta t^2. \end{cases} \tag{A1}$$

Rewriting $\dot{\alpha}$ and $\dot{\beta}$ in terms of Hamiltonian (Eq. 17), the second time derivatives are

$$\begin{cases} \ddot{\alpha} = -\dfrac{d}{dt}\left(\dfrac{\partial H}{\partial \beta}\right) = \dfrac{\partial}{\partial \alpha}\left(\dfrac{\partial H}{\partial \beta}\right)^2 - \dfrac{\partial}{\partial \beta}\left(\dfrac{\partial H}{\partial \alpha}\dfrac{\partial H}{\partial \beta} + \dfrac{\partial H}{\partial t}\right) \\ \ddot{\beta} = \dfrac{d}{dt}\left(\dfrac{\partial H}{\partial \alpha}\right) = \dfrac{\partial}{\partial \beta}\left(\dfrac{\partial H}{\partial \alpha}\right)^2 - \dfrac{\partial}{\partial \alpha}\left(\dfrac{\partial H}{\partial \alpha}\dfrac{\partial H}{\partial \beta} - \dfrac{\partial H}{\partial t}\right) \end{cases} \tag{A2}$$

(see also Lichtenberg and Lieberman, 1992; their equation (5.4.10), p. 322).

Combining equations Eqs A1, A2, 17, we have

$$\begin{cases} \Delta\alpha = -\dfrac{\partial H}{\partial \beta}\Delta t + \dfrac{(\Delta t)^2}{2}\left(\dfrac{\partial}{\partial \alpha}\left(\dfrac{\partial H}{\partial \beta}\right)^2 - \dfrac{\partial}{\partial \beta}\left(\dfrac{\partial H}{\partial \alpha}\dfrac{\partial H}{\partial \beta} + \dfrac{\partial H}{\partial t}\right)\right) \\ \Delta\beta = \dfrac{\partial H}{\partial \alpha}\Delta t + \dfrac{(\Delta t)^2}{2}\left(\dfrac{\partial}{\partial \beta}\left(\dfrac{\partial H}{\partial \alpha}\right)^2 - \dfrac{\partial}{\partial \alpha}\left(\dfrac{\partial H}{\partial \alpha}\dfrac{\partial H}{\partial \beta} - \dfrac{\partial H}{\partial t}\right)\right). \end{cases} \tag{A3}$$

To the second order in Δt, we also have

$$\begin{cases} (\Delta\alpha)^2 = \left(\dfrac{\partial H}{\partial \beta}\right)^2(\Delta t)^2 \\ (\Delta\beta)^2 = \left(\dfrac{\partial H}{\partial \alpha}\right)^2(\Delta t)^2 \\ \Delta\alpha\Delta\beta = -\dfrac{\partial H}{\partial \alpha}\dfrac{\partial H}{\partial \beta}(\Delta t)^2. \end{cases} \tag{A4}$$

Thus,

$$\begin{cases} \dfrac{1}{2}\dfrac{\partial}{\partial \alpha}(\Delta\alpha)^2 = \dfrac{1}{2}\dfrac{\partial}{\partial \alpha}\left(\dfrac{\partial H}{\partial \beta}\right)^2(\Delta t)^2 \\ \dfrac{1}{2}\dfrac{\partial}{\partial \beta}(\Delta\beta)^2 = \dfrac{1}{2}\dfrac{\partial}{\partial \beta}\left(\dfrac{\partial H}{\partial \alpha}\right)^2(\Delta t)^2 \\ \dfrac{1}{2}\dfrac{\partial}{\partial \alpha}(\Delta\beta\Delta\alpha) = -\dfrac{1}{2}\dfrac{\partial}{\partial \alpha}\left(\dfrac{\partial H}{\partial \alpha}\dfrac{\partial H}{\partial \beta}\right)(\Delta t)^2 \\ \dfrac{1}{2}\dfrac{\partial}{\partial \beta}(\Delta\alpha\Delta\beta) = -\dfrac{1}{2}\dfrac{\partial}{\partial \beta}\left(\dfrac{\partial H}{\partial \alpha}\dfrac{\partial H}{\partial \beta}\right)(\Delta t)^2. \end{cases} \tag{A5}$$

Combining Eqs A3–A5 in terms of expected values for the variations, we have

$$-[\Delta\alpha] + \frac{1}{2}\frac{\partial[(\Delta\alpha)^2]}{\partial \alpha} + \frac{1}{2}\frac{\partial[\Delta\alpha\Delta\beta]}{\partial \beta} = \left[\frac{\partial}{\partial \beta}\left(H + \frac{\Delta t}{2}\frac{\partial H}{\partial t}\right)\right]\Delta t, \tag{A6}$$

$$-[\Delta\beta] + \frac{1}{2}\frac{\partial[(\Delta\beta)^2]}{\partial \beta} + \frac{1}{2}\frac{\partial[\Delta\beta\Delta\alpha]}{\partial \alpha} = -\left[\frac{\partial}{\partial \alpha}\left(H + \frac{\Delta t}{2}\frac{\partial H}{\partial t}\right)\right]\Delta t. \tag{A7}$$

Assuming that the time interval, Δt, is very small in comparison with the characteristic time for the time variation of the Hamiltonian:

$$\Delta t \ll H/(\partial H/\partial t), \tag{A8}$$

with $\langle\Delta\alpha\rangle = [\Delta\alpha]/\Delta t$ and $\langle\Delta\beta\rangle = [\Delta\beta]/\Delta t$, the rates of change of the expected values for the variations, we obtain

$$\begin{cases} -\langle\Delta\alpha\rangle + \dfrac{1}{2}\dfrac{\partial\langle(\Delta\alpha)^2\rangle}{\partial \alpha} + \dfrac{1}{2}\dfrac{\partial\langle\Delta\alpha\Delta\beta\rangle}{\partial \beta} = \left[\dfrac{\partial H}{\partial \beta}\right] = -[\dot{\alpha}] \\ -\langle\Delta\beta\rangle + \dfrac{1}{2}\dfrac{\partial\langle(\Delta\beta)^2\rangle}{\partial \beta} + \dfrac{1}{2}\dfrac{\partial\langle\Delta\beta\Delta\alpha\rangle}{\partial \alpha} = -\left[\dfrac{\partial H}{\partial \alpha}\right] = -[\dot{\beta}]. \end{cases} \tag{A9}$$

Glossary

$(\boldsymbol{\alpha},\boldsymbol{\beta})$	Euler potentials
$\mathbf{A}$	magnetic vector potential
$\mathbf{B}$	magnetic field
$\boldsymbol{B}_{\mathrm{E}}$	magnetic equatorial field at the Earth's surface
$\mathbf{D}_{\mathrm{XY}}$	diffusion coefficient with respect to the X and Y coordinates
$\mathbf{f},\mathbf{F}$	distribution functions
$\boldsymbol{\Gamma}$	drift contour
$\mathbf{H}$	Hamiltonian proportional to the total energy of the guiding center
$\mathbf{J}_{\mathrm{i=1..3}}$	action variable, proportional to the adiabatic invariant coordinates
$\mathbf{J}$	stands for J_3, the adiabatic invariant associated with the drift motion
$\mathbf{L}^*$	"L-star" or "L-Roederer" inversely proportional to the third adiabatic invariant, J
$\mathbb{L}$	"double-struck L" or "L-Euler", inversely proportional to the Euler potential α
$\mathbf{MLT}$	magnetic local time
$\mathbf{q}$	electric charge of a particle
$\mathbf{r}$	radial distance to the center of the dipole magnetic moment
$\mathbf{R}_{\mathrm{E}}$	Earth's equatorial radius
$\boldsymbol{\varphi},\boldsymbol{\varphi}_{\mathrm{E}}$	azimuthal location (i.e., magnetic local time, in radians), azimuthal location of the footpoint at $r = R_E$ for the field line passing through the location considered
$\boldsymbol{\Sigma}$	surface encompassed by the drift contour, Γ
$\boldsymbol{\theta},\boldsymbol{\theta}_{\mathrm{E}}$	magnetic colatitude, magnetic colatitude of the footpoint at $r = R_E$ for the field line passing through the location considered
$\mathbf{t},\Delta\mathbf{t}$	time, small time interval
$\mathbf{T}$	kinetic energy
$\mathbf{V}$	electric potential
$[]$	square brackets = expected value (average value of an ensemble of fluctuations) of the bracketed quantity
$\langle\rangle$	angle brackets = average change per unit time of the bracketed quantity (= $[]/\Delta t$)
$\propto$	proportionality symbol.

frontiers | Frontiers in Astronomy and Space Sciences

TYPE Original Research
PUBLISHED 08 August 2023
DOI 10.3389/fspas.2023.1232512

OPEN ACCESS

EDITED BY
Qianli Ma,
Boston University, United States

REVIEWED BY
Greg Cunningham,
Los Alamos National Laboratory (DOE), United States
Xin Tao,
University of Science and Technology of China, China

*CORRESPONDENCE
Solène Lejosne,
solene@berkeley.edu

RECEIVED 31 May 2023
ACCEPTED 13 July 2023
PUBLISHED 08 August 2023

CITATION
Lejosne S, Albert JM and Walton SD (2023), Drift phase resolved diffusive radiation belt model: 2. implementation in a case of random electric potential fluctuations.
Front. Astron. Space Sci. 10:1232512.
doi: 10.3389/fspas.2023.1232512

Drift phase resolved diffusive radiation belt model: 2. implementation in a case of random electric potential fluctuations

Solène Lejosne[1]*, Jay M. Albert[2] and Samuel D. Walton[1]

[1]Space Sciences Laboratory, University of California, Berkeley, CA, United States, [2]Air Force Research Laboratory, Kirtland AFB, Albuquerque, NM, United States

In the first part of this work, we highlighted a drift-diffusion equation capable of resolving the magnetic local time dimension when describing the effects of trapped particle transport on radiation belt intensity. Here, we implement these general considerations in a special case. Specifically, we determine the various transport and diffusion coefficients required to solve the drift-diffusion equation for equatorial electrons drifting in a dipole magnetic field in the presence of a specific model of time-varying electric fields. Random electric potential fluctuations, described as white noise, drive fluctuations of trapped particle drift motion. We also run a numerical experiment that consists of tracking trapped particles' drift motion. We use the results to illustrate the validity of the drift-diffusion equation by showing agreement in the solutions. Our findings depict how a structure initially localized in magnetic local time generates drift-periodic signatures that progressively dampen with time due to the combined effects of radial and azimuthal diffusions. In other words, we model the transition from a drift-dominated regime, to a diffusion-dominated regime. We also demonstrate that the drift-diffusion equation is equivalent to a standard radial diffusion equation once the distribution function is phase-mixed. The drift-diffusion equation will allow for radiation belt modeling with a better spatiotemporal resolution than radial diffusion models once realistic inputs, including localized transport and diffusion coefficients, are determined.

KEYWORDS

radiation belts, fokker-planck equation, adiabatic invariants, radial transport, radial diffusion, azimuthal diffusion, cross-terms, electric fields

1 Introduction

The effects of trapped particle spatial transport on radiation belt intensity are usually described by the radial diffusion paradigm. According to this model, in the absence of any other process besides spatial transport, the time evolution of radiation belt intensity is described by a one-dimensional diffusion equation:

$$\frac{\partial f(L^*,t)}{\partial t} = L^{*2}\frac{\partial}{\partial L^*}\left(\frac{D_{LL}}{L^{*2}}\frac{\partial f}{\partial L^*}\right) \quad (1)$$

where f is a distribution function proportional to phase space density, L^* is inversely proportional to the third adiabatic invariant, and $D_{LL} = \left\langle \left(\Delta L^*\right)^2 \right\rangle / 2$ is the radial diffusion coefficient (Roederer, 1970). Since all the quantities involved in Eq. 1 are *drift-averaged*, i.e., averaged over all three gyration, bounce and drift phases, there is no information on trapped particle drift phase—or equivalently, on the magnetic local time (MLT) dimension. In a companion paper (Lejosne and Albert, 2023), we discussed the limitations associated with the inability to resolve the drift phase. We also proposed a theoretical solution to address this difficulty. Namely, we highlighted a two-dimensional drift-diffusion equation to describe trapped particle transport effects on radiation belt intensity (Birmingham et al., 1967). According to this model, in the absence of any other process besides transport, radiation belt intensity varies such that:

$$\frac{\partial F(\mathbb{L},\varphi,t)}{\partial t} = -[\dot{\mathbb{L}}]\frac{\partial F}{\partial \mathbb{L}} - [\dot{\varphi}]\frac{\partial F}{\partial \varphi} + \mathbb{L}^2 \frac{\partial}{\partial \mathbb{L}}\left(\frac{D_{\mathbb{L}\mathbb{L}}}{\mathbb{L}^2}\frac{\partial F}{\partial \mathbb{L}}\right) + \mathbb{L}^2 \frac{\partial}{\partial \mathbb{L}}\left(\frac{D_{\mathbb{L}\varphi}}{\mathbb{L}^2}\frac{\partial F}{\partial \varphi}\right) + \frac{\partial}{\partial \varphi}\left(D_{\varphi\mathbb{L}}\frac{\partial F}{\partial \mathbb{L}}\right) + \frac{\partial}{\partial \varphi}\left(D_{\varphi\varphi}\frac{\partial F}{\partial \varphi}\right) \tag{2}$$

where F is a distribution function proportional to the number of particles per unit of surface, $d\mathbb{L}d\varphi$, φ is the azimuthal location (i.e., MLT, in radians), and the "double-struck L" (or "L-Euler") coordinate is: $\mathbb{L} = 1/\sin^2\theta_E$, with θ_E the magnetic colatitude of the intersection between the Earth's surface and the footpoint of the field line passing through the location considered. The parameters $D_{\mathbb{L}\mathbb{L}}$, $D_{\varphi\varphi}$, $D_{\mathbb{L}\varphi}$ and $D_{\varphi\mathbb{L}}$ are the MLT-dependent diffusion coefficients, and the parameters $[\dot{\mathbb{L}}]$ and $[\dot{\varphi}]$, also MLT-dependent, are the mean time rates of change of $\mathbb{L}$ and φ. All the quantities involved in Eq. 2 are *bounce-averaged* quantities that depend on MLT. In particular, the coordinate double-struck L, $\mathbb{L}$, corresponds to the normalized equatorial radius of the field line on which trapped particles would bounce if all non-dipolar contributions to the magnetic field were turned off on a timescale comparable to a few bounce periods. There are various benefits of using L-Euler as a coordinate for radial transport over L-McIlwain or L-Roederer. From the theoretical standpoint, the set of coordinates $(\mathbb{L},\varphi)$ is proportional to a set of canonical variables, which allows for a reduction of the general two-dimensional Fokker-Planck equation into a drift-diffusion equation (Eq. 2) (Lejosne and Albert, 2023). In addition, computing the L-Euler, $\mathbb{L}$, is much less expensive than computing the L-Roederer, L^*, coordinate: The former only requires local field line tracing, while the latter requires computing the magnetic flux through the instantaneous drift shell. The set of coordinates $(\mathbb{L},\varphi)$ can also be used to parameterize both trapped and quasi-trapped populations (since the definition of L-Euler, $\mathbb{L}$, only requires a closed local field line). On the other hand, the L^* parameter requires a closed instantaneous drift shell, meaning that it can only parameterize trapped populations. Thus, the L-Euler, $\mathbb{L}$, is an appropriate coordinate for modeling the trapping and de-trapping of energetic particles at transition regions (e.g., close to the magnetopause, or at low L regions, below the inner radiation belt).

In the following, we specify the field and particle characteristics assumed to compute the transport and diffusion coefficients introduced in Eq. 2 in a special case. For the sake of simplicity, we focus on the magnetic equator and assume dipolar magnetic field lines thereafter. In this context, $\mathbb{L} = L = r/R_E$, where r is the equatorial radius and $R_E = 6,370\,\text{km}$ is one Earth's equatorial radius.

2 Theoretical setup

The objective of this section is to show how to determine the localized transport ($[\dot{\mathbb{L}}]$ and $[\dot{\varphi}]$) and diffusion ($D_{\mathbb{L}\mathbb{L}}$, $D_{\varphi\varphi}$, $D_{\mathbb{L}\varphi}$ and $D_{\varphi\mathbb{L}}$) coefficients in the simple case of equatorially mirroring particles trapped in a magnetic dipole field with a drift motion perturbed by a special case of random electric potential fluctuations. The characteristics of the fields are provided in Section 2.1, and their effects on the drift motion of trapped particles are detailed in Section 2.2.

2.1 Fields

We assume a magnetic dipole field, **B,** and an electric potential, V, whose random time variations lead to small perturbations of trapped particle drift motion. The dipole field at the magnetic equator in spherical coordinates (r,θ,φ) is:

$$\mathbf{B} = \begin{pmatrix} 0 \\ -\frac{B_E R_E^3}{r^3} \\ 0 \end{pmatrix} \tag{3}$$

where $B_E = 30,000\,\text{nT}$ is the magnetic equatorial field at the Earth's surface. We model the total electric potential, V, as the sum of a well-determined corotation potential, and some *ad hoc* fluctuations proportional to a random variable, w:

$$V = -\frac{C}{r} + w(t) r\cos\varphi \tag{4}$$

where $C = \Omega_E B_E R_E^3$ is a constant, with $\Omega_E = 2\pi/86400\,\text{s} \cong 7.3\,e^{-5}\,\text{s}^{-1}$ the angular velocity of the Earth's rotation, so $-C/r$ is the corotation potential. The electric field, $\mathbf{E} = -\nabla V$, at the magnetic equator is:

$$\mathbf{E} = \begin{pmatrix} -\frac{C}{r^2} - w(t)\cos\varphi \\ 0 \\ w(t)\sin\varphi \end{pmatrix} \tag{5}$$

Characteristics of the electric fluctuation: The electric fluctuation, w(t) (in V/m), is assumed to be not well known. This lack of determination in field variations is what drives the need for a stochastic model, rather than a deterministic one. We view the electric fluctuation, w(t), as a sequence of possible outcomes by a random variable. In this first implementation, we favor practicality over realism to characterize the properties of the variable. Specifically, we assume that the variable, w, is a white noise. We describe it as a piecewise constant function: the value stays constant for a set amount of time, T (in seconds), and it updates instantaneously and unpredictably at the end of every time interval. We choose the size of the time interval, T, such that the time variations of the electric fluctuation, w(t), result in the variation of the third adiabatic invariant, while conserving the first two invariants of the population considered. In other words, we

require that $\tau_B \ll T \ll \tau_D$, where τ_B and τ_D are the bounce and drift periods, respectively. This assumption differs from the drift resonance condition, where $T \sim \tau_D$.

The standard deviation of the white noise, W, is a parameter that we set arbitrarily. The mean value of the white noise, [w], is theoretically 0, by definition. Yet, when considering a finite sequence of values for w(t), the ensemble average is not necessarily 0 in practice. Thereafter, we consider that the average value, [w], remains small enough that: $[w]^2 \ll \Omega T W^2$, where $\Omega/2\pi$ is the unperturbed drift frequency. This assumption is verified in our numerical experiment, and it simplifies mathematical derivations.

2.2 Trapped particles

2.2.1 Computation of the localized transport and diffusion coefficients

The objective of this Section is to determine $D_{\mathbb{L}\mathbb{L}}$, $D_{\varphi\varphi}$, $D_{\mathbb{L}\varphi}$ and $D_{\varphi\mathbb{L}}$, the diffusion coefficients, and $[\dot{\mathbb{L}}]$ and $[\dot{\varphi}]$, the transport coefficients, defined as the mean time rates of change of the radial and azimuthal locations, respectively. This is done for a population of equatorially trapped particles drifting in the fields described in Section 2.1. Generally speaking, a diffusion coefficient for a set of variables, X and Y, is:

$$D_{XY} = \frac{\langle \Delta X \Delta Y \rangle}{2} \tag{6}$$

where $\langle \Delta X \Delta Y \rangle = [\Delta X \Delta Y]/\Delta t$ is the rate of change of the expected value for the product of the time variations of X and Y during a time interval, Δt:

$$[\Delta X \Delta Y] = [(X(t+\Delta t) - X(t))(Y(t+\Delta t) - Y(t))] \tag{7}$$

In our case, the time interval, Δt, is long with respect to the bounce period, but very small in comparison with the drift period, $\tau_B \ll \Delta t \ll \tau_D$. Thus, we need to compute the time variations for the radial and azimuthal locations of the trapped particles, Δr and $\Delta\varphi$, respectively, to determine the diffusion coefficients.

The equations for the drift motion of equatorial particles trapped in the fields described in Section 2.1 are:

$$\begin{pmatrix} \dot{r} \\ 0 \\ \dot{\varphi} \end{pmatrix} = \begin{pmatrix} \frac{r^3}{B_E R_E^3} w(t) \sin\varphi \\ 0 \\ -\frac{3M}{\gamma q r^2} + \Omega_E + \frac{r^2}{B_E R_E^3} w(t) \cos\varphi \end{pmatrix} \tag{8}$$

where M is the first adiabatic invariant, q is the electric charge of the particle and γ is the Lorentz factor. Given that $\dot{\mathbb{L}} = \dot{r}/R_E$ at the magnetic equator of a dipole field, the transport coefficients are:

$$\begin{cases} [\dot{\mathbb{L}}] = \frac{\mathbb{L}^3 [w]}{B_E R_E} \sin\varphi \\ [\dot{\varphi}] = \Omega + \frac{\mathbb{L}^2 [w]}{B_E R_E} \cos\varphi \end{cases} \tag{9}$$

where $\Omega = -3M/\gamma q R_E^2 \mathbb{L}^2 + \Omega_E$ is the unperturbed angular drift velocity. In the presence of an ideal white noise signal ($[w] = 0$) the transport coefficients become $[\dot{\mathbb{L}}] = 0$ and $[\dot{\varphi}] = \Omega$.

Using Eq. 8, the general expressions for the total variations in radial and azimuthal locations after a time interval Δt are, respectively:

$$\begin{cases} \Delta r = \frac{1}{B_E R_E^3} \int_t^{t+\Delta t} r^3(u) w(u) \sin\varphi(u) du \\ \Delta\varphi = -\frac{3M}{q} \int_t^{t+\Delta t} \frac{1}{\gamma(u) r^2(u)} du + \Omega_E \Delta t + \frac{1}{B_E R_E^3} \int_t^{t+\Delta t} r^2(u) w(u) \cos\varphi(u) du \end{cases} \tag{10}$$

We consider a time interval, Δt, very small in comparison with the drift period ($\Delta t \ll \tau_D$), but long enough to have many small fluctuations during Δt ($T \ll \Delta t$). We also assume small radial displacements ($\Delta r/r \ll 1$). As detailed in the **Appendix**, it results that:

$$\begin{cases} \langle (\Delta r)^2 \rangle = \frac{r^6 W^2 T}{B_E^2 R_E^6} \sin^2\varphi \\ \langle (\Delta\varphi)^2 \rangle = \frac{r^4 W^2 T}{B_E^2 R_E^6} \cos^2\varphi \\ \langle \Delta r \Delta\varphi \rangle = \langle \Delta\varphi \Delta r \rangle = \frac{r^5 W^2 T}{B_E^2 R_E^6} \sin\varphi \cos\varphi \end{cases} \tag{11}$$

With the definition provided Eq. 6, the MLT-localized diffusion coefficients are:

$$\begin{cases} D_{\mathbb{L}\mathbb{L}} = \frac{\mathbb{L}^6 W^2 T}{2 B_E^2 R_E^2} \sin^2\varphi \\ D_{\varphi\varphi} = \frac{\mathbb{L}^4 W^2 T}{2 B_E^2 R_E^2} \cos^2\varphi \\ D_{\mathbb{L}\varphi} = D_{\varphi\mathbb{L}} = \frac{\mathbb{L}^5 W^2 T}{2 B_E^2 R_E^2} \sin\varphi \cos\varphi \end{cases} \tag{12}$$

We note that the diffusion coefficients provided in Eq. 12 are functions of magnetic local time, φ. This is in contrast with the standard radial diffusion coefficient, independent of magnetic local time by definition, which involves drift-phase averaging (e.g., Lejosne and Kollmann, 2020). The relationship between these coefficients and the standard radial diffusion framework is further discussed in Section 3.1.

The diffusion coefficients provided in Eq. 12 are also proportional to W^2T, the product of the variance of the random signal, w, and a time, T, that is similar to an autocorrelation time. This finding is consistent with theoretical expectations: the higher the variance, the stronger the perturbation, the higher the diffusion. We also expect electric field perturbations that stay correlated for a longer time interval to be more efficient in perturbing drift motion. On the other hand, the coefficients are independent of the energy of the trapped population considered, provided that the updating time, T, remains very small in comparison with the drift period (see also the discussion in **Appendix**). The coefficients are also independent of the charge of the population. These findings would need to be reassessed in the presence of more realistic field perturbations.

2.2.2 Contextualization using Hamiltonian equations

We expect a relationship between the first and second moments characterizing transport. Indeed, assuming small variations over the course of a couple of bounce periods,we have shown in the first part

of this work (Lejosne and Albert, 2023) that:

$$\begin{cases} -\langle\Delta\alpha\rangle + \frac{1}{2}\frac{\partial\langle(\Delta\alpha)^2\rangle}{\partial\alpha} + \frac{1}{2}\frac{\partial\langle\Delta\alpha\Delta\beta\rangle}{\partial\beta} = -[\dot{\alpha}] \\ -\langle\Delta\beta\rangle + \frac{1}{2}\frac{\partial\langle(\Delta\beta)^2\rangle}{\partial\beta} + \frac{1}{2}\frac{\partial\langle\Delta\beta\Delta\alpha\rangle}{\partial\alpha} = -[\dot{\beta}] \end{cases} \tag{13}$$

where (α,β) are the Euler potentials. In a dipole field at the magnetic equator, given that $\alpha \propto 1/r$, and $\beta = \varphi$, this set of equations is equivalent to:

$$\begin{cases} -\langle\Delta r\rangle + \frac{r^2}{2}\frac{\partial}{\partial r}\left(\frac{\langle(\Delta r)^2\rangle}{r^2}\right) + \frac{1}{2}\frac{\partial}{\partial\varphi}(\langle\Delta r\Delta\varphi\rangle) = -[\dot{r}] \\ -\langle\Delta\varphi\rangle + \frac{1}{2}\frac{\partial\langle(\Delta\varphi)^2\rangle}{\partial\varphi} + \frac{r^2}{2}\frac{\partial}{\partial r}\left(\frac{\langle\Delta\varphi\Delta r\rangle}{r^2}\right) = -[\dot{\varphi}] \end{cases} \tag{14}$$

A second-order Taylor expansion of Eq. 10 yields

$$\begin{cases} \langle\Delta r\rangle = \frac{r^3[\mathrm{w}]}{\mathrm{B_E R_E^3}}\sin\varphi + \frac{\mathrm{r^5 W^2 T}}{\mathrm{B_E^2 R_E^6}}\left(\frac{1}{2} + \sin^2\varphi\right) \\ \langle\Delta\varphi\rangle = \Omega + \frac{r^2[\mathrm{w}]}{\mathrm{B_E R_E^3}}\cos\varphi + \frac{\mathrm{r^4}W^2T}{2\mathrm{B_E^2 R_E^6}}\sin\varphi\cos\varphi \end{cases} \tag{15}$$

Leveraging Eqs 9, 11 and 15, it is straightforward to verify Eq. 14. A notable consequence of this result is that:

$$\langle\Delta r\rangle \neq \frac{r^2}{2}\frac{\partial}{\partial r}\left(\frac{\langle(\Delta r)^2\rangle}{r^2}\right) \tag{16}$$

when the drift phase is resolved. In other words, the commonly assumed relationship between the first and second moments of radial transport, $\langle\Delta r\rangle$ and $\langle(\Delta r)^2\rangle$ (e.g., Fälthammar, 1968, their Eq. 3), is verified only on average over all magnetic local times.

3 On the drift-diffusion equation

3.1 Equivalence with a radial diffusion equation in the case of an azimuthally symmetric distribution function

We leverage the coefficients computed in Section 2.2 to demonstrate that Eq. 2 is like a radial diffusion equation (Eq. 1) when the distribution function is independent of MLT, i.e., when $\partial F/\partial\varphi = 0$. Eq. 2 becomes:

$$\frac{\partial F}{\partial t} = -[\dot{\mathbb{L}}]\frac{\partial F}{\partial\mathbb{L}} + \mathbb{L}^2\frac{\partial}{\partial\mathbb{L}}\left(\frac{D_{\mathbb{L}\mathbb{L}}}{\mathbb{L}^2}\frac{\partial F}{\partial\mathbb{L}}\right) + \frac{\partial}{\partial\varphi}\left(D_{\varphi\mathbb{L}}\right)\frac{\partial F}{\partial\mathbb{L}} \tag{17}$$

when $\partial F/\partial\varphi = 0$. This is also:

$$\frac{\partial F}{\partial t} = -[\dot{\mathbb{L}}]\frac{\partial F}{\partial\mathbb{L}} + D_{\mathbb{L}\mathbb{L}}\frac{\partial^2 F}{\partial\mathbb{L}^2} + \left(\mathbb{L}^2\frac{\partial}{\partial\mathbb{L}}\left(\frac{D_{\mathbb{L}\mathbb{L}}}{\mathbb{L}^2}\right) + \frac{\partial}{\partial\varphi}\left(D_{\varphi\mathbb{L}}\right)\right)\frac{\partial F}{\partial\mathbb{L}} \tag{18}$$

Leveraging Equations 9, 12 yields:

$$\begin{aligned}\frac{\partial F}{\partial t} = &-\frac{\mathbb{L}^3[\mathrm{w}]}{\mathrm{B_E R_E}}\sin\varphi\frac{\partial F}{\partial\mathbb{L}} + \frac{\mathbb{L}^6 W^2 T}{2\mathrm{B_E^2 R_E^2}}\sin^2\varphi\frac{\partial^2 F}{\partial\mathbb{L}^2} \\ &+ \left(\frac{\mathbb{L}^5\mathrm{W^2T}}{2\mathrm{B_E^2 R_E^2}}\left(1 + 2\sin^2\varphi\right)\right)\frac{\partial F}{\partial\mathbb{L}}\end{aligned} \tag{19}$$

Averaging over all MLT-phases, we have that:

$$\frac{\partial F}{\partial t} = \frac{\mathbb{L}^6 W^2 T}{4\mathrm{B_E^2 R_E^2}}\frac{\partial^2 F}{\partial\mathbb{L}^2} + \frac{\mathbb{L}^5\mathrm{W^2T}}{\mathrm{B_E^2 R_E^2}}\frac{\partial F}{\partial\mathbb{L}} \tag{20}$$

Introducing the drift-averaged diffusion coefficient, D_{LL}, as:

$$D_{LL} = \frac{\mathbb{L}^6 W^2 T}{4\mathrm{B_E^2 R_E^2}} \tag{21}$$

Equation 20 also becomes:

$$\frac{\partial F}{\partial t} = L^2\frac{\partial}{\partial L}\left(\frac{D_{LL}}{L^2}\frac{\partial F}{\partial L}\right) \tag{22}$$

We emphasize that $\mathbb{L} = L = r/R_E$ in this demonstration, since we assume a dipole magnetic field. Given that the phase-averaged distribution function, f, is proportional to the bounce-averaged distribution function, F, by a physical constant when F is independent on MLT, Eq. 22 can be rewritten as:

$$\frac{\partial f}{\partial t} = L^2\frac{\partial}{\partial L}\left(\frac{D_{LL}}{L^2}\frac{\partial f}{\partial L}\right) \tag{23}$$

Thus, we have shown how the drift-diffusion Eq. 2 relates to the standard radial diffusion Eq. 1 when the distribution function is phase-mixed (i.e., independent of MLT). We have also shown that the corresponding radial diffusion coefficient, D_{LL}, is the MLT-average of the localized radial diffusion coefficient, $D_{\mathbb{L}\mathbb{L}}$. The expression for D_{LL} provided Eq. 21 is the same as the one that would be obtained by following standard procedures to compute radial diffusion coefficients (e.g., Schulz and Lanzerotti, 1974, their section III.3).

3.2 Change of variables to remove the cross terms

The drift-diffusion equation (Eq. 2) contains cross-terms ($\mathrm{D\mathbb{L}\varphi} = \mathrm{D\varphi\mathbb{L}} \neq 0$), which poses numerical challenges to guarantee positivity of the solution (Tao et al., 2008; 2009; 2016). Albert and Young (2005) and Albert (2018) discussed changes of coordinates to address this difficulty. In the present situation, the determinant of the 2×2 diffusion matrix is 0:

$$D_{\mathbb{L}\mathbb{L}}D_{\varphi\varphi} - D_{\mathbb{L}\varphi}^2 = 0 \tag{24}$$

This means that 0 is an eigenvalue of the diffusion matrix, and there exists a system of coordinates in which the diffusive part of the drift-diffusion equation is one-dimensional. We introduce a new set of variables:

$$\begin{cases} x = \mathbb{L}\cos\varphi \\ y = \mathbb{L}\sin\varphi \end{cases} \tag{25}$$

which corresponds to a conversion from polar to Cartesian coordinates. In this coordinate system, with the values of the diffusion coefficients provided Eq. 12, Eq. 2 becomes:

$$\frac{\partial F}{\partial t} = -[\dot{x}]\frac{\partial F}{\partial x} - [\dot{y}]\frac{\partial F}{\partial y} + \left(x^2 + y^2\right)^{\frac{3}{2}}\frac{\partial}{\partial y}\left(\frac{D_{yy}}{\left(x^2 + y^2\right)^{\frac{3}{2}}}\frac{\partial F}{\partial y}\right) \tag{26}$$

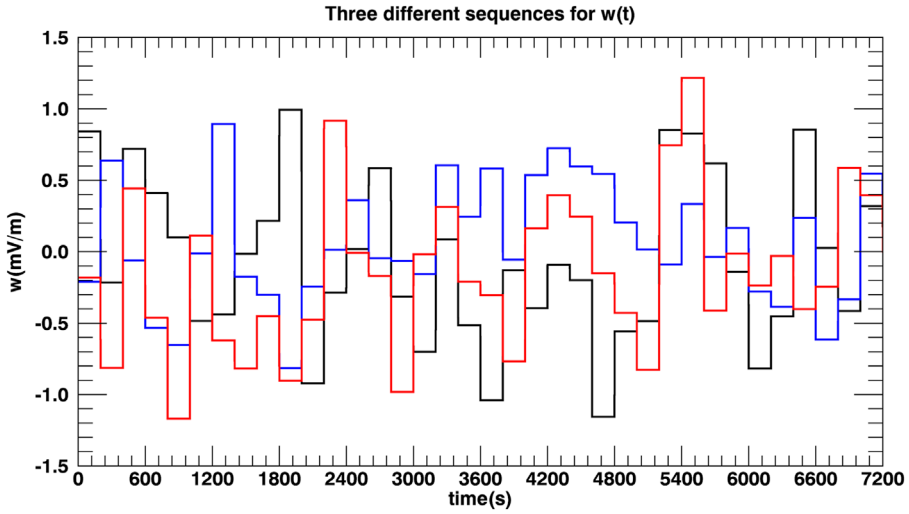

FIGURE 1
Three different sequences of randomly generated outcomes for the white noise signal, *w* (t), are represented in black, blue and red over a 2-h time interval. The signal is updated every T = 200 s. The expected (i.e., average) value is 0 mV/m, and the standard deviation is set to 0.5 *mV/m*.

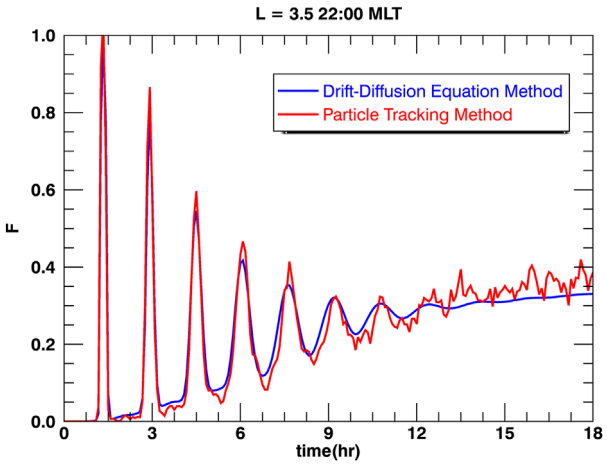

FIGURE 2
Time evolution of the distribution function centered at L = 3.5 and 22:00 MLT. The magnitude of the flux oscillation characteristic of trapped particle injections decreases with time until it vanishes after a time characteristic of phase mixing. This figure compares numerical results from (in red) a test particle simulation and (in blue) the solution of the drift-diffusion equation. It illustrates the transition from a drift-dominated regime (with the presence of drift periodic oscillations in the distribution function) to a diffusion-dominated regime (characterized by a slow and steady variation of the distribution function).

with

$$D_{yy} = \frac{W^2 T}{2B_E^2 R_E^2}(x^2 + y^2)^3 \tag{27}$$

Looking back at the drift motion equations (Eq. 8), we notice that the perturbation of the drift velocity is indeed along the *y*-direction: The velocity perturbation is along $\sin\varphi \boldsymbol{e_r} + \cos\varphi \boldsymbol{e_\varphi} = \boldsymbol{e_y}$, where $\boldsymbol{e_y}$ and $\boldsymbol{e_r}, \boldsymbol{e_\varphi}$ are unit vectors associated with the Cartesian and polar frames of reference.

In the following, we assume [w] = 0 for the sake of simplicity. This means that $[\dot{\mathbb{L}}] = 0$ and $[\dot{\varphi}] = \Omega$. As a result, Eq. 26 is also:

$$\frac{\partial F}{\partial t} = -\Omega \frac{\partial F}{\partial \varphi} + \mathbb{L}^3 \frac{\partial}{\partial y}\left(\frac{D_{yy}}{\mathbb{L}^3}\frac{\partial F}{\partial y}\right) \tag{28}$$

This latest equation is the one used for numerical implementation, as discussed in Section 4.

4 Numerical simulations

4.1 Numerical setups and methods

Parameters: Since this work assumes electric potential fluctuations in a time-stationary dipole field, we focus on a region where this is most likely to happen, namely, the inner belt and slot region (below L = 4). We consider populations that have been associated with drift period structures in this region, i.e., electrons in the tens to hundreds of keV energy range (e.g., Ukhorskiy et al., 2014). Specifically, we focus on equatorial electrons with kinetic energy of 200 keV at $L = 3$. These electrons have a first adiabatic invariant of M = 21.5 MeV/G, and a second adiabatic invariant of $J = 0$. The standard deviation of the white noise, W, is a parameter that we set to a plausible value of about 0.5 mV/m ($W^2 = 2.5 \times 10^{-7} V^2/m^2$). We set the updating time (i.e., the duration between changes in value) for the sequence of outcomes w(t) to be $T = 200s$. At L = 3, the bounce and drift periods of the electrons considered are $\tau_B \sim 0.4s$ and $\tau_D \sim 1.5hr$, so the ordering, $\tau_B \ll T \ll \tau_D$, is verified. With this set of parameters, the coefficient of proportionality for the diffusion coefficients is $W^2 T/2B_E^2 R_E^2 = 6.8 \times 10^{-10} s^{-1} = 5.9 \times 10^{-5} day^{-1}$. Therefore, given Eq. 21, the drift-averaged diffusion coefficient D_{LL} is set to $D_{LL} \sim 3.0 \times 10^{-5} L^6 day^{-1}$ ($2.2 \times 10^{-2} day^{-1}$ at L =

3 for instance). This order of magnitude is consistent with previous estimates for radial diffusion in the inner belt and slot region (e.g., Selesnick, 2012; O'Brien et al., 2016, their Figure 4).

Method for particle tracking: We solve Eq. 8 to determine trapped particle drift motion. We launch particles in many different sequences of outcomes for w (t). We use the RANDOMN function from IDL, which returns pseudorandom numbers from a Gaussian distribution to generate an original time sequence of outcomes. Every different sequence is created by randomly reordering (permuting) the vector indices of the original sequence of outcomes. To create a permutation of the vector indices, we use the RANDOMU function from IDL, which returns an array of uniformly distributed random numbers. An illustration of the approach is provided in Figure 1. It represents three different permutations for the sequence of outcomes for w(t), over a time intervals of 2 h. For the numerical experiment, we perform 200 different permutations. We track more than 10,000 particle drift trajectories for 18 h every time, recording their locations every 5 min. The particle initial locations are distributed homogeneously, following the initial condition described hereafter.

Initial condition: To solve numerically Eq. 28, we consider a simple initial condition, assuming that:

- Particles are present homogeneously at all MLTs at $3.8\,R_E$ and above (up to 7 R_E).
- Particles are also present homogeneously in an area mimicking a localized injection, extending from $r = 2.5\,R_E$ to $r = 3.8\,R_E$, and initially centered around 00:00 MLT (from 22:15 to 01:45).

The distribution function, F, is chosen to be initially constant and normalized (= 1) at all locations where particles are present. It is set to zero otherwise.

Method for numerical simulation: To solve numerically Eq. 28, we use an operator splitting method. At each time step, we first solve the transport part of the equation, using the method of characteristics. We then use the updated function to solve the diffusive part of the equation, using an explicit scheme for the sake of simplicity. We record the value of the distribution function, F, every 5 min over a 24-h interval.

4.2 Results

4.2.1 Comparison between the results of the test particle experiments and the solution of the drift-diffusion equation

We compare: a) the outputs of the particle tracking experiment with b) the solution of Eq. 28. First, we focus on one location (L = 3.5 ± 0.05 and 22:00 MLT ± 00:15): We record the time evolution of the distribution functions derived from the drift-diffusion equation and from the particle tracking experiment. The results, presented in Figure 2**,** highlight the consistency of the two approaches. The location is initially out of the artificial injection region thus $F(t = 0) = 0$. As the particles drift eastwards starting from the midnight region, no particles are visible for a moment. Then, they briefly drift through the location, creating a transient peak in the distribution function, and so on. Figure 2 shows how the distribution function oscillates at the trapped particles'

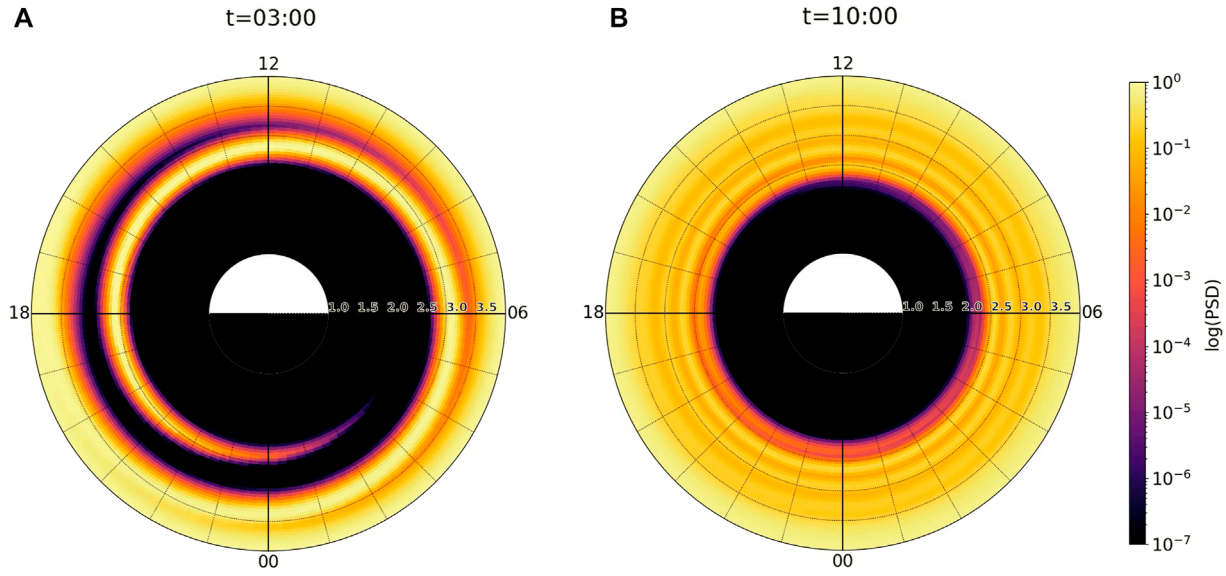

FIGURE 3
Time evolution of a distribution function (initially centered around 00:00 MLT for $2.5\,R_E < r < 3.8\,R_E$, and constant at all MLTs for $r \geq 3.8\,R_E$) **(A)** At t = 3:00 h, the MLT-dependent structure is visible. It creates a spiral around the Earth due to the L-dependence of the drift frequency. As a result, the distribution function is strongly dependent on MLT for r between ~ $2.5\,R_E$ and $3.8\,R_E$ **(B)** At t = 10:00 h, the MLT-dependent structure has disappeared: The distribution function is barely dependent on MLT. The effect of transport on radiation belt intensity is now more consistent with the radial diffusion paradigm.

unperturbed drift frequency. With time, the magnitude of the peak decreases, and the width of the peak increases: This is due to the combined effects of radial and azimuthal diffusions. In parallel, new particles transported radially from L ≥ 3.8 fill the region: The drift-averaged minimum of the distribution function increases with time. After some time, the drift-periodic signature disappears and the regime is purely diffusive. In other words: In this numerical experiment, the radial diffusion equation represents a valid description of the system after ~15 h at L = 3.5 (or about 9 drift periods for the population considered). For shorter times, it is necessary to use the drift-diffusion equation to represent the time evolution of drift echoes. In general, we expect the magnitude of the typical phase-mixing time scale to be a function of: (a) the initial condition for the distribution function (the more MLT-localized the inhomogeneity, the longer it will take to cover all MLT sectors), (b) the magnitude of the diffusion coefficients (the higher the coefficient, the most efficient at smoothing MLT-dependent fluctuations, thus the shorter the characteristic time for phase mixing) and (c) the drift frequency (the higher the drift frequency, the shorter the characteristic time for phase mixing).

4.2.2 Visualization of the solution of the drift-diffusion equation

A 2D video of the simulation run for the solution of the drift-diffusion equation over a 24 h interval is provided in Supplementary Material. Two screenshots (at t = 3:00 h and t = 10:00 h) are provided in Figure 3.

From the video, it is clear that the effect of the azimuthal drift on radiation belt intensity is at first more striking than the effects of radial and azimuthal diffusion. That said, drift alone would only lead to trajectories wrapping around, meaning that the distribution function would only become more structured. Radial and azimuthal diffusions act to smooth out the MLT-dependent structure, dampening it until it disappears and the distribution becomes independent of MLT. This *phase-mixing* process is consistent with observations. It allows for the transition from a drift-dominated regime to a diffusion-dominated regime.

5 Conclusion

We have shown how the drift-diffusion equation is capable of modeling phase mixing, allowing for a transition from drift-resolved structures (e.g., drift-periodic fluctuations associated with MLT-localized sources or losses) to the standard radial diffusion framework. We illustrated our case using simple assumptions, focusing on the magnetic equator of a dipole field and modeling electric potential fluctuations by a white noise. A next step of physical importance is to model the effect of the thermospheric wind driven electric field fluctuations on radiation belt dynamics. Indeed, electric potential fluctuations are present in the inner belt. They are viewed as the primary driver of radial diffusion in this region (e.g., O'Brien et al., 2016). In particular, electric fluctuations associated with quiet time wind dynamo have significant day-to-day variability, even during geomagnetically quiet periods (e.g., Fejer, 1993). Thermospheric wind driven electric fields are also known to shape the inner belt drift shells (Lejosne et al., 2021). Future work should consist of determining a more realistic form for the electric perturbation using information on thermospheric wind driven electric field fluctuations. Going back to the general expression of the drift-diffusion equation, future work should also consist of determining the various transport and diffusion coefficients in the presence of a time varying magnetic field. Once realistic inputs, including localized transport and diffusion coefficients, are determined, the drift-diffusion equation will enable operational radiation belt modeling with a better spatiotemporal resolution than current radial diffusion models.

Data availability statement

The raw data supporting the conclusion of this article will be made available by the authors, without undue reservation.

Author contributions

We describe contributions to the paper using the CRediT (Contributor Roles Taxonomy) categories (Brand et al., 2015). Conceptualization, Writing—Original Draft: SL and JA Writing—Review and Editing: All authors. Visualization: SL and SW. All authors contributed to the article and approved the submitted version.

Funding

SL work was performed under NASA Grant Awards 80NSSC18K1223 and 80NSSC20K1351. SW work was performed under NASA Grant Award 80NSSC20K1351. JA was supported by NASA grant 80NSSC20K1270, AFOSR grant 22RVCOR002, and the Space Vehicles Directorate of the Air Force Research Laboratory.

Conflict of interest

The authors declare that the research was conducted in the absence of any commercial or financial relationships that could be construed as a potential conflict of interest.

Publisher's note

Author disclaimer

The views expressed are those of the authors and do not reflect the official guidance or position of the United States Government, the Department of Defense or of the United States Air Force. The appearance of external hyperlinks does not constitute endorsement by the United States Department of Defense (DoD) of the linked websites, or the information, products, or services contained therein. The DoD does not exercise any editorial, security, or other control over the information you may find at these locations.

Supplementary material

The Supplementary Material for this article can be found online at: https://www.frontiersin.org/articles/10.3389/fspas.2023.1232512/abstract#supplementary-material

References

Albert, J. M. (2018). Diagonalization of diffusion equations in two and three dimensions. *J. Atmos. Solar-Terrestrial Phys.* 177, 202–207. doi:10.1016/j.jastp.2017.08.008

Albert, J. M., and Young, S. L. (2005). Multidimensional quasi-linear diffusion of radiation belt electrons. *Geophys. Res. Lett.* 32, L14110. doi:10.1029/2005GL023191

Birmingham, T. J., Northrop, T. G., Fälthammar, (1967). Charged particle diffusion by violation of the third adiabatic invariant. *Phys. Fluids* 10, 2389. Number 11. doi:10.1063/1.1762048

Brand, A., Allen, L., Altman, M., Hlava, M., and Scott, J. (2015). Beyond authorship: Attribution, contribution, collaboration, and credit. *Learn. Pub.* 28, 151–155. doi:10.1087/20150211

Fälthammar, C.-G. (1968), Radial diffusion by violation of the third adiabatic invariant, in *Earth's particles and fields*. B. M. McCormac (New York: Reinhold), 157

Fejer, B. G. (1993). F region plasma drifts over Arecibo: Solar cycle, seasonal, and magnetic activity effects. *J. Geophys. Res.* 98 (8), 13645–13652. doi:10.1029/93JA-00953

Lejosne, S., Fedrizzi, M., Maruyama, N., and Selesnick, R. S. (2021). Thermospheric neutral winds as the cause of drift shell distortion in Earth's inner radiation belt. *Front. Astron. Space Sci.* 8, 725800. doi:10.3389/fspas.2021.725800

Lejosne, S., and Albert, J. M. (2023). Drift phase resolved diffusive radiation belt model: 1. Theoretical framework. *Front. Astron. Space Sci.* 10, 1200485. doi:10.3389/fspas.2023.1200485

Lejosne, S., and Kollmann, P. (2020). Radiation belt radial diffusion at Earth and beyond. *Space Sci. Rev.* 216, 19. doi:10.1007/s11214-020-0642-6

O'Brien, T. P., Claudepierre, S. G., Guild, T. B., Fennell, J. F., Turner, D. L., Blake, J. B., et al. (2016). Inner zone and slot electron radial diffusion revisited. *Geophys. Res. Lett.* 43, 7301–7310. doi:10.1002/2016GL069749

Roederer, J. G. (1970). *Dynamics of geomagnetically trapped radiation*. Heidelberg: Springer Berlin. doi:10.1007/978-3-642-49300-3

Schulz, M., and Lanzerotti, L. J. (1974). *Particle diffusion in the radiation belts*. Berlin: Springer. doi:10.1007/978-3-642-65675-0

Selesnick, R. S. (2012). Atmospheric scattering and decay of inner radiation belt electrons. *J. Geophys. Res.* 117, A08218. doi:10.1029/2012JA017793

Tao, X., Albert, J. M., and Chan, A. A. (2009). Numerical modeling of multidimensional diffusion in the radiation belts using layer methods. *J. Geophys. Res.* 114, A02215. doi:10.1029/2008JA013826

Tao, X., Chan, A. A., Albert, J. M., and Miller, J. A. (2008). Stochastic modeling of multidimensional diffusion in the radiation belts. *J. Geophys. Res.* 113, A07212. doi:10.1029/2007JA012985

Tao, X., Zhang, L., Wang, C., Li, X., Albert, J. M., and Chan, A. A. (2016). An efficient and positivity-preserving layer method for modeling radiation belt diffusion processes. *J. Geophys. Res. Space Phys.* 121, 305–320. doi:10.1002/2015JA022064

Ukhorskiy, A., Sitnov, M., Mitchell, D., Takahashi, K., Lanzerotti, L. J., and Mauk, B. H. (2014). Rotationally driven 'zebra stripes' in Earth's inner radiation belt. *Nature* 507, 338–340. doi:10.1038/nature13046

Whipple, E. C. (1978). U, B, K) coordinates: A natural system for studying magnetospheric convection. *J. Geophys. Res.* 83 (A9), 4318–4326. doi:10.1029/JA083iA09p04318

Appendix

We explain how we derived the expressions for $\langle(\Delta r)^2\rangle$, $\langle(\Delta\varphi)^2\rangle$, and $\langle\Delta r\Delta\varphi\rangle$ (Eq. 11), in order to obtain the diffusion coefficients required to solve the drift-diffusion equation.
A first-order Taylor expansion for the expressions of the total variations in radial and azimuthal locations (Eq. 10) yields:

$$\begin{cases} \Delta r = \dfrac{r_o^3}{B_E R_E^3}\displaystyle\int_t^{t+\Delta t} w(u)\sin(\varphi_o+\Omega u)du \\ \Delta\varphi = \Omega\Delta t \\ \quad +\dfrac{3M}{\gamma_o q B_E R_E^3}\left(2-\dfrac{3MB_E R_E^3}{\gamma_o^2 E_o r_o^3}\right)\displaystyle\int_t^{t+\Delta t}\int_t^u w(x)\sin(\varphi_o+\Omega x)dxdu \\ \quad +\dfrac{r_o^2}{B_E R_E^3}\displaystyle\int_t^{t+\Delta t} w(u)\cos(\varphi_o+\Omega u)du \end{cases} \tag{A1}$$

where r_o, φ_o, γ_o are the values for the radial and azimuthal locations, and Lorentz factor, at time, t, respectively.
The expression for the ensemble average of the square of the total variation of the radial displacement is:

$$[(\Delta r)^2] = \frac{r_o^6}{B_E^2 R_E^6}\int_t^{t+\Delta t}\int_t^{t+\Delta t}[w(u)w(v)]\sin(\varphi_o+\Omega u)\sin(\varphi_o+\Omega v)dudv \tag{A2}$$

Since $\Omega\Delta t \ll 1$, the variation in phase is not significant, and Eq. A2 becomes

$$[(\Delta r)^2] = \frac{r_o^6\sin^2(\varphi_o)}{B_E^2 R_E^6}\int_t^{t+\Delta t}\int_t^{t+\Delta t}[w(u)w(v)]dudv \tag{A3}$$

Since the signal w is a piecewise constant function, we have that:

$$w(u) = w_i \text{ for } iT \le u < (i+1)T \tag{A4}$$

And by definition of the white noise sequence, $[w_i w_j] = W^2\delta_{ij}$, where δ_{ij} is the Kronecker delta. As a result, expressing the time interval, Δt, as $\Delta t = NT + k$, where N is an integer, and $0 < k < T$:

$$[(\Delta r)^2] = \frac{r_o^6 W^2\sin^2(\varphi_o)}{B_E^2 R_E^6}(NT^2+k^2) \cong \frac{r_o^6 W^2 T\sin^2(\varphi_o)}{B_E^2 R_E^6}\Delta t \tag{A5}$$

As a result:

$$\langle(\Delta r)^2\rangle = \frac{[(\Delta r)^2]}{\Delta t} = \frac{r_o^6 W^2 T}{B_E^2 R_E^6}\sin^2(\varphi_o) \tag{A6}$$

A similar approach allows for a computation of $[(\Delta\varphi)^2]$, and $[(\Delta r\Delta\varphi)^2]$ as first order functions of Δt, yielding analytical expressions for $\langle(\Delta\varphi)^2\rangle$, and $\langle\Delta r\Delta\varphi\rangle$. Alternatively, the total variation in phase, $\Delta\varphi$, can also be related the total variation in radial displacement, Δr, and the time variation, Δt, by considering a multivariate Taylor expansion for the expression of total energy conservation (e.g., Whipple, 1978):

$$\begin{aligned} &E_k(r_o+\Delta r, \varphi_o+\Delta\varphi, t+\Delta t) + qV(r_o+\Delta r, \varphi_o+\Delta\varphi, t+\Delta t) \\ &\quad = E_k(r_o,\varphi_o,t) + qV(r_o,\varphi_o,t) \end{aligned} \tag{A7}$$

where $E_k = E_o\left(\sqrt{1+2MB/E_o}-1\right)$ is the kinetic energy, with E_o the rest mass energy.
The formula provided Eq. A6 is not dependent on the energy of the particles considered, provided that the drift period is very long in comparison with the updating time, T. If we were to consider particles of higher energies, with a drift period smaller than the updating time, T, the magnitude of the radial diffusion coefficient would drop, in accordance with theoretical expectations. Indeed, with $\Delta t = k < T$, $N = 0$, and $[(\Delta r)^2]$ Eq. (A5) would become proportional to $W^2\Delta t^2 (< W^2 T\Delta t)$. In parallel, the ensemble average of the signal, $[w]$, would not be 0 anymore during Δt: this means that the effects of field fluctuations would be accounted for through the transport coefficients, $[\dot{\mathbb{L}}]$ and $[\dot{\varphi}]$ (Eq. 9).

Glossary

(α,β)	Euler potentials
$\boldsymbol{B}$	Magnetic field
B_E	Magnetic equatorial field at the Earth's surface
C	constant to model the corotation potential
D_{XY}	Diffusion coefficient with respect to the X and Y coordinates
$\boldsymbol{E}$	electric field
f,F	Distribution functions
γ	Lorentz factor
J	second adiabatic invariant
L^*	L-star, inversely proportional to the third adiabatic invariant
$\mathbb{L}$	double-struck L, or L-Euler
L	normalized equatorial radial distance
M	first adiabatic invariant
Ω_E	angular velocity of the Earth's rotation
$\Omega/2\pi$	unperturbed drift frequency
q	electric charge of a particle
r	radial location at the magnetic equator
R_E	Earth's equatorial radius
φ	Azimuthal location (i.e., magnetic local time, in radians)
τ_B	Bounce period
τ_D	Drift period
$t,\Delta t$	Time, small time interval
T	updating time for the sequence of outcomes w(t)
V	Electric potential
w	random variable
W	standard deviation of the random variable w
[ ]	Square brackets = expected value (average value over an ensemble of fluctuations) of the bracketed quantity
< >	Angle brackets = average change per unit time of the bracketed quantity ($= \frac{[]}{\Delta t}$)
∝	Proportionality symbol

frontiers | Frontiers in Astronomy and Space Sciences

TYPE Original Research
PUBLISHED 23 August 2023
DOI 10.3389/fspas.2023.1231578

OPEN ACCESS

EDITED BY
Xiao-Jia Zhang,
The University of Texas at Dallas,
United States

REVIEWED BY
Chao Yue,
Peking University, China
Alexander Lukin,
The University of Texas at Dallas,
United States

*CORRESPONDENCE
Sheng Huang,
hs2015@bu.edu
Wen Li,
wenli77@bu.edu

RECEIVED 30 May 2023
ACCEPTED 09 August 2023
PUBLISHED 23 August 2023

CITATION
Huang S, Li W, Ma Q, Shen X-C, Capannolo L, Hanzelka M, Chu X, Ma D, Bortnik J and Wing S (2023), Deep learning model of hiss waves in the plasmasphere and plumes and their effects on radiation belt electrons. *Front. Astron. Space Sci.* 10:1231578. doi: 10.3389/fspas.2023.1231578

Deep learning model of hiss waves in the plasmasphere and plumes and their effects on radiation belt electrons

Sheng Huang[1]*, Wen Li[1]*, Qianli Ma[1,2], Xiao-Chen Shen[1], Luisa Capannolo[1], Miroslav Hanzelka[1,3], Xiangning Chu[4], Donglai Ma[2], Jacob Bortnik[2] and Simon Wing[5]

[1]Center for Space Physics, Boston University, Boston, MA, United States, [2]Department of Atmospheric and Oceanic Sciences, University of California, Los Angeles, CA, United States, [3]Department of Space Physics, Institute of Atmospheric Physics of the Czech Academy of Sciences, Prague, Czechia, [4]Laboratory for Atmospheric and Space Physics, University of Colorado Boulder, Boulder, CO, United States, [5]Applied Physics Laboratory, The Johns Hopkins University, Laurel, MD, United States

Hiss waves play an important role in removing energetic electrons from Earth's radiation belts by precipitating them into the upper atmosphere. Compared to plasmaspheric hiss that has been studied extensively, the evolution and effects of plume hiss are less understood due to the challenge of obtaining their global observations at high cadence. In this study, we use a neural network approach to model the global evolution of both the total electron density and the hiss wave amplitudes in the plasmasphere and plume. After describing the model development, we apply the model to a storm event that occurred on 14 May 2019 and find that the hiss wave amplitude first increased at dawn and then shifted towards dusk, where it was further excited within a narrow region of high density, namely, a plasmaspheric plume. During the recovery phase of the storm, the plume rotated and wrapped around Earth, while the hiss wave amplitude decayed quickly over the nightside. Moreover, we simulated the overall energetic electron evolution during this storm event, and the simulated flux decay rate agrees well with the observations. By separating the modeled plasmaspheric and plume hiss waves, we quantified the effect of plume hiss on energetic electron dynamics. Our simulation demonstrates that, under relatively quiet geomagnetic conditions, the region with plume hiss can vary from L = 4 to 6 and can account for up to an 80% decrease in electron fluxes at hundreds of keV at L > 4 over 3 days. This study highlights the importance of including the dynamic hiss distribution in future simulations of radiation belt electron dynamics.

KEYWORDS

total electron density, hiss, plasmasphere, plume, deep learning, radiation belt electrons, fokker planck simulation

1 Introduction

Hiss waves are a type of whistler mode, broadband emission that typically exists in the Earth's high density plasmasphere and plume regions (Thorne et al., 1973; Chan and Holzer, 1976; Larkina and Likhter, 1982; Hayakawa et al., 1986; Meredith, 2004; Ripoll et al., 2020). Since their early discovery (Dunckel and Helliwell, 1969; Russell et al., 1969), hiss waves have

been extensively studied, and many of their properties have been revealed (Hayakawa and Sazhin, 1992; Li et al., 2015a; Tsurutani et al., 2015).

Through cyclotron resonant interactions, hiss can pitch-angle scatter electrons with energies ranging from tens of keV up to several MeV (Horne and Thorne, 1998; Li et al., 2007; Ni et al., 2014; Ma et al., 2016). They are responsible for creating the slot region between the inner and outer radiation belts and are believed to be the main driver of the outer belt electron decay during quiet times (Lam et al., 2007; Ma et al., 2015), thus playing an important role in controlling the structure and dynamics of the radiation belts.

Hiss waves are believed to have multiple generation mechanisms, which are still under active research (e.g., Green, 2005; Bortnik J. et al., 2009; Liu et al., 2020). Lightning-generated whistlers from low altitudes can propagate and evolve into hiss (Sonwalkar and Inan, 1989; Bortnik et al., 2003), but they account for only a portion of the wave power at frequencies >2 kHz at L < 3.5 (Meredith et al., 2006). In recent years, more and more observations and ray-tracing simulations have linked hiss waves with chorus waves propagating into the plasmasphere (Church and Thorne, 1983; Santolík et al., 2006; Bortnik et al., 2008; Chen et al., 2012a; 2012b). This correlation is supported by statistical analyses of wave distribution (Meredith et al., 2013; Agapitov et al., 2018) as well as direct observations through event analyses (Bortnik Jacob et al., 2009; Li et al., 2015b). In addition to lightning-generated whistlers and chorus waves propagating into the plasmasphere, electron cyclotron instability can also be a possible energy source for hiss by locally amplifying it to observable levels (Kennel and Petschek, 1966; Thorne et al., 1979). Although the wave growth rate is generally weak (Church and Thorne, 1983; C. Y; Huang et al., 1983), recent studies have shown that the high-frequency hiss waves may be locally generated (Fu et al., 2021; Meredith et al., 2021). In addition, the sharp density gradient near the plasmapause and a fresh injection of anisotropic hot electrons drifting from the nightside plasma sheet can aid in generating intense low-frequency hiss, particularly favored when plasmaspheric plumes are present (Li et al., 2013; Chen et al., 2014; Su et al., 2018; Wu et al., 2022). Plume hiss is thus gaining more and more attention due to its potential role in controlling radiation belt dynamics (Summers et al., 2008). In the era of Van Allen Probes, hiss is found to be prevalent inside plumes (Shi et al., 2019; Zhang et al., 2019), and both observations and simulations recognize its importance in precipitating electrons in the outer radiation belt (Li et al., 2019; Ma et al., 2021; Millan et al., 2021; Qin et al., 2021). However, the observation of plume hiss is highly limited during individual events due to a lack of global coverage, and simulations are usually performed based on the statistical properties of plume hiss. Therefore, the spatiotemporal evolution of plume hiss and its effects on energetic electron dynamics remain elusive, though they are believed to critically affect the loss rate of energetic electrons in radiation belts.

In this study, we propose a deep learning approach to model the global evolution of hiss and total electron density, inspired by Bortnik et al. (Bortnik et al., 2016; Bortnik et al., 2018). Deep learning techniques have shown promising results in space weather modeling by analyzing information from large datasets (Chu et al., 2017a, b; 2021; Ma et al., 2022; Wing et al., 2005; 2022). We present the methodology for our model in Section 2. In Section 3, we analyze the model performance and apply it to a geomagnetic storm event where the complete evolution of plume hiss is predicted. Then, we simulate the energetic electron evolution based on the modeled hiss and total electron density, and quantify the effects of plume hiss. In Section 4, we discuss our findings, followed by our conclusions in Section 5.

2 Data and deep learning model

2.1 Van Allen Probes data

We train the model using observations from the twin Van Allen Probes (also known as RBSP; Mauk et al., 2013) throughout the majority of their operational time (2013–2019). The Electric and Magnetic Field Instrument Suite and Integrated Science (Kletzing et al., 2013) suite onboard RBSP provides *in-situ* measurements of the field and waves with a time resolution of −6 s for the survey mode. Total electron density (N_e) is inferred from the upper hybrid resonance frequency (Kurth et al., 2015) based on the measurements from the High Frequency Receiver (HFR). The WaveForm Receiver (WFR) measures wave activity, which we use to calculate the amplitude of hiss waves following Li et al. (2015a) summarized as follows.

1) wave ellipticity >0.7;
2) wave planarity >0.2;
3) spectral frequency range over 20–4,000 Hz.

When the satellites are outside the plasmasphere or plume (according to the wave power of electron cyclotron harmonic waves; Shen et al., 2019), the wave amplitude is set to 0.2 pT to indicate no hiss wave. The whole hiss wave dataset has a similar trend to the statistics by Li et al. (2015a) that hiss wave tends to occur on the dayside during enhanced levels of substorm activity (not shown here). The satellite location is also used for training purposes, including L shell, magnetic local time (MLT), and magnetic latitude (MLAT). The MLT is converted into sin (MLT/12*π) and cos (MLT/12*π) to account for the discontinuity at MLT = 24. Additionally, the spin-averaged electron fluxes measured by the Magnetic Electron Ion Spectrometer (MagEIS) instrument (Blake et al., 2013) in the Energetic Particle Composition and Thermal Plasma (ECT) suite (Spence et al., 2013) are used to compare with the results of radiation belt simulations using our density and wave models.

2.2 Geomagnetic indices

To model both the electron density and wave amplitude at a specific location observed by satellites, we use the geomagnetic indices SML, SMU, Hp30, and SYM-H, which measure the level of geomagnetic disturbance at different latitudes. The SML and SMU indices (Gjerloev, 2012; Newell and Gjerloev, 2011; from SuperMAG Web Service) provide better time coverage (to include recent year data) compared to the more commonly used AL and AU indices. The Hp30 index (Matzka et al., 2021; from GFZ German Research Centre for Geosciences) is designed to improve the temporal resolution of Kp index from 3 h to 30 min. To capture

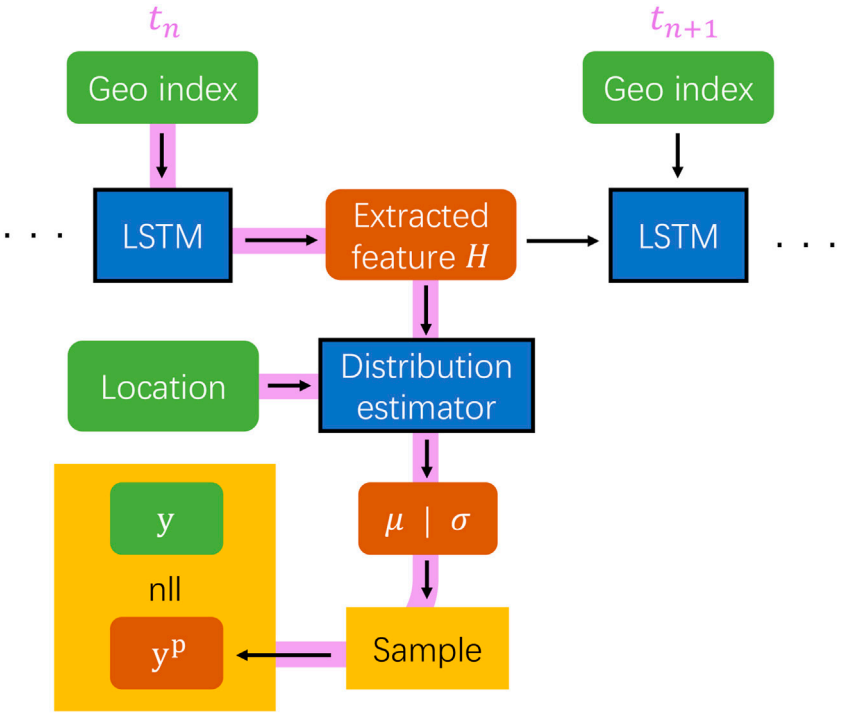

FIGURE 1
Model structure and workflow. Purple line: data flow at time t_n; Green box: model input; Blue box: neural network model modules; Red box: (intermediate) model output; Yellow box: data operation. After the hidden state H is encoded by LSTM from the geomagnetic indices, a probability distribution is estimated at the satellite location, and a prediction y^p is sampled from this distribution. The negative log likelihood (nll) is calculated between the prediction y^p and satellite observation y, and is further used to update the model parameters through backpropagation. y denotes either total electron density or hiss wave amplitude.

the most variation in the data without introducing many artifacts from interpolation, all satellite observations and geomagnetic indices are interpolated to a time resolution of 1 min.

2.3 Deep learning model

We adopt a similar model structure to that of Huang et al. (2022), as illustrated in Figure 1. In this framework, geomagnetic indices are used as the inputs to a neural network module, known as Long Short-Term Memory (Hochreiter and Schmidhuber, 1997). LSTM is well-suited for modeling data sequences in time-series format and can effectively capture the temporal evolution within the data (Karim et al., 2018; Siami-Namini et al., 2019). The extracted output feature H at time t_n can be viewed as a representation of the inner magnetospheric state at time t_n , described solely based on the geomagnetic indices. Subsequently, H is used to fit the satellite observations (both total electron density and hiss wave amplitude), with corresponding satellite location as an input (see Section 2.4). By employing LSTM to process geomagnetic indices alone (without any RBSP data), the temporal evolution is decoupled from the location information, which enables our model to simultaneously learn the complex spatial dependence and the smooth transition along the satellite orbital observations over time.

As hiss wave amplitude varies significantly in different regions, models tend to estimate the average activity while treating the variation as noise, thus underestimating the wave activity (trained with the same model structure as Huang et al. (2022) on hiss wave; not shown here). To better capture the dynamic nature of hiss wave activity, instead of directly predicting a quantity in a deterministic approach, we use a neural network module that estimates the wave probability distribution (modeling both the mean μ and standard deviation σ) at a specific location and time. This approach essentially introduces an estimation of the uncertainty (Blundell et al., 2015) in the data and is critical to model quantities with large variations (Tasistro-Hart et al., 2021). We avoid applying significant smoothing to the RBSP data to retain the full information carried in the variation. We sample a prediction y^p from the modeled mean and standard deviation and calculate the negative log likelihood

$$nll = \sum_i \left(\log\sqrt{2\pi\sigma^2} + \frac{(y_i - \mu)^2}{2\sigma^2} \right)$$

between the observation and model prediction. This process essentially maximizes the possibility of measuring the observed quantity given the estimated distribution. The calculated loss is then used to update the model parameters through the standard backpropagation procedure.

To address the issue of an unbalanced dataset in training the hiss wave model, we have implemented a weighted sampler. While we dedicate considerable attention to geomagnetically active times, it is important to note that quiet times are more common and generally exhibit low wave activities. When the model is trained on the entire

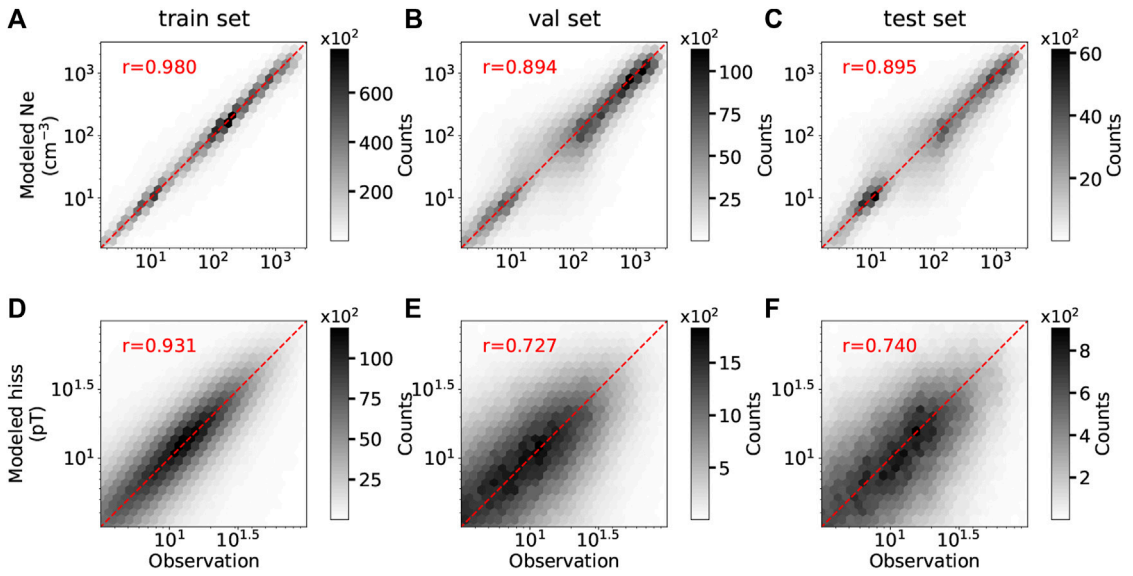

FIGURE 2
Overall model performance of electron density **(A–C)** and hiss wave amplitude **(D–F)** for different datasets. *X*-axis: observed quantity; *Y*-axis: modeled quantity. The correlation coefficient is calculated and labeled as "r." The Red dashed line denotes the data pair where the model prediction matches the observed value perfectly.

dataset, it tends to learn more efficiently from weaker waves, resulting in an underestimation of wave activity. To mitigate this imbalance, we use a weighted sampler that selects training samples based on a probability proportional to the largest wave amplitude within the subsequent 1-h period. Consequently, periods with stronger wave activity are more likely to be included in the training process than those with weak wave activity, leading to a model with improved performance during geomagnetically active times.

We include more details of the model structure and optimization procedure in Appendix A.

2.4 Data processing

The data from 2013 to 2019 is divided into 7-day blocks, with 70% randomly assigned as the training set, 20% as the validation set, and 10% as the test set. The period 13–19 May 2019 is also kept in the test set for further simulation (see Section 3.2). This division into 7-day blocks is chosen to avoid data leakage that is common in time-series modeling, and is short enough to allow for a large number of blocks, and long enough to prevent information leakage, while also considering long-term seasonal and solar cycle variations. After the training time range is settled (7-day blocks that belong to the training set combined), during each runtime we generate training samples with a weighted sampler using the following procedure. 1) Before the training starts, both Van Allen Probe A and B observations that fall within these 7-day blocks are assigned with a sequence of weights. Each weight that corresponds to a certain timestamp is calculated to be proportional to the largest wave amplitude within the subsequent 1-h period. The resulting weight sequence has the same length as satellite observations. 2) During the training, starting times of the satellite observations are randomly picked given the weight sequence, and for each selected time, a period of 10-h that follows the selected time is used in the training process. Each 10-h period of observation is then paired with the corresponding 10 h of geomagnetic indicies and the preceding 24 h of historical geomagnetic indices at 1-min resolution to provide information on the state of the inner magnetosphere. In summary, for each 10-h period, the model takes 24 h of historical geomagnetic indices (consisting of 1,440 data points) as inputs, followed by another 10 h of geomagnetic indices (consisting of 600 data points) and satellite location (L, sin (MLT/12*π), cos (MLT/12*π), MLAT) at the same time. The model predicts the total electron density and hiss wave amplitude within the 10-h period. The negative log likelihood is calculated between observation and model prediction over each 10-h period. Loss is accumulated over a number of sequences trained at the same time, until it backpropagates to update the neural network parameters.

3 Results

3.1 Model performance

The overall model performance is shown in Figure 2 for total electron density (A-C) and hiss wave amplitude (D-F) for different datasets, respectively. The *x*-axis represents the observed quantity y (density or hiss wave amplitude), while the *y*-axis represents the corresponding modeled quantity y^p. The color represents how many $y - y^p$ pairs are located in that region. The red dashed diagonal line indicates a perfect model prediction ($y = y^p$). The darker areas, concentrated near the red line, indicate good model performance for the majority of the data. This is also quantified by the correlation coefficient between $\log_{10} y$ and $\log_{10} y^p$ denoted by "r" in each panel. The model performance for electron density is

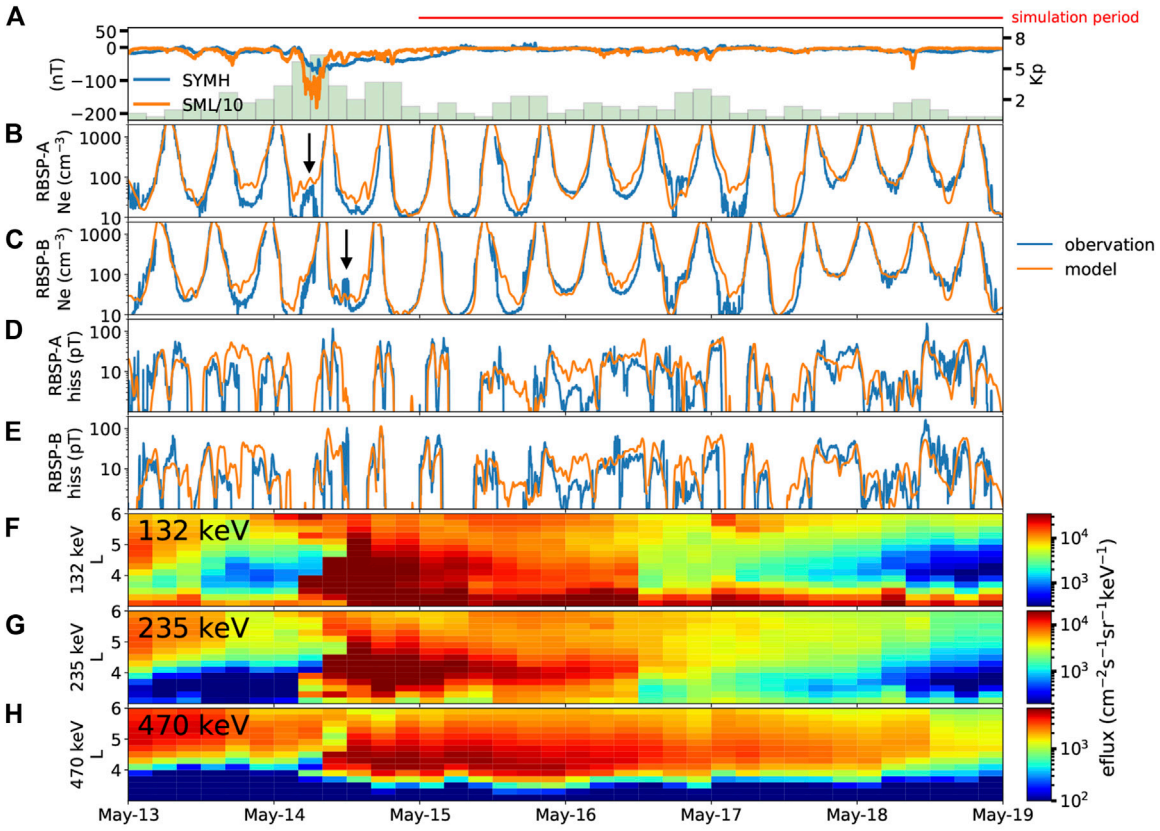

FIGURE 3
Overview of the geomagnetic storm during 13–19 May 2019. **(A)** SYM-H, SML, and Kp indices during the event. **(B–C)** Comparison between modeled electron density (orange) and satellite observation (blue) for RBSP-A and -B, respectively. Black arrows indicate plume features observed by the satellites. **(D–E)** Same as **(B–C)**, but for hiss wave amplitude. **(F–H)** Measured spin-averaged electron flux at different energy channels.

similar to that of Huang et al. (2022), where the Pearson correlation coefficient for the test dataset (Figure 2C) is about 0.9, close to that of the validation set (Figure 2B) indicating that the model generalization ability is good. The mean square error (MSE) and median error are 0.16 and 0.017, respectively. This indicates that the error is evenly distributed along the true values, signifying that the model both generalizes well and performs well in modeling electron density. For the hiss wave amplitude, there is more spread of the darker areas (Figure 2F) with r = 0.74, mse = 0.53 and median = −0.009 for the test dataset, which suggests that the model performance is worse for the hiss amplitude than electron density. This is partly because the wave activity is highly dynamic, exhibiting fluctuations on short timescales, and thus is less predictable compared to the cold plasma density. Nevertheless, by adopting a probability-based approach, our model reproduces the general global wave evolution fairly well, as presented in the following section.

3.2 Event study

We present a case study focusing on the global evolution of hiss waves and evaluate their effects on the energetic electron dynamics during a storm event on 14 May 2019, which is intentionally excluded from the training set. RBSP observations reveal the formation of a plasmaspheric plume and intensification of hiss waves over 13–19 May 2019, as shown in Figure 3. The SYM-H and SML indices (Figure 3A) peaked on May 14 when RBSP was on the dayside and observed a clear signature of the plasmaspheric plume (first by RBSP-A and later by RBSP-B, marked with black arrows in Figures 3B,C, respectively). Hiss wave amplitude intensified during the event (Figures 3D–H). show binned satellite observations of energetic electron fluxes at energies of 132 keV, 235 keV, and 470 keV, respectively. The electron flux increased by an order of magnitude from L~ 5 to L~3 within several hours during the main phase of the storm, which occurred at 7 UT on May 14. After the storm main phase, the electron flux decayed gradually over the subsequent days due to radial diffusion and pitch-angle scattering by waves that we will model later. We plot the modeled electron density and hiss wave amplitude in panels (B)–(E) and show a line-by-line comparison between the model (orange) and the observation (blue) during the event. Overall, the model accurately captures the evolution of the plasmapause location, especially during the latter half of the event when SYM-H and SML were very quiet while Kp varied. There were instances when RBSP measured very low density (<10 cm^{-3}), but the model predicted slightly higher density (−30 cm^{-3}). Although the relative error is significant, the absolute error remains relatively low. The modeled hiss wave amplitude generally follows the observations, successfully capturing most of the peak values.

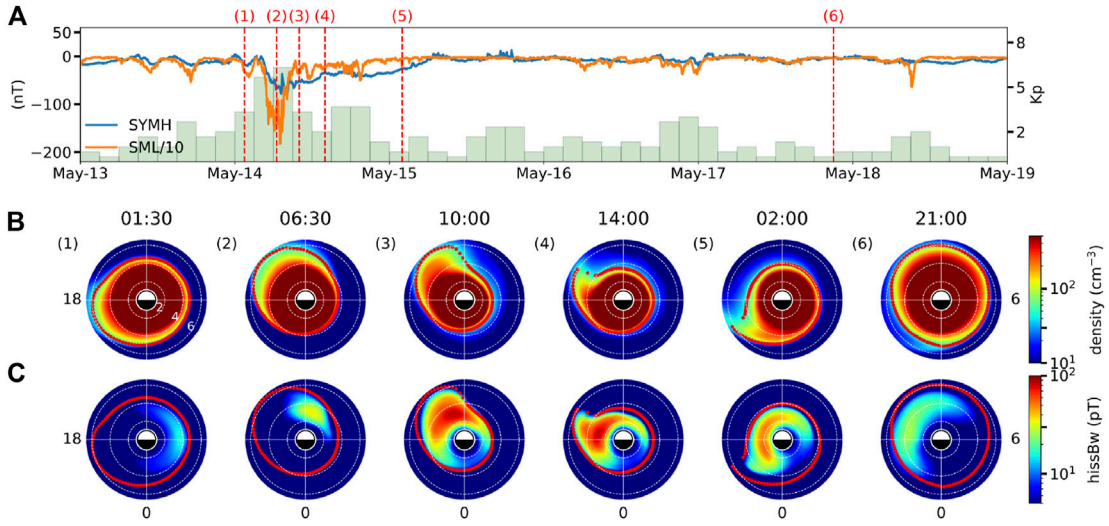

FIGURE 4
Snapshots of a geomagnetic storm event during 13–19 May 2019. **(A)** SYM-H, SML, and Kp indices during the event. **(B)** Modeled total electron density on the equatorial plane at different times, indicated by red dashed lines in panel **(A)**. The contour of electron density of 50 cm^{-3} is overplotted as a red line to indicate the plasmapause. White dashed circles represent L = 2, 4, and 6. **(C)** Same as panel **(B)**, but for hiss wave amplitude.

Figure 4 provides several snapshots illustrating the modeled global evolution of both electron density and hiss waves, allowing for a more comprehensive understanding of their dynamics during and following the storm event. As indicated by SYM-H and SML in panel (A), we select six specific times (1-6) to examine the modeled electron density (B) and hiss wave amplitude (C) before, during, and after the storm. Before the storm onset (1), the plasmasphere was relatively quiet and extended up to L = 6 on the dusk side. Correspondingly, hiss wave activity was low, which is expected during quiet conditions (Li et al., 2015a; Kim et al., 2015). As the storm intensified (2) with higher Kp and decreased SYM-H, the plasmasphere was pushed to the dayside due to the enhanced convection electric field, and hiss waves were intensified in the dawn-to-noon sector, probably related to the enhanced injection from the nightside plasma sheet. As the storm progressed (3), the plasmaspheric plume was formed, and the region with strong hiss waves shifted to the dusk side. The intensified waves predominantly occurred at high L, showing a good spatial correlation with the plume, in agreement with the statistical results of plume hiss (Shi et al., 2019). During the recovery phase from (3) to (5), the model predicted a rotating and narrowing plume, consistent with physical simulation results (De Pascuale et al., 2018), with hiss waves rotating and decaying simultaneously. After the storm, instances of persistent moderate hiss wave activity were observed (6). During the entire period, the majority of the wave power was concentrated near the plasmapause, in agreement with statistical results (Malaspina et al., 2017).

3.3 Event simulation

We use the UCLA 3-D diffusion code (Ma et al., 2015; 2018) to simulate the energetic electron evolution, considering radial diffusion and local resonant interactions with hiss waves. The simulation starts at 00 UT on May 15, following a period of significant local electron acceleration period and the extension of the plasmapause beyond L = 4. During the following four quiet days, the electron flux gradually decayed, providing a unique opportunity to model the effects of pitch angle scattering caused by hiss waves. The observed electron fluxes at 00 UT on May 15 are used as the initial condition for all L shells, as well as the time-varying boundary conditions at L = 2.6 and L = 6. The energy range in the simulation is set from 374 keV to 4.5 MeV at L = 2.6 and from 40 keV to 1 MeV at L = 6, maintaining the conservation of the first adiabatic invariant. The pitch angle gradients of phase space density at $\alpha = 0^{\circ}$ and $\alpha = 90^{\circ}$ are set to be 0. The modeling results of energetic electron fluxes are not sensitive to the energy boundary condition assumptions because the energy diffusion coefficients due to hiss are much smaller than the pitch angle diffusion coefficients (e.g., Ni et al., 2013; Thorne et al., 2013). Radial diffusion coefficients are calculated using the formulation by Liu et al. (2016) with pitch angle dependence from Schulz (1991, p229). The pitch angle, momentum, and their mixed diffusion coefficients are computed based on the total plasma density and hiss wave amplitude obtained from the deep learning model with a time cadence of 5 min. The wave frequency spectrum is derived from the Van Allen Probes statistics (Li et al., 2015b), and wave normal angles are assumed to be quasi field-aligned near the magnetic equator, gradually becoming highly oblique at higher latitudes (Ni et al., 2013). The deep learning model provides the time-varying total electron density and hiss wave amplitude as functions of L shell and MLT at the equator, which are used as inputs to the 3-D diffusion code.

Figure 5 shows the modeled MLT-averaged hiss wave amplitude (A) and the simulated energetic electron flux evolution (B-D) in the same energy channels as shown in Figure 3. At the start of the simulation on May 15, the energetic electron fluxes were initially high in the outer radiation belt. As a result of both radial diffusion and scattering by hiss waves, the electron flux gradually decayed over

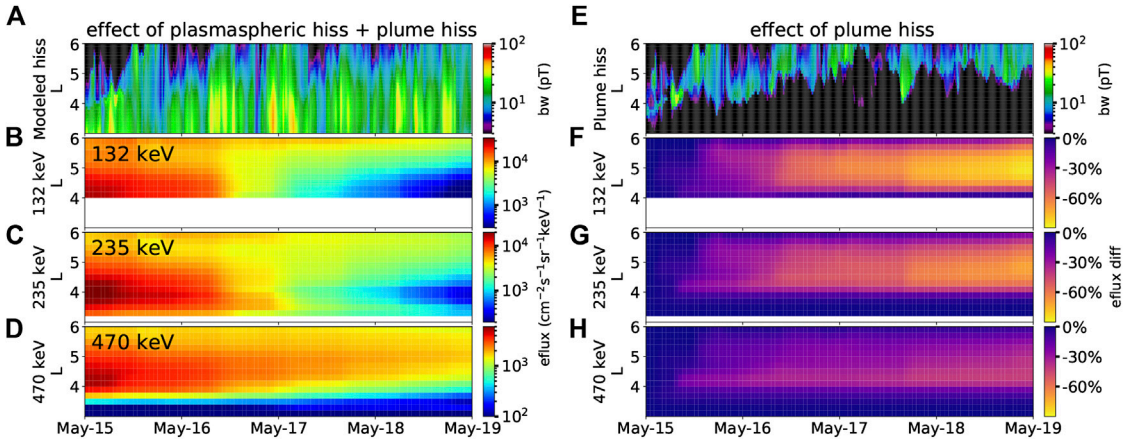

FIGURE 5
Simulated energetic flux evolution during a quiet period. **(A)** MLT-averaged hiss wave amplitude as a function of L and time from the deep learning model. **(B)** Simulated electron flux evolution for 132 keV electrons as a function of L and time, starting at L > 4. **(C)** Same as panel **(B)** but for 235 keV electrons. **(D)** Same as panel **(B)** but for 470 keV electrons. **(E)** Modeled MLT-averaged plume hiss wave amplitude. **(F)** Difference in simulated electron flux with and without plume hiss for 132 keV electrons. **(G)** Same as panel **(F)** but for 235 keV electrons. **(H)** Same as panel **(F)** but for 470 keV electrons.

the following 1–3 days. Instances of faster decay and slumps in the electron flux were successfully reproduced by the simulation at 0 and 18 UT on May 17, consistent with the RBSP observations. These slumps can be attributed to the enhanced wave activity, which causes stronger pitch angle scattering. To quantify the role of plume hiss in energetic electron dynamics, we divided the modeled global distribution of hiss waves into plume hiss and plasmaspheric hiss based on the modeled total electron density. We defined the plume as the region with a total electron density in the range 20–200 cm^{-3}, as identified from the global maps of modeled electron density, in agreement with typical plume statistics (Moldwin, 2004; Darrouzet et al., 2008). Although this definition may include the outer plasmasphere, as well as attached or detached plumes, it serves our purpose as this region exhibits similar characteristics that allow access for energetic electrons, potentially providing a source of free energy for whistler mode wave intensification (e.g., Li et al., 2013; Shi et al., 2019). Figure 5E displays the modeled plume hiss, characterized by an MLT-averaged wave amplitude of ~10–20 pT. The majority of the plume hiss was located at L ~ 5, although the coverage was sometimes extended to L > 6. Despite its high variability, a clear trend emerged during the first 3 days, indicating that the inner edge of the plume hiss moved from L = 4 to 5 due to the refilling of the plasmasphere after the storm.

To assess the impact of plume hiss on energetic electron flux, we conducted simulations considering only plasmaspheric hiss and compared them with simulations that included the effects of both plasmaspheric and plume hiss (the simulated electron fluxes are denoted as J_1 and J_2, respectively). The difference in electron fluxes between these simulations, quantified by $(J_1 - J_2)/J_1$, represents the sole effect of plume hiss, as shown in panels (F-H). When the plume hiss effect was included, there was a consistent decrease in electron fluxes over the 100–500 keV energy range. After a few days of simulation, the plume hiss accounted for an −80% decrease in 132 keV electron flux and a −40% decrease in 470 keV electron flux at L–4.5, near the heart of the outer radiation belt. At higher L,

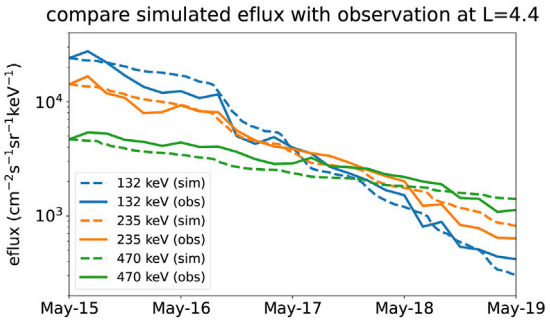

FIGURE 6
Comparison between the simulated (dashed line) and the observed electron flux evolution (solid line) at L = 4.4. Each color represents a different energy channel.

the plume hiss also contributed significantly to electron losses, resulting in a −30%–70% decrease in electron flux at L–5.5. It is worth noting that the hiss wave activity depicted in Figure 5A is relatively modest, but the peak wave amplitude reached up to −100 pT. The averaged value of hiss wave amplitude during the recovery phase of this event is lower than the averaged statistical wave amplitude (−100 pT) on the dayside during strong geomagnetic conditions with AL* < −500 nT (Li et al., 2015a). It is interesting to note that there have been instances where hiss wave amplitudes in plumes exceeded 1,000 pT (Su et al., 2018). Therefore, we expect that plume hiss waves would have a much stronger impact during periods of higher geomagnetic activity.

Figure 6 presents a comparison between the simulated (dashed line) and the observed electron flux evolution (solid line) at L = 4.4. This L shell is located in the heart of the outer radiation belt, where the electron flux decay is most prominent. Moreover, choosing L = 4.4 ensures that it is sufficiently distant from the simulation

boundary, thus the change at this distance is mostly from the simulation itself, minimizing the potential impact of using observations as boundary conditions. In all three energy channels, the simulation exhibits a gradual flux decay from May 15 to 16, followed by a faster decay from 16 to 17. The simulation accurately captures the electron flux decay rate until the end of May 18, when the observation reveals a faster decay of higher-energy electrons. This faster decay could be attributed to the influence of waves other than hiss waves alone, as discussed below.

4 Discussion

Although the simulated electron flux reproduced the observed flux for most of the period, there was a slightly faster decay rate in the observed flux on the last day of the simulation. Several potential factors could contribute to this discrepancy, which are discussed below.

1. The presence of waves other than hiss waves can affect energetic electron dynamics. For example, chorus waves can also scatter electrons in the energy range of hundreds of keV, especially on the nightside where the plasmapause is often located at L < −5. When performing simulations that include both chorus and hiss waves, the effects of these waves will be taken into consideration. However, this is beyond the scope of the present study, as we focus solely on modeling the hiss wave distribution in the plasmasphere and plume and their quantitative scattering effects on electrons.
2. The presence of other waves may not scatter particles directly, but instead enhance the efficiency of hiss waves in scattering energetic electrons into the loss cone. Previous studies have shown that when electromagnetic ion cyclotron (EMIC) waves and hiss waves coexist at the same L shell, MeV electrons can be first scattered by hiss waves and subsequently scattered and precipitated by EMIC waves (Ma et al., 2015; Drozdov et al., 2020), resulting in a significant reduction in their lifetimes (Li et al., 2007; Zhang et al., 2017). Fast magnetosonic waves can induce additional scattering at intermediate pitch angles, leading to increased electron losses compared to scattering by hiss alone (Hua et al., 2018). Non-linear phase trapping by chorus waves can accelerate 300–500 keV electrons, which may then resonate with EMIC waves, resulting in their rapid scattering into the loss cone (Bashir et al., 2022). The combined effects of different wave modes on the radiation belt dynamics are beyond the scope of the present study and are left for future investigations.

There are different ways to define plumes used in simulations. In our study, we define the plume region as an area with a total electron density ranging from 20 to 200 cm^{-3} at $L < 6$. This definition typically encompasses the outer plasmasphere or the plume, where energetic electrons (>−10s keV) can access, thus leading to highly variable wave activity over time and space. We have found a considerable amount of hiss wave power at L > 4, and the outermost extension of hiss waves has been observed to vary from L = 4 to 6, even during relatively quiet periods indicated by the geomagnetic indices. The commonly used density and wave statistical models, which are often expressed as simple functions of Kp and/or AE (O'Brien and Moldwin, 2003; Golden et al., 2012; Spasojevic et al., 2015; Saikin et al., 2022), do not capture such variability since the underlying geomagnetic indices might not exhibit strong variations during the period. These statistical models predict a constant wave power at a given location for a range of geomagnetic indices. Our findings demonstrate that even under relatively quiet conditions, hiss wave activity could exhibit dynamic evolution, and such spatial variation plays a crucial role in the evolution of energetic electron fluxes over time at different L shells, as shown in Figure 5.

5 Conclusion

We have developed a neural network model to simultaneously reconstruct the global evolution of both electron density and hiss wave amplitude in the Earth's plasmasphere and plume. Unlike traditional deterministic models, our approach estimates the distribution of these quantities, allowing for a better representation of variations in the data on both large and small scales.

To quantify the evolution and effects of plume hiss, we focused on the storm event that occurred over 13–19 May 2019, during which RBSP observed the formation of a plasmaspheric plume, followed by a gradual decay in the electron fluxes at a few hundred keV. Our model successfully captured the global evolution of the plume, as well as the plume hiss within it during the entire event. As geomagnetic activity increased, hiss wave power intensified and shifted from dawn to dusk, where the plume was formed later. The plume and plume hiss exhibited a strong spatial correlation and rotated together as the geomagnetic activity became weaker. The plume wrapped around the Earth and became thinner over the nightside, where hiss wave power diminished rapidly. During the recovery phase, the plasmasphere was gradually refilled, and hiss wave activity remained relatively low in general. Our model provided valuable insights into the relationship between the plume structure (as seen in the plasma density) and plume hiss on a global scale.

To quantify the impact of plume hiss, we separated the modeled total hiss wave population into plasmaspheric hiss and plume hiss, and simulated the energetic electron flux evolution with and without plume hiss. By including both plasmaspheric and plume hiss, together with radial diffusion, the simulated electron flux decay reproduces the observation very well. The remaining differences in the electron flux decay may be attributed to scattering effects from other waves. Although the MLT-averaged wave amplitude was −10–20 pT, plume hiss alone was responsible for an additional −80% decrease in 132 keV electron flux at L−4.5 within 3 days, and −30% decrease in 470 keV electron flux at L−5.5. These results highlight the dynamic nature of hiss wave evolution even during geomagnetically quiet conditions, and emphasize the significant role played by plume hiss in shaping the energetic electron dynamics, especially in the outer radiation belt, which should be considered in future simulations of radiation belt dynamics.

Data availability statement

The datasets presented in this study can be found in online repositories. The names of the repository/repositories and accession

number(s) can be found below: The Van Allen Probes data from the EMFISIS instrument were obtained from http://emfisis.physics.uiowa.edu/Flight/. Data from the ECT instrument were obtained from https://rbsp-ect.newmexicoconsortium.org/data_pub/. The geomagnetic indices used in the model training are available at https://omniweb.gsfc.nasa.gov/form/omni_min.html (SYM-H); https://supermag.jhuapl.edu (SML and SMU); https://www.gfz-potsdam.de/en/hpo-index/ (Hp30). All data used to produce figures, as well as the Python script defining the model structure, are publicly available at https://doi.org/10.6084/m9.figshare.22817531.

Author contributions

SH and WL developed the study concept and lead the project. SH designed, implemented, and trained the neural network model, and performed the event analysis. QM performed the Fokker-Planck simulation and produced Figure 5. X-CS processed the wave spectrum data from EMFISIS and generated the dataset of hiss. LC contributed to the model design and event analysis. XC, DM, JB, MH, and SW contributed to the model design. SH wrote the first draft of the manuscript. All authors contributed to the article and approved the submitted version.

Funding

This research at Boston University is supported by the NASA Grants 80NSSC19K0845, 80NSSC20K0196, 80NSSC20K0704, and 80NSSC21K1312, and the NSF Grants AGS-1847818 and AGS-2225445. SH gratefully acknowledges the NASA FINESST Grant 80NSSC21K1385. SW acknowledges the support of NASA Grant 80NSSC20K0704. JB and DM gratefully acknowledge support from subgrant No. 1559841 to the University of California, Los Angeles, from the University of Colorado Boulder under NASA Prime Grant agreement No. 80NSSC20K1580.

Acknowledgments

We gratefully acknowledge the Van Allen Probes Mission, especially EMFISIS and ECT teams, for the use of their data. We also acknowledge the OMNI team, SuperMAG collaborators, GFZ collaborators, and the PyTorch team.

Conflict of interest

The authors declare that the research was conducted in the absence of any commercial or financial relationships that could be construed as a potential conflict of interest.

Publisher's note

References

Agapitov, O., Mourenas, D., Artemyev, A., Mozer, F. S., Bonnell, J. W., Angelopoulos, V., et al. (2018). Spatial extent and temporal correlation of chorus and hiss: statistical results from multipoint themis observations. *J. Geophys. Res. Space Phys.* 123 (10), 8317–8330. doi:10.1029/2018JA025725

Bashir, M. F., Artemyev, A., Zhang, X., and Angelopoulos, V. (2022). Energetic electron precipitation driven by the combined effect of ULF, EMIC, and whistler waves. *J. Geophys. Res. Space Phys.* 127 (1). doi:10.1029/2021JA029871

Blake, J. B., Carranza, P. A., Claudepierre, S. G., Clemmons, J. H., Crain, W. R., Dotan, Y., et al. (2013). The magnetic electron ion spectrometer (MagEIS) instruments aboard the radiation belt storm probes (RBSP) spacecraft. *Space Sci. Rev.* 179 (1–4), 383–421. doi:10.1007/s11214-013-9991-8

Blundell, C., Cornebise, J., Kavukcuoglu, K., and Wierstra, D. (2015). Weight uncertainty in neural networks. Retrieved from http://arxiv.org/abs/1505.05424.

Bortnik, Jacob, Thorne, R. M., and Meredith, N. P. (2009b). Plasmaspheric hiss overview and relation to chorus. *J. Atmos. Solar-Terrestrial Phys.* 71 (16), 1636–1646. doi:10.1016/j.jastp.2009.03.023

Bortnik, J. (2003). Frequency-time spectra of magnetospherically reflecting whistlers in the plasmasphere. *J. Geophys. Res.* 108 (A1), 1030. doi:10.1029/2002JA009387

Bortnik, J., Li, W., Thorne, R. M., Angelopoulos, V., Cully, C., Bonnell, J., et al. (2009a). An observation linking the origin of plasmaspheric hiss to discrete chorus emissions. *Science* 324 (5928), 775–778. doi:10.1126/science.1171273

Bortnik, J., Thorne, R. M., and Meredith, N. P. (2008). The unexpected origin of plasmaspheric hiss from discrete chorus emissions. *Nature* 452 (7183), 62–66. doi:10.1038/nature06741

Chan, K.-W., and Holzer, R. E. (1976). ELF hiss associated with plasma density enhancements in the outer magnetosphere. *J. Geophys. Res.* 81 (13), 2267–2274. doi:10.1029/JA081i013p02267

Chen, L., Bortnik, J., Li, W., Thorne, R. M., and Horne, R. B. (2012a). Modeling the properties of plasmaspheric hiss: 1. Dependence on chorus wave emission. *J. Geophys. Res. Space Phys.* 117 (A5). doi:10.1029/2011JA017201

Chen, L., Bortnik, J., Li, W., Thorne, R. M., and Horne, R. B. (2012b). Modeling the properties of plasmaspheric hiss: 2. Dependence on the plasma density distribution. *J. Geophys. Res. Space Phys.* 117 (A5). doi:10.1029/2011JA017202

Chen, L., Thorne, R. M., Bortnik, J., Li, W., Horne, R. B., Reeves, G. D., et al. (2014). Generation of unusually low frequency plasmaspheric hiss. *Geophys. Res. Lett.* 41 (16), 5702–5709. doi:10.1002/2014GL060628

Church, S. R., and Thorne, R. M. (1983). On the origin of plasmaspheric hiss: ray path integrated amplification. *J. Geophys. Res.* 88 (A10), 7941. doi:10.1029/JA088iA10p07941

Darrouzet, F., De Keyser, J., Décréau, P. M. E., El Lemdani-Mazouz, F., and Vallières, X. (2008). Statistical analysis of plasmaspheric plumes with Cluster/WHISPER observations. *Ann. Geophys.* 26 (8), 2403–2417. doi:10.5194/angeo-26-2403-2008

De Pascuale, S., Jordanova, V. K., Goldstein, J., Kletzing, C. A., Kurth, W. S., Thaller, S. A., et al. (2018). Simulations of van allen probes plasmaspheric electron density observations. *J. Geophys. Res. Space Phys.* 123 (11), 9453–9475. doi:10.1029/2018JA025776

Drozdov, A. Y., Usanova, M. E., Hudson, M. K., Allison, H. J., and Shprits, Y. Y. (2020). The role of hiss, chorus, and EMIC waves in the modeling of the dynamics of the multi-MeV radiation belt electrons. *J. Geophys. Res. Space Phys.* 125 (9). doi:10.1029/2020JA028282

Dunckel, N., and Helliwell, R. A. (1969). Whistler-mode emissions on the OGO 1 satellite. *J. Geophys. Res.* 74 (26), 6371–6385. doi:10.1029/JA074i026p06371

Fu, H., Yue, C., Ma, Q., Kang, N., Bortnik, J., Zong, Q., et al. (2021). Frequency-dependent responses of plasmaspheric hiss to the impact of an interplanetary shock. *Geophys. Res. Lett.* 48 (20). doi:10.1029/2021GL094810

Gjerloev, J. W. (2012). The SuperMAG data processing technique: technique. *J. Geophys. Res. Space Phys.* 117 (A9). doi:10.1029/2012JA017683

Golden, D. I., Spasojevic, M., Li, W., and Nishimura, Y. (2012). Statistical modeling of plasmaspheric hiss amplitude using solar wind measurements and geomagnetic indices: modeling HISS with solar wind. *Geophys. Res. Lett.* 39 (6). doi:10.1029/2012GL051185

Green, J. L. (2005). On the origin of whistler mode radiation in the plasmasphere. *J. Geophys. Res.* 110 (A3), A03201. doi:10.1029/2004JA010495

Hayakawa, M., and Sazhin, S. S. (1992). Mid-latitude and plasmaspheric hiss: A review. *Planet. Space Sci.* 40 (10), 1325–1338. doi:10.1016/0032-0633(92)90089-7

Hayakawa, M., Ohmi, N., Parrot, M., and Lefeuvre, F. (1986). Direction finding of ELF hiss emissions in a detached plasma region of the magnetosphere. *J. Geophys. Res.* 91 (A1), 135. doi:10.1029/JA091iA01p00135

Hochreiter, S., and Schmidhuber, J. (1997). Long short-term memory. *Neural Comput.* 9 (8), 1735–1780. doi:10.1162/neco.1997.9.8.1735

Horne, R. B., and Thorne, R. M. (1998). Potential waves for relativistic electron scattering and stochastic acceleration during magnetic storms. *Geophys. Res. Lett.* 25 (15), 3011–3014. doi:10.1029/98GL01002

Hua, M., Ni, B., Fu, S., Gu, X., Xiang, Z., Cao, X., et al. (2018). Combined scattering of outer radiation belt electrons by simultaneously occurring chorus, exohiss, and magnetosonic waves. *Geophys. Res. Lett.* 45 (19). doi:10.1029/2018GL079533

Huang, C. Y., Goertz, C. K., and Anderson, R. R. (1983). A theoretical study of plasmaspheric hiss generation. *J. Geophys. Res.* 88 (A10), 7927. doi:10.1029/JA088iA10p07927

Huang, S., Li, W., Shen, X., Ma, Q., Chu, X., Ma, D., et al. (2022). Application of recurrent neural network to modeling Earth's global electron density. *J. Geophys. Res. Space Phys.* 127 (9). doi:10.1029/2022JA030695

Karim, F., Majumdar, S., Darabi, H., and Chen, S. (2018). LSTM fully convolutional networks for time series classification. *IEEE Access* 6, 1662–1669. doi:10.1109/ACCESS.2017.2779939

Kennel, C. F., and Petschek, H. E. (1966). Limit on stably trapped particle fluxes. *J. Geophys. Res.* 71 (1), 1–28. doi:10.1029/JZ071i001p00001

Kim, K., Lee, D., and Shprits, Y. (2015). Dependence of plasmaspheric hiss on solar wind parameters and geomagnetic activity and modeling of its global distribution. *J. Geophys. Res. Space Phys.* 120 (2), 1153–1167. doi:10.1002/2014JA020687

Kletzing, C. A., Kurth, W. S., Acuna, M., MacDowall, R. J., Torbert, R. B., Averkamp, T., et al. (2013). The electric and magnetic field instrument suite and integrated science (EMFISIS) on RBSP. *Space Sci. Rev.* 179 (1–4), 127–181. doi:10.1007/s11214-013-9993-6

Kurth, W. S., De Pascuale, S., Faden, J. B., Kletzing, C. A., Hospodarsky, G. B., Thaller, S., et al. (2015). Electron densities inferred from plasma wave spectra obtained by the Waves instrument on Van Allen Probes. *J. Geophys. Res. Space Phys.* 120 (2), 904–914. doi:10.1002/2014JA020857

Lam, M. M., Horne, R. B., Meredith, N. P., and Glauert, S. A. (2007). Modeling the effects of radial diffusion and plasmaspheric hiss on outer radiation belt electrons. *Geophys. Res. Lett.* 34 (20), L20112. doi:10.1029/2007GL031598

Larkina, V. I., and Likhter, Ja. I. (1982). Storm-time variations of plasmaspheric ELF hiss. *J. Atmos. Terr. Phys.* 44 (5), 415–423. doi:10.1016/0021-9169(82)90048-4

Li, W., Chen, L., Bortnik, J., Thorne, R. M., Angelopoulos, V., Kletzing, C. A., et al. (2015b). First evidence for chorus at a large geocentric distance as a source of plasmaspheric hiss: coordinated themis and van allen probes observation. *Geophys. Res. Lett.* 42 (2), 241–248. doi:10.1002/2014GL062832

Li, W., Ma, Q., Thorne, R. M., Bortnik, J., Kletzing, C. A., Kurth, W. S., et al. (2015a). Statistical properties of plasmaspheric hiss derived from Van Allen Probes data and their effects on radiation belt electron dynamics. *J. Geophys. Res. Space Phys.* 120 (5), 3393–3405. doi:10.1002/2015JA021048

Li, W., Shen, X. -C., Ma, Q., Capannolo, L., Shi, R., Redmon, R. J., et al. (2019). Quantification of energetic electron precipitation driven by plume whistler mode waves, plasmaspheric hiss, and exohiss. *Geophys. Res. Lett.* 46 (7), 3615–3624. doi:10.1029/2019GL082095

Li, W., Shprits, Y. Y., and Thorne, R. M. (2007). Dynamic evolution of energetic outer zone electrons due to wave-particle interactions during storms. *J. Geophys. Res. Space Phys.* 112 (A10). doi:10.1029/2007JA012368

Li, W., Thorne, R. M., Bortnik, J., Reeves, G. D., Kletzing, C. A., Kurth, W. S., et al. (2013). An unusual enhancement of low-frequency plasmaspheric hiss in the outer plasmasphere associated with substorm-injected electrons: amplification of low-frequency HISS. *Geophys. Res. Lett.* 40 (15), 3798–3803. doi:10.1002/grl.50787

Liu, N., Su, Z., Gao, Z., Zheng, H., Wang, Y., Wang, S., et al. (2020). Comprehensive observations of substorm-enhanced plasmaspheric hiss generation, propagation, and dissipation. *Geophys. Res. Lett.* 47 (2). doi:10.1029/2019GL086040

Liu, W., Tu, W., Li, X., Sarris, T., Khotyaintsev, Y., Fu, H., et al. (2016). On the calculation of electric diffusion coefficient of radiation belt electrons with *in situ* electric field measurements by THEMIS. *Geophys. Res. Lett.* 43 (3), 1023–1030. doi:10.1002/2015GL067398

Ma, Q., Li, W., Bortnik, J., Thorne, R. M., Chu, X., Ozeke, L. G., et al. (2018). Quantitative evaluation of radial diffusion and local acceleration processes during GEM challenge events. *J. Geophys. Res. Space Phys.* 123 (3), 1938–1952. doi:10.1002/2017JA025114

Ma, Q., Li, W., Thorne, R. M., Bortnik, J., Reeves, G. D., Kletzing, C. A., et al. (2016). Characteristic energy range of electron scattering due to plasmaspheric hiss. *J. Geophys. Res. Space Phys.* 121 (12). doi:10.1002/2016JA023311

Ma, Q., Li, W., Thorne, R. M., Ni, B., Kletzing, C. A., Kurth, W. S., et al. (2015). Modeling inward diffusion and slow decay of energetic electrons in the Earth's outer radiation belt. *Geophys. Res. Lett.* 42 (4), 987–995. doi:10.1002/2014GL062977

Ma, Q., Li, W., Zhang, X. J., Bortnik, J., Shen, X. -C., Connor, H. K., et al. (2021). Global survey of electron precipitation due to hiss waves in the Earth's plasmasphere and plumes. *J. Geophys. Res. Space Phys.* 126 (8). doi:10.1029/2021JA029644

Malaspina, D. M., Jaynes, A. N., Hospodarsky, G., Bortnik, J., Ergun, R. E., and Wygant, J. (2017). Statistical properties of low-frequency plasmaspheric hiss. *J. Geophys. Res. Space Phys.* 122 (8), 8340–8352. doi:10.1002/2017JA024328

Matzka, J., Stolle, C., Yamazaki, Y., Bronkalla, O., and Morschhauser, A. (2021). The geomagnetic *kp* index and derived indices of geomagnetic activity. *Space weather.* 19 (5). doi:10.1029/2020SW002641

Mauk, B. H., Fox, N. J., Kanekal, S. G., Kessel, R. L., Sibeck, D. G., and Ukhorskiy, A. (2013). Science objectives and rationale for the radiation belt storm probes mission. *Space Sci. Rev.* 179 (1–4), 3–27. doi:10.1007/s11214-012-9908-y

Meredith, N. P., Bortnik, J., Horne, R. B., Li, W., and Shen, X. (2021). Statistical investigation of the frequency dependence of the chorus source mechanism of plasmaspheric hiss. *Geophys. Res. Lett.* 48 (6). doi:10.1029/2021GL092725

Meredith, N. P., Horne, R. B., Bortnik, J., Thorne, R. M., Chen, L., Li, W., et al. (2013). Global statistical evidence for chorus as the embryonic source of plasmaspheric hiss. *Geophys. Res. Lett.* 40 (12), 2891–2896. doi:10.1002/grl.50593

Meredith, N. P., Horne, R. B., Clilverd, M. A., Horsfall, D., Thorne, R. M., and Anderson, R. R. (2006). Origins of plasmaspheric hiss. *J. Geophys. Res.* 111 (A9), A09217. doi:10.1029/2006JA011707

Meredith, N. P. (2004). Substorm dependence of plasmaspheric hiss. *J. Geophys. Res.* 109 (A6), A06209. doi:10.1029/2004JA010387

Millan, R. M., Ripoll, J.-F., Santolík, O., and Kurth, W. S. (2021). Early-time non-equilibrium pitch angle diffusion of electrons by whistler-mode hiss in a plasmaspheric plume associated with BARREL precipitation. *Front. Astronomy Space Sci.* 8, 776992. doi:10.3389/fspas.2021.776992

Moldwin, M. B. (2004). Plasmaspheric plumes: CRRES observations of enhanced density beyond the plasmapause. *J. Geophys. Res.* 109 (A5), A05202. doi:10.1029/2003JA010320

Newell, P. T., and Gjerloev, J. W. (2011). Evaluation of SuperMAG auroral electrojet indices as indicators of substorms and auroral power: supermag auroral electrojet indices. *J. Geophys. Res. Space Phys.* 116 (A12). doi:10.1029/2011JA016779

Ni, B., Bortnik, J., Thorne, R. M., Ma, Q., and Chen, L. (2013). Resonant scattering and resultant pitch angle evolution of relativistic electrons by plasmaspheric hiss. *J. Geophys. Res. Space Phys.* 118 (12), 7740–7751. doi:10.1002/2013JA019260

Ni, B., Li, W., Thorne, R. M., Bortnik, J., Ma, Q., Chen, L., et al. (2014). Resonant scattering of energetic electrons by unusual low-frequency hiss. *Geophys. Res. Lett.* 41 (6), 1854–1861. doi:10.1002/2014GL059389

O'Brien, T. P., and Moldwin, M. B. (2003). Empirical plasmapause models from magnetic indices. *Geophys. Res. Lett.* 30 (4), 2002GL016007. doi:10.1029/2002GL016007

Qin, M., Li, W., Ma, Q., Woodger, L., Millan, R., Shen, X., et al. (2021). Multi-point observations of modulated whistler-mode waves and energetic electron precipitation. *J. Geophys. Res. Space Phys.* 126 (12). doi:10.1029/2021JA029505

Ripoll, J.-F., Denton, M., Loridan, V., Santolík, O., Malaspina, D., Hartley, D. P., et al. (2020). How whistler mode hiss waves and the plasmasphere drive the quiet decay of radiation belts electrons following a geomagnetic storm. *J. Phys. Conf. Ser.* 1623, 012005. doi:10.1088/1742-6596/1623/1/012005

Russell, C. T., Holzer, R. E., and Smith, E. J. (1969). OGO 3 observations of ELF noise in the magnetosphere: 1. Spatial extent and frequency of occurrence. *J. Geophys. Res.* 74 (3), 755–777. doi:10.1029/JA074i003p00755

Saikin, A. A., Drozdov, A. Y., and Malaspina, D. M. (2022). Low frequency plasmaspheric hiss wave activity parameterized by plasmapause location: models and simulations. *J. Geophys. Res. Space Phys.* 127 (9). doi:10.1029/2022JA030687

Santolík, O., Chum, J., Parrot, M., Gurnett, D. A., Pickett, J. S., and Cornilleau-Wehrlin, N. (2006). Propagation of whistler mode chorus to low altitudes: spacecraft observations of structured elf hiss. *J. Geophys. Res.* 111 (A10), A10208. doi:10.1029/2005JA011462

Schulz, M. (1991). "The magnetosphere," in *Geomagnetism* (Elsevier), Amsterdam, Netherlands 87–293. doi:10.1016/B978-0-12-378674-6.50008-X

Shen, X., Li, W., Ma, Q., Agapitov, O., and Nishimura, Y. (2019). Statistical analysis of transverse size of lower band chorus waves using simultaneous multisatellite observations. *Geophys. Res. Lett.* 46 (11), 5725–5734. doi:10.1029/2019GL083118

Shi, R., Li, W., Ma, Q., Green, A., Kletzing, C. A., Kurth, W. S., et al. (2019). Properties of whistler mode waves in Earth's plasmasphere and plumes. *J. Geophys. Res. Space Phys.* 124 (2), 1035–1051. doi:10.1029/2018JA026041

Siami-Namini, S., Tavakoli, N., and Namin, A. S. (2019). The performance of LSTM and BiLSTM in forecasting time series. In Proceedings of the 2019 IEEE International Conference on Big Data (Big Data). Los Angeles, CA, USA.doi:10.1109/BigData47090.2019.9005997

Sonwalkar, V. S., and Inan, U. S. (1989). Lightning as an embryonic source of VLF hiss. *J. Geophys. Res. Space Phys.* 94 (A6), 6986–6994. doi:10.1029/JA094iA06p06986

Spasojevic, M., Shprits, Y. Y., and Orlova, K. (2015). Global empirical models of plasmaspheric hiss using Van Allen Probes. *J. Geophys. Res. Space Phys.* 120 (12). doi:10.1002/2015JA021803

Spence, H. E., Reeves, G. D., Baker, D. N., Blake, J. B., Bolton, M., Bourdarie, S., et al. (2013). Science goals and overview of the radiation belt storm probes (RBSP) energetic particle, composition, and thermal plasma (ECT) suite on NASA's van allen probes mission. *Space Sci. Rev.* 179 (1–4), 311–336. doi:10.1007/s11214-013-0007-5

Su, Z., Liu, N., Zheng, H., Wang, Y., and Wang, S. (2018). Multipoint observations of nightside plasmaspheric hiss generated by substorm-injected electrons. *Geophys. Res. Lett.* 45 (20). doi:10.1029/2018GL079927

Summers, D., Ni, B., Meredith, N. P., Horne, R. B., Thorne, R. M., Moldwin, M. B., et al. (2008). Electron scattering by whistler-mode ELF hiss in plasmaspheric plumes. *J. Geophys. Res.* 17. doi:10.1029/2007JA012678

Tasistro-Hart, A., Grayver, A., and Kuvshinov, A. (2021). Probabilistic geomagnetic storm forecasting via deep learning. *J. Geophys. Res. Space Phys.* 126 (1). doi:10.1029/2020JA028228

Thorne, Richard M., Smith, E. J., Burton, R. K., and Holzer, R. E. (1973). Plasmaspheric hiss. *J. Geophys. Res.* 78 (10), 1581–1596. doi:10.1029/JA078i010p01581

Thorne, R. M., Church, S. R., and Gorney, D. J. (1979). On the origin of plasmaspheric hiss: the importance of wave propagation and the plasmapause. *J. Geophys. Res.* 84 (A9), 5241. doi:10.1029/JA084iA09p05241

Thorne, R. M., Li, W., Ni, B., Ma, Q., Bortnik, J., Baker, D. N., et al. (2013). Evolution and slow decay of an unusual narrow ring of relativistic electrons near L ~ 3.2 following the September 2012 magnetic storm. *Geophys. Res. Lett.* 40, 3507–3511. doi:10.1002/grl.50627

Tsurutani, B. T., Falkowski, B. J., Pickett, J. S., Santolik, O., and Lakhina, G. S. (2015). Plasmaspheric hiss properties: observations from polar. *J. Geophys. Res. Space Phys.* 120 (1), 414–431. doi:10.1002/2014JA020518

Wing, S., Johnson, J. R., Jen, J., Meng, C.-I., Sibeck, D. G., Bechtold, K., et al. (2005). Kp forecast models: kp forecast models. *J. Geophys. Res. Space Phys.* 110 (A4). doi:10.1029/2004JA010500

Wing, S., Turner, D. L., Ukhorskiy, A. Y., Johnson, J. R., Sotirelis, T., Nikoukar, R., et al. (2022). Modeling radiation belt electrons with information theory informed neural networks. *Space weather.* 20 (8). doi:10.1029/2022SW003090

Wu, Z., Su, Z., Goldstein, J., Liu, N., He, Z., Zheng, H., et al. (2022). Nightside plasmaspheric plume-to-core migration of whistler-mode hiss waves. *Geophys. Res. Lett.* 49 (16). doi:10.1029/2022GL100306

Zhang, W., Ni, B., Huang, H., Summers, D., Fu, S., Xiang, Z., et al. (2019). Statistical properties of hiss in plasmaspheric plumes and associated scattering losses of radiation belt electrons. *Geophys. Res. Lett.* 46 (11), 5670–5680. doi:10.1029/2018GL081863

Zhang, X. J., Mourenas, D., Artemyev, A. V., Angelopoulos, V., and Thorne, R. M. (2017). Contemporaneous EMIC and whistler mode waves: observations and consequences for mev electron loss. *Geophys. Res. Lett.* 44 (16), 8113–8121. doi:10.1002/2017GL073886

10.3389/fspas.2023.1231578

Appendix A: Model structure and optimization procedure

We optimize the hyperparameters in our model following the steps described by Huang et al. (2022).

After careful tuning, we used the following set of optimal hyperparameters for our model: a) 2 LSTM layers, each with a size of 256. b) To output with an estimation of mean, 5 fully connected layers with each of size (260, 128, 128, 128, 128, 1) and SELU as activation function are applied. c) To output with an estimation of standard deviation, 5 fully connected layers with sizes (260, 128, 128, 128, 128, 1) and SELU as activation function are applied, with an additional soft-plus operation that converts the output to be positive. d) The encoder length is 24 h e) The decoder length is 10 h.

The detailed script that defines the model structure and weighted sampler can be found in the file uploaded in the figshare archive.

frontiers | Frontiers in Astronomy and Space Sciences

TYPE Original Research
PUBLISHED 11 September 2023
DOI 10.3389/fspas.2023.1232702

OPEN ACCESS

EDITED BY
Xiao-Jia Zhang,
The University of Texas at Dallas,
United States

REVIEWED BY
Hong Zhao,
Auburn University, United States
Ruoxian Zhou,
Wuhan University, China

*CORRESPONDENCE
Qianli Ma,
qianlima@ucla.edu

RECEIVED 01 June 2023
ACCEPTED 11 August 2023
PUBLISHED 11 September 2023

CITATION
Ma Q, Chu X, Ma D, Huang S, Li W, Bortnik J and Shen X-C (2023), Evaluating the performance of empirical models of total electron density and whistler-mode wave amplitude in the Earth's inner magnetosphere. *Front. Astron. Space Sci.* 10:1232702. doi: 10.3389/fspas.2023.1232702

Evaluating the performance of empirical models of total electron density and whistler-mode wave amplitude in the Earth's inner magnetosphere

Qianli Ma[1,2]*, Xiangning Chu[3], Donglai Ma[2], Sheng Huang[1], Wen Li[1], Jacob Bortnik[2] and Xiao-Chen Shen[1]

[1]Center for Space Physics, Boston University, Boston, MA, United States, [2]Department of Atmospheric and Oceanic Sciences, University of California, Los Angeles, Los Angeles, CA, United States, [3]Laboratory for Atmospheric and Space Physics, University of Colorado Boulder, Boulder, CO, United States

Empirical models have been previously developed using the large dataset of satellite observations to obtain the global distributions of total electron density and whistler-mode wave power, which are important in modeling radiation belt dynamics. In this paper, we apply the empirical models to construct the total electron density and the wave amplitudes of chorus and hiss, and compare them with the observations along Van Allen Probes orbits to evaluate the model performance. The empirical models are constructed using the Hp30 and SME (or SML) indices. The total electron density model provides an overall high correlation coefficient with observations, while large deviations are found in the dynamic regions near the plasmapause or in the plumes. The chorus wave model generally agrees with observations when the plasma trough region is correctly modeled and for modest wave amplitudes of 10–100 pT. The model overestimates the wave amplitude when the chorus is not observed or weak, and underestimates the wave amplitude when a large-amplitude chorus is observed. Similarly, the hiss wave model has good performance inside the plasmasphere when modest wave amplitudes are observed. However, when the modeled plasmapause location does not agree with the observation, the model misidentifies the chorus and hiss waves compared to observations, and large modeling errors occur. In addition, strong (>200 pT) hiss waves are observed in the plumes, which are difficult to capture using the empirical model due to their transient nature and relatively poor sampling statistics. We also evaluate four metrics for different empirical models parameterized by different indices. Among the tested models, the empirical model considering a plasmapause and controlled by Hp* (the maximum Hp30 during the previous 24 h) and SME* (the maximum SME during the previous 3 h) or Hp* and SML has the best performance with low errors and high correlation coefficients. Our study indicates that the empirical models are applicable for predicting density and whistler-mode waves with modest power, but large errors could occur, especially near the highly-dynamic plasmapause or in the plumes.

KEYWORDS

empirical model, total electron density, chorus wave amplitude, hiss wave amplitude, error metric, radiation belt, space weather prediction

1 Introduction

The dynamic evolution of Earth's outer radiation belt electron fluxes is strongly affected by whistler-mode waves and the cold electron density through the wave-particle interaction processes (Thorne et al., 2021). After the electrons are injected from the nightside plasma sheet, whistler-mode chorus waves scatter the energetic electrons at ~1–100 keV energies, causing their fluxes to decay along the drift trajectory in the magnetosphere and precipitate them into the Earth's upper atmosphere (Thorne et al., 2010; Tao et al., 2011; Ma et al., 2012). Following the commencement of geomagnetic storm and the subsequent substorms, chorus waves accelerate relativistic electrons at ~100 s keV - 10 MeV energies to build up the Earth's outer radiation belt (Reeves et al., 2013; Thorne et al., 2013; Li et al., 2016b; Ma et al., 2018). Hiss waves in the plasmasphere and plumes scatter the electrons at ~10 keV–1 MeV energies, causing the radiation belt electron flux to decay during the storm recovery phase (Ni et al., 2013; Ma et al., 2016a). The energy-dependent slot region forms between the inner and outer radiation belts due to the dominant pitch angle scattering loss by hiss (Reeves et al., 2016; Ripoll et al., 2016; Zhao et al., 2019). The total electron density affects the electron resonance energy due to chorus and hiss waves and the efficiencies of pitch angle scattering and acceleration (Summers et al., 2007).

Whistler-mode chorus waves are commonly observed in the low-density plasma trough over the nightside-dawn-dayside magnetic local time (MLT) sectors (Li et al., 2009; Meredith et al., 2012; 2020; Agapitov et al., 2013). Chorus waves on the nightside are strong near the equator, and the waves on dayside have a broad latitudinal coverage with maximum power observed at off-equatorial latitudes (Agapitov et al., 2018). Chorus waves are generated by the unstable anisotropic hot electrons injected from the nightside plasma sheet (Li et al., 2008; Fu et al., 2014), with wave intensities closely related to electron injection events (Kasahara et al., 2009; Ma J. et al., 2022). The statistical wave power is well correlated with the auroral electrojet index of AE or AL, which indicates the strength of substorm injections. Chorus waves with high magnetic power are mainly observed to be quasi-parallel propagating. Another group of highly oblique chorus waves have high occurrence rates over the nightside-dawn sector close to the Earth (Li et al., 2016a).

Hiss waves are commonly observed in the high-density plasmasphere and plumes in the dayside and afternoon sectors (Summers et al., 2008; Li et al., 2015; Meredith et al., 2018; Kim and Shprits, 2019; Zhang et al., 2019). The major sources of hiss include the wave amplification by anisotropic electron distributions in the plumes or near the outer edge of the plasmasphere (Chen et al., 2012a; 2014; Li et al., 2013), the chorus waves propagating into the plasmasphere from the plasma trough (Bortnik et al., 2008; 2009; Meredith et al., 2021), and the lightning generated whistlers leaking from the ionosphere to the magnetosphere at low L shells (Sonwalkar and Inan, 1989; Bortnik et al., 2003; Meredith et al., 2006). The statistical wave power is stronger during more disturbed geomagnetic conditions (Kim et al., 2015; Spasojevic et al., 2015). The density structures in the outer plasmasphere or plumes modulate the hiss wave intensity (Malaspina et al., 2016; Li et al., 2019; Shi et al., 2019). In addition to the preferred wave amplification regions, the wave propagation could be focused, and enhanced in local high-density regions (Chen et al., 2012b).

Using multiple satellite mission data in the magnetosphere, previous statistical studies have revealed the global distribution of wave power and their dependence on geomagnetic activities. The empirical models are widely used to construct the global wave distributions and simulate the radiation belt electron evolution (Horne et al., 2013; Glauert et al., 2014; Drozdov et al., 2015; Ma et al., 2015). The radiation belt simulation using empirical wave models could produce a reasonable estimate of the electron flux decay and acceleration over a period longer than several days. However, event-specific wave distributions from *in situ* observations or other techniques are required to simulate the dynamic electron evolution in a short timescale or during high geomagnetic activities (Li et al., 2016b; Ma et al., 2018).

In this paper, we evaluate the performance of empirical models of total electron density and amplitudes of whistler-mode chorus and hiss waves in the Earth's inner magnetosphere. Section 2 presents two events of total electron density and whistler-mode waves observed by Van Allen Probes. Section 3 presents the empirical model based on the statistics of the Van Allen Probes dataset, and the data distribution comparison between observation and modeling. Section 4 compares the performance of different models using error metrics and the Pearson correlation coefficient. Finally, in Section 5, we summarize and discuss our results.

2 Van Allen Probes observation of total electron density and whistler-mode waves

We use Van Allen Probes (RBSP) measurements (Mauk et al., 2013) to obtain the total electron density (N_e) and whistler-mode wave amplitudes (B_w) at $L < 6.5$ in the Earth's inner magnetosphere. The Electric and Magnetic Field Instrument Suite and Integrated Science (EMFISIS) measures the DC magnetic fields and the AC signals of wave electric and magnetic fields over a broad frequency range (Kletzing et al., 2013). The background magnetic fields in three orthogonal directions are measured by the fluxgate magnetometer. The wave electric and magnetic power spectral densities at 10 Hz–12 kHz frequencies are measured by the Waveform Receiver (WFR), which also provides the wave polarization properties, including the wave normal angle, ellipticity, and planarity, calculated using the Singular Value Decomposition (SVD) method (Santolík et al., 2003). The High Frequency Receiver (HFR) measures the wave electric power spectral density from 10 kHz to 400 kHz, capturing the upper hybrid resonance band waves. The total electron density is calculated using the measured upper hybrid resonance frequency (Kurth et al., 2015). We also use the total electron density inferred using the spacecraft potential measured by the Electric Field and Waves (EFW) instrument (Wygant et al., 2013) when the upper hybrid resonance frequency is unavailable from HFR measurements. The density measurements from EFW have been calibrated against the more accurate EMFISIS density measurements (Breneman et al., 2022). We use the L shell from TS05 magnetic field model (Tsyganenko and Sitnov, 2005), provided by the ephemeris data products of Van Allen Probes.

In this section, we describe the total electron density and whistler-mode wave measurements during two events when Van Allen Probes apogees were at different MLTs. Then, we will compare modeling and observation during the two events in Section 3.3.

2.1 Observations on 01 March 2023

Figure 1 shows the total electron density and whistler-mode waves measured over a full day by Van Allen Probe A (panels C–F) and Probe B (panels G–J) on 01 March 2013. Figure 1A shows the geomagnetic *Hp30* index (black) and *Hp** values (blue). The *Hp30* index is analogous to the *Kp* index but has a 30-min resolution (Matzka et al., 2022), and we define *Hp** as the maximum *Hp30* index during the previous 24 h. The 24 h timescale is chosen following the plasmapause models by Carpenter and Anderson (1992) and O'Brien and Moldwin (2003). Figure 1B shows the SuperMAG (Gjerloev, 2012) Auroral Electrojet index *SML* and the negative of *SME**, where *SME** is defined as the maximum *SME* index during the previous 3 h. The *SML* and *SME* indices are derived using SuperMAG magnetometer chains from more than 100 sites, and can more accurately indicate the substorm activity than auroral electrojet indices *AL* and *AE* (Newell and Gjerloev, 2011). A modest geomagnetic storm occurred on 01 March 2013, as analyzed by Ma et al. (2016b) and Bortnik et al. (2018). The maximum *Hp30* index was close to 6, and the minimum *SML* index was about −1,400 nT, indicating a disturbed geomagnetic condition and particle injection activities.

The Van Allen Probes apogees were on the nightside (Figures 1C, G), suitable for measuring the whistler-mode chorus waves during this event. The measured total electron densities (Figures 1D, H) show a clear plasmapause structure with a large density gradient, the separation of the dense plasmasphere (blue) and tenuous plasma trough (black). Using the method described by Ma et al. (2021), we identified the high-density region (blue), including the plasmasphere and plumes, and the low-density region (black) of the plasma trough. We traced the density variations from perigee to apogee for each half orbit of the spacecraft. The region is first flagged as high-density from perigee. A low-density flag is triggered when a large value of negative density gradient is observed, and then a high-density flag is triggered when a large value of positive density gradient is observed. The densities inside identified high- and low-density regions are further compared to the empirical models to confirm the results. The detailed criteria are described by Ma et al. (2021) and not repeated here. The density data were averaged into a 1-min time cadence which is used in the statistical analysis in the following sections.

The wave magnetic power spectrograms (Figures 1E, I) show intense chorus waves at frequencies above (upper-band) and below (lower-band) 0.5 f_{ce}, where f_{ce} is the equatorial electron gyrofrequency. The chorus waves were observed over a wide range of MLTs on the nightside. The hiss waves at frequencies from ~50 Hz to 1 kHz were observed mainly at $L < 3.5$ during this event, with weaker intensities compared to the chorus. We selected the whistler-mode wave intensities from the wave power spectrograms at frequencies from 20 Hz (or the equatorial proton gyrofrequency f_{cp} when $f_{cp} >$ 20 Hz) to f_{ce} (or 10 kHz when $f_{ce} > 10$ kHz). In addition, we excluded the highly oblique magnetosonic waves by requiring that the wave ellipticity is greater than 0.5, the wave normal angle is below 80°, and the wave planarity is above 0.2. The chorus and hiss wave amplitudes were calculated in both the low-density and high-density regions, respectively, as shown by the black and blue lines in Figures 1F, J. During this event, the peak of chorus wave amplitude reached about 500 pT, and the hiss waves had weak amplitudes of tens of pT. We calculated the root-mean-square (RMS) wave amplitudes during each 1-min time cadence for statistical purposes.

2.2 Observations on 02 September 2013

Figure 2 shows the density and waves measurements made over a full day by Van Allen Probe A (panels C–F) and Probe B (panels G–J) on 02 September 2013. The maximum Hp30 index (Figure 2A) was 4, and the minimum *SML* index (Figure 2B) was about −900 nT, indicating a modestly disturbed geomagnetic condition.

The Van Allen Probes apogees were located on the dusk side (Figures 2C, G), which is suitable for measuring the plasmaspheric plumes and hiss waves during this event, as analyzed by Li et al. (2019). The measured total electron densities (Figures 2D, H) show evident density perturbations during each orbit of Van Allen Probes except for the Probe B observation after 16:00 UT. For example, during 13–21 UT, Figure 2D shows that Van Allen Probe A first traveled from the plasmasphere (blue) to the plasma trough (black), encountered plumes (blue) during 16:00–18:30 UT, and then traveled from the plasma trough (black) back to the plasmasphere (blue). The density measurements on different orbits suggest a highly dynamic variation of the plume on the dusk side.

Figures 2E, I show hiss wave activities with extended coverage in the high-density plasmasphere and plumes. The hiss waves at frequencies of ~50 Hz–1 kHz are correlated with the high-density region, both during the extended plume period of 16:00–18:30 UT measured by Van Allen Probe A (Figures 2D, E) and for the short periods of density variations during 01–04 UT measured by Van Allen Probe B (Figures 2I, J). The magnetosonic waves were also observed below 50 Hz during 6–7 UT by Probe A (Figure 2E) and during 7–9 UT by Probe B (Figure 2I), but they were excluded from our wave data using the spectral criteria described above. The chorus waves were observed in the plasma trough during 19:00–22:30 UT by Probe B (Figure 2I). Figures 2F, J show that the peaks of hiss wave amplitudes (blue) are about 100 pT both in the plasmasphere and plumes.

3 Empirical model

3.1 Development of the empirical model

In previous studies, the surveys of whistler-mode chorus and hiss waves were usually modeled separately, and the full *L*-MLT distributions of both chorus and hiss waves were parameterized for different solar wind or geomagnetic conditions. However, the chorus and hiss waves are usually separated in space, with the chorus observed in the low-density plasma trough and the hiss observed in the high-density plasmasphere or plumes (e.g., Meredith et al., 2018; 2020). Therefore, an additional model of the

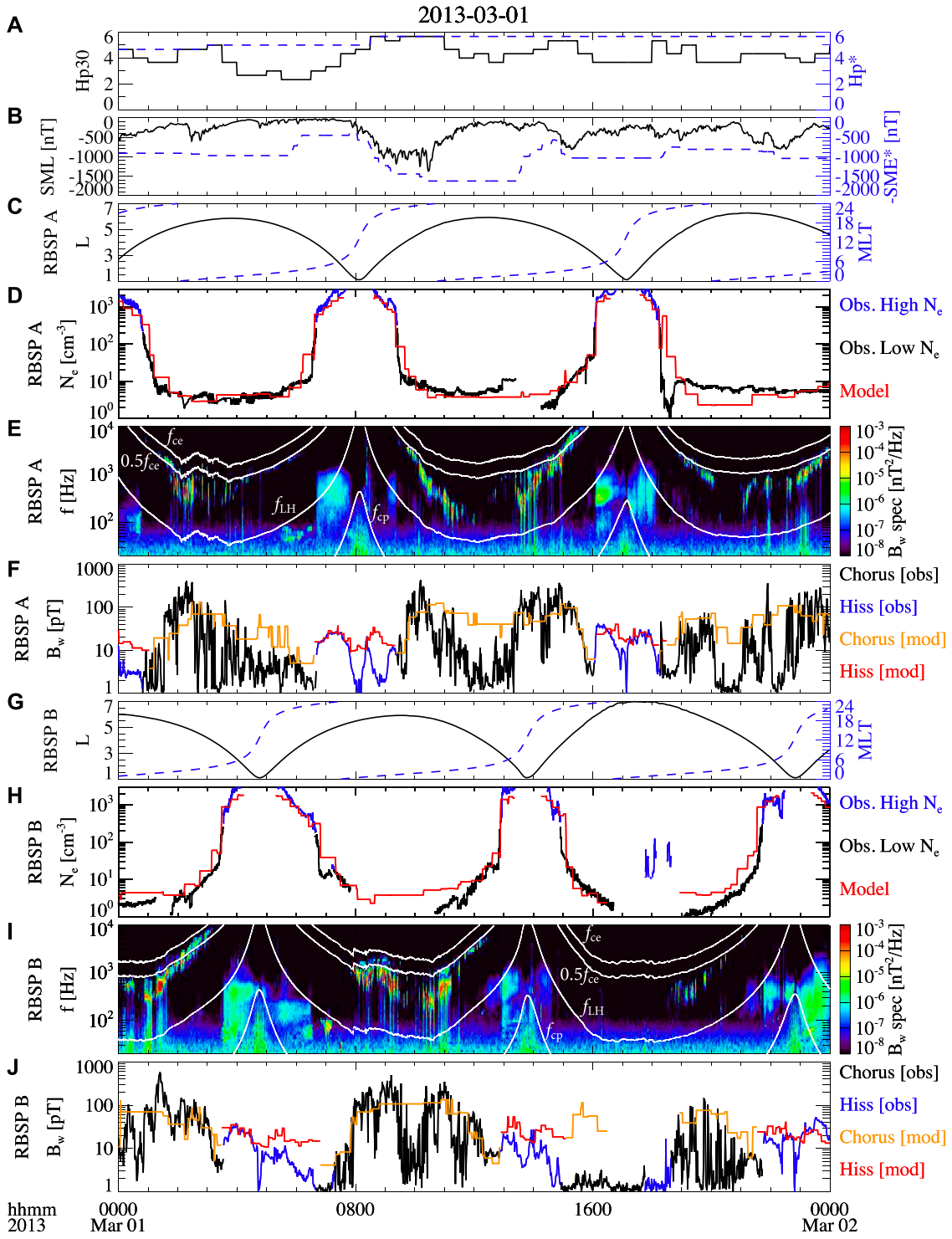

FIGURE 1
Van Allen Probes observation and empirical modeling of the total electron density and whistler-mode chorus and hiss waves on 01 March 2013. **(A)** Geomagnetic *Hp30* index and *Hp**, which is the maximum *Hp30* index during the previous 24 h; **(B)** geomagnetic *SML* index and *SME**, which is the maximum *SME* index in the previous 3 h; **(C)** *L* shell and MLT of Van Allen Probe A; **(D)** total electron densities observed by Van Allen Probe A in the high-density plasmasphere or plume (blue) and in the low-density plasma trough (black), and produced by the empirical model (red); **(E)** magnetic power spectrogram at 20 Hz–10 kHz frequencies observed by Van Allen Probe A, where the four white lines are equatorial electron gyrofrequency (f_{ce}), 0.5 f_{ce}, lower hybrid resonance frequency (f_{LH}), and proton gyrofrequency (f_{cp}); **(F)** chorus (black) and hiss (blue) wave amplitudes observed by Van Allen Probe A, and chorus (orange) and hiss (red) wave amplitudes produced from the empirical model. **(G–J)** Same as **(C–F)** except for the density and waves along the trajectory of Van Allen Probe **(B)**.

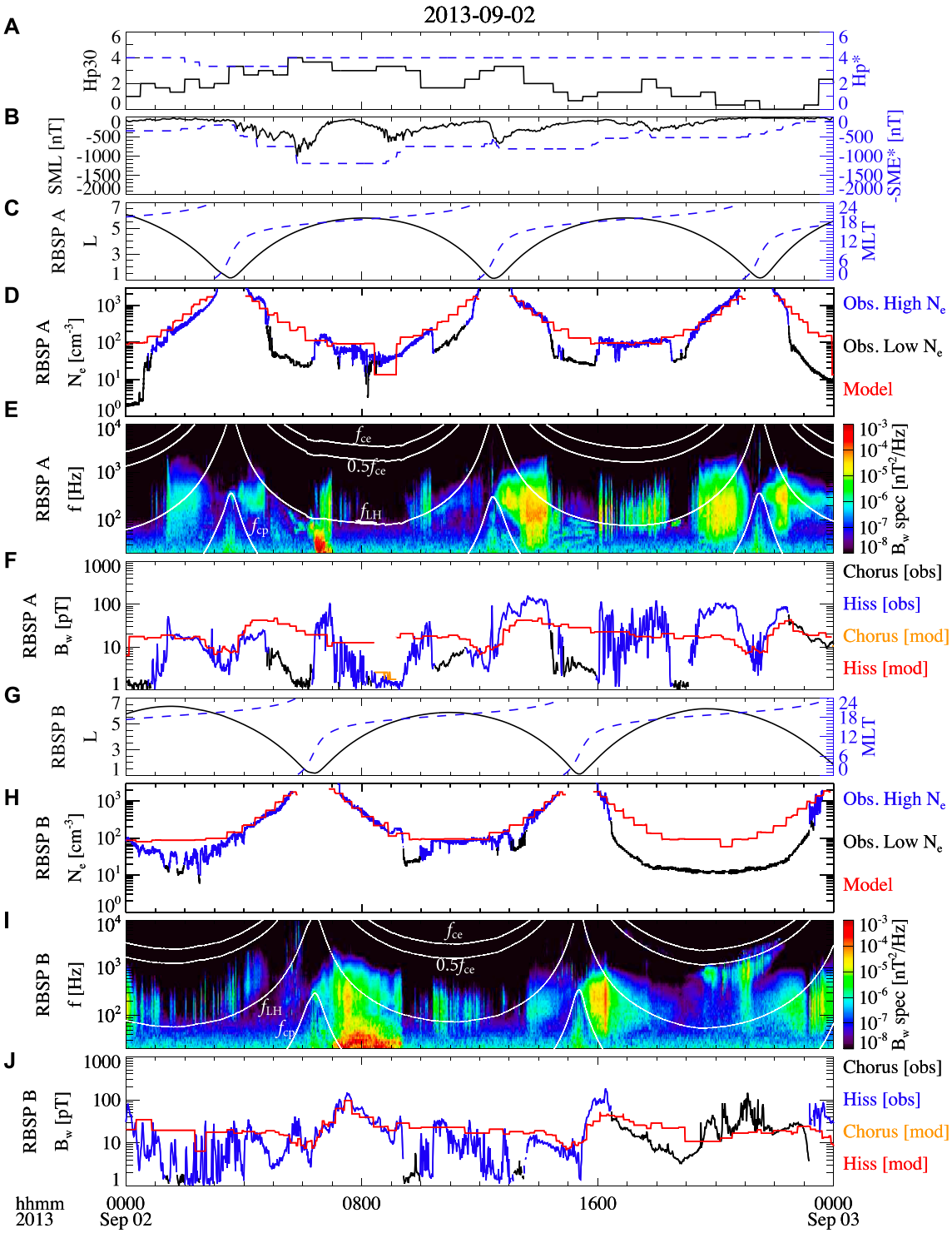

FIGURE 2
Same as Figure 1 except for the event on 02 September 2013.

plasmapause location or plasma density is required to construct the global distributions of chorus and hiss using the previous models.

We performed a survey using a unified dataset to analyze the total electron density, chorus wave amplitudes, and hiss wave amplitudes. This approach allowed us to construct consistent statistical distributions among them. Van Allen Probes measurements from September 2012 to October 2019 were used. To obtain the global distributions, we selected data when the magnetic latitude was within 10° from the magnetic equator. The

survey of total electron density was performed at $2 < L < 6.5$, considering that the density at $L < 2$ may not be reliable when the upper hybrid resonance frequency is higher than 500 kHz (Hartley et al., 2023). Surveys of chorus and hiss were performed at $1 < L < 6.5$. The whistler-mode waves at $L < 2$ were identified as hiss throughout our survey. The data of average density and root-mean-square wave amplitudes were binned in every 1 h MLT and 0.5 L shell.

We used the combination of Hp^* and SME^* (or SML) indices to categorize the statistical distributions of the total electron density, chorus wave amplitude, and hiss wave amplitude. The plasmapause location in L-MLT was previously fitted as a function of the maximum Kp index in the previous 24–36 h by O'Brien and Moldwin (2003). The large amplitude chorus waves were generally found to be correlated with electron injections. The hiss waves are also related to the AE index, and were previously categorized by AE^* by Li et al. (2015). Using the combination of Hp^* and SME^* or Hp^* and SML, the model may better capture the plasmapause location and the wave activity. We set 7 levels of Hp^* ($Hp^* \leq 1$, $1 < Hp^* \leq 2$, $2 < Hp^* \leq 3$, … $Hp^* > 6$), and up to 4 levels of SME^* (or SML) within each range of Hp^*. The ranges of SME^* (or SML) were set so that the data sample number is sufficient in each combination of Hp^* and SME^* (or SML), and the possible variation of SME^* (or SML) is captured.

Using the Van Allen Probes dataset, we first obtained the occurrence rates of high-density (plasmasphere or plume) and low-density (plasma trough) flags in each L-MLT bin under each category of Hp^* and SME^*. Then, to construct a deterministic empirical model, we set the regions with a high-density occurrence rate higher than 0.5 to be the modeled plasmasphere or plume, and the regions with a low-density occurrence rate higher than 0.5 to be the modeled plasma trough.

The total electron densities with a high-density flag (blue) or a low-density flag (black) in Figures 1D, H, 2D, H were averaged in each L-MLT bin under each combination of Hp^* and SME^*. To construct the global density distribution, we used the average densities in the high-density region as the densities in the modeled plasmasphere or plume, and the average densities in the low-density region as the densities in the modeled plasma trough.

Similar to the density, we obtained the root-mean-square amplitudes of chorus and hiss waves in each L-MLT bin under each geomagnetic condition. To construct the global distributions for a certain geomagnetic condition, we assigned the chorus wave amplitudes in the modeled plasma trough, and hiss wave amplitudes in the modeled plasmasphere or plume. The modeled chorus and hiss waves are well separated in the space. Note that the chorus and hiss waves could be modeled using different parameters after the low- and high-density regions were modeled. For example, we first identified the high- and low-density flags using Hp^* and SME^* indices, and used Hp^* and SML to model chorus in the high-density regions and Hp^* and SME^* to model hiss in the low-density regions. The model performances for different parameters are discussed in Section 4. The performance of the chorus wave amplitude model using Hp^* and SML is found to be close to the performance of the model using Hp^* and SME^*.

3.2 Statistical distributions

Figure 3 shows the statistical distributions of the total electron density (panels A–D), chorus wave amplitude (panels E–H), and hiss wave amplitude (panels I–L) for the selected Hp^*, SME^*, and SML conditions. The sample numbers are shown in Figures 3M–T. The chorus waves are shown in the modeled plasma trough region, and hiss waves are shown in the modeled plasmasphere or plume. During quiet times (Figures 3A, E, I), the modeled plasmapause is mainly located at $L > 6.5$, and thus the densities mainly represent the plasmaspheric density, and the hiss waves are widely distributed at $L < 6.5$, consistent with an extended plasmasphere region. As geomagnetic conditions become more disturbed, the total electron densities are eroded over the nightside-dawn-dayside sectors, showing an MLT-dependent plasmapause. The high density in the dusk sector during the disturbed time (Figure 3D) includes the data samples of plumes or extended plasmasphere compared to other MLTs. The chorus wave power is enhanced over the nightside-dawn-dayside sectors as the geomagnetic activity becomes more disturbed (Figures 3F–H). Figures 3I–L show that the hiss wave powers are enhanced on the dayside and the dusk side at high L shells when Hp^* and SME^* increase, although the overall spatial coverage becomes more limited due to the erosion of the plasmapause. The statistical distributions of total electron density and whistler-mode waves are consistent with the previous survey results (e.g., Sheeley et al., 2001; Li et al., 2009; 2015; Meredith et al., 2018; 2020). Compared to the mean values, the standard deviation of total electron density is generally lower than the mean value, while the standard deviations of chorus and hiss wave amplitudes could be comparable or larger than the mean values (Supplementary Figure S1). Although the distributions under 4 conditions of Hp^* and SME^* (or SML) are shown in Figure 3, the empirical models cover all geomagnetic conditions and the full models are provided in the data repository.

3.3 Comparison between observation and modeling during the events

For a given value of Hp^* and SME^* (or SML) at a specific time, the empirical model provides the distribution of density and whistler-mode waves on a global scale by selecting data from the corresponding geomagnetic categories. The total electron density and whistler-mode wave amplitudes were modeled along the L shell and MLT of Van Allen Probes from September 2012 to October 2019. The modeled results were produced at $2 < L < 6.5$ for the density and $1 < L < 6.5$ for the wave amplitudes at a 1-min time cadence to compare with the observation. It is worth noting that the empirical model was developed using the data samples within 10° from the equator, while the Van Allen Probes measurements had additional sampling at latitudes up to 20°.

Figures 1D, F, H, J show the comparison between observation and modeling on 01 March 2013, when the Van Allen Probes apogees were on the nightside. The model (red) well captures the location of plasmapause and the density values in the plasmasphere and plasma trough (Figures 1D, H). The modeling was not performed during 16:30–19:00 UT on Van Allen Probe B (Figure 1H) because the L shell was larger than 6.5. The wave mode of chorus (orange) or hiss (red) is also correctly identified

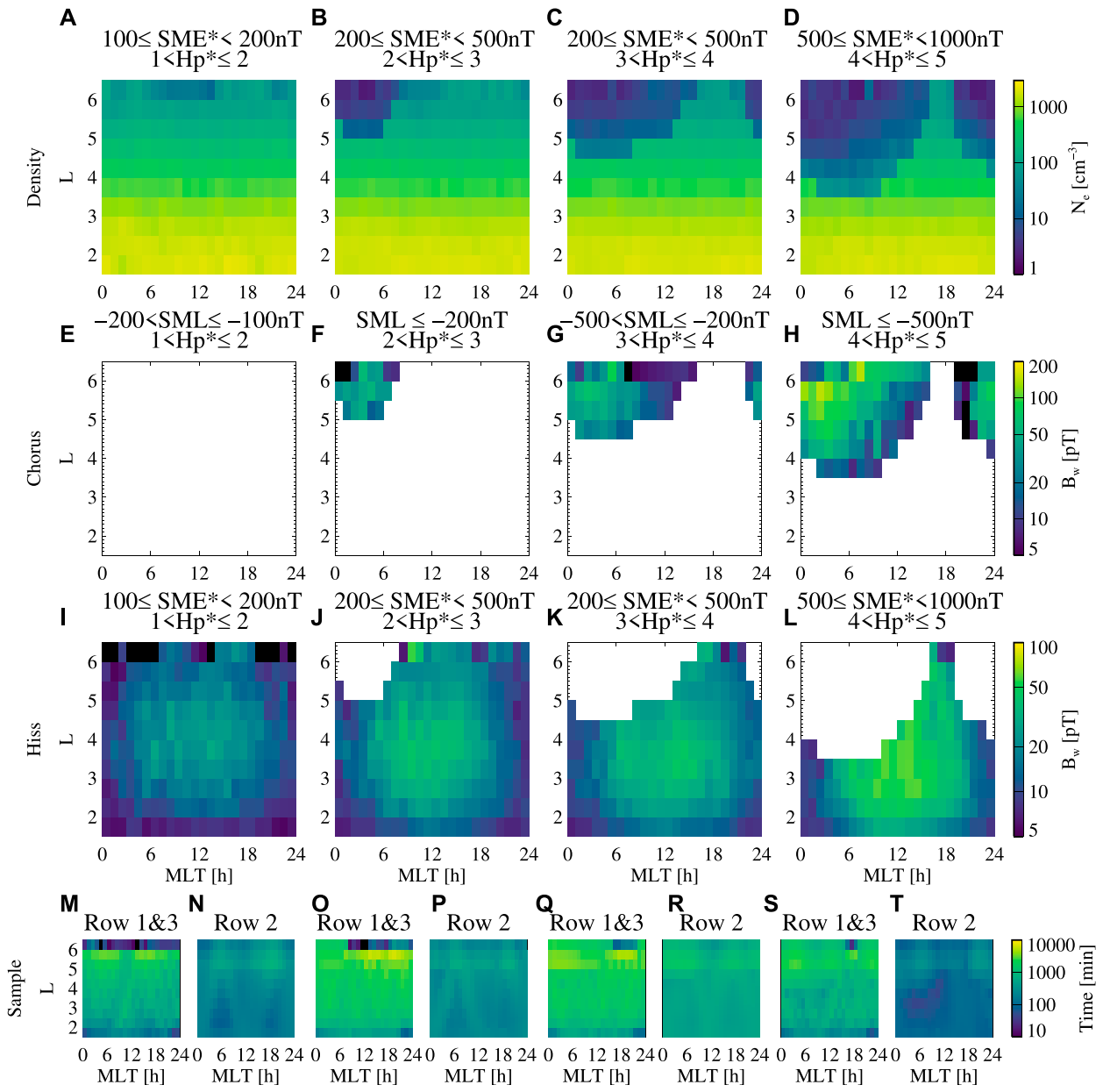

FIGURE 3
Statistical surveys of average total electron density **(A–D)**, and root-mean-square amplitude of chorus **(E–H)** and hiss **(I–L)** as a function of MLT and *L* shell, categorized by different *Hp** and *SME** or *Hp** and *SML* indices. **(M)** Total sample time under the geomagnetic condition for total electron density (Row 1, Panel A) or hiss (Row 3, Panel I), and **(N)** total sample time under the geomagnetic condition for chorus (Row 2, Panel E). **(O–T)** Same as **(M,N)** except for different geomagnetic conditions. **(E–H)** only show the data in the region where the low-density occurrence rate is higher than the high-density occurrence rate; **(I–L)** only show the data in the region where the high-density occurrence rate is higher.

by the model (Figures 1F, J). Overall, the observations of chorus (black) and hiss (blue) show larger wave amplitude fluctuations than the modeling. The modeled chorus and hiss waves are persistently present in the low- and high-density regions, respectively, and may not reproduce the strong bursts or rapid disappearance of the observed waves. The large discrepancies are found at the peak of observed wave amplitude or when the whistler-mode waves were absent, i.e., at the extreme amplitudes. The modeling significantly overestimates the observed chorus waves during 15:00–16:30 UT observed by Probe B (Figure 1H), but the satellite was at high latitudes before traveling towards $L \sim 7$, and the chorus waves were possibly damped in the nightside high-latitude region.

Figures 2D, F, H, J show the comparison on 02 September 2013 when the satellite apogees were on the dusk side. Plasmaspheric plumes were observed by Van Allen Probes (blue), which were not captured by the modeling. In Figure 2D, the modeling (red) shows the density structures of the plasmasphere and plasma trough during 04–12 UT, and only the plasmasphere during 13–21 UT. The

modeling agrees with the observation when the high- and low-density regions are identified correctly.

Because the high- and low-density regions are potentially mis-identified by the model, the model predicts hiss waves when chorus waves are observed, and *vice versa*. The discrepancies in the wave amplitude modeling are larger than those in Figure 1 due to the mis-identification of the wave modes. For example, after 22:30 UT in Figure 2F, the observation shows that chorus $B_w > 10$ pT and hiss $B_w = 0$, and the modeling suggests that chorus $B_w = 0$ and hiss $B_w > 10$ pT. This causes an additional major source of modeling error, especially for the waves inside and near the plumes, in addition to the error sources found in Figure 1.

The two events in Figures 1, 2 are examples for the good model performance and for the potential issue in the empirical modeling, respectively, The plasmasphere was compressed to $L \lesssim 3$ during the event on 01 March 2013 (Figure 1), but the plasmapause structure was clear and the satellite did not observe plume structures. The modelled density agrees with the observation since the modeled plasmapause location was accurate. Plasmaspheric plumes were observed at the afternoon sector near the satellite apogee during the event on 02 September 2013 (Figure 2). Because the plasmaspheric plumes are highly dynamic and cause large density variations, they are less predictable using an empirical model which assumes a static state for a certain geomagnetic condition category. Machine learning technique may improve the performance for the electron densities during plasmaspheric plume activities.

3.4 Comparision of data distributions from observation and modeling

We compare the data distribution from observations and modeling using the ~7-year dataset at 1-min time cadence. In this comparison and the evaluation of modeling performance discussed in Section 4, we only used the data when the Van Allen Probes were located within 10° from the equator. The entire dataset including all geomagnetic conditions is compared in Figure 4.

Figures 4A, D, G show the average total electron density, RMS amplitude of chorus, and RMS amplitude of hiss wave as a function of L. The observation generally agrees with the modeling results. The high- and low-density regions were modeled using a criterion of occurrence rate at 0.5 (see Section 3.1), causing the slight overestimate (underestimate) of chorus (hiss) B_w at $L > 4.5$, and slight underestimate (overestimate) of chorus (hiss) B_w at $L < 4.5$. If the average density and RMS B_w were weighted by the occurrence rates of high- and low-density regions in the models, the modeling would perfectly match the observation. However, such a model would not be very useful because it mixes the plasmasphere and plasma trough densities, and the modeled chorus and hiss waves appear simultaneously.

Figure 4B shows the probability density function (PDF) between the modeled and observed total electron densities. Most of the data are distributed around the diagonal line, suggesting a good model performance. The overall Pearson correlation coefficient (R) is 0.89. To examine the modeled data distribution for a fixed observation, Figure 4C shows the PDF divided by the sum of probability density in each range of observed N_e, denoted as the normalized PDF. The total normalized PDF for each range of observation is 1, so the good model will show a normalized PDF of ~0.5–1 along the diagonal line. Figure 4C indicates good model performance when the observed density is higher than 100 cm^{-3}. The modeled data shows a wide spread for the observed densities from 10 cm^{-3} to 100 cm^{-3}, suggesting a large deviation at and near the plasmapause or plumes. For the observed densities below 10 cm^{-3}, the modeled density is mainly at 3–10 cm^{-3}, suggesting that the model correctly identifies the low-density region of the plasma trough, but the modeled density is overall higher than the observation when the observed density is below 3 cm^{-3}.

Figure 4E shows the probability density function for chorus waves. The modeled and observed chorus waves with 0 pT amplitude, including the high-density region data (chorus $B_w = 0$) in the modeling and observation, are included at $B_w < 2$ pT bins, and considered when evaluating the model performance. The high PDF at observed $B_w < 2$ pT and modeled $B_w < 2$ pT suggests that the majority of the plasmasphere regions are correctly modeled. A second group of data are found at observed $B_w > 2$ pT and modeled $B_w < 2$ pT, representing the times when the satellite was outside the plasmapause and observed chorus wave activity while the model suggests a high-density region. Similarly, the group of data at observed $B_w < 2$ pT and modeled $B_w > 2$ pT represents the times when the satellite was inside the plasmapause or chorus was not observed outside the plasmapause, while the model suggests a low-density region with chorus wave activity. Figure 4F shows the normalized PDF for each range of observed chorus B_w. The model underestimates the strong chorus wave amplitudes for observed $B_w >$ 100 pT; specifically, the model most likely predicts a wave amplitude of 100–200 pT for the observed wave amplitude of 500–1,000 pT. The model provides a good estimate of the chorus wave amplitude for the observed chorus B_w from 10 pT to 100 pT. For the weak chorus waves with $B_w < 10$ pT, the model most likely overestimates the observation with modeled B_w of 10–20 pT. The overall Pearson correlation coefficient for chorus B_w is 0.67, which is lower than that of the density model. The correlation coefficient is affected by the groups of data at observed $B_w > 2$ pT and modeled $B_w < 2$ pT, and at observed $B_w < 2$ pT and modeled $B_w > 2$ pT; i.e., the R is strongly affected by the mis-identification of the plasmasphere or plasma trough.

Figure 4H shows the probability density function for hiss. The data distribution and scattering are similar to those of the chorus waves, while the amplitudes of observed and modeled hiss waves are overall lower than those of chorus. The group of data at observed $B_w > 2$ pT and modeled $B_w < 2$ pT represents the times when the spacecraft was in the high-density region and the model suggests a low-density region. The data group at observed $B_w < 2$ pT and modeled $B_w > 2$ pT represents the times when the spacecraft was in the low-density region or hiss was not observed, while the model suggests hiss wave activity in a high-density region. The normalized PDF distribution (Figure 4I) suggests that the modeling agrees with observation for observed B_w from 10 pT to 50 pT, underestimates for observed $B_w > 50$ pT, and overestimates for observed $B_w <$ 10 pT. In addition, another evident group of data is found for observed $B_w > 200$ pT and modeled $B_w < 2$ pT in Figure 4I. The very large amplitude hiss waves, despite their overall low occurrence, are usually observed with large density variations or in the plumes (Shi et al., 2019). The empirical model may not fully capture the density variations, plume structures, or their evolution. Instead,

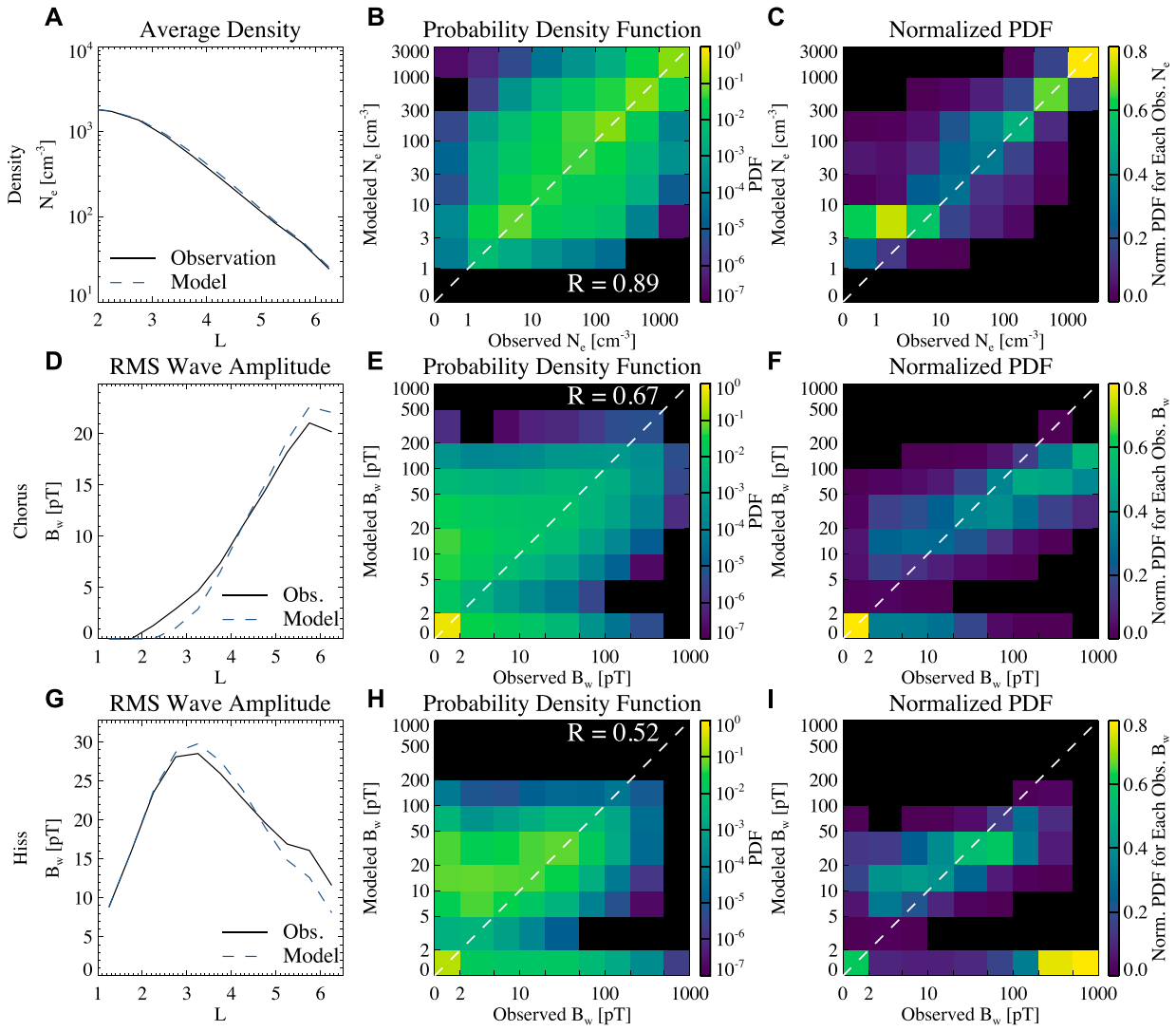

FIGURE 4
The comparison between observation and the empirical model, considering the *Hp**, *SME** index and modeled plasmapause for density and hiss, and considering the *Hp**, *SML* index and modeled plasmapause for chorus. **(A)** The average density as a function of *L*, where the solid and dashed lines are observation and modeling results, respectively; **(B)** probability density distribution as a function of modeled and observed densities; **(C)** probability densities divided by the total probability density within each bin of observed density. **(D–F)** Same as **(A–C)** except for the chorus wave amplitude. **(G–I)** Same as **(A–C)** except for the hiss wave amplitude.

these regions are likely mis-identified as the low-density plasma trough by the model, since the *L* shell of the perturbed density is usually high, and the geomagnetic condition is usually disturbed (Shi et al., 2019). As a result, the empirical model cannot capture the very large amplitude hiss waves. The Pearson correlation coefficient for hiss is 0.53, which is lower than that of chorus.

4 Performance of different models

4.1 Metrics for evaluating the model performance

We further evaluate the model performances using various error metrics and correlation coefficients for different *L* shells. In each *L* shell bin, we consider the data in the range $\Delta L = \pm 0.25$. Following Morley et al. (2018), we consider Mean Absolute Error (MAE), Root Mean Square Error (RMSE), Median Symmetric Accuracy (MSA), and Pearson correlation coefficient. Below we define x as the observed N_e or B_w and y as the modeled N_e or B_w.

We calculate Mean Absolute Error normalized by the average of N_e or RMS of B_w as

$$MAE/Mean = \overline{|y-x|}/\bar{x} \quad \text{for } N_e \tag{1}$$

$$MAE/RMS = \overline{|y-x|}/\sqrt{\overline{x^2}} \quad \text{for } B_w \tag{2}$$

The Root Mean Square Error normalized by the average of N_e or RMS of B_w is calculated as

$$RMSE/Mean = \sqrt{\overline{(y-x)^2}}/\bar{x} \quad \text{for } N_e \tag{3}$$

$$RMSE/RMS = \sqrt{\overline{(y-x)^2}}/\sqrt{\overline{x^2}} \quad \text{for } B_w \tag{4}$$

The Median Symmetric Accuracy is calculated as

$$MSA = 100\left(e^{Median\left(\left|\ln\frac{y}{x}\right|\right)} - 1\right) \quad \text{for } N_e \text{ and } B_w \tag{5}$$

The Pearson correlation coefficient is calculated as

$$R = \frac{\sum(x-\bar{x})(y-\bar{y})}{\sqrt{\sum(x-\bar{x})^2(y-\bar{y})^2}} \quad \text{for } N_e \text{ and } B_w \tag{6}$$

All data, including the observed or modeled $B_w = 0$, are considered in Eqs 1–4, 6. To calculate MSA in Eq. 5, the logarithm function is used, so we consider all density data, and only the wave amplitude data with observed and modeled $B_w > 10$ pT. The good model is evaluated as having low MAE, low RMSE, low MSA, and high R.

Although the MSA cannot be calculated for $B_w = 0$, it provides a symmetric error for underestimate and overestimate in terms of the multiplication factor, while MAE and RMSE provide symmetric errors in terms of the percentage relative to the observation. For example, if $y = 0.5x$, then $MAE = 0.5$, $RMSE = 0.5$, $MSA = 100$; if $y = 2x$, then $MAE = 1$, $RMSE = 1$, $MSA = 100$ (same as for $y = 0.5x$); if $y = 1.5x$, then $MAE = 0.5$ (same as for $y = 0.5x$), $RMSE = 0.5$ (same as for $y = 0.5x$), $MSA = 50$.

4.2 Comparing different models

We evaluate the performances of 6 models categorized by different combinations of *Hp30* or *Hp**, and *SML* or *SME** indices, and the incorporation of the plasmapause. For each model, the surveys of total electron density, chorus wave amplitude, and hiss wave amplitude are performed using the same combination of geomagnetic indices. The statistical methods are the same as those described in Section 3 except for those described below. We perform the surveys of density and wave amplitudes using

- Empirical model 1: use *Hp30* and *SML* indices, and consider the low- and high-density categorizations in the models (same as the density categorization method described in Section 3.1, and denoted as "PP");
- Empirical model 2: use *Hp30* index, and consider the low- and high-density categorizations;
- Empirical model 3: we perform the surveys of density and wave amplitudes using *SML* index, and consider the low- and high-density categorizations;
- Empirical model 4: use *Hp** and *SML* indices, and consider the low- and high-density categorizations;

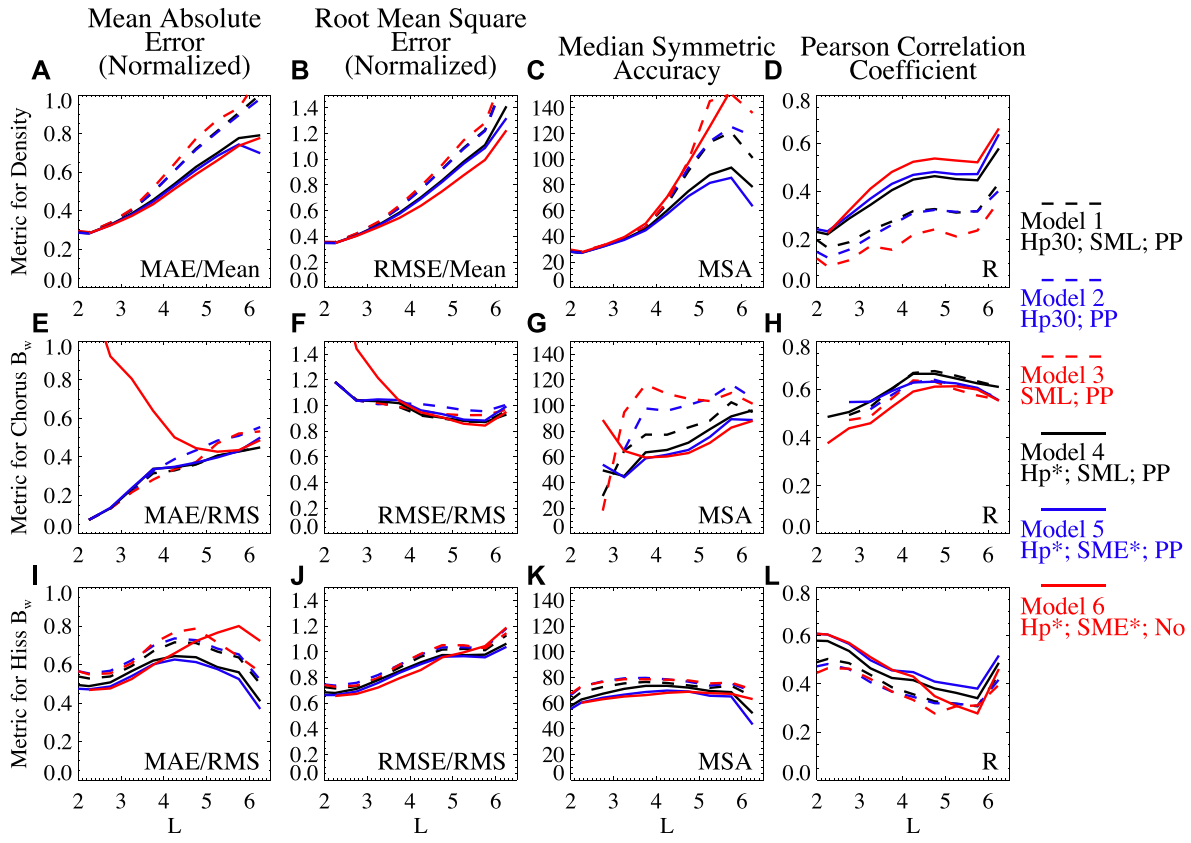

FIGURE 5
The performance of different empirical models evaluated using four metrics for different *L* shells. **(A–D)** Total electron density; **(E–H)** chorus wave amplitude; **(I–L)** hiss wave amplitude. The metrics include: Mean Absolute Error divided by the average of N_e or by the RMS B_w (chorus and hiss); Root Mean Square Error divided by the average of N_e or by the RMS B_w; Median Symmetric Accuracy; Pearson Correlation Coefficient *R*. The different empirical models are illustrated by different line styles or colors.

TABLE 1 The overall performance of different empirical models evaluated using four metrics. The best performance evaluated by each metric is highlighted in bold blue font; the second best is highlighted in blue font; the worst performance is highlighted in bold black font.

Model	Mean absolute error			Root mean square error			Median symmetric accuracy			Pearson correlation coefficient		
	MAE/Mean for N_e MAE/RMS for B_w			RMSE/Mean for N_e RMSE/RMS for B_w			MSA			R		
	Density N_e	Chorus B_w	Hiss B_w	Density N_e	Chorus B_w	Hiss B_w	Density N_e	Chorus B_w	Hiss B_w	Density N_e	Chorus B_w	Hiss B_w
Hp30, *SML*, PP	0.427	**0.366**	0.647	0.72	0.927	0.946	69.5	163	58.8	0.881	**0.679**	0.45
Hp30, PP	0.428	0.433	0.668	0.724	**1.01**	**0.966**	71.1	162	60.2	0.88	0.649	0.441
SML, PP	**0.441**	0.421	0.68	**0.732**	0.976	0.965	77.6	**243**	**61**	**0.876**	**0.634**	**0.432**
*HP**, *SML*, PP	0.398	0.368	0.585	0.697	0.929	0.911	60.8	102	59.4	0.888	0.672	0.491
*HP**, *SME**, PP	**0.393**	0.369	**0.562**	**0.691**	0.945	**0.894**	**57.8**	104	57.1	**0.89**	0.653	**0.517**
*HP**, *SME**, No PP	0.401	**0.451**	**0.682**	0.702	**0.926**	0.908	**84.3**	**89.3**	**51.8**	0.888	0.637	0.475

- Empirical model 5: use *Hp** and *SME** indices, and consider the low- and high-density categorizations;
- Empirical model 6: use *Hp** and *SME** indices; the low- and high-density categorization is not considered, but the model adopts the averages over both low- and high-density conditions weighted by their occurrence rates (denoted as "No PP").

Models 1–3 only use the instantaneous geomagnetic conditions, and models 4–6 also consider the most disturbed *Hp* condition in the past 24 h. Model 6 is equivalent to the method of directly using the models of density, chorus, and hiss waves without imposing a plasmapause. The density and wave models are not coupled, the plasmaspheric density could be mixed with the plasma trough density, and the chorus and hiss wave could appear simultaneously in the same location. For Models 1–5, the empirical model of high- and low-density region is developed using the occurrence rates of high- and low-density flags for each individual model using the corresponding indices.

Figure 5 shows the metrics for different models as a function of the *L* shell. For the total electron density (Figures 5A–D), models 4 and 5 using *Hp** have lower MAE, lower RMSE, lower MSA and higher *R*, than models 1, 2 and 3 using the *Hp30* index. Although model 6 has a slightly lower RMSE and higher *R* than models 4 and 5, the MSA of model 6 is much higher than that of models 4 and 5. The best density model is model 5 using *Hp**, *SME**, and PP, with slightly lower errors and a higher correlation coefficient than model 4. Note that the *R* for the density data in each *L* shell bin is much lower than the overall *R* for all *L* shells (0.89 in Figure 4B). This is because the total electron density has a persistent *L*-dependence with high densities generally at low *L* shells, contributing to the high correlation coefficient when the data at different *L* shells are included in the *R* calculation.

For the chorus B_w (Figures 5E–H), models 4 and 5 have slightly lower MAE and RMSE and slightly higher *R* at $L < 4$ than models 1, 2, and 3, and the improvement evaluated using MSA is significant. The different error trend for MSA compared to MAE or RMSE could be caused by the different penalization rules for underestimate and overestimate, different data samples used for error calculation (see Section 4.1), and non-Gaussian distribution of the data. Although model 6 shows the lowest RMSE and MSA at $L > 3.5$, it has the lowest *R* overall and significantly large MAE at $L < 4$. The best chorus wave models are 4 and 5 considering *Hp**, *SML* (or *SME**), and PP, and the *R* of model 4 is slightly higher than model 5.

For the hiss B_w (Figures 5I–L), models 4 and 5 have slightly lower RMSE and MSA than models 1, 2, and 3, and noticeable improvement evaluated using MAE and *R*. Compared to models 4 and 5, model 6 shows large MAE at $L > 4$ and low *R* at $4 < L < 6$, and the performances at other regions or for other metrics are similar. The best model for hiss is model 5 considering *Hp**, *SME**, and PP, with higher *R* than model 4.

The performances between Model 4 and Model 5 are overall similar. We also performed a modeling using *Hp** and *SME* indices and considering the low- and high-density categories (Supplementary Figure S2). Figure 5 shows slight improvement for modeling hiss B_w when *SME** is considered compared to using *SML*, and the improvement for modeling chorus B_w is also shown by the model comparison between Model 5 and the model using *Hp** and *SME* (Supplementary Figure S2).

The overall metrics for different models of density, chorus B_w and hiss B_w are also tabulated in Table 1, considering the data at all different L shells. Similar to the discussions above, the overall best model is model 4 for the density and hiss and model 5 for chorus, while their performance difference is very small. Significant modeling improvement is obtained using the Hp^* index compared to the *Hp30* index, and considering the low- and high-density categorization in the model.

5 Conclusion and discussions

We evaluated the performance of a number of empirical models describing the total electron density and whistler-mode wave amplitudes in the Earth's inner magnetosphere. The empirical models of density, chorus, and hiss waves were developed using the ~7 years of Van Allen Probes data, categorized using *Hp30*, *SME*, *SML* indices, and their past maximum values, with a classification of high- or low-density regions (i.e., plasmasphere, plume or plasma trough). The models were used to reproduce the density and wave amplitudes along the Van Allen Probes trajectories, and the data distribution was compared between the observation and modeling results. We further used 4 metrics to compare the performances of 6 different models, categorized using different geomagnetic indices or excluding the density region classification. Our model performance evaluation indicates that:

- Incorporating the plasmapause (i.e., classifying the high- and low-density regions) significantly improves the modeling of total electron density as well as the amplitudes of chorus and hiss waves.
- Using the maximum values of geomagnetic indices during the past 3 h for SME and 24 h for Hp30 improves the modeling results compared to using only the instantaneous indices.
- The total electron density is well-modeled with high Pearson correlation coefficients using geomagnetic indices. The model agrees with the observation when the observed $N_e > 3$ cm^{-3} and overestimates for smaller density observations. The additional errors are near the plasmapause or in the plumes, causing the large data spread in the probability density function distribution.
- The amplitudes of whistler-mode chorus and hiss waves are well-modeled when the observed wave amplitudes are moderate, with amplitudes between 10 and 100 pT. For the observed amplitude $B_w < 10$ pT or in the absence of whistler-mode waves, the chorus and hiss models tend to provide the average wave amplitudes, which overestimate the observation. The models underestimate the whistler-mode wave amplitudes when the observed amplitude is intense (>100 pT). The model cannot capture the very large amplitude (>200 pT) hiss waves, probably because these hiss waves are present in the plume region at high L shells during disturbed conditions, which is identified as the plasma trough by the model.
- The mis-identification of the plume region or the errors in identifying the plasmapause boundary causes large errors in modeling chorus and hiss wave amplitudes, because the chorus and hiss waves are mis-labeled by the model.
- To investigate the model performance properly, it is necessary to evaluate multiple error metrics and correlation coefficients. Using a single metric may provide a biased judgment for the model comparison.

Although we evaluated the performances of 6 different models, the chosen 'best' model is not yet optimized. For example, our model comparison mainly focused on the *Hp30* and *SME* (or *SML*) indices and their derivatives, while the impacts of other geomagnetic indices and solar wind parameters have not been investigated. The solar wind dynamic pressure may significantly impact the whistler-mode waves at $L > 6$ due to the compression of the magnetosphere (Zhou et al., 2015; Yue et al., 2017). Following previous studies (O'Brien and Moldwin, 2003; Li et al., 2015), we incorporated the history of *Hp30* and *SME* indices by simply using their maximum values in the past 24 h and 3 h, respectively. The history lengths of the indices are not tested, and the alternative method of using mean values of the indices is not investigated. The model optimization requires significant work efforts for an empirical model. However, the machine learning models inherently optimize the dependences of the model target on the parameters (Bortnik et al., 2016; Chu et al., 2017; 2021; Ma D. et al., 2022; Huang et al., 2022). The test of different empirical models could directly suggest the importance of each parameter, while the machine learning technique is more efficient in providing the best model fit for many parameters.

Our empirical models are developed using the Van Allen Probes data within 10° from the magnetic equator at $L < 6.5$. Additional data from the other spacecraft missions (THEMIS, Cluster, MMS, and Arase) provide the waves and density measurements at higher L shells or higher latitudes. In this paper, the comparison between Van Allen Probes data and the model results is limited to latitudes within ±10°. The chorus waves are confined close to the equator at the nightside, while the high powers of the dayside chorus are found at higher latitudes (Agapitov et al., 2018). A more comprehensive wave model in L shell, MLT, and magnetic latitude is required to properly capture the high-latitude wave power. The evaluation of the model performance in other regions is left as a future work.

Although the accuracy of the empirical models may be lower than the accuracy of machine learning models, the empirical model inherently provides the average density and wave power under a certain condition, which is stable and generally matches the data averaged over a sufficiently long period. The empirical model is robust if the data sampling time is sufficiently high in each category. The empirical models of total electron density and whistler-mode wave power are applicable to radiation belt modeling on a timescale longer than several days (Horne et al., 2013; Glauert et al., 2014; Drozdov et al., 2015), or under quiet to modestly disturbed geomagnetic conditions (Ma et al., 2015; 2017). During a short and disturbed period, the chorus and hiss wave amplitudes may be underestimated, or the plume regions may be misidentified. Therefore, the wave model based on observation (Li et al., 2016b; Ma et al., 2018) or from machine learning prediction (Bortnik et al., 2018) may provide better radiation belt modeling results. Our study of the empirical model performance provides a reference for the future development of machine learning models, by investigating the different error metrics and revealing the key factors affecting the model performance.

Data availability statement

The datasets presented in this study can be found in online repositories (https://doi.org/10.6084/m9.figshare.22762247). The names of the repository/repositories and accession number(s) can be found in the article/Supplementary Material.

Author contributions

QM performed the surveys using satellite data, constructed the empirical models, made model-data comparisons, evaluated the model performance, and wrote the manuscript. XC, DM, and SH performed machine learning modeling, which helped inspire the evaluation methods for the performance of the empirical models, discussed the strengths and weaknesses of the empirical model, and revised the manuscript. WL and JB discussed the results of this project, suggested improvements to the models, revised the manuscript, and provided support for this project. X-CS helped with the data preparation and global surveys, verified the data distribution, and revised the manuscript. All authors contributed to the article and approved the submitted version.

Funding

This work is supported by NASA grants 80NSSC19K0911, 80NSSC20K0196, and 80NSSC22K1023. In addition, we acknowledge NASA grants 80NSSC19K0845 and 80NSSC20K0698, 80NSSC20K0704 and the NSF grants AGS-1847818 and AGS-2225445. SH gratefully acknowledges the NASA FINESST grant 80NSSC21K1385. JB acknowledges support from the Defense Advanced Research Projects Agency under the Department of the Interior award D19AC00009.

Acknowledgments

We are grateful to the NASA and NSF agencies for their support of our research. The details of each grant are listed in the "Funding" section above. We acknowledge the efforts by Geospace Environment Modeling focus group Self-Consistent Inner Magnetospheric Modeling. We also acknowledge the Van Allen Probes teams for providing the data.

Conflict of interest

The authors declare that the research was conducted in the absence of any commercial or financial relationships that could be construed as a potential conflict of interest.

Publisher's note

All claims expressed in this article are solely those of the authors and do not necessarily represent those of their affiliated organizations, or those of the publisher, the editors and the reviewers. Any product that may be evaluated in this article, or claim that may be made by its manufacturer, is not guaranteed or endorsed by the publisher.

Supplementary material

The Supplementary Material for this article can be found online at: https://www.frontiersin.org/articles/10.3389/fspas.2023.1232702/full#supplementary-material

References

Agapitov, O., Artemyev, A., Krasnoselskikh, V., Khotyaintsev, Y. V., Mourenas, D., Breuillard, H., et al. (2013). Statistics of whistler-mode waves in the outer radiation belt: cluster STAFF-SA measurements. *J. Geophys. Res. Space Phys.* 118, 3407–3420. doi:10.1002/jgra.50312

Agapitov, O. V., Mourenas, D., Artemyev, A. V., Mozer, F. S., Hospodarsky, G., Bonnell, J., et al. (2018). Synthetic empirical chorus wave model from combined Van Allen Probes and Cluster statistics. *J. Geophys. Res. Space Phys.* 123, 297–314. doi:10.1002/2017JA024843

Bortnik, J., Chu, X., Ma, Q., Li, W., Zhang, X., Thorne, R. M., et al. (2018). "Artificial neural networks for determining magnetospheric conditions," in *Machine learning techniques for space weather* (Elsevier), 279–300. doi:10.1016/b978-0-12-811788-0.00011-1

Bortnik, J., Inan, U. S., and Bell, T. F. (2003). Frequency-time spectra of magnetospherically reflecting whistlers in the plasmasphere. *J. Geophys. Res.* 108 (A1), 1030. doi:10.1029/2002JA009387

Bortnik, J., Li, W., Thorne, R. M., and Angelopoulos, V. (2016). A unified approach to inner magnetospheric state prediction. *J. Geophys. Res. Space Phys.* 121 (3), 2423–2430. doi:10.1002/2015ja021733

Bortnik, J., Li, W., Thorne, R. M., Angelopoulos, V., Cully, C., Bonnell, J., et al. (2009). An observation linking the origin of plasmaspheric hiss to discrete chorus emissions. *Science* 324 (5928), 775–778. doi:10.1126/science.1171273

Bortnik, J., Thorne, R. M., and Meredith, N. P. (2008). The unexpected origin of plasmaspheric hiss from discrete chorus emissions. *Nature* 452, 62–66. doi:10.1038/nature06741

Breneman, A. W., Wygant, J. R., Tian, S., Cattell, C. A., Thaller, S. A., Goetz, K., et al. (2022). The van allen Probes electric field and waves instrument: science results, measurements, and access to data. *Space Sci. Rev.* 218, 69. doi:10.1007/s11214-022-00934-y

Carpenter, D. L., and Anderson, R. R. (1992). An ISEE/whistler model of equatorial electron density in the magnetosphere. *J. Geophys. Res.* 97, 1097–1108. doi:10.1029/91ja01548

Chen, L., Li, W., Bortnik, J., and Thorne, R. M. (2012a). Amplification of whistler-mode hiss inside the plasmasphere. *Geophys. Res. Lett.* 39, L08111. doi:10.1029/2012GL051488

Chen, L., Thorne, R. M., Bortnik, J., Li, W., Horne, R. B., Reeves, G. D., et al. (2014). Generation of unusually low frequency plasmaspheric hiss. *Geophys. Res. Lett.* 41, 5702–5709. doi:10.1002/2014GL060628

Chen, L., Thorne, R. M., Li, W., Bortnik, J., Turner, D., and Angelopoulos, V. (2012b). Modulation of plasmaspheric hiss intensity by thermal plasma density structure. *Geophys. Res. Lett.* 39, L14103. doi:10.1029/2012GL052308

Chu, X., Bortnik, J., Li, W., Ma, Q., Denton, R., Yue, C., et al. (2017). A neural network model of three-dimensional dynamic electron density in the inner magnetosphere. *J. Geophys. Res. Space Phys.* 122 (9), 9183–9197. doi:10.1002/2017ja024464

Chu, X., Ma, D., Bortnik, J., Tobiska, W. K., Cruz, A., Bouwer, S. D., et al. (2021). Relativistic electron model in the outer radiation belt using a neural network approach. *Space weather.* 19, e2021SW002808. doi:10.1029/2021SW002808

Drozdov, A. Y., Shprits, Y. Y., Orlova, K. G., Kellerman, A. C., Subbotin, D. A., Baker, D. N., et al. (2015). Energetic, relativistic, and ultrarelativistic electrons: comparison of long-term VERB code simulations with van allen Probes measurements. *J. Geophys. Res. Space Phys.* 120, 3574–3587. doi:10.1002/2014JA020637

Fu, X., Cowee, M. M., Friedel, R. H., Funsten, H. O., Gary, S. P., Hospodarsky, G. B., et al. (2014). Whistler anisotropy instabilities as the source of banded chorus: van Allen Probes observations and particle-in-cell simulations. *J. Geophys. Res. Space Phys.* 119, 8288–8298. doi:10.1002/2014JA020364

Gjerloev, J. W. (2012). The SuperMAG data processing technique. *J. Geophys. Res.* 117, A09213. doi:10.1029/2012JA017683

Glauert, S. A., Horne, R. B., and Meredith, N. P. (2014). Three-dimensional electron radiation belt simulations using the BAS Radiation Belt Model with new diffusion models for chorus, plasmaspheric hiss, and lightning-generated whistlers. *J. Geophys. Res. Space Phys.* 119, 268–289. doi:10.1002/2013JA019281

Hartley, D. P., Cunningham, G. S., Ripoll, J.-F., Malaspina, D. M., Kasahara, Y., Miyoshi, Y., et al. (2023). Using Van Allen Probes and Arase observations to develop an empirical plasma density model in the inner zone. *J. Geophys. Res. Space Phys.* 128, e2022JA031012. doi:10.1029/2022ja031012

Horne, R. B., Glauert, S. A., Meredith, N. P., Boscher, D., Maget, V., Heynderickx, D., et al. (2013). Space weather impacts on satellites and forecasting the Earth's electron radiation belts with SPACECAST. *Space weather.* 11, 169–186. doi:10.1002/swe.20023

Huang, S., Li, W., Shen, X.-C., Ma, Q., Chu, X., Ma, D., et al. (2022). Application of recurrent neural network to modeling Earth's global electron density. *J. Geophys. Res. Space Phys.* 127, e2022JA030695. doi:10.1029/2022JA030695

Kasahara, Y., Miyoshi, Y., Omura, Y., Verkhoglyadova, O. P., Nagano, I., Kimura, I., et al. (2009). Simultaneous satellite observations of VLF chorus, hot and relativistic electrons in a magnetic storm "recovery" phase. *Geophys. Res. Lett.* 36, L01106. doi:10.1029/2008GL036454

Kim, K., Lee, D., and Shprits, Y. (2015). Dependence of plasmaspheric hiss on solar wind parameters and geomagnetic activity and modeling of its global distribution. *J. Geophys. Res. Space Phys.* 120, 1153–1167. doi:10.1002/2014JA020687

Kim, K.-C., and Shprits, Y. (2019). Statistical analysis of hiss waves in plasmaspheric plumes using Van Allen Probe observations. *J. Geophys. Res. Space Phys.* 124, 1904–1915. doi:10.1029/2018JA026458

Kletzing, C. A., Kurth, W. S., Acuna, M., MacDowall, R. J., Torbert, R. B., Averkamp, T., et al. (2013). The electric and magnetic field instrument suite and integrated science (EMFISIS) on RBSP. *Space Sci. Rev.* 179, 127–181. doi:10.1007/s11214-013-9993-6

Kurth, W. S., De Pascuale, S., Faden, J. B., Kletzing, C. A., Hospodarsky, G. B., Thaller, S., et al. (2015). Electron densities inferred from plasma wave spectra obtained by the Waves instrument on Van Allen Probes. *J. Geophys. Res. Space Phys.* 120, 904–914. doi:10.1002/2014JA020857

Li, W., Ma, Q., Thorne, R. M., Bortnik, J., Kletzing, C. A., Kurth, W. S., et al. (2015). Statistical properties of plasmaspheric hiss derived from Van Allen Probes data and their Effects on radiation belt electron dynamics. *J. Geophys. Res. Space Phys.* 120, 3393–3405. doi:10.1002/2015JA021048

Li, W., Ma, Q., Thorne, R. M., Bortnik, J., Zhang, X., Li, J., et al. (2016b). Radiation belt electron acceleration during the 17 March 2015 geomagnetic storm: observations and simulations. *J. Geophys. Res. Space Phys.* 121, 5520–5536. doi:10.1002/2016JA022400

Li, W., Santolik, O., Bortnik, J., Thorne, R. M., Kletzing, C. A., Kurth, W. S., et al. (2016a). New chorus wave properties near the equator from Van Allen Probes wave observations. *Geophys. Res. Lett.* 43, 4725–4735. doi:10.1002/2016GL068780

Li, W., Shen, X.-C., Ma, Q., Capannolo, L., Shi, R., Redmon, R. J., et al. (2019). Quantification of energetic electron precipitation driven by plume whistler mode waves, plasmaspheric hiss, and exohiss. *Geophys. Res. Lett.* 46, 3615–3624. doi:10.1029/2019GL082095

Li, W., Thorne, R. M., Angelopoulos, V., Bortnik, J., Cully, C. M., Ni, B., et al. (2009). Global distribution of whistler-mode chorus waves observed on the THEMIS spacecraft. *Geophys. Res. Lett.* 36, L09104. doi:10.1029/2009GL037595

Li, W., Thorne, R. M., Bortnik, J., Reeves, G. D., Kletzing, C. A., Kurth, W. S., et al. (2013). An unusual enhancement of low-frequency plasmaspheric hiss in the outer plasmasphere associated with substorm-injected electrons. *Geophys. Res. Lett.* 40, 3798–3803. doi:10.1002/grl.50787

Li, W., Thorne, R. M., Meredith, N. P., Horne, R. B., Bortnik, J., Shprits, Y. Y., et al. (2008). Evaluation of whistler mode chorus amplification during an injection event observed on CRRES. *J. Geophys. Res.* 113, A09210. doi:10.1029/2008JA013129

Ma, D., Chu, X., Bortnik, J., Claudepierre, S. G., Tobiska, W. K., Cruz, A., et al. (2022a). Modeling the dynamic variability of sub-relativistic outer radiation belt electron fluxes using machine learning. *Space weather.* 20, e2022SW003079. Available at: https://doi-org.colorado.idm.oclc.org/10.1029/2022SW003079.

Ma, J., Gao, X., Chen, H., Tsurutani, B. T., Ke, Y., Chen, R., et al. (2022b). The effects of substorm injection of energetic electrons and enhanced solar wind ram pressure on whistler-mode chorus waves: A statistical study. *J. Geophys. Res. Space Phys.* 127, e2022JA030502. doi:10.1029/2022JA030502

Ma, Q., Li, W., Bortnik, J., Thorne, R. M., Chu, X., Ozeke, L. G., et al. (2018). Quantitative evaluation of radial diffusion and local acceleration processes during GEM challenge events. *J. Geophys. Res. Space Phys.* 123, 1938–1952. doi:10.1002/2017JA025114

Ma, Q., Li, W., Thorne, R. M., Bortnik, J., Reeves, G. D., Kletzing, C. A., et al. (2016a). Association between glycated hemoglobin A1c levels with age and gender in Chinese adults with no prior diagnosis of diabetes mellitus. *J. Geophys. Res. Space Phys.* 121 (11), 737–740. doi:10.3892/br.2016.643

Ma, Q., Li, W., Thorne, R. M., Bortnik, J., Reeves, G. D., Spence, H. E., et al. (2017). Diffusive transport of several hundred keV electrons in the Earth's slot region. *J. Geophys. Res. Space Phys.* 122 (10), 235–310. doi:10.1002/2017JA024452

Ma, Q., Li, W., Thorne, R. M., Ni, B., Kletzing, C. A., Kurth, W. S., et al. (2015). Modeling inward diffusion and slow decay of energetic electrons in the Earth's outer radiation belt. *Geophys. Res. Lett.* 42, 987–995. doi:10.1002/2014GL062977

Ma, Q., Li, W., Thorne, R. M., Nishimura, Y., Zhang, X., Reeves, G. D., et al. (2016b). Simulation of energy-dependent electron diffusion processes in the Earth's outer radiation belt. *J. Geophys. Res. Space Phys.* 121, 4217–4231. doi:10.1002/2016JA022507

Ma, Q., Li, W., Zhang, X. -J., Bortnik, J., Shen, X. -C., Connor, H. K., et al. (2021). Global survey of electron precipitation due to hiss waves in the Earth's plasmasphere and plumes. *J. Geophys. Res. Space Phys.* 126, e2021JA029644. doi:10.1029/2021JA029644

Ma, Q., Ni, B., Tao, X., and Thorne, R. M. (2012). Evolution of the plasma sheet electron pitch angle distribution by whistler-mode chorus waves in non-dipole magnetic fields. *Ann. Geophys.* 30 (4), 751–760. doi:10.5194/angeo-30-751-2012

Malaspina, D. M., Jaynes, A. N., Boulé, C., Bortnik, J., Thaller, S. A., Ergun, R. E., et al. (2016). The distribution of plasmaspheric hiss wave power with respect to plasmapause location. *Geophys. Res. Lett.* 43, 7878–7886. doi:10.1002/2016GL069982

Matzka, J., Bronkalla, O., Kervalishvili, G., Rauberg, J., and Yamazaki, Y. (2022). Geomagnetic hpo index. V. 2.0. *GFZ Data Serv.* doi:10.5880/Hpo.0002

Mauk, B. H., Fox, N. J., Kanekal, S. G., Kessel, R. L., Sibeck, D. G., and Ukhorskiy, A. (2013). Science objectives and rationale for the radiation belt storm Probes mission. *Space Sci. Rev.* 179, 3–27. doi:10.1007/s11214-012-9908-y

Meredith, N. P., Bortnik, J., Horne, R. B., Li, W., and Shen, X.-C. (2021). Statistical investigation of the frequency dependence of the chorus source mechanism of plasmaspheric hiss. *Geophys. Res. Lett.* 48, e2021GL092725. doi:10.1029/2021gl092725

Meredith, N. P., Horne, R. B., Clilverd, M. A., Horsfall, D., Thorne, R. M., and Anderson, R. R. (2006). Origins of plasmaspheric hiss. *J. Geophys. Res.* 111, A09217. doi:10.1029/2006JA011707

Meredith, N. P., Horne, R. B., Kersten, T., Li, W., Bortnik, J., Sicard, A., et al. (2018). Global model of plasmaspheric hiss from multiple satellite observations. *J. Geophys. Res. Space Phys.* 123, 4526–4541. doi:10.1029/2018JA025226

Meredith, N. P., Horne, R. B., Shen, X.-C., Li, W., and Bortnik, J. (2020). Global model of whistler mode chorus in the near-equatorial region ($|\lambda_m|< 18°$). *Geophys. Res. Lett.* 47, e2020GL087311. doi:10.1029/2020GL087311

Meredith, N. P., Horne, R. B., Sicard-Piet, A., Boscher, D., Yearby, K. H., Li, W., et al. (2012). Global model of lower band and upper band chorus from multiple satellite observations. *J. Geophys. Res.* 117, A10225. doi:10.1029/2012JA017978

Morley, S. K., Brito, T. V., and Welling, D. T. (2018). Measures of model performance based on the log accuracy ratio. *Space weather.* 16, 69–88. doi:10.1002/2017SW001669

Newell, P. T., and Gjerloev, J. W. (2011). Evaluation of SuperMAG auroral electrojet indices as indicators of substorms and auroral power. *J. Geophys. Res.* 116, A12211. doi:10.1029/2011JA016779

Ni, B., Bortnik, J., Thorne, R. M., Ma, Q., and Chen, L. (2013). Resonant scattering and resultant pitch angle evolution of relativistic electrons by plasmaspheric hiss. *J. Geophys. Res. Space Phys.* 118, 7740–7751. doi:10.1002/2013JA019260

O'Brien, T. P., and Moldwin, M. B. (2003). Empirical plasmapause models from magnetic indices. *Geophys. Res. Lett.* 30, 1152. doi:10.1029/2002GL016007

Reeves, G. D., Friedel, R. H. W., Larsen, B. A., Skoug, R. M., Funsten, H. O., Claudepierre, S. G., et al. (2016). Energy-dependent dynamics of keV to MeV electrons in the inner zone, outer zone, and slot regions. *J. Geophys. Res. Space Phys.* 121, 397–412. doi:10.1002/2015JA021569

Reeves, G., Spence, H. E., Henderson, M. G., Morley, S. K., Friedel, R. H. W., Funsten, H. O., et al. (2013). Electron acceleration in the heart of the Van Allen radiation belts. *Science* 341 (6149), 991–994. doi:10.1126/science.1237743

Ripoll, J.-F., Reeves, G. D., Cunningham, G. S., Loridan, V., Denton, M., Santolík, O., et al. (2016). Reproducing the observed energy-dependent structure of Earth's electron radiation belts during storm recovery with an event-specific diffusion model. *Geophys. Res. Lett.* 43, 5616–5625. doi:10.1002/2016GL068869

Santolík, O., Parrot, M., and Lefeuvre, F. (2003). Singular value decomposition methods for wave propagation analysis. *Radio Sci.* 38 (1), 1010. doi:10.1029/2000RS002523

Sheeley, B. W., Moldwin, M. B., Rassoul, H. K., and Anderson, R. R. (2001). An empirical plasmasphere and trough density model: CRRES observations. *J. Geophys. Res.* 106 (A11), 25631–25641. doi:10.1029/2000JA000286

Shi, R., Li, W., Ma, Q., Green, A., Kletzing, C. A., Kurth, W. S., et al. (2019). Properties of whistler mode waves in Earth's plasmasphere and plumes. *J. Geophys. Res. Space Phys.* 124, 1035–1051. doi:10.1029/2018JA026041

Sonwalkar, V. S., and Inan, U. S. (1989). Lightning as an embryonic source of VLF hiss. *J. Geophys. Res.* 94 (A6), 6986–6994. doi:10.1029/JA094iA06p06986

Spasojevic, M., Shprits, Y. Y., and Orlova, K. (2015). Global empirical models of plasmaspheric hiss using Van Allen Probes. *J. Geophys. Res. Space Phys.* 120 (10), 370–410. doi:10.1002/2015JA021803

Summers, D., Ni, B., Meredith, N. P., Horne, R. B., Thorne, R. M., Moldwin, M. B., et al. (2008). Electron scattering by whistler-mode ELF hiss in plasmaspheric plumes. *J. Geophys. Res.* 113, A04219. doi:10.1029/2007JA012678

Summers, D., Ni, B., and Meredith, N. P. (2007). Timescales for radiation belt electron acceleration and loss due to resonant wave-particle interactions: 2. Evaluation for VLF chorus, ELF hiss, and electromagnetic ion cyclotron waves. *J. Geophys. Res.* 112, A04207. doi:10.1029/2006JA011993

Tao, X., Thorne, R. M., Li, W., Ni, B., Meredith, N. P., and Horne, R. B. (2011). Evolution of electron pitch angle distributions following injection from the plasma sheet. *J. Geophys. Res.* 116, A04229. doi:10.1029/2010JA016245

Thorne, R. M., Bortnik, J., Li, W., and Ma, Q. (2021), Wave-particle interactions in the Earth's magnetosphere, doi:10.1002/9781119815624.ch6

Thorne, R. M., Li, W., Ni, B., Ma, Q., Bortnik, J., Chen, L., et al. (2013). Rapid local acceleration of relativistic radiation belt electrons by magnetospheric chorus. *Nature* 504, 411–414. doi:10.1038/nature12889

Thorne, R. M., Ni, B., Tao, X., Horne, R. B., and Meredith, N. P. (2010). Scattering by chorus waves as the dominant cause of diffuse auroral precipitation. *Nature* 467, 943–946. doi:10.1038/nature09467

Tsyganenko, N. A., and Sitnov, M. I. (2005). Modeling the dynamics of the inner magnetosphere during strong geomagnetic storms. *J. Geophys. Res.* 110, A03208. doi:10.1029/2004JA010798

Wygant, J. R., Bonnell, J. W., Goetz, K., Ergun, R. E., Mozer, F. S., Bale, S. D., et al. (2013). The electric field and waves instruments on the radiation belt storm Probes mission. *Space Sci. Rev.* 179, 183–220. doi:10.1007/s11214-013-0013-7

Yue, C., Chen, L., Bortnik, J., Ma, Q., Thorne, R. M., Spence, H. E., et al. (2017). The characteristic response of whistler mode waves to interplanetary shocks. *J. Geophys. Res. Space Phys.* 122 (10), 047. doi:10.1002/2017JA024574

Zhang, W., Ni, B., Huang, H., Summers, D., Fu, S., Xiang, Z., et al. (2019). Statistical properties of hiss in plasmaspheric plumes and associated scattering losses of radiation belt electrons. *Geophys. Res. Lett.* 46, 5670–5680. doi:10.1029/2018GL081863

Zhao, H., Ni, B., Li, X., Baker, D. N., Johnston, W. R., Zhang, W., et al. (2019). Plasmaspheric hiss waves generate a reversed energy spectrum of radiation belt electrons. *Nat. Phys.* 15 (4), 367–372. doi:10.1038/s41567-018-0391-6

Zhou, C., Li, W., Thorne, R. M., Bortnik, J., Ma, Q., An, X., et al. (2015). Excitation of dayside chorus waves due to magnetic field line compression in response to interplanetary shocks. *J. Geophys. Res. Space Phys.* 120, 8327–8338. doi:10.1002/2015JA021530

frontiers | Frontiers in Astronomy and Space Sciences

TYPE Methods
PUBLISHED 26 September 2023
DOI 10.3389/fspas.2023.1239160

OPEN ACCESS

EDITED BY
Robert Demajistre,
Johns Hopkins University, United States

REVIEWED BY
Alex Degeling,
Shandong University, Weihai, China
Alexander Chernyshov,
Space Research Institute (RAS), Russia

*CORRESPONDENCE
Anthony A. Chan,
aac@rice.edu
Scot R. Elkington,
scot.elkington@lasp.colorado.edu

RECEIVED 12 June 2023
ACCEPTED 21 August 2023
PUBLISHED 26 September 2023

CITATION
Chan AA, Elkington SR, Longley WJ, Aldhurais SA, Alam SS, Albert JM, Jaynes AN, Malaspina DM, Ma Q and Li W (2023), Simulation of radiation belt wave-particle interactions in an MHD-particle framework. *Front. Astron. Space Sci.* 10:1239160. doi: 10.3389/fspas.2023.1239160

Simulation of radiation belt wave-particle interactions in an MHD-particle framework

Anthony A. Chan[1]*, Scot R. Elkington[2]*, William J. Longley[1,3], Suhail A. Aldhurais[1,4,5], Shah S. Alam[1], Jay M. Albert[6], Allison N. Jaynes[7], David M. Malaspina[2,8], Qianli Ma[9] and Wen Li[9]

[1]Department of Physics and Astronomy, Rice University, Houston, TX, United States, [2]Laboratory for Atmospheric and Space Physics, University of Colorado, Boulder, CO, United States, [3]Center for Solar-Terrestrial Research, New Jersey Institute of Technology, Newark, NJ, United States, [4]Applied Physics Graduate Program, Smalley-Curl Institute, Rice University, Houston, TX, United States, [5]Physics Department, King Fahd University of Petroleum and Minerals, Dhahran, Saudi Arabia, [6]Air Force Research Laboratory, Kirtland AFB, NM, United States, [7]Department of Physics and Astronomy, University of Iowa, Iowa, IA, United States, [8]Astrophysical and Planetary Sciences Department, University of Colorado, Boulder, CO, United States, [9]Center for Space Physics, Boston University, Boston, MA, United States

In this paper we describe K2, a comprehensive simulation model of Earth's radiation belts that includes a wide range of relevant physical processes. Global MHD simulations are combined with guiding-center test-particle methods to model interactions with ultra low-frequency (ULF) waves, substorm injections, convective transport, drift-shell splitting, drift-orbit bifurcations, and magnetopause shadowing, all in self-consistent MHD fields. Simulation of local acceleration and pitch-angle scattering due to cyclotron-scale interactions is incorporated by including stochastic differential equation (SDE) methods in the MHD-particle framework. The SDEs are driven by event-specific bounce-averaged energy and pitch-angle diffusion coefficients. We present simulations of electron phase-space densities during a simplified particle acceleration event based on the 17 March 2013 event observed by the Van Allen Probes, with a focus on demonstrating the capabilities of the K2 model. The relative wave-particle effects of global scale ULF waves and very-low frequency (VLF) whistler-mode chorus waves are compared, and we show that the primary acceleration appears to be from the latter. We also show that the enhancement with both ULF and VLF processes included exceeds that of VLF waves alone, indicating a synergistic combination of energization and transport processes may be important.

KEYWORDS

radiation belts of magnetized planets, wave-particle interaction, energetic particles, magnetospheric plasma waves, quasilinear and non-linear theory, numerical simulation

1 Introduction

The inner magnetosphere supports a host of physical processes driving acceleration, transport, and loss of radiation belt electrons, including acceleration and transport by drift-interaction with ultra low-frequency (ULF) waves, local acceleration and loss by cyclotron-interaction with higher frequency (VLF and ELF) plasma waves, transport due to substorm activity and large-scale convection, and loss by particle scattering into the atmosphereor interaction with the magnetopause. A fundamental challenge in

constructing physical models of the radiation belts is capturing this broad range of processes across many different time and spatial scales.

Recent radiation belt research has been summarized in two comprehensive reviews, and references therein, by Li and Hudson (2019) and Ripoll et al. (2020). As described in those reviews, the main current method of modeling Earth's radiation belts is solution of a three-dimensional Fokker-Planck equation that uses quasilinear diffusion coefficients, as in the following codes: the ONERA Salammbô code (e.g., Beutier and Boscher, 1995; Maget et al., 2015), the BAS (British Antarctic Survey) code (e.g., Glauert et al., 2014), the AFRL code (e.g., Albert et al., 2009), the UCLA code (e.g., Li et al., 2016; Ma et al., 2016), the VERB code (Shprits et al., 2009; Drozdov et al., 2015), the LANL DREAM-3D code (e.g., Tu et al., 2014), the CEA CEVA code (e.g., Ripoll et al., 2016), the STEERB code (e.g., Su et al., 2011), and the REM SDE (stochastic differential equation) code developed at Rice University (Zheng et al., 2014) that was later developed into the UBER SDE code (Zheng et al., 2021).

Although 3-D radiation belt diffusion codes have had success in reproducing some features of radiation belt observations, there is still much work to be done to assess their quantitative agreement between the simulations and observations (Tu et al., 2019), and there are still some basic unanswered questions regarding the applicability of the diffusion approach, particularly for the use of radial diffusion (see Lejosne and Kollmann (2020), for example). Specifically, the following questions are active research areas: What are the relative roles of local acceleration and radial transport? (as discussed in Drozdov et al. (2022), for example.) Is there sufficient phase randomization to justify a quasilinear diffusion approach? What are the relative roles of diffusive versus advective transport? How important are nonlinear wave-particle interactions, either for cyclotron-frequency wave-particle interactions or for drift-frequency wave-particle interactions?

In this Methods paper we describe K2, a comprehensive radiation belt modeling code especially designed for event simulations, that contains the basic physics of radial transport, local acceleration, and loss; all of which are important processes in solving the questions of the previous paragraph (Elkington et al., 2004; Chan et al., 2010). The code is named after the mountain K2 in the northwestern Karakoram Range, the second-highest mountain on Earth. This paper outlines the method used in the K2 modeling framework, and provides an example of its use in the context of the geomagnetic storm beginning on 17 March 2013. This event was chosen because it is a well-known radiation belt enhancement event (Li W et al., 2014; Tu et al., 2014), and because the chorus wave diffusion coefficients that are an important input to the K2 code were available from the NSF Geopsace Environment Modeling (GEM) QARBM (Quantitative Assessment of Radiation Belt Models) focus group challenge (Ma et al., 2018). In the subsequent sections, we describe the general MHD/test particle method and history; give an overview of the SDE method used to simulate local wave-particle interactions; discuss how event-specific chorus wave diffusion coefficients may be obtained and implemented with a test particle method; and follow up with a discussion of initial simulation results for the 17 March 2013 geomagnetic event.

2 MHD-particle simulations and stochastic differential equations

2.1 MHD-particle simulations

MHD-particle simulations have been used to elucidate the physics and dynamics of the radiation belts for a broad range of phenomena, including the effects of CMEs/shocks in the solar wind (Li et al., 1993; Hudson et al., 1998; Elkington et al., 2002; Hudson et al., 2015; Li et al., 2015), radial transport driven by ULF waves (Elkington et al., 1999; Elkington et al., 2003; Fei et al., 2006), effects of substorms and advective injections of particles from the plasma sheet (Birn et al., 1997; Kim et al., 2000; Elkington et al., 2005; Kress et al., 2014; Merkin et al., 2019), and in recent plasma sheet, ring current and radiation belt simulations (Sorathia et al., 2018; Sorathia et al., 2021).

We now summarize the main features of the MHD-particle methods that form the basis for the K2 framework, based on our earlier work (Elkington et al., 2002; Elkington et al., 2004). The MHD model uses solar wind conditions observed at L_1 to provide time-dependent, event-specific upstream boundary conditions for the MHD model, and the magnetohydrodynamic state vector is solved on a grid. An example of the output of an MHD simulation is indicated in Figure 1, showing an equatorial snapshot of the electric and magnetic field values (color scale and contours, respectively), and the direction and relative magnitude of magnetospheric plasma flow velocities (vectors). Flow channels associated with substorm activity are clearly shown in the pre- and post-midnight tail regions. Such activity is difficult to model in diffusive Fokker-Planck simulations of the radiation belts because those models do not contain magnetospheric fields with these spatial and temporal scales and they do not contain associated non-diffusive advective transport. In contrast, effects of such activity on radiation belt particles are a natural feature of the MHD-particle method. Solar wind conditions driving the MHD simulation are indicated in the right-hand panels of Figure 1.

The test particle portion of the MHD-particle method uses the electric and magnetic field values from the MHD simulation, interpolated in space and time from the MHD solution grid to each test particle's location, and these values are used to advance the particle's position in time using a 3d guiding center approximation. The validity of the guiding center approximation must be checked at each point in the particle's trajectory to ensure that the instantaneous particle gyroradius is much smaller than both parallel and perpendicular gradients in the local magnetic fields, and that the gyrofrequency is much larger than the corresponding temporal changes in the local fields. These particle simulations may comprise 10^5-10^6 test particles representing a range of energies and pitch angles, and may be conducted either forward or backward in time (e.g., Kress et al., 2015). By assigning a phase-space density to each test particle based on either initial or boundary conditions and invoking Liouville's theorem, the aggregate dynamics of the radiation belts may be simulated as a function of driving solar wind conditions.

We note that the accuracy of any MHD/particle simulation will be limited by the accuracy of the underlying geomagnetic field model. For example, inadequate representation of the ring

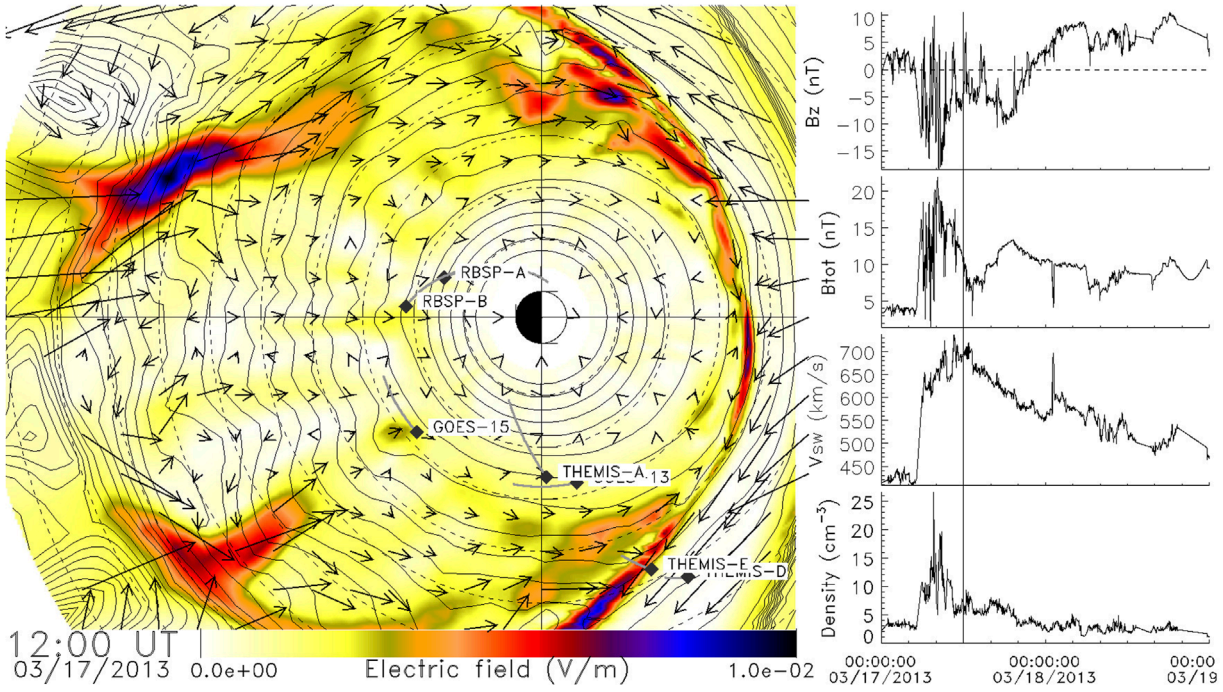

FIGURE 1
Snapshot of the equatorial results of an MHD simulation driven by the upstream solar wind conditions in the right-hand panel. Contours of constant magnetic field strength are shown, with plasma flow velocities indicated by vectors and the associated electric field magnitude indicated on the color scale. The location of several spacecraft at this time is also shown.

or tail current in an MHD model will lead to a reduction in the stretching and overall morphology of individual field lines (e.g., Wiltberger et al., 2000), and thus lead to inaccurate drift and bounce trajectories. Similarly, inaccuracies in the cold plasma distribution in the inner magnetosphere will change the propagation characteristics of Alfvénic wave activity in these regions, leading to errors in the rates and effect of radial transport in the simulation.

2.2 Stochastic differential equations

The application of SDEs to solving radiation belt Fokker-Planck equations has been developed and described by Tao et al. (2008), Tao et al. (2009), Selesnick et al. (2013), Zheng et al. (2014), Zheng et al. (2021), and references therein. Essentially, an n-dimensional Fokker-Planck equation is equivalent to n SDEs. Solving the SDEs generates an ensemble of random walk trajectories, and each of those trajectories carries information about the phase-space density from either a boundary or from an initial condition, as illustrated in Figure 2. Using SDEs, complicated general boundary conditions and initial conditions can be implemented easily, and the solution of the SDEs is highly parallelizable.

In this work, we incorporate cyclotron-frequency wave-particle interactions into an MHD-particle simulation code by following Hamiltonian guiding center particle motion (Brizard and Chan, 2001; Tao et al., 2007), and by using SDEs to give random kicks to the equatorial pitch angle and momentum of each particle (or to an equivalent pair of particle variables, such as the first adiabatic invariant and the parallel momentum). The random kicks are made according to bounce-averaged diffusion coefficients for the wave-particle interactions (details of the coefficients are given in the next section). The SDEs used in K2 that advance the equatorial pitch-angle α_0 and momentum p of each particle from an "initial" value (before the kick) to a "final" value (after the kick, corresponding to a time interval Δs) are (Tao et al., 2008):

$$\alpha_f = \alpha_i + b_1\Delta s + \sigma_{11}\sqrt{\Delta s}N_1 + \sigma_{12}\sqrt{\Delta s}N_2 \quad (1)$$

$$p_f = p_i + b_2\Delta s + \sigma_{21}\sqrt{\Delta s}N_3 + \sigma_{22}\sqrt{\Delta s}N_4 \quad (2)$$

where N_1, N_2, N_3, and N_4 are Gaussian random numbers with zero mean and unit variance, and on the σ and b coefficients we use a subscript 1 for α_0 and a subscript 2 for p. For convenience we make the choice $\sigma_{12} = 0$, and then the other σ coefficients are:

$$\sigma_{11} = \sqrt{2D_{11}/p_i}, \qquad \sigma_{21} = \sqrt{2}D_{12}/\sqrt{D_{11}}, \qquad \sigma_{22} = \sqrt{2D_{22} - \sigma_{21}^2}, \quad (3)$$

and the b_1, b_2 coefficients are given by

$$b_1(t,\alpha_0,p) = \frac{1}{Gp}\frac{\partial}{\partial\alpha_0}(GD_{11}/p) + \frac{1}{G}\frac{\partial}{\partial p}(GD_{12}/p) \quad (4)$$

$$b_2(t,\alpha_0,p) = \frac{1}{Gp}\frac{\partial}{\partial\alpha_0}(GD_{12}) + \frac{1}{G}\frac{\partial}{\partial p}(GD_{22}). \quad (5)$$

We have the freedom to choose $\sigma_{12} = 0$ because i) the matrix σ only needs to satisfy the condition $\sigma\sigma^T = a$ [where σ^T is the transpose and where a is a diffusion matrix that appears in Equation 2 of Tao et al. (2008)], but that condition is not sufficient to uniquely fix σ; and ii) as described below Equation 5 of Tao et al. (2008), because of

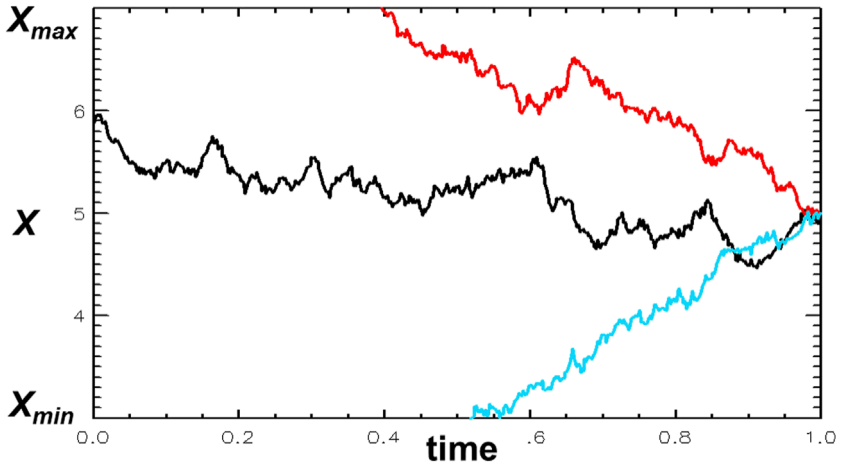

FIGURE 2
An illustration of SDE random walk trajectories, followed backwards in time from a phase-space position X at time t. A trajectory may either encounter a boundary (the red and blue trajectories) or an initial condition (the black trajectory), and contributions from those locations are summed to find the overall phase-space density at X and t. For a Dirichlet boundary condition the value at the boundary contributes directly, and for a Neumann boundary condition the trajectory is reflected and then followed until it encounters a Dirichlet boundary or an initial condition (Tao et al., 2008).

Levy's theorem, different choices of σ generate equivalent stochastic processes that yield the same solution of the diffusion equation.

Consistent with the magnetic dipole field approximations assumed in the diffusion coefficients themselves, the Jacobian is given by the dipole formula $G = p^2 T(\alpha_0)\sin(\alpha_0)\cos(\alpha_0)$, where the normalized bounce period is $T(\alpha_0) \approx 1.3801730 - 0.639693\sin^{4/3}(\alpha_0)$ (Schulz and Lanzerotti, 1974).

Quantitatively assessing the effect of these dipole field approximations is difficult without doing the full non-dipolar field calculations. Orlova and Shprits (2010) have calculated diffusion coefficients in a Tsyganenko 89c (non-dipolar) magnetic field, and they compared corresponding scattering rates with those calculated in a dipole field. They demonstrated that on the dayside the effects of a non-dipolar magnetic field are negligible at distances less than six Earth radii, and on the nightside the diffusion coefficients may significantly depend on the assumed field model. We regard the dipole approximation as temporary at this stage–we assume it is reasonable in the inner magnetosphere, but the non-dipolar effects should be studied in future work (with the caveat that the amount of computation involved in calculating the diffusion coefficients would increase significantly).

3 Implementation in K2

3.1 Chorus wave diffusion coefficients

The K2 model can use any set of pre-computed diffusion coefficients for wave-particle interactions using the SDE method (2.2). In this paper we use a set of event specific chorus diffusion coefficients for the 17 March 2013 geomagnetic storm from Ma et al. (2018). These coefficients are calculated using quasilinear theory, with the chorus wave intensity estimated from National Oceanic and Atmospheric Administration (NOAA) Polar Orbiting Environmental Satellites (POES) measurements of precipitating and trapped electron fluxes using the method in Li et al. (2013) and Ni et al. (2014). The diffusion coefficients used in this study do not include the effects of a changing ω_{pe}/ω_{ce} ratio, which can substantially affect the wave power estimated from POES observations (Longley et al., 2022). The set of coefficients in Ma et al. (2018) are calculated separately for upper and lower band chorus with Gaussian frequency and wave normal angle distributions in each band. The limited orbital coverage of POES means the coefficients are binned in 1 hour time increments, L values of $3.0, 3.5, \ldots, 7.0$, and MLT bins of 00:00-04:00, 04:00-08:00, 08:00-12:00, and 20:00-24:00. The diffusion coefficients are assumed 0 in the 12:00-20:00 MLT interval. This assumption is made because the frequent presence of whistler waves in plumes in the afternoon to dusk sector introduces a higher level of uncertainty in the POES technique, which used the empirical plasmatrough density model (Sheeley et al., 2001) to infer chorus wave amplitudes. Pitch angle is resolved in 2° intervals from 1° to 89° with an additional point at 89.5°, and energy is resolved from 0.1 keV to 10 MeV with 71 values equally spaced. Figure 3 shows the pitch angle, momentum, and mixed diffusion coefficients at several times for an L-shell of 5, and MLT in the range of 00:00-04:00.

Diffusion coefficients are computed in the framework of the Fokker-Planck equation, with units of 1/s. For use in K2, we convert precomputed coefficients to the Langevin equation formalism in Section 2.2. To avoid discretization errors, we compute the derivatives with respect to momentum in log space using

$$\frac{\partial}{\partial p} \rightarrow \frac{d(\log E)}{dp}\frac{\partial}{\partial(\log E)} \tag{6}$$

A centered finite difference is used for both the $\partial/\partial p$ and $\partial/\partial\alpha_0$ derivatives. The diffusion coefficients are computed and pre-processed independently from K2. K2 then reads in the pre-processed file at runtime and stores the set of diffusion coefficients in memory. A linear interpolation provides the diffusion coefficient

10.3389/fspas.2023.1239160

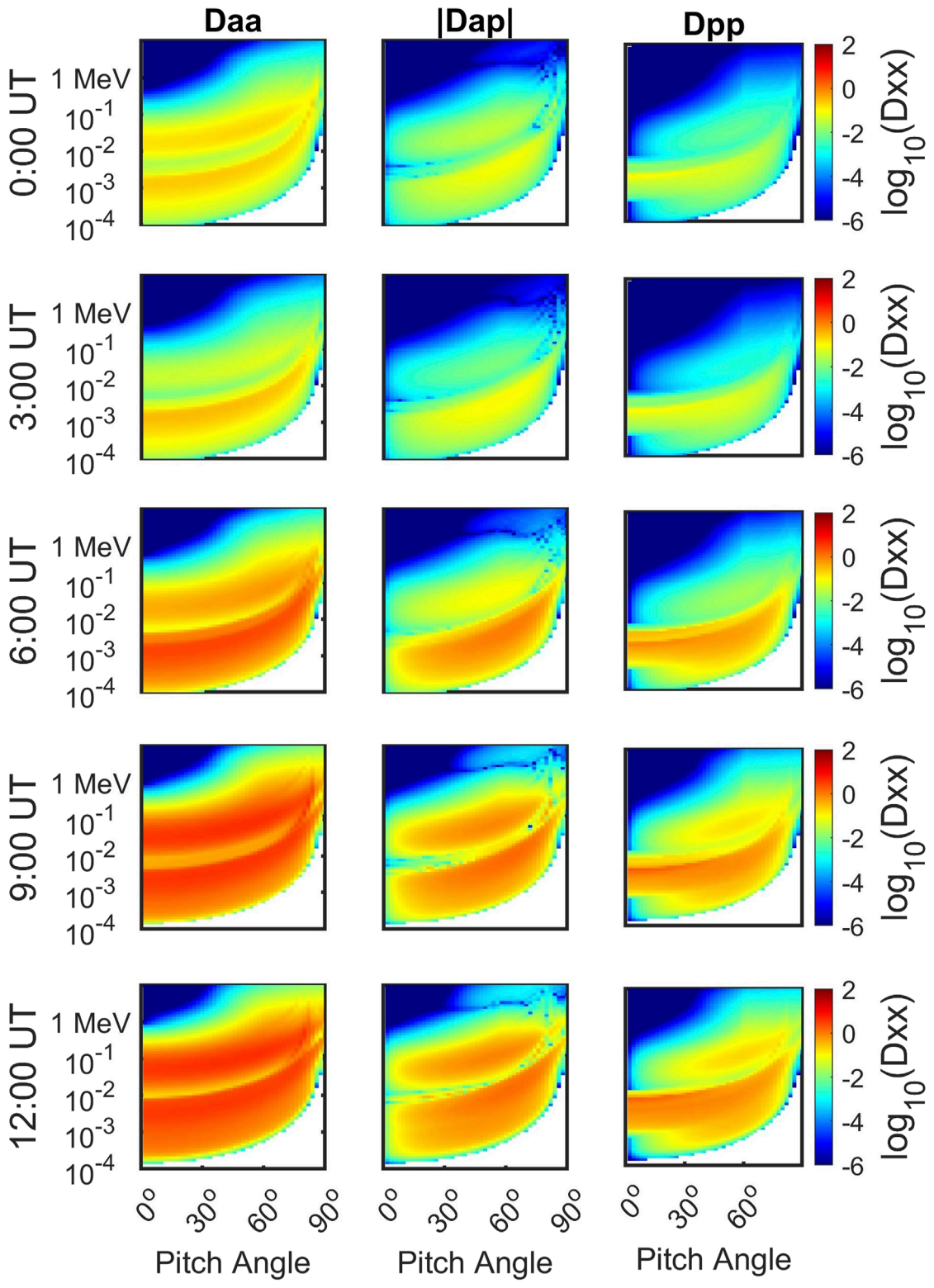

FIGURE 3
The chorus wave diffusion coefficients are plotted for several times during the event on 17 March 2013. Here Daa, Dap, and Dpp represent the $\alpha_0\alpha_0$, $\alpha_0 p$, and *pp* diffusion coefficients, and the Dxx label on the color bar represents any of those three coefficients. The coefficients are for an L-shell of 5, and an MLT range of 00:00-04:00. Note the colorbar and axes are the same in each subplot, and each coefficient is in units of 1/hours.

at any L-shell, energy, and equatorial pitch angle for a fixed MLT (magnetic local time) bin.

3.2 Implementing SDE kicks

The SDE method tracking the effects of whistler-mode chorus on energetic particles is combined with a global 3d test particle code capable of tracking the radial transport of the particles under the influence of ULF wave activity, substorm injections, and perturbations in the solar wind. The fields in this effort were taken from an MHD simulation of the solar wind/magnetosphere interaction driven by upstream boundary conditions measured at L_1. The global MHD code used in this simulation was the Lyon-Fedder-Mobarry (LFM) MHD code (Lyon et al., 2004), although the method described can use any gridded simulation output or analytic model of the background electric and magnetic fields.

The test particle code is based on that described by (Elkington et al., 2002; Elkington et al., 2004). The 3d Hamiltonian guiding center equations (Brizard and Chan, 2001) are solved using a Runge-Kutta method with an adaptive time step (Cash and Karp, 1990), with background fields interpolated to the location of each test particle from a regular grid containing the MHD electric and magnetic fields as they evolve in time. In the examples shown in this paper, the MHD field grids are Cartesian with a uniform grid spacing of $0.2R_E$ in all dimensions; basic benchmark tests indicate that errors in the drift trajectories due to field interpolation are not larger than those resulting from the relative local truncation error tolerance set in our adaptive Runge-Kutta solver (here 10^{-4}/step). The test particle code is capable of being run either in a time-forward or a time-backward fashion; in this work, we run time-backward to minimize the number of points in phase space from which particles need to be initialized. Each particle is run backward in time until it hits either a boundary condition or initial condition, and a phase-space density is assigned to that particle based on that boundary/initial condition. In this work, we use the AE-8max trapped electron model (Vette, 1991) to assign phase-space densities to those particles that intersect an initial condition. In the current version of K2, time-backward simulations for longer and longer time intervals become more computationally costly quite rapidly (approximately quadratically in the time interval). In future work we plan to investigate ways to improve the efficiency of K2 to reduce computation time. We are considering variance-reduction methods and/or source-biasing methods, and we may apply methods developed by Woodroffe et al. (2018).

The effects of wave-particle interactions are simulated by periodically "kicking" the particle pitch angle and momentum in accordance with Eqs 1, 2. The particle may be allowed to traverse through several bounce periods before the trajectory is modified through simulated interaction with chorus waves via the SDE solver, so long as the time between SDE kicks is much less than a drift period. For the particle simulations described in this paper, the number of bounces N_b between kicks was experimentally varied between $N_b = 3$ and $N_b = 60$ with no significant change in the aggregate results of the test particle results, but with a small increase in code efficiency as we increased N_b. The results shown here, we used $N_b = 15$ as a compromise between code efficiency and temporal fidelity of the chorus wave interactions.

The time-backward trajectory of each test particle is tracked throughout its bounce motion, noting the time and spatial location at which the particle passes through its local magnetic minimum on each bounce. Once the specified number of bounces, N_b, has been completed, the particle location, momentum, and time are reset to the most recent traversal of the magnetic minimum, and Eqs 1, 2 are solved to give updated equatorial pitch angle and momentum. The Gaussian random number generator used in this step is based on the Mersenne Twister as described in Matsumoto and Nishimura (1998). Once the pitch angle and momentum is updated, the particle trajectory continues to be tracked backward in time through the next interval of N_b bounces, and the next update to the momentum and pitch angle applied. Examples of the trajectory of individual particles undergoing combined drift motion and interaction with chorus-mode whister waves is shown in Figure 4. Here the first adiabatic invariant (solid line) and energy (dashed line) are shown in the left-hand panel of the figure, with the equatorial parallel momentum (solid line) and equatorial pitch angle (dashed line) shown in the right-hand panel as the particle drifts in time about the Earth. The local time variation in the effects of the inferred chorus wave activity is clearly evident in the drift trajectories, with regions of little to no chorus activity evident in the trajectory plots centered around 500s simulation time and again centered around ~1250s simulation time.

The first-order numerical scheme for integrating the SDEs in Eqs 1, 2 is known as the Euler-Murayama scheme. Because the transport terms on the right-hand side of those equations are a small perturbation to the overall guiding center motion, the first-order errors accumulated in integrating the SDEs with the Euler-Murayama method become higher-order infinitesimals in the final results. The insensitivity of the calculated PSD to the value of ds, as described in the previous two paragraphs, justifies this approach. We note that there are also higher-than-first-order schemes of integrating SDEs, but these would greatly increase the computational cost and would require more stringent restrictions on the smoothness of the equation coefficients, so in practice the Euler-Maruyama scheme used in this paper is by far the most commonly used numerical solver for SDE calculations.

4 K2 simulations of a storm-time enhancement event

We have applied the K2 code to an idealized simulation of a radiation belt enhancement event, with drivers and inputs motivated by the 17 March 2013 storm (Li Z et al., 2014). This storm was characterized by a strong CME shock first depleting the phase-space density, with a subsequent rapid increase in electron phase-space density (PSD) and energies beginning first around $L = 4$ (Thorne et al., 2013; Li W et al., 2014). The solar wind conditions during this event are indicated in Figure 1 and discussed in more detail in Li et al. (2015). We used event-specific bounce-averaged chorus wave diffusion coefficients calculated for the NSF GEM QARBM (Quantitative Assessment of Radiation Belt Models) focus group challenge (Ma et al., 2018). In this section we have plotted K2 simulated PSD profiles, event-specific averaged chorus wave diffusion coefficients, and the spatial distribution of precipitated particles.

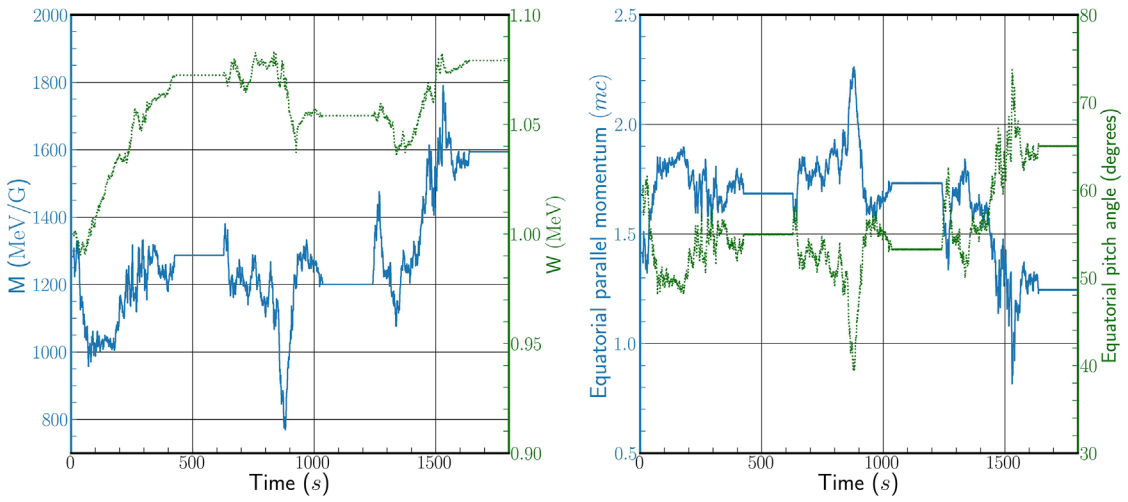

FIGURE 4
Example of a particle drifting about the Earth in a dipole field and undergoing interactions with whistler-mode chorus at different local times. In the left-hand figure, the particle's first invariant M (blue, solid) and energy W (green, dotted) are shown; in the right-hand figure, the particle's equatorial parallel momentum (blue, solid; in units of particle mass times *c*) and equatorial pitch angle (green, dotted) are shown. The effect of azimuthal variations in the chorus-based local diffusion coefficients are clearly visible as the particle drifts through local times.

In these K2 simulations we have not yet implemented contributions to the PSD from a possible low-energy (~100 keV) boundary population of particles (analogous to the blue random walk in Figure 2). Thus the current K2 PSDs are due to contributions from the initial condition only (the black random walk in Figure 2). This simplifies the interpretation of the simulated PSD profiles, but it omits potentially important contributions to PSD and precludes a comparison with measured PSDs. In later work we plan to implement a time-varying low-energy PSD boundary condition (corresponding to a time-dependent seed population for the radiation belt electrons) and compare K2 simulation results with measurements from spacecraft missions, such as the NASA Van Allen Probes mission and the ERG (Arase) mission.

Figure 5 plots K2 values of PSD $f(M,K,L)$ vs. L, for $M = 500$ MeV/G and $K = 0.056\ R_E\sqrt{\text{G}}$, and averaged $D_{\alpha\alpha}$ diffusion coefficients vs. L, for UT = 0 to UT = 12 on 17 March 2013. In these plots L is the distance, in Earth radii, from the center of Earth to the crossing point of the dipole field line of a given guiding center particle and the magnetic equatorial plane. Thus L is a dipole approximation to L^*, the Roederer L value. In this work, we attempt to minimize the effects of this approximation by starting our time-backward particle simulations from four local times (noon, dusk, midnight, and dawn) and averaging the results over each of these local times. In ongoing related work, we are beginning to calculate PSD as a function of M, K, and L^*, but more code development and testing of those calculations is needed before they are incorporated into the K2 code. In Figure 5 the black solid line for UT = 0 shows the initial PSD profile, taken from the AE8MAX empirical model (Vette, 1991). Also, solid lines are used for UT = 1 to UT = 7, and dashed lines are used for UT = 8 to UT = 12.

Figure 5A shows PSD profiles calculated in MHD fields with SDE wave-particle interactions; thus it includes effects of radial transport and chorus wave-particle interactions. The resulting PSD profiles vary significantly and in a complicated way in L and time. In order to better understand these dynamic PSD profiles, in Figures 5B, C we first isolate the chorus wave-particle interactions and the radial transport, respectively, and then we will return to a discussion of Figure 5A.

Figure 5B shows PSD profiles calculated in a static dipole magnetic field with SDE wave-particle interactions; thus it isolates effects of chorus wave-particle interactions on the PSD profiles. At all times, the absence of changes in the PSD profiles for $L \geq 7$ is because the QARBM diffusion coefficients are zero there. We note two main increases in PSD: i) for UT = 1 to UT = 7 PSD profiles in the range $5 < L < 7$ increase (while PSD profiles below $L = 5$ are unchanged), and ii) from UT = 8 to UT = 10, PSD profiles in the range $3.4 < L < 5.4$ increase (while PSD profiles in the range $6 < L < 7$ decrease mildly). This results in PSD values between $L = 3.4$ and $L = 7$ that are significantly higher than the initial condition, with a maximum increase near $L = 4$ by a factor of about 30. Overall, we see that PSD increases predominantly at early times at large L, and then at late times at small L. In the next paragraph we argue that the two main PSD increases can be identified with changes in the chorus wave diffusion coefficients.

For comparison with Figures 5B, D plots averaged values of the $D_{\alpha\alpha}$ diffusion coefficients over the course of the simulation. These values are plotted as a function of L, and are taken on a surface of constant $K = 0.056\ R_E\sqrt{\text{G}}$ with $M = 500$ MeV/G to match the simulations, and then averaged over the four MLT sectors. We have plotted $D_{\alpha\alpha}$ values, but corresponding plots of $D_{\alpha p}$ and D_{pp} have very similar L and t dependence, as can be seen in Figure 3. Averaged diffusion coefficients below about 0.042/hour (corresponding to a diffusion time scale above about 24 h) result in negligible changes in PSD over this 12-h simulation. Two main features of the L and t dependence of the averaged $D_{\alpha\alpha}$ diffusion coefficients can be identified with the two main PSD increases in Figure 5B. First,

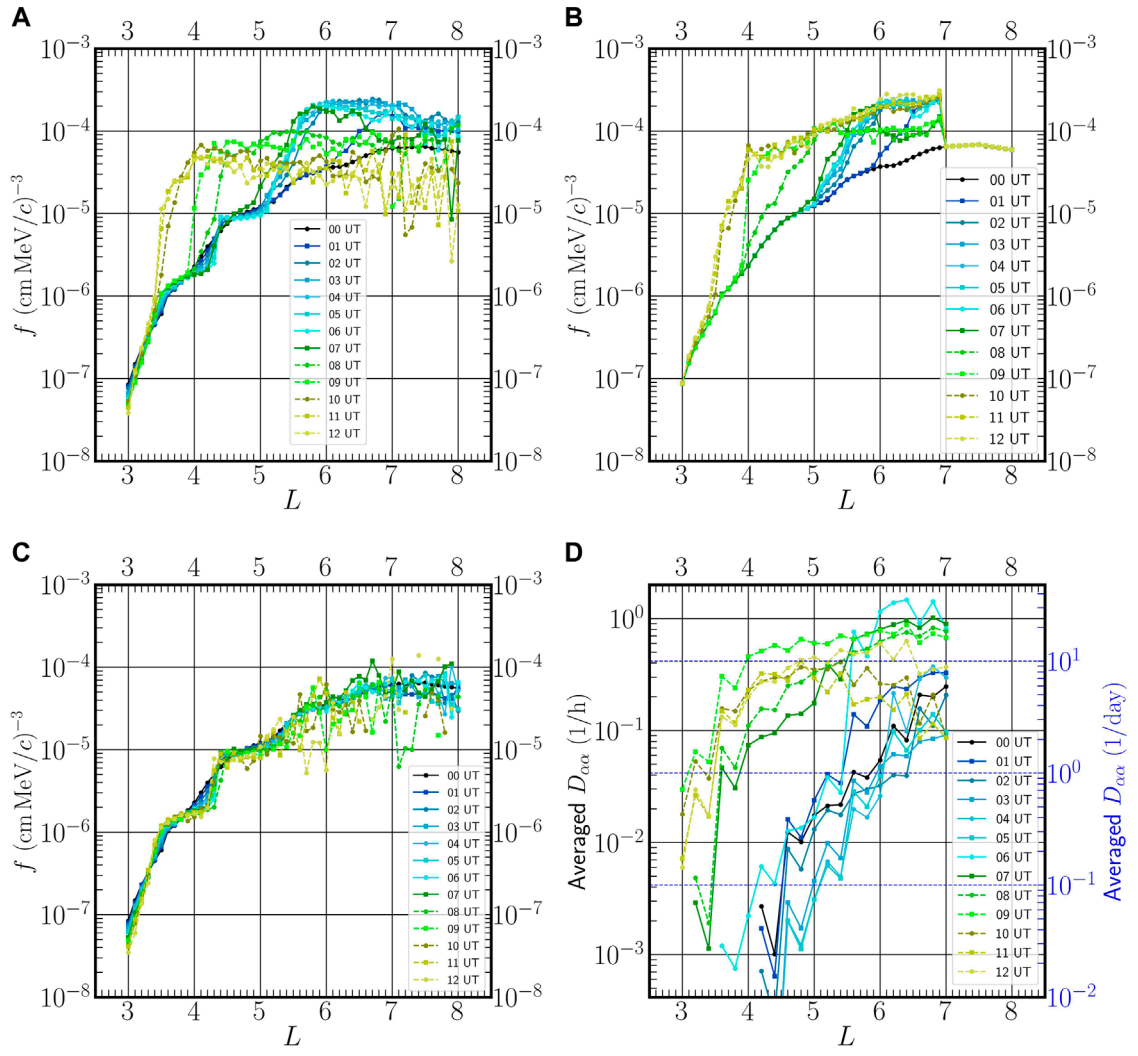

FIGURE 5
Phase-space density f in units (cm MeV/c)$^{-3}$, for electrons with M = 500 MeV/G and K = 0.056 R_E $\sqrt{G}$ (corresponding to 1.32 MeV electrons with equatorial pitch angle 62° and mirror point latitude 13.7° at L = 4 in a dipole magnetic field) and averaged $D_{\alpha\alpha}$ diffusion coefficients. L is a dipole approximation to the Roederer L value. Times are UT on 17 March 2013. Solid lines are used for UT = 1 to UT = 7, and dashed lines are used for UT = 8 to UT = 12. **(A)** PSD calculated with MHD fields and SDE wave-particle effects included. **(B)** PSD calculated with a static dipole magnetic field and SDE wave-particle effects (to isolate the SDE effects). **(C)** PSD calculated with MHD fields, but no SDE wave-particle effects (to isolate the MHD-driven radial transport). **(D)** Averaged $D_{\alpha\alpha}$ diffusion coefficients, for comparison with **(A,B)**. See the text for further details.

for $L > 5$ and UT = 1 to UT = 6 the averaged diffusion rates have relatively high values (between about 0.042/hour and 1.0/hour), and this can be identified with the PSD increases described in item i) of the previous paragraph. Second, for $L \lesssim 5.4$ and for UT = 7 to UT = 10 the averaged diffusion rates are much higher than at earlier times for $L \lesssim 5.4$; and this can be identified with the large PSD increases described in item ii) of the previous paragraph. Therefore, large increases in PSD can be identified with large local chorus wave diffusion coefficients.

Figure 5C shows PSD profiles calculated in MHD fields, but without SDE wave-particle interactions; thus it isolates effects of MHD-induced radial transport on the PSD profiles. Throughout the 12 h of the simulation the PSD profiles are relatively constant. They show small deviations from the initial condition for $L \lesssim 5.5$, and larger, more-variable fluctuations for $L \gtrsim 5.5$. The latter are due to insufficient numbers of particles contributing to the PSD (including several cases of zero contributions that occur because the particle's backward-in-time trajectory does not reach the initial condition), and as a result, for UT = 8 to UT = 12 PSD values for $L \gtrsim 5.5$ are not reliable. We usually start with around N = 10,000 backward trajectories to obtain each final value of f. Because the relative error scales as $1/\sqrt{N}$ (we checked this numerically) this typically results in relative errors of around 1%, which we regard as sufficiently small relative to other errors and uncertainties. Sometimes significant numbers of time-backward trajectories do not reach the initial condition and this can give poor statistics; in this case, we run more backward trajectories, but even then, the statistics may not improve very much (and the relatively weak $1/\sqrt{N}$ scaling is costly). Further

work will be needed to diagnose and improve the low statistics at these times and L values, but loss by magnetopause shadowing no doubt plays a role, especially for $L \gtrsim 7$.

Revisiting Figure 5A we can now identify and interpret the main features of the overall PSD evolution in MHD fields with SDE wave-particle interactions included. First, for UT = 1 to UT = 7 the PSD profiles between L = 5 and L = 7 increase almost an order of magnitude, associated primarily with local acceleration, while the PSD increase for $L > 7$ is consistent with outward radial diffusion. Note that the sharp gradient in Figure 5B at L = 7 is smoothed out within 1 hour. Second, for UT = 7 to UT = 10 the PSD profiles for $L \lesssim 5$ increase rapidly, also associated primarily with local acceleration; in particular, near L = 4.1 PSD increases by an order of magnitude within 1 hour (from UT = 8 to UT = 9). Note that combined radial transport and chorus wave-particle interactions can result in PSD increases that are larger than the increase with SDEs alone (for example, the PSD increase near L = 3.5 at UT = 11 is larger in Figure 5A than in Figure 5B). Third, for UT = 10-12 the PSD profiles for $L \gtrsim 7$ have decreased compared to UT = 8, probably due to magnetopause shadowing and outward radial transport, but these values are less reliable because of low statistics and large error bars. Further work is needed to better model PSD at these late times and large L values.

Just as we calculate PSD in Figure 5 from the mean of the PSD values from all the contributing time-reversed trajectories, we have calculated the error bars from the corresponding standard deviation of those PSD values. In general, except for late times and large L values in Figure 5A, the error bars are mostly smaller than, or comparable to, the size of the plotting symbols. We also note that for this Methods paper, we chose to show results for only one pair of M and K values, in order to demonstrate the capabilities of the K2 code, and we plan to investigate the dependence of our simulation results on changing values of M and K in future work.

Figure 6 replots the same data as Figure 5 using the same four panels, but using heatmap plots rather than line plots. Comparing Figure 5 and Figure 6 we see that the heatmap format can be better for visualizing certain features of the data. For example, the heatmap plots better show the noisy low-statistics PSD values and the zero PSD values seen at late times and large L, particularly in Figures 5A versus Figure 6A and Figures 5C versus Figure 6C. This is primarily because the noisy overlapping lines in Figure 5 are difficult to separate visually. Also, the grey regions of the heatmap plots clearly show regions with zero values, whereas the zero values are omitted from the line plots.

In Figure 7 we show how the K2 code may be used to examine particle loss to the atmosphere as a result of scattering via interactions with whistler-mode chorus waves. Here, particles were launched in the interval L = [3.0,8.0] with a constant initial value of K; in this instance, we chose K = .0561 $R_E\sqrt{G}$ corresponding to a particle mirroring 15° from the SM (solar magnetic) equatorial plane at L = 6 in a dipole field. Particle trajectories were tracked in the dynamic MHD fields using event-specific SDE wave-particle interactions, corresponding to the situation shown in Figure 5A. Those particle trajectories that intersected the inner boundary of the MHD simulation domain at ~2.3 R_E were removed from the simulation, and the location at which the particles intersected the boundary traced down to 1.1 R_E using a dipole approximation. The inner boundary at ~2.3 R_E occurs because below that value the Alfvén speed becomes fast enough that MHD time steps become prohibitively small, and the value 1.1 R_E corresponds roughly to the top of Earth's atmosphere.

Figure 7 marks the location of each precipitated electron as a function of latitude and longitude, integrated over the full 12 h duration of the simulation. We note that the density of marks varies with both latitude and longitude, reflecting the local time variation of the event-specific local diffusion coefficients used in this simulation. In particular, we note a relatively high density of marks in the southern hemisphere between 0 and -5 h LT. This feature may be appearing because the event-specific diffusion coefficients

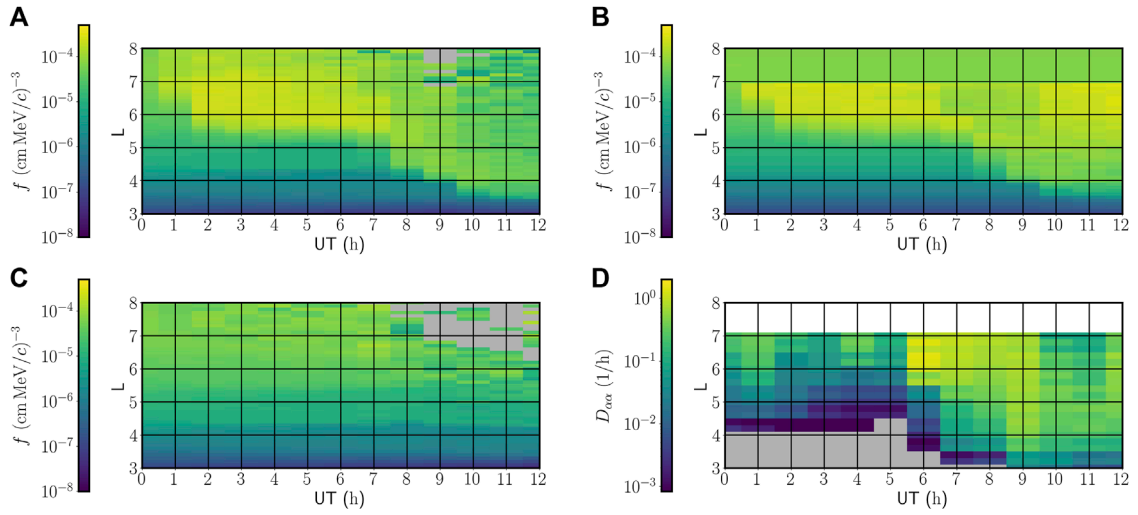

FIGURE 6
Phase-space densities f and averaged $D_{\alpha\alpha}$ diffusion coefficients from Figure 5, re-plotted in L-t heatmap format. The subfigure labels **(A–D)** correspond to the same labels in Figure 5. Grey pixels show zero values and white indicates no values were calculated there.

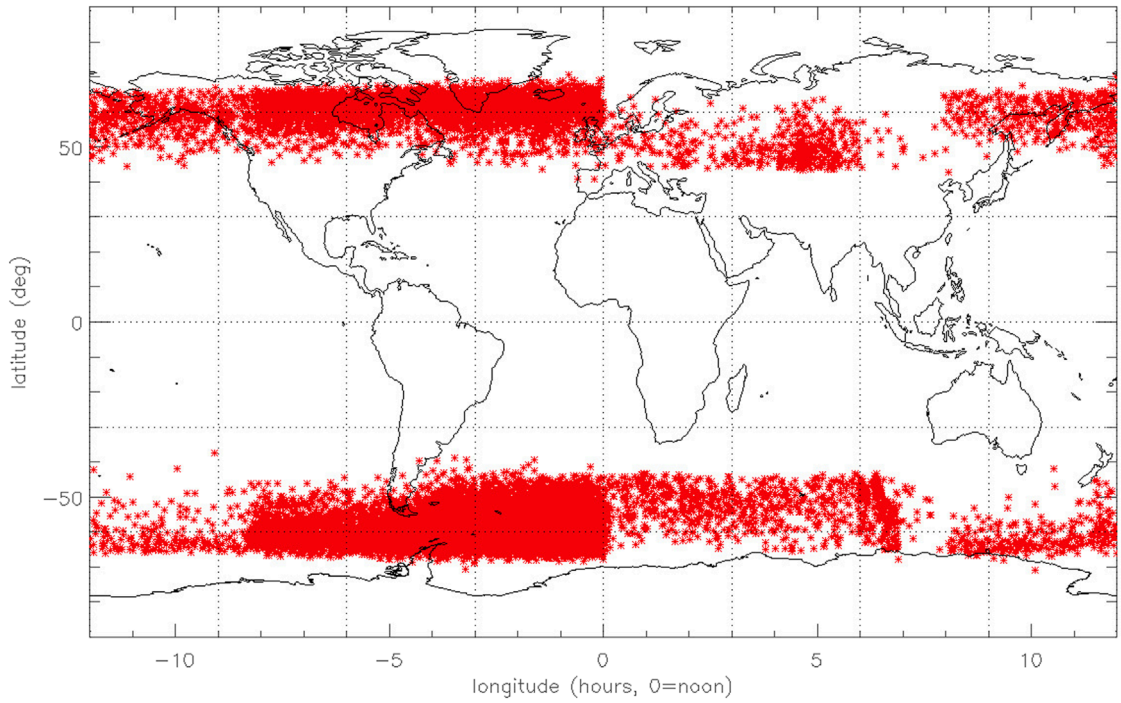

FIGURE 7
Figure showing the location where individual test particles intersect the inner boundary of the MHD simulation at ~2.3R_E, traced down to 1.1R_E using a dipole approximation. This figure shows how the K2 method can be used to quantify precipitated particle loss during geomagnetic storms.

we use are determined from POES precipitation data, which would be enhanced near the South Atlantic Anomaly (SAA); we note that this feature is not in the expected latitudinal range of the SAA (namely, between about 50° south and the equator), but because the MHD simulations do not contain the dipole field offset associated with the SAA, we do not expect to accurately reproduce the SAA location. We also note a North-South asymmetry in the number of test particles precipitating into the atmosphere, which we suggest is a result of the prevailing dipole tilt during this 12 h period of the simulation.

Test particles are also self-consistently lost from the simulation as they intersect the magnetopause: during periods of southward IMF, these test particles fail a check on the conservation of the first adiabatic invariant as they transition from the northward fields interior to the magnetopause, to the southward fields in the magnetosheath and solar wind. During periods of northward IMF, those test particles intersecting the magnetopause and not failing the adiabaticity check simply drift with the solar wind until they reach an outer boundary of the simulation domain. Further work contrasting the time history and phase-space density of precipitating particles to those lost to the magnetopause will allow us to examine the conditions and extent to which each loss process affects the dynamics of the radiation belts.

5 Summary and discussion

In summary, the main conclusions of this work are:

1. SDEs provide a powerful and general method to incorporate stochastic cyclotron-frequency wave-particle interactions into MHD-particle simulation codes. This includes quasilinear wave-particle interactions (WPIs) and stochastic nonlinear WPIs. The methods are adaptable to full-particle, guiding center, and bounce-center particle tracing.
2. In the K2 code, we have implemented the SDE methods into a guiding-center MHD-particle simulation code for Earth's radiation belts.
3. The K2 code can comprehensively simulate radiation belt dynamics, including radial transport (which may be diffusive or non-diffusive), mesoscale magnetospheric field effects (such as magnetopause shadowing and drift-orbit bifurcation), and effects of cyclotron-frequency WPIs (such as precipitation losses to the ionosphere, local acceleration, and cross-term energy and pitch-angle diffusion).
4. We have performed a K2 radiation belt simulation motivated by the 17 March 2013 storm (e.g., Li W et al., 2014). We used event-specific bounce-averaged chorus wave diffusion coefficients calculated for the NSF GEM QARBM (Quantitative Assessment of Radiation Belt Models) focus group challenge, and plotted PSD profiles, averaged event-specific diffusion coefficients, and a spatial distribution of precipitated particles.
5. In this K2 simulation we find that local chorus wave-particle interactions can give rapid ($\lesssim$ 1 hour) changes in PSD, MHD-driven radial transport can smooth out sharp radial PSD gradients within 1 hour, combined chorus wave-particle interactions and radial transport can give PSD incresaes greater than chorus wave-particle interactions alone, and losses seen in

the simulation are qualitatively consistent with magnetopause shadowing and chorus wave-induced precipitation.

Compared to other radiation belt models, K2 has a number of strengths. First, unlike 3D diffusion models, K2 is not bounded by a last closed drift shell. Second, K2 contains both diffusive and nondiffusive radial transport. Third, K2 includes effects of off-diagonal radial-energy and radial-pitch-angle scattering associated with drift-shell splitting, and Shabansky orbits are automatically included. Fourth, K2 contains dynamic meso-scale magnetospheric field effects such as magnetopause shadowing and subsequent outward radial transport. The K2 code contains similar basic physics (bounce-averaged particle dynamics and quasilinear cyclotron wave interactions) to existing 4D radiation belt transport models described by Jordanova et al. (2008), Fok et al. (2008), and Shprits et al. (2015), but the main advantage of the K2 code over those models is the use of dynamic global MHD fields, which is especially important for event simulations. That said, K2 is computationally demanding and storage intensive, both in terms of the underlying global MHD simulations used to drive the test particles, and the test particle simulations themselves. The high time resolution required to fully resolve the bounce-drift motion of the particles makes this method better-suited to simulating radiation belt dynamics during individual geomagnetic events, rather than simulating weeks or months of radiation belt evolution.

We note that the background fields provided by the LFM MHD simulation code are susceptible to the sources of error discussed in Section 2.1. In the case of the results presented here, we used a version of the LFM code that is coupled with the Rice Convection Model (RCM) (Pembroke et al., 2012). The RCM provides a representation of the inner magnetospheric ring current, reducing errors in the stretching and morphology of the global magnetic field. The RCM also provides a model plasmasphere that dynamically changes with solar wind driving conditions, reducing errors in ULF wave propagation and the resulting radial transport of energetic particles. However, the version of the LFM used in this manuscript does not include potentially-relevant physical effects such as self-consistent plasmaspheric refilling via ionospheric outflow. Coupling the K2 framework to MHD models with better representations of the ring current and plasmasphere could improve the overall accuracy of the test particle simulation results.

While these preliminary results show the promise of the comprehensive global simulations made possible by K2, there are still several areas where the current framework may be improved. For example, the results shown here commonly assume a dipole field geometry in initializing the particle populations (e.g., in the calculation of the invariant K and corresponding initialization latitudes of test particles), as well as in the ordering of simulation results (e.g., assuming an L corresponding to a dipole field rather than the MHD fields distorted by external fields associated with magnetospheric currents). To that end, we are implementing an efficient iterative method that allows fast calculation of adiabatic invariants in dynamically-evolving MHD fields, to be described in another manuscript. Also, we currently assume a constant low-energy (keV) seed population given by the AE-8 trapped electron model; future improvements will use data-driven low-energy seed particle populations to provide time-dependent boundary conditions based on (where available) observations. Similarly, a non-zero outer boundary condition corresponding to energetic particles in the plasmasheet and near-Earth tail may be implemented to model the effects of those particles that may be convectively trapped in the inner magnetosphere or injected via substorm activity. With these improvements, we expect the K2 model to provide a comprehensive framework for simulating a wide range of physical processes, and allow detailed comparison of global radiation belt dynamics to those provided by *in situ* measurements.

Data availability statement

The datasets presented in this study can be found in online repositories. The names of the repository/repositories and accession number(s) can be found below: https://doi.org/10.5281/zenodo.8030588, https://doi.org/10.6084/m9.figshare.23405129.

Author contributions

AC and SE developed the concepts and implementation of the K2 model and wrote the first draft of the manuscript. SSA and WJL assisted with the incorporation of the chorus wave diffusion coefficients into K2. SAA contributed to the K2 coding and plotting of the results. JA discussed the conceptual basis of K2 with AC. AJ and DM contributed to the conception and development of this paper. QM and WL provided the chorus wave diffusion coefficients. All authors contributed to the article and approved the submitted version.

Funding

SE, AC, WJL, and SAA were supported by NASA LWS grant number 80NSSC21K1323. AJ, DM, SE, AC, and WJL were supported by NASA H-SR grant number NNX17AI51G. WL would like to acknowledge the NASA grants 80NSSC19K0845 and 80NSSC20K0698. QM is supported by the NASA grant 80NSSC20K0196.

Acknowledgments

The authors acknowledge Professor Xin Tao and Dr. Liheng Zheng for important contributions to the development of the radiation belt SDE methods that were adapted for use in the K2 model.

Conflict of interest

The authors declare that the research was conducted in the absence of any commercial or financial relationships that could be construed as a potential conflict of interest.

Publisher's note

References

Albert, J. M., Meredith, N. P., and Horne, R. B. (2009). Three-dimensional diffusion simulation of outer radiation belt electrons during the 9 October 1990 magnetic storm. *J. Geophys. Res. Space Phys.* 114. doi:10.1029/2009JA014336

Beutier, T., and Boscher, D. (1995). A three-dimensional analysis of the electron radiation belt by the Salammbô code. *J. Geophys. Res.* 100, 14853. doi:10.1029/94JA03066

Birn, J., Thomsen, M. F., Borovsky, J. E., Reeves, G. D., McComas, D. J., and Belian, R. D. (1997). Characteristic plasma properties during dispersionless substorm injections at geosynchronous orbit. *J. Geophys. Res.* 102, 2309–2324. doi:10.1029/96JA02870

Brizard, A. J., and Chan, A. A. (2001). Relativistic bounce-averaged quasilinear diffusion equation for low-frequency electromagnetic fluctuations. *Phys. Plasmas* 8, 4762–4771. doi:10.1063/1.1408623

Cash, J. R., and Karp, A. H. (1990). A variable order Runge-Kutta method for initial value problems with rapidly varying right-hand sides. *ACM Trans. Math. Softw.* 16, 201–222. doi:10.1145/79505.79507

Chan, A. A., Elkington, S. R., and Albert, J. M. (2010). Development of MHD-SDE methods for radiation belt simulations. *38th COSPAR Sci. Assem.* 38, 4.

Drozdov, A. Y., Blum, L. W., Hartinger, M., Zhao, H., Lejosne, S., Hudson, M. K., et al. (2022). Radial transport versus local acceleration: the long-standing debate. *Earth Space Sci.* 9. doi:10.1029/2022EA002216

Drozdov, A. Y., Shprits, Y. Y., Orlova, K. G., Kellerman, A. C., Subbotin, D. A., Baker, D. N., et al. (2015). Energetic, relativistic, and ultrarelativistic electrons: comparison of long-term VERB code simulations with van allen probes measurements. *J. Geophys. Res. Space Phys.* 120, 3574–3587. doi:10.1002/2014JA020637

Elkington, S. R., Baker, D. N., and Wiltberger, M. (2005). "Injection of energetic ions during the 31 March 2001 0630 substorm," in *The inner magnetosphere: Physics and modeling*. Editors T. I. Pulkkinen, N. A. Tsyganenko, R. H. W. Friedel, and D. C. Washington (American Geophysical Union). vol. 155 of Geophysical Monographs, 147. doi:10.1029/155GM17

Elkington, S. R., Hudson, M. K., and Chan, A. A. (1999). Acceleration of relativistic electrons via drift-resonant interaction with toroidal-mode Pc-5 ULF oscillations. *Geophys. Res. Lett.* 26, 3273–3276. doi:10.1029/1999gl003659

Elkington, S. R., Hudson, M. K., and Chan, A. A. (2003). Resonant acceleration and diffusion of outer zone electrons in an asymmetric geomagnetic field. *J. Geophys. Res.* 108, 1116. doi:10.1029/2001JA009202

Elkington, S. R., Hudson, M. K., Wiltberger, M. J., and Lyon, J. G. (2002). MHD/Particle simulations of radiation belt dynamics. *J. Atmos. Sol. Terr. Phys.* 64, 607–615. doi:10.1016/S1364-6826(02)00018-4

Elkington, S. R., Wiltberger, M., Chan, A. A., and Baker, D. N. (2004). Physical models of the geospace radiation environment. *J. Atmos. Sol. Terr. Phys.* 66, 1371–1387. doi:10.1016/j.jastp.2004.03.023

Fei, Y., Chan, A. A., Elkington, S. R., and Wiltberger, M. J. (2006). Radial diffusion and MHD particle simulations of relativistic electron transport by ULF waves in the September 1998 storm. *J. Geophys. Res.* 111, A12209. doi:10.1029/2005JA011211

Fok, M.-C., Horne, R. B., Meredith, N. P., and Glauert, S. A. (2008). Radiation belt environment model: application to space weather nowcasting. *J. Geophys. Res.* 113, A03S08. doi:10.1029/2007JA012558

Glauert, S. A., Horne, R. B., and Meredith, N. P. (2014). Three-dimensional electron radiation belt simulations using the BAS radiation belt model with new diffusion models for chorus, plasmaspheric hiss, and lightning-generated whistlers. *J. Geophys. Res. Space Phys.* 119, 268–289. doi:10.1002/2013JA019281

Hudson, M. K., Marchenko, V. A., Roth, I., Temerin, M., Blake, J. B., and Gussenhoven, M. S. (1998). Radiation belt formation during storm sudden commencements and loss during main phase. *Adv. Space Res.* 21, 597–607. doi:10.1016/s0273-1177(97)00969-1

Hudson, M. K., Paral, J., Kress, B. T., Wiltberger, M., Baker, D. N., Foster, J. C., et al. (2015). Modeling CME-shock driven storms in 2012-2013: MHD-test particle simulations. *J. Geophys. Res.* 120, 1168–1181. doi:10.1002/2014JA020833

Jordanova, V. K., Albert, J., and Miyoshi, Y. (2008). Relativistic electron precipitation by EMIC waves from self-consistent global simulations. *J. Geophys. Res.* 113, A00A10. doi:10.1029/2008JA013239

Kim, H.-J., Chan, A. A., Wolf, R. A., and Birn, J. (2000). Can substorms produce relativistic electrons? *J. Geophys. Res.* 105, 7721–7735. doi:10.1029/1999JA900465

Kress, B. T., Hudson, M. K., and Paral, J. (2014). Rebuilding of the Earth's outer electron belt during 8–10 October 2012. *Geophys. Res. Lett.* 41, 749–754. doi:10.1002/2013GL058588

Kress, B. T., Hudson, M. K., Selesnick, R. S., Mertens, C. J., and Engel, M. (2015). Modeling geomagnetic cutoffs for space weather applications. *J. Geophys. Res.* 120, 5694–5702. doi:10.1002/2014JA020899

Lejosne, S., and Kollmann, P. (2020). Radiation belt radial diffusion at Earth and beyond. *Space Sci. Rev.* 216, 19. doi:10.1007/s11214-020-0642-6

Li, W., and Hudson, M. K. (2019). Earth's van allen radiation belts: from discovery to the van allen probes era. *J. Geophys. Res.* 124, 8319–8351. doi:10.1029/2018JA025940

Li, W., Ma, Q., Thorne, R. M., Bortnik, J., Zhang, X.-J., Li, J., et al. (2016). Radiation belt electron acceleration during the 17 March 2015 geomagnetic storm: observations and simulations. *J. Geophys. Res. Space Phys.* 121, 5520–5536. doi:10.1002/2016JA022400

Li, W., Ni, B., Thorne, R. M., Bortnik, J., Green, J. C., Kletzing, C. A., et al. (2013). Constructing the global distribution of chorus wave intensity using measurements of electrons by the POES satellites and waves by the Van Allen Probes. *Geophys. Res. Lett.* 40, 4526–4532. doi:10.1002/grl.50920

Li, W., Thorne, R. M., Ma, Q., Ni, B., Bortnik, J., Baker, D. N., et al. (2014). Radiation belt electron acceleration by chorus waves during the 17 March 2013 storm. *J. Geophys. Res.* 119, 4681–4693. doi:10.1002/2014JA019945

Li, X., Roth, I., Temerin, M., Wygant, J. R., Hudson, M. K., and Blake, J. B. (1993). Simulation of the prompt energization and transport of radiation belt particles during the March 24, 1991 SSC. *Geophys. Res. Lett.* 20, 2423–2426. doi:10.1029/93gl02701

Li, Z., Hudson, M. K., Jaynes, A. N., Boyd, A. J., Malaspina, D. M., Thaller, S. A., et al. (2014). Modeling gradual diffusion changes in radiation belt electron phase space density for the March 2013 Van Allen Probes case study. *J. Geophys. Res.* 119, 8396–8403. doi:10.1002/2014JA020359

Li, Z., Hudson, M., Kress, B., and Paral, J. (2015). Three-dimensional test particle simulation of the 17-18 March 2013 CME shock-driven storm. *Geophys. Res. Lett.* 42, 5679–5685. doi:10.1002/2015gl064627

Longley, W. J., Chan, A. A., Jaynes, A. N., Elkington, S. R., Pettit, J. M., Ross, J. P. J., et al. (2022). Using MEPED observations to infer plasma density and chorus intensity in the radiation belts. *Front. Astronomy Space Sci.* 9. doi:10.3389/fspas.2022.1063329

Lyon, J. G., Fedder, J. A., and Mobarry, C. M. (2004). The Lyon–Fedder–Mobarry (LFM) global MHD magnetospheric simulation code. *J. Atmos. Sol. Terr. Phys.* 66, 1333–1350. doi:10.1016/j.jastp.2004.03.020

Ma, Q., Li, W., Bortnik, J., Thorne, R. M., Chu, X., Ozeke, L. G., et al. (2018). Quantitative evaluation of radial diffusion and local acceleration processes during GEM challenge events. *J. Geophys. Res. Space Phys.* 123, 1938–1952. doi:10.1002/2017JA025114

Ma, Q., Li, W., Thorne, R. M., Nishimura, Y., Zhang, X.-J., Reeves, G. D., et al. (2016). Simulation of energy-dependent electron diffusion processes in the Earth's outer radiation belt. *J. Geophys. Res. Space Phys.* 121, 4217–4231. doi:10.1002/2016JA022507

Maget, V., Sicard-Piet, A., Bourdarie, S., Lazaro, D., Turner, D. L., Daglis, I. A., et al. (2015). Improved outer boundary conditions for outer radiation belt data assimilation using THEMIS-SST data and the Salammbo-EnKF code. *J. Geophys. Res. Space Phys.* 120, 5608–5622. doi:10.1002/2015JA021001

Matsumoto, M., and Nishimura, T. (1998). Mersenne twister: a 623-dimensionally equidistributed uniform pseudo-random number generator. *ACM Trans. Model. Comp. Sim.* 8, 3–30. doi:10.1145/272991.272995

Merkin, V. G., Panov, E. V., Sorathia, K. A., and Ukhorskiy, A. Y. (2019). Contribution of bursty bulk flows to the global dipolarization of the magnetotail during an isolated substorm. *J. Geophys. Res.* 124, 8647–8668. doi:10.1029/2019JA026872

Ni, B., Li, W., Thorne, R. M., Bortnik, J., Green, J. C., Kletzing, C. A., et al. (2014). A novel technique to construct the global distribution of whistler mode chorus wave intensity using low-altitude POES electron data. *J. Geophys. Res. Space Phys.* 119, 5685–5699. doi:10.1002/2014JA019935

Orlova, K. G., and Shprits, Y. Y. (2010). Dependence of pitch-angle scattering rates and loss timescales on the magnetic field model. *Geophys. Res. Lett.* 37, L05105. doi:10.1029/2009GL041639

Pembroke, A., Toffoletto, F., Sazykin, S., Wiltberger, M., Lyon, J., Merkin, V., et al. (2012). Initial results from a dynamic coupled magnetosphere-ionosphere-ring current model. *J. Geophys. Res.* 117, A02211. doi:10.1029/2011JA016979

Ripoll, J.-F., Claudepierre, S. G., Ukhorskiy, A. Y., Colpitts, C., Li, X., Fennell, J. F., et al. (2020). Particle dynamics in the Earth's radiation belts: review of current research and open questions. *J. Geophys. Res. Space Phys.* 125, e2019JA026735. doi:10.1029/2019ja026735

Ripoll, J. F., Reeves, G. D., Cunningham, G. S., Loridan, V., Denton, M., Santolík, O., et al. (2016). Reproducing the observed energy-dependent structure of Earth's electron radiation belts during storm recovery with an event-specific diffusion model. *Geophys. Res. Lett.* 43, 5616–5625. doi:10.1002/2016GL068869

Schulz, M., and Lanzerotti, L. J. (1974). "Particle diffusion in the radiation belts," in *Physics and chemistry in space, vol. 7* (New York: Springer-Verlag). doi:10.1007/978-3-642-65675-0

Selesnick, R. S., Hudson, M. K., and Kress, B. T. (2013). Direct observation of the CRAND proton radiation belt source. *J. Geophys. Res. Space Phys.* 118, 7532–7537. doi:10.1002/2013JA019338

Sheeley, B. W., Moldwin, R., Rassoul, H. K., and Anderson, R. R. (2001). An empirical plasmasphere and trough density model: CRRES observations. *J. Geophys. Res.* 106, 25631–25641. doi:10.1029/2000JA000286

Shprits, Y. Y., Kellerman, A. C., Drozdov, A. Y., Spence, H. E., Reeves, G. D., and Baker, D. N. (2015). Combined convective and diffusive simulations: VERB-4D comparison with 17 March 2013 van allen probes observations. *Geophys. Res. Lett.* 42, 9600–9608. doi:10.1002/2015GL065230

Shprits, Y. Y., Subbotin, D., and Ni, B. (2009). Evolution of electron fluxes in the outer radiation belt computed with the VERB code. *J. Geophys. Res. Space Phys.* 114. doi:10.1029/2008JA013784

Sorathia, K. A., Michael, A., Merkin, V., Ukhorskiy, A., Turner, D. L., Lyon, J., et al. (2021). The role of mesoscale plasma sheet dynamics in ring current formation. *Front. Astronomy Space Sci.* 8. 761875. doi:10.3389/fspas.2021.761875

Sorathia, K. A., Ukhorskiy, A. Y., Merkin, V. G., Fennell, J. F., and Claudepierre, S. G. (2018). Modeling the depletion and recovery of the outer radiation belt during a geomagnetic storm: combined mhd and test particle simulations. *J. Geophys. Res. Space Phys.* 123, 5590–5609. doi:10.1029/2018JA025506

Su, Z., Xiao, F., Zheng, H., and Wang, S. (2011). CRRES observation and STEERB simulation of the 9 October 1990 electron radiation belt dropout event. *Geophys. Res. Lett.* 38, L06106. doi:10.1029/2011GL046873

Tao, X., Albert, J. M., and Chan, A. A. (2009). Numerical modeling of multidimensional diffusion in the radiation belts using layer methods. *J. Geophys. Res.* 114, A02215. doi:10.1029/2008JA013826

Tao, X., Chan, A. A., Albert, J. M., and Miller, J. A. (2008). Stochastic modeling of multidimensional diffusion in the radiation belts. *J. Geophys. Res.* 113, A07212. doi:10.1029/2007JA012985

Tao, X., Chan, A. A., and Brizard, A. J. (2007). Hamiltonian theory of adiabatic motion of relativistic charged particles. *Phys. Plasmas* 14, 092107. doi:10.1063/1.2773702

Thorne, R. M., Li, W., Ni, B., Ma, Q., Bortnik, J., Chen, L., et al. (2013). Rapid local acceleration of relativistic radiation-belt electrons by magnetospheric chorus. *Nature* 504, 411–414. doi:10.1038/nature12889

Tu, W., Cunningham, G. S., Chen, Y., Morley, S. K., Reeves, G. D., Blake, J. B., et al. (2014). Event-specific chorus wave and electron seed population models in DREAM3D using the Van Allen Probes. *Geophys. Res. Lett.* 41, 1359–1366. doi:10.1002/2013GL058819

Tu, W., Li, W., Albert, J. M., and Morley, S. K. (2019). Quantitative assessment of radiation belt modeling. *J. Geophys. Res. Space Phys.* 124, 898–904. doi:10.1029/2018JA026414

Vette, J. I. (1991). *The AE-8 trapped electron model environment*. Tech. Rep. NSSDC/WDC-A-R&S 91-24. Greenbelt, MD: NASA Goddard Space Flight Center.

Wiltberger, M., Pulkkinen, T. I., Lyon, J. G., and Goodrich, C. C. (2000). MHD simulation of the magnetotail during the December 10, 1996, substorm. *J. Geophys. Res.* 105, 27649–27663. doi:10.1029/1999ja000251

Woodroffe, J., Brito, T., Jordanova, V., Henderson, M., Morley, S., and Denton, M. (2018). Data-optimized source modeling with the backwards Liouville test–kinetic method. *J. Atmos. Solar-Terrestrial Phys.* 177, 125–130. doi:10.1016/j.jastp.2017.09.010

Zheng, L., Chan, A. A., Albert, J. M., Elkington, S. R., Koller, J., Horne, R. B., et al. (2014). Three-dimensional stochastic modeling of radiation belts in adiabatic invariant coordinates. *J. Geophys. Res. Space Phys.* 119, 7615–7635. doi:10.1002/2014JA020127

Zheng, L., Chen, L., Chan, A. A., Wang, P., Xia, Z., and Liu, X. (2021). UBER v1.0: a universal kinetic equation solver for radiation belts. *Geosci. Model Dev.* 14, 5825–5842. doi:10.5194/gmd-14-5825-2021

frontiers | Frontiers in Astronomy and Space Sciences

TYPE Original Research
PUBLISHED 10 October 2023
DOI 10.3389/fspas.2023.1251563

OPEN ACCESS

EDITED BY
Xiao-Jia Zhang,
The University of Texas at Dallas, United States

REVIEWED BY
Jun Liang,
University of Calgary, Canada
Xiangrong Fu,
New Mexico Consortium, United States

*CORRESPONDENCE
Miroslav Hanzelka,
mirekhanzelka@gmail.com

RECEIVED 01 July 2023
ACCEPTED 26 September 2023
PUBLISHED 10 October 2023

CITATION
Hanzelka M, Li W, Ma Q, Qin M, Shen X-C, Capannolo L and Gan L (2023), Full-wave modeling of EMIC wave packets: ducted propagation and reflected waves.
Front. Astron. Space Sci. 10:1251563.
doi: 10.3389/fspas.2023.1251563

Full-wave modeling of EMIC wave packets: ducted propagation and reflected waves

Miroslav Hanzelka[1,2]*, Wen Li[1], Qianli Ma[1,3], Murong Qin[1], Xiao-Chen Shen[1], Luisa Capannolo[1] and Longzhi Gan[1]

[1]Center for Space Physics, Boston University, Boston, MA, United States, [2]Department of Space Physics, Institute of Atmospheric Physics of the Czech Academy of Sciences, Prague, Czechia, [3]Department of Atmospheric and Oceanic Sciences, UCLA, Los Angeles, CA, United States

Electromagnetic ion cyclotron (EMIC) waves can scatter radiation belt electrons with energies of a few hundred keV and higher. To accurately predict this scattering and the resulting precipitation of these relativistic electrons on short time scales, we need detailed knowledge of the wave field's spatio-temporal evolution, which cannot be obtained from single spacecraft measurements. Our study presents EMIC wave models obtained from two-dimensional (2D) finite-difference time-domain (FDTD) simulations in the Earth's dipole magnetic field. We study cases of hydrogen band and helium band wave propagation, rising-tone emissions, packets with amplitude modulations, and ducted waves. We analyze the wave propagation properties in the time domain, enabling comparison with *in situ* observations. We show that cold plasma density gradients can keep the wave vector quasiparallel, guide the wave energy efficiently, and have a profound effect on mode conversion and reflections. The wave normal angle of unducted waves increases rapidly with latitude, resulting in reflection on the ion hybrid frequency, which prohibits propagation to low altitudes. The modeled wave fields can serve as an input for test-particle analysis of scattering and precipitation of relativistic electrons and energetic ions.

KEYWORDS

EMIC waves, wave propagation properties, full-wave simulation, mode conversion, ducted waves, reflected waves, cold plasma, Earth's inner magnetosphere Frontiers

1 Introduction

The electromagnetic ion cyclotron (EMIC) wave is a type of electromagnetic emission that is generated by unstable anisotropic ion distributions (Cornwall, 1965; Anderson et al., 1996; Min et al., 2015) and interacts with relativistic and ultrarelativistic electrons in the Earth's radiation belts (Horne and Thorne, 1998; Summers et al., 1998; Li and Hudson, 2019; Baker, 2021). The wave frequencies are typically extremely low, ranging from $f = 0.1$ Hz to $f = 5.0$ Hz (Saito, 1969). More precisely, the upper-frequency limit is determined by the proton cyclotron frequency (f_{cp}) in the source, which is much smaller than the electron gyrofrequency f_{ce}. Therefore, the wavenumber is the dominant term in the evaluation of the electron cyclotron-resonant energy (Chen L. et al., 2019). In addition, the small phase velocities of EMIC waves limit the efficiency of electron acceleration, making pitch-angle scattering the main component of the wave-particle interaction (Kersten et al., 2014). EMIC waves also play a role in the acceleration and losses of energetic protons in the inner

magnetosphere (Cornwall et al., 1970; Jordanova et al., 2001; Lyu et al., 2022) and in heating the thermal ion populations (Ma et al., 2019).

Nonnegligible concentrations of He+ and O+ ions in the Earth's magnetosphere create a complicated structure of cold plasma dispersion branches with cutoffs and resonances (Stix, 1992). Due to the close spacing between ion gyrofrequencies f_{ci} (with i standing for protons, helium ions, or oxygen ions), the wavenumber is very sensitive to changes in the f/f_{cp} ratio and also strongly depends on the electron plasma-to-gyrofrequency ratio f_{pe}/f_{ce} (in the rest of the text, we will sometimes use angular wave frequencies denoted by ω, with Ω being reserved for angular gyrofrequencies). The waves are typically generated near the B_0-field minimum along a given field line in the left-hand polarized mode and propagate to higher latitudes, where they can switch to right-handed polarization as they reach the local crossover frequency f_{cr} (Rauch and Roux, 1982; Grison et al., 2018). The wave vectors in the source are observed to be quasiparallel, but the wave normal angles (WNA) become increasingly more oblique during propagation to higher latitudes (Hu et al., 2010; Allen et al., 2015; Chen et al., 2019). On the other hand, perpendicular cold plasma density gradients can act as guiding structures for EMIC waves, limiting the growth of WNA with latitude (Thorne and Horne, 1997). Depending on the wave vector directions along the trajectory, the waves may propagate to the ground through mode conversion and tunneling (Johnson et al., 1995; Kim and Johnson, 2016). Because helium band waves encounter only one stop band during propagation, they are more likely to be observed on the ground in conjugation with spacecraft than hydrogen band emissions (Bräysy and Mursula, 2001). The occurrence of oxygen band waves, which do not encounter any stop bands during propagation, is low on both spacecraft and ground stations (Bräysy et al., 1998; Saikin et al., 2015; Wang et al., 2017).

Statistical surveys of EMIC emissions in the inner magnetosphere have shown that they can reach very high amplitudes, up to above 1{%} of the background field (Meredith et al., 2003; Engebretson et al., 2015; Zhang et al., 2016). These amplitudes can facilitate nonlinear growth and formation of rising-tone and falling-tone spectral elements (Omura et al., 2010; Nakamura et al., 2016; Sigsbee et al., 2023). Furthermore, the interaction of electrons with high-amplitude EMIC waves can lead to nonlinear phase-trapping and phase-bunching effects (Omura and Zhao, 2012; Grach and Demekhov, 2020). The resonant particle evolution is often studied with test-particle simulations, which are easy to implement and parallelize, but cannot provide self-consistent evolution of the electromagnetic field. The EMIC wave fields in those simulations are often based on simple one-dimensional (1D) models that assume constant frequency and amplitude along the field line (Bortnik et al., 2022; Hanzelka et al., 2023). In contrast, spacecraft observations demonstrate that high-amplitude EMIC waves can have complicated spectra displaying frequency drifts, amplitude modulations, and phase discontinuities, combined with significant spatial variations (Grison et al., 2016; Ojha et al., 2021). Therefore, assessing the importance of nonlinear interactions and the overall efficiency of relativistic electron pitch-angle scattering by EMIC emissions requires constructing more realistic wave field models.

Several studies aimed to provide a better understanding of EMIC wave propagation properties through numerical simulations. Ray tracing simulations in hot plasma (Horne and Thorne, 1993; Chen et al., 2010) have been used to obtain wave power and wave normal angle distributions in the meridional plane. Ray propagation in cold plasma density gradients (Thorne and Horne, 1997), plasmaspheric plumes (Chen et al., 2009), and field-aligned density enhancements (de Soria-Santacruz et al., 2013) has been studied, showing the ducting properties of these structures. However, the geometric optics approximation employed in these simulations requires that the characteristic scales of inhomogeneities in the background medium must be much larger than the wavelength, a condition that often cannot be satisfied. Furthermore, ray simulations cannot predict the energy transfer during mode conversions and tunneling and need to be restarted to trace a new mode (Horne and Miyoshi, 2016). Johnson et al. (1995) and Johnson and Cheng (1999) presented full-wave solutions of one-dimensional EMIC wave propagation from their source region to the ionosphere, demonstrating that large portions of L-mode wave power can be converted to R-mode and reach low altitudes. Here we use the terms R-mode and L-mode to refer to any right-hand and left-hand polarized dispersion branches below f_{cp}, without regard to the possibly highly elliptical (nearly linear) states of polarization. Kim and Johnson (2016) conducted a two-dimensional (2D) propagation study with a FEM (Finite Element Method) solver of Maxwell equations and have shown that with an equatorial source of quasiparallel waves, nearly all wave power transfers to the R-mode, but the wave is then reflected at the ion hybrid frequency surface. However, a narrow wave source (comparable to a single wavelength) will produce moderately oblique waves that reach the ion hybrid frequency surface with quasiparallel wave vectors and continue on an earthward trajectory. While computationally efficient, the FEM approach is limited to finding the eigenmodes and does not support sources with time-dependent frequency and amplitude. 2D hybrid simulations (Hu and Denton, 2009; Denton et al., 2019) can provide dynamic wave fields along with the evolution of electron phase space density but are computationally expensive and require smoothing and filtering in the Fourier space to achieve good accuracy and stability.

Here we present 2D full-wave models of EMIC waves based on the FDTD (Finite-Difference Time-Domain) solutions of Maxwell equations. This method was successfully used before to study the propagation properties of the whistler-mode chorus in an inhomogeneous environment (Hosseini et al., 2021; Hanzelka and Santolík, 2022), and to study the effects of ion hybrid resonance (also called the Buchsbaum resonance) on the propagation of EMIC waves inside the plasmasphere (Pakhotin et al., 2022). Unlike FEM, the FDTD method can incorporate time-dependent sources, allowing us to study the propagation of rising-tone emissions with amplitude modulations. This advantage comes at the expense of a much higher computational cost. However, compared to the similarly expensive hybrid simulations, we are not restricted by frequency filtering. To make the best use of the FDTD method, we study not only the propagation of constant-frequency waves but also the propagation of rising-tone emissions and ducted waves. Wave propagation analysis is conducted in the time domain, providing quantities comparable to spacecraft data. 2D numerical models of rising-tone ducted and unducted EMIC waves obtained by FDTD methods can be used as input for test-particle simulations in studies of nonlinear wave-particle interactions on short timescales.

The contents of this paper are organized as follows: Sections 2.1 and 2.2 describe our implementation of the FDTD method and density models, with data processing and input parameters described in Sections 2.3 and 2.4, respectively. In Section 3.1, we present simulation results for constant-frequency H-band waves. Section 3.2 focuses on constant-frequency helium band waves and demonstrates the effects of a narrow-width cold current source. Wave ducting of H-band emissions on a density gradient is analyzed in Section 3.3, and Section 3.4 deals with rising-tone emissions and their spectra. Section 4 discusses our results in the context of previous works, and a brief summary and future outlooks are given in Section 5.

2 Materials and methods

2.1 Finite-difference time-domain simulations

We solve Maxwell's curl equations together with the equation of motion (Lorentz force equation) for a cold plasma fluid. The system of equations can be written as

$$\nabla \times \boldsymbol{B} = \sum_{i}^{N_p} \mu_0 \left(\boldsymbol{J}_{si} + \boldsymbol{J}_i\right) + \frac{1}{c^2}\frac{\partial \boldsymbol{E}}{\partial t}, \tag{1}$$

$$\nabla \times \boldsymbol{E} = -\frac{\partial \boldsymbol{B}}{\partial t}, \tag{2}$$

$$\frac{\partial \left(\mu_0 \boldsymbol{J}_i\right)}{\partial t} = \frac{\omega_{pi}^2}{c^2}\boldsymbol{E} + \mu_0 \boldsymbol{J}_i \times \boldsymbol{\Omega}_i. \tag{3}$$

Here we use the SI system of units, with c standing for the speed of light and μ_0 for vacuum permeability. $\boldsymbol{E}$ and $\boldsymbol{B}$ represent the dynamic electric and magnetic fields, while the static dipole field $\boldsymbol{B_0}$ is implicitly included through the signed vector gyrofrequency

$$\boldsymbol{\Omega}_i = \frac{q_i \boldsymbol{B}_0}{m_i}, \tag{4}$$

where the index i stands for particle species in the cold plasma: electrons and the three ions H+, He+, and O+ (number of particle species $N_p = 4$). The assumption $|\boldsymbol{B_0}| \gg |\boldsymbol{B}|$ was used in Eq. 3 to remove the nonlinear term $\boldsymbol{J} \times \boldsymbol{B}$. The number density n_i of individual species is introduced through the plasma frequency

$$\omega_{pi} = \sqrt{\frac{n_i q_i^2}{\varepsilon_0 m_i}}. \tag{5}$$

The symbols q_i, m_i, and ε_0 stand for the particle charge, mass, and vacuum permittivity, respectively. $\boldsymbol{J}_i$ stands for current density associated with the fields $\boldsymbol{E}$ and $\boldsymbol{B}$, and $\mathbf{J}_{si}$ is the external current source. For the purposes of EMIC wave propagation, the electron mass can be replaced by $m_{e,num} > m_e$ to gain a major computational performance boost at the expense of minor inaccuracies in wave propagation properties near the resonance cone—see the Supplementary Material for a short discussion of these inaccuracies.

The equations are solved by implementing the finite-difference time-domain (FDTD) method described by Pokhrel et al. (2018), where the Boris method is used to evolve the current $\boldsymbol{J}_i$. In the case of ion cyclotron waves, the time step Δt in the numerical solution of the Maxwell equations is typically much larger than the time step Δt_c required by the Boris algorithm to advance the Lorentz equation for current with good precision. The singular update method from Pokhrel et al. (2018) provides matrix equations which advance $\boldsymbol{J}$ by $M\Delta t_c = \Delta t$ in a single step, where M is an integer. A 2D version of the staggered Yee grid is used (Yee, 1966), with the current being placed symmetrically at the center of the Yee cell.

The minimum required size of each cell is determined by wavelength λ_w of the modes supported by the plasma fluid confined in the chosen simulations box and must be generally tested before each run. The time step Δt must not violate the Courant-Friedrichs-Lewy (CFL) condition

$$\Delta t < \Delta t_{CFL} = \frac{1/c}{\sqrt{1/\Delta z^2} + \sqrt{1/\Delta x^2}}, \tag{6}$$

where Δz and Δx are the dimensions of a grid cell (Gedney, 2011). The CFL stability condition is necessary but not sufficient, so an even lower time step might be required, depending on the choice of Δz and Δx. The grid is located in the meridional plane and represented in Cartesian coordinates, with z aligned with the dipole axis and x pointing away from the Earth. The origin $(z, x) = (0, 0)$ sits in the center of the source region.

Similarly to Hosseini et al. (2021) and Hanzelka and Santolík (2022), we use a 1D current density source located along $z = 0$ with a finite halfwidth w_J. The current amplitude distribution is described by the shape function

$$G(x) = \cos^2\left(\frac{\pi x}{2w_J}\right) \quad \text{if} \quad |x| < w_J \tag{7}$$

$$G(x) = 0 \quad \text{otherwise.} \tag{8}$$

Time-dependence of the current amplitude is incorporated in the function

$$T(t) = T_t(t)\, T_m(t) \quad \text{if} \quad 0 < t < t_{max} \tag{9}$$

$$T(t) = 0 \quad \text{otherwise,} \tag{10}$$

where T_t is a tapering function

$$T_t = \cos^2\left(\frac{\pi\left(t - t_{ramp}\right)}{2t_{ramp}}\right) \quad \text{if} \quad t < t_{ramp} \tag{11}$$

$$T_t = 1 \quad \text{if} \quad t_{ramp} \le t \le t_{max} - t_{ramp} \tag{12}$$

$$T_t = \cos^2\left(\frac{\pi\left(t - t_{max} + t_{ramp}\right)}{2t_{ramp}}\right) \quad \text{if} \quad t > t_{max} - t_{ramp}, \tag{13}$$

and T_m represents subpacket modulations. Subpackets are defined by $N_s - 1$ local modulation minima and N_s local maxima, with the adjacent minima and maxima being connected by $\cos^2$ functions, similarly to the tapering function above.

The components of the source current must be obtained from the cold plasma dispersion relation. Considering that the EMIC waves are generated through the first-order cyclotron resonance with ions that propagate along the field line, it is reasonable to assume that the current should be near-circularly polarized, producing quasiparallel electromagnetic emissions. Nevertheless, the simulation code is not

limited to any specific wave mode and allows for an arbitrary value of θ_k, so the full 3D field description is given in the following. We start by defining time-dependent frequency $\omega(t)$ and wave normal angle $\theta_k(t)$. As the next step, the refractive index μ and the complex conductivity tensor $\boldsymbol{\sigma}_i$ are obtained (e.g., Gurnett and Bhattacharjee (2017), Chapter 4). We continue by calculating the complex electric field with E_x normalized to $-1j$, where j is the imaginary unit. The corresponding magnetic field is obtained from Faraday's law in the Fourier space,

$$B_x = -k_z E_y/\omega \tag{14}$$

$$B_y = \left(k_z E_x - k_x E_z\right)/\omega \tag{15}$$

$$B_z = -k_x E_y/\omega, \tag{16}$$

where the azimuthal angle was set to zero, and thus $k_y = 0$. Since the calculations are performed at the equator, the solar magnetic coordinates used for the Cartesian grid coincide with field-aligned coordinates. The fields are then renormalized so that $|B| = 1$, and after that multiplied by $G(x)T(t)B_{w0}$, where B_{w0} is the desired equatorial peak amplitude of EMIC wave field. Having the properly normalized electric field, we employ the generalized Ohm's law and obtain the current

$$\boldsymbol{J}_i = \boldsymbol{\sigma}\boldsymbol{E}. \tag{17}$$

As a final step, we need to consider the effects of discretization. Because the current source behaves as a delta function in the z direction, but the grid cells are finite, an additional numerical factor must enter into the initialization of our simulation. This factor $g(\ell)$ depends purely on $\ell = \lambda_w/\Delta z$ and has to be determined numerically. We ran simulations with ℓ going from 8 to 24 and found the least-squares power law fit

$$g(\ell) = 2.201\ell^{-0.891} \tag{18}$$

with a coefficient of determination $R^2 = 0.9991$.

The source current vector can be formally written as (dropping the particle index i)

$$\boldsymbol{J_s} = \left(J_x \cos\psi(x,t), -J_y \sin\psi(x,t), J_z \cos\psi(x,t)\right), \tag{19}$$

where the J_x, J_y, and J_z components are obtained from Eq. 17 with the correction introduced in Eq. 18, and

$$\psi(x,t) = \psi_0 - \int_{-w_j}^{x} \mathrm{d}\tilde{x} k_x(\tilde{x},t) + \int_0^t \mathrm{d}\tilde{t}\,\omega'(\tilde{t}) \tag{20}$$

is the harmonic phase (ψ_0 chosen such that $\psi(0,0) = 0$). Assuming a constant θ_k and constant frequency, we get

$$\frac{\partial\psi}{\partial x} = -k_x \tag{21}$$

$$\frac{\partial\psi}{\partial t} = \omega. \tag{22}$$

However, in a general case, the frequencies appearing in (20) and 22 are different. With a constant wave normal angle θ_k (i.e., time-independent k_x) an a chirp rate $r_c = (\omega_1 - \omega_0)/t_{max}$, setting $\omega'(t) = \omega_0 + r_c t$ will result in $\omega = \omega'$ in Eq. 22. When $k_x(t)$ includes explicit time dependence, it will enter the time derivative of phase and introduce a spatial gradient of frequency: $\omega = \omega' - x\partial k_x(t)/\partial t$. For simplicity, we will further consider only sources with a fixed $\boldsymbol{k}$-vector direction.

Wave reflection at the simulation box boundaries is mitigated by implementing damping regions. Following Umeda et al. (2001), we introduce a masking factor $f_m \leq 1$ and multiply the electromagnetic fields by this factor in each time step. At distances from the boundary larger than d_{damp}, we set $f_m = 1$. In the damping region near box boundaries, f_m decreases parabolically. The optimal rate at which the masking factor should decrease depends on the time step and the phase velocity. The efficiency of damping improves with increasing d_{damp}, which is usually chosen as a small integer multiple of a typical wavelength. Due to the variability of wave vectors and frequencies in our simulations, there is no simple method that would prescribe the best choice of damping parameters. We therefore numerically tested the efficiency of damping to ensure that the power of reflected waves in results presented in Section 3 is less than $10^{-3.5}$ of the incident waves.

2.2 Density models

The cold electron density distribution is based on the empirical model from Denton et al. (2002) adapted for dipole. The latitudinal dependence is described by

$$n_e = \frac{n_{e0}}{(\cos\lambda)^{2\alpha}}, \tag{23}$$

where n_{e0} is the equatorial profile, and the formula for the exponential factor in SI base units reads

$$\alpha = 36.08 - 6.36\log_{10} n_{e0} + 0.28\log_{10}^2 n_{e0} - 0.43L. \tag{24}$$

The equatorial profile uses the best-fit power law for the plasmatrough (Denton et al., 2004)

$$n_{e0} = 10.13 - 4.1\log_{10} L \tag{25}$$

rescaled to coincide with the prescribed $\omega_{pe0} = \omega_{pe}$ ($z = 0, x = 0$). The rescaled model does not represent the best fit, but the radial density gradient remains within the range predicted by the various density models discussed by Denton et al. (2004).

The cold electron density in our model can be further modified by density crests (increase) and troughs (decrease) with a Gaussian radial profile, which can be used to simulate ducted propagation. Symbolically, $n_{e,tot} = n_e n_d$, where

$$n_d = 1 + \sum_{j=1}^{N_d} \delta n_j \mathrm{e}^{\frac{-\left(L-L_{dj}\right)^2}{2\sigma_{Lj}}}. \tag{26}$$

The duct parameters are: number of ducts N_d, relative density change δn, central L-shell of the duct L_d, and characteristic width σ_L. As noted by Hanzelka and Santolík (2022), these ducts are different from the commonly assumed 3D tubes (Angerami, 1970; Koons, 1989); instead, they behave as density slabs, infinite in the y-direction. Dispersive properties of 2D and 3D ducted wave modes are principally different (Zudin et al., 2019), and therefore, the wave propagation properties in the 2D model may differ from *in situ* observations, especially where the azimuthal wave vector angle ϕ_k is concerned. Unfortunately, full-wave numerical investigations of 3D

EMIC wave propagation are beyond our computational possibilities; furthermore, there is no suitable *in-situ* data we could use for comparison with the hypothetical 3D numerical results.

The dispersive properties of hydrogen and helium band EMIC waves strongly depend on the concentration of heavy ions (Lee et al. (2021) and references therein). The concentrations of the three ions in our simulations (η_p, η_{He}, and η_O) are set to be constant across the whole computational domain. Their impact can be seen in the behavior of characteristic frequencies below the proton gyrofrequency Ω_p. Specifically, the following three frequencies have an impact on the propagation and mode conversion of hydrogen band waves: the crossover frequency ω_{cr}, where the L-mode and R-mode become coupled and have linear polarization; the L-mode cutoff frequency ω_{lc}, which creates a stopband and leads to reflection of incident waves; and the ion hybrid frequency ω_{ih}, which can cause reflection of oblique R-mode waves. A similar triplet of frequencies exists in the helium band (but not in the oxygen band). Approximate formulas from Chen et al. (2014) are used in this paper to evaluate the characteristic frequencies.

2.3 Wave propagation analysis

The simulation code provides all six electromagnetic components and $3N_p$ cold current components with sampling rate $f_s = 1/\Delta t$ on a fine spatial grid with cell size $\Delta z \times \Delta x$. In most practical cases, this data is too large to be stored. Instead, we save a small number of snapshots of the fine grid and a continuous time evolution on a coarse grid $\Delta_g z \times \Delta_g x$ with sampling rate $f_{sg} = 1/\Delta_g t \ll 1/\Delta t$. Wave propagation properties are calculated in the time domain based on the coarse-grid data.

The data analysis process can be divided into four steps. First, the field components are transformed to the field-aligned system, $(x, y, z) \to (x', y', z')$, where $z' \| \boldsymbol{B_0}$, x' is perpendicular to the field line and lies in the x-z plane, and $y' = y$. In the second step, the fields are converted to analytic signals with Hilbert transform. As the third step, we construct spectral matrices and average them over a short time interval (typically a small integer multiple of the average wave period T_{avg} given on the input). As the fourth and last step, we use the SVD methods (Santolík et al., 2003) and get normalized wave vectors, from which we can obtain various wave propagation properties: wave normal angle θ_k, azimuthal angle ϕ_k, B-ellipticity, and B-planarity. The angles are defined so that $\theta_k = 0°$ represents parallel propagation, $\theta_k = 180°$ anti-parallel propagation, and waves with $\phi_k = 0°$ propagate outward in the x' direction. The Poynting vector and its polar and azimuthal angles θ_S and ϕ_S can be obtained directly from the cross-spectral components (Santolík et al., 2010). The instantaneous frequency of each B-field component is obtained by a simple forward difference of the analytic signal's phase.

We also pick several grid cells (probes) and save the field data from those cells at a higher sampling rate. These high-resolution time series are used to construct spectrograms with the STFT (Short-Time Fourier Transform) method. Hann window with a 15/16 overlap is applied. Wave propagation properties in each time-frequency bin are obtained by the same SVD methods as described above, without any additional time averaging.

2.4 Input parameters

We use four different sets of input parameters to simulate the propagation of

Set 1: Constant-frequency hydrogen band wave,
Set 2: Constant-frequency helium band wave,
Set 3: Constant-frequency hydrogen band wave on a steep density gradient (ducted propagation),
Set 4: Rising-tone hydrogen band wave with amplitude modulations.

Some values of the input parameters are shared across all runs. Firstly, we set $\theta_k = 0°$ in the calculation of the conductivity tensor $\boldsymbol{\sigma}$ appearing in Eq. 17. We justify this choice by assuming that the waves are generated from an anisotropy-driven ion cyclotron instability, which is most unstable in the exactly parallel direction of propagation (Yoon, 1992). We choose the central L-shell of the source to be $L_0 = 5.5$, which passes through regions with high occurrence of intense EMIC waves (Saikin et al., 2015; Jun et al., 2021). The width of the damping regions is three times the time-averaged equatorial wavelength λ_{avg}, with a masking factor of 0.998 at the box boundaries. The equatorial strength of the dipole magnetic field at the Earth's surface is set to $B_{surf} = 3.1 \cdot 10^{-5}$ T. The electron mass is increased sixteen times, $m_{e,num} = 16 m_e$, to speed up the calculations (see the Supplementary Material and Supplementary Figures S1, S2 for further discussion of the increased electron mass).

A number of shared input parameters have no direct impact on wave propagation. Those are: Peak source amplitude $B_{w0} = 0.01$, coarse grid sampling time $T_{avg}/12$, coarse grid spatial sampling $\lambda_{avg}/4$, probe data time step $\Delta t/16$, probe positions $x' = \{-1,500\text{ km}, -750\text{ km}, 0\text{ km}, 750\text{ km}, 1,500\text{ km}\}$ and $\lambda = \{0.5°, 2.5°, 5.0°, 10.0°, 15.0°, 20.0°\}$ ($5 \cdot 6 = 30$ probes in total), and 128 Boris time steps per electron gyroperiod (the smallest gyroperiod over the whole simulation box is taken).

All the other input parameters are listed in Table 1, with two exceptions. The density structure in the ducted case (Set 3) is composed of $N_d = 3$ Gaussians with characteristic equatorial widths $750\text{ km} \sim \sigma_L = 0.118$, amplitudes $\delta n = 1$ and centers $L = L_0 + \{0, -2\sigma_L, -4\sigma_L\}$. Due to the properties of the Gaussian function, the sum of these three ducts creates a near constant elevation between L_0 and $L_0 - 4\sigma_L$ with an increase of $\sim 1.2\delta n$. Such structure can represent the plasmaspheric plume (Darrouzet et al., 2009). The rising-tone emission (Set 4) exhibits amplitude modulations of the source, with maxima of $\{0.5, 1.0, 1.0, 0.5\} B_{w0}$ at $\{0.125, 0.375, 0.625, 0.875\} t_{max}$ and minima of $\{0.25, 0.50, 0.25\} B_{w0}$ at $\{0.25, 0.5, 0.75\} t_{max}$.

3 Results

3.1 Constant-frequency hydrogen band wave

We first analyze the wave propagation properties of a simple hydrogen band EMIC wave packet with no amplitude modulations and a constant frequency. The corresponding input parameters can be found in Table 1, Set 1. In Figure 1, we plot the total

TABLE 1 Four sets of input parameters of four separate simulation runs.

Input parameter	Symbol	Unit	Set 1 value	Set 2 value	Set 3 value	Set 4 value
Initial frequency	f_0	Hz	1.70	0.43	1.70	1.28
Final frequency	f_1	Hz	1.70	0.43	1.70	1.85
H+ concentration	η_p	_	0.8	0.8	0.8	0.93
He + concentration	η_{He}	_	0.17	0.17	0.17	0.06
O+ concentration	η_O	_	0.03	0.03	0.03	0.01
Source halfwidth	w_J	km	1500	1075	1125	1400
Source duration	t_{max}	s	33.33	33.33	33.33	26
Ramp-up time	t_{ramp}	t_{max}	0.5	0.5	0.5	0.0
Left box boundary	z_L	km	−2500	−2500	−2500	−3000
Right box boundary	z_R	km	17,000	17,000	17,000	17,000
Lower box boundary	x_D	km	−11500	−11500	−11500	−13000
Upper box boundary	x_U	km	5000	5000	5000	5000
Simulation time	t_{sim}	s	50	50	50	50
Grid cell size	$\Delta z, \Delta x$	λ_{avg}	1/16	1/24	1/16	1/16
Avg. initial wavelength	λ_{avg}	km	680	970	680	470
Time step	Δt	Δt_{CFL}	1/6	1/12	1/6	1/4
CFL time step	$10^5 \Delta t_{CFL}$	s	10.0	10.6	10.0	7.1
Plasma frequency	ω_{pe0}	Ω_{e0}	5	10	5	5

The cold plasma frequency in the source ω_{pe0} refers to a density profile without ducting structures. The wave frequencies correspond to $\omega_0 = 0.6\Omega_{p0}$ in Set 1 and Set 3, $\omega_0 = 0.6\Omega_{He0}$ in Set 2, and $\omega_0 = 0.45\Omega_{p0}$ and $\omega_1 = 0.65\Omega_{p0}$ in Set 4. ω_{pe0}, Ω_{e0}, Ω_{p0} and Ω_{He0} are the frequencies at the magnetic equator.

magnetic and electric fields at time $t = 25$ s along with selected field components. Because the source is symmetric, we will discuss only the waves propagating towards $z > 0$ (northward); the fields propagating towards $z < 0$ (southward) quickly enter the damping region near box boundaries and dissipate.

Several important features of unducted EMIC wave propagation can be discerned from these snapshots. The magnetic and electric fields in Figures 1A,B display spatial oscillations with a period of $\lambda_w/2$, hinting at a rapid increase in ellipticity away from the source. Highly elliptical polarization suggests oblique wave vector direction, which can be confirmed by observing the angle between wave crests and field lines. When the wave frequency approaches the ion hybrid frequency (represented by the red curves in Figure 1), the magnetic field diminishes, while the electric field remains strong, confirming that the oblique EMIC wave is becoming electrostatic at the hybrid resonance.

The perpendicular component $B_{x'}$ plotted in Figure 1C disappears near the crossover frequency (magenta curves) because the wave becomes near linearly polarized with most of its magnetic amplitude in the y' direction. Because the source width $2w_J$ is about 4.4 equatorial wavelengths, the plane wave approximation is not heavily violated, and $\boldsymbol{E} \cdot \boldsymbol{B} = 0$ implies that the $B_{y'}$ component will have a spatial distribution similar to $E_{x'}$ (Figure 1D).

Figure 1E shows the magnetic field component $B_{z'}$, which reveals weak parts of the wave field moving across field lines, deviating from the expected quasi-parallel propagation of energy. Most of these can be shown to be right-handed and are related to mode conversions near characteristic frequencies—they will be described with the help of polarization analysis in the following paragraphs. However, some of these weak R-mode waves originate directly in the source. This observation may seem surprising since the source current density was obtained based on the assumption of a left-handed circular polarization. However, those calculations relied on the plane wave approximation in a homogeneous plasma, which is not exactly satisfied when the source is finite and the electron density in the radial direction changes by about 10{%} per wavelength. How the finite 1D source affects wave properties can be shown by constructing the magnetic field wave equation from Eqs 1, 2 (dropping the particle species index i)

$$\nabla \times (\nabla \times \boldsymbol{B}) = \mu_0 \nabla \times \boldsymbol{J_s} - \frac{1}{c^2} \frac{\partial^2 \boldsymbol{B}}{\partial t^2}. \tag{27}$$

The circularly polarized current can be represented by

$$\boldsymbol{J_s} = J_{s0}(x)(\cos\psi, \sin\psi, 0), \tag{28}$$

where $J_{s0}(x)$ represents the amplitude profile. If we take the curl of $\mathbf{J_s}$, we get

$$\nabla \times \boldsymbol{J_s} = \left(J_{s0} k_z \cos\psi, J_{s0} k_z \sin\psi, \left(\partial J_{s0}/\partial x\right) \sin\psi\right). \tag{29}$$

The z-component will propagate into the calculation of $\boldsymbol{B}$ and cause deviations from the circular polarization. This behavior is confirmed in Figure 1E, where we show $B_{z'}$ to be nonzero in the source for $z = 0$, $x \neq 0$. The resulting wave field can be

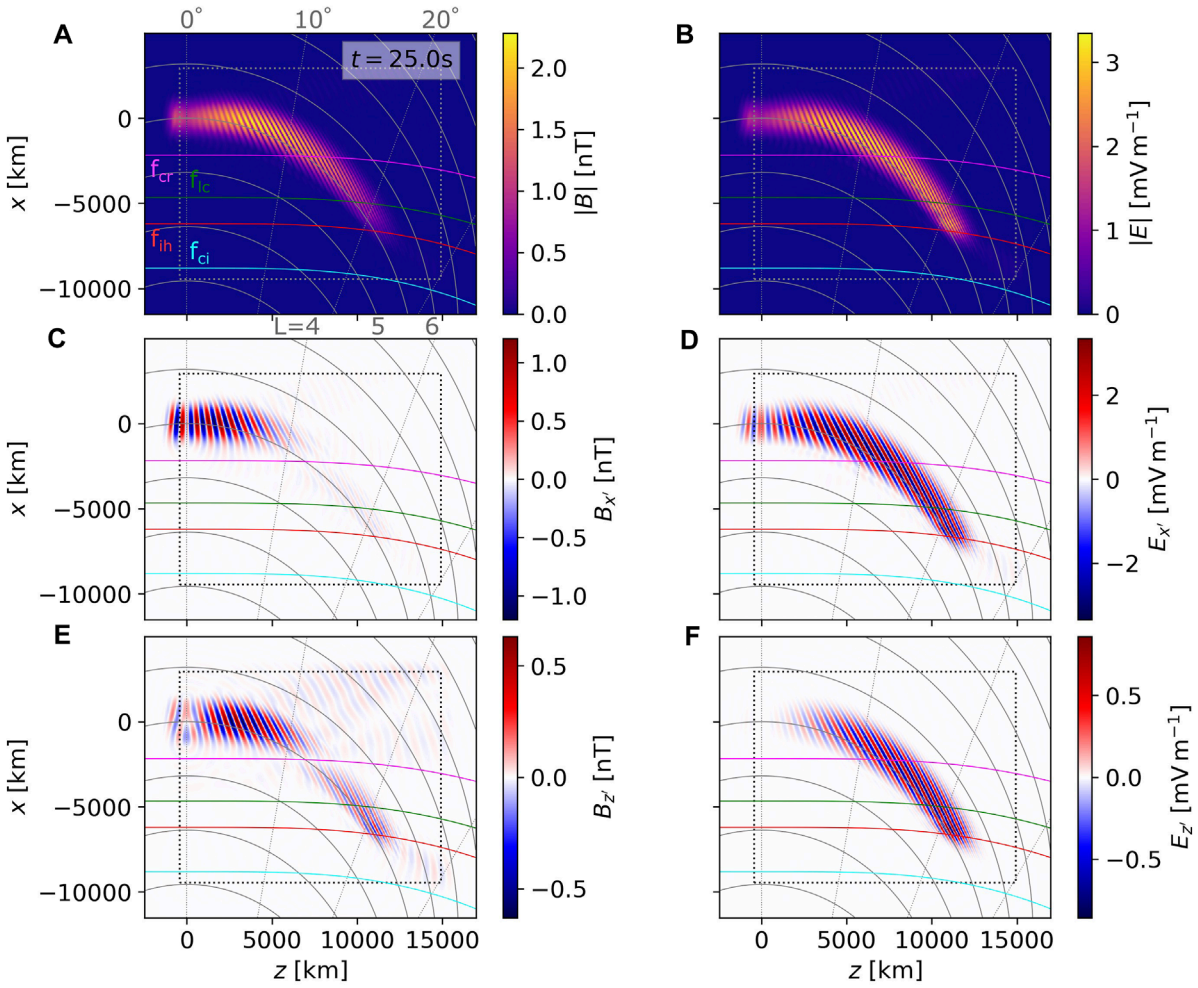

FIGURE 1
Snapshots of magnetic and electric fields from the simulation run with input parameter Set 1 (constant-frequency unducted hydrogen band wave packet with a single amplitude maximum). **(A)** Amplitude of the wave magnetic field $|\boldsymbol{B}|$. This panel shows the time stamp $t = 25$ s, labels of the radial lines of constant latitude, L-shell labels, and characteristic frequency labels: magenta curve for wave frequency encountering the crossover frequency f_{cr}, green for the L-cutoff frequency f_{lc}, red for the ion hybrid frequency f_{ih}, and cyan for the cyclotron frequency f_{ci} (helium gyrofrequency in this case). The dotted rectangle represents boundaries of the damping region. **(B)** Amplitude of the wave electric field $|\boldsymbol{E}|$. **(C)** Magnetic field component $B_{x'}$ perpendicular to the local field line (parallel to the meridional plane). **(D)** Electric field component $E_{x'}$. **(E)** Magnetic field component $B_{z'}$. **(F)** Electric field component $E_{z'}$.

decomposed into left-hand and right-hand polarized components, and thus the finite source supports both the L-mode and the R-mode. However, because the plane wave approximation is violated only weakly, the corresponding R-mode wave field is also weak. With decreasing w_J, the source is becoming increasingly point-like, supporting radiation in directions far away from $\theta_k = 0°$. For the sake of completeness, we may also construct the electric field wave equation

$$-\nabla \times (\nabla \times \boldsymbol{E}) = \mu_0 \frac{\partial \boldsymbol{J_s}}{\partial t} + \frac{1}{c^2} \frac{\partial^2 \boldsymbol{E}}{\partial t^2}. \tag{30}$$

The spatial derivatives of current density are not present here; therefore, the electric field component $E_{z'}$ remains zero in the source, as documented in Figure 1F.

To better understand the wave propagation and polarization properties, we run SVD analysis on the coarse grid, following the methods described in Section 2.3. The results are shown in Figure 2, using the same snapshot as in Figure 1. Figure 2A presents the Poynting flux amplitude $|\mu_0 \boldsymbol{S}|$ in units of nT mV^{-1}. The lower threshold for all data is set to $10^{-3.5}$ of the maximum Poynting flux in the chosen snapshot. As expected, the peak energy flux follows the starting field line $L = 5.5$, with only a slight deviation towards high L-shells, which is further confirmed by the low values of polar angle of the Poynting vector θ_S. The only regions where θ_S becomes large are the reflection region near the hybrid resonance, and the southern hemisphere (which will not be further discussed). Figure 2C shows that the wave starts as near left-hand circularly polarized, then becomes linearly polarized when crossing $f = f_{cr}$, and in the reflection region, a mixture of left-hand and right-hand polarization appears. The wave normal angle θ_k in Figure 2D shows a steady increase from near zero in the source up to 90° during reflection. However, the WNA values are somewhat noisy, especially

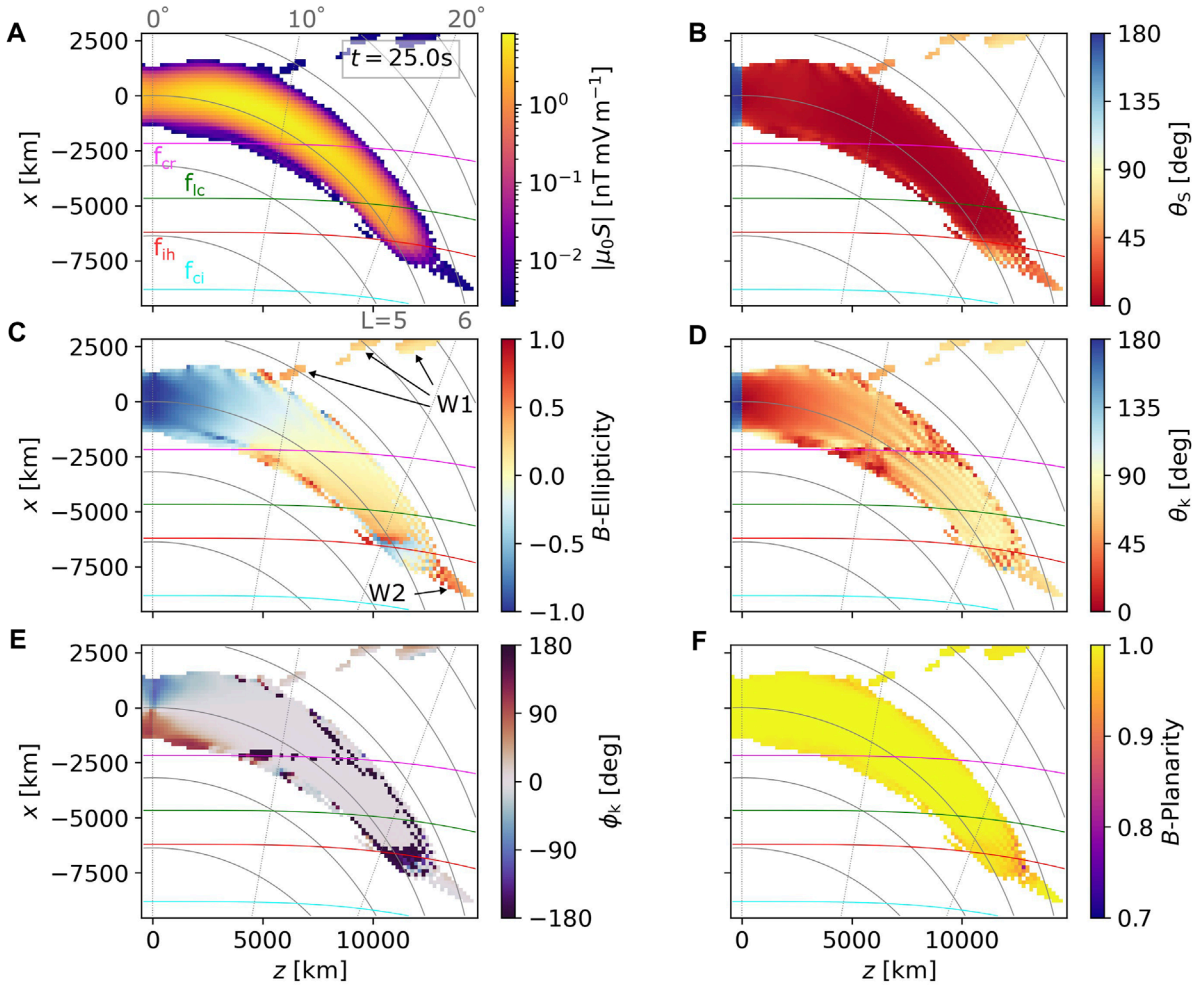

FIGURE 2
Snapshots of wave propagation and polarization properties from Set 1, taken at the same time $t = 25$ s as the wave fields in Figure 1. The plotted data range has been changed from Figure 1 to exclude the damping region. **(A)** Magnitude of the Poynting flux. **(B)** Polar angle of the Poynting vector. **(C)** Ellipticity of the magnetic field. Labels W1 and W2 point to weaker fields whose propagation properties differ from the main packet. **(D)** Wave normal angle. **(E)** Azimuthal angle of the wave vector. **(F)** Planarity of the magnetic field. All quantities were obtained through SVD methods with spectral averaging over three equatorial wave periods, as described in Section 2.3.

near f_{cr}, near f_{ih}, and at the edges of the wave packet. Similar features are displayed by the azimuthal angle ϕ_k in Figure 2E, with the values jumping from 0° to 180°. At the two above-mentioned characteristic frequencies, the B-field polarization ellipse is degenerate (linear polarization), and thus the direction of the wave vector cannot be determined. At the wave packet edges, the variations come from the mixing of L-mode with the very weak R-mode. The planarity stays above 0.7 (Figure 2F), confirming that the use of the SVD analysis is meaningful.

A peculiar behavior can be seen near the source, where the azimuthal angle shows large eastward and westward deviations (Figure 2E). An explanation can be provided through the same calculations that led to Eq. 29. The additional part of the B_z component arising from the $\partial/\partial x$ gradient has a phase shift of 90° with respect to B_x, differing from the 180° shift expected in an oblique EMIC plane wave propagating in the meridional plane. This phase difference is demonstrated by Figures 1C,E where $B_{x'}$ is almost zero in the source while $B_{z'}$ attains its maximum or minimum at the same time. However, as long as the wave normal angle is small, the deviations in ϕ_k have little impact on wave propagation away from the source.

Apart from the main field-aligned packet, weaker fields with an oblique energy propagation direction appear in Figure 2, labeled W1 and W2. The W1 field has both θ_S and θ_k moderately or highly oblique (>50°), is right-hand elliptically polarized, and has origin in the weak R-mode radiated from the source. This origin can be confirmed by looking at $B_{z'}$ (Figure 1E) and tracing it back in time. A portion of the W1 field first propagates through the f_{cr}, experiences polarization reversal, reflects at the L-cutoff, and then goes through a second polarization reversal before arriving at the point of observation. The W2 field has similar properties but shows a smaller obliquity of θ_S and represents waves that were initially quasiparallel, did not experience reflection at the ion hybrid frequency and became unguided.

Neglecting the weak W1 and W2 fields, we may conclude that in a cold plasma with a high He + concentration (17{%}), an unducted hydrogen band wave that started with low values of WNA near the source will be entirely reflected back to the equator. To further confirm this conclusion, we show the evolution of the wave packet in three snapshots plotted in Figure 3. Figures 3A–F cover the initial stage before reflection, where we can clearly see the W1 field escaping away from $L = 5.5$ and the main field going through polarization reversal. We skip over the intermediate stage already discussed in Figure 2 and go to the final stage at $t = 45$ s, where the majority of the wave packet has been reflected. The reflected wave goes through a second polarization reversal and reaches the source region as a very oblique, left-hand highly elliptically polarized EMIC emission. Due to the slight deviation of $\boldsymbol{S}$ from the field-aligned direction, the reflected wave passes above the center of the wave source when it returns to the equatorial plane. A space probe flying through the source region can, therefore, easily miss the reflected wave, depending on the probe's precise position and velocity. Our results demonstrate that more data from multi-spacecraft observations at close separations are needed to evaluate the occurrence and physical properties of reflected EMIC waves.

3.2 Constant-frequency helium band wave

In a cold plasma with the three ions H+, He+, and O+, the dispersive properties of the helium band EMIC wave are generally similar to those of the hydrogen band wave, with the most significant difference being in wavenumber. However, because He-band is associated with higher densities (Meredith et al., 2014), even the wavenumbers can be close in value. One clear distinction appears once waves pass through the L-mode stopband: while the H-band waves will encounter another stopband at higher latitudes, the He-band can propagate unimpeded down to ionospheric altitudes. Moreover, low oxygen concentrations in the plasmatrough can push the characteristic frequencies close to Ω_O.

In the simulation run with input parameter Set 2, we choose $\omega_0/\Omega_{He0} = 0.6$, which is the same value as ω_0/Ω_{p0} in Set 1. The plasma frequency is doubled, which still makes the wavelength larger than in the hydrogen band case. Furthermore, the source extent is decreased from ±1,500 km to ±1,075 km. The full source width $2w_J$ is now only about two equatorial wavelengths, which leads to enhanced radiation in oblique directions. This change in the radiation pattern is demonstrated in Figures 4A,B, where the magnetic field components $B_{x'}$ and $B_{z'}$ show oblique wave crests emanating from the source. The power of these weak oblique fields is about two orders of magnitude below the peak of the main packet (Figure 4C), making them more significant than in the wide-source case from Figure 2. The polar angle θ_S reveals that some of these weaker waves stay at latitudes below 10°, displaying very oblique propagation of energy, while some are more parallel and quickly (i.e., at time $t = 27.5$ s) reach latitudes up to above 20°. The first group is marked W1 in Figure 4E and has two components. The outward propagating component is right-hand polarized and quickly reaches the damping boundary—its properties are similar to the W1 field from Figure 2, hence the shared label. The second component propagates inward, experiences polarization reversal, and reflects at the L-cutoff. The second group, labeled W2, propagates in a quasiparallel fashion down to the lower box boundary without experiencing any notable changes in propagation properties, becoming unguided after passing below f_{ih}. We may notice in Figure 4F that at the boundaries between L-mode-dominated and R-mode-dominated regions, the wave normal angle appears to be near 90°.

The narrow source not only affects the amplitude of the weak R-mode, but also changes the propagation properties of the main L-mode packet. This is easier to observe during later times of the wave field evolution, as demonstrated by the three snapshots in Figure 5. At $t = 17.5$ s (Figures 5A–C), the separation into the main packet and secondary R-mode packets is already clear. At a later time, $t = 32.4$ s (Figures 5D–F), we notice that a part of the main packet near the bottom edge, labeled W3 in Figure 5E, has a near-circular left-hand polarization and quasiparallel wave vector. In Figures 5G–I (snapshot $t = 40.0$ s), this W3 field is shown to propagate through the crossover frequency without any significant loss of wave power and remain mostly left-hand polarized, while the more oblique portion of the main wave packet undergoes polarization reversal. However, a small amount of wave energy is transferred into a reflected R-mode component near $f = f_{cr}$, labeled W4 in Figure 5H. The above-discussed weak fields W1 and W2 are also marked for comparison with Figure 4.

3.3 Ducted hydrogen band wave

After inspecting the propagation of unducted EMIC waves in Sections 3.1 and Sections 3.2, we turn to ducted propagation on steep density gradients (input parameter Set 3). In this ducted H-band simulation, the source width is smaller than in Set 1, $w_J = 1,125$ km, but the wavelengths are shorter due to the increased density in the ducting structure. Because of the large radial density gradients, the wavelength in the source cannot be well represented by a single value. Nonetheless, in the chosen setup, the source is still wide enough to emit only negligible power into the oblique directions.

The $B_{x'}$ component plotted in Figure 6A shows stark differences from the unducted picture in Figure 1C. When reaching f_{cr}, the wave crests follow the field line, and the L-value of this field line matches well with the region of steep density drop off (see Figure 6B for a plot of 2D ω_{pe}/Ω_{e0} distribution). As shown in Figures 6C,D, most of the wave power reaches the hybrid resonance and passes towards higher latitudes. However, a significant amount of wave power becomes reflected near the $f = f_{cr}$ and $f = f_{lc}$ surfaces. In Figure 6E, we can see that the quasiparallel ducted EMIC wave turns into a mixture of L-mode and R-mode after passing through the crossover. The left-handed part reflects to higher L-shells and goes through a polarization reversal—we label it S3, as it has a similar propagation path to W3, except for being stronger due to ducting. S2' is an R-mode wave, which has similar properties to the weak field W2 but originates in the polarization reversal instead of being generated directly in the source. Additionally, a weak part of the main packet gets reflected at the crossover and becomes right-hand polarized (W4 in Figure 6E). Due to the mixture of R-mode and L-mode waves with similar power, the wave normal angles plotted in Figure 6F are

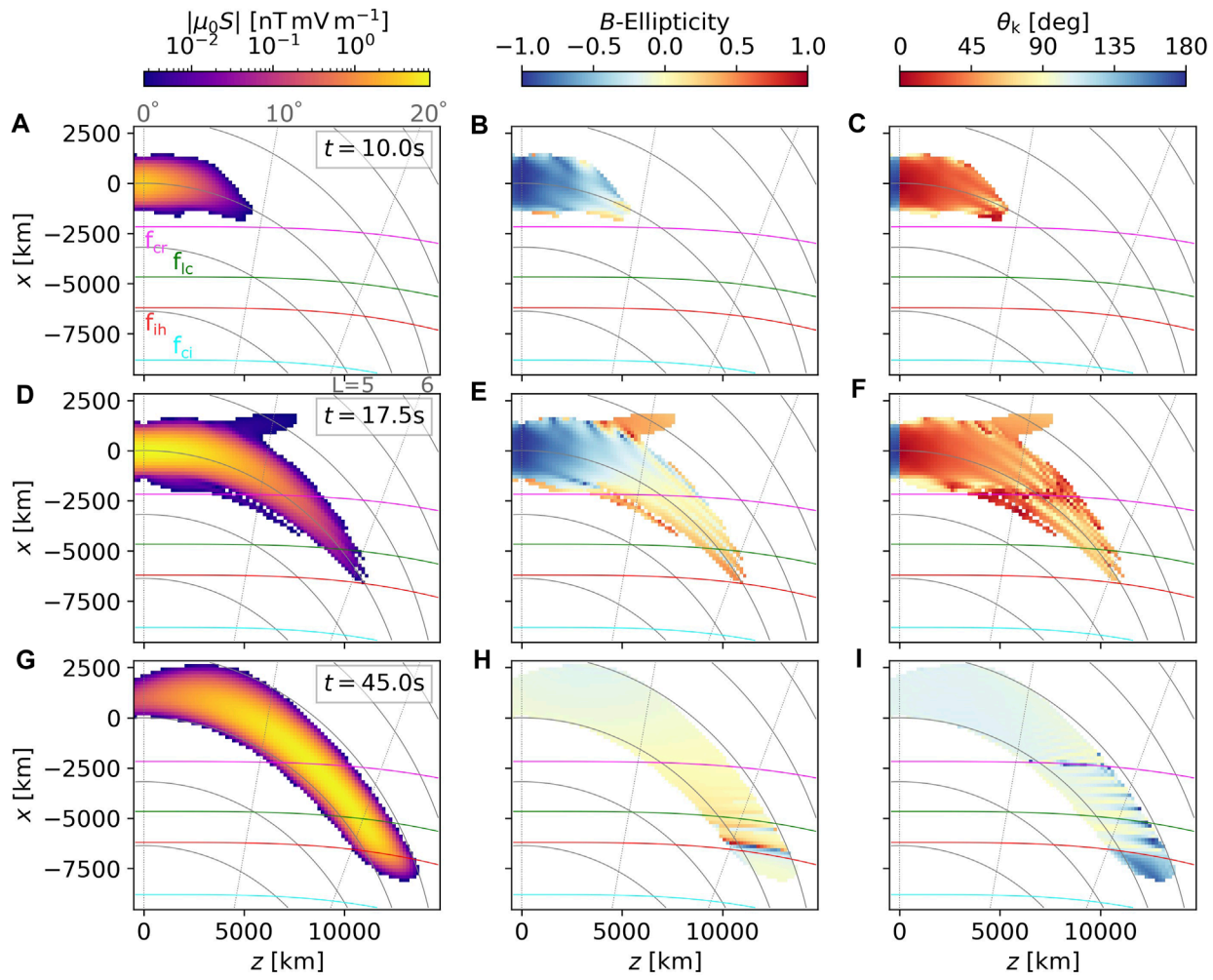

FIGURE 3
Poynting vector magnitude, B-field ellipticity, and wave normal angle calculated for three different snapshots from Set 1: $t = 10$ s in panels **(A–C)**, $t = 17.5$ s in panels **(D–F)**, and $t = 45.0$ s in panels **(G–I)**.

difficult to interpret, but the quasiparallel component at the center of the wave packet can still be traced.

Values of θ_k below the $f = f_{ih}$ surface suggest moderate obliquity, which means that these waves are decoupled from the R-mode at $\omega < \Omega_O$, and most of their energy will be reflected before reaching low altitudes. However, the simulation would give nearly identical results for He-band with a similar wavenumber (requiring a high-density background), up to minor differences related to the ion composition. The S2' wave field would then propagate through down to the ionosphere.

3.4 Rising-tone hydrogen band wave

In the previous sections, the current density source was not dynamic, except for the slow changes in amplitude that formed the single-peaked wave packet envelope. We now modulate the wave field into four subpackets and introduce a constant frequency chirp from the initial frequency $\omega_0 = 0.45\Omega_{p0}$ to the final frequency $\omega_1 = 0.65\Omega_{p0}$. As listed in Table 1, the concentration of He+ and O+ has been decreased to prevent the $f_0 = f_{cr}$ surface from crossing the source. The source width is very slightly (by ~7 %) smaller than in Set 1 and the initial wavelength is larger, making the source relatively more narrow. This can be noticed in the $B_{y'}$ plot in Figure 7A, where a weak quasiparallel field appears at the inner edge of the wave field. In Figure 7B, we show the instantaneous frequency at time $t = 15$ s, shortly before the reflection of the first subpacket at the hybrid resonance. At the local minimum between the first and second subpacket, which is located near 10° of latitude, the frequency can be seen to have a localized decrease, despite the linearly rising frequency of the source. These are the effects of group velocity dispersion consistent with $\partial V_g/\partial\omega < 0$, which have been previously discussed in the context of rising-tone chorus elements by Hanzelka and Santolík (2022).

To provide another view on the evolution of wave frequency and the effects of reflected waves, we process data from two selected simulation probes, P1 and P2, whose position is shown in Figure 7B (P1 near the source, P2 at the f_{cr} crossing of the first

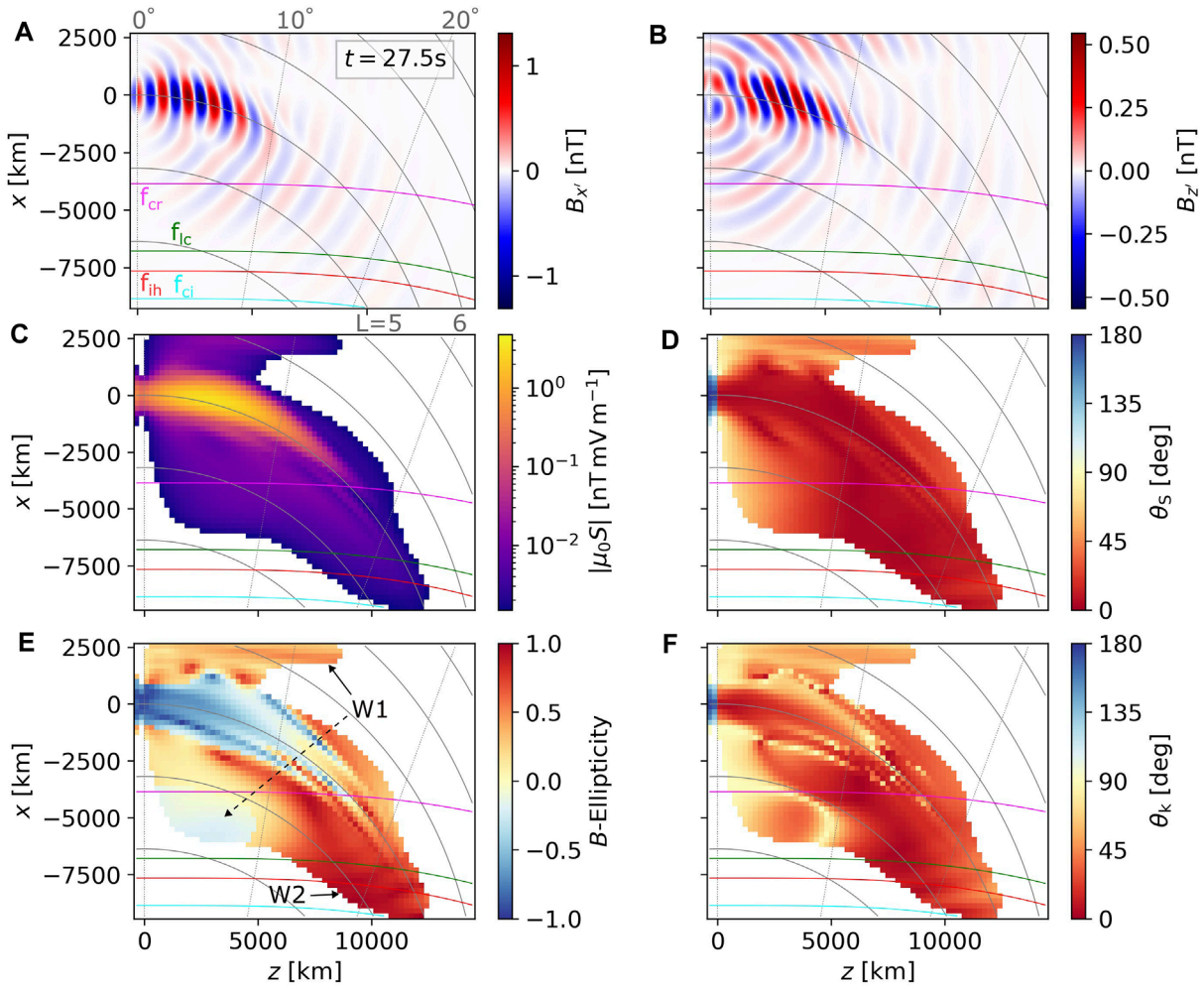

FIGURE 4
Snapshots of wave fields and propagation properties from the simulation run with input parameter Set 2 (constant-frequency unducted helium band wave packet with a single amplitude maximum) taken at $t = 27.5$ s. **(A)** Magnetic field component $B_{x'}$ perpendicular to the local field line (parallel to the meridional plane). **(B)** Magnetic field component $B_{z'}$. **(C)** Magnitude of the Poynting flux. **(D)** Polar angle of the Poynting vector. **(E)** Ellipticity of the magnetic field. Labels W1 and W2 point to weaker fields whose propagation properties differ from the main packet. **(F)** Wave normal angle. Note that the colored curves now represent crossings with characteristic frequencies in the helium band, with f_{ci} standing for the oxygen gyrofrequency.

subpacket). Unlike in the presentation of the constant-frequency wave propagation (Section 3.1), we can show the whole time evolution in one plot, but we are limited to a single point in space. Figure 7C presents the amplitude envelopes of all three magnetic field components $B_{x'}$, $B_{y'}$, and $B_{z'}$, as well as the total magnetic field $|\boldsymbol{B}|$. Before $t \sim 30$ s, the four northward propagating subpackets have a negligible parallel component, and the peak amplitude is near equal to $B_0/100$, as dictated by the source properties. The two perpendicular components have similar magnitudes, suggesting circular polarization, which is further confirmed by the negligible oscillations in $|\boldsymbol{B}|$. After $t \sim 30$ s, the reflected wave packet passes over probe P1, but its amplitude is diminished, with the second subpacket having less than 15{%} of its original amplitude. The $B_{y'}$ component dominates, and $|\boldsymbol{B}|$ exhibits strong oscillations at two times the wave frequency, which are signs of linear polarization and high obliquity in the hydrogen band L-mode. The frequencies near the source (Figure 7D) are linearly growing, except for minor oscillations in the frequency derived from $B_{z'}$. The chirp rate within subpackets of the reflected wave is higher than the initial value, which is again the effect of group velocity dispersion that we already noted when describing Figure 7B.

Moving to probe P2, we observe the behavior of two linearly polarized waves propagating in opposite directions. This overlap creates multiple very short subpackets associated with large variations in the instantaneous frequency. When such a structure is observed, we must separate the two modes, either by the Hilbert-Huang transform (HHT; for an application on EMIC waves, see (Ojha et al., 2021)) or by inspection of time-frequency spectrograms. We choose the latter method and plot spectrograms of power spectral density (PSD) and propagation properties in Figure 8. The PSD near equator, as shown in Figure 8A, confirms that the reflected emission has a considerably lower power (down by almost two orders of magnitude) than the forward propagating wave. Depending on the signal-to-noise ratio of the original wave

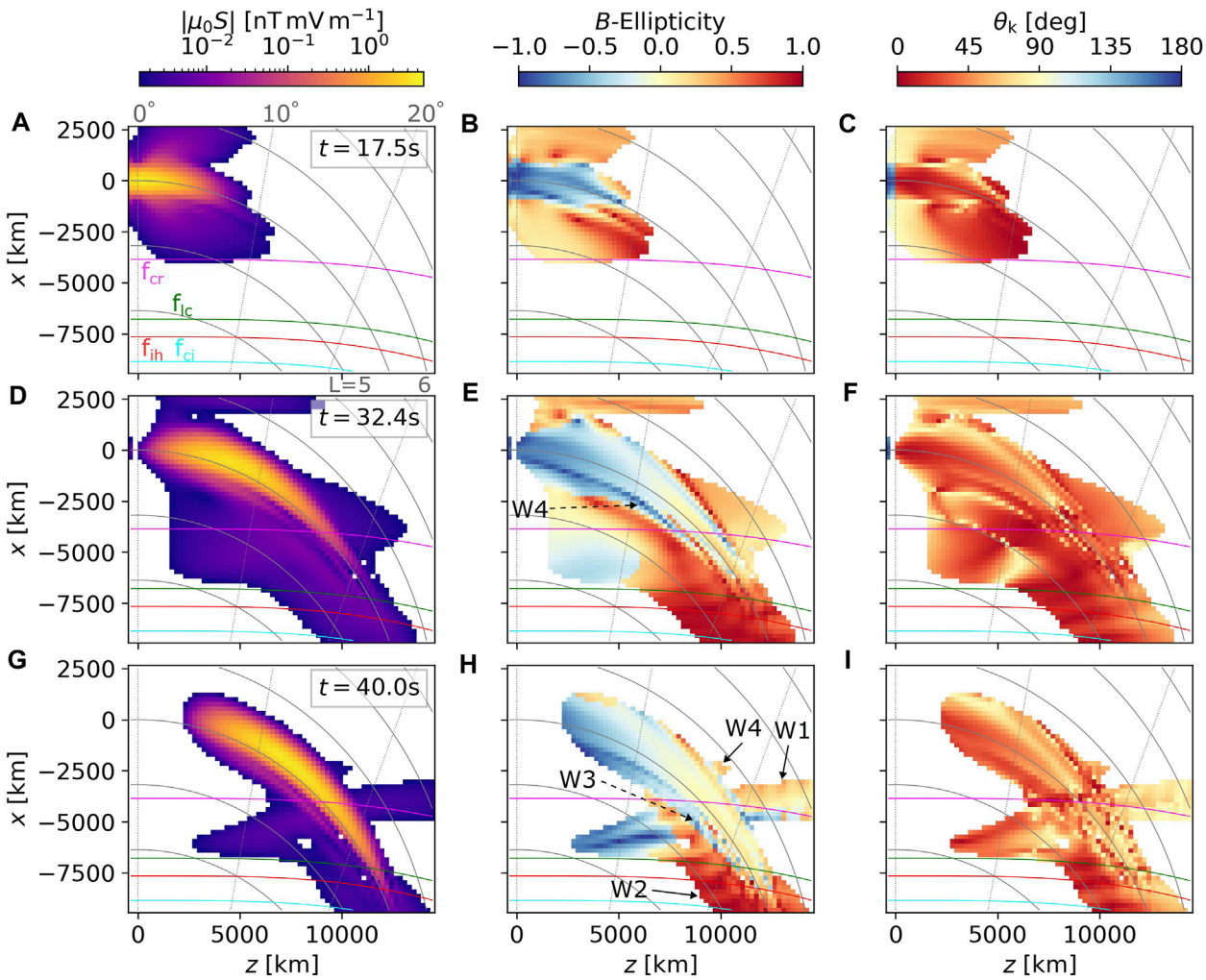

FIGURE 5
Several snapshots of wave propagation properties of the helium band propagation, presented in the same format as the hydrogen band data in Figure 3. **(A–C)** $t = 17.5$ s, **(D–F)** $t = 32.4$ s, **(G–I)** $t = 40.0$ s. Labels, W1, W2, W3, and W4 point to weaker components of the wave field with special propagation and polarization properties.

packet, only parts of the reflected riser may be visible, or none at all. It is of note that the rising-tone element has a considerable spectral width, which is the consequence of the Fourier uncertainty principle for short wave packets. Even with the 93.75{%} overlap of the STFT time windows, the frequency resolution is too low to determine whether the individual subpackets are chirping—the line plots obtained from Hilbert transform are better suited for this purpose but might require some form of mode decomposition like the one included within HHT. Figure 8 supports our previous assessment of the reflected wave's propagation properties, clearly showing the near-linear polarization and highly oblique wave normal angle.

Finally, Figures 8E–H show spectrograms constructed from the probe P2 data. Due to the close frequencies of the two wave packets, it is not immediately clear from the power spectrum in Figure 8E that we are indeed observing two risers propagating in opposite directions. Fortunately, the polar angle θ_S in Figure 8H shows a clear division into two northward and southward propagating elements. Figures 8F,G further show that one element has θ_k about 65° and ellipticty of −0.2, while the other has $\theta_k \approx 100°$ and positive ellipticity <0.1 (these values slightly differ between subpackets). However, in practical applications with the presence of noise, these small differences in WNA and ellipticity could not serve as reliable criteria, and the Poynting flux data would be needed. Before we conclude this section, we must note that the probe P2 was shifted to a slightly higher L-shell than P1 to ensure similar wave powers of the forward-propagating and reflected element—a property that is not necessarily satisfied within real spacecraft data.

4 Discussion

The results of constant-frequency wave simulations from Section 3.1 can be compared to the 2D finite-element method (FEM) simulations of hydrogen band EMIC waves conducted by Kim

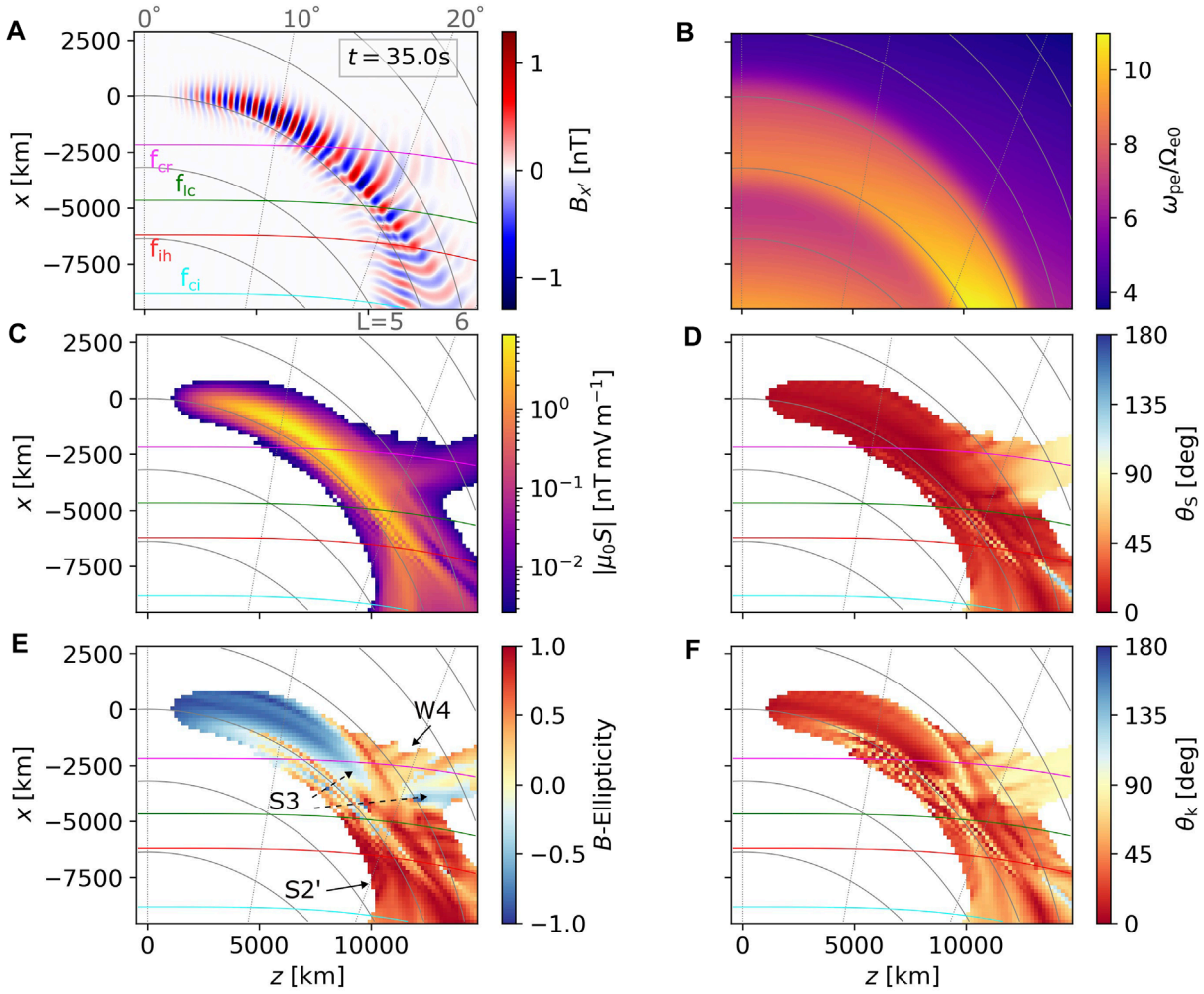

FIGURE 6
Snapshots of wave fields and propagation properties from the simulation run with input parameter Set 3 (constant-frequency ducted hydrogen band wave packet with a single amplitude maximum) taken at $t = 35.0$ s. Compared to Figure 4, we replaced the $B_{z'}$ plot in panel B with a 2D distribution of ω_{pe}/Ω_{e0}, which shows the shape of the density structure responsible for guided propagation. The rest of the panels **(A–F)** show the same type of data as Figure 4. In panel E, certain weak and strong parts of the wave field with special properties are labeled as S2′, S3, and W4.

and Johnson (2016). The FEM approach is used to solve Maxwell equations as a boundary value problem, with the result being the spatial distribution of eigenmodes (Fourier space solutions). This approach differs from our initial value problem, but the fixed frequency and slowly changing source amplitude allow for a meaningful comparison. Kim and Johnson (2016) show that with a wide source region (about four equatorial wavelengths, similar to our Set 1), the wave propagation is initially nearly parallel but becomes significantly oblique before encountering the crossover frequency. Most of those waves reflect at the hybrid resonance after going through polarization reversal, with only a negligible amount passing through to lower altitudes. This weak wave that does not experience reflection corresponds to our W2 field in Figure 2. The R-mode wave W1 emanating from the source was not clearly detected in the FEM simulations, likely because of a stricter power threshold. Due to different ion compositions and density models, the reflected wave in the FEM simulation went to a higher L-shell than in our case and quickly encountered an absorbing boundary, so its propagation properties were not analyzed.

Kim and Johnson (2016) further analyzed a propagation scenario with a very narrow source, which can be compared to our Set 2. As in the previous case, the W1 field is not very apparent in the FEM simulation—it is possible that differences in the initialization (1D current density source in contrast to a 2D electric field source) are behind this disagreement. What the simulations agree on is the presence of a quasiparallel L-mode component at the inner edge of the wave packet (W3 in Figure 5). Some of these left-handed waves preserve their polarization and continue to f_{lc}, while some reflect at f_{cr} and become right-handed (W4 in Figure 5A in Figure 4 of Kim and Johnson (2016)). Unlike in the FEM simulation, the dispersion of R-mode at f_{ih} is unclear due to the overlap with the weak field W2, which originates in the narrow source. We must also point out that we simulated a helium band wave in Set 2, in contrast to the hydrogen band wave in the FEM simulation, so the comparison can

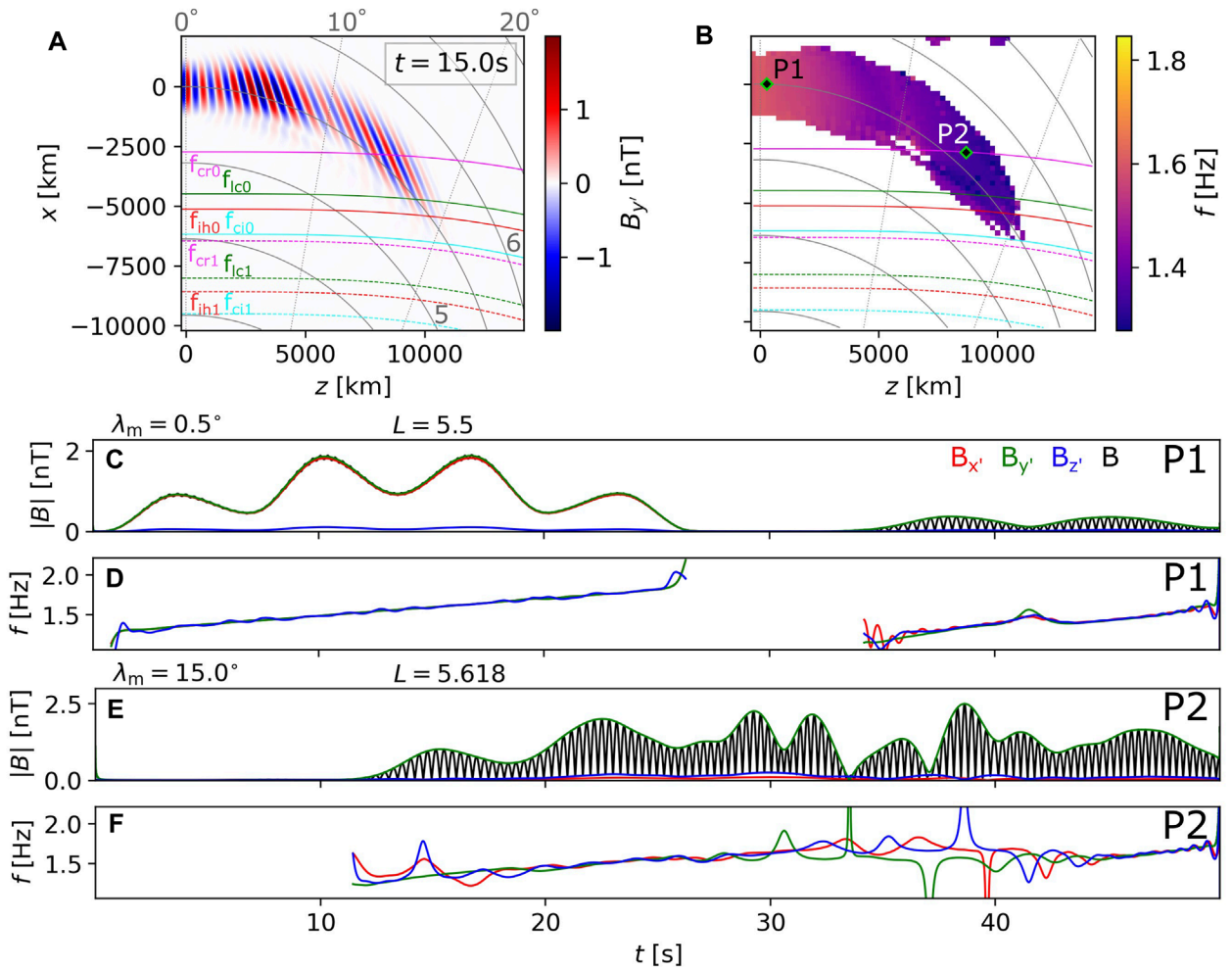

FIGURE 7
Field components and propagation properties of waves from simulation run with input parameter Set 4 (rising-tone unducted hydrogen band wave packet with four subpackets). **(A)** Magnetic field component $B_{x'}$ perpendicular to the local field line (perpendicular to the meridional plane). Snapshot taken at $t = 15$ s. Crossings of characteristic frequencies for wave at frequency ω_0 are represented by solid lines as before, and the crossing for the final frequency ω_1 are plotted with dashed lines. **(B)** Instantaneous wave frequency snapshot, obtained as a power-weighted average of frequencies of the three magnetic components. Labels P1 and P2 show positions of probes that collected data analyzed in the following panels and in Figure 8C Probe P1 measured amplitude envelopes of the magnetic field components $B_{x'}$, $B_{y'}$, and $B_{z'}$ plotted in red, green, and blue, respectively. The total magnetic field $|\boldsymbol{B}|$ is plotted with a black line. **(D)** Instantaneous frequencies from Probe P1, color coded as in the previous panel. **(E, F)** Same as panels **(C, D)**, but with data from probe P2.

be only qualitative. In qualitative terms, the polarization reversal and mode conversion observed near $f = f_{cr}$ in our simulations also agree with the theoretical and numerical full-wave analysis conducted by Johnson and Cheng (1999) and Johnson et al. (1995).

The 2D FDTD full-wave simulations of EMIC propagation on a steep density gradient (Figure 6) are, to our knowledge, unique and cannot be directly compared to previous literature. de Soria-Santacruz et al. (2013) performed hot plasma ray tracing simulations in field-aligned density irregularities, showing that density enhancements can guide quasiparallel waves. However, the widths of those enhancements (minimum to minimum) were ~2500 km and ~625 km, with typical wavelengths ranging from 500 km to 800 km. Under such conditions, the changes in density gradients over a single wavelength are significant, and the plane wave approximation inherent to ray tracing cannot accurately predict wave propagation properties. Furthermore, ray simulations cannot be used to inspect wave energy flow during mode conversion and tunneling. In the full-wave simulation we presented in Figure 6, the H-band EMIC waves guided on the outer edge of a density enhancement are partly reflected on the L-cutoff and partly continue as the quasiparallel R-mode that propagates to lower altitudes. This behavior is similar to the case analyzed by Kim and Johnson (2016) where a moderately oblique wave ($\theta_k \approx 40°$) launched from the equator partly converts to R-mode and avoids reflection at the hybrid resonance. The ducted mode seems to be more efficient at carrying wave energy to lower altitudes, but this is expected to depend on the exact density model and input wave parameters.

The R-mode waves which penetrated through the $f = f_{ih}$ surface (see the bottom right corner of Figure 6F) are shown to have a

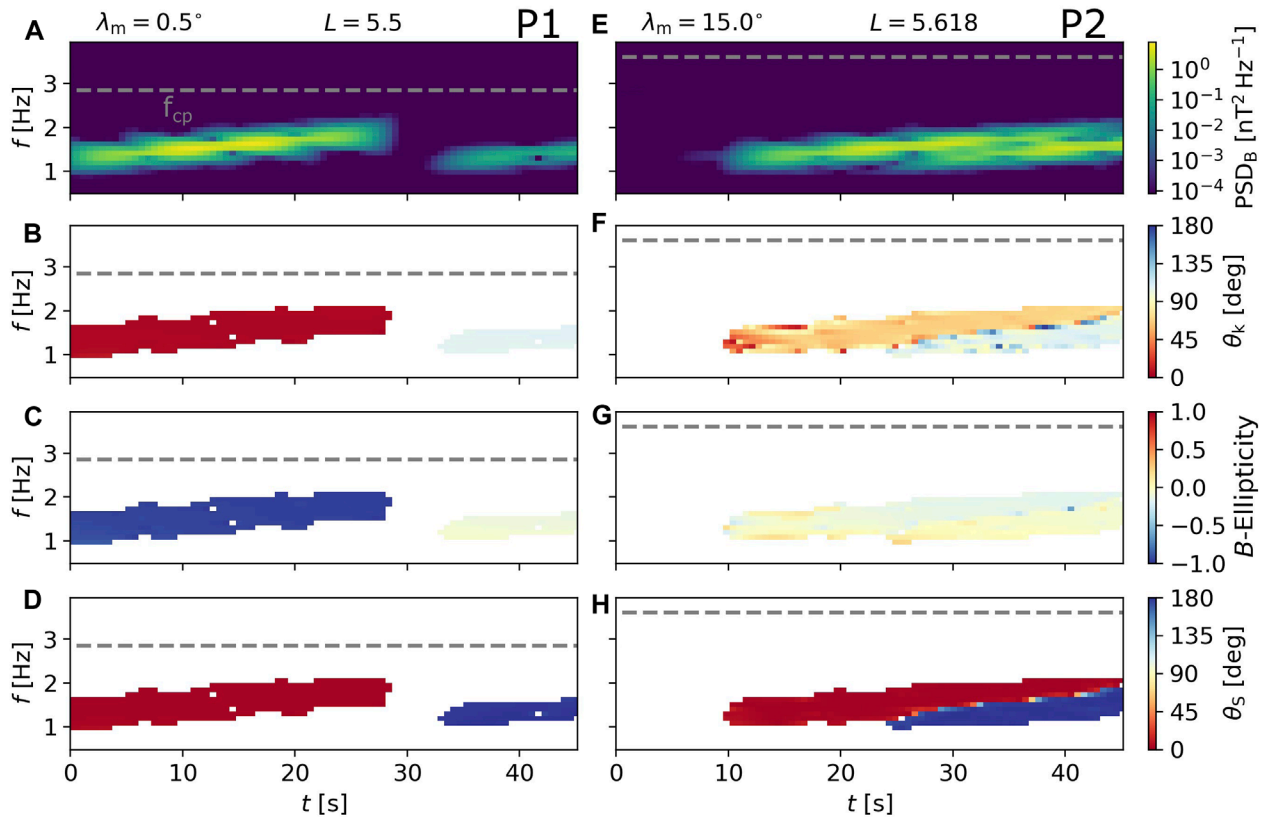

FIGURE 8
Time-frequency spectrograms constructed from time series of wave magnetic field captured by probes P1 **(A–D)** and P2 **(E–H)** placed inside the rising-tone EMIC wave field. **(A)** Magnetic field power spectral density, with the dashed grey line representing the local proton gyrofrequency. **(B)** Wave normal angle. **(C)** Ellipticity of the magnetic field. **(D)** Polar angle of the Poynting vector. **(E–H)** Same as panels **(A–D)**, but with data from probe P2.

broad range of propagation directions. Extending the simulation box down to the ionosphere is beyond our current computational possibilities, but we may assume that a portion of wave energy will be further guided along the gradient, and another portion will propagate towards lower *L*-shells. The former can be linked to observations of R-mode waves in the 0.1 – 1.0 Hz range made by the LEO (Low Earth Orbit) satellite DEMETER above and at the ionospheric trough (Parrot et al., 2014). Ducting along the outer edge of plasmaspheric plumes could also explain why the majority of hydrogen band EMIC observed by Polar (Bräysy and Mursula, 2001) and GOES satellites (Noh et al., 2022) are also detected at conjugate ground stations. Another analysis of DEMETER data by Píša et al. (2015) revealed the presence of 1 – 15 Hz R-mode waves at very low *L*-shells and linked them to He-band EMIC waves. Assuming a strong plasmasphere compression, He-band waves generated at the plasmapause (Fraser and Nguyen, 2001) will fit into this frequency range; therefore, the unguided waves from our ducted simulation can be linked to these observations. We must note that while our density enhancement model was presented as a plume model, the waves never reached its inner boundary, and so it can be seen as a plasmapause model as well.

As far as we know, the 2D full-wave EMIC rising-tone simulations presented in Figures 7, 8 are also unique. Due to the time-dependent nature of the source, such simulations must be performed in the time domain, precluding comparison with FEM models (Kim and Johnson, 2016; 2023). Unlike in the chorus rising-tone simulations of Hanzelka and Santolík (2022), small-scale density irregularities (~1 – 100 km) can be neglected since waveguide modes of structures with sizes far below a single wavelength will not be excited (Zudin et al., 2019). Moreover, Landau damping of oblique EMIC waves is typically very weak (Thorne and Horne, 1992), and so it is meaningful to use cold plasma approximation to study unducted wave propagation and reflections, as long as we neglect the impact of warm ions on the dispersive properties near characteristic frequencies (Chen et al., 2011). The spectra of the forward-propagating and reflected risers in Figure 8 can be compared to the spectral analysis of reflected EMIC risers found in Cluster spacecraft data by Grison et al. (2016). The wave normal angles are nearly perpendicular in both cases and the reflected wave power is observed to be slightly reduced. However, while the direction of the Poynting vector in the simulation is nearly parallel (or anti-parallel), the Cluster observations show angles within a 70°–110° interval. Such conditions are possible only when $f < f_{ih}$ (unguided waves; compare with Supplementary Figure S1C in the Supplementary Material), suggesting that the waves are

reflecting slightly below the $f = f_{ih}$ surface. Thus, despite the similarity in spectra, we are observing a different type of reflection. The importance of unguided waves for propagation of EMIC energy down to the ionosphere has been studied numerically by Pakhotin et al. (2022) using sources at lower L-shells ($L = 3.3$).

The simulated propagation properties of ducted and unducted EMIC waves can be used to draw conclusions about wave-particle interactions and scattering of resonant electrons and protons. In all unducted cases, the waves become moderately oblique (WNA around 40° and higher) before reaching $\lambda = 10°$. Thus the high-order cyclotron resonances (Ma et al., 2019), fractional resonances (Hanzelka et al., 2023), and the Landau resonance (Cao et al., 2019) can become efficient before the wave encounters the crossover frequency. On the other hand, ducted waves remain quasiparallel up to $\lambda > 20°$, keeping the first-order cyclotron resonance as the dominant cause of scattering. However, since the L-mode typically cannot pass through the L-cutoff and ω_{pe}/Ω_e decreases with increasing latitude, interactions with ~1 MeV and sub-MeV electrons will be limited to the near-equatorial region, where the resonance energy reaches its lowest values.

Last but not least, we should discuss some of the choices made when developing our 2D FDTD simulation code and possible subsequent limitations. The restriction to a cold plasma medium results in the lack of a feedback loop between waves and resonant particles. This limitation is especially noticeable in studies of rising-tone EMIC emissions, which are generated by resonant currents formed through nonlinear processes. These currents have an impact on wave properties during propagation in the near-equatorial region and can be properly captured only by including the hot plasma component (Shoji and Omura, 2013; Denton et al., 2019). Another choice affecting the core of the simulation code is the initialization of the wave field. While some authors prefer to initialize the simulation with an electric (Streltsov et al., 2006; Kim and Johnson, 2016) or magnetic field (Xu et al., 2020), others feed current into the simulation box, which then generates the waves (Hosseini et al., 2021; Hanzelka and Santolík, 2022; Pakhotin et al., 2022). The initialization with magnetic field is likely the most straightforward, but we consider the initialization with current density to be more natural, as it resembles wave growth due to hot plasma current. Reduction of the source to one dimension requires the use of an additional numerical factor (Eq. 18), but it removes the need to estimate the unknown field-aligned extent of the source, and it dramatically decreases the size of the input data for time-dependent sources (instead of two spatial dimensions and one temporal, we have only one spatial and one temporal). The deviations from the meridional plane shown in Figure 2E cannot be adequately studied and addressed in a 2D simulation. Implementing a 3D FDTD solver would not be difficult, and it would allow us to construct realistic models of density ducts. Unfortunately, memory constraints would prevent the investigation of wave propagation further away from the equator, where the mode conversion and polarization reversals occur. Adopting spherical coordinates as done by Xu et al. (2020) or Pakhotin et al. (2022) would reduce the box size in cases of field-aligned propagation, boosting the performance in both 2D and 3D simulations, but would not be very beneficial when studying duct leakages and unguided waves. 3D Ray tracing codes thus remain the best method for studies of azimuthal propagation of EMIC waves (Xiao et al., 2012; Chen et al., 2014; Santolík et al., 2016; Hanzelka et al., 2022).

5 Conclusion

The results presented in this paper can be summarized into five points:

1. Two-dimensional finite-difference time-domain simulations can be efficiently used to simulate the propagation of EMIC wave fields generated by time-varying sources in the magnetosphere.
2. Simulated mode conversions and wave reflections corroborate the previous results of Kim and Johnson (2016). Namely, we observed polarization reversal and mode conversions near the crossover frequency, and reflections at the L-cutoff and ion hybrid resonance.
3. A finite and narrow 1D source of left-hand polarized current produces not only a quasiparallel L-mode wave, but also weak R-mode waves propagating into a wide range of directions.
4. Density gradients at the outer edge of plasmaspheric plumes (or plasmapause) can guide wave energy to high latitudes and are a strong candidate for explaining frequent observations of EMIC waves at low altitudes. On the other hand, unducted waves quickly become oblique and experience reflection at the ion hybrid resonance after going through a polarization reversal.
5. Reflected rising-tone EMIC emissions can be observed when the probes are fortuitously positioned, but the propagation properties in our simulation differ from those in Cluster observations of reflected waves (Grison et al., 2016).

We have shown four different scenarios of EMIC wave propagation (unducted H-band, unducted He-band, ducted H-band, unducted rising-tone H-band), but we have not studied the sensitivity of our results to changes in input parameters. A sampling of initial wave frequencies and cold plasma densities could be used to investigate the wave distribution during different geomagnetic conditions. The numerical code also has capabilities to simulate the effects of spatial variability in ion concentrations (Min et al., 2015), branch splitting by minority ions (Miyoshi et al., 2019), falling-tone triggered emissions (Nakamura et al., 2016), propagation of waves generated by an oblique source, spreading of short EMIC pulses, and many other concepts that were before thoroughly investigated with 2D FDTD numerical models. Furthermore, the resulting wave fields can be used as an input in test-particle simulations to study the scattering and precipitation of energetic ions and relativistic electrons. These topics will be investigated in our future research.

Data availability statement

The datasets presented in this study can be found in online repositories. The names of the repository/repositories and accession

number(s) can be found below: https://figshare.com/s/9d05a8bf0646fdceac8a.

Author contributions

MH created the full-wave simulation code, analyzed the resulting simulated wave fields, and wrote the original manuscript. WL secured the funding. MH and WL initiated the study. WL, QM, and MQ provided consultations on EMIC wave propagation properties based on experimental observations. LC, X-CS, and LG provided helpful comments during the course of the project. All authors contributed to the article and approved the submitted version.

Funding

The research at Boston University is supported by NASA grants 80NSSC20K0698, 80NSSC20K1270, and 80NSSC21K1312, as well as the NSF grant AGS-2019950. QM would like to acknowledge the NASA grant 80NSSC20K0196 and the NSF grant AGS-2225445. LG gratefully acknowledges the NASA FINESST grant 80NSSC20K1506.

Conflict of interest

The authors declare that the research was conducted in the absence of any commercial or financial relationships that could be construed as a potential conflict of interest.

Publisher's note

Supplementary material

The Supplementary Material for this article can be found online at: https://www.frontiersin.org/articles/10.3389/fspas.2023.1251563/full#supplementary-material

References

Allen, R. C., Zhang, J. C., Kistler, L. M., Spence, H. E., Lin, R. L., Klecker, B., et al. (2015). A statistical study of EMIC waves observed by cluster: 1. Wave properties. *J. Geophys. Res. Space Phys.* 120, 5574–5592. doi:10.1002/2015JA021333

Anderson, B. J., Denton, R. E., Ho, G., Hamilton, D. C., Fuselier, S. A., and Strangeway, R. J. (1996). Observational test of local proton cyclotron instability in the Earth's magnetosphere. *J. Geophys. Res.* 101, 21527–21543. doi:10.1029/96JA01251

Angerami, J. J. (1970). Whistler duct properties deduced from VLF observations made with the Ogo 3 satellite near the magnetic equator. *J. Geophys. Res.* 75, 6115–6135. doi:10.1029/JA075i031p06115

Baker, D. N. (2021). Wave-particle interaction effects in the Van Allen belts. *Earth Planets Space* 73, 189. doi:10.1186/s40623-021-01508-y

Bortnik, J., Albert, J. M., Artemyev, A., Li, W., Jun, C.-W., Grach, V. S., et al. (2022). Amplitude dependence of nonlinear precipitation blocking of relativistic electrons by large amplitude EMIC waves. *Geophys. Res. Lett.* 49, e2022GL098365. doi:10.1029/2022GL098365

Bräysy, T., and Mursula, K. (2001). Conjugate observations of electromagnetic ion cyclotron waves. *J. Geophys. Res.* 106, 6029–6041. doi:10.1029/2000JA003009

Bräysy, T., Mursula, K., and Marklund, G. (1998). Ion cyclotron waves during a great magnetic storm observed by Freja double-probe electric field instrument. *J. Geophys. Res.* 103, 4145–4155. doi:10.1029/97JA02820

Cao, X., Ni, B., Summers, D., Shprits, Y. Y., Gu, X., Fu, S., et al. (2019). Sensitivity of EMIC wave-driven scattering loss of ring current protons to wave normal angle distribution. *Geophys. Res. Lett.* 46, 590–598. doi:10.1029/2018GL081550

Chen, H., Gao, X., Lu, Q., and Wang, S. (2019a). Analyzing EMIC waves in the inner magnetosphere using long-term van allen probes observations. *J. Geophys. Res. (Space Phys.* 124, 7402–7412. doi:10.1029/2019JA026965

Chen, L., Jordanova, V. K., Spasojević, M., Thorne, R. M., and Horne, R. B. (2014). Electromagnetic ion cyclotron wave modeling during the geospace environment modeling challenge event. *J. Geophys. Res. Space Phys.* 119, 2963–2977. doi:10.1002/2013JA019595

Chen, L., Thorne, R. M., and Bortnik, J. (2011). The controlling effect of ion temperature on EMIC wave excitation and scattering. *Geophys. Res. Lett.* 38, L16109. doi:10.1029/2011GL048653

Chen, L., Thorne, R. M., and Horne, R. B. (2009). Simulation of EMIC wave excitation in a model magnetosphere including structured high-density plumes. *J. Geophys. Res. Space Phys.* 114, A07221. doi:10.1029/2009JA014204

Chen, L., Thorne, R. M., Jordanova, V. K., Wang, C.-P., Gkioulidou, M., Lyons, L., et al. (2010). Global simulation of EMIC wave excitation during the 21 April 2001 storm from coupled RCM-RAM-HOTRAY modeling. *J. Geophys. Res. Space Phys.* 115, A07209. doi:10.1029/2009JA015075

Chen, L., Zhu, H., and Zhang, X. (2019b). Wavenumber analysis of EMIC waves. *Geophys. Res. Lett.* 46, 5689–5697. doi:10.1029/2019GL082686

Cornwall, J. M., Coroniti, F. V., and Thorne, R. M. (1970). Turbulent loss of ring current protons. *J. Geophys. Res.* 75, 4699–4709. doi:10.1029/JA075i025p04699

Cornwall, J. M. (1965). Cyclotron instabilities and electromagnetic emission in the ultra low frequency and very low frequency ranges. *J. Geophys. Res.* 70, 61–69. doi:10.1029/JZ070i001p00061

Denton, R. E., Goldstein, J., Menietti, J. D., and Young, S. L. (2002). Magnetospheric electron density model inferred from Polar plasma wave data. *J. Geophys. Res. Space Phys.* 107, 1386. doi:10.1029/2001JA009136

Darrouzet, F., Gallagher, D. L., André, N., Carpenter, D. L., Dandouras, I., Décréau, P. M. E., et al. (2009). Plasmaspheric density structures and dynamics: properties observed by the CLUSTER and IMAGE missions. *Space Sci. Rev.* 145, 55–106. doi:10.1007/s11214-008-9438-9

de Soria-Santacruz, M., Spasojevic, M., and Chen, L. (2013). EMIC waves growth and guiding in the presence of cold plasma density irregularities. *Geophys. Res. Lett.* 40, 1940–1944. doi:10.1002/grl.50484

Denton, R. E., Menietti, J. D., Goldstein, J., Young, S. L., and Anderson, R. R. (2004). Electron density in the magnetosphere. *J. Geophys. Res. Space Phys.* 109, A09215. doi:10.1029/2003JA010245

Denton, R. E., Ofman, L., Shprits, Y. Y., Bortnik, J., Millan, R. M., Rodger, C. J., et al. (2019). Pitch angle scattering of sub-MeV relativistic electrons by electromagnetic ion cyclotron waves. *J. Geophys. Res. Space Phys.* 124, 5610–5626. doi:10.1029/2018JA026384

Engebretson, M. J., Posch, J. L., Wygant, J. R., Kletzing, C. A., Lessard, M. R., Huang, C. L., et al. (2015). Van Allen probes, NOAA, GOES, and ground observations of an intense EMIC wave event extending over 12 h in magnetic local time. *J. Geophys. Res. Space Phys.* 120, 5465–5488. doi:10.1002/2015JA021227

Fraser, B. J., and Nguyen, T. S. (2001). Is the plasmapause a preferred source region of electromagnetic ion cyclotron waves in the magnetosphere? *J. Atmos. Sol.-Terr. Phys.* 63, 1225–1247. doi:10.1016/S1364-6826(00)00225-X

Gedney, S. D. (2011). *Introduction to the finite-difference time-domain (FDTD) Method for electromagnetics. Synthesis lectures on computational electromagnetics*. Morgan & Claypool Publishers. doi:10.2200/S00316ED1V01Y201012CEM027

Grach, V. S., and Demekhov, A. G. (2020). Precipitation of relativistic electrons under resonant interaction with electromagnetic ion cyclotron wave packets. *J. Geophys. Res. Space Phys.* 125, e27358. doi:10.1029/2019JA027358

Grison, B., Darrouzet, F., Santolík, O., Cornilleau-Wehrlin, N., and Masson, A. (2016). Cluster observations of reflected EMIC-triggered emission. *Geophys. Res. Lett.* 43, 4164–4171. doi:10.1002/2016GL069096

Grison, B., Hanzelka, M., Breuillard, H., Darrouzet, F., Santolík, O., Cornilleau-Wehrlin, N., et al. (2018). Plasmaspheric plumes and EMIC rising tone emissions. *J. Geophys. Res. Space Phys.* 123, 9443–9452. doi:10.1029/2018JA025796

Gurnett, D. A., and Bhattacharjee, A. (2017). *Introduction to plasma Physics: With space, laboratory and astrophysical applications*. Cambridge University Press.

Horne, R. B., and Thorne, R. M. (1993). On the preferred source location for the convective amplification of ion cyclotron waves. *J. Geophys. Res.* 98, 9233–9247. doi:10.1029/92JA02972

Hanzelka, M., Li, W., and Ma, Q. (2023). Parametric analysis of pitch angle scattering and losses of relativistic electrons by oblique EMIC waves. *Front. Astronomy Space Sci.* 10, 1163515. doi:10.3389/fspas.2023.1163515

Hanzelka, M., Němec, F., Santolík, O., and Parrot, M. (2022). Statistical analysis of wave propagation properties of equatorial noise observed at low altitudes. *J. Geophys. Res. Space Phys.* 127, e30416. doi:10.1029/2022JA030416

Hanzelka, M., and Santolík, O. (2022). Effects of field-aligned cold plasma density filaments on the fine structure of chorus. *Geophys. Res. Lett.* 49, e2022GL101654. doi:10.1029/2022GL101654

Horne, R. B., and Miyoshi, Y. (2016). Propagation and linear mode conversion of magnetosonic and electromagnetic ion cyclotron waves in the radiation belts. *Geophys. Res. Lett.* 43, 039. doi:10.1002/2016GL070216

Horne, R. B., and Thorne, R. M. (1998). Potential waves for relativistic electron scattering and stochastic acceleration during magnetic storms. *Geophys. Res. Lett.* 25, 3011–3014. doi:10.1029/98GL01002

Hosseini, P., Agapitov, O., Harid, V., and Gołkowski, M. (2021). Evidence of small scale plasma irregularity effects on whistler mode chorus propagation. *Geophys. Res. Lett.* 48, e92850. doi:10.1029/2021GL092850

Hu, Y., Denton, R. E., and Johnson, J. R. (2010). Two-dimensional hybrid code simulation of electromagnetic ion cyclotron waves of multi-ion plasmas in a dipole magnetic field. *J. Geophys. Res. Space Phys.* 115, A09218. doi:10.1029/2009JA015158

Hu, Y., and Denton, R. E. (2009). Two-dimensional hybrid code simulation of electromagnetic ion cyclotron waves in a dipole magnetic field. *J. Geophys. Res. Space Phys.* 114, A12217. doi:10.1029/2009JA014570

Johnson, J. R., Chang, T., and Crew, G. B. (1995). A study of mode conversion in an oxygen-hydrogen plasma. *Phys. Plasmas* 2, 1274–1284. doi:10.1063/1.871339

Johnson, J. R., and Cheng, C. Z. (1999). Can ion cyclotron waves propagate to the ground? *Geophys. Res. Lett.* 26, 671–674. doi:10.1029/1999GL900074

Jordanova, V. K., Farrugia, C. J., Thorne, R. M., Khazanov, G. V., Reeves, G. D., and Thomsen, M. F. (2001). Modeling ring current proton precipitation by electromagnetic ion cyclotron waves during the May 14-16, 1997, storm. *J. Geophys. Res.* 106, 7–22. doi:10.1029/2000JA002008

Jun, C.-W., Miyoshi, Y., Kurita, S., Yue, C., Bortnik, J., Lyons, L., et al. (2021). The characteristics of EMIC waves in the magnetosphere based on the van allen probes and arase observations. *J. Geophys. Res. Space Phys.* 126, e29001. doi:10.1029/2020JA029001

Kersten, T., Horne, R. B., Glauert, S. A., Meredith, N. P., Fraser, B. J., and Grew, R. S. (2014). Electron losses from the radiation belts caused by EMIC waves. *J. Geophys. Res. Space Phys.* 119, 8820–8837. doi:10.1002/2014JA020366

Kim, E.-H., and Johnson, J. R. (2016). Full-wave modeling of EMIC waves near the He^+ gyrofrequency. *Geophys. Res. Lett.* 43, 13–21. doi:10.1002/2015GL066978

Kim, E.-H., and Johnson, J. R. (2023). Magnetic tilt effect on externally driven electromagnetic ion cyclotron (EMIC) waves. *Geophys. Res. Lett.* 50, e2022GL101544. doi:10.1029/2022GL101544

Koons, H. C. (1989). Observations of large-amplitude, whistler mode wave ducts in the outer plasmasphere. *J. Geophys. Res.* 94, 15393–15397. doi:10.1029/JA094iA11p15393

Lee, J. H., Blum, L. W., Chen, L., and Kwon, Y. J. (2021). Relationship between muscle mass and non-alcoholic fatty liver disease. *Front. Astron. Space Sci.* 8, 122. doi:10.3390/biology10020122

Li, W., and Hudson, M. K. (2019). Earth's van allen radiation belts: from discovery to the van allen probes era. *J. Geophys. Res. Space Phys.* 124, 8319–8351. doi:10.1029/2018JA025940

Lyu, X., Ma, Q., Tu, W., Li, W., and Capannolo, L. (2022). Modeling the simultaneous dropout of energetic electrons and protons by EMIC wave scattering. *Geophys. Res. Lett.* 49, e2022GL101041. doi:10.1029/2022GL101041

Ma, Q., Li, W., Yue, C., Thorne, R. M., Bortnik, J., Kletzing, C. A., et al. (2019). Ion heating by electromagnetic ion cyclotron waves and magnetosonic waves in the Earth's inner magnetosphere. *Geophys. Res. Lett.* 46, 6258–6267. doi:10.1029/2019GL083513

Meredith, N. P., Horne, R. B., Kersten, T., Fraser, B. J., and Grew, R. S. (2014). Global morphology and spectral properties of EMIC waves derived from CRRES observations. *J. Geophys. Res. Space Phys.* 119, 5328–5342. doi:10.1002/2014JA020064

Meredith, N. P., Horne, R. B., Thorne, R. M., and Anderson, R. R. (2003). Favored regions for chorus-driven electron acceleration to relativistic energies in the Earth's outer radiation belt. *Geophys. Res. Lett.* 30, 1871. doi:10.1029/2003GL017698

Min, K., Liu, K., Bonnell, J. W., Breneman, A. W., Denton, R. E., Funsten, H. O., et al. (2015). Study of EMIC wave excitation using direct ion measurements. *J. Geophys. Res. Space Phys.* 120, 2702–2719. doi:10.1002/2014JA020717

Miyoshi, Y., Matsuda, S., Kurita, S., Nomura, K., Keika, K., Shoji, M., et al. (2019). EMIC waves converted from equatorial noise due to M/Q = 2 ions in the plasmasphere: observations from van allen probes and arase. *Geophys. Res. Lett.* 46, 5662–5669. doi:10.1029/2019GL083024

Nakamura, S., Omura, Y., and Angelopoulos, V. (2016). A statistical study of EMIC rising and falling tone emissions observed by THEMIS. *J. Geophys. Res. Space Phys.* 121, 8374–8391. doi:10.1002/2016JA022353

Noh, S.-J., Kim, H., Lessard, M., Engebretson, M., Pilipenko, V., Kim, E.-H., et al. (2022). Statistical study of EMIC wave propagation using space-ground conjugate observations. *J. Geophys. Res. Space Phys.* 127, e30262. doi:10.1029/2022JA030262

Ojha, B., Omura, Y., Singh, S., and Lakhina, G. S. (2021). Multipoint analysis of source regions of EMIC waves and rapid growth of subpackets. *J. Geophys. Res. Space Phys.* 126, e29514. doi:10.1029/2021JA029514

Omura, Y., and Zhao, Q. (2012). Nonlinear pitch angle scattering of relativistic electrons by EMIC waves in the inner magnetosphere. *J. Geophys. Res. Space Phys.* 117, A08227. doi:10.1029/2012JA017943

Omura, Y., Pickett, J., Grison, B., Santolik, O., Dandouras, I., Engebretson, M., et al. (2010). Theory and observation of electromagnetic ion cyclotron triggered emissions in the magnetosphere. *J. Geophys. Res. Space Phys.* 115, A07234. doi:10.1029/2010JA015300

Pakhotin, I. P., Mann, I. R., Sydorenko, D., and Rankin, R. (2022). Novel EMIC wave propagation pathway through Buchsbaum resonance and inter-hemispheric wave interference: swarm observations and modeling. *Geophys. Res. Lett.* 49, e98249. doi:10.1029/2022GL098249

Parrot, M., Němec, F., and Santolík, O. (2014). Analysis of fine ELF wave structures observed poleward from the ionospheric trough by the low-altitude satellite DEMETER. *J. Geophys. Res. (Space Phys.* 119, 2052–2060. doi:10.1002/2013JA019557

Píša, D., Parrot, M., Santolík, O., and Menietti, J. D. (2015). EMIC waves observed by the low-altitude satellite DEMETER during the November 2004 magnetic storm. *J. Geophys. Res. (Space Phys.* 120, 5455–5464. doi:10.1002/2014JA020233

Pokhrel, S., Shankar, V., and Simpson, J. J. (2018). 3-D FDTD modeling of electromagnetic wave propagation in magnetized plasma requiring singular updates to the current density equation. *IEEE Trans. Antennas Propag.* 66, 4772–4781. doi:10.1109/TAP.2018.2847601

Rauch, J. L., and Roux, A. (1982). Ray tracing of ULF waves in a multicomponent magnetospheric plasma: consequences for the generation mechanism of ion cyclotron waves. *J. Geophys. Res.* 87, 8191–8198. doi:10.1029/JA087iA10p08191

Saikin, A. A., Zhang, J. C., Allen, R. C., Smith, C. W., Kistler, L. M., Spence, H. E., et al. (2015). The occurrence and wave properties of H^+-He^+-and O^+-band EMIC waves observed by the Van Allen Probes. *J. Geophys. Res. Space Phys.* 120, 7477–7492. doi:10.1002/2015JA021358

Saito, T. (1969). Geomagnetic pulsations. *Space Sci. Rev.* 10, 319–412. doi:10.1007/BF00203620

Santolík, O., Parrot, M., and Lefeuvre, F. (2003). Singular value decomposition methods for wave propagation analysis. *Radio Sci.* 38, 1010. doi:10.1029/2000RS002523

Santolík, O., Parrot, M., and Němec, F. (2016). Propagation of equatorial noise to low altitudes: decoupling from the magnetosonic mode. *Geophys. Res. Lett.* 43, 6694–6704. doi:10.1002/2016GL069582

Santolík, O., Pickett, J. S., Gurnett, D. A., Menietti, J. D., Tsurutani, B. T., and Verkhoglyadova, O. (2010). Survey of Poynting flux of whistler mode chorus in the outer zone. *J. Geophys. Res. Space Phys.* 115, A00F13. doi:10.1029/2009JA014925

Shoji, M., and Omura, Y. (2013). Triggering process of electromagnetic ion cyclotron rising tone emissions in the inner magnetosphere. *J. Geophys. Res. Space Phys.* 118, 5553–5561. doi:10.1002/jgra.50523

Sigsbee, K., Kletzing, C. A., Faden, J., and Smith, C. W. (2023). Occurrence rates of electromagnetic ion cyclotron (EMIC) waves with rising tones in the van allen probes data set. *J. Geophys. Res. Space Phys.* 128, e2022JA030548. doi:10.1029/2022JA030548

Stix, T. (1992). *Waves in plasmas*. Melville NY: American Institute of Physics).

Streltsov, A. V., Lampe, M., Manheimer, W., Ganguli, G., and Joyce, G. (2006). Whistler propagation in inhomogeneous plasma. *J. Geophys. Res. Space Phys.* 111, A03216. doi:10.1029/2005JA011357

Summers, D., Thorne, R. M., and Xiao, F. (1998). Relativistic theory of wave-particle resonant diffusion with application to electron acceleration in the magnetosphere. *J. Geophys. Res.* 103, 20487–20500. doi:10.1029/98JA01740

Thorne, R. M., and Horne, R. B. (1997). Modulation of electromagnetic ion cyclotron instability due to interaction with ring current O^+ during magnetic storms. *J. Geophys. Res.* 102, 14155–14163. doi:10.1029/96JA04019

Thorne, R. M., and Horne, R. B. (1992). The contribution of ion-cyclotron waves to electron heating and SAR-arc excitation near the storm-time plasmapause. *Geophys. Res. Lett.* 19, 417–420. doi:10.1029/92GL00089

Umeda, T., Omura, Y., and Matsumoto, H. (2001). An improved masking method for absorbing boundaries in electromagnetic particle simulations. *Comput. Phys. Commun.* 137, 286–299. doi:10.1016/S0010-4655(01)00182-5

Wang, X. Y., Huang, S. Y., Allen, R. C., Fu, H. S., Deng, X. H., Zhou, M., et al. (2017). The occurrence and wave properties of EMIC waves observed by the Magnetospheric Multiscale (MMS) mission. *J. Geophys. Res. Space Phys.* 122, 8228–8240. doi:10.1002/2017JA024237

Xiao, F., Zhou, Q., He, Z., and Tang, L. (2012). Three-dimensional ray tracing of fast magnetosonic waves. *J. Geophys. Res. Space Phys.* 117, A06208. doi:10.1029/2012JA017589

Xu, X., Zhou, C., Chen, L., Xia, Z., Liu, X., Simpson, J. J., et al. (2020). Two dimensional full-wave modeling of propagation of low-altitude hiss in the ionosphere. *Geophys. Res. Lett.* 47, e86601. doi:10.1029/2019GL086601

Yee, K. (1966). Numerical solution of initial boundary value problems involving maxwell's equations in isotropic media. *IEEE Trans. Antennas Propag.* 14, 302–307. doi:10.1109/TAP.1966.1138693

Yoon, P. H. (1992). Quasilinear evolution of Alfvén-ion-cyclotron and mirror instabilities driven by ion temperature anisotropy. *Phys. Fluids B* 4, 3627–3637. doi:10.1063/1.860371

Zhang, X. J., Li, W., Thorne, R. M., Angelopoulos, V., Bortnik, J., Kletzing, C. A., et al. (2016). Statistical distribution of EMIC wave spectra: observations from van allen probes. *Geophys. Res. Lett.* 43, 12. doi:10.1002/2016GL071158

Zudin, I. Y., Zaboronkova, T. M., Gushchin, M. E., Aidakina, N. A., Korobkov, S. V., and Krafft, C. (2019). Whistler waves' propagation in plasmas with systems of small-scale density irregularities: numerical simulations and theory. *J. Geophys. Res. Space Phys.* 124, 4739–4760. doi:10.1029/2019JA026637

frontiers | Frontiers in Astronomy and Space Sciences

TYPE Original Research
PUBLISHED 22 February 2024
DOI 10.3389/fspas.2024.1253668

OPEN ACCESS

EDITED BY
Xu-Zhi Zhou,
Peking University, China

REVIEWED BY
Li Li,
Peking University, China
Ze-Fan Yin,
Peking University, China

*CORRESPONDENCE
Murong Qin,
mqin1@bu.edu
Wen Li,
wenli77@bu.edu

RECEIVED 05 July 2023
ACCEPTED 12 February 2024
PUBLISHED 22 February 2024

CITATION
Qin M, Li W, Ma Q, Shen X-C, Woodger L, Millan R and Angelopoulos V (2024), Large-scale magnetic field oscillations and their effects on modulating energetic electron precipitation.
Front. Astron. Space Sci. 11:1253668.
doi: 10.3389/fspas.2024.1253668

Large-scale magnetic field oscillations and their effects on modulating energetic electron precipitation

Murong Qin[1]*, Wen Li[1]*, Qianli Ma[1,2], Xiao-Chen Shen[1], Leslie Woodger[3], Robyn Millan[3] and Vassilis Angelopoulos[4]

[1]Center for Space Physics, Boston University, Boston, MA, United States, [2]Department of Atmospheric and Oceanic Sciences, University of California, Los Angeles, Los Angeles, CA, United States, [3]Department of Physics and Astronomy, Dartmouth College, Hanover, NH, United States, [4]Earth, Planetary, and Space Sciences Department, University of California, Los Angeles, Los Angeles, CA, United States

In this study, we present simultaneous multi-point observations of magnetospheric oscillations on a time scale of tens of minutes (forced-breathing mode) and modulated whistler-mode chorus waves, associated with concurrent energetic electron precipitation observed through enhanced BARREL X-rays. Similar fluctuations are observed in X-ray signatures and the compressional component of magnetic oscillations, spanning from ~9 to 12 h in MLT and 5 to 11 in *L* shell. Such magnetospheric oscillations covering an extensive region in the pre-noon sector have been suggested to play a potential role in precipitating energetic electrons by either wave scattering or loss cone modulation, showing a high correlation with the enhancement in X-rays. In this event, the correlation coefficients between chorus waves (smoothed over 8 min), ambient magnetic field oscillations and X-rays are high. We perform an in-depth quasi-linear modeling analysis to evaluate the role of magnetic field oscillations in modulating energetic electron precipitation in the Earth's magnetosphere through modulating whistler-mode chorus wave amplitude, resonance condition between chorus waves and electrons, as well as loss cone size. Model results further show that the modulation of chorus wave amplitude plays a dominant role in modulating the electron precipitation. However, the effect of the modulation in the resonant energy between chorus waves and energetic electrons due to the background magnetic field oscillations cannot be neglected. The bounce loss cone modulation, affected by the magnetic oscillations, has little influence on the electron precipitation modulation. Our results show that the low frequency magnetospheric oscillations could play a significant role in modulating the electron precipitation through modulating chorus wave intensity and the resonant energy between chorus waves and electron.

KEYWORDS

wave-particle interaction, magnetic field oscillations, ULF waves, whistler waves, electron precipitation

1 Introduction

Pitch angle diffusion of energetic electrons into the atmospheric bounce loss cone has been considered to be an important loss mechanism of radiation belt electrons. In this process, energetic electrons are precipitated into the atmosphere through resonant interactions with various plasma waves (e.g., Millan and Thorne., 2007), such as electromagnetic ion cyclotron (EMIC) waves (Summers and Thorne, 2003; Clilverd et al., 2015; Hendry et al., 2017; Qin et al., 2018; Qin et al., 2019; Qin et al., 2020; Capannolo et al., 2019a; Capannolo et al., 2019b; Zhang et al., 2021), whistler-mode chorus waves (e.g., Nishimura et al., 2010; Thorne, 2010; Ma et al., 2020) and hiss waves in the plasmasphere and plumes (Summers et al., 2008; Li et al., 2019; Ma et al., 2021).

Fluctuations with frequencies below tens of millihertz (mHz) have been extensively observed in the signatures of energetic electron precipitation from riometer pulsations (Heacock and Hunsucker, 1977; Spanswick et al., 2005), radars (Buchert et al., 1999), optical auroral emissions (Rae et al., 2007; Jaynes et al., 2015) and balloon X-ray spectra (Brito et al., 2012; Motoba et al., 2013; Breneman et al., 2015; Halford et al., 2015; Rae et al., 2018; Breneman et al., 2020; Qin et al., 2021). These fluctuations have been shown to be usually associated with ultra-low frequency (ULF) waves or quasi-static breathing mode of the magnetosphere with similar periodicities. Pc 3–5 ULF waves (1.7–100 mHz, Jacobs et al., 1964) can be driven by upstream solar wind dynamic pressure impulses (e.g., Claudepierre et al., 2009; Claudepierre et al., 2010; Shen et al., 2015; Shen et al., 2017), solar wind speed changes (Mathie and Mann, 2000), as well as internal sources like substorms (e.g., Olson, 1999; Hsu and McPherron, 2007). The magnetosphere also responds to external solar wind conditions via a quasi-static forced breathing mode, with periods longer than the Alfven wave travel time in the dayside magnetosphere (~4 min, 4 mHz) (Kepko et al., 2002; Kepko and Spence, 2003; Kepko and Viall, 2019). Because the period of these ambient magnetic field oscillations is much longer than the gyroperiod and the bounce period of energetic electrons, they are only supposed to be in drift resonance with electrons (Elkington et al., 2003), rather than directly scatter the electrons into loss cone through cyclotron-resonance interaction.

Many mechanisms have been employed to explain the commonly observed energetic electron precipitation modulated by ULF wave or forced-breathing mode oscillations. Theoretically, ULF waves or forced-breathing mode magnetic field fluctuations

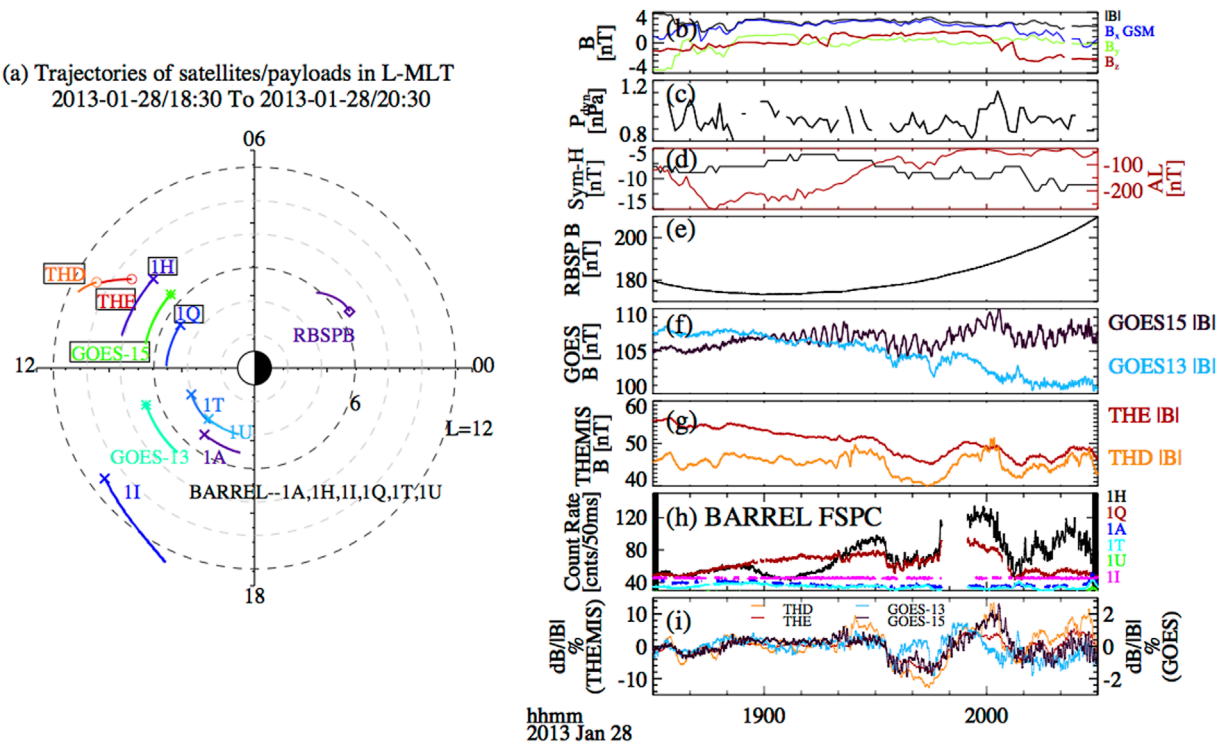

FIGURE 1
(A) Trajectories of BARREL payloads, RBSP, THEMIS and GOES satellites in the *L*-MLT map (IGRF model) during 18:30–20:30 UT. The circle, cross, asterisk, and diamond symbols indicate the start point of THEMIS, BARREL, RBSP and GOES. Satellites and payloads that observed the similar features of fluctuation are highlighted in the black box. The observations from the solar wind, magnetospheric spacecraft and BARREL payloads are shown in Panels **(B–G)**. **(B)** Total magnetic field (black), Bx (blue), By (green), and Bz component (red) of the interplanetary magnetic field in GSM coordinates and **(C)** solar wind dynamic pressure obtained from OMNI database (a compilation of records made on ACE, WIND, and IMP-8 spacecraft that were time-shifted to the Earth's bow shock subsolar point); **(D)** Sym-H (black) and AL indices (red) showing a substorm onset at ~18:30 UT; **(E)** Total magnetic field measured by RBSP-B; **(F)** Total magnetic field strength measured by GOES-13 (cyan) and 15 (black); **(G)** Total magnetic field measured by THEMIS D (orange) and E (red); **(H)** 25–180 keV X-ray count rate (smoothed over 0.5 s) measured by BARREL 1A (blue), 1H (black), 1I (magenta), 1Q (red), 1T (cyan) and 1U (green); **(I)** Percent variation (over 60 min smoothed background) of the magnetic field observed by THEMIS-D (orange), THEMIS-E (red), GOES-13 (cyan) and GOES-15 (black) relative to their 60 min smoothed data.

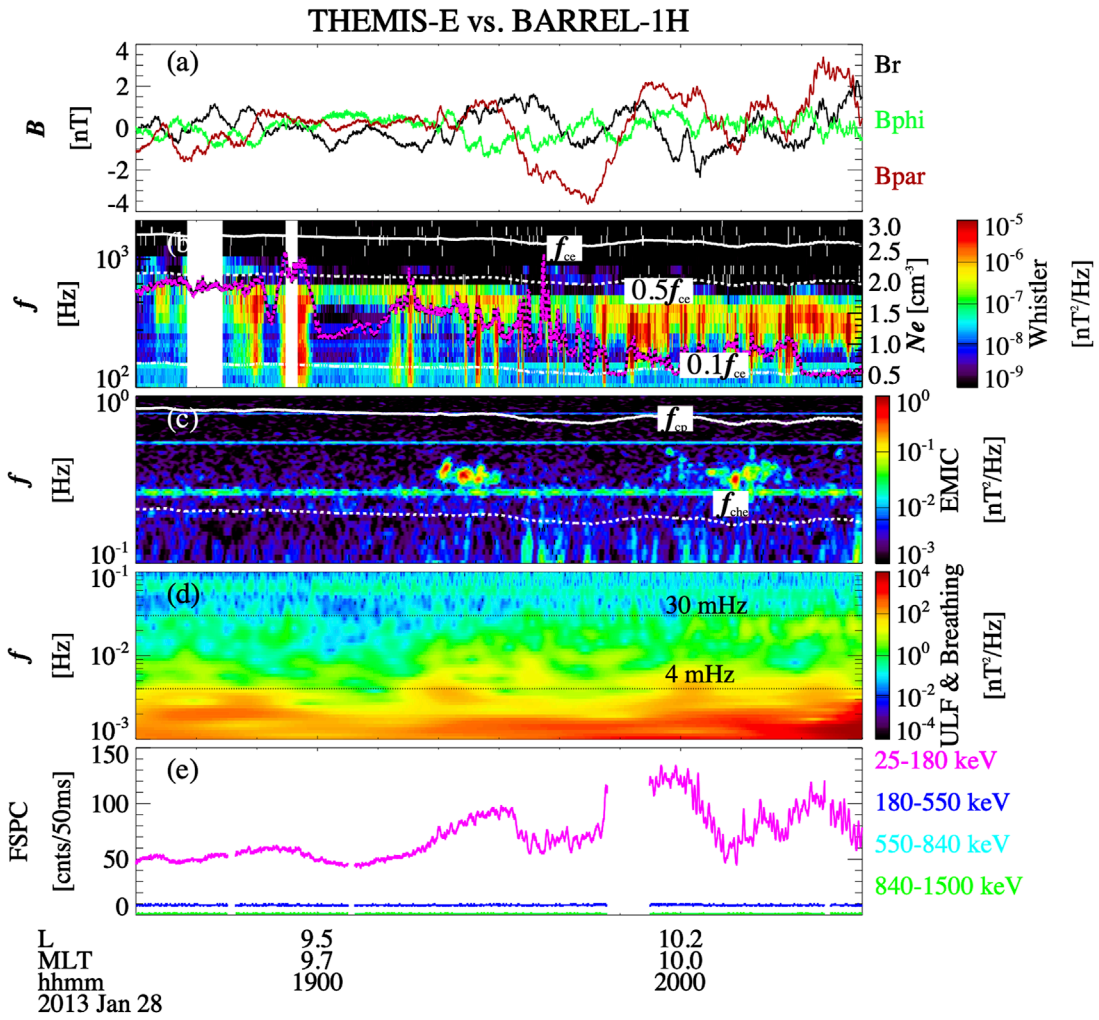

FIGURE 2
(A) Three components of the magnetic field in field-aligned coordinates (black: radial component, green: azimuthal component, red: compressional component) detrended over 60 min. **(B)** Magnetic spectral density observed by the Search Coil Magnetometer (SCM) onboard THEMIS-E. The white lines in panel **(B)** represent the electron cyclotron frequency (f_{ce}), 0.5 f_{ce} and 0.1 f_{ce} from top to bottom. The superimposed magenta line is the total electron density obtained from the spacecraft potential. **(C)** Magnetic spectral density calculated from the fluxgate magnetometer (FGM) onboard THEMIS-E. The white lines in panel **(C)** indicate proton, helium, and oxygen cyclotron frequencies. **(D)** Wavelet analysis of the magnetometer measurements, where the 4 and 30 mHz frequencies are shown as the two black dotted lines. **(E)** BARREL 1H fast spectrum X-rays at energies of 25–180 (pink), 180–550 (blue), 550–840 (cyan), and 840–1,500 keV (green).

can modulate electron precipitation mainly in three ways. 1) ULF waves/breathing mode oscillations can modulate the EMIC wave and whistler-mode wave growth rate. Breneman et al. (2015) showed that 1–10 min ULF modulations of X-rays generated by electron precipitation on a Balloon Array for Radiation-belt Relativistic Electron Losses (BARREL) balloon (Millan et al., 2013; Woodger et al., 2015) were nearly identical to modulations in whistler-mode hiss amplitude observed by the Van Allen Probes (RBSP, Mauk et al., 2013) during a close magnetic conjunction. Breneman et al. (2020) reported large-scale electron precipitation observed as X-rays on BARREL. Their analysis suggested that hiss waves modulated by forced-breathing mode magnetic field fluctuations are directly responsible for the observed loss. 2) ULF waves/breathing mode oscillations could modulate the resonance condition and thus cause an increase/decrease of the resonant energy with electrons by modulating the ambient magnetic field or total electron density. Zhang et al. (2019) investigated the mechanism of electron precipitation through quasi-linear pitch angle scattering by EMIC waves when simultaneous ULF waves exist. It was shown that the ULF wave fluctuations could lead to a significant decrease in the minimum resonant energy when the magnetic field diminishes. 3) ULF waves can cause electron precipitation by modulating the size of the bounce loss cone (BLC) (Rae et al., 2018) and electron pitch angles (Brito et al., 2012; Brito et al., 2015; Yin et al., 2023). Brito et al. (2012); Brito et al. (2015) used MHD simulations to show that when electrons encounter compressional magnetic field oscillations, their trajectories move closer to the Earth into a stronger magnetic field with shorter field lines where the loss cone is larger, leading to enhanced precipitation. However, due to a lack of equatorial

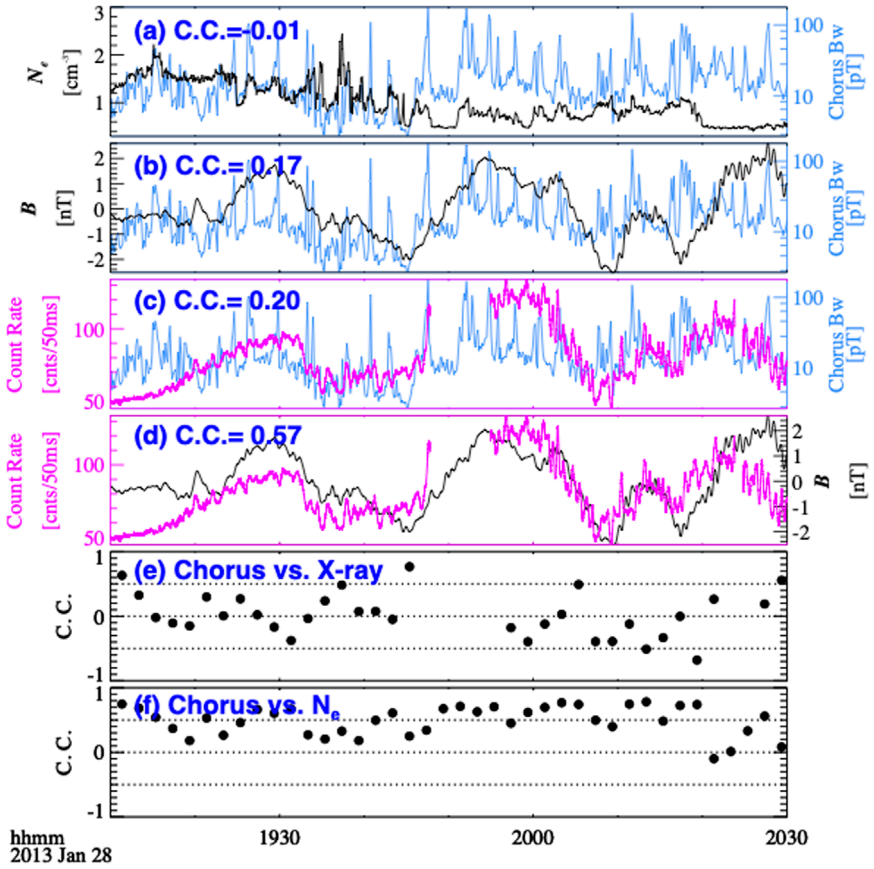

FIGURE 3
(A) Total electron density (black) obtained from spacecraft potential and chorus wave amplitude (blue) observed by THEMIS-E. **(B)** Ambient magnetic field fluctuations (0.5–30 mHz, black) and chorus wave amplitude (blue) observed by THEMIS-E with the time resolution of 4 s and 8 s, respectively. **(C)** Fast spectrum X-ray count rate (25–180 keV) from BARREL smoothed over 0.5 s (magenta) and chorus wave amplitude (blue). **(D)** Fast spectrum X-ray count rate (25–180 keV) from BARREL smoothed over 0.5 s (magenta) and ambient magnetic field fluctuations (0.5–30 mHz, black). Correlation coefficient between **(E)** chorus wave amplitude and X-ray count rate and **(F)** chorus wave amplitude and electron density. Correlation coefficients in panels **(A–D)** are calculated over the entire time window (19:10–20:30), while in panels **(E–F)**, the correlation coefficients are calculated within a 4-min box with a time-shifted window of 2 min.

wave observations and direct comparison between observed and simulated electron precipitation features, it remains unclear whether ULF waves were fully responsible for the electron precipitation or act as a minor role in modulating electron precipitation. ULF waves/breathing mode oscillations could also modulate the BLC by modulating the ambient magnetic field (Rae et al., 2018). Although the direct modulation of the BLC by ULF waves/quasi-static breathing mode only influences electrons near the loss cone, it could potentially enhance the modulation of precipitation during the presence of EMIC/whistler-mode waves due to pitch angle scattering. However, in Rae et al. (2018), there are no means to test other precipitation sources, such as pitch angle scattering by whistler-mode waves, due to the lack of conjugated high frequency wave measurement near the equatorial plane.

In this paper, we primarily use observations from BARREL-1H (Millan et al., 2013) and THEMIS-E (Angelopoulos, 2008), which were in close conjunction, to separately evaluate the effect of whistler-mode chorus wave amplitude, loss cone size and the resonant energy (between plasma waves and electrons) in modulating energetic electron precipitation in the Earth's magnetosphere. We also augment our observations with other equatorial satellite magnetometer data from THEMIS-D, RBSP-A, B and GOES-13, 15 (Singer et al., 1996), as well as the observations of X-rays generated by electron precipitation from other BARREL payloads (BARREL 1A, 1I, 1Q, 1T and 1U). The BARREL payloads drift slowly in space, enabling the investigation of temporal evolution features of electron precipitation. The THEMIS spacecraft were operating in near-equatorial orbits to measure waves and plasma parameters.

The content of the paper is outlined as follows. In Section 2, an overview of the event and detailed correlation between the measured chorus emissions, BARREL X-rays and quasi-static breathing mode fluctuations are presented. In Section 3, through a physics-based technique based on the quasi-linear theory, we quantify the role of background magnetic field in modulating the chorus-driven electron precipitation by turning on and off the background quasi-static magnetic field fluctuations respectively and compare the time evolution of the modeled electron precipitation with the observed modulated X-rays. In Section 4, we discuss the potential

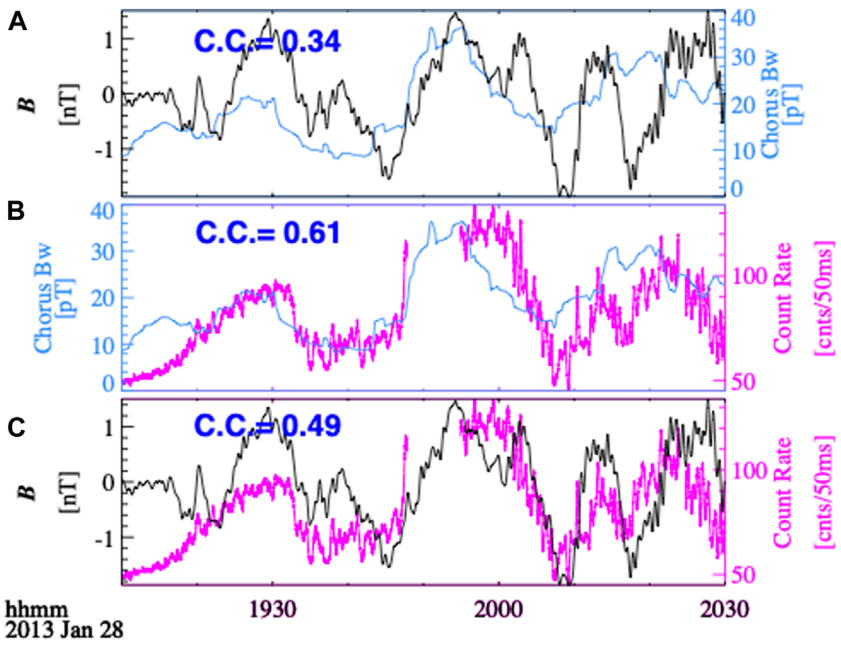

FIGURE 4
(A) Ambient magnetic field fluctuations (0.5–30 mHz, black) and chorus wave amplitude smoothed over 8 min (blue) observed by THEMIS-E with the time resolution of 4 s and 8 s, respectively. **(B)** Fast spectrum X-ray count rate (25–180 keV) from BARREL smoothed over 0.5 s (magenta) and chorus wave amplitude smoothed over 8 min (blue). **(C)** Fast spectrum X-ray count rate (25–180 keV) from BARREL smoothed over 0.5 s (magenta) and ambient magnetic field fluctuations (0.5–30 mHz, black).

roles of loss cone change and the shift of resonant energy in modulating the energetic electron precipitation. The conclusions are summarized in Section 5.

2 Observation

2.1 Event overview

Figure 1A shows the trajectories of the available equatorial satellites (THEMIS-D, E; RBSP-B and GOES-13, 15) and BARREL payloads (BARREL 1A, 1H, 1I, 1Q, 1T and 1U) in the *L*-MLT map (determined using the IGRF magnetic field model) over 18:30 UT—20:30 UT on 28 January 2013. Figures 1B–D show solar wind and geomagnetic conditions, indicating little change in the interplanetary magnetic field and the solar wind dynamic pressure, as well as a modest substorm activity at around 18:30 UT. Figures 1F, G show the fluxgate magnetometer data from GOES and THEMIS. During this event, GOES-15 and GOES-13 were located in the pre-noon and post-noon sectors respectively (Figure 1A), providing observations of magnetic field at geosynchronous orbit with 0.512 s time resolution. THEMIS-D and THEMIS-E were located in the pre-noon sector outside the geosynchronous orbit. Following the substorm onset (18:30 UT), similar magnetic field modulations (correlation coefficient >0.5) on a timescale of ~10 s of minutes (forced-breathing mode) were observed by GOES-15, THEMIS-D, and THEMIS-E. Such low frequency magnetospheric oscillations are often related to solar wind pressure variations (Kepko et al., 2002; Kepko and Spence, 2003). In this event, frequency analysis (not shown) suggests that source of the forced-breathing mode magnetic oscillations lies in the solar wind speed (OMNI database, propagated from measurements at the Lagrange-1 point by either ACE or Wind satellite to the Earth's bow shock nose). GOES-13, which was located near post-noon, however, shows a different modulation in the background magnetic field (Figure 1F).

Observations from the full BARREL array are shown in the 25–180 keV X-ray fast spectrum smoothed over 0.5 s (Millan et al., 2013; Woodger et al., 2015) in Figure 1H. Similar modulations were observed on BARREL 1H and 1Q, which were located in the prenoon sector. The count rate level of X-rays was higher for BARREL 1H (L ~ 8) than 1Q (L ~ 5), which might be either caused by the different trapped flux levels at different L shells or the location of the plasmapause. Enhancements were not observed on BARREL-1A, 1I, 1T and 1U, which were located in the afternoon sector. Those satellites and payloads with similar fluctuations (correlation coefficient >0.5) are highlighted in the black boxes in Figure 1A. The spatial scale with the similar modulation timescale is large, with MLT spanning from ~9 to 12 and L shell from 5 to 11. It was also shown that moderate changes in the ambient magnetic field can cause a significant change in the BLC (Rae et al., 2018), the plasma wave growth rate and the resonance condition between waves and energetic electrons (Zhang et al., 2019). In this case, the relative change (relative to the 60 min smoothed data) of the magnetic field on THEMIS-D and E reached up to around 10% (Figure 1I). Our results indicate a potential link between the low frequency magnetic field fluctuations and the electron precipitation observed through BARREL X-rays.

To explore the large-scale background magnetic field fluctuations in modulating the electron precipitation, we analyze the observations from BARREL-1H and THEMIS-E which were in closer conjunction (Figure 2). Figure 2A shows three components of the magnetic field in the field-aligned coordinates observed by THEMIS-E fluxgate magnetometers (FGM) (Auster et al., 2008), which were detrended over 60 min to show the ULF/quasi-static forced breathing mode variations. It is shown that the compressional component (red line) has a similar fluctuation to the BARREL X-rays shown in Figure 2E. Figure 2B shows the magnetic spectral density observed by the Search Coil Magnetometer (SCM) (Roux et al., 2008), which detects low-frequency magnetic field fluctuations and waves in three directions over a frequency bandwidth up to ~8 kHz. The superimposed magenta line represents total electron density inferred from the spacecraft potential (Pedersen et al., 2008) measured by the Electric Field Instrument (EFI) (Bonnell et al., 2008). The lower-band chorus wave was also observed by THEMIS-E and the wave intensity was positively correlated with the total electron density, with the lower cutoff frequency of waves extending down to a lower value with a higher density. The density modulation can lead to modulation of chorus wave growth through modulating the fraction of resonant electrons (Li et al., 2011a) or through wave trapping by density crests or troughs (Chen et al., 2012; Liu et al., 2021). Figure 2C shows the magnetic spectral density calculated from the low frequency fluctuations (up to 64 Hz) of the background magnetic field measured by the FGM instrument, using fast Fourier transform method with a window size of 256 s and a shifted time window by 32 s. EMIC waves were also detected during this event. However, the enhancement in X-rays were only observed in the lowest energy channel (25–180 keV). EMIC waves, which are known to interact with high-energy electrons (>~ a few hundred keV; Capannolo et al., 2019a; Capannolo et al., 2019b; Grach et al., 2022) and would lead to enhanced X-ray count rates in higher energy channels (Li et al., 2014), are unlikely to play a major role during this precipitation event. Figure 2D shows the Morlet mother wavelet analysis of the FGM measurement. The horizontal lines in panel (d) indicate frequencies of 4 and 30 mHz. ULF waves between 4 mHz and 30 mHz were relatively weak, while the quasi-static forced breathing mode, with wave frequency lower than 4 mHz, was stronger. The forced breathing mode of the magnetosphere was associated with the enhancement of the 25–180 keV BARREL X-rays with a similar fluctuation, as shown in Figure 2E.

2.2 Modulation of waves and electron precipitation

In order to examine the correlation between the observed electron precipitation and the chorus waves or ambient magnetic field oscillations, we show the correlation coefficients (C. C.) between them in Figure 3. During this period, chorus waves were observed outside the plasmasphere, as shown in Figure 2B. The blue line in Figure 3A shows chorus wave amplitude (8-s time resolution, blue line) observed by THEMIS-E, which was calculated by integrating the wave intensity over the frequency range from 100 to 1,000 Hz. The black line in Figure 3A shows the total electron density inferred from the spacecraft potential. It shows that the chorus wave intensity has similar fluctuations with the local electron density on a timescale of approximately 1 minute. However, when considering a longer time scale (10 s of minutes), the fluctuations of chorus waves and electron density are quite different. This is evident in the correlation coefficient over the entire time window (19:10–20:30), which is close to 0 (Figure 3A). To analyze the correlation on a shorter timescale, Figure 3F presents the calculation of the correlation coefficient within a 4-min box with a time-shifted window of 2 min. Figure 3F shows that the chorus wave intensity is highly correlated (>0.5 at most times) with the local electron density, further supporting that the chorus waves are modulated by local density. Figure 3B shows the amplitudes of chorus waves (blue line) and the compressional component of the ambient magnetic field oscillations (0.5–30 mHz, 4-s time resolution, black line), with a low correlation coefficient only about 0.17. Figure 3C shows the X-ray count rate (black line) and the chorus wave amplitude (blue line), also with a low correlation of about 0.20. Similarly, we calculate the short-time scale correlation, which is shown in Figure 3E and further demonstrates the overall low correlation (C. C. < 0.5 at most times). Figure 3D shows the compressional component of the ambient magnetic field oscillations (black line) and the X-ray count rate (magenta line), with a correlation coefficient ~0.57, much higher than that between X-ray count rate and chorus wave amplitude. This indicates that the breathing mode fluctuations observed by THEMIS-E is highly correlated with the enhancement in X-rays. Combining with the fact that a similar modulation (C. C. > 0.5) was also observed by BARREL-1Q and GOES-15 (Figure 1A), we conclude that the quasi-static breathing mode may have played a significant role in modulating the electron precipitation. Previous studies show high correlation between chorus waves and ASI auroral intensity when the electron precipitation is driven by chorus waves (Nishimura et al., 2011; Hosokawa et al., 2020). In those work, the observations were specifically chosen at latitudes with the highest correlation (corresponding to highest correlation L shell), within a narrow window of a few minutes. In this case, however, the correlation is calculated on a point-to-point basis, rather than the point-to-plane comparison (Nishimura et al., 2011; Hosokawa et al., 2020). The low correlation between chorus wave amplitude and X-ray count rate (Figure 3E) might be due to the spatial difference of THEMIS-E and BARREL-1H, which were at rough conjugate locations with a separation in L shell of ~1.5–2.5. This is much larger than the coherent scale size of the chorus elements, which is about hundreds to thousands of kilometers (Agapitov et al., 2017; Shen et al., 2019), thus the electron precipitation is not expected to have one-to-one correspondence with the chorus wave elements.

The chorus wave intensity is not only shown to be correlated (at times) with the local electron density (Figure 3F), but also tends to increase (decrease) when the ambient background magnetic field increases (decreases). The ambient magnetic field oscillations can modulate the whistler mode growth rate by modulating the magnetic field inhomogeneity (Zhou et al., 2015) and the radial transport of resonant electron populations (Brenaman et al., 2020). To smooth out the modulation in association with local plasma density, whistler-mode chorus wave amplitude is smoothed over 8 min to evaluate the temporal modulation on forced-breathing time scale. The results are shown in Figure 4, which is similar to Figure 3 except that chorus wave amplitude is smoothed over 8 min. The analysis reveals that there is a notable increase in the correlation coefficient between chorus wave intensity (smoothed

over 8-min) and the amplitude of the ambient magnetic field fluctuations (Figure 4A), reaching 0.39. This value is higher when compared to the correlation coefficient of 0.17 for unsmoothed chorus wave amplitude in Figure 3B. Additionally, the correlation coefficient between the smoothed chorus wave amplitude and X-ray count rate (Figure 4B) increased to 0.61. This value is much higher compared to the unsmoothed case in Figure 3C (C. C. ~ 0.2) and comparable to the correlation coefficient between the ambient magnetic field fluctuations and X-ray count rate (Figure 4C). These findings suggest that the overall temporal evolution of chorus wave amplitude is also modulated by quasi-static breathing mode oscillations of the ambient magnetic field, which can further modulate the X-ray count rate generated by electron precipitation. Since the magnetic field oscillations can also modulate electron precipitation through modulating resonance condition and the loss cone size, the correlation analysis itself cannot determine the main driver of the electron precipitation modulation. To further examine the role of each mechanism, a further physics-based modeling is performed in Section 3 and Section 4.

3 Comparison between observations and simulations

Figure 5A shows the modulation in equatorial bounce loss cone (blue) due to large amplitude magnetic field oscillations (black). The equatorial bounce loss cone α_{LC} is defined as the maximum pitch angle of particles at the equatorial plane that have a mirror point below 100 km altitude in the atmosphere ($sin^2\,\alpha_{LC} = B_0/B_m$, where B_0 is the equatorial magnetic field and B_m is the magnetic field at 100 km altitude). Since the variation in B_m is only a small fraction of B_m as compared to B_0, we assume that the variation in α_{LC} is mainly caused by modulation in B_0 with very little loss in accuracy (Rae et al., 2018). Magnetic field strength of B_m was calculated by mapping the THEMIS-E position to the foot point at 100 km using the IGRF magnetic field model. The ratio of the corresponding background magnetic field and loss cone size under the two circumstances are shown in Figure 5G, where the black line represents magnetic field and the blue line is for the equatorial loss cone size. When B_0 increases, the equatorial loss cone size also increases, which allows more particles to be precipitated. It is shown that there is an up to 8% variation in loss cone size caused by ambient magnetic field fluctuations.

The pitch angle scattering rates driven by chorus waves are quantified using a physics-based approach with the Full Diffusion Code to calculate the quasi-linear diffusion coefficients (Ni et al., 2008). Landau resonance and multiple cyclotron harmonic resonances (−10 to 10) are considered. It is assumed that chorus wave normal angles are quasi-parallel to the magnetic field line near the equatorial plane and increase as magnetic latitudes increase (Ni et al., 2013). Total electron density is derived from the spacecraft potential measured by THEMIS-E and assumed to be constant along the field lines. With the diffusion coefficient $< D_{\alpha\alpha}>_{LC}$ and the electron flux near the equatorial loss cone α_{LC}, we then determine the equatorial pitch angle distribution of electrons inside the loss cone using the solution for the Fokker-Planck equation under the quasi-equilibrium state (Kennel and Petschek, 1966; Li et al., 2011b; Ma et al., 2020; Ma et al., 2021), which can be estimated as:

$$J_{in}\left(\alpha_{eq,in},E\right) = \frac{S(E)}{D^*}\left\{\frac{I_0\left(\frac{\alpha_{eq,in}}{\alpha_{LC}}z_0\right)}{z_0 I_1(z_0)}\right\} \quad (1)$$

where $I_0\,and\,I_1$ are the modified Bessel functions; $S(E)$ is the rate that the particles enter the loss cone, which is calculated based on the electron flux measured by solid state telescope (SST) onboard THEMIS-E at the lowest pitch angle bin (11.25°); $D^* \approx < D_{aa} >_{LC} \times cos\left(\alpha_{LC}\right)$ and $z_0 = \frac{\alpha_{LC}}{\sqrt{D^*\tau}}$, where τ is a quarter of the electron bounce period. The integral electron flux inside the loss cone is further calculated as:

$$J_{integral}(E) = \int_0^{\alpha_{LC}} J_{in}\left(\alpha_{eq,in},E\right) \bullet sin\,\alpha \bullet d\alpha \quad (2)$$

In order to evaluate the effects of ambient magnetic field oscillations in electron precipitation through modulating the resonance condition and loss cone size, we perform simulations by turning on ("modulated") and turning off ("smoothed") the background ambient magnetic field fluctuations in the Full Diffusion Code and in calculating the resultant integral electron precipitation inside the loss cone using Eqs 1, 2. In the "modulated" case, the modulation of chorus wave amplitude and modulation of the resonant energy are included to calculate the diffusion coefficients with the Full Diffusion Code (Figure 5B) and the modulation of the loss cone size is further included to calculate the resultant electron precipitation using Eqs 1, 2 (Figure 5C). In the "smoothed" case, only the modulation of the chorus wave amplitude is included to calculate the diffusion coefficients (Figure 5E) and the electron precipitation (Figure 5F). The ratios of them are shown in the right panels (g-i).

The diffusion coefficients at the loss cone $< D_{\alpha\alpha}>_{LC}$ corresponding to these two circumstances are shown in Figure 5B (Modulated) and 5e (Smoothed). The superimposed black lines are BARREL X-ray counts at 25–180 keV. Figure 5H is the ratio between them. When background magnetic field increases, chorus waves tend to interact with higher energy electrons more efficiently, leading to a higher ratio in $<D_{\alpha\alpha}>_{LC}$ (modulated/smoothed) at higher energies and a lower ratio at lower energies. Above 30 keV, breathing mode can decrease the diffusion coefficient to half at minimum B_0 and increase the diffusion coefficient by 50% at maximum B_0. The modulations of $<D_{\alpha\alpha}>_{LC}$ caused by chorus wave amplitude variations are more noticeable than the difference of $<D_{\alpha\alpha}>_{LC}$ caused by the modulation of resonant condition (mainly due to the modulation of background magnetic field), as shown in Figures 5B, E. This indicates that the temporal modulation of the chorus wave amplitude dominates the fluctuations in electron precipitation.

Figures 5C, F show the integral precipitating flux under the two circumstances and Figure 5I is the ratio between them. It was shown that the integral precipitating flux is similar for the two circumstances when the background magnetic field fluctuation is turned on (Figure 5C) and turned off (Figure 5F). The ratio in Figure 5I further shows that the precipitating fluxes at higher energy (>~100 keV) are significantly modulated. The modeled precipitation can increase by 1.5–3 times as magnetic field varies from the minimum to maximum value when we turn on the

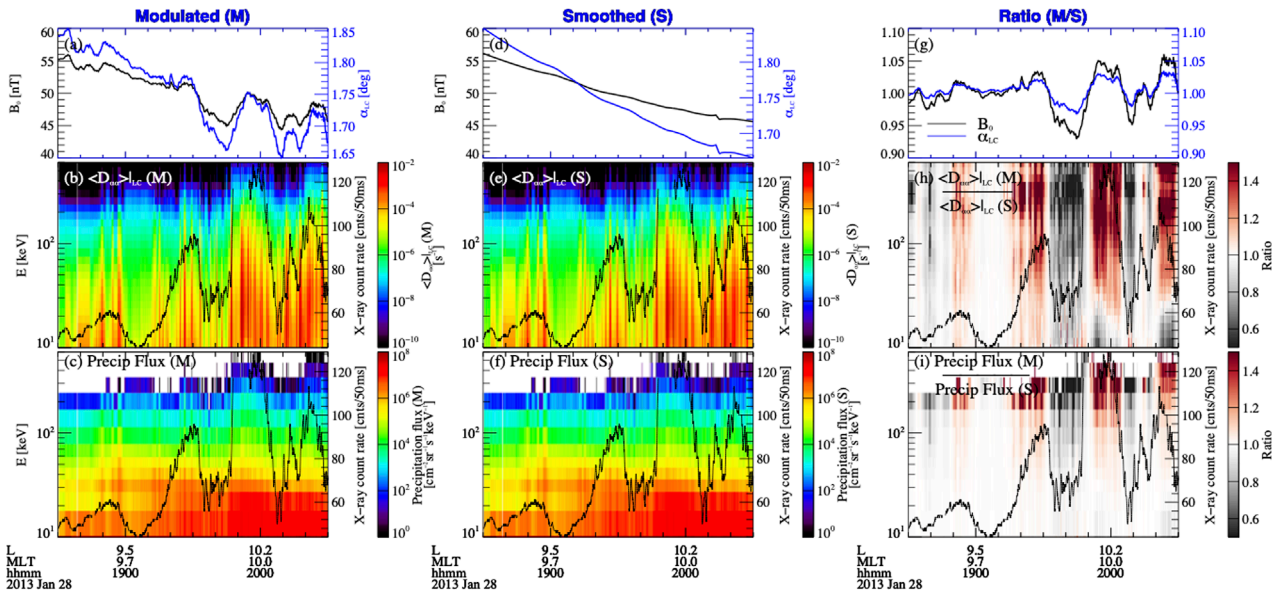

FIGURE 5
Analysis of electron precipitation due to chorus waves when the quasi-static breathing mode magnetic field modulation is considered **(A–C)** and excluded **(D–F)**. **(A)** Measured ambient magnetic field strength and the corresponding bounce loss cone size calculated from the IGRF model; **(B)** Bounce-averaged pitch angle diffusion coefficients at the loss cone as a function of time and electron energy; **(C)** Model calculated electron precipitation at the equilibrium state from the quasi-linear theory as a function of time and electron energy. **(D, E)** Same format as panels **(A–C)** but with the quasi-static breathing mode turned off (Smoothed). Right panels **(G–I)** show the ratio between the left panels and the middle panels. The superimposed black lines in the bottom two rows represent fast spectrum X-ray count rate (25–180 keV) observed by BARREL.

breathing mode fluctuation. This result indicates that although the temporal modulation of the chorus wave amplitude dominates the fluctuations in electron precipitation, the effects of the modulation of resonance condition through modulating the background magnetic field cannot be neglected.

4 Discussion

In this work, we evaluate the role of large-scale forced-breathing mode magnetic field oscillations in modulating the electron precipitation. Although the ambient magnetic field oscillations alone only affect the small electron population near the loss cone, they can play an important role in modulating the electron precipitation ratio with the presence of chorus waves, through modulating the chorus wave amplitude, the resonance condition and the loss cone size.

ULF waves/forced-breathing mode magnetic field fluctuations can modulate the electron precipitation through modulating chorus wave growth rate (e.g., Li et al., 2011a; Breneman et al., 2015; Jaynes et al., 2015; Xia et al., 2016; Qin et al., 2021). In our study, the whistler-mode chorus wave amplitude is modulated by both magnetic field fluctuations (Figure 4A) and local electron density (Figure 3F). The correlation coefficient between chorus wave amplitude (8 s time resolution without smoothing) and the electron precipitation is low (0.22). This is because the separation in L shell between chorus wave and electron precipitation is ~1.5–2.5, much larger than the coherent scale size of the chorus elements, which is about hundreds to thousands of kilometers (Agapitov et al., 2017; Shen et al., 2019). Therefore, the electron precipitation is not expected to have one-to-one correspondence with the chorus wave elements. The smoothed chorus wave amplitude, which shows the averaged properties of a group of chorus wave elements, however, exhibits a higher correlation (0.62) with X-ray count rate (Figure 4B). This suggests that the magnetic field oscillations could modulate the electron precipitation through modulating the whistler-mode chorus wave amplitude. The maximum value of the smoothed chorus wave amplitude is about 4 times larger than the minimum value, which can lead to a significant modulation (16 times) in the electron precipitation. Unfortunately, chorus wave intensity measured at the exactly same location as BARREL was not available, and thus the accurate role of the modulation of chorus wave intensity in modulating the energetic electron precipitation is difficult to quantify.

ULF waves/forced-breathing mode magnetic field fluctuations can also modulate the electron precipitation through modulating the resonance condition and the loss cone size. On one hand, the minimum energy of electrons to interact with chorus waves depends on the background magnetic field strength (Li et al., 2011a). It was shown that the minimum resonant energy increases when the magnetic field increases. On the other hand, chorus waves can move electrons toward pitch angles near the loss cone through cyclotron resonance. The quasi-static breathing mode magnetic field oscillations can then take over and enhance (reduce) the precipitation by increasing (decreasing) the loss cone size, as suggested by Rae et al. (2018). In our case, we show that magnetic field fluctuations could affect the resonant energy and the pitch angle diffusion rate (Figure 5). When the magnetic field increases (decreases), the minimum energy for electrons to be in resonance with chorus waves increases (decreases, approximately ~10%). For electrons above 30 keV, the diffusion coefficients at the loss cone

10.3389/fspas.2024.1253668

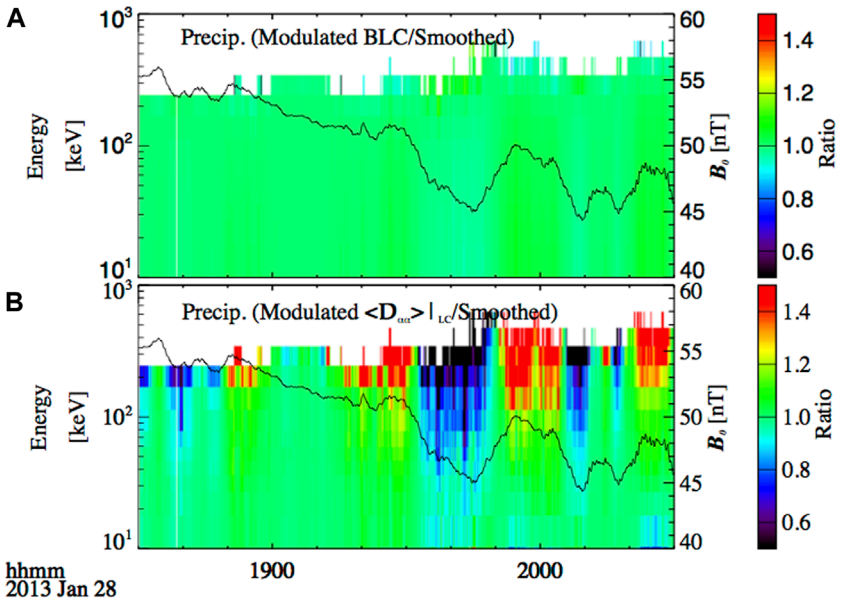

FIGURE 6
(A) Ratio of the calculated precipitating electron flux inside the loss cone with quasi-static breathing mode modulation of the equatorial loss cone size (Modulated BLC) to the precipitating flux without quasi-static breathing mode modulation (Smoothed). **(B)** Ratio of the calculated precipitating electron flux inside the loss cone with quasi-static breathing mode modulation of $<D_{\alpha\alpha}>_{LC}$ to the precipitating flux without quasi-static breathing mode modulation (Smoothed). The superimposed black lines represent the background magnetic field strength observed by THEMIS-E.

increase by up to ~1.5 times when the magnetic field increases by 5%. Correspondingly, the diffusion coefficients for electrons with energy below 30 keV show an anti-correlation with the magnetic field oscillations. Since BARREL X-rays are only sensitive to electrons with energy approximately above 30 keV, the X-ray count rate is expected to increase when the background magnetic field increases.

In order to separate the effect of bounce loss cone size modulation and the effect of diffusion coefficient modulation on the precipitating flux, we further compare the simulation results corresponding to three cases: 1) in the "smoothed" case, only the modulation of the chorus wave amplitude is included to calculate the diffusion coefficient and electron precipitation; 2) in the case of "modulated loss cone," the modulation of the chorus wave amplitude is included to calculate the diffusion coefficient and the modulation of loss cone is further included to calculate the electron precipitation (the modulation of resonant energy is not included to calculate the diffusion coefficient and the resultant integral electron precipitation inside the loss cone); 3) in the case of "modulated diffusion coefficient", both modulation of the chorus wave amplitude and modulation of the resonant energy are included to calculate the diffusion coefficient. Variation of loss cone size is not included when calculating the resultant electron precipitation using Eqs 1, 2. We calculate the ratio of the modeled precipitating flux with modulation of the equatorial loss cone size ("Modulated α_{LC}") to the precipitating flux without ambient magnetic field modulation ("Smoothed") (Figure 6A), as well as the ratio of the precipitating flux with modulated $< D_{\alpha\alpha}>_{LC}$ to the precipitating flux without modulation in $<D_{\alpha\alpha}>_{LC}$ ("Smoothed") (Figure 6B). Rae et al. (2018) showed that the percent change in precipitating flux driven by the change in the equatorial loss cone depends significantly on electron pitch angle distribution close to the loss cone. In our case, it is shown that when there is only bounce loss cone modulation (Figure 6A), the precipitating flux increases (decreases) about 10% when magnetic field increases (decreases) by 10% for electrons with a broad range of energy (10–300 keV). However, for higher energy electrons, the precipitating flux shows an opposite trend, i.e., increases when α_{LC} decreases. This is caused by the competing effects of the loss cone size and averaged flux inside the loss cone. When loss cone size increases, it is harder for these higher energy electrons to form a filled loss cone under the equilibrium between pitch angle scattering and precipitation into the atmosphere, and the averaged flux inside the loss cone is smaller, leading to a lower value of total integrated precipitation. When there is only modulation in $<D_{\alpha\alpha}>_{LC}$ (Figure 6B), the change in electron precipitation ratio also depends on their energies, increasing (decreasing) by up to about 20% for electrons with energy at 30 keV and about 50% for ~100 keV electrons when B_0 increases (decreases). We conclude that the magnetic field oscillation-driven modulation in $<D_{\alpha\alpha}>_{LC}$, i.e., the resonance condition in precipitating rates, are larger than the effects of modulation in loss cone size by the ambient magnetic field oscillations.

5 Summary

We present simultaneous multi-point observations of whistler-mode chorus waves and magnetospheric oscillations on a time scale of ~10 s min, associated with concurrent energetic electron precipitation observed through enhanced BARREL X-rays. Similar fluctuations on a time scale of ~10 s min are observed in X-ray signatures and the compressional component of magnetic field

oscillations. The spatial scale of oscillations spans from ~9 to 12 h in MLT and from 5 to 11 in *L* shell. Such large-scale magnetic field oscillations, which have been suggested to play a potential role in precipitating energetic electrons by either wave amplitude, resonance energy or loss cone modulation, show high correlations with enhancement in X-rays.

We evaluate the relative role of breathing mode magnetic field oscillations in modulating the electron precipitation through modulating the minimum resonant energy, the loss cone size and the chorus wave amplitude. We show that the modulation in energetic electron precipitation is dominated by the modulation of chorus wave amplitude. However, the effects of modulation in the resonance condition due to breathing mode magnetic field oscillations cannot be neglected. The ambient magnetic field oscillation could significantly modulate the electron precipitation observed through BARREL X-ray (25–180 keV), increasing the precipitating flux by 50% when magnetic field increases by 5% by modulating the resonance condition. The modulation in the loss cone size has a much smaller effect on the electron precipitation modulation, increasing the precipitating flux by 10% when the ambient magnetic field increases by 5%.

The study examines the relative role of different mechanisms that could be responsible for the electron precipitation modulated on ULF timescales or a longer period, which is important for understanding the radiation belt electron loss. Nevertheless, multi-case or statistical studies are needed in the future to systematically evaluate the relative roles of various mechanisms in different events and regions.

Data availability statement

The original contributions presented in the study are included in the article/supplementary material, further inquiries can be directed to the corresponding authors.

Author contributions

MQ: Writing–original draft. WL: Supervision, Writing–review and editing. Qianli Ma: Methodology, Writing–review and editing. X-CS: Writing–review and editing. LW: Data curation, Writing–review and editing. RM: Writing–review and editing. VA: Data curation, Writing–review and editing.

Funding

The author(s) declare that financial support was received for the research, authorship, and/or publication of this article. NASA grants of 80NSSC20K0698, 80NSSC19K0845, 80NSSC20K0196, 80NSSC21K1312, and the NSF grant of AGS-1847818.

Acknowledgments

WL, QM, and X-CS would like to acknowledge NASA grants of 80NSSC20K0698, 80NSSC19K0845, 80NSSC20K0196, 80NSSC21K1312, and the NSF grant of AGS-1847818. We acknowledge the BARREL team developers of IDL BDAS program for use of BARREL data. We thank the NOAA National Geophysical Data Center for GOES data. We acknowledge VA for use of data from the THEMIS mission. We also acknowledge, specifically, C.W. Carlson and J. P. McFadden for use of ESA data; K.H. Glassmeier, U. Auster, and W. Baumjohann for the use of FGM data provided under the lead of the Technical University of Braunschweig. The content of this manuscript has been presented in part at EGU22, the 24th EGU General Assembly. Citation: MQ, WL, QM, X-CS: Global magnetic field oscillations on the breathing-mode timescale and their effects on energetic electron precipitation, EGU General Assembly 2022, Vienna, Austria, 23–27 May 2022, EGU22-4057, https://doi.org/10.5194/egusphere-egu22-4057, 2022.

Conflict of interest

The authors declare that the research was conducted in the absence of any commercial or financial relationships that could be construed as a potential conflict of interest.

Publisher's note

All claims expressed in this article are solely those of the authors and do not necessarily represent those of their affiliated organizations, or those of the publisher, the editors and the reviewers. Any product that may be evaluated in this article, or claim that may be made by its manufacturer, is not guaranteed or endorsed by the publisher.

References

Agapitov, O., Blum, L. W., Mozer, F. S., Bonnell, J. W., and Wygant, J. (2017). Chorus whistler wave source scales as determined from multipoint Van Allen Probe measurements. *Geophys. Res. Lett.* 44, 2634–2642. doi:10.1002/2017GL072701

Angelopoulos, V. (2008). The THEMIS mission. *Space Sci. Rev.* 141, 5–34. doi:10.1007/s11214-008-9336-1

Auster, H. U., Glassmeier, K. H., Magnes, W., Aydogar, O., Baumjohann, W., Constantinescu, D., et al. (2008). The THEMIS fluxgate magnetometer. *Space Sci. Rev.* 141, 235–264. doi:10.1007/s11214-008-9365-9

Bonnell, J. W., Mozer, F. S., Delory, G. T., Hull, A. J., Ergun, R. E., Cully, C. M., et al. (2008). The electric field instrument (EFI) for THEMIS. *Space Sci. Rev.* 141, 303–341. doi:10.1007/s11214-008-9469-2

Breneman, A. W., Halford, A., Millan, R., McCarthy, M., Fennell, J., Sample, J., et al. (2015). Global-scale coherence modulation of radiation-belt electron loss from plasmaspheric hiss. *Nature* 523 (7559), 193–195. doi:10.1038/nature14515

Breneman, A. W., Halford, A. J., Millan, R. M., Woodger, L. A., Zhang, X.-J., Sandhu, J. K., et al. (2020). Driving of outer belt electron loss by solar wind dynamic pressure structures: analysis of balloon and satellite data. *J. Geophys. Res. Space Phys.* 125 (12). doi:10.1029/2020ja028097

Brito, T., Hudson, M., Kress, B., Paral, J., Halford, A., Millan, R., et al. (2015). Simulation of ULF wave-modulated radiation belt electron precipitation during the 17 March 2013 storm. *J. Geophys. Res. Space Phys.* 120 (5), 3444–3461. doi:10.1002/2014ja020838

Brito, T., Woodger, L., Hudson, M., and Millan, R. (2012). Energetic radiation belt electron precipitation showing ULF modulation. *Geophys. Res. Lett.* 39 (22). doi:10.1029/2012gl053790

Buchert, S. C., Fujii, R., and Glassmeier, K.-H. (1999). Ionospheric conductivity modulation in ULF pulsations. *J. Geophys. Res. Space Phys.* 104 (A5), 10119–10133. doi:10.1029/1998ja900180

Capannolo, L., Li, W., Ma, Q., Chen, L., Shen, X.-C., Spence, H. E., et al. (2019a). Direct observation of subrelativistic electron precipitation potentially driven by EMIC waves. *Geophys. Res. Lett.* 46 (22), 12711–12721. doi:10.1029/2019gl084202

Capannolo, L., Li, W., Ma, Q., Shen, X.-C., Zhang, X.-J., Redmon, R. J., et al. (2019b). Energetic electron precipitation: multievent analysis of its spatial extent during EMIC wave activity. *J. Geophys. Res. Space Phys.* 124 (4), 2466–2483. doi:10.1029/2018ja026291

Chen, L., Thorne, R. M., Li, W., Bortnik, J., Turner, D., and Angelopoulos, V. (2012). Modulation of plasmaspheric hiss intensity by thermal plasma density structure. *Geophys. Res. Lett.* 39, L14103. doi:10.1029/2012GL052308

Claudepierre, S., Hudson, M., Lotko, W., Lyon, J., and Denton, R. (2010). Solar wind driving of magnetospheric ULF waves: field line resonances driven by dynamic pressure fluctuations. *J. Geophys. Res.* 115, A11202. doi:10.1029/2010ja015399

Claudepierre, S. G., Wiltberger, M., Elkington, S. R., Lotko, W., and Hudson, M. K. (2009). Magnetospheric cavity modes driven by solar wind dynamic pressure fluctuations. *Geophys. Res. Lett.* 36, L13101. doi:10.1029/2009gl039045

Clilverd, M. A., Duthie, R., Hardman, R., Hendry, A. T., Rodger, C. J., Raita, T., et al. (2015). Electron precipitation from EMIC waves: a case study from 31 May 2013. *J. Geophys. Res. Space Phys.* 120 (5), 3618–3631. doi:10.1002/2015ja021090

Elkington, S. R., Hudson, M. K., and Chan, A. A. (2003). Resonant acceleration and diffusion of outer zone electrons in an asymmetric geomagnetic field. *J. Geophys. Res.* 108, 1116. doi:10.1029/2001ja009202

Grach, V. S., Artemyev, A. V., Demekhov, A. G., Zhang, X.-J., Bortnik, J., Angelopoulos, V., et al. (2022). Relativistic electron precipitation by EMIC waves: importance of nonlinear resonant effects. *Geophys. Res. Lett.* 49, e2022GL099994. doi:10.1029/2022GL099994

Halford, A., McGregor, S., Murphy, K., Millan, R., Hudson, M., Woodger, L., et al. (2015). BARREL observations of an ICME-shock impact with the magnetosphere and the resultant radiation belt electron loss. *J. Geophys. Res. Space Phys.* 120 (4), 2557–2570. doi:10.1002/2014ja020873

Heacock, R., and Hunsucker, R. (1977). A study of concurrent magnetic field and particle precipitation pulsations, 0.005 to 0.5 Hz, recorded near College, Alaska. *J. Atmos. Terr. Phys.* 39 (4), 487–501. doi:10.1016/0021-9169(77)90158-1

Hendry, A. T., Rodger, C. J., and Clilverd, M. A. (2017). Evidence of sub-MeV EMIC-driven electron precipitation. *Geophys. Res. Lett.* 44 (3), 1210–1218. doi:10.1002/2016gl071807

Hosokawa, K., Miyoshi, Y., Ozaki, M., Oyama, S. I., Ogawa, Y., Kurita, S., et al. (2020). Multiple time-scale beats in aurora: precise orchestration via magnetospheric chorus waves. *Sci. Rep.* 10, 3380. doi:10.1038/s41598-020-59642-8

Hsu, T., and McPherron, R. L. (2007). A statistical study of the relation of Pi 2 and plasma flows in the tail. *J. Geophys. Res.* 112, A05209. doi:10.1029/2006ja011782

Jacobs, J. A., Kato, Y., Matsushita, S., and Troitskaya, V. A. (1964). Classification of geomagnetic micropulsations. *J. Geophys. Res.* 69 (1), 180–181. doi:10.1029/JZ069i001p00180

Jaynes, A., Lessard, M., Takahashi, K., Ali, A., Malaspina, D., Michell, R., et al. (2015). Correlated Pc4–5 ULF waves, whistler-mode chorus, and pulsating aurora observed by the Van Allen Probes and ground-based systems. *J. Geophys. Res. Space Phys.* 120 (10), 8749–8761. doi:10.1002/2015ja021380

Kennel, C. F., and Petschek, H. E. (1966). Limit on stably trapped particle fluxes. *J. Geophys. Res.* 71 (1), 1–28. doi:10.1029/jz071i001p00001

Kepko, L., and Spence, H. E. (2003). Observations of discrete, global magnetospheric oscillations directly driven by solar wind density variations. *J. Geophys. Res.* 108 (A6), 1257. doi:10.1029/2002JA009676

Kepko, L., Spence, H. E., and Singer, H. J. (2002). ULF waves in the solar wind as direct drivers of magnetospheric pulsations. *Geophys. Res. Lett.* 29 (8). doi:10.1029/2001GL014405

Kepko, L., and Viall, N. M. (2019). The source, significance, and magnetospheric impact of periodic density structures within stream interaction regions. *J. Geophys. Res. Space Phys.* 124, 7722–7743. doi:10.1029/2019JA026962

Li, W., Bortnik, J., Thorne, R. M., Nishimura, Y., Angelopoulos, V., and Chen, L. (2011b). Modulation of whistler mode chorus waves: 2. Role of density variations. *J. Geophys. Res.* 116, A06206. doi:10.1029/2010ja016313

Li, W., Shen, X.-C., Ma, Q., Capannolo, L., Shi, R., Redmon, R. J., et al. (2019). Quantification of energetic electron precipitation driven by plume whistler mode waves, plasmaspheric hiss, and exohiss. *Geophys. Res. Lett.* 46 (7), 3615–3624. doi:10.1029/2019gl082095

Li, W., Thorne, R. M., Bortnik, J., Nishimura, Y., and Angelopoulos, V. (2011a). Modulation of whistler mode chorus waves: 1. Role of compressional Pc4–5 pulsations. *J. Geophys. Res.* 116, A06205. doi:10.1029/2010ja016312

Li, Z., Millan, R. M., Hudson, M. K., Woodger, L. A., Smith, D. M., Chen, Y., et al. (2014). Investigation of EMIC wave scattering as the cause for the BARREL 17 January 2013 relativistic electron precipitation event: a quantitative comparison of simulation with observations. *Geophys. Res. Lett.* 41, 8722–8729. doi:10.1002/2014GL062273

Liu, X., Gu, W., Xia, Z., Chen, L., and Horne, R. B. (2021). Frequency-dependent modulation of whistler-mode waves by density irregularities during the recovery phase of a geomagnetic storm. *Geophys. Res. Lett.* 48, e2021GL093095. doi:10.1029/2021GL093095

Ma, Q., Connor, H. K., Zhang, X.-J., Li, W., Shen, X.-C., Gillespie, D., et al. (2020). Global survey of plasma sheet electron precipitation due to whistler mode chorus waves in Earth's magnetosphere. *Geophys. Res. Lett.* 47, e2020GL088798. doi:10.1029/2020GL088798

Ma, Q., Li, W., Zhang, X.-J., Bortnik, J., Shen, X.-C., Connor, H. K., et al. (2021). Global survey of electron precipitation due to hiss waves in the Earth's plasmasphere and plumes. *J. Geophys. Res. Space Phys.* 126, e2021JA029644. doi:10.1029/2021JA029644

Mathie, R. A., and Mann, I. R. (2000). A correlation between extended intervals of ULF wave power and storm-time geosynchronous relativistic electron flux enhancements. *Geophys. Res. Lett.* 27 (20), 3261–3264. doi:10.1029/2000gl003822

Millan, R. M., McCarthy, M. P., Sample, J. G., Smith, D. M., Thompson, L. D., McGaw, D. G., et al. (2013). The balloon array for RBSP relativistic electron losses (BARREL). *Space Sci. Rev.* 179 (1-4), 503–530. doi:10.1007/s11214-013-9971-z

Millan, R. M., and Thorne, R. M. (2007). Review of radiation belt relativistic electron losses. *J. Atmos. Sol. Terr. Phys.* 69, 362–377. doi:10.1016/j.jastp.2006.06.019

Motoba, T., Takahashi, K., Gjerloev, J., Ohtani, S., and Milling, D. (2013). The role of compressional Pc5 pulsations in modulating precipitation of energetic electrons. *J. Geophys. Res. Space Phys.* 118 (12), 7728–7739. doi:10.1002/2013ja018912

Ni, B., Bortnik, J., Thorne, R. M., Ma, Q., and Chen, L. (2013). Resonant scattering and resultant pitch angle evolution of relativistic electrons by plasmaspheric hiss. *J. Geophys. Res. Space Phys.* 118, 7740–7751. doi:10.1002/2013JA019260

Ni, B., Thorne, R. M., Shprits, Y. Y., and Bortnik, J. (2008). Resonant scattering of plasma sheet electrons by whistler-mode chorus: contribution to diffuse auroral precipitation. *Geophys. Res. Lett.* 35, L11106. doi:10.1029/2008GL034032

Nishimura, Y., Bortnik, J., Li, W., Thorne, R. M., Chen, L., Lyons, L. R., et al. (2011). Multievent study of the correlation between pulsating aurora and whistler mode chorus emissions. *J. Geophys. Res.* 116, A11221. doi:10.1029/2011JA016876

Nishimura, Y., Bortnik, J., Li, W., Thorne, R. M., Lyons, L. R., Angelopoulos, V., et al. (2010). Identifying the driver of pulsating aurora. *Science* 330, 81–84. doi:10.1126/science.1193186

Olson, J. V. (1999). Pi2 pulsations and substorm onsets: a review. *J. Geophys. Res.* 104 (17), 17499–17520. doi:10.1029/1999ja900086

Pedersen, A., Lybekk, B., André, M., Eriksson, A., Masson, A., Mozer, F. S., et al. (2008). Electron density estimations derived from spacecraft potential measurements on Cluster in tenuous plasma regions. *J. Geophys. Res.* 113, A07S33. doi:10.1029/2007JA012636

Qin, M., Hudson, M., Li, Z., Millan, R., Shen, X., Shprits, Y., et al. (2019). Investigating loss of relativistic electrons associated with EMIC waves at low L values on 22 june 2015. *J. Geophys. Res. Space Phys.* 124 (6), 4022–4036. doi:10.1029/2018ja025726

Qin, M., Hudson, M., Millan, R., Woodger, L., and Shekhar, S. (2018). Statistical investigation of the efficiency of EMIC waves in precipitating relativistic electrons. *J. Geophys. Res. Space Phys.* 123 (8), 6223–6230. doi:10.1029/2018ja025419

Qin, M., Hudson, M., Millan, R., Woodger, L., and Shen, X. (2020). Statistical dependence of EMIC wave scattering on wave and plasma parameters. *J. Geophys. Res. Space Phys.* 125 (4). doi:10.1029/2020ja027772

Qin, M., Li, W., Ma, Q., Woodger, L., Millan, R., Shen, X.-C., et al. (2021). Multi-point observations of modulated whistler-mode waves and energetic electron precipitation. *J. Geophys. Res. Space Phys.* 126, e2021JA029505. doi:10.1029/2021ja029505

Rae, I. J., Mann, I. R., Dent, Z. C., Milling, D. K., Donovan, E. F., and Spanswick, E. (2007). Multiple field line resonances: optical, magnetic and absorption signatures. *Planet. Space Sci.* 55 (6), 701–713. doi:10.1016/j.pss.2006.02.009

Rae, J. I., Murphy, K. R., Watt, C. E., Halford, A. J., Mann, I. R., Ozeke, L. G., et al. (2018). The role of localized compressional ultra-low frequency waves in energetic electron precipitation. *J. Geophys. Res. Space Phys.* 123 (3), 1900–1914. doi:10.1002/2017ja024674

Roux, A., Le Contel, O., Coillot, C., Bouabdellah, A., de la Porte, B., Alison, D., et al. (2008). The search coil magnetometer for THEMIS. *Space Sci. Rev.* 141, 265–275. doi:10.1007/s11214-008-9455-8

Shen, X., Zong, Q.-G., Shi, Q., Tian, A., Sun, W., Wang, Y., et al. (2015). Magnetospheric ULF waves with increasing amplitude related to solar wind dynamic pressure changes: the time history of events and macroscale interactions during substorms (THEMIS) observations. *J. Geophys. Res. Space Phys.* 120, 7179–7190. doi:10.1002/2014ja020913

Shen, X.-C., Li, W., Ma, Q., Agapitov, O., and Nishimura, Y. (2019). Statistical analysis of transverse size of lower band chorus waves using simultaneous multisatellite observations. *Geophys. Res. Lett.* 46, 5725–5734. doi:10.1029/2019GL083118

Shen, X. C., Shi, Q. Q., Zong, Q., Tian, A. M., Nowada, M., Sun, W. J., et al. (2017). Dayside magnetospheric ULF wave frequency modulated by a solar wind dynamic pressure negative impulse. *J. Geophys. Res. Space Phys.* 122, 1658–1669. doi:10.1002/2016ja023351

Singer, H., Matheson, L., Grubb, R., Newman, A., and Bouwer, D. (1996). "Monitoring space weather with the GOES magnetometers," in *GOES-8 and beyond* (Bellingham, Washington: International Society for Optics and Photonics), 299–308. doi:10.1117/12.254077

Spanswick, E., Donovan, E., and Baker, G. (2005). Pc5 modulation of high energy electron precipitation: particle interaction regions and scattering efficiency. *Ann. Geophys.* 23 (5), 1533–1542. doi:10.5194/angeo-23-1533-2005

Summers, D., Ni, B., Meredith, N. P., Horne, R. B., Thorne, R. M., Moldwin, M. B., et al. (2008). Electron scattering by whistler-mode ELF hiss in plasmaspheric plumes. *J. Geophys. Res.* 113, A04219. doi:10.1029/2007ja012678

Summers, D., and Thorne, R. M. (2003). Relativistic electron pitch-angle scattering by electromagnetic ion cyclotron waves during geomagnetic storms. *J. Geophys. Res.* 108 (A4), 1143. doi:10.1029/2002JA009489

Thorne, R. M. (2010). Radiation belt dynamics: the importance of wave-particle interactions. *Geophys. Res. Lett.* 37, L22107. doi:10.1029/2010gl044990

Woodger, L. A., Halford, A. J., Millan, R. M., McCarthy, M. P., Smith, D. M., Bowers, G. S., et al. (2015). A summary of the BARREL campaigns: technique for studying electron precipitation. *J. Geophys. Res. Space Phys.* 120, 4922–4935. doi:10.1002/2014JA020874

Xia, Z., Chen, L., Dai, L., Claudepierre, S. G., Chan, A. A., Soto-Chavez, A. R., et al. (2016). Modulation of chorus intensity by ULF waves deep in the inner magnetosphere. *Geophys. Res. Lett.* 43, 9444–9452. doi:10.1002/2016GL070280

Yin, Z.-F., Zhou, X.-Z., Li, W., Shen, X.-C., Rankin, R., Liu, J., et al. (2023). Characteristics of electron precipitation directly driven by poloidal ULF waves. *J. Geophys. Res. Space Phys.* 128, e2022JA031163. doi:10.1029/2022JA031163

Zhang, X.-J., Mourenas, D., Artemyev, A. V., Angelopoulos, V., and Sauvaud, J.-A. (2019). Precipitation of MeV and sub-MeV electrons due to combined effects of EMIC and ULF waves. *J. Geophys. Res. Space Phys.* 124, 7923–7935. doi:10.1029/2019ja026566

Zhang, X.-J., Mourenas, D., Shen, X.-C., Qin, M., Artemyev, A. V., Ma, Q., et al. (2021). Dependence of relativistic electron precipitation in the ionosphere on EMIC wave minimum resonant energy at the conjugate equator. *J. Geophys. Res.* 126 (5), e2021JA029193. doi:10.1029/2021ja029193

Zhou, C., Li, W., Thorne, R. M., Bortnik, J., Ma, Q., An, X., et al. (2015). Excitation of dayside chorus waves due to magnetic field line compression in response to interplanetary shocks. *J. Geophys. Res. Space Phys.* 120, 8327–8338. doi:10.1002/2015JA021530

frontiers | Frontiers in Physics

TYPE Original Research
PUBLISHED 28 May 2024
DOI 10.3389/fphy.2024.1254024

OPEN ACCESS

EDITED BY
Chuanfei Dong,
Boston University, United States

REVIEWED BY
Mehran Shahmansouri,
Arak University, Iran
Xu Liu,
The University of Texas at Dallas, United States
Hongyang Zhou,
University of Helsinki, Finland

*CORRESPONDENCE
Xinliang Gao,
gaoxl@ustc.edu.cn
Yangguang Ke,
keyg@ustc.edu.cn

RECEIVED 06 July 2023
ACCEPTED 15 April 2024
PUBLISHED 28 May 2024

CITATION
Shao T, Gao X, Ke Y, Lu Q and Wang X (2024), The effects of plasma density structure on the propagation of magnetosonic waves: 1-D particle-in-cell simulations.
Front. Phys. 12:1254024.
doi: 10.3389/fphy.2024.1254024

The effects of plasma density structure on the propagation of magnetosonic waves: 1-D particle-in-cell simulations

Tong Shao[1,2,3], Xinliang Gao[1,2,3]*, Yangguang Ke[1,2,3]*, Quanming Lu[1,2,3] and Xueyi Wang[4]

[1]Deep Space Exploration Laboratory, School of Earth and Space Sciences, University of Science and Technology of China, Hefei, China, [2]CAS Center for Excellence in Comparative Planetology, Hefei, China, [3]Collaborative Innovation Center of Astronautical Science and Technology, Harbin, China, [4]Physics Department, Auburn University, Auburn, AL, United States

Magnetosonic (MS) waves, i.e., ion Bernstein mode waves, are one of the common plasma waves in the Earth's magnetosphere, which are important for regulating charged particle dynamics. How MS waves propagate in the magnetosphere is critical to understanding the global distribution of the waves, but it remains unclear. Although previous studies present that MS waves can be reflected by fine-scale density structures, the dissipation of waves by background plasma has long been neglected. In this study, we perform one-dimensional (1-D) particle-in-cell (PIC) simulations to study the propagation of MS waves through density structures, where both absorption and reflection have been included. We find that absorption is as important as reflection when considering the propagation of MS waves through density structures, and both of them are strongly dependent on the shape of density structures. Specifically, the reflectivity of MS waves is positively and negatively correlated with the height and width of density structures, respectively, while the absorptivity of MS waves has a positive correlation with both the height and width of density structures. Our study demonstrates the significance of absorption during the propagation of MS waves, which may help better understand the distribution of MS waves in the Earth's magnetosphere.

KEYWORDS

magnetosonic wave, wave propagation, density structure, magnetosphere, paticlein-cell simulation, wave-particle interaction

1 Introduction

Magnetosonic (MS) waves, also known as ion Bernstein mode waves, are one of the intense electromagnetic emissions observed in the Earth's inner magnetosphere [1]. These waves were first detected by the OGO 3 satellite and named "equatorial noise" due to their occurrence within about ± 2° of the magnetic equator [2–4]. Recent observations made by Cluster and THEMIS satellites [5,6] have shown that MS waves can occur both inside and outside the plasmasphere near the magnetic equator. The waves are excited at harmonics of the proton gyrofrequency [7] and at large (~90°) wave normal angles [8,9] by ring velocity distributions of ring current protons [10,11]. MS waves play a significant role in regulating the dynamics of charged particles in the Earth's magnetosphere [12–18]. They have been proposed as a candidate

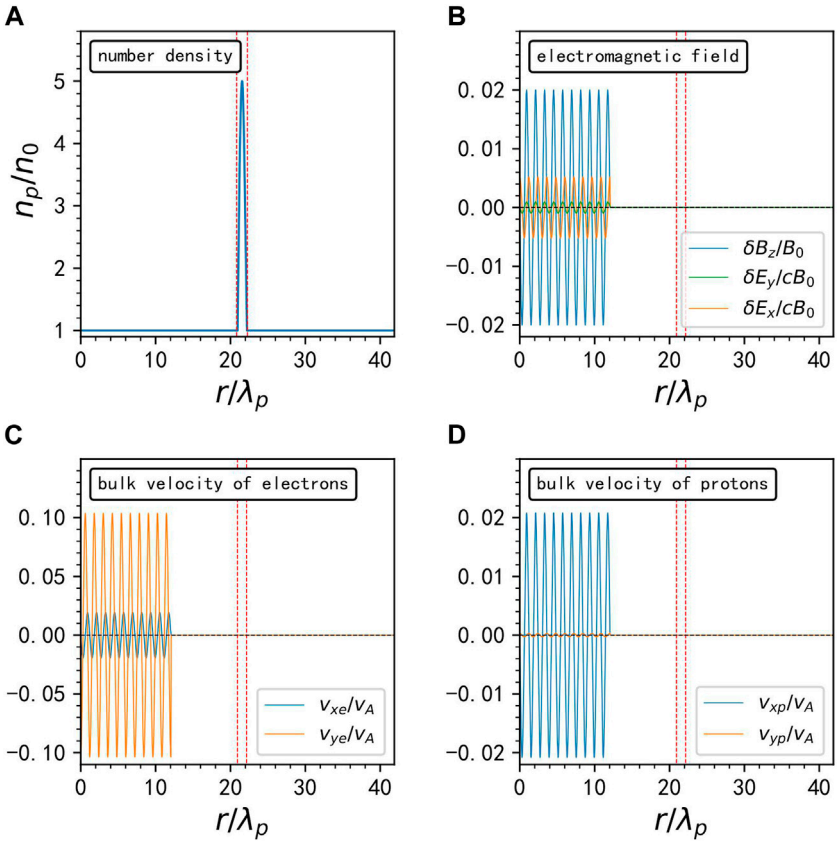

FIGURE 1
The initialization of the spatial distribution of **(A)** plasma number density, **(B)** wave fields δB_z (blue line), δE_x (orange line), δE_y (green line) **(C)** bulk velocities of electrons v_{xe} (blue line), v_{ye} (orange line) and **(D)** bulk velocities of protons v_{xp} (blue line), v_{yp} (orange line) at $t\Omega_{cp} = 0$ in Run 1. The central vertical red dashed lines denote the position of the density structure.

for accelerating ~100 keV electrons up to relativistic energies in the outer radiation belt [14]. Additionally, scattering by MS waves may explain the formation of butterfly distributions of radiation belt electrons [19,18,21–23]. Furthermore, MS waves can effectively energize the background cold protons and electrons [24,25].

Understanding the propagation of MS waves in the Earth's magnetosphere is crucial in comprehending the global distributions of these waves and their impact on energy transfer among different particle populations. Satellite observations indicate that the occurrence rate of MS waves strongly depends on the magnetic local time (MLT) outside the plasmapause, but remains nearly uniform inside the plasmapause [26]. This coincides with the scenario that MS waves are initially generated outside the plasmasphere in the noon and dusk sectors and then propagate both outward and inward, crossing the plasmapause and migrating globally over MLT [27,28]. Moreover, the occurrence rate and intensity of MS waves outside the plasmapause are higher than inside it [26] and the majority of MS waves inside the plasmapause have lower frequencies than the local proton cyclotron frequency [7,22], making radial propagation the most plausible explanation [5,6,29].

The propagation of MS waves is strongly influenced by the inhomogeneous background plasma density. By performing one-dimensional (1-D) full wave simulations with the finite difference time domain (FDTD) method, Liu et al. [30] have found that MS waves can propagate deep into the plasmasphere with only a small fraction of the MS wave power being reflected by the plasmapause. Instead, the fine-scale density structures near the outer edge of the plasmapause can effectively reflect MS waves. Such fine-scale density structures have been widely observed in the Earth's magnetosphere [29,30–31]. However, previous simulations have also revealed that MS waves can be significantly damped by the background cold plasma [17,24,34], which was neglected in the study of Liu et al. [30] due to the limitation of their model. Therefore, we utilize the 1-D PIC model to simulate the propagation of MS waves through the fine-scale density structures, where both absorption and reflection have been considered. We have also quantified the reflectivity and absorptivity of MS waves passing through the density structure and investigated their dependences on the shape of the density structure.

2 Simulation model and method

In this study, we employ a 1-D PIC simulation model to investigate the effects of density structures on the propagation of

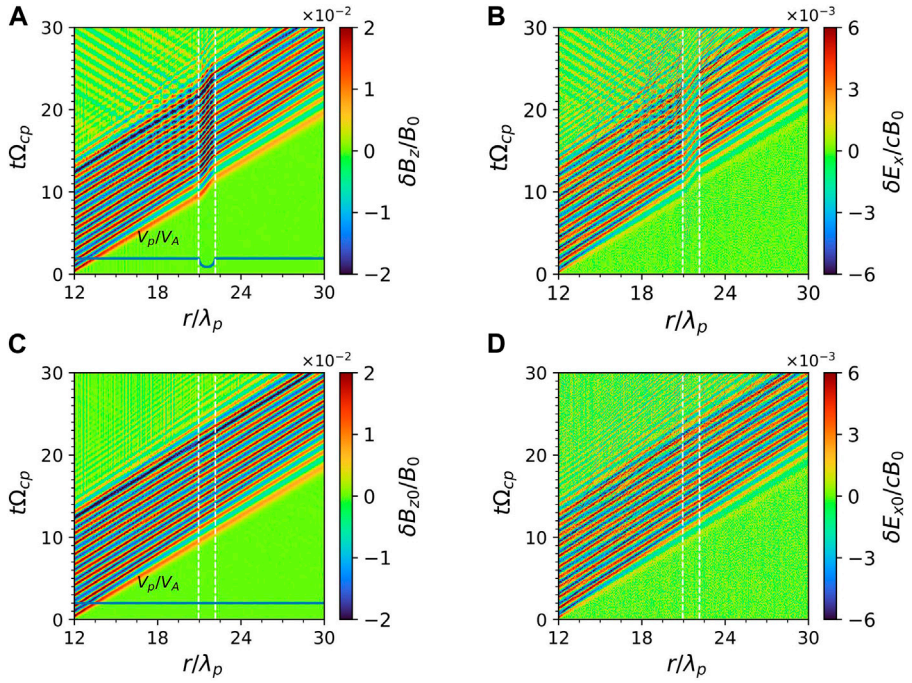

FIGURE 2
The temporal evolution of wave **(A)** magnetic field and **(B)** electric field in Run 1, and wave **(C)** magnetic field and **(D)** electric field in Run 2.The blue curves in **(A, C)** denote the variation of phase velocity along the simulation direction.

MS waves. The background magnetic field $\boldsymbol{B_0}$ is directed along the z-axis, and the wave vector of MS waves is lying in the x-z plane. Here, the simulation box is along the wave vector (or the propagating direction), which is defined as the r direction. This model includes full three-dimensional electromagnetic fields and velocities but only allows spatial variations in the r direction. The periodic boundary conditions are adopted. The units of time and space are the inverse of the proton gyrofrequency Ω_{cp}^{-1}, and the proton inertial length λ_p, respectively. The plasma system only consists of background protons and electrons which are denoted by subscripts "p" and "e" hereafter. Both protons and electrons satisfy a Maxwellian velocity distribution and have the same temperature $T_p = T_e = 1eV$. To reduce computational costs, the mass ratio of proton to electron m_p/m_e is set to 1600, and the ratio of light speed to the Alfven speed c/V_A is set to 20. The simulation domain with a length of $41.89\lambda_p$ is divided equally into 30000 grids. The average number of superparticles in each grid is approximately 100 for each species, and the time step is set to $\Delta t = 3.125 \times 10^{-5}\Omega_{cp}^{-1}$.

The angle between the wave vector and the background magnetic field is defined as θ, i.e., the wave normal angle. Here we will consider two categories of MS waves: perpendicular ($\theta = 90°$) and quasi-perpendicular waves ($\theta = 85°$). For each run, we initially pump the monochromatic MS wave from the left boundary to $r = 10\lambda_w$ (λ_w is the wavelength) by assigning fluctuating wave fields on each grid and fluctuating bulk velocity to each particle in the form of $A_i e^{ikr}$ (A_i is the related parameter and k is the wave number, respectively) along the r direction. Based on the dispersion relation of MS waves in a cold plasma, we can obtain the wave fields by the following relations:

$$B_{wx} = -\frac{1}{tan\,\theta}B_{wz} \tag{1}$$

$$B_{wy} = \frac{-i(n^2 - S)P}{Dtan\theta(P - n^2 sin^2\theta)}B_{wz} \tag{2}$$

$$E_{wy} = \frac{\omega}{ksin\theta}B_{wz} \tag{3}$$

$$E_{wx} = \frac{n^2 - S}{iD}E_{wy} \tag{4}$$

$$E_{wz} = \frac{n^2 sin^2\theta - P}{n^2\,sin\,\theta\,cos\,\theta}E_{wx} \tag{5}$$

$$n = \frac{ck}{\omega} = \frac{RL}{S} \tag{6}$$

where P, D, R, L, and S are the Stix parameters [35,36] and n is the refraction index in Eqs 1–6. Besides, the corresponding bulk velocities of protons and electrons are given by Eqs 7–9:

$$v_{xj}(r,t) = \left\{\frac{-iq_j}{m_j\omega}\left[\frac{1}{\left(\Omega_{cj}/\omega\right)^2 - 1}E_{wx} + i\frac{\Omega_{cj}/\omega}{\left(\Omega_{cj}/\omega\right)^2 - 1}E_{wy}\right]\right\} \tag{7}$$

$$v_{yj}(r,t) = \mathrm{Re}\left\{\frac{-iq_j}{m_j\omega}\left[-i\frac{\Omega_{cj}/\omega}{\left(\Omega_{cj}/\omega\right)^2 - 1}E_{wx} + \frac{1}{\left(\Omega_{cj}/\omega\right)^2 - 1}E_{wy}\right]\right\} \tag{8}$$

$$v_{zj}(r,t) = Re\left(\frac{iq_j}{m_j\omega}E_{wz}\right) \tag{9}$$

where q_j, m_j, and Ω_{cj} denote the charge, mass, and cyclotron frequency of the j-component of plasma (j indicates p or e),

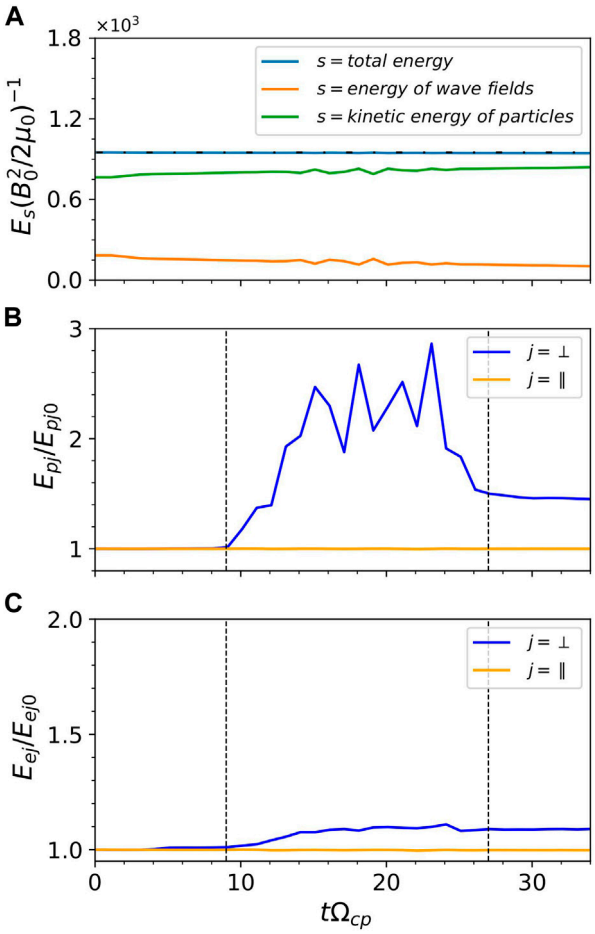

FIGURE 3
(A) The time evolution of the energy of the electromagnetic fields (green line), the kinetic energy of the particles (orange line), and their sum (blue line), respectively. The horizontal black dash-dotted line denotes the initial value of the total energy. The time evolution of kinetic energy of **(B)** protons and **(C)** electrons. Blue lines and orange lines denote the perpendicular direction and parallel direction, respectively. E_{pj0} denotes the kinetic energy of species j at $t\Omega_{cp} = 0$. The black dashed lines in **(B, C)** denote the time of wave arrival and departure of the density structure.

respectively. In each run, the B_{wz} is set to $0.02B_0$, and other parameters can be calculated according to the above relations.

For convenience, the density structure is assumed as the sinusoidal variation of density, so the plasma density as a function of r is given by Eq. 10:

$$n_p = \begin{cases} n_0\left[1 + (H-1)\sin\left(\dfrac{r - r_0 + \dfrac{\Delta L}{2}}{\Delta L}\pi\right)\right], r_0 - \dfrac{\Delta L}{2} \le r \le r_0 + \dfrac{\Delta L}{2} \\ n_0, otherwise \end{cases} \tag{10}$$

where n_0 is the ambient number density (outside the density structure), and H is the height of the density structure which is the ratio of the peak density to the ambient density n_0. r_0 and ΔL denote the location and width of the density structure, respectively. The location of the density structure is fixed at $r_0 = 20.95\lambda_p$ in each run.

In the following section, we will present the simulation results of three runs in detail: Run 1 with $\theta = 90°$, $H = 5$, and $\Delta L = 1\lambda_w$, Run 2 with $\theta = 90°$ and no structure, and Run 3 with $\theta = 85°$, $H = 5$, and $\Delta L = 1\lambda_w$. To show how we initialize the simulation model, we present the spatial profiles of (a) plasma density, (b) wave fields, bulk velocities of (c) electrons, and (d) protons at $t = 0$ for Run 1 in Figure 1. There is a density structure located at $r_0 = 20.95\lambda_p$ with the width $\Delta L = 1.2\lambda_p = 1\lambda_w$ and the height $H = 5$ (Figure 1A). The MS waves are launched within the region of $0 \le r \le 12\lambda_p$ (i.e., $10\lambda_w$). For the perpendicular MS wave, there are only one component of fluctuating magnetic fields (δB_z) and two components of fluctuating electric fields (δE_x and δE_y) (Figure 1B). The bulk velocities of protons and electrons are shown in Figures 1C, D, respectively. Although the corresponding fluctuating density is not initialized, the density fluctuation will be self-consistently coupled to the MS wave very quickly in the PIC model

3 Simulation results

3.1 Perpendicular waves: $\theta = 90°$

Figure 2 displays the propagation of the MS waves in Run 1 with a density structure and in Run 2 without it. Without the density

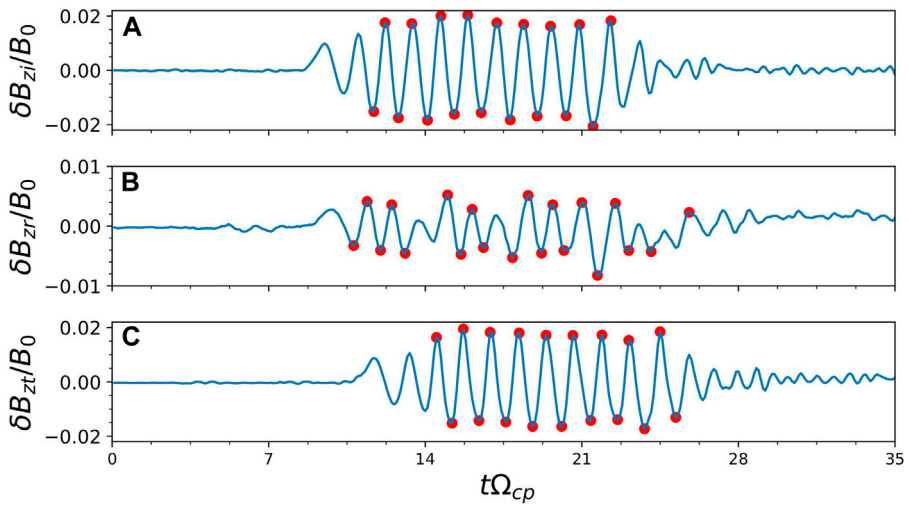

FIGURE 4
The time evolution of the fluctuating magnetic field of **(A)** the incident MS wave (δB_{zi}) and **(B)** reflected MS wave (δB_{zr}) at the left boundary ($x_1 = 20.94\lambda_p$) of the density structure, and of **(C)** the transmitted MS wave (δB_{zt}) at the right boundary ($x_2 = 22.15\lambda_p$) of the density structure for the Run 1. Red circles denote the wave peaks used to calculate the wave magnetic amplitude.

structure, the MS waves propagate along the r direction (x-axis) with a constant speed of $0.96V_A$, which is consistent with the linear dispersion relation (Figures 2C, D). As expected, we can find that the wave amplitude is gradually decreasing during the propagation due to the dissipation caused by background plasma. In Run 1, the MS wave encounters the density structure at about $9\Omega_{cp}^{-1}$, and then there appears the weak backward propagating MS wave emitting from the left boundary of the density structure. Such a wave is just reflected by the density structure. Besides, the phase velocity inside the density structure becomes smaller than that outside the structure due to the enhanced plasma density (Figure 2A). Meanwhile, the wave fields δB_z and δE_x become larger and smaller inside the density structure (Figures 2A, B), respectively, consistent with the results of Liu et al. [30].

Figure 3A shows the time evolution of the energy of MS wave fields (orange line), the kinetic energy of charged particles (green line), and their sum (blue line) for Run 1. First of all, the total energy in our model is well conserved within a 0.06% margin of error. Secondly, it is clearly shown that the wave energy decreases as the particle kinetic energy increases with time, suggesting the wave dissipation takes effect during the propagation. We further display the time evolution of kinetic energies of protons and electrons inside the density structure in Figures 3B, C, respectively, where the vertical dashed lines mark the tie when the wave enters and leaves this structure. For both protons and electrons, their parallel kinetic energy remains nearly unchanged, since the perpendicular MS wave does not have the parallel electric field and cannot energize particles in the parallel direction. The perpendicular kinetic energy of protons $E_{p\perp}$ rapidly increases as the wave enters the density structure mainly due to the pick-up process. After the wave leaves the density structure, the $E_{p\perp}$ rapidly drops, but there is still the obvious net increase of kinetic energy (Figure 3B), which is caused by the perpendicular heating by the MS wave (also see Supplementary Material). However, the net increase of kinetic energy for electrons is not significant (Figure 3C).

To quantify the effects of the density structure on the propagation of MS waves, we need to calculate the reflectivity R_M, absorptivity A_M, and transmissivity T_M of MS waves. Here, the R_M, T_M, A_M are estimated based on the following formulas:

$$R_M = \frac{P_r}{P_i} = \left(\frac{\bar{B}_{wzr}}{\bar{B}_{wzi}}\right)^2 \tag{11}$$

$$T_M = \frac{P_t}{P_i} = \left(\frac{\bar{B}_{wzt}}{\bar{B}_{wzi}}\right)^2 \tag{12}$$

$$A_M = 1 - R_M - T_M \tag{13}$$

where P_i, P_r, and P_t are the Poynting flux of the incident, reflected, and transmitted waves, respectively, and the corresponding amplitudes are $\bar{B}_{wzi}$, $\bar{B}_{wzr}$, and $\bar{B}_{wzt}$. The waveform of transmitted waves is shown in Figure 4C, which is directly obtained by recording the time series of δB_z at the right boundary of the density structure. The eight clearest wavelengths are selected by marking the peaks and troughs with red dots, and then the amplitude of transmitted wave $\bar{B}_{wzt}$ is given by their average. However, the reflected and incident MS waves cannot be directly obtained, since the incident and reflected waves are mixed at the left boundary in Run 1. Instead, we use the recorded waveform at the left boundary of the density structure in Run 2 to represent the incident wave (Figure 4A), and the amplitude $\bar{B}_{wzi}$ is the average of those marked points. Then, the waveform of reflected waves is obtained by subtracting the reflected waveform shown in Figure 4A from the mixed waveform recorded at the left boundary in Run 1, and the amplitude $\bar{B}_{wzr}$ is calculated as above. For Run 1, the $\bar{B}_{wzi}$, $\bar{B}_{wzr}$, and $\bar{B}_{wzt}$ are estimated as 0.01783, 0.00392, and 0.01683, so the R_M, A_M, and T_M are 4.83%, 6.07%, and 89.1% according to Eqs 11–13. It is clearly found that the absorption of MS wave by the density structure is even more significant than the reflection in this case.

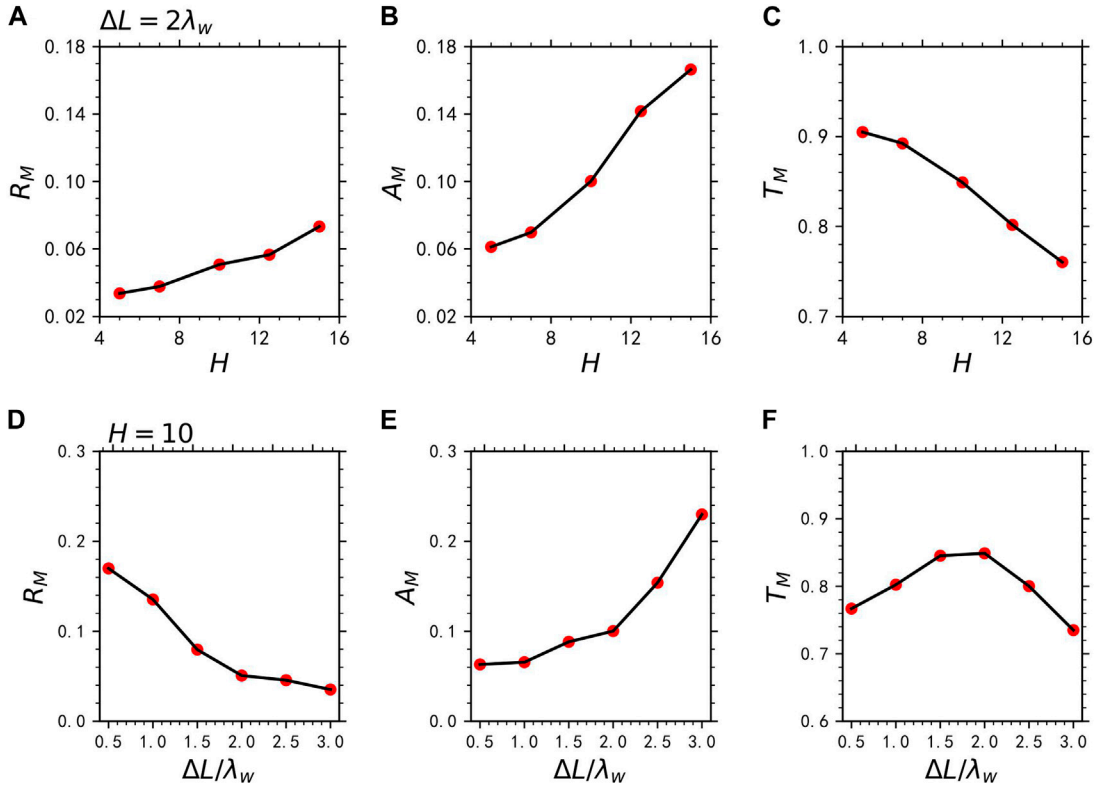

FIGURE 5
The **(A)** reflectivity R_M, **(B)** absorptivity A_M and **(C)** transmissivity T_M as a function of various heights with a constant width $\Delta L = 2\lambda_w$, and the **(D)** reflectivity R_M, **(E)** absorptivity A_M, and **(F)** transmissivity T_M as a function of various widths with a constant height $H = 10$. Red dots are the simulation runs with different parameters when the pump wave propagates exactly perpendicularly.

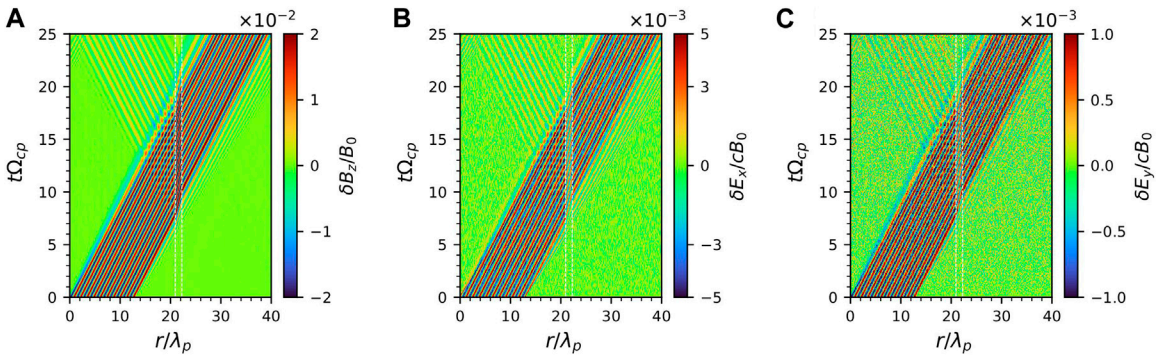

FIGURE 6
Temporal evolution of wave magnetic field **(A)** δB_z, electric field **(B)** δE_x, **(C)** δE_y in Run 3.

Furthermore, we have also studied the effects of the shape of density structure on the reflection and absorption of MS wave by considering the various widths ΔL and heights H. Figure 5 summarizes the simulation results (32 additional runs). First of all, there is a clear trend that both the R_M and A_M are positively correlated with the height of density structure H (Figures 5A, B). Just as expected, the corresponding transmissivity T_M must be decreasing with the height H (Figure 5C). However, with the increasing ΔL, the R_M decreases while the A_M increases (Figures 5D, E). Their opposite correlation with the width of density structure ΔL results in the particular dependence of T_M on the ΔL. With the increasing ΔL, the T_M first increases and then decreases, leading to a maximum on a certain value of ΔL (Figure 5F). Moreover, comparing the A_M with T_M, we can find that the absorptivity

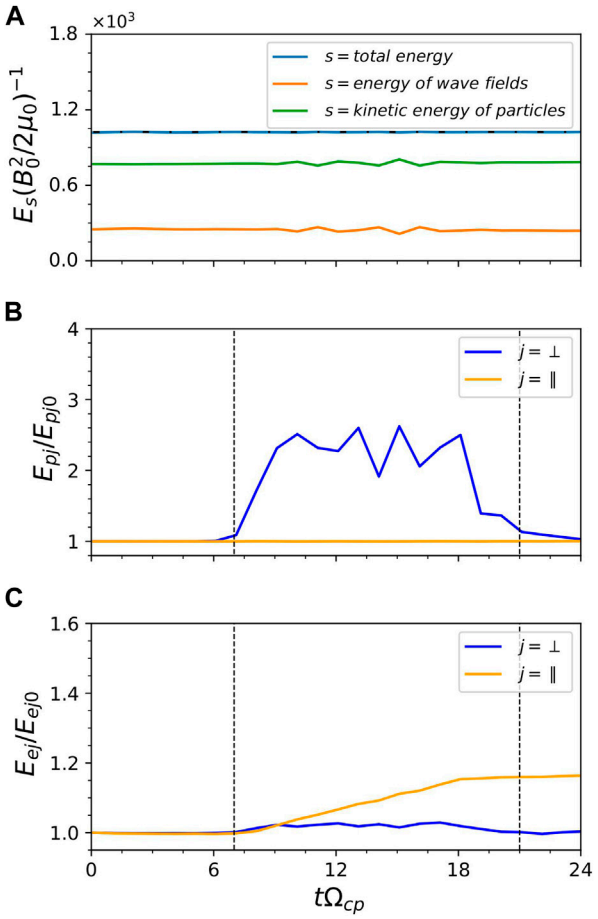

FIGURE 7
(A) The time evolution of the energy of the electromagnetic fields (green line), the kinetic energy of the particles (orange line), and their sum (blue line), respectively. The horizontal black dash-dotted line denotes the initial value of the total energy. The time evolution of kinetic energy of **(B)** protons and **(C)** electrons. Blue lines and orange lines denote the perpendicular direction and parallel direction, respectively. E_{pj0} denotes the kinetic energy of species j at $t\Omega_{cp} = 0$. The black dashed lines in **(B, C)** denote the time of wave arrival and departure of the density structure.

A_M is comparable to or even larger than the reflectivity R_M in most cases, suggesting the absorption of waves should not be neglected when modeling the propagation of MS wave through the density structure.

3.2 Quasi-perpendicular waves: $\theta = 85°$

Besides the strictly perpendicular waves, we have also studied the propagation of MS waves with $\theta = 85°$ through the density structure due to the different interactions with charged particles [24]. Figure 6 shows the spatial-temporal evolution of wave fields for Run 3. Similar to Run1, the reflected wave immediately shows up when the MS wave encounters the left boundary of the density structure at $t \approx 7\Omega_{cp}^{-1}$, and the transmitted waves become weaker after the MS wave leaves the density structure.

Figure 7A displays the time history of the wave energy and particle kinetic energy for Run 3. The total energy (blue line) is well conserved in this simulation model, and the energy exchange between MS wave and plasma can be easily found. Figures 7B, C present the time evolution of the kinetic energies of protons and electrons inside the density structure, respectively. The perpendicular kinetic energy of protons and electrons inside the structure first increases as the wave enters the density structure and then decreases after the wave leaves, with a weak net increase. However, the parallel kinetic energy of electrons gradually increases when the wave passes through the structure and then remains nearly constant after the wave leaves. This is due to the efficient parallel heating of electrons by quasi-parallel MS waves (Supplementary Figure S2).

We further investigate the effects of the shape of density structure on the reflection and absorption of the MS wave with $\theta = 85°$. The calculation method of R_M, A_M, and T_M is the same as above. The simulation results marked by red dots and solid lines are summarized in Figure 8. Similar to the perpendicular MS wave, the R_M and A_M increase with the increasing H, resulting in the decreasing T_M. Then, the A_M and the R_M have a positive correlation and an anti-correlation with the ΔL, respectively, leading to a maximum of T_M at a certain ΔL. Although the trends of A_M, R_M, and T_M with the H and ΔL are very similar to the perpendicular cases, the reflectivity R_M and the

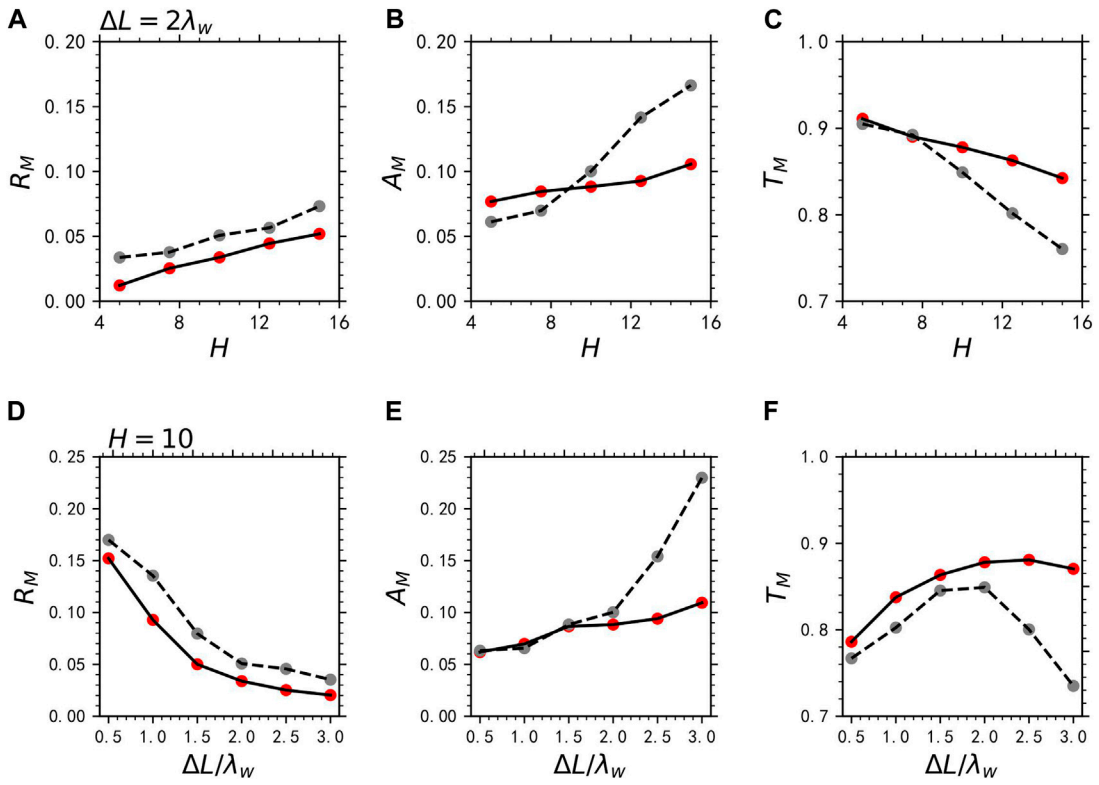

FIGURE 8
The **(A)** reflectivity R_M, **(B)** absorptivity A_M, and **(C)** transmissivity T_M as a function of various heights with a constant width $\Delta L = 2\lambda_w$, and **(D)** the reflectivity R_M, **(E)** absorptivity A_M, and **(F)** transmissivity T_M as a function of various widths with a constant height $H = 10$. Red dots are the simulation runs with different parameters when the pump wave propagates quasi-perpendicularly. The gray dots and black dashed lines denote the result of Figure 5.

absorptivity A_M of the quasi-perpendicular MS waves are smaller than those of the MS waves with $\theta = 90°$, which may imply that the quasi-perpendicular MS waves can propagate further than those perpendicular waves in the magnetosphere.

4 Conclusion and discussion

The effects of density structures on MS waves are important to understand the distribution and propagation of MS waves in the Earth's magnetosphere, which are attracting more and more attention. However, previous simulations and theoretical models [30,36] only include the reflection of MS waves caused by the density structure. To include both the absorption and reflection of waves, we utilize a self-consistent model, i.e., PIC model, to study the propagation of MS waves across density structures. We find that both perpendicular and quasi-perpendicular propagating MS waves can be effectively reflected and absorbed by the fine-scale density structure. Generally, the absorption of MS waves is as important as the reflection when MS waves propagate through the density structure, and they are strongly dependent on the shape of the density structure. The reflection of MS waves is positively correlated with the height but is inversely related to the width of a density structure. While the absorption of MS waves is positively correlated with the height and width of a density structure. Our simulation results reveal that the absorption also plays an important role in the propagation of MS waves in the Earth's magnetosphere, which can help better understand the properties and distribution of MS waves.

To obtain the reliable reflectivity, absorptivity, and transmissivity of the MS waves, we must ensure that the total energy of this system is conserved. As shown in Figures 3A, 7A, it is clear shown that the total energy is well conserved within a margin of error below 0.1%, which is much lower than the energy change (>5%) of charged particles or wave fields. This is true for all simulation runs in this study. Thus, the dependences of reflectivity and absorptivity of MS waves on the shape of density structure as shown in Figures 5, 8 are quite reliable. Since the reflectivity of MS wave is strongly dependent on the density gradient, so the R_M will increase with the increase of the height or the decrease of width, i.e., steep density structure. While, the absorptivity should be positively correlated with the number of particles inside the density structure, so the A_M increases with the increase of the height or width, i.e., large density structure. However, because the corresponding transmissivity T_M relies on the sum of R_M and A_M, the dependence of T_M on the shape of density structure is somehow unpredictable.

Data availability statement

The original contributions presented in the study are included in the article/supplementary materials, further inquiries can be directed to the corresponding author/s. Figure data are available at https://cstr.cn/14804.41.sciencedb.space.00813.00D00D7D.

Author contributions

TS: Writing–original draft. XG: Writing–review and editing. YK: Writing–review and editing. QL: Writing–original draft, Writing–review and editing, Supervision. XW: Writing–original draft, Writing–review and editing, Validation.

Funding

The author(s) declare that no financial support was received for the research, authorship, and/or publication of this article. This work was supported by the NSFC grant 41774151, 42104155, B-type Strategic Priority Program of the Chinese Academy of Sciences, Grant No. XDB41000000.

Conflict of interest

The authors declare that the research was conducted in the absence of any commercial or financial relationships that could be construed as a potential conflict of interest.

Publisher's note

Supplementary material

The Supplementary Material for this article can be found online at: https://www.frontiersin.org/articles/10.3389/fphy.2024.1254024/full#supplementary-material

References

1. Santolík O, Němec F, Gereová K, Macúšová E, de Conchy Y, Cornilleau-Wehrlin N. Systematic analysis of equatorial noise below the lower hybrid frequency. *Ann Geophys* (2004) 22:2587–95. doi:10.5194/angeo-22-2587-2004

2. Russell C, Holzer R, Smith E. OGO 3 observations of ELF noise in the magnetosphere: 1. Spatial extent and frequency of occurrence. *J Geophys Res* (1969) 74:755–77. doi:10.1029/JA074i003p00755

3. Russell CT, Holzer RE, Smith EJ. OGO 3 observations of ELF noise in the magnetosphere 2. The nature of the equatorial noise. *J Geophys Res* (1970) 75:755–68. doi:10.1029/JA075i004p00755

4. Gurnett DA. Plasma wave interactions with energetic ions near the magnetic equator. *J Geophys Res* (1976) 81:2765–70. doi:10.1029/JA081i016p02765

5. Xiao F, Zhou Q, He Y, Yang C, Liu S, Baker DN, et al. Penetration of magnetosonic waves into the plasmasphere observed by the Van Allen Probes. *Geophys Res Lett* (2015) 42:7287–94. doi:10.1002/2015GL065745

6. Ma Q, Li W, Thorne RM, Angelopoulos V. Global distribution of equatorial magnetosonic waves observed by THEMIS. *Geophys Res Lett* (2013) 40:1895–901. doi:10.1002/grl.50434

7. Boardsen SA, Hospodarsky GB, Min K, Averkamp TF, Bounds SR, Kletzing CA, et al. Determining the wave vector direction of equatorial fast magnetosonic waves. *Geophys Res Lett* (2018) 45(16):7951–9. doi:10.1029/2018GL078695

8. Kasahara Y, Kenmochi H, Kimura I. Propagation characteristics of the ELF emissions observed by the satellite Akebono in the magnetic equatorial region. *Radio Sci* (1994) 29(4):751–67. doi:10.1029/94RS00445

9. Ke Y, Chen L, Gao X, Lu Q, Wang X, Chen R, et al. Whistler-mode waves trapped by density irregularities in the earth's magnetosphere. *Geophys Res Lett* (2021) 48:e2020GL092305. doi:10.1029/2020GL092305

10. Meredith N, Horne R, Anderson R. Survey of magnetosonic waves and proton ring distributions in the Earth's inner magnetosphere. *J Geophys Res* (2008) 113:A06213. doi:10.1029/2007JA012975

11. Min K, Němec F, Liu K, Denton RE, Boardsen SA. Equatorial propagation of the magnetosonic mode across the plasmapause: 2-D PIC simulations. *J Geophys Res Space Phys* (2019) 124:4424–44. doi:10.1029/2019JA026567

12. Bortnik J, Thorne RM. Transit time scattering of energetic electrons due to equatorially confined magnetosonic waves. *J Geophys Res* (2010) 115:A07213. doi:10.1029/2010JA015283

13. Bortnik J, Thorne RM, Ni B, Li J. Analytical approximation of transit time scattering due to magnetosonic waves. *Geophys Res Lett* (2015) 42:1318–25. doi:10.1002/2014GL062710

14. Horne RB, Thorne RM, Glauert SA, Meredith NP, Pokhotelov D, Santolık O. Electron acceleration in the Van Allen radiation belts by fast magnetosonic waves. *Geophys Res Lett* (2007) 34(17):L17107. doi:10.1029/2007GL030267

15. Horne RB, Wheeler GV, Alleyne HSCK. Proton and electron heating by radially propagating fast magnetosonic waves. *J Geophys Res* (2000) 105(27):27597–610. doi:10.1029/2000JA000018

16. Li X, Tao X. Validation and analysis of bounce resonance diffusion coefficients. *J Geophys Res Space Phys* (2018) 123:104–13. doi:10.1002/2017JA024506

17. Chen L, Sun J, Lu Q, Wang X, Gao X, Wang D, et al. Two-dimensional particle-in-cell simulation of magnetosonic wave excitation in a dipole magnetic field. *Geophys Res Lett* (2018) 45:8712–20. doi:10.1029/2018GL079067

18. Li J, Bortnik J, Thorne RM, Li W, Ma Q, Baker DN, et al. Ultrarelativistic electron butterfly distributions created by parallel acceleration due to magnetosonic waves. *J Geophys Res Space Phys* (2016) 121:3212–22. doi:10.1002/2016JA022370

19. Xiao FL, Yang C, Su ZP, Zhou QH, He ZG, He YH, et al. Wave-driven butterfly distribution of Van Allen belt relativistic electrons. *Nat Commun* (2015) 6(1):8590. doi:10.1038/ncomms9590

20. Ni BB, Zou ZY, Fu S, Cao X, Gu XD, Xiang Z. Resonant scattering of radiation belt electrons by off-equatorial magnetosonic waves. *Geophys Res Lett* (2018) 45(3):1228–36. doi:10.1002/2017GL075788

21. Yang C, Su Z, Xiao F, Zheng H, Wang Y, Wang S, et al. A positive correlation between energetic electron butterfly distributions and magnetosonic waves in the radiation belt slot region. *Geophys Res Lett* (2017) 44:3980–90. doi:10.1002/2017GL073116

22. Ma QL, Li W, Thorne RM, Bortnik J, Kletzing CA, Kurth WS, et al. Electron scattering by magnetosonic waves in the inner magnetosphere. *J Geophys Res Space Phys* (2016) 121(1):274–85. doi:10.1002/2015JA021992

23. Sun J, Gao X, Lu Q, Chen L, Liu X, Wang X, et al. Spectral properties and associated plasma energization by magnetosonic waves in the Earth's magnetosphere: particle-in-cell simulations. *J Geophys Res Space Phys* (2017) 122:5377–90. doi:10.1002/2017JA024027

24. Yuan Z, Yu X, Huang S, Qiao Z, Yao F, Funsten HO. Cold ion heating by magnetosonic waves in a density cavity of the plasmasphere. *J Geophys Res Space Phys* (2018) 123:1242–50. doi:10.1002/2017JA024919

25. Zhou Q, Jiang Z, Yang C, He Y, Liu S, Xiao F. Correlated observation on global distributions of magnetosonic waves and proton rings in the radiation belts. *J Geophys Res Space Phys* (2021) 126:e2020JA028354. doi:10.1029/2020JA028354

26. Chen L, Thorne RM. Perpendicular propagation of magnetosonic waves. *Geophys Res Lett* (2012) 39:L14102. doi:10.1029/2012GL052485

27. Xiao F, Zhou Q, He Z, Tang L. Three-dimensional ray tracing of fast magnetosonic waves. *J Geophys Res* (2012) 117:A06208. doi:10.1029/2012JA017589

28. Santolík O, Parrot M, Němec F. Propagation of equatorial noise to low altitudes: decoupling from the magnetosonic mode. *Geophys Res Lett* (2016) 43:6694–704. doi:10.1002/2016GL069582

29. Liu X, Chen L, Yang L, Xia Z, Malaspina DM. One-dimensional full wave simulation of equatorial magnetosonic wave propagation in an inhomogeneous magnetosphere. *J Geophys Res Space Phys* (2018) 123:587–99. doi:10.1002/2017JA024336

30. Mauk BH, Fox NJ, Kanekal SG, Kessel RL, Sibeck DG, Ukhorskiy A. Science objectives and rationale for the radiation belt storm probes mission. *Space Sci Rev* (2013) 179(1):3–27. doi:10.1007/s11214-012-9908-y

31. Ma Q, Li W, Chen L, Thorne RM, Angelopoulos V. Magnetosonic wave excitation by ion ring distributions in the Earth's inner magnetosphere. *J Geophys Res Space Phys* (2014) 119:844–52. doi:10.1002/2013JA019591

32. Boardsen SA, Hospodarsky GB, Kletzing CA, Pfaffff RF, Kurth WS, Wygant JR, et al. Van Allen Probe observations of periodic rising frequencies of the fast magnetosonic mode. *Geophys Res Lett* (2014) 41:8161–8. doi:10.1002/2014GL062020

33. Sun J, Lu Q, Wang X, Liu X, Gao X, Yang H. Modulation of magnetosonic waves by background plasma density in a dipole magnetic field: 2-D PIC simulation. *J Geophys Res Space Phys* (2021) 126:e2021JA029729. doi:10.1029/2021JA029729

34. Stix. *Waves in plasmas*. College Park, MD: American Institute of Physics (1992).

35. Streltsov AV, Goyal R. Whistlers in micro ducts. *J Geophys Research:SpacePhysics* (2021) 126:e2021JA029868. doi:10.1029/2021JA029868

36. Yu X, Yuan Z, Ouyang Z, Yao F. Effects of the plasmapause on the radial propagation of fast magnetosonic waves: an analytical approach. *J Geophys Res Space Phys* (2021) 126:e2020JA028330. doi:10.1029/2020JA028330

Frontiers in
Astronomy and Space Sciences

Explores planetary science and extragalactic astronomy in all wavelengths

Advances the understanding of our universe - from planetary science to extragalactic astronomy, to high-energy and astroparticle physics.

Discover the latest Research Topics

See more →

Frontiers

Avenue du Tribunal-Fédéral 34
1005 Lausanne, Switzerland
frontiersin.org

Contact us

+41 (0)21 510 17 00
frontiersin.org/about/contact